Transactions of the ASME, Journal of Heat Transfer (ISSN 0022-1481) is published monthly by The American Society of Mechanical Engineers, Three Park Avenue, New York, NY 10016. Periodicals postage paid at New York, NY and additional mailing offices. POSTMASTER: Send address changes to Transactions of the ASME, Journal of Heat Transfer, c/o THE AMERICAN SOCIETY OF MECHANICAL ENGINEERS, 22 Law Drive, Box 2300, Fairfield, NJ 07007-2300. **CHANGES OF ADDRESS** must be received at Society headquarters seven weeks before they are to be effective. Please send old label and new address. **STATEMENT from By-Laws.** The Society shall not be responsible for statements or opinions advanced in papers or ... printed in its publications (B7.1, Para. 3).

Journal of Heat Transfer

Published Monthly by ASME

VOLUME 132 • NUMBER 12 • DECEMBER 2010

RESEARCH PAPERS

(**Contents continued on inside back cover**)

This journal is printed on acid-free paper, which exceeds the ANSI Z39.48-1992 specification for permanence of paper and library materials. ♾™
♻ 85% recycled content, including 10% post-consumer fibers.

Journal of Heat Transfer Volume 132, Number 12 DECEMBER 2010

The ASME Journal of Heat Transfer is abstracted and indexed in the following:

Applied Science and Technology Index, Chemical Abstracts, Chemical Engineering and Biotechnology Abstracts (Electronic equivalent of Process and Chemical Engineering), Civil Engineering Abstracts, Compendex (The electronic equivalent of Engineering Index), Corrosion Abstracts, Current Contents, E & P Health, Safety, and Environment, Ei EncompassLit, Engineered Materials Abstracts, Engineering Index, Enviroline (The electronic equivalent of Environment Abstracts), Environment Abstracts, Environmental Engineering Abstracts, Environmental Science and Pollution Management, Fluidex, Fuel and Energy Abstracts, Index to Scientific Reviews, INSPEC, International Building Services Abstracts, Mechanical & Transportation Engineering Abstracts, Mechanical Engineering Abstracts, METADEX (The electronic equivalent of Metals Abstracts and Alloys Index), Petroleum Abstracts, Process and Chemical Engineering, Referativnyi Zhurnal, Science Citation Index, SciSearch (The electronic equivalent of Science Citation Index), Theoretical Chemical Engineering

Hosein Molavi
Researcher
Department of Mechanical Engineering,
Tarbiat Modares University,
Tehran, 14115-143, Iran
e-mail: hn.molavi@gmail.com

Ali Hakkaki-Fard
Department of Mechanical Engineering,
McGill University Montreal,
QC H3A 2T5, Canada
e-mail: ali.hakkaki-fard@mail.mcgill.ca

Ramin K. Rahmani
Affiliate Research Scholar
e-mail: rkhrahmani@yahoo.com

Anahita Ayasoufi
Affiliate Research Scholar
e-mail: aayasoufi@yahoo.com

Department of Mechanical, Industrial, and
Manufacturing Engineering,
University of Toledo,
Toledo, OH 43606

Mehdi Molavi
Department of Mechanical Engineering,
Azad University of Tehran,
Tehran, Tehran 1777613651, Iran

A Novel Methodology for Combined Parameter and Function Estimation Problems

This article presents a novel methodology, which is highly efficient and simple to implement, for simultaneous retrieval of a complete set of thermal coefficients in combined parameter and function estimation problems. Moreover, the effect of correlated unknown variables on convergence performance is examined. The present methodology is a combination of two different classical methods: The conjugate gradient method with adjoint problem (CGMAP) and Box–Kanemasu method (BKM). The methodology uses the benefit of CGMAP in handling function estimation problems and BKM for parameter estimation problems. One of the unique features about the present method is that the correlation among the separate unknowns does not disrupt the convergence of the problem. Numerical experiments using measurement errors are performed to verify the efficiency of the proposed method in solving the combined parameter and function estimation problems. The results obtained by the present approach show that the combined procedure can efficiently and reliably estimate the values of the unknown thermal coefficients.
[DOI: 10.1115/1.4002283]

Keywords: Box–Kanemasu method, conjugate gradient method, function estimation, parameter estimation

1 Introduction

The object of an inverse heat conduction problem (IHCP) is the estimation of unknown functions or parameters (e.g., heat flux or thermophysical properties) appearing in the mathematical model, given the measured temperature histories of a heat-conducting space along with a computational "estimator" algorithm. This happens when the direct measurement of boundary conditions or of the thermophysical properties of a system is unfeasible. The IHCP is considered to be a "difficult" problem [1] as the unavoidable noise imbedded in the data can produce large or even unbounded deviations in the solution. This is due to "ill-posed" nature of the IHCP [1]. In general, solution of the IHCP involves minimization of a sum of squared error function, which is defined based on the difference between the calculated and the measured temperatures [2]. The thermal coefficients (i.e., thermophysical properties, boundary or initial conditions) that minimize the aforementioned error function are the solutions of the IHCP. An excellent review of literature and comprehensive bibliography on the topic may be found in the textbooks of Beck et al. [1], Alifanov [3], and Beck and Arnold [4].

IHCPs are usually categorized as parameter and function estimation problems. The parameter estimation problems show the identification of a relatively small number of unknowns; the parameters are often coefficients in the governing equations. Examples of these parameters are thermal conductivity, thermal emittance, convection coefficient, specific heat, density, and even the parameters that appear in the studies of turbulent flows. Many researchers have employed different inverse methods to determine unknown parameters [5–10]. On the other hand, a function estimation problem determines functions represented by numerous unknowns, which may vary spatially and/or temporally. Function estimation problems have been the subject of extensive investigations, thanks to their numerous and various applications [2,11–17]. The function estimation and parameter estimation problems have similar attributes and are closely related. It is worth mentioning that an IHCP may be a combined parameter and function estimation problem. An illustration can be found in the simultaneous prediction of heat flux and specific heat of a heat-conducting body, which is exposed to an unknown heat flux. Assessment of thermophysical properties utilizing experimental techniques not only demands the knowledge of recorded temperature history during the test but also the transient heat flux profile should be valid. Most of studies have considered uncertainty in temperature measurements as the only mode of noise in experiment. However, experiments have shown that achievement of the ideal profile of heat flux is very difficult or even impossible. Under this situation, recognizing actual boundary conditions can provide valuable insight to the methods, particularly since actual experimental data is used. Dowding et al. [18] estimated the thermal properties of carbon-carbon composite using simultaneously temperature measurements as well as measurement of the time-varying heat flux. Subsequently, they solved another inverse problem for predicting the profile of heat flux. Comparison between the values of the measured heat fluxes and those obtained by their algorithm verified the consistency of their method. A different heat flux causes an impact of the temperature response, which in turn alters the estimated unknowns. Recent parameter estimation works by the current authors [8,9] revealed that the net surface heat flux at the boundary is what drives the problem. As reported, this function depends on the thermal properties and wall tempera-

Contributed by the Heat Transfer Division of ASME for publication in the JOURNAL OF HEAT TRANSFER. Manuscript received March 4, 2009; final manuscript received July 22, 2010; published online September 17, 2010. Assoc. Editor: Patrick H. Oosthuizen.

ture and recovers as part of the formulation. All noted works indicate the feasibility and the importance of application of the combined parameter and function estimation problems. These problems are highly subjected to correlation between separate unknowns as well as the high condition number of the sensitivity matrix, which cause the divergence of the common known IHCP methods. Paradoxically, the bibliography on combined parameter and function estimation in the fundamental equation of the heat transfers is very limited; Loulou and Artioukhine [19] discussed the application of numerical algorithms based on gradient-type methods for recovering unknown variables. As the descent variable in gradient-type methods is chosen to be the same for the independent unknowns, the very slow or no convergence at all of the gradient-type methods can be observed. To overcome this difficulty, Loulou and Artioukhine [19] presented a discussion of the implementation of the iterative algorithms for solving the general problem of recovering a complete set of thermal coefficients, introduced a vectorial descent variable, and reported a considerable increase in the convergence rate. Based on the aforementioned method, Loulou and Scott [20] estimated simultaneously time dependent blood perfusion and thermal contact conductance between the probe and the tissue. Later, Loulou [21] validated this method against a benchmark experiment of Beck and Arnold [4].

The purpose of this research is to develop an efficient and uncomplicated method to implement for simultaneously predicting the unknown parameters and functions in an IHCP. The method is quite different from the previous method of Loulou and Artioukhine [19], which was developed to solve the combined problems based on the modified conjugate gradient method (MCGM). Although their approach appeared to be effective for improving the computational efficiency of iterative algorithms for simultaneous estimation of the one parameter and one function problems, its applicability for more than two separate unknowns (e.g., one function and two parameters) as well as versatility for different unknowns has never been examined (to the best of the authors' knowledge). To accomplish this, the authors have developed the same strategy of Ref. [19] and found the convergence of the method to the correct values of the unknowns is strongly contingent upon the initial guess. As reported in Ref. [20], when the unknown parameter is thermal contact conductance in combined problem, the results are greatly affected by the initial guess of this parameter. Without sufficient preliminary knowledge of this parameter, achieving a converged estimation is very complicated. On the other hand, with the author's experience about this methodology, when the unknown parameter is thermal contact resistance, the method does not converge at all. Furthermore, for estimating more than two unknowns, this method needs perfect initial guess to be able to reach the correct answer. Despite starting with the suitable initial guess and applying exact data (noise-free data), there is no guarantee that the method converges to accurate results. To overcome the limitation in the previous work, a framework is developed to take advantage of the classical methods in combined parameter and function estimation problems. On the basis of the proposed approach, the determination of the unknown thermal coefficients includes two steps per iteration of the estimation algorithm, namely, the function estimation step and the parameter estimation step. A flowchart showing the sequence of calculations in the algorithm is given in Fig. 1. After initial setting of the unknown parameters and function, the solver repeatedly cycles through the following steps. (1) In the function estimation process, by using initial guess values for the unknown thermophysical properties, the IHCP becomes a function estimation problem. Estimated function (heat flux) by using conjugate gradient method with adjoint problem (CGMAP) is then used for parameter estimation procedure. (2) In this procedure, the parameters will denote as the unknown variables and will recover using Box–Kanemasu method (BKM) based on the knowledge of function estimated at the previous step. It should be noted that this procedure repeats for each unknown parameter. (3) Then, an intermediate set of the thermal coefficient values is substituted for the unknown parameters and function in the following analysis. Several iterations are needed before obtaining the undetermined thermal coefficients. The method outlined here is computationally simple and does not encounter difficulties with the correlation problem as a limiting factor for the converged application of common gradient-based estimation procedures, as different unknowns are estimated by different procedures. One of the main advantages of the present method to the previous work available in literature is its capability of overcoming the existing restrictions in the determination of the appropriate initial guess. Moreover, in some occasions, when the MCGM shows instabilities resulting in nonconvergence while implemented in special case, the current methodology generates precise results. To summarize, the presented method simultaneously predicts the unknown parameters and functions in an IHCP with wide range values on the initial guess for reaching the correct answer. The method produces results with excellent agreement with the exact solutions when exact measurements are available. Also, it produces high accuracy results when error exists in the data while the existing methods may not even converge to any solution at all with or without errors in simulated data. In other words, the convergence is now possible with the present methodology where it was not possible using the other methods.

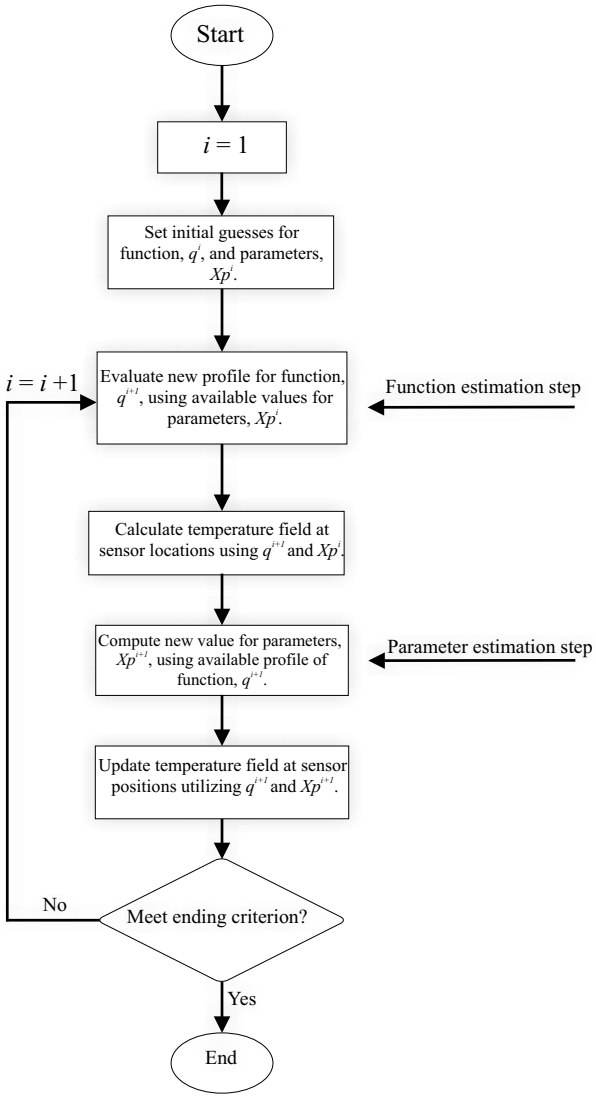

Fig. 1 A flowchart of the combined parameter and function estimation strategy

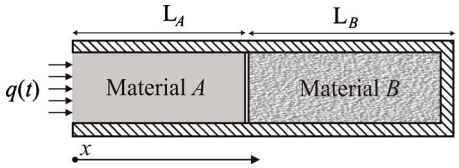

Fig. 2 Problem geometry

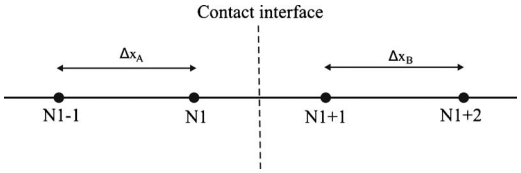

Fig. 3 Schematic of grid spacing at contact interface

2 Analysis

2.1 Direct Problem. In order to show the versatility, usability, and appropriateness of the proposed method in handling different unknown variables, a suitable heat conduction problem is considered. Two solid materials are placed together (with a nonperfect contact surface condition) enabling heat to flow from one material to the other. All the nonshared boundaries of the two materials but one are insulated to ensure heat only flows in the x-direction (Fig. 2). A time dependent heat flux is applied to the remaining boundary (the left edge of material *A* in Fig. 2). The mathematical formulation for this transient heat conduction problem is written as

$$\rho_A Cp_A \frac{\partial T_A}{\partial t} = k_A \frac{\partial^2 T_A}{\partial x^2} \quad 0 \le x \le L_A \tag{1}$$

$$\rho_B Cp_B \frac{\partial T_B}{\partial t} = k_B \frac{\partial^2 T_B}{\partial x^2} \quad L_A \le x \le L_B \tag{2}$$

$$-k_A \frac{\partial T_A}{\partial x} = q(t) \quad x = 0 \tag{3}$$

$$-k_A \frac{\partial T_A}{\partial x} = -k_B \frac{\partial T_B}{\partial x} = \frac{(T_A - T_B)}{R} \quad x = L_A \tag{4}$$

$$\frac{\partial T_B}{\partial x} = 0 \quad x = L_A + L_B \tag{5}$$

$$T_A(x,0) = T_B(x,0) = T_0 \quad t = 0 \tag{6}$$

where T is the temperature, L, ρ, Cp, and k are the length, density, specific heat, and thermal conductivity of the specimens, respectively, T_0 is the initial temperature, $q(t)$ is the time dependent heat flux, and R is the thermal contact resistance. Subscripts A and B represent the materials A and B, respectively.

The finite difference method, implicit in time, is used to solve Eqs. (1)–(6). To avoid temperature oscillations at the contact surface, the Fourier number is set the same for the two parts, as follows:

$$\mathrm{Fo} = \frac{\alpha_A \Delta t}{\Delta x_A^2} = \frac{\alpha_B \Delta t}{\Delta x_B^2} \tag{7}$$

In IHCP, the numerical time step size is usually equal to the measurement interval; spatial domain is discretized in such a way that satisfies Eq. (7). Then, internal energy balance equation for each material can be discretized as

$$\rho_{\mathrm{mat}} Cp_{\mathrm{mat}} \frac{T_i^{n+1} - T_i^n}{\Delta t} = k_{\mathrm{mat}} \frac{T_{i-1}^{n+1} - 2T_i^{n+1} + T_{i+1}^{n+1}}{\Delta x_{\mathrm{mat}}^2} \tag{8}$$

where superscript n denotes the time level and subscript *mat* specifies the material A or B. By referring to Fig. 3, boundary conditions at contact interface are discretized as follows:

$$-k_A \frac{T_{N1}^{n+1} - T_{N1-1}^{n+1}}{\Delta x_A} = \frac{T_{N1}^{n+1} - T_{N1+1}^{n+1}}{R} \tag{9}$$

$$-k_B \frac{T_{N1+2}^{n+1} - T_{N1+1}^{n+1}}{\Delta x_B} = \frac{T_{N1}^{n+1} - T_{N1+1}^{n+1}}{R} \tag{10}$$

where $N1$ denotes the last node in material A. Rearrangement and applying boundary conditions allow the preceding discretization equations to be as follows:

$$a_i T_{i-1} + b_i T_i + c_i T_{i+1} = d_i \quad for \;\; i = 1,2,\ldots,K \tag{11}$$

where K denotes the number of nodes. Equation (11) can be extended into a tridiagonal matrix system and solved by the tridiagonal matrix algorithm [22].

2.2 Inverse Problem. For the inverse problem considered in this study, the heat flux and one of the parameters in Eqs. (1)–(6) (i.e., thermal conductivities, specific heats, or thermal contact resistance) are regarded as being unknown and to be estimated from measured temperatures by sensors. These unknown variables are gathered in a single unknown vector $\boldsymbol{P}=[q(t), X_P]$. The solution of present inverse problem is to be sought in such a way that the following functional is minimized:

$$S(\boldsymbol{P}) = \sum_{j=1}^{N} \int_{t=0}^{t_f} [Y_j(t) - T(x_j,t;\boldsymbol{P})]^2 dt \tag{12}$$

where $Y_j(t)$ are the measured temperatures and $T(x_j,t)$ are the estimated temperatures at the measurement locations obtained by the proposed method. N is the number of the mounted sensors. As the problem is simultaneously of parameter and function estimation type, one difficulty is that the unknown thermal coefficients are correlated. A strong correlation among quantities means that they cannot be independently determined by the data set, which leads to an ill-conditioned system of equations. In this situation, the common gradient-based IHCP methods do not tend to converge. To overcome this difficulty, a combined procedure can be employed to circumvent difficulties of nonconvergence in cases when the thermal coefficients are correlated or nearly so. This procedure is based on two different methods, namely, CGMAP for the function estimation stage (i.e., heat flux) and BKM for the parameter estimation stage. The results obtained by the present method are compared with the ones of the MCGM [19]. In addition, the methodology for investigation of the correlation among the diverse thermal coefficients is presented.

2.3 Function Estimation Process. In the function estimation stage, initial values are assumed for the unknown parameters (i.e., the initial guess values, which are improved during the iterative process) and then the unknown function (i.e., heat flux) can be estimated by using temperature measurements taken within the slab.[1] The components of heat flux function are determined via minimization of the following functional:

$$J[q(t)] = \sum_{j=1}^{N} \int_{t=0}^{t_f} \{Y_j(t) - T[x_j,t;q(t)]\}^2 dt \tag{13}$$

[1]Three test cases are studied in this paper. The thermal contact resistance is the unknown in the first one and values of thermal conductivity for two different materials are the unknowns in the second case. In the third one, the specific heat values for two different materials are the unknowns.

To accomplish this, we consider the iterative procedure of the conjugate gradient method given in Refs. [3,23].

$$q^{i+1}(t) = q^i(t) - \beta^i d^i(t) \tag{14}$$

where i is the iteration number, β^i is the search step size, and $d^i(t)$ is the direction of descent given by

$$d^i(t) = -\nabla J[q^i(t)] + \gamma^i d^{i-1}(t) \tag{15}$$

The conjugation coefficient γ^i can be computed from different expressions available in literature. In this work, we use the expression of Flecther–Reeves, which is given in Refs. [3,23].

$$\gamma^i = \frac{\int_{t=0}^{t_f} \{\nabla J[q^i(t)]\}^2 dt}{\int_{t=0}^{t_f} \{\nabla J[q^{i-1}(t)]\}^2 dt} \quad \text{for } i = 1,2,\ldots \quad \text{with } \gamma^0 = 0 \quad \text{for } i = 0 \tag{16}$$

The search step size β^i is chosen as the one that minimizes the function $J[q(t)]$ at each iteration i. By using a first-order Taylor series approximation and performing the minimization, the following expression results for the search step size:

$$\beta^i = \frac{\sum_{j=1}^{N} \int_{t=0}^{t_f} \{T[x_j,t] - Y_j(t)\} \Delta T[x_j,t:d^i(t)] dt}{\sum_{j=1}^{N} \int_{t=0}^{t_f} \{\Delta T[x_j,t:d^i(t)]\}^2 dt} \tag{17}$$

For the implementation of the iterative procedure described here the sensitivity term $\Delta T\,[x_j,t:d^i(t)]$ and gradient $\nabla J[q^i(t)]$ are required. The former is determined by employing the sensitivity problem and the latter by employing the adjoint problem. Both problems are briefly described next.

2.3.1 The Sensitivity Problem. The sensitivity problem is used to determine the variation of the dependent variables due to changes in the unknown quantity. Therefore, the sensitivity problem can be obtained by assuming that the temperature $T(x,t)$ is perturbed by an arbitrary amount $\Delta T(x,t)$ when the unknown heat flux $q(t)$ is perturbed by $\Delta q(t)$ in the specific search direction. Thus, the following problem for the sensitivity function $\Delta T(x,t)$ can be obtained:

$$\rho_A Cp_A \frac{\partial \Delta T_A}{\partial t} = k_A \frac{\partial^2 \Delta T_A}{\partial x^2} \quad 0 \le x \le L_A \tag{18}$$

$$\rho_B Cp_B \frac{\partial \Delta T_B}{\partial t} = k_B \frac{\partial^2 \Delta T_B}{\partial x^2} \quad L_A \le x \le L_B \tag{19}$$

$$-k_A \frac{\partial \Delta T_A}{\partial x} = \Delta q(t) \quad x = 0 \tag{20}$$

$$-k_A \frac{\partial \Delta T_A}{\partial x} = -k_B \frac{\partial \Delta T_B}{\partial x} = \frac{(\Delta T_A - \Delta T_B)}{R} \quad x = L_A \tag{21}$$

$$\frac{\partial \Delta T_B}{\partial x} = 0 \quad x = L_A + L_B \tag{22}$$

$$\Delta T_A(x,0) = \Delta T_B(x,0) = 0 \quad t = 0 \tag{23}$$

2.3.2 The Adjoint Problem. In order to derive the adjoint problem for heat flux, Eqs. (1) and (2) are multiplied by the Lagrange multiplier functions $\lambda_A(x,t)$ and $\lambda_B(x,t)$, and the resulting expressions are integrated over the time and the space domain. Then, the results are added to the right hand side of Eq. (13), which leads to the following expression for the functional $J[q(t)]$

$$J[q(t)] = \sum_{j=1}^{N} \int_{t=0}^{t_f} \{Y_j(t) - T[x_j,t:q(t)]\}^2 dt + \int_{t=0}^{t_f} \int_{x=0}^{L_A} \lambda_A(x,t) \times \left(k_A \frac{\partial^2 T_A}{\partial x^2} - \rho_A Cp_A \frac{\partial T_A}{\partial t} \right) dx dt + \int_{t=0}^{t_f} \int_{x=L_A}^{L_A+L_B} \lambda_B(x,t) \times \left(k_B \frac{\partial^2 T_B}{\partial x^2} - \rho_B Cp_B \frac{\partial T_B}{\partial t} \right) dx dt \tag{24}$$

The variation ΔJ is obtained by perturbing q by Δq and T by ΔT in Eq. (24), subtracting from the resulting expression the original Eq. (24) and neglecting the second-order terms. We, thus, find

$$\Delta J[q(t)] = 2\sum_{j=1}^{N} \int_{t=0}^{t_f} \{Y_j(t) - T[x_j,t:q(t)]\} \Delta T dt + \int_{t=0}^{t_f} \int_{x=0}^{L_A} \lambda_A(x,t) \times \left(k_A \frac{\partial^2 \Delta T_A}{\partial x^2} - \rho_A Cp_A \frac{\partial \Delta T_A}{\partial t} \right) dx dt + \int_{t=0}^{t_f} \int_{x=L_A}^{L_A+L_B} \lambda_B(x,t) \times \left(k_B \frac{\partial^2 \Delta T_B}{\partial x^2} - \rho_B Cp_B \frac{\partial \Delta T_B}{\partial t} \right) dx dt \tag{25}$$

Using integration by parts, as well as the boundary and initial conditions, the derivatives are transferred to the Lagrange multiplier function. After some algebraic manipulations, the following adjoint differential equations are obtained for the Lagrange multiplier functions $\lambda_A(x,t)$ and $\lambda_B(x,t)$

$$\rho_A Cp_A \frac{\partial \lambda_A}{\partial t} + k_A \frac{\partial^2 \lambda_A}{\partial x^2} + 2\sum_{j=1}^{N} [T(x_j,t) - Y_j(t)] \delta(x - x_j) = 0 \quad \text{for } 0 \le x \le L_A \tag{26}$$

$$\rho_B Cp_B \frac{\partial \lambda_B}{\partial t} + k_B \frac{\partial^2 \lambda_B}{\partial x^2} + 2\sum_{j=1}^{N} [T(x_j,t) - Y_j(t)] \delta(x - x_j) = 0 \quad \text{for } L_A \le x \le L_B \tag{27}$$

$$-k_A \frac{\partial \lambda_A}{\partial x} = 2\sum_{j=1}^{N} [T(x_j,t) - Y_j(t)] \delta(x - x_j) \quad x = 0 \tag{28}$$

$$-k_A \frac{\partial \lambda_A}{\partial x} = -k_B \frac{\partial \lambda_B}{\partial x} = \frac{(\lambda_A - \lambda_B)}{R} - 2\sum_{j=1}^{N} [T(x_j,t) - Y_j(t)] \delta(x - x_j) \quad x = L_A \tag{29}$$

$$k_B \frac{\partial \lambda_B}{\partial x} = 2\sum_{j=1}^{N} [T(x_j,t) - Y_j(t)] \delta(x - x_j) \quad x = L_A + L_B \tag{30}$$

$$\lambda_A(x,t_f) = \lambda_B(x,t_f) = 0 \quad t = 0 \tag{31}$$

where x_j denotes the sensor locations. When $\lambda_A(x,t)$ and $\lambda_B(x,t)$ satisfy the above differential equation, the functional given by Eq. (25) reduces to

$$\Delta J[q(t)] = \int_{t=0}^{t_f} \Delta q(t) \lambda_A(0,t) dt \tag{32}$$

By definition, the functional increment can be presented as

$$\Delta J[q(t)] = \int_{t=0}^{t_f} \Delta q(t)\, \nabla J[q(t)]dt \tag{33}$$

A comparison of Eqs. (32) and (33) leads to the following expression for the gradient of functional $\nabla J[q^k(t)]$:

$$\nabla J[q(t)] = \lambda_A(0,t) \tag{34}$$

2.4 Parameter Estimation Process. In the parameter estimation stage, the parameters will denote as the unknown variables and will recover based on the knowledge about the estimated function at the previous stage. The solution to the present inverse problem can be determined by satisfying the following equation:

$$F(X_p) = \sum_{j=1}^{N} \int_{t=0}^{t_f} \{Y_j(t) - T[x_j,t;X_p]\}^2 dt \tag{35}$$

where X_P denotes to one of the parameters in Eqs. (1)–(6). One of the prevalent iterative methods for minimizing the objective function F is the BKM, which is a modification to the Gauss method [4,23] that could improve the convergence rate in some cases. The computational procedure for the estimation of the unknown parameters at iteration i can be summarized as follows.

1. Solve the direct problem with available estimated X_P in order to obtain temperature field within the slab $T(X_P^{(i)})$.
2. Compute F from the Eq. (35).
3. Compute the sensitivity matrix X defined by the following equation:

$$X = \left[\frac{\partial T_{1,1}}{\partial X_P} \quad \frac{\partial T_{1,2}}{\partial X_P} \quad . \quad . \quad \frac{\partial T_{1,M}}{\partial X_P} \quad \frac{\partial T_{2,1}}{\partial X_P} \quad \frac{\partial T_{2,2}}{\partial X_P} \quad . \quad . \quad \frac{\partial T_{2,M}}{\partial X_P} \quad . \quad . \quad \frac{\partial T_{N,M}}{\partial X_P} \right]^T \tag{36}$$

Since corresponding inverse problem is nonlinear, the sensitivity coefficients with regard to each of the unknown parameters in each iteration step should be calculated by the following equation:

$$\frac{\partial T}{\partial X_p} = \frac{T(X_p + \varepsilon X_p) - T(X_p)}{\varepsilon X_p} + O(\varepsilon X_p) \tag{37}$$

where ε is a small number (10^{-5} in this study).

4. Solve the following linear system of equation to find $\Delta X_P^{(i)}$:

$$[X^{T(i)}X^{(i)}]\Delta X_P^{(i)} = X^{T(i)}(\boldsymbol{T}^{(i)} - \boldsymbol{Y}^{(i)}) \tag{38}$$

where superscript T denotes transpose sign, and vectors $\boldsymbol{T}$ and $\boldsymbol{Y}$ are defined as

$$\boldsymbol{T}^{(i)} = [T_{1,1}, T_{1,2}, \ldots, T_{1,M}, T_{2,1}, T_{2,2}, \ldots, T_{2,M}, \ldots, T_{N,M}]^{(i)} \tag{39}$$

$$\boldsymbol{Y}^{(i)} = [Y_{1,1}, Y_{1,2}, \ldots, Y_{1,M}, Y_{2,1}, Y_{2,2}, \ldots, Y_{2,M}, \ldots, Y_{N,M}]^{(i)} \tag{40}$$

5. The updating rule for the BKM's algorithm is then applied to determine the unknown parameter

$$X_P^{(i+1)} = X_P^{(i)} + \hat{h}\Delta X_P^{(i)} \tag{41}$$

where $\hat{h}$ is the scalar interpolation factor and the Gauss method is indicated by $\hat{h}=1$.

6. Solve the direct problem with this new estimated $X_P^{(i+1)}$ in order to obtain $T(X_P^{(i+1)})$ and then compute F, as defined by Eq. (35).
7. Check the stopping (convergence) criterion given by Eq. (42)

$$F(X_P^{(n)}) < \varepsilon \tag{42}$$

8. Stop the iteration procedure if Eq. (42) is satisfied; otherwise, replace i by $i+1$ and return to step 3.

2.5 Correlation Analysis. The commonly used gradient-based estimation methods show instabilities resulting in nonconvergence, when implemented with models that contain correlated or nearly correlated variables. A sense of the magnitude of the sensitivity coefficients is gained through normalizing the sensitivity coefficients. Normalization is performed by multiplying the unknowns, resulting in units of temperature for all the scaled sensitivity coefficients. One way to investigate a correlation is to simply plot the scaled sensitivity coefficients against each other. If they appear to be nearly linear dependent, the corresponding thermal coefficients are correlated [4]. In the current study, the following equations are used to determine sensitivity coefficients for the heat flux, thermal conductivity, specific heat, and thermal contact resistance. Then, these coefficients will be normalized.

2.5.1 Sensitivity Problem for Heat Flux.

$$\rho_A Cp_A \frac{\partial \Delta T_A}{\partial t} = k_A \frac{\partial^2 \Delta T_A}{\partial x^2} \quad 0 \le x \le L_A \tag{43}$$

$$\rho_B Cp_B \frac{\partial \Delta T_B}{\partial t} = k_B \frac{\partial^2 \Delta T_B}{\partial x^2} \quad L_A \le x \le L_B \tag{44}$$

$$-k_A \frac{\partial \Delta T_A}{\partial x} = 1 \quad x = 0 \tag{45}$$

$$-k_A \frac{\partial \Delta T_A}{\partial x} = -k_B \frac{\partial \Delta T_B}{\partial x} = \frac{(\Delta T_A - \Delta T_B)}{R} \quad x = L_A \tag{46}$$

$$\frac{\partial \Delta T_B}{\partial x} = 0 \quad x = L_A + L_B \tag{47}$$

$$\Delta T_A(x,0) = \Delta T_B(x,0) = 0 \quad t = 0 \tag{48}$$

2.5.2 Sensitivity Problem for Thermal Conductivity. For the problem under consideration, sensitivity coefficients for thermal conductivity of material A can be obtained by the following equations:

$$\rho_A Cp_A \frac{\partial \Delta T_A}{\partial t} = k_A \frac{\partial^2 \Delta T_A}{\partial x^2} + \frac{\partial^2 T_A}{\partial x^2} \quad 0 \le x \le L_A \tag{49}$$

$$\rho_B Cp_B \frac{\partial \Delta T_B}{\partial t} = k_B \frac{\partial^2 \Delta T_B}{\partial x^2} \quad L_A \le x \le L_B \tag{50}$$

$$k_A \frac{\partial \Delta T_A}{\partial x} = \frac{\partial T_A}{\partial x} \quad x = 0 \tag{51}$$

$$-k_A\frac{\partial \Delta T_A}{\partial x}-\frac{\partial T_A}{\partial x}=-k_B\frac{\partial \Delta T_B}{\partial x}=\frac{(\Delta T_A-\Delta T_B)}{R} \quad x=L_A \tag{52}$$

$$\frac{\partial \Delta T_B}{\partial x}=0 \quad x=L_A+L_B \tag{53}$$

$$\Delta T_A(x,0)=\Delta T_B(x,0)=0 \quad t=0 \tag{54}$$

2.5.3 Sensitivity Problem for Specific Heat. For the problem studied here, sensitivity coefficients for specific heat of material *A* can be achieved by the following expressions.

$$\rho_A Cp_A\frac{\partial \Delta T_A}{\partial t}+\rho_A\frac{\partial T_A}{\partial t}=k_A\frac{\partial^2 \Delta T_A}{\partial x^2} \quad 0\le x\le L_A \tag{55}$$

$$\rho_B Cp_B\frac{\partial \Delta T_B}{\partial t}=k_B\frac{\partial^2 \Delta T_B}{\partial x^2} \quad L_A\le x\le L_B \tag{56}$$

$$k_A\frac{\partial \Delta T_A}{\partial x}=0 \quad x=0 \tag{57}$$

$$-k_A\frac{\partial \Delta T_A}{\partial x}=-k_B\frac{\partial \Delta T_B}{\partial x}=\frac{(\Delta T_A-\Delta T_B)}{R} \quad x=L_A \tag{58}$$

$$\frac{\partial \Delta T_B}{\partial x}=0 \quad x=L_A+L_B \tag{59}$$

$$\Delta T_A(x,0)=\Delta T_B(x,0)=0 \quad t=0 \tag{60}$$

2.5.4 Sensitivity Problem for Thermal Contact Resistance.

$$\rho_A Cp_A\frac{\partial \Delta T_A}{\partial t}=k_A\frac{\partial^2 \Delta T_A}{\partial x^2} \quad 0\le x\le L_A \tag{61}$$

$$\rho_B Cp_B\frac{\partial \Delta T_B}{\partial t}=k_B\frac{\partial^2 \Delta T_B}{\partial x^2} \quad L_A\le x\le L_B \tag{62}$$

$$k_A\frac{\partial \Delta T_A}{\partial x}=0 \quad x=0 \tag{63}$$

$$-k_A\frac{\partial \Delta T_A}{\partial x}=-k_B\frac{\partial \Delta T_B}{\partial x}=\frac{(\Delta T_A-\Delta T_B)}{R}-\frac{(T_A-T_B)}{R^2} \quad x=L_A \tag{64}$$

$$\frac{\partial \Delta T_B}{\partial x}=0 \quad x=L_A+L_B \tag{65}$$

$$\Delta T_A(x,0)=\Delta T_B(x,0)=0 \quad t=0 \tag{66}$$

3 Computational Procedure for Inverse Methodology

The computational procedure for the estimation of the unknown parameters can be summarized as follows.

(1) Choose initial guess q^0 and X_p^0.
(2) Solve the direct problem with q^i and X_p^i to obtain temperature at sensor locations.
(3) Evaluate the objective functional S using Eq. (12).
(4) Calculate heat flux q^{i+1} as described in the function estimation stage.
(5) Solve the direct problem with estimated heat flux at previous stage q^{i+1} in order to obtain temperatures at sensor locations.
(6) The updating rule for the BKM's algorithm is then applied to determine the unknown parameters, X_P^{i+1}. This procedure applies individually for each parameter.
(7) Check the stopping (convergence) criterion given by Eq. (67).

$$S(\boldsymbol{P}^{(i+1)})<\varepsilon \tag{67}$$

(8) Stop the iteration procedure if it is satisfied; otherwise, replace i by $i+1$ and return to step 2.

If the measured temperatures contain no errors (noise), the ε in Eq. (67) can be chosen to be an arbitrary small value.

However, as measured data are always degraded by noise, a stopping criterion is needed for the case of measurement errors. The iterative process is then stopped in accordance with the discrepancy principle criterion [3], i.e., upon satisfaction of the following condition:

$$\varepsilon=N\times M\times \sigma^2 \tag{68}$$

where M is the total number of time steps and σ is the standard deviation of the errors in the temperature. The criterion given by Eq. (68) is based on terminating the procedure as soon as the observation function is in the order of magnitude of the ε, which represents that the best evaluation expected in the order of the data error.

4 Results and Discussion

In order to demonstrate the accuracy and efficiency of the present method, a simulated test case for simultaneous parameter and function estimation is considered. The following values are used for the materials properties, boundary, and initial conditions in this test case: $k_A=63.9$ W/m K, $k_B=2$ W/m K, $\rho_A=7832$ kg/m^3, $\rho_B=2349$ kg/m^3, $Cp_A=434$ J/kg K, $Cp_B=900$ J/kg K, $R=0.002$ m^2 K/W, $L_A=1$ cm, $L_B=1$ cm, and $T_0=300$ K, and the heat flux function, $q(t)$, is assumed to have a rectangular (or pulsed) form. The duration of the experiment was assumed to be 10 s. A grid spacing of 0.001 cm for material A was used for all the results presented below. The measured data $Y(t)$ were simulated by adding random errors with zero mean and constant standard deviation to their exact values $Y_{\text{exact}}(t)$.

$$Y(t)=Y_{\text{exact}}(t)+\omega\sigma \tag{69}$$

where ω is a random variable being within -2.576–2.576 for a 99% confidence bound. In order to improve an experimental design, different factors such as sensor positions, heating time, boundary conditions, and number of sensors must be optimized. This subject matter is out of the scope of this work and will not be examined here. Two sensors are assumed to be used here. The temperature values were obtained using the direct heat conduction calculations and their values at sensor locations are saved and used as sensors data. The effect of the sensors location in each material is examined here. Three situations for sensors position are investigated. (I) Two sensors are located in material A at x = 0 cm and x = 0.5 cm. (II) One sensor is embedded in material *A* at x = 0 cm and another sensor in material B at x = 1.1 cm. (III) Sensors are placed in material *A* at x = 1.1 cm and x = 2 cm.

To quantify the deviation of the estimated thermal coefficients ($\hat{q}(t)$ and $\hat{X}_P$) from the exact ones ($q(t)$ and X_P), relative errors are defined as follows:

$$q_{\text{err}}=\frac{\displaystyle\int_{t=0}^{t_f}[q(t_i)-\hat{q}(t_i)]^2dt}{\displaystyle\int_{t=0}^{t_f}[q(t_i)]^2dt}\times 100\% \tag{70}$$

$$Xp_{\text{err}}=\left|\frac{X_P-\hat{X}_P}{X_P}\right|\times 100\% \tag{71}$$

Table 1 Effect of sensors arrangements on the results (test case 1)

Configuration	Value of objective function	No. of iterations
I	5×10^{-9}	356
II	9×10^{-9}	323
III	2.37	500

4.1 Numerical Test Case 1. This example deals with the simultaneous estimation of thermal contact resistance and heat flux. At the first stage, impact of sensors location on the convergence of combined procedure is examined. The data acquisition time step for each sensor is assumed to be 0.1 s. As previously mentioned, two sensors were used for this problem and therefore, the total number of temperature readings was 202 samples. The initial guess values of 1000 W/m^2 (0.1 W/cm^2) for heat flux and 0.001 m^2 K/W for thermal contact resistance were used. Table 1 summarizes the results obtained for different sensors location without the presence of any noise. A comparison of the estimation error for three different sensors configuration shows the same order magnitude of accuracy for the first two configurations. The value of objective function approaches to 2.37 after 500 iterations when sensors are installed in material B. The second sensors arrangement shows a faster convergence rate than other arrangements and will be considered for the estimation procedure. At the next step, the influence of initial guess on the results is examined. It was realized that values lower than 5.2×10^{-4} m^2 K/W as an initial guess for R do not satisfy the convergence criterion. Meanwhile, the estimation procedure is not sensitive to initial guess for the heat flux. With knowledge of the sensors position and suitable ranges of initial guess, the effect of the temperature reading time on the inverse solution can be explored. Three sets of interval time for simulated data are considered here (0.01 s, 0.1 s, and 0.4 s). No impact is observed on the results when noise-free data is used. Table 2 presents the relative errors obtained by the present strategy. It shows that the error of the estimated unknowns is small in comparison to the added noise and reliable results can still be obtained when measurement errors are included. As expected, the increases in the measurement errors cause decreases in the accuracy of the inverse solution. Moreover, it is seen that by using the smaller sampling interval time, the profile of heat flux is better reconstructed. However, when the sampling time step is 0.4 s, the parameter R cannot be approximated as accurately as another sampling interval times. Considering sampling time step equals to 0.1, the estimated thermal contact resistances for exact and noisy data are shown in Table 3. The excellent agreement between the exact solutions and the estimated results from errorless data can be seen. In the case of exact measurements $\sigma=0.0$, the estimated heat flux recovers its exact value. For these cases, the method of Ref. [19] does not converge. The estimated heat flux using inexact measurement ($\sigma=1$) is shown in Fig. 4. The relative errors between the exact and estimated values for $q(t)$ and R are listed in Table 2. These small relative errors show that the proposed scheme is highly accurate for solving the combined parameter and function estimation problem.

Table 2 Relative error between exact and estimated unknowns for different values of noise and time step (test case 1)

	Noisy data ($\sigma=1$)		Noisy data ($\sigma=2$)	
Sampling interval time	q_{err}%	R_{err}%	q_{err}%	R_{err}%
0.4	0.13	0.53	0.53	0.53
0.1	0.217	0.4	0.9	0.49
0.01	0.4	0.3	1	0.58

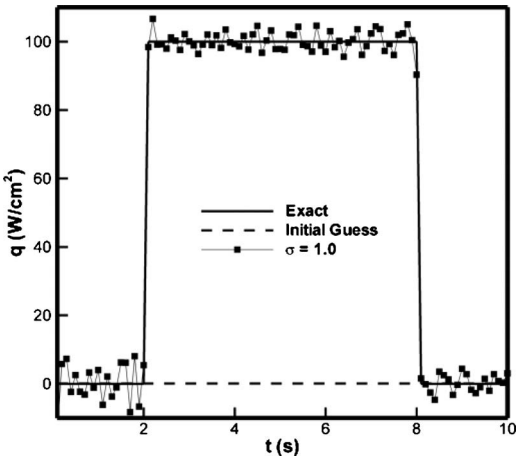

Fig. 4 The exact and estimated values of heat flux

Figure 5 compares the reduction of the objective function with respect to the number of iterations for different levels of measurements. The fluctuation in objective functional indicates the difficulty associated with the estimation procedure. As expected, using exact (noise-free) data leads to significantly small values for the objective function. However, the objective function remains almost constant (in the order of 10^2 for $\sigma=1$ and 400 for $\sigma=2$) for noisy data after about 50 iterations. It should be noted that the results in this section reported at iteration 50 in which the value of objective function satisfies Eq. (68). To investigate the correlation among the heat flux and contact resistance, scaled sensitivity coefficients for $q(t)$ and R are illustrated in Fig. 6. As it is indicated in Fig. 7, $q(t)$ and R are almost negatively correlated at $x=1.1$. Moreover, a large magnitude difference between the scaled sensitivity coefficients at $x=0$ has more negative impact on the accuracy of the estimated values than the correlation among the unknowns. These limiting factors to the stability may explain the nonconvergence behavior of the traditional gradient-type methods.

4.2 Numerical Test Case 2. In this case, the simultaneous prediction of heat flux and thermal conductivities of two materials is considered. It is assumed that two sensors are positioned at 0 cm and 0.5 cm for this test case (it was found that when both sensors are installed in the material A, the rate of convergence is faster). Furthermore, it was observed that the results are independent of initial guess for heat flux. However, the algorithm cannot reach a solution using small values as the initial guess for thermal conductivities. The initial guess values for $q(t)$, k_A, and k_B in the current algorithm are taken to be 1000 W/m^2, 5 W/m K, and 5 W/m K, respectively. Additional computations were indicated

Table 3 Estimated thermal contact resistance (test case 1)

Data	Initial guess (m^2 K/W)	Exact value (m^2 K/W)	Estimated value by proposed method (m^2 K/W)	Estimated value by Ref. [19] (m^2 K/W)
Errorless	0.001000	0.002000	0.002000	Not converged
Noisy ($\sigma=1$)	0.001000	0.002000	0.002008	Not converged
Noisy ($\sigma=2$)	0.001000	0.002000	0.0020098	Not converged

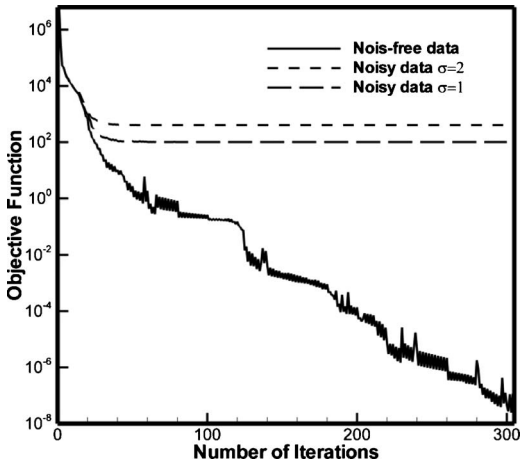

Fig. 5 Reduction histories of the objective function for different level of measurements

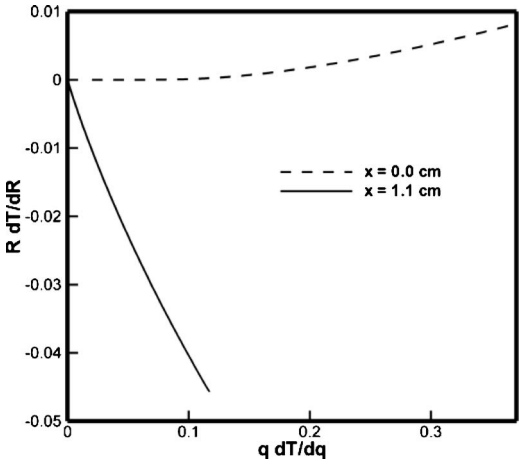

Fig. 7 Study of the linear dependence between the scaled sensitivity coefficients of $q(t)$ and R

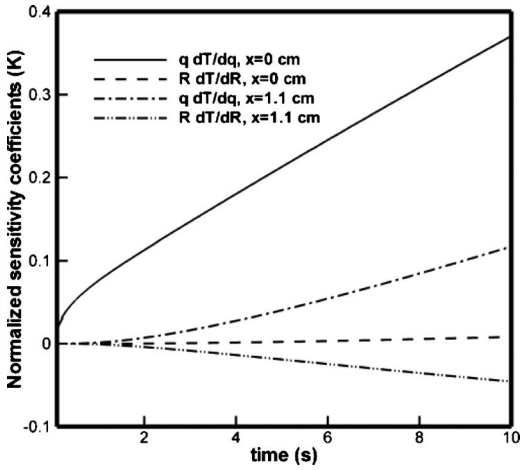

Fig. 6 Normalized sensitivity coefficients for $q(t)$ and R

that if the small value for time step (0.01 s) is used, there is enough numerical noise for the heat flux to be highly fluctuating. In addition, relative error in the evaluated thermal conductivities was bigger than those obtained by larger time steps (i.e., 0.1 s and 0.4 s). On the other hand, using a time step equal to 0.4 s can cause difficulty in estimating thermal conductivity of material B. In this situation, when the value of the objective function remains almost constant, k_B experiences a wide range of values during iterative procedure. Hence, the time step for this simulated experiment is considered to be 0.1 s. The results obtained by the proposed methodology are compared with MCGM and are presented in Table 4. No convergence is achieved with or without errors in simulated data when the method of Ref. [19] is employed. It should be pointed out using better initial guesses that the strategy of Ref. [19] did not meet stopping criterion. This makes the aforementioned method inefficient to be applied for this class of IHCPs. Using noise-free data, $q(t)$, k_A, and k_B recovered their theoretical values and the error is to the machine zero. Figure 8 shows the reconstructed heat flux by the proposed method when noisy data ($\sigma=1$) is utilized. The largest errors appear in the initiation of test where the heat flux and temperature field have their minimum values and artificial noises in the real data (Eq. (69)) are most sensible. Table 5 shows relative errors between the exact and estimated values of thermal coefficients. The relative errors of the estimated heat flux and thermal conductivities are not distinguishable, indicating that the proposed algorithm is effective.

To demonstrate the robustness of the proposed method against the correlated thermal coefficients, normalized sensitivity coefficients for $q(t)$, k_A, and k_B are presented in Fig. 9. These coefficients are semilinearly dependent, as indicated by Fig. 10. A large magnitude difference between the scaled sensitivity coefficients of $q(t)$ and k_B at $x=0$ has a negative effect on the accuracy of the estimates. These features characterized an ill-posed estimation problem that does not allow for an accurate estimation of $q(t)$, k_A, and k_B by the traditional conjugate gradient method (TCGM) and also entails correlations between the sensitivity coefficients, as shown earlier.

4.3 Numerical Test Case 3. In this numerical experiment, the simultaneous evaluation of heat flux and specific heats of two materials is discussed. It was found when sensors are embedded in material A, estimation of Cp_B becomes difficult. Thus, the sensors are assumed to be installed in both materials. The results obtained by the inverse technique are not influenced by initial guess for heat flux. Initial guess above 100 J/kg K for specific heat of material A and in the range of 100–650 J/kg K for material B produced acceptable results. In this case, the computations can start using $q=1000$ W/m^2, $Cp_A=500$ J/kg K, and $Cp_B=500$ J/kg K

Table 4 Estimated thermal conductivity values (test case 2)

	Initial guess			Exact value (W/m K)		Estimated value by proposed method (W/m K)		Estimated value by Ref. [19] (W/m K)	
Data	k_A (W/m K)	k_B (W/m K)	q (W/m^2)	k_A	k_B	k_A	k_B	k_A	k_B
Errorless	5	5	1000	63.9	2	63.9	2	Not converged	Not converged
Noisy ($\sigma=1$)	5	5	1000	63.9	2	63.75	2.0057	Not converged	Not converged
Noisy ($\sigma=2$)	5	5	1000	63.9	2	63.48	2.07	Not converged	Not converged

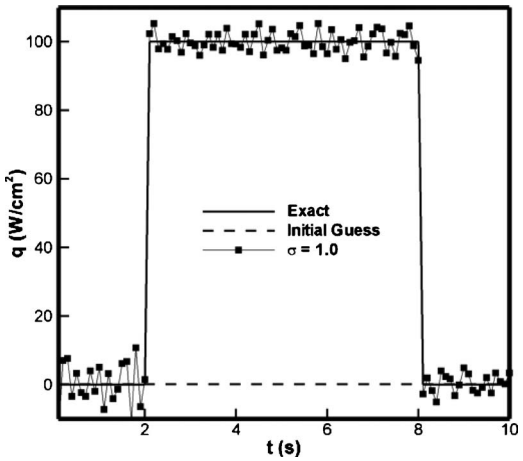

Fig. 8 The exact and estimated values of heat flux

as initial guess. Discussion of selecting suitable value for time step showed that reliable results can be obtained when the recording time for each sensor is 0.1 s. The results for unknown parameters are presented for different levels of measurement in Table 6. The exact solution is very close to the estimated specific heats from errorless data. Furthermore, the accuracy of the estimated results from noisy data is demonstrated to be high. The measured temperatures with error $\sigma=1.0$ are obtained according to Eq. (69), which represent temperature rise from 0.47% to 1.67% during simulated experiment. When the MCGM [19] is employed, no convergence with or without errors in temperature measurement was observed. It might be worth mentioning that MGCM converges when a better initial guess is utilized, but its results are not as accurate as the ones obtained by the present method. The retrieval heat fluxes using exact and inexact measurements are shown on Fig. 11. Existence of discontinuities in the profile of heat flux does not prevent methodology from recovering its distribution. Although oscillation of the estimated values is observed, the estimated values are in good agreement with the exact values of the heat flux. As expected, the largest errors appear during the first 2 s of test in which the ratio of the noise magnitude to the measured temperature is maximized. The estimated values for the heat flux follow the discontinuities with some dissipation. The values for the relative errors are presented in Table 7. The estimation error for different unknowns is less than 0.5%, whereas the MCGM leads to larger errors even with the usage of good initial guess.

The scaled sensitivity coefficients for $q(t)$, Cp_A, and Cp_B are shown in Fig. 12. It can be seen from Fig. 13 that $q(t)$ and Cp_A are semilinearly dependent. This may be a reason for convergence difficulties of TCGM and ordinary estimation procedures and it restricts their applications. Furthermore, because of significant magnitude differences between the sensitivity coefficients of $q(t)$ and Cp_B at $x=0$, the simultaneous estimation was limited by gradient-type methods.

At the end of this paper, it might be worth clarifying that it is possible to estimate two thermal conductivities (or two specific heats) and heat flux by the present method. Then, heat flux and two parameters can be estimated. One could consider the case that the heat flux and two parameters (i.e., thermal conductivity and specific heat) are unknowns. In the case that no information about the material and its environment is known, it is not possible to estimate the heat flux and/or thermal conductivity and specific heat by the methodology described here.

5 Conclusions

A framework is developed for exploiting the classical methods in combined parameter and function estimation problems and broadening their appeal through a basic understanding of their application. To gain the benefits of the conjugate gradient method in handling function estimation problems as well as the Box–Kanemasu method advantages in parameter estimation problems, a joint method for solving combined parameter and function estimation problems was introduced in this paper. The most tangible artifact of this work is the successful simultaneous estimation of correlated unknowns. Numerical results indicated the significance

Table 5 Relative error between exact and estimated quantities (test case 2)

Errorless data			Noisy data ($\sigma=1$)			Noisy data ($\sigma=2$)		
q_{err}%	k_{Aerr}%	K_{Berr}%	q_{err}%	k_{Aerr}%	K_{Berr}%	q_{err}%	k_{Aerr}%	K_{Berr}%
0.0	0.0	0.0	0.25	0.23	0.28	0.92	0.66	3.5

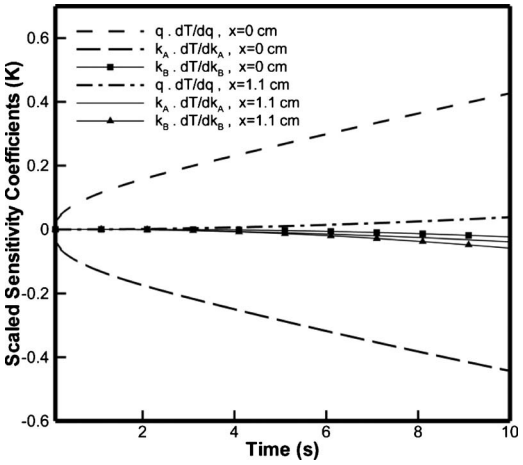

Fig. 9 Normalized sensitivity coefficients for $q(t)$, k_A, and k_B

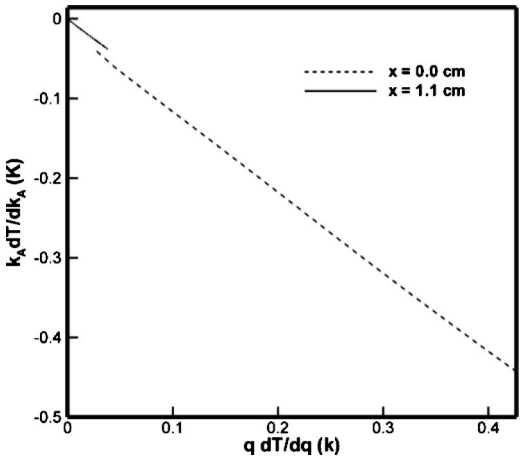

Fig. 10 Study of the linear dependence between the scaled sensitivity coefficients of $q(t)$ and k_A

Table 6 Estimated specific heats (test case 3)

Data	Initial guess Cp_A (J/kg K)	Initial guess Cp_B (J/kg K)	Initial guess q (W/m^2)	Exact value (J/kg K) Cp_A	Exact value (J/kg K) Cp_B	Estimated value by proposed method (J/kg K) Cp_A	Estimated value by proposed method (J/kg K) Cp_B	Estimated value by Ref. [19] (J/kg K) Cp_A	Estimated value by Ref. [19] (J/kg K) Cp_B
Errorless	500	500	1000	434	900	434	900	Not converged	Not converged
Errorless	500	500	1×10^6	434	900	434	900	473.18	837.26
Noisy	500	500	1000	434	900	432.09	904.53	Not converged	Not converged
Noisy	500	500	1×10^6	434	900	432.12	904.50	470.94	843

Table 7 Relative error between exact and estimated quantities (test case 3)

Data	Initial guess Cp_A (J/kg K)	Initial guess Cp_B (J/kg K)	Initial guess q (W/m^2)	Proposed method Cp_{Aerr}%	Proposed method Cp_{Berr}%	Proposed method q_{err}%	Ref. [19] Cp_{Aerr}%	Ref. [19] Cp_{Berr}%	Ref. [19] q_{err}%
Errorless	500	500	1000	0.0	0.0	0.0	-	-	-
Errorless	500	500	1×10^6	0.0	0.0	0.0	9.03	6.97	0.508
Noisy	500	500	1000	0.44	0.5	0.221	-	-	-
Noisy	500	500	1×10^6	0.433	0.5	0.22	8.51	6.33	1.117

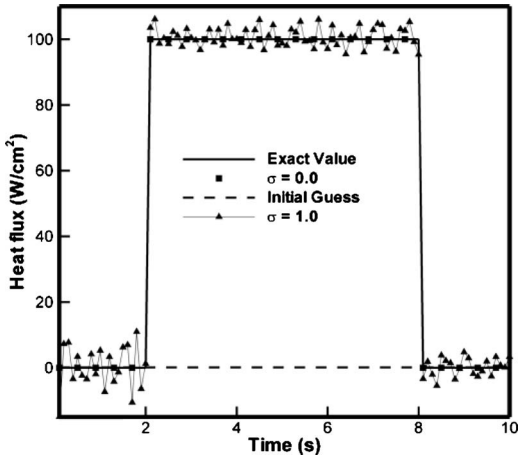

Fig. 11 The exact and estimated values of heat flux

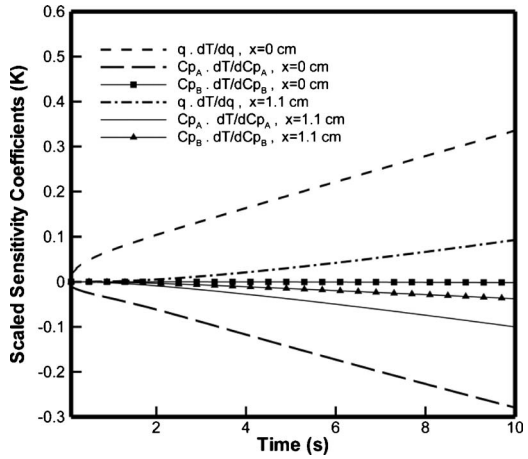

Fig. 12 Normalized sensitivity coefficients for $q(t)$, Cp_A, and Cp_B

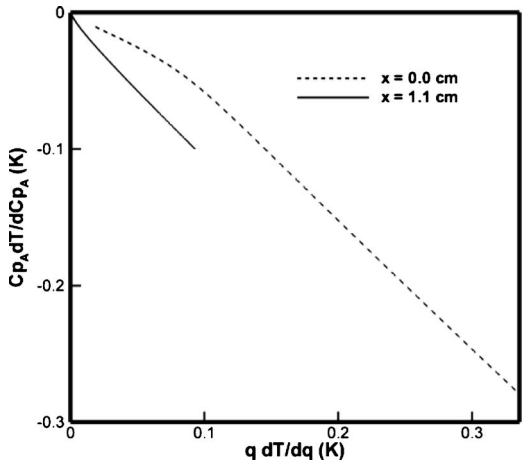

Fig. 13 Study of the linear dependence between the scaled sensitivity coefficients of $q(t)$ and Cp_A

of the proposed method in finding the accurate values of the thermal coefficients from exact (noise-free) data in inverse heat conduction problems for cases that the commonly used gradient-base methods fail in dealing with the correlation among thermal coefficients. Moreover, the method showed excellent stability in the presence of imperfect or noisy data and high accuracy of the estimated results.

Nomenclature

- c_p = specific heat
- d = descent direction
- F = the objective functional for parameter estimation problem
- Fo = Fourier number
- $\hat{h}$ = scalar interpolation factor used in Eq. (41)
- J = the objective functional for function estimation problem
- k = thermal conductivity
- L = slab thickness
- M = total number of temperature readings
- N = number of sensors
- N_P = number of unknowns

P = vector of unknowns
$q(t)$ = unknown surface heat flux
R = thermal contact resistance
S = the objective functional for combined parameter and function estimation problem
T = temperature
T_0 = initial temperature
t = time
t_f = final time
X = sensitivity matrix
X_P = unknown parameter
x = space variable
Y = temperature measured by sensors
α = thermal diffusivity
β = descent variable
γ = variable in decent direction
Δ = small variation
ΔT = sensitivity function
δ = Dirac delta function
ε = very small value
λ = adjoint variable
ρ = density
σ = standard deviation of the errors in the measured temperatures
ω = random variable
∇J = gradient of the objective functional for function estimation problem

Subscripts

A, B = materials A and B, respectively

Superscripts

i = iteration number
T = transpose of a matrix

References

[1] Beck, J. V., Blackwell, B., and St. Clair, C. R., 1985, *Inverse Heat Conduction: Ill-Posed Problems*, Wiley, New York.
[2] Hakkaki-Fard, A., and Kowsary, F., 2008, "Heat Flux Estimation in a Charring Ablator," Numer. Heat Transfer, Part A, **53**, pp. 543–560.
[3] Alifanov, O. M., 1994, *Inverse Heat Transfer Problems*, Springer, New York.
[4] Beck, J. V., and Arnold, K. J., 1977, *Parameter Estimation in Engineering and Science*, Wiley, New York.
[5] Dowding, K. J., Beck, J. V., and Blackwell, B. F., 1999, "Estimating Temperature-Dependent Thermal Properties of Carbon-Carbon Composite," J. Thermophys. Heat Transfer, **13**, pp. 328–336.
[6] Aviles-Ramos, C., Haji-Sheikh, A., Beck, J. V., and Dowding, K. J., 2001, "Estimation of Thermophysical Properties by the Spectral Method—Development and Evaluation," ASME J. Heat Transfer, **123**, pp. 24–30.
[7] Veiseh, S., Hakkaki-Fard, A., and Kowsary, F., 2009, "Determining of the Air/Fiber Conductivity of Mineral Wool Insulations in Building Applications Using Parameter Estimation Methods," Journal of Building Physics, **32**, pp. 243–260.
[8] Molavi, H., Hakkaki-Fard, A., Pourshaban, I., Mahbubi Fard, M., and Rahmani, R. K., 2009, "Estimation of Temperature-Dependent Thermophysical Properties of Noncharring Ablators," J. Thermophys. Heat Transfer, **23**, pp. 50–58.
[9] Molavi, H., Pourshaban, I., Hakkaki-Fard, A., Molavi, M., Ayasoufi, A., and Rahmani, R. K., 2009, "Inverse Identification of Thermal Properties of Charring Ablators," Numer. Heat Transfer, Part B, **56**, pp. 478–501.
[10] Allahdadi-Mehrabadi, M., Sadeghy, K., Hakkaki-Fard, A., and Sefidgar, M., 2008, "On the Use of Inverse Methods to Parameter Estimation in Turbulent Pipe Flows of Drag Reducing Polymers," J. Soc. Rheol., Jpn., **36**, pp. 241–251.
[11] Petrushevsky, V., and Cohen, S., 1999, "Nonlinear Inverse Heat Conduction With a Moving Boundary: Heat Flux and Surface Recession Estimation," ASME J. Heat Transfer, **121**, pp. 708–711.
[12] Kim, S. K., and Daniel, I. M., 2004, "Gradient Method for Inverse Heat Conduction Problem in Nanoscale," Int. J. Numer. Methods Eng., **60**, pp. 2165–2181.
[13] Dowding, K. J., and Beck, J. V., 1999, "A Sequential Gradient Method for the Inverse Heat Conduction Problem (IHCP)," ASME J. Heat Transfer, **121**, pp. 300–306.
[14] Kowsary, F., Behbahani-nia, A., and Pourshaghaghy, A., 2006, "Transient Heat Flux Function Estimation Utilizing the Variable Metric Method," Int. Commun. Heat Mass Transf., **33**, pp. 800–810.
[15] Molavi, H., Rahmani, R. K., Pourshaghaghy, A., Sharifi Tashnizi, E., and Hakkaki-Fard, A., 2010, "Heat Flux Estimation in a Nonlinear Inverse Heat Conduction Problem With Moving Boundary," ASME J. Heat Transfer, **132**, p. 081301.
[16] Rahmani, R. K., Molavi, H., and Ayasoufi, A., 2009, "A Novel Gradient-Type Method Based on Maximum Entropy Principle Applied to the Inverse Radiation Problems," ASME Early Career Technical Journal, **8**, pp. 3.1–3.9.
[17] Rahmani, R. K., Molavi, H., Ayasoufi, A., Koomullil, R. P., and Cheng, G., 2010, "Solution of Radiative Boundary Design Problems Using a Combined Optimization Technique," Numer. Heat Transfer, Part B, **57**, pp. 348–371.
[18] Dowding, K. J., Beck, J. V., Ulbrich, A., Blackwell, B., and Hayes, J., 1995, "Estimation of Thermal Properties and Surface Heat Flux in Carbon-Carbon Composite," J. Thermophys. Heat Transfer, **9**, pp. 345–351.
[19] Loulou, T., and Artioukhine, E., 2003, "Optimal Choice of Descent Steps in Gradient-Type Methods When Applied to Combined Parameter and Function or Multi-Function Estimation," Inverse Probl. Eng., **11**, pp. 273–288.
[20] Loulou, T., and Scott, E. P., 2006, "An Inverse Heat Conduction Problem With Heat Flux Measurements," Int. J. Numer. Methods Eng., **67**, pp. 1587–1616.
[21] Loulou, T., 2007, "Combined parameter and Function Estimation With Application to Thermal Conductivity and Surface Heat Flux," ASME J. Heat Transfer, **129**, pp. 1309–1320.
[22] Patankar, S. V., 1986, *Numerical Heat Transfer and Fluid Flows*, Hemisphere, London.
[23] Ozisik, M. N., and Orlande, H. R. B., 2000, *Inverse Heat Transfer Fundamentals and Applications*, Taylor & Francis, New York.

Analytical Solution to Nonlinear Thermal Diffusion: Kirchhoff Versus Cole–Hopf Transformations

Peter Vadasz
Professor
Fellow ASME
Department of Mechanical Engineering,
Northern Arizona University,
P.O. Box 15600,
Flagstaff, AZ 86011;
Faculty of Engineering,
University of Kwa-Zulu Natal,
Durban 4041, South Africa

The Kirchhoff transformation is the classical method of solution to the nonlinear thermal diffusion problem with temperature dependent properties. It essentially converts the nonlinear problem into a linear one if the thermal diffusivity is approximately constant. Unfortunately, with the only exception of an exponential dependence of the thermal conductivity on temperature, all other thermal conductivity functions produce an inconvenient form for the inverse transform. This paper shows that the Kirchhoff transformation is a particular consequence of the more general Cole–Hopf transformation. However, the classical presentation of the Kirchhoff transformation in terms of a definite integral is more restrictive than the result obtained from the Cole–Hopf transformation and it is this restrictiveness that causes the practical inconvenience in the form of the inverse transform. It is shown that a more compact and practically convenient form of the inverse transform can be obtained by using directly the result from the Cole–Hopf transformation, hence, making its application more attractive. [DOI: 10.1115/1.4002325]

Keywords: nonlinear conduction, Kirchhoff transformation, Cole–Hopf transformation, nonlinear thermal diffusion, temperature dependent properties

1 Introduction

Nonlinear thermal diffusion occurs typically when the material properties, such as the thermal conductivity and possibly the heat capacity, are temperature dependent [1,2]. In such cases, useful transformations may in certain circumstances transform the nonlinear problem into a linear one. Nonlinear diffusion occurs also in problems involving radiation in cellular porous media, such as porous foams. Viskanta [3], for example, mentioned that cellular foams formed from plastics, ceramics, and metals were strongly attenuating, and radiative transfer in such foams even of small thickness can often be treated as a diffusion process. Kuznetsov and Nield [4] applied such a temperature dependent thermal conductivity in dealing with the Cheng–Minkowycz convection problem in porous media [5] and in forced convection in porous media [6] as well as on the onset of natural convection in a porous layer heated from below [7]. As these applications involve convection, the transformations discussed in this paper apply to such problems only when the porous layer is heated from above and cooled from below or when it is heated from below but it is well in the subcritical regime or for a porous layer differentially heated for the sides but within the conduction regime (small Rayleigh numbers) such that the velocity field is perpendicular to the temperature gradient causing the convection effects to vanish. The latter is reflected by the term $\boldsymbol{V}\cdot\nabla T$ in the energy equation, hence, when $\boldsymbol{V}$ is perpendicular to ∇T, it yields $\boldsymbol{V}\cdot\nabla T=0$. Therefore, the importance of treating the problem of temperature dependent properties is also revealed in all these applications.

The Kirchhoff transformation is the classical method of obtaining analytical solutions to the nonlinear thermal diffusion problem when the properties are temperature dependent [1,2]. While the thermal conductivity k and the heat capacity ρc_p of a fluid or solid (in the case of solids c replaces c_p) are considered temperature dependent, the Kirchhoff transformation is applicable when their ratio $\alpha=k/\rho c_p$ can be assumed approximately constant. Carslaw and Jaeger [2] indicated that "it is a fact that in many cases the variation of α with temperature is much less important that that of k, so that, to a reasonable approximation, it may be taken constant; for example, for metals near the absolute zero, both k and c are approximately proportional to the absolute temperature," and for solids $\rho\approx$constant, therefore, $\alpha\approx$constant. The method was reviewed by Knight and Philip [8] and was applied to steady state heat conduction problems too by Bonani and Ghione [9]. Essentially, the Kirchhoff transformation is expressed in the form of a definite integral that transforms the nonlinear diffusion problem into a linear one. The inverse transform, however, appears in the form of a nonlinear algebraic equation and therefore, obtaining the temperature field requires the solution of this nonlinear algebraic equation, leading to a practical inconvenience that can be substantially reduced by using the more general Cole–Hopf transformation for the solution to the same problem. It is demonstrated in this paper that the Kirchhoff transformation is actually a result of the Cole–Hopf transformation but its presentation in the form of a definite integral limits its attractiveness due to the inconvenient inverse transform. Examples of the application of the general result obtained from the Cole–Hopf transformation to specific thermal conductivity functions in the nonlinear thermal diffusion problem are presented, demonstrating its practicality and convenience of use. More applications of the Cole–Hopf transformation beyond heat conduction can be found in Whitham [10].

2 Problem Formulation

The thermal diffusion process applicable to temperature dependent properties involves functional relationship between the thermal conductivity and the temperature that may have one of the following forms, presented only as examples:

$$k(\tilde{T}) = k_o \exp[\sigma(\tilde{T}-\tilde{T}_o)] \tag{1}$$

Contributed by the Heat Transfer Division of ASME for publication in the JOURNAL OF HEAT TRANSFER. Manuscript received November 1, 2009; final manuscript received July 23, 2010; published online September 22, 2010. Assoc. Editor: Ofodike A. Ezekoye.

$$k(\tilde{T}) = k_o[1 + \beta_k(\tilde{T} - \tilde{T}_o)] \tag{2}$$

$$k(\tilde{T}) = k_o[1 + \beta_1(\tilde{T} - \tilde{T}_o) + \beta_2(\tilde{T} - \tilde{T}_o)^2] \tag{3}$$

where $\tilde{T}$ is the temperature, k is the thermal conductivity, k_o and $\tilde{T}_o$ are the constant reference values of k and $\tilde{T}$, respectively, such that $k=k_o$ when $\tilde{T}=\tilde{T}_o$, and σ, β_k, β_1, and β_2 are the constants representing coefficients of thermal conductivity affinity to temperature. Actually, since the variation of thermal conductivity with temperature may take so many functional forms, Eqs. (2) and (3) are extremely useful as they represent first and second order Taylor series approximations, respectively, of any functional form around the reference temperature $\tilde{T}_o$. It is convenient to introduce the notation of the temperature taken with respect to its reference value in the form

$$T = \tilde{T} - \tilde{T}_o \tag{4}$$

Subject to notation (4), Eqs. (1)–(3) take the form

$$k(T) = k_o \exp(\sigma T) \tag{5}$$

$$k(T) = k_o(1 + \beta_k T) \tag{6}$$

$$k(T) = k_o(1 + \beta_1 T + \beta_2 T^2) \tag{7}$$

The heat capacity $\gamma(T)=\rho c_p$ is also temperature dependent and is assumed to have functional forms similar to the thermal conductivity functions with approximately the same values of their coefficients such that the thermal diffusivity, $\alpha=k/\gamma$, is approximately constant, i.e., $\alpha \approx$ constant, as presented by Carslaw and Jaeger [2]. The nonlinear thermal diffusion equation has the general form

$$\gamma(T)\frac{\partial T}{\partial t} = \nabla \cdot [k(T)\,\nabla\, T] + \dot{q} \tag{8}$$

where $\dot{q}(\boldsymbol{X})$ is the heat generation per unit volume $(\mathrm{W/m^3})$, which may vary within the domain but is assumed independent of time. The latter may be produced by Ohm's heating for example but is not necessarily limited to the latter. The space variable $\boldsymbol{X}$ represents the position vector and is defined in Cartesian coordinates in the form

$$\boldsymbol{X} = x\hat{\boldsymbol{e}}_x + y\hat{\boldsymbol{e}}_y + z\hat{\boldsymbol{e}}_z \tag{9}$$

where $\hat{\boldsymbol{e}}_x, \hat{\boldsymbol{e}}_y, \hat{\boldsymbol{e}}_z$ are the unit vectors in the x, y, and z directions, respectively, and similar forms are applicable to other coordinate systems.

For the application of the Cole–Hopf transformation, Eq. (8) is presented in the following equivalent form obtained by using the chain rule in applying the divergence operator on the first term on the right hand side of Eq. (8):

$$\gamma(T)\frac{\partial T}{\partial t} = k(T)\nabla^2 T + \frac{\mathrm{d}k}{\mathrm{d}T}(\nabla T \cdot \nabla T) + \dot{q} \tag{10}$$

The nonlinear thermal diffusion problem governed by Eq. (8) or its equivalent form (10) has to be solved subject to the following boundary and initial conditions (any other combination of Dirichlet and Neumann boundary conditions are possible):

$$[\boldsymbol{q} \cdot \hat{\boldsymbol{e}}_{\boldsymbol{n}}]_{B_1} = q_o; \quad [T]_{B_2} = T_{b2}; \quad [T]_{B_3} = T_{b3} \tag{11}$$

where $\boldsymbol{q}$ represents the heat flux vector, $\hat{\boldsymbol{e}}_{\boldsymbol{n}}$ is a unit vector perpendicular to the boundary, and B_1, B_2, B_3 are different portions of the boundary B such that $B=B_1 \cup B_2 \cup B_3$. The values of the imposed heat flux and temperature q_o, T_{b2}, T_{b3} on the boundaries are not necessarily constant but they are assumed independent of time. The initial conditions are expressed in the form

$$t = 0: T = T_o(\boldsymbol{X}) \tag{12}$$

3 Kirchhoff Transformation

The Kirchhoff transformation introduces a new dependent variable that has the following form [1,2]:

$$\theta = \frac{1}{k_o}\int_0^T k(f)\mathrm{d}f \tag{13}$$

where f is a dummy variable used for the integration of $k(T)$. One may obtain the following derivatives of θ by using the Leibnitz rule of differentiation under the integral sign:

$$\frac{\partial \theta}{\partial t} = \frac{k}{k_o}\frac{\partial T}{\partial t} \tag{14}$$

$$\nabla \theta = \frac{k}{k_o}\nabla\, T \tag{15}$$

and therefore, their substitution into Eq. (8) yields

$$\frac{1}{\alpha}\frac{\partial \theta}{\partial t} = \nabla^2 \theta + \frac{\dot{q}}{k_o} \tag{16}$$

which is a linear equation for the new variable $\theta(t,\boldsymbol{X})$ if $\alpha=k/\gamma \approx$ constant.

To demonstrate the application of the Kirchhoff transformation (13) to specific thermal diffusion problems, we use as examples the three thermal conductivity functions presented in Eqs. (5)–(7). While functional form (5) is very specific, Eqs. (6) and (7) represent the first and second order Taylor series approximations of any general function $k(T)$ around any reference value of temperature. By substituting Eq. (5) into Eq. (13) one obtains explicitly

$$\theta = \frac{1}{\sigma}[\exp(\sigma T) - 1] \tag{17}$$

leading to the following inverse transformation:

$$T = \frac{1}{\sigma}\ln(\sigma\theta + 1) \tag{18}$$

In this particular case of an exponential function for the thermal conductivity, the inverse transformation is a simple explicit function that allows a convenient way of converting the linear solution obtained in terms of $\theta(t,\boldsymbol{X})$ by solving the linear Eq. (16) subject to simply converted boundary and initial conditions (11) and (12). For any other functions, the inverse transformation is, however, more complicated. By substituting Eq. (6) into Eq. (13) it yields

$$\theta = T + \frac{\beta_k}{2}T^2 \tag{19}$$

and the inverse transformation is obtained as the solution of the quadratic algebraic equation

$$T^2 + \frac{2}{\beta_k}T - \frac{2}{\beta_k}\theta = 0 \tag{20}$$

leading to

$$T = \frac{1}{\beta_k}[-1 \pm \sqrt{1 + 2\beta_k\theta}] \tag{21}$$

It is convenient to select the positive root in Eq. (21) by choosing the positive sign in front of the square root if $\beta_k > 0$ and the negative sign if $\beta_k > 0$. In any case, Eq. (21) demonstrates the practical inconvenience related to the inverse transformation in the case of a linear approximation for the thermal conductivity function. The result gets even worse when a second order approximation as presented in Eq. (7) is employed. Substituting Eq. (7) into Eq. (13) yields the following explicit transformation:

$$\theta = \int_0^T (1 + \beta_1 f + \beta_2 f^2)\mathrm{d}f = T + \frac{\beta_1}{2}T^2 + \frac{\beta_2}{3}T^3 \tag{22}$$

and the inverse transformation is obtained as the solution of the cubic algebraic equation

$$T^3 + \frac{3}{2}\frac{\beta_1}{\beta_2}T^2 + \frac{3}{\beta_2}T - \frac{3}{\beta_2}\theta = 0 \tag{23}$$

Equation (23) has closed form analytical solutions that can be expressed more conveniently by using the notation

$$a_1 = \frac{3}{2}\frac{\beta_1}{\beta_2}; \quad a_2 = \frac{3}{\beta_2}; \quad a_3 = -\frac{3\theta}{\beta_2}$$

$$Q = \frac{3a_2 - a_1}{9}; \quad R = \frac{9a_1a_2 - 27a_3 - 2a_1^3}{54} \tag{24}$$

One real root is obtained if the discriminant

$$\Delta = Q^3 + R^2 \tag{25}$$

is positive, i.e., if $\Delta > 0$, and three real roots exist when the discriminant is negative $\Delta < 0$. When $\Delta > 0$, the real root has the form

$$T = S + P - \frac{1}{3}a_1 \tag{26}$$

where

$$S = [R + \Delta^{1/2}]^{1/3}; \quad P = [R - \Delta^{1/2}]^{1/3} \tag{27}$$

When $\Delta < 0$, the presentation is simplified by the use of trigonometry in the form

$$T_1 = 2\sqrt{-Q}\cos\left(\frac{\varphi}{3}\right) - \frac{1}{3}a_1 \tag{28}$$

where

$$\varphi = \cos^{-1}\left[\frac{R}{(-Q)^{3/2}}\right] \tag{29}$$

and the other two real roots are

$$T_2 = 2\sqrt{-Q}\cos\left(\frac{\varphi}{3} + \frac{2\pi}{3}\right) - \frac{1}{3}a_1 \tag{30}$$

and

$$T_3 = 2\sqrt{-Q}\cos\left(\frac{\varphi}{3} + \frac{4\pi}{3}\right) - \frac{1}{3}a_1 \tag{31}$$

Since the transformation $T \rightarrow \theta$ is unique, the inverse transformation $\theta \rightarrow T$ can be performed by using any of the roots, Eq. (28), (30), or (31), without loss of generality and therefore, the choice of Eq. (28) seems the most convenient. In any case, this demonstration just emphasizes the inconvenient form of the inverse transform when using the Kirchhoff transformation method for solving nonlinear thermal diffusion problems. This practical inconvenience is the result of expressing the transformation in terms of a definite integral as presented in Eq. (13). In the next section, we will show that Kirchhoff transformation is a consequence of the more general Cole–Hopf transformation and can be, therefore, presented in a less restrictive fashion so that the inverse transformation involving general thermal conductivity functions can be adjusted to more convenient practical forms.

4 Cole–Hopf Transformation

While one could apply the transformation straight on Eq. (8), a process that could be seen as a simpler approach, we selected to apply it to its equivalent form represented by Eq. (10) because the former may obscure the fact that we deal with a Cole–Hopf transformation while the latter makes the identification of the Cole–Hopf transformation more obvious. We are seeking a transformation of the form

$$T = f(\theta) \tag{32}$$

such that the nonlinear term that corresponds to $\nabla T \cdot \nabla T$ in Eq. (10) vanishes. By using Eq. (32), one may evaluate the derivatives applicable to Eq. (10) as follows:

$$\frac{\partial T}{\partial t} = f'\frac{\partial \theta}{\partial t}; \quad \nabla T = f'\nabla\theta; \quad \nabla T \cdot \nabla T = f'^2 \nabla\theta \cdot \nabla\theta;$$

$$\nabla^2 T = f'\nabla^2\theta + f''\nabla\theta \cdot \nabla\theta \tag{33}$$

where f' represents the derivative of f with respect to θ, i.e., $f' = \mathrm{d}f/\mathrm{d}\theta$ and $f'' = \mathrm{d}^2 f/\mathrm{d}\theta^2$. Substitution of Eq. (33) into Eq. (10) yields the following form:

$$\gamma(f)f'\frac{\partial\theta}{\partial t} = k(f)f'\nabla^2\theta + \underbrace{\left[k(f)f'' + \frac{\mathrm{d}k}{\mathrm{d}f}f'^2\right]}_{=0}(\nabla\theta\cdot\nabla\theta) + \dot{q} \tag{34}$$

The objective of the transformation is to set the square brackets in Eq. (34) equal to zero and therefore, causing the nonlinear term that includes $\nabla\theta\cdot\nabla\theta$ to become 0. The function $f(\theta)$ that provides such a property is obtained as the solution of the ordinary differential equation that results from imposing the condition that the square brackets in Eq. (34) be equal to 0, i.e.,

$$k(f)\frac{\mathrm{d}^2 f}{\mathrm{d}\theta^2} + \frac{\mathrm{d}k}{\mathrm{d}f}\left(\frac{\mathrm{d}f}{\mathrm{d}\theta}\right)^2 = 0 \tag{35}$$

that can be expressed in the following integrable form:

$$\frac{\mathrm{d}}{\mathrm{d}\theta}\left[k(f)\frac{\mathrm{d}f}{\mathrm{d}\theta}\right] = 0 \tag{36}$$

Integrating Eq. (36) yields

$$k(f)\frac{\mathrm{d}f}{\mathrm{d}\theta} = A \tag{37}$$

where A is the integration constant, implying that $k(f)f' = A$ and the coefficient to $\nabla^2\theta$ in Eq. (34) is a constant. Also from Eq. (37), we have $f' = A/k(f)$, which upon substitution into the first term in Eq. (34), and introducing the definition $\alpha = k/\gamma$ converts Eq. (34) into the following linear form if $\alpha \approx$ constant:

$$\frac{1}{\alpha}\frac{\partial\theta}{\partial t} = \nabla^2\theta + \frac{\dot{q}}{A} \tag{38}$$

To find the explicit transformation function, one needs to integrate Eq. (37) to yield

$$\int k(f)\mathrm{d}f = A\theta + C_o \tag{39}$$

which may be expressed explicitly as

$$\theta = \frac{1}{A}\int k(f)\mathrm{d}f + C_1 \tag{40}$$

We may already observe that Eq. (40) has a form similar to the Kirchhoff transformation (13) except that it is presented in terms of an indefinite integral. The integration constants A and C_1 are arbitrary constants (except that $A \neq 0$) as for any constants A and C_1 (except $A \neq 0$), Eq. (40) will cause the transformation of Eq. (34) into the linear Eq. (38). The choice

$$A = k_o \tag{41}$$

and

$$C_1 = -\frac{1}{k_o}\left[\int k(f)\mathrm{d}f\right]_{f=0} \tag{42}$$

reproduces accurately the Kirchhoff transformation (13) as follows:

$$\theta = \frac{1}{k_o}\left\{\left[\int k(f)\mathrm{d}f\right]_{f=T} - \left[\int k(f)\mathrm{d}f\right]_{f=0}\right\} = \frac{1}{k_o}\int_0^T k(f)\mathrm{d}f \tag{43}$$

However, this choice is arbitrary, not necessary and if avoided, it leaves the choice of the integration constants open to adjustment in such a way that for any given thermal conductivity function, the inverse transform (32) is a convenient function for practical evaluations. Note that Eq. (32) represents the inverse transform $\theta \rightarrow T$ while Eq. (40) represents the direct one $T \rightarrow \theta$. We will demonstrate the advantage of using the more general form expressed by Eq. (40) rather than the more restricted form expressed by the Kirchhoff transformations (13) and (43) in the next section.

The linear boundary and initial conditions formulated in Eqs. (11) and (12) for the nonlinear diffusion problem formulated in Eq. (8) or (10) yields linear boundary and initial conditions in the transformed space, i.e., when expressed in terms of θ, the boundary conditions can be expressed in the form

$$[\boldsymbol{q}\bullet\hat{\boldsymbol{e}}_{\boldsymbol{n}}]_{B_1} = [-k(T)\,\nabla T\bullet\hat{\boldsymbol{e}}_{\boldsymbol{n}}]_{B_1} = q_o$$
$$\Rightarrow [-k(f)f'\,\nabla\theta\bullet\hat{\boldsymbol{e}}_{\boldsymbol{n}}]_{B_1} = q_o \underbrace{\Rightarrow}_{(37)} [-A\,\nabla\theta\bullet\hat{\boldsymbol{e}}_{\boldsymbol{n}}]_{B_1} = q_o$$

leading to

$$[\nabla\theta\bullet\hat{\boldsymbol{e}}_{\boldsymbol{n}}]_{B_1} = -\frac{q_o}{A} \tag{44}$$

and

$$[T]_{B_2} = T_{b2} \Rightarrow [\theta]_{B_2} = f^{-1}(T_{b2}); \quad [T]_{B_3} = T_{b3} \Rightarrow [\theta]_{B_3} = f^{-1}(T_{b3}) \tag{45}$$

where $f^{-1}(\bullet)$ is the direct transform (40) applied to the boundary conditions in the form

$$[\theta]_{B_2} = \frac{1}{A}\left[\int k(f)\mathrm{d}f\right]_{B_2} + C_1; \quad [\theta]_{B_3} = \frac{1}{A}\left[\int k(f)\mathrm{d}f\right]_{B_3} + C_1 \tag{46}$$

5 Practical Applications of the Cole–Hopf Transformation

To demonstrate the application of the Cole–Hopf transformation (40) to specific thermal diffusion problems, we use as examples the same three thermal conductivity functions presented in Eqs. (5)–(7). While the functional form (5) is very specific, Eqs. (6) and (7) represent the first and second order Taylor series approximations of any general function $k(T)$ around any reference value of temperature. For the exponential function by substituting of Eq. (5) into Eq. (40), one obtains explicitly

$$\theta = \frac{k_o}{A}\int \exp(\sigma f)\mathrm{d}f + C_1 = \frac{k_o}{\sigma A}\exp(\sigma T) + C_1 \tag{47}$$

The inverse transform takes, therefore, the form

$$T = \frac{1}{\sigma}\ln\left[\frac{\sigma A}{k_o}(\theta - C_1)\right] \tag{48}$$

In Kirchhoff's transformation, the choice of the constants for this case is $A = k_o$ and $C_1 = -1/\sigma$, leading to the result presented in Eq. (18). As the choice of the integration constants A and C_1 is arbitrary, we can make the following more convenient choice $C_1 = 0$ and $A = k_o/\sigma$ such that the direct transformation (47) becomes:

$$\theta = \exp(\sigma T) \tag{49}$$

and the inverse transform (48) becomes

$$T = \frac{1}{\sigma}\ln\theta \tag{50}$$

leading to an inverse transform slightly simpler than in the Kirchhoff transformation (18). The major difference is revealed in the next two applications.

By using the linear thermal conductivity function (6) into Eq. (40), it yields

$$\theta = \frac{k_o}{A}\left[T + \frac{\beta_k}{2}T^2\right] + C_1 \tag{51}$$

and the inverse transform is the solution to the algebraic quadratic equation

$$T^2 + \frac{2}{\beta_k}T + \frac{2A(C_1 - \theta)}{k_o\beta_k} = 0 \tag{52}$$

producing the following roots:

$$T = \frac{1}{\beta_k}\left[-1 \pm \sqrt{1 + \frac{2A(\theta - C_1)\beta_k}{k_o}}\right]$$
$$= \frac{1}{\beta_k}\left[-1 \pm \sqrt{\frac{2A\beta_k\theta + k_o - 2AC_1\beta_k}{k_o}}\right] \tag{53}$$

In principle, we are at the same point that we have been with the Kirchhoff inverse transform with this linear function of thermal conductivity. The distinction is that this time, we have the flexibility to adjust the values of the integration constants to our advantage and in this case, the choice that simplifies the square root in Eq. (53), i.e., $A = k_o/2\beta_k$ and $C_1 = k_o/2\beta_k A = 1$ leading upon substitution into Eq. (53)

$$T = \frac{1}{\beta_k}(\pm\sqrt{\theta} - 1) \tag{54}$$

where one may choose the positive sign when $\beta_k > 0$ and the negative sign when $\beta_k < 0$. The direct transform applicable is obtained by substituting of the selected values of the integration constants $A = k_o/2\beta_k$ and $C_1 = k_o/2\beta_k A = 1$ into Eq. (51)

$$\theta = \beta_k^2\left[T^2 + \frac{2}{\beta_k}T\right] + 1 \tag{55}$$

The inverse transform (54) has certainly a simpler and more convenient form than its corresponding Kirchhoff inverse transform represented by Eq. (21). The linear transformed equation for this choice of constants substituted into Eq. (38) takes the following explicit form:

$$\frac{1}{\alpha}\frac{\partial\theta}{\partial t} = \nabla^2\theta + \frac{2\beta_k}{k_o}\dot{q} \tag{56}$$

and the linear boundary and initial conditions formulated in Eqs. (11) and (12) for the nonlinear diffusion problem formulated in Eq. (8) or (10) yield linear boundary and initial conditions in the transformed space, i.e., when expressed in terms of θ, the boundary conditions have the form obtained from Eqs. (44) and (46)

$$[\nabla\theta\bullet\hat{\boldsymbol{e}}_{\boldsymbol{n}}]_{B_1} = -\frac{2\beta_k}{k_o}q_o \tag{57}$$

$$[\theta]_{B_2} = 2\beta_k\left[T_{b2} + \frac{\beta_k}{2}T_{b2}^2\right]; \quad [\theta]_{B_3} = 2\beta_k\left[T_{b3} + \frac{\beta_k}{2}T_{b3}^2\right] \tag{58}$$

The application of the quadratic thermal conductivity function produces even more impressive results. By using the quadratic thermal conductivity function (7) into Eq. (40), it yields

$$\theta = \frac{k_o}{A}\left[T + \frac{\beta_1}{2}T^2 + \frac{\beta_2}{3}T^3\right] + C_1 \tag{59}$$

and the inverse transform is obtained as the solution of the cubic algebraic equation

$$T^3 + \frac{3\beta_1}{2\beta_2}T^2 + \frac{3}{\beta_2}T + \frac{3A}{k_o\beta_2}(C_1 - \theta) = 0 \tag{60}$$

Equation (60) has closed form analytical solutions that can be expressed more conveniently by using the notation

$$a_1 = \frac{3}{2}\frac{\beta_1}{\beta_2}; \quad a_2 = \frac{3}{\beta_2}; \quad a_3 = \frac{3A}{k_o\beta_2}(C_1 - \theta)$$

$$Q = \frac{3a_2 - a_1}{9}; \quad R = \frac{9a_1a_2 - 27a_3 - 2a_1^3}{54} \tag{61}$$

One real root is obtained if the discriminant

$$\Delta = Q^3 + R^2 \tag{62}$$

is positive, i.e., if $\Delta > 0$, and three real roots exist when the discriminant is negative $\Delta < 0$. When $\Delta > 0$, the real root has the form

$$T = S + P - \frac{1}{3}a_1 \tag{63}$$

where

$$S = [R + \Delta^{1/2}]^{1/3}; \quad P = [R - \Delta^{1/2}]^{1/3} \tag{64}$$

When $\Delta < 0$, the presentation is simplified by the use of trigonometry in the form

$$T_1 = 2\sqrt{-Q}\cos\left(\frac{\varphi}{3}\right) - \frac{1}{3}a_1 \tag{65}$$

where

$$\varphi = \cos^{-1}\left[\frac{R}{(-Q)^{3/2}}\right] \tag{66}$$

and the other two real roots are

$$T_2 = 2\sqrt{-Q}\cos\left(\frac{\varphi}{3} + \frac{2\pi}{3}\right) - \frac{1}{3}a_1 \tag{67}$$

and

$$T_3 = 2\sqrt{-Q}\cos\left(\frac{\varphi}{3} + \frac{4\pi}{3}\right) - \frac{1}{3}a_1 \tag{68}$$

Evaluating Q, R, Δ, S, and P yields

$$Q = \frac{(4\beta_2 - \beta_1^2)}{4\beta_2^2}; \quad R = \frac{3A}{2k_o\beta_2}\theta + \underbrace{\left(\frac{3\beta_1}{2\beta_2^2} - \frac{\beta_1^3}{8\beta_2^3} - \frac{3A}{2k_o\beta_2}C_1\right)}_{=0} \tag{69}$$

and we can chose the value of C_1 such that the brackets in the expression for R in Eq. (69) becomes 0, hence

$$R = \frac{3A}{2k_o\beta_2}\theta \tag{70}$$

and we can chose A such that

$$R^2 = Q^3\theta^2 \tag{71}$$

and therefore

$$\Delta = Q^3 + R^2 = Q^3(1 + \theta^2) \tag{72}$$

The values of C_1 and A, which lead to these simplifications, are

$$A = \frac{2k_o\beta_2}{3}Q^{3/2}; \quad A = \frac{2k_o\beta_2}{3}Q^{3/2} \tag{73}$$

The only real root then is obtained from Eqs. (64) and (63)

$$T = Q^{1/2}\{[\theta + (1 + \theta^2)^{1/2}]^{1/3} + [\theta - (1 + \theta^2)^{1/2}]^{1/3}\} - \frac{1}{2}\frac{\beta_1}{\beta_2} \tag{74}$$

with the value of Q given explicitly by the first expression in Eq. (69). This inverse transformation, although not completely simple, is yet manageable as distinct from the corresponding inverse transform in the Kirchhoff transformation where the choice of $A = k_o$ and $C_1 = 0$ resulted in such a complicated inverse transform that we even avoided presenting its lengthy expression explicitly. This present inverse transform (74) applies to the case when $\Delta > 0$. The latter implies by using Eq. (72) that $Q^3 > 0 \Rightarrow Q > 0$. From the definition of Q in Eq. (69), this condition means $\beta_2 > \beta_1^2/4$. In the opposite case, when $\Delta < 0 \Rightarrow Q < 0 \Rightarrow \beta_2 < \beta_1^2/4$, the choice

$$A = \frac{2k_o\beta_2}{3}(-Q)^{3/2}; \quad C_1 = (-Q)^{-3/2}\left(\frac{3\beta_1}{2\beta_2^2} - \frac{\beta_1^3}{8\beta_2^3}\right) \tag{75}$$

such that

$$R^2 = (-Q)^3\theta^2 \tag{76}$$

is the appropriate simplification leading to the real solutions

$$T_1 = 2\sqrt{-Q}\cos\left(\frac{\varphi}{3}\right) - \frac{1}{2}\frac{\beta_1}{\beta_2} \tag{77}$$

where the phase angle is related to the known linear solution θ in the simple form

$$\varphi = \cos^{-1}\theta \tag{78}$$

and the other two real roots are

$$T_2 = 2\sqrt{-Q}\cos\left(\frac{\varphi}{3} + \frac{2\pi}{3}\right) - \frac{1}{2}\frac{\beta_1}{\beta_2} \tag{79}$$

and

$$T_3 = 2\sqrt{-Q}\cos\left(\frac{\varphi}{3} + \frac{4\pi}{3}\right) - \frac{1}{2}\frac{\beta_1}{\beta_2} \tag{80}$$

Since the transformation $T \rightarrow \theta$ is unique, the inverse transformation $\theta \rightarrow T$ can be performed by using any of the roots (77) and (79), or (80) without loss of generality and therefore, the choice of using Eq. (77) seems the most convenient. Again, this inverse transformation (77) and (78) although not entirely simple, is yet manageable as distinct from the corresponding inverse transform in the Kirchhoff transformation. The linear transformed equation for this choice of constants substituted into Eq. (38) takes the following explicit form:

$$\frac{1}{\alpha}\frac{\partial\theta}{\partial t} = \nabla^2\theta + \frac{3}{2k_o\beta_2\xi}\dot{q} \tag{81}$$

where $\xi = Q^{3/2}$ $\forall \Delta > 0$, i.e., $\forall \beta_2 > \beta_1^2/4$, and $\xi = (-Q)^{3/2}$ $\forall \Delta < 0$, i.e., $\forall \beta_2 < \beta_1^2/4$. The linear boundary conditions expressed in terms of θ have the form obtained from Eqs. (44) and (46)

$$[\nabla\theta \cdot \hat{\boldsymbol{e}}_n]_{B_1} = -\frac{3}{2k_o\beta_2\xi}q_o \tag{82}$$

$$[\theta]_{B_2} = \frac{3}{2\beta_2\xi}\left[T_{b2} + \frac{\beta_1}{2}T_{b2}^2 + \frac{\beta_2}{3}T_{b2}^3\right]$$

$$[\theta]_{B_2} = \frac{3}{2\beta_2 \xi}\left[T_{b3} + \frac{\beta_1}{2}T_{b3}^2 + \frac{\beta_2}{3}T_{b3}^3\right] \tag{83}$$

These examples of practical applications of the Cole–Hopf transformation reflect its simplicity as compared with the Kirchhoff transformation.

Further effort is needed in developing a way of applying the same method for the experimental evaluation of the thermal conductivity in cases when the latter is not constant but rather a function of temperature. The "transient hot wire" experimental method for evaluating experimentally the thermal conductivity of solids and fluids, as well as other similar experimental methods, are excellent methods for cases of constant thermal conductivities. They do not apply to cases of temperature dependent thermal conductivities. Furthermore, the applicability of the latter to two-phase and composite materials as suggested by Vadasz [11] needs also further exploration in cases where the thermal conductivity is temperature dependent.

6 Conclusions

The classical Kirchhoff transformation that is useful in producing analytical solutions to the nonlinear heat conduction problem with temperature dependent properties was shown to be a particular case of the more general Cole–Hopf transformation. The latter result was shown to have significant implications in the practical convenience of solving such problems because the formulation of Kirchhoff's transformation is too restrictive while the use of the more general result obtained from the Cole–Hopf transformation in terms of an indefinite integral allows the adjustment of the transform via the arbitrary choice of their integration constant. Such a choice can then be tuned to the most convenient and desirable form of the inverse transform, hence, simplifying the results and their practical evaluation.

References

[1] Ozisik, M. N., 2002, *Boundary Value Problems of Heat Conduction*, Dover, New York, p. 353.

[2] Carslaw, H. S., and Jaeger, J. C., 1959, *Conduction of Heat in Solids*, 2nd ed., Oxford University Press, Oxford, UK, pp. 10–11.

[3] Viskanta, R., 2009, "Overview of Radiative Transfer in Cellular Porous Materials," *Proceedings of the ASME 2009 Heat Transfer Summer Conference*, San Francisco, CA, Jul. 19–23.

[4] Kuznetsov, A. V., and Nield, D. A., 2009, "The Cheng–Minkowycz Problem for Cellular Porous Materials: Effect of Temperature Dependent Conductivity Arising From Radiative Transfer," Int. J. Heat Mass Transfer, **53**(13-14), pp. 2676–2679.

[5] Cheng, P., and Minkowycz, W. J., 1977, "Free Convection About a Vertical Plate Embedded in a Porous Medium With Application to Heat Transfer From a Dike," J. Geophys. Res., **82**(14), pp. 2040–2044.

[6] Nield, D. A., and Kuznetsov, A. V., 2009, "The Onset of Convection in a Layer of Cellular Porous Material: Effect of Temperature-Dependent Conductivity Arising From Radiative Transfer," J. Heat Transfer, **132**(7), pp. 074503.

[7] Nield, D. A., and Kuznetsov, A. V., 2009, "Forced Convection in Cellular Porous Materials: Effect of Temperature-Dependent Conductivity Arising From Radiative Transfer," Int. J. Heat Mass Transfer, **53**(13-14), pp. 2680–2684.

[8] Knight, J. H., and Philip, J. R., 1974, "Exact Solutions in Nonlinear Diffusion," J. Eng. Math., **8**(3), pp. 219–227.

[9] Bonani, F., and Ghione, G., 1995, "On the Application of the Kirchhoff Transformation to the Steady State Thermal Analysis of Semiconductor Devices With Temperature Dependent and Piecewise Inhomogeneous Thermal Conductivity," Solid-State Electron., **38**(7), pp. 1409–1412.

[10] Whitham, G. B., 1999, *Linear and Nonlinear Waves*, Wiley, New York.

[11] Vadasz, P., 2010, "Rendering the Transient Hot Wire Experimental Method for Thermal Conductivity Estimation to Two-Phase Systems—Theoretical Leading Order Results," ASME J. Heat Transfer, **132**(8), p. 081601.

Measurement of Entropy Generation in Microscale Thermal-Fluid Systems

Meghdad Saffaripour
Research Assistant
e-mail: msaffari@engmail.uwaterloo.ca

Richard Culham
Professor
e-mail: rix@mhtlab.uwaterloo.ca

Department of Mechanical and Mechatronics Engineering,
Microelectronics Heat Transfer Laboratory,
University of Waterloo,
Waterloo, ON, N2L 3G1, Canada

A new nonintrusive and whole field method for the measurement of entropy generation in microscale thermal-fluid devices is presented. The rate of entropy generation is a measure of the thermodynamic losses or irreversibilities associated with viscous effects and heat transfer in thermal-fluid systems. This method provides the entropy generation distribution in the device, thus enabling the designers to find and modify the areas producing high energy losses characterized by large entropy production rates. The entropy generation map is obtained by postprocessing the velocity and temperature distribution data, measured by micro particle image velocimetry and laser induced fluorescence methods, respectively. The velocity and temperature measurements lead to the frictional and thermal terms of entropy generation. One main application of this method is optimizing the efficiency of microchannel heatsinks, used in cooling of electronic devices. The minimum amount of entropy generation determines the optimum design parameters of heatsinks, leading to highest heat removal rates and at the same time, the lowest pressure drop across the heatsink. To show the capability of this technique, the entropy generation field in the transition region between a 100 μm wide and a 200 μm wide rectangular microchannel is measured. This method is used to measure thermal and frictional entropy generation rates in three different flow area transition geometries. The results can be used to determine which geometry has the highest thermal and hydraulic efficiencies. [DOI: 10.1115/1.4002026]

Keywords: microscale thermal-fluid systems, microchannel heatsinks, entropy generation measurement

1 Introduction

An increase in the functional power and the feature density of integrated circuits is accompanied by a steady increase in the dissipative heat generation of these devices, driving the demand for novel thermal management technologies. The power dissipation of high performance computer processors is predicted to rise from 90 W in 1999 to 198 W in 2022 [1,2]. Assuming the ideal processor temperature to be 85°C and the ambient temperature to be 45°C, the thermal resistance to the ambient would need to decrease from 0.44°C/W to 0.20°C/W, i.e., more than a two fold decrease. Similarly, it is anticipated that the heat dissipation of low-cost processors for personal computers will increase from 111 W in 2008 to 151 W in 2022, which translates into a thermal resistance decrease from 0.36°C/W to 0.26°C/W. This sharp increase in power dissipation necessitates the development of innovative cooling methods. One such novel technology is forced convection microchannel liquid cooling. This method was first introduced in Ref. [3] in 1981 and succeeded in dissipating 790 W/cm^2 from a chip, with a maximum thermal resistance of 0.09°C/W. This method provides a more efficient and more compact arrangement than conventional air cooling methods due to the higher wetted surface area to volume ratio in microchannels as well as higher thermal conductivity and specific heat of liquids compared with air.

The generally laminar nature of flow in microchannel heatsinks implies that the Nusselt number is inversely proportional to channel's hydraulic diameter. Consequently, by scaling down the cross-sectional size of the microchannels, higher heat removal rates are achieved. However, the huge rise in pressure drop across the heatsink, caused by fluid friction, limits the minimization process. Increasing the heat transfer rate and minimizing the pressure drop at the same time is crucial in optimizing the performance of cooling devices.

The performance of thermal-fluid systems is degraded due to flow irreversibilities. In microchannel heatsinks, the irreversibilities cause irreversible conversion of available energy into internal energy, thus lowering the cooling capability of the flow. Irreversibilities also diminish the operating efficiency of microchannel heatsinks by increasing the pressure difference required to transport the fluid into the channels. The two most common sources of flow irreversibilities in thermal systems are heat transfer across a finite temperature difference and fluid friction [4].

Entropy generation is used in thermodynamics as an indicator to quantify the significance of irreversibilities. Entropy production characterizes the extent of the dissipation of mechanical energy into internal energy and includes both thermal and frictional irreversibilities. The second law of thermodynamics provides a general and unique way of optimizing the design of thermal-fluid devices both thermally and hydrodynamically through minimizing the sum of thermal and frictional entropy generation terms. A set of optimal operating and design conditions is obtained that minimizes the irreversibilities in the system.

Only a few studies attempted the simultaneous thermal and hydraulic optimization of microchannel heatsinks, and other microscale systems, by minimizing the entropy generation. Khan et al. [5] developed general expressions for the entropy generation rate in microchannel heatsinks and optimized the overall performance of the device analytically, using an entropy generation minimization procedure. They studied the effect of Knudsen number, flow rate, channel aspect ratio, and accommodation coefficient on the efficiency in the slip flow regime. Abbassi [6] analyzed the entropy generation in uniformly heated microchannel heatsinks ana-

Contributed by the Heat Transfer Division of ASME for publication in the JOURNAL OF HEAT TRANSFER. Manuscript received January 1, 2009; final manuscript received May 22, 2010; published online September 17, 2010. Assoc. Editor: Kenneth Goodson.

lytically, based on a porous medium model. The effect of aspect ratio, Brinkman number, thermal conductivity, and channel porosity on the local and average entropy production rates and heatsink performance is investigated. Chen [7] studied the entropy generation and transfer in microchannels for different thermal boundary conditions, neglecting the lateral temperature and velocity gradients. They found that the local entropy production rates only depend on temperature gradients in the flow direction. Erbay et al. [8] numerically studied the entropy generation during laminar transient forced convection in the combined entrance region of parallel plate microchannels. The effect of moving the bottom plate and other flow parameters were investigated. Hooman [9] presented closed form solutions for the entropy generation due to forced convection in parallel plate microchannels and micropipes, taking into account the effect of temperature jump and velocity slip near the walls. Ogedengbe et al. [10] numerically investigated the effect of velocity slip on fluid motion and the dissipative kinetic to internal energy exchange in microchannels, using the finite volume method.

2 Method

To analytically optimize the second law efficiency of a thermal system, functional expressions for the entropy generation in the system should be developed and minimized by the methods of differential calculus. This approach is limited only to simple geometries. The numerical analysis involves the development of reliable and accurate numerical models and solution algorithms. Experimental methods for the measurement of local entropy generation values are required to validate the numerical predictions. Previous entropy generation measurement methods could detect the losses globally by measuring the pressure drop and heat transfer across the microchannels and represented it by a loss coefficient.

This work presents a new nonintrusive and whole field method for the measurement of local entropy generation rates in microscale flows. This method provides the designers with a map of entropy generation distribution within the device, thereby allowing them to locate and redesign the areas with high irreversibility, characterized by large entropy generation rates, to improve the overall performance of the device. As microscale thermofluid devices become more complex, employing such measurement methods is necessary to achieve the theoretical upper limits of device efficiency.

The experimental method described here involves the application of micro particle image velocimetry (PIV) and micro laser induced fluorescence (LIF) techniques for measuring velocity and temperature distribution within a device. Entropy generation is a function of velocity and temperature gradients; thus it can be calculated by postprocessing the PIV and LIF data.

The method for the measurement of local entropy generation rates from the velocity and temperature data was first introduced by Adeyinka and Naterer [11]. Their procedure combines particle image velocimetry and planar laser induced fluorescence methods to determine the velocity and temperature distributions in the laminar natural convection flow of water within a $39\times39\times59$ mm^3 cavity. By postprocessing the results, spatial gradients of velocity and temperature are found that constitute the frictional and thermal entropy generation terms, respectively. They have reported the results for the velocity and frictional entropy generation rates only, without considering the heat transfer term of entropy generation. The local entropy generation rates have also been determined numerically, using a finite element formulation. There is excellent agreement between the predicted and measured results. In another work [12], Naterer and Adeyinka employed this technique to measure the instantaneous entropy generation rate in a $60\times60\times60$ mm^3 magnetic stirrer rotating at 90 rpm. Particle image velocimetry is used to find the velocity gradients, leading to the frictional entropy generation term.

By applying the second law of thermodynamics to an infinitesimal Cartesian control volume in a two-dimensional flow field, we can develop the following expression for the rate of entropy production per unit volume [4]:

$$\dot{S}_g''' = \frac{1}{T}\nabla\cdot\mathbf{q} - \frac{1}{T^2}\mathbf{q}\cdot\nabla T + \rho\frac{Ds}{Dt} \tag{1}$$

where $\dot{S}_g'''$ is the volumetric rate of entropy generation, $\mathbf{q}$ is the vectorial heat transfer rate, T is the local fluid temperature, s is the specific entropy, and ρ is the local fluid density. Using the conservation of energy principal, Fourier's law of heat conduction, and Gibbs equation, we obtain the volumetric rate of entropy generation in terms of measurable quantities, namely, velocity and temperature,

$$\dot{S}_g''' = \frac{2\mu}{T}\left\{\left[\left(\frac{\partial u}{\partial x}\right)^2+\left(\frac{\partial v}{\partial y}\right)^2\right]+\frac{1}{2}\left(\frac{\partial u}{\partial y}+\frac{\partial v}{\partial x}\right)^2\right\}+\frac{k}{T^2}\left[\left(\frac{\partial T}{\partial x}\right)^2+\left(\frac{\partial T}{\partial y}\right)^2\right] \tag{2}$$

where u and v are velocity components in the x and y directions. The first term on the right represents the entropy generation due to frictional losses and the second term represents the entropy produced due to heat transfer. For irreversible processes such as heat transfer and viscous fluid flows, the second law of thermodynamics dictates that the entropy generation rate is positive because mechanical energy is irreversibly being converted to internal energy. The right side of the above equation is a sum of square terms and always positive; thus Eq. (2) is called the positive definite equation for entropy generation [11].

Local entropy generation rates are measured indirectly, based on the above formulations, using the micro-PIV and LIF methods. The measured velocity and temperature data are displayed by the software over a discrete grid. The local entropy generation rates are determined by spatial differencing Eq. (2) over the discrete grid and substituting values measured by the PIV and LIF for velocity components and local temperatures. The discretized representation of Eq. (2) is

$$\dot{S}_{gati,j}''' = \frac{k}{T_{i,j}^2}\left[\left(\frac{T_{i+1}-T_{i-1}}{\Delta x}\right)^2+\left(\frac{T_{j+1}-T_{j-1}}{\Delta y}\right)^2\right]+\frac{2\mu}{T_{i,j}}\left[\left(\frac{u_{i+1}-u_{i-1}}{\Delta x}\right)^2+\left(\frac{v_{j+1}-v_{j-1}}{\Delta y}\right)^2+\frac{1}{2}\left(\frac{u_{j+1}-u_{j-1}}{\Delta y}+\frac{v_{i+1}-v_{i-1}}{\Delta x}\right)^2\right] \tag{3}$$

3 Experimental Procedure

Micron resolution particle image velocimetry was created by Santiago et al. [13] in 1998 to measure the instantaneous velocity distribution in microfluidic devices. Due to the lack of optical access and significant diffraction, generating a light sheet to illuminate microscale flows is not possible as in large systems. Therefore, they developed a volume illumination approach, in which the images of the particles within the depth of field of the objective, as well as the image of the out of focus particles, are recorded by the camera. The high level of background noise produced by the out of focus particles, along with the very low intensity of the reflected light from submicron particles, put significant constraints on recording optics and processing algorithms.

The schematic of a Micro-PIV system is presented in Fig. 1. The illumination source is a two cavity new wave neodymium-doped yttrium aluminum garnet (Nd:YAG) laser, which generates 532 nm green light at 30 mJ/pulse. The illumination light is delivered to an inverted Nikon-TE2000E microscope via a liquid filled light guide. A Nikon plan fluor objective with a magnification of 10 and a numerical aperture of 0.3 is used for the mea-

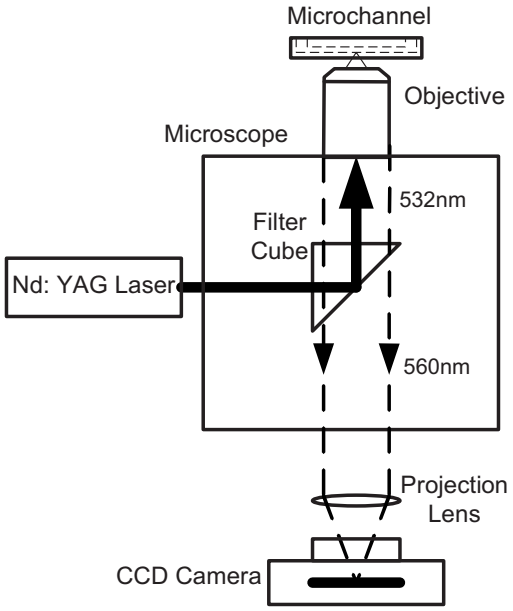

Fig. 1 Schematic of a micro-PIV system

surements. The required working distance, field of view, and resolution, as well as the size of the seeding particles, are the parameters that determine the power and type of the objective. Red fluorescent particles from Duke Scientific (Waltham, MA) with a diameter of 500 nm are used to seed the flow. The particles absorb the 532 nm illumination light and emit at a wavelength of 560 nm. The reflected light goes through a set of optical filters to separate the light reflected by the particles at 560 nm from the light reflected by the microchannel walls at 532 nm. A 14-10 PIVCAM camera from TSI (Shoreview, MN) with a charge-coupled device (CCD) size of 1376 pixels $\times$ 1040 pixels and a pixel size of 6.45 μm, along with a 2$\times$ projection lens, is used for image recording. A computer controlled synchronizer coordinates the timing of laser pulses and camera frames. The timing parameters are set so that the camera captures two singly exposed images. As a rule of thumb, pulse separation, i.e., the delay between the two exposures, is set such that the particle displacements are roughly 1/4 of the interrogation area size. Pulse separation is the key parameter in matching the flow velocity with the system and in this work varies from 5.5 μs to 20 μs for flow rates of 500 μl/min and 100 μl/min. The image is divided into 32 pixel $\times$ 32 pixel uniformly spaced interrogation areas with 50% overlap, resulting in a vector spacing of approximately 5 μm. A minimum intensity image, which is an estimate of the background light level, is constituted from over 500 images taken in each acquisition and subtracted from the images to increase the signal to noise ratio. The PIV images are processed using the INSIGHT-3G software, from TSI, by a fast Fourier transform cross-correlation technique.

Laser induced fluorescence is a laser-based nonintrusive method for the measurement of temperature (or other scalar quantities). The working fluid is mixed with a dye whose fluorescent intensity is proportional to its temperature, Rhodamine B in this work. Rhodamine B molecules are excited to a higher energy state by the 532 nm laser light. To return to the ground state, the molecules emit photons at a wavelength of 570 nm. The optical filters installed within the microscope block the illumination light reflected on the microchannel walls and let only the fluorescent reflection of Rhodamine B to reach the camera, with the same mechanism as in Micro-PIV. There are two major obstacles to implementing the LIF method at the microscale. The first one is the adverse effect of volume illumination and the second one is the very short timescales of thermal transport in microscale, which makes the instantaneous measurements by continuous lasers impossible [14].

The fluorescent emission intensity of Rhodamine B is a function of the intensity of the excitation light, I_0, concentration of the dye, C, molecular absorptivity, α, and temperature dependant quantum efficiency, $\phi(T)$, by the following relationship:

$$I = I_0 C \alpha \phi(T) \tag{4}$$

For a fixed concentration and illumination intensity, the quantum efficiency decreases with rising temperature. This dependence of quantum efficiency on temperature is the basis of LIF measurements.

Ross et al. [15] successfully used the above method, referred to as single-dye LIF method, to measure the temperature distribution resulted by Joule heating in various electrokinetically pumped microfluidic circuits. In fused silica capillary tubes and straight acrylic microchannels, the precision of their results ranges from 0.03°C near room temperature to 0.07°C at 85°C. A 1 cm long microchannel with a series of 14 constrictions was also examined and the reported precision is 2.4°C near room temperature and 3.5°C at high temperatures.

Although keeping a constant dye concentration is feasible, maintaining a stable and uniform illumination light is not achievable. In practice, the fluorescent intensity of the dye includes the effect of variations in illumination as well as variations in temperature. Thereby, the accuracy of the single-dye LIF is limited by the uniformity and stability of the laser light source. To overcome this problem, Sakakibara et al. [16] suggested adding a second dye to the working fluid whose fluorescence has very little dependence on temperature. The fluorescent intensity of the temperature dependent dye includes the effect of temperature and illumination; however, the fluorescent intensity of the second dye embodies only the effect of illumination light variations. By normalizing the fluorescent intensity of the temperature dependent dye with that of the temperature independent dye, the effect of illumination nonuniformities can be removed. The ratio of the fluorescent emissions of the two dyes is

$$\frac{I_1}{I_2} = \frac{I_0 \phi_1 \varepsilon_1}{I_0 \phi_2 \varepsilon_2} \tag{5}$$

The above ratio is independent of the illumination light intensity but depends on temperature through ϕ_1/ϕ_2. Assuming that the two dyes fluoresce at different wavelengths with no overlap, their fluorescent intensities can be recorded by using two sets of filters and two cameras. For the case of an imperfect separation of the fluorescent emissions, see Ref. [14].

Natrajan et al. [14] implemented a two-color LIF technique to measure the one-dimensional, steady state temperature gradient in an array of seven parallel 25 μm wide and 100 μm deep microchannels located between two large constant temperature reservoirs. The mean value of the temperature measurements in ethanol are within $\pm$0.4°C of the predicted values with a standard deviation of $\pm$0.48–0.59°C. Kim et al. [17] used this method to measure temperature inside a 1 mm heated cuvette and achieved a rms fluctuation of $\pm$0.92°C from the numerical predictions.

The single-dye LIF method is used for the measurement of temperature in this work. The first step in performing LIF temperature measurements is calibration, i.e., correlating the fluorescent intensities with temperature. To perform the calibration, Rhodamine B solution at a fixed concentration is imaged at several known temperatures. Figure 2 shows the normalized intensities, averaged over 50 successive images, versus temperature along with a quadratic curve fit. The intensity at each point is obtained by averaging the intensity of all the pixels (1376 $\times$ 1040) in each image. To ensure repeatability, the calibration process was performed three times. The concentration of Rhodamine B is 0.1 mM, which provides a satisfactory gradient of

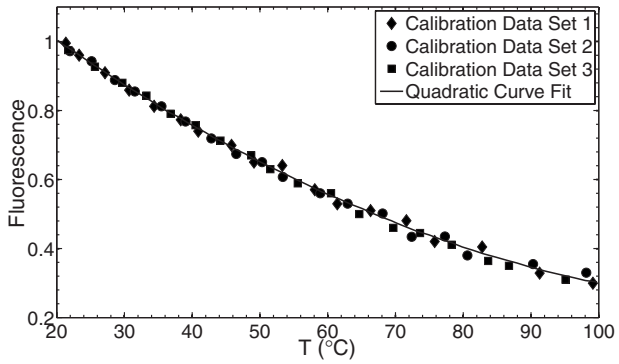

Fig. 2 LIF calibration curve

fluorescent intensity with temperature. Temperature and velocity fields were measured in separate sets of experiments, with a single camera and optical filter set.

To demonstrate the feasibility of this method, the entropy production rate at the transition between a wide and a narrow rectangular microchannel, with different transition geometries, is measured and some selected results are presented. The results of this study are useful to determine which expansion and contraction geometry has the highest thermal and hydraulic efficiency. Three geometries for the transition at the entrance and exit of the narrow channel have been selected in this study, namely, rectangular, triangular, and circular. The narrow channel is 100 μm wide and 2 cm long, located between 200 μm wide and 1 cm long channels to ensure parallel and disturbance free flow at the entrance to the narrow channel. The depth of the microchannels is 100 μm everywhere. A schematic of the microchannels under study in this work is sketched in Fig. 3.

A PHP-2000 Harvard Apparatus syringe pump provides a constant and accurate flow rate that ranges from 100 μl/min to 500 μl/min, resulting in average velocities of 0.17–0.83 m/s in the narrow channel. The Reynolds number, defined as $\mathrm{Re} = \rho \bar{U} D_{\mathrm{hyd}} / \mu$, is controlled by adjusting the volume flow rate and varies between 19.8 and 99.1, for water at room temperature. In this range of Reynolds number, the flow is essentially laminar and the hydrodynamic and thermal entrance lengths are 0.5 mm and 2.9 mm, respectively, at a flow rate of 500 μl/min.

Microchannels are etched in silicon using an ALCATEL-601E deep reactive ion etching system. This process allows the fabrication of high aspect ratio vertical trenches in a substrate. In ordinary etching techniques, the top of a trench is exposed to the etching ions for a longer time; therefore, the structures are wider on the top. On the contrary, deep reactive ion etching allows deep, high aspect ratio structures to be etched in silicon. An approach called alternate etching and chemical vapor deposition or Bosch process is undertaken in this work for the deep etching of the substrate, in which chemical vapor deposition is used to protect the side walls.

First, the areas to be etched are defined by coating the silicon wafer with a thin layer of photoresist, which is patterned by the photolithographically process. This process results in the photoresist being washed away from the areas to be etched and the rest of the wafer remains protected. Bosch process consists of two steps, etching and deposition. In the etching step which lasts for 7 s, the substrate is etched by a flow of SF_6 gas ions. In the deposition step, a 10 nm layer of fluorocarbon polymer is deposited on the trench walls by exposing the substrate to a flow of C_4F_8 for 3 s. In each etching step, the polymer film at the bottom of the trench and the silicon substrate are etched by the direct bombardment of ions, while the polymer film on the side walls protect it from being etched by the ions bouncing back from the bottom. The etch front advances into the substrate at a rate of 7 μm/min and the whole process takes about 15 min. The substrate is then diced into 1

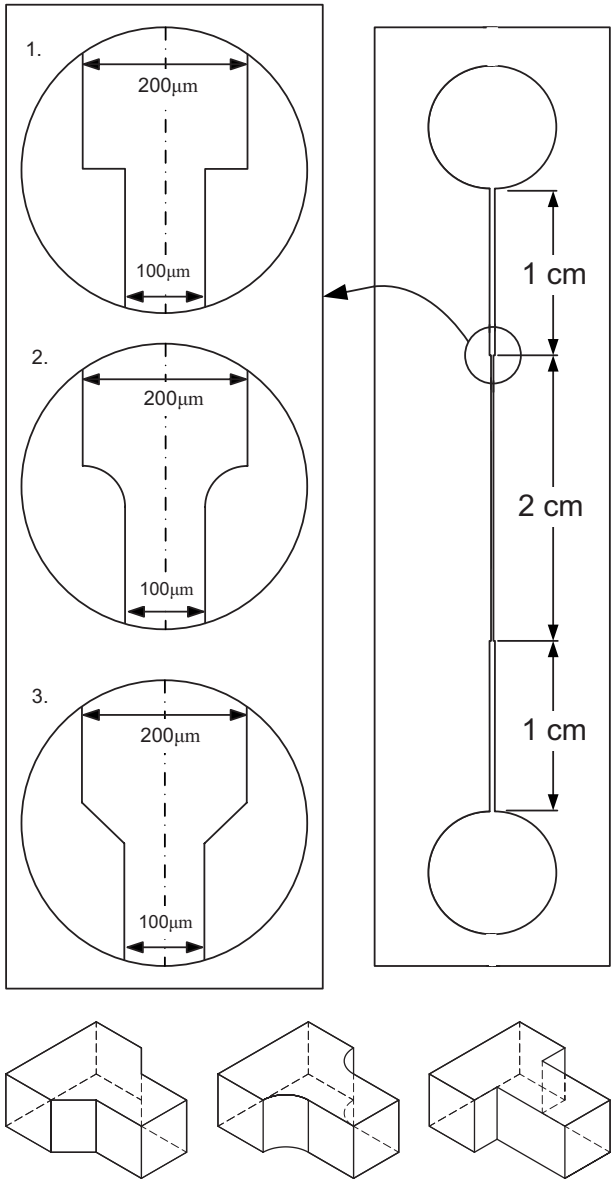

Fig. 3 (*a*) Schematic of the microchannels under study. (*b*) Three-dimensional schematic of the expansion/contraction geometries.

$\times 3$ in.^{2} (2.54×7.62 cm^2) specimens and through holes are drilled in the plenums for the fluid to enter and exit the devices. The next step is covering the structured silicon wafers with glass. SU-8 2015 negative-tone photoresist is used as an adhesive (see Ref. [18]). A 13 μm layer of SU-8 was spin coated on a 700 μm thick glass wafer in a two step process for a uniform thickness. One structured silicon slide is placed in the middle of the glass wafer and baked in an oven for 30 min at 150 °C without applying any external forces. The resultant bond is strong enough to tolerate the pressure inside the channel and no leakage was observed. It must be noted that SU-8 is completely transparent for wavelengths above 400 nm. Finally, the inlet and outlet ports, from Upchurch Scientific (Oak Harbor, WA), are attached on top of the holes drilled in the plenums.

A schematic of the measurement test setup is shown in Fig. 4. A flexible heater, from Minco (Minneapolis, MN), is attached on top of the silicon microchannels using a layer of thermal interface material, from Thermagon (Chesterfield, MO). The measurements are done under the constant surface temperature boundary condi-

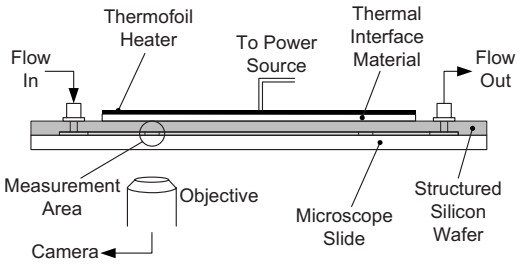

Fig. 4 Microfluidic assembly for PIV and LIF measurements

tion, at 90°C. The temperature on the side walls of the microchannel is expected to be uniform, due to the very small thickness and high conductivity of the silicon substrate. The temperature on the microchannel top surface is recorded using thermocouples placed between the thermal interface layer and the microchannel.

4 Uncertainty Analysis

Following a procedure used in Ref. [19], an uncertainty analysis in a fully developed region of the flow is performed to verify the accuracy of the technique. Because entropy generation is a postprocessed variable, the uncertainties of velocity and temperature measurements should be calculated first.

The total velocity measurement uncertainty is divided into a bias component, $\delta_{u,b}$, a calibration component, $\delta_{u,c}$, and a precision component, $\delta_{u,p}$.

At a fully developed flow section of the channels, local fluid velocities are reduced by $u=\Delta X/\Delta t$, where ΔX is the displacement vector in pixels calculated by the software, and Δt is the time interval between the two frames in seconds. The total bias uncertainty is related to the elementary bias uncertainties by the following expression:

$$\delta_{u,b}^2 = \eta_{\Delta X}^2 \delta_{\Delta X}^2 + \eta_{\Delta t}^2 \delta_{\Delta t}^2 \tag{6}$$

where $\delta_{u,b}$ is the bias uncertainty of velocity measurement due to detectability, $\delta_{\Delta X}$ is the uncertainty of particle displacement measurement by the PIV software, and $\delta_{\Delta t}$ is the uncertainty in the laser pulse separation reported by the manufacturer. The sensitivity coefficient, η_ϕ, is defined as $\partial u/\partial \phi$.

$\delta_{\Delta X}$ is equal to one-tenth of the effective particle image diameter [20], except very close to the side walls where particles do not faithfully follow the flow and the amount of light reaching the camera is small (see Refs. [21–23] for near-wall effects). The effective diameter of the recorded image of the particles can be estimated as the convolution of the point-spread function, originating from the diffraction of light in the objective, and the geometric image. Approximating these functions as Gaussian, the effective image diameter will be

$$d_e = \sqrt{(Md_p)^2 + d_s^2} \tag{7}$$

where M is the magnification of the objective, d_p is the diameter of the particles, and d_s is the diameter of the point-spread function estimated by the following relationship:

$$d_s = 2.44(M+1)f^{\#}\lambda \tag{8}$$

in which $f^{\#}$ is the f-number of the lens and λ is the wavelength of the light [20].

In this work, the diameter of the point-spread function is approximately 45.6 μm and the geometrical particle image diameter is 10 μm. Thus, the effective particle image diameter would be 46.7 μm in the image plane or 7.2 pixels. The cross-correlation peak can be detected by the software with an uncertainty of ± 4.67 μm in the image plane. Combining the contributions of displacement measurement and laser pulse separation errors result in a bias uncertainty of 1.6% at the center of the microchannel and 7.3% adjacent to the wall, in a flow rate of 500 μl/min. Percentage values are obtained by dividing the uncertainties by the velocities close to side walls or at the center of the channel.

Another source of error in the results is the calibration process. In order to convert the velocity results produced by the software in pixels/s to the velocity in m/s, we have to multiply the displacements in pixels by the length in the flow domain corresponding to a unit pixel in the image:

$$u = \frac{\Delta X}{\Delta t} \times \frac{L_{\text{flow}}}{L_{\text{image}}} \tag{9}$$

The ratio $L_{\text{flow}}/L_{\text{image}}$ is obtained by calibrating the system, using a microscope calibration ruler. L_{flow} is the distance between two lines on the calibration ruler in meters, and L_{image} is the length of the image of the same section of the ruler in pixels. There is some level of error associated with the calibration of the system. The accuracy of the ruler is reported as ± 2 μm over 150 mm. There is also an uncertainty of about ± 1 pixels in reading the image of the distances between the ruler lines in the software. The calibration error is evaluated as follows:

$$\delta_{u,c}^2 = \eta_{L_{\text{flow}}}^2 \delta_{L_{\text{flow}}}^2 + \eta_{L_{\text{image}}}^2 \delta_{L_{\text{image}}}^2 \tag{10}$$

where $\delta_{u,c}$ is the velocity measurement calibration error, $\delta_{L_{\text{flow}}}$ is the uncertainty in the distance between two lines on the ruler, and $\delta_{L_{\text{image}}}$ is the uncertainty in reading the image of the same distance in pixels. A calibration uncertainty of 3.1% is obtained by using this method.

Two sets of velocity measurements were performed, with 500 ensemble averaged image pairs in each acquisition. The precision uncertainty of the velocity measurement about an average velocity is [24]

$$\pm \frac{t_{\nu,P}\sigma_V}{\sqrt{M}} \tag{11}$$

where $t_{\nu,P}$ is a confidence coefficient called t-estimator at a probability of P%, ν is the degree of freedom (equal to number of measurements in each acquisition minus one), σ_V is the standard deviation, and M is the number of acquisition sets, 2 in this study.

The standard deviation of the measured velocities is defined as

$$\sigma_{V(x,y)} = \left(\frac{1}{N-1} \sum_{i=1}^{N} (V_i(x,y) - \overline{V}(x,y))^2 \right)^{1/2} \tag{12}$$

where N is the number of image pairs and $(\overline{V})$ is the velocity mean value given by

$$\overline{V}(x,y) = \frac{1}{N} \sum_{i=1}^{N} V_i(x,y) \tag{13}$$

The precision uncertainties within a 95% confidence interval are 0.6% and 0.8% at the point of maximum velocity and near the wall, respectively.

As mentioned in Sec. 3, the major drawback of the single-dye LIF method is its poor accuracy caused mainly by the nonhomogeneous and unstable illumination light as well as the high out of focus noise level due to volume illumination. In the following, an estimate of the uncertainties associated with the single-dye LIF method used in this work is provided.

The standard deviation of the calibration data from the quadratic curve fit is one source of uncertainty in the temperature field measurements. The highest standard deviations from the calibration curve are 5.5°C and 0.7°C at elevated temperatures and near room temperature, respectively. The calibration uncertainty in the temperature measurements is obtained by using Eq. (11) with $t_{\nu,P}=2.01$ for a 95% confidence interval, 50 data points, and $M=3$ for three sets of acquisitions [24]. The resulting uncertainty near the side walls is 6.4°C and at the center of the channel is 0.8°C.

The maximum standard deviation of the temperature field measurements near the side walls of the microchannel is about 7.0°C and at the center of the channel is 1.2°C. The precision uncertainty with $t_{\nu,P}=1.96$, 500 data point, and $M=2$ is 9.7°C and 1.7°C near the side walls and at the center, respectively.

An instrumental bias uncertainty of ±0.5°C is included to account for the thermocouple used to record the temperature of the microchannel substrate. An estimate of the total uncertainty in the temperature measurements can be obtained by taking the root of the sum of the squares of the elemental uncertainties, i.e., calibration, precision, and bias uncertainty terms [24]:

$$\delta_{u,T} = \pm \sqrt{u_c^2 + u_p^2 + u_b^2} \tag{14}$$

The resulting uncertainty near the side walls is 11.6°C and at the center of the channel is 1.9°C. An estimate of the percentage values of the uncertainties are 13% and 8%, obtained by dividing the uncertainty at the wall and at the center line by 90°C and 23°C, the temperatures of the microchannel substrate and centerline temperature at the inlet, respectively.

Based on the data reduction equation for entropy generation, Eq. (2), and neglecting the errors in reported viscosity and thermal conductivity of the water, the total uncertainty in the fully developed region of the flow becomes

$$\delta_{S_{\text{gen}}}^2 = \eta_T^2\delta_T^2 + \eta_{\Delta y}^2\delta_{\Delta y}^2 + \eta_{\Delta u}^2\delta_{\Delta u}^2 + \eta_{\Delta T}^2\delta_{\Delta T}^2 \tag{15}$$

The uncertainty in $\Delta u = u_{i+1} - u_{i-1}$ is defined as

$$\delta_{\Delta u}^2 = \eta_{u_{i+1}}^2\delta_{u_{i+1}}^2 + \eta_{u_{i-1}}^2\delta_{u_{i-1}}^2 \tag{16}$$

where

$$\eta_{u_{i+1}} = \frac{\partial(\Delta u)}{\partial u_{i+1}} = 1 \quad \text{and} \quad \eta_{u_{i-1}} = \frac{\partial(\Delta u)}{\partial u_{i-1}} = -1 \tag{17}$$

The uncertainties in ΔT and Δy are similarly calculated and substituted in Eq. (15). The uncertainties of the frictional entropy generation, determined by the above procedure and based on a 95% confidence interval, are 13.9% near the wall and 6.6% at the centerline. The uncertainties of the thermal entropy generation near the wall and at the centerline are 17.5% and 11.2%, respectively.

In this work, the thermal entropy generation rate is orders of magnitude larger than the frictional entropy generation rate. Therefore, the uncertainty of the frictional entropy generation is only a very small fraction of the total entropy generation uncertainty. Practical limitations, specifically leakage, did not allow increasing the flow rate to make the frictional and thermal components comparable.

5 Results

As stated earlier, entropy generation has two components: a frictional component caused by viscous dissipation within the fluid flow and a heat transfer component caused by the convection process in the flow between the high temperature side walls and the low temperature fluid stream. In this section, selected results of velocity measurements with micro-PIV and the frictional component of the entropy generation will be presented first. Next, the results of temperature measurements performed with micro-LIF will be used to determine the thermal entropy generation term. Summation of these two terms results in the total entropy generation. The measurement plane is located at the middle of the channel's height (see Fig. 5). The depth of the measurement volume, or the depth of correlation, is about 25.5 μm [25]. The measurements are averaged over this volume and considered as the result in the midplane of the channel. The general shape of the velocity and temperature profiles and their variations with flow rate are similar at different heights; hence the results at a certain height can qualitatively represent the results for the entire channel.

The measured velocity profiles in the flow direction, V, and normal to it, U, in a fully developed region of the microchannel is sketched and compared with the fully developed analytical profile [26] in Fig. 6. The measured profile is in excellent agreement with the analytical profile except very close to the walls (see Sec. 4). As expected, the normal velocities are nearly zero. The insignificant negative values of normal velocity are due to the small tilt of the microchannel.

Figure 7 illustrates the velocity vectors at the three flow rates of 100 μl/min, 300 μl/min, and 500 μl/min in the sudden expansion with rectangular shoulders ((a)–(c)) and at 500 μl/min in the

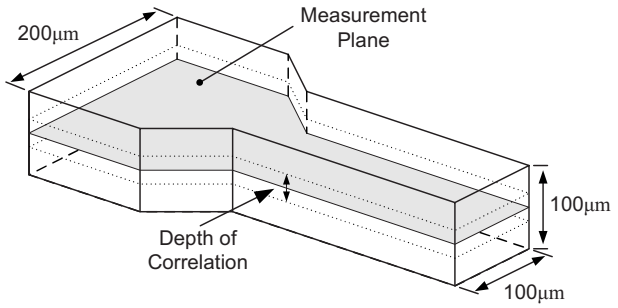

Fig. 5 Schematic of the measurement plane relative to the geometry under study

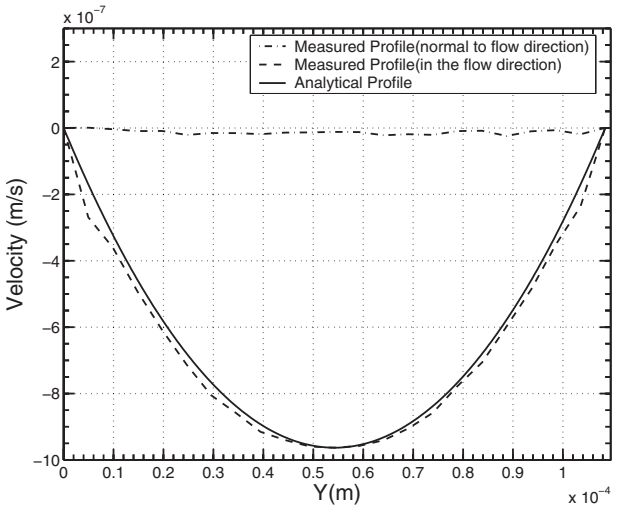

Fig. 6 Streamwise and normal velocity profiles in a fully developed region of the channel compared with analytical fully developed velocity profile [18]

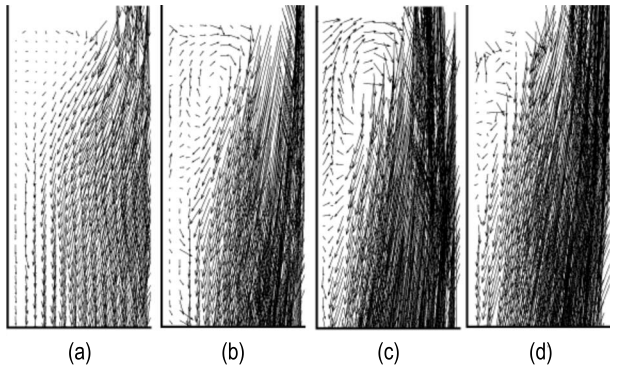

Fig. 7 Velocity field at the sudden expansion with rectangular shoulders, at flow rates of (*a*) 100 μl/min, (*b*) 300 μl/min, and (*c*) 500 μl/min. (*d*) Velocity field at the rounded expansion at a flow rate of 500 μl/min.

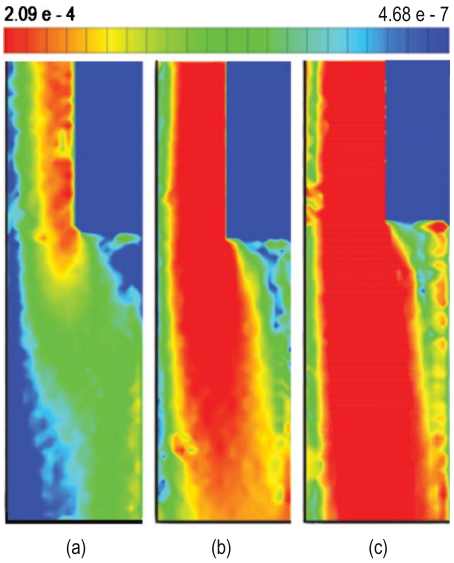

Fig. 8 Contours of constant frictional entropy generation at the expansion with rounded shoulders, at flow rates of (*a*) 100 μl/min, (*b*) 300 μl/min, and (*c*) 500 μl/min

rounded expansion (d). It is shown that there is a region of circulating flow, size and intensity of which depend on the geometry and flow rate. As expected, the separated flow region grows with flow rate and is larger in the sudden expansion.

By postprocessing the velocity measurement data, the frictional entropy generation rates at the exit of the microchannels are calculated. The entropy generation distribution map is plotted in Fig. 8. The highest rates of entropy generation occur in the regions with highest shear stresses, i.e., close to the walls of the 100 μm wide channel and in the high velocity gradient shear layer of the exiting flow. Higher flow rates magnify the velocity gradients, hence increasing the entropy generation rates. The amount of entropy produced in the separated region is small, due to small velocities and velocity gradients. In other words, the entropy generated due to frictional effects are more significant than the entropy produced due to a sudden change in flow area and pressure drop, which is expected in the low Reynolds number flows.

The results of the frictional entropy measurements in Fig. 9(*a*) show that the entropy produced in the rounded and triangular expansion geometries are larger than the entropy produced in the rectangular expansion at similar flow rates. The reason is the increased length of the side walls in the transition and higher wall shear effects. The velocity vector field at the rounded expansion (Fig. 7(*d*)) shows the formation of a small circulating flow region that explains the smaller frictional entropy generation produced in the rounded expansion compared with the triangular expansion.

On the other hand, in flow area contractions, the maximum frictional entropy generation is expected to occur in the sudden contraction due to flow separation and losses after the vena contracta. In practice, however, sharp corners cannot be created by the deep etching method and the shoulders of the contraction are rounded; hence, this behavior cannot be seen. In Fig. 9(*b*) the frictional entropy generation rate for the three contraction geometries is shown versus flow rate. The entropy produced in the rectangular and rounded geometries are very close due to the above fabrication constraint. However, the frictional entropy production increases with flow rate in all the expansion and contraction geometries due to larger velocity gradients at higher flow rates.

The isotherms in the rounded expansion have been plotted in Fig. 10. At smaller flow rates, in the expansion region, the fluid is exposed to the hot channel walls for a longer period of time; therefore, heat can penetrate deeper into the fluid and the core of

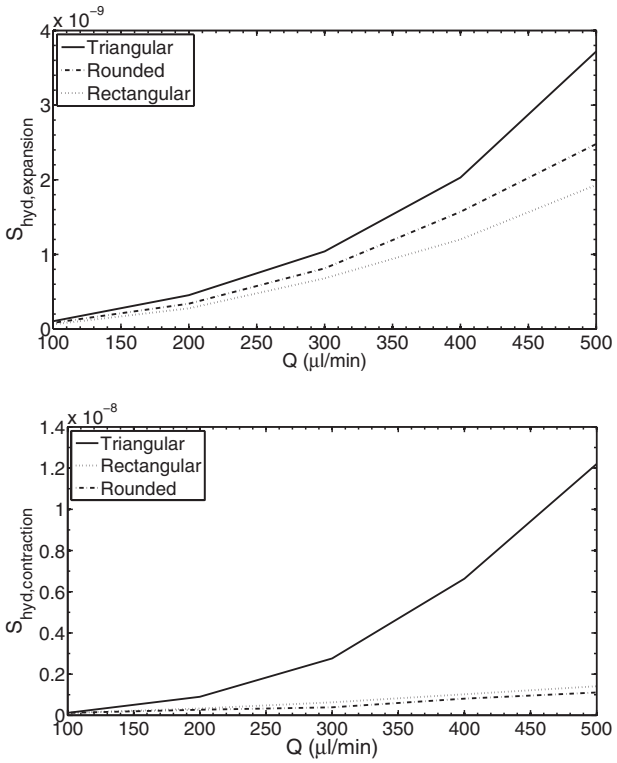

Fig. 9 Frictional entropy generation at a plane in the middle of the expansion (*a*) and contraction (*b*) section as a function of flow rate

the flow is affected by the high temperature on the walls. As the flow rate increases, the thickness of the high temperature fluid layer, adjacent to the walls, decreases and the temperature at the center of the flow does not change significantly. Figure 10 clearly shows this trend in the rounded exit of the microchannel. At a flow rate of 100 μl/min, the entire area of the flow is influenced by the heat transfer from the side walls, while at a flow rate of

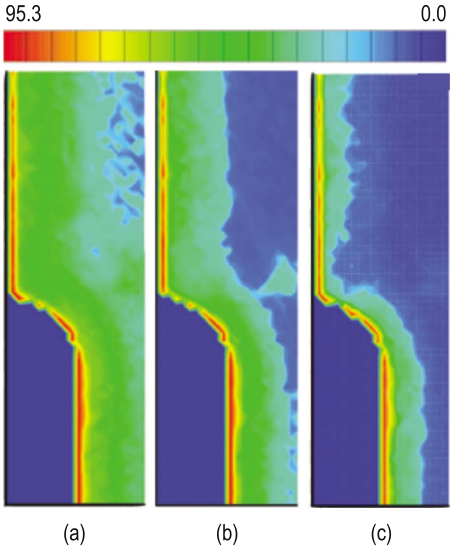

Fig. 10 Temperature distribution in the flow at the expansion with rounded shoulders, at a constant surface wall temperature of 90°C, at flow rates of (*a*) 100 μl/min, (*b*) 300 μl/min, and (*c*) 500 μl/min

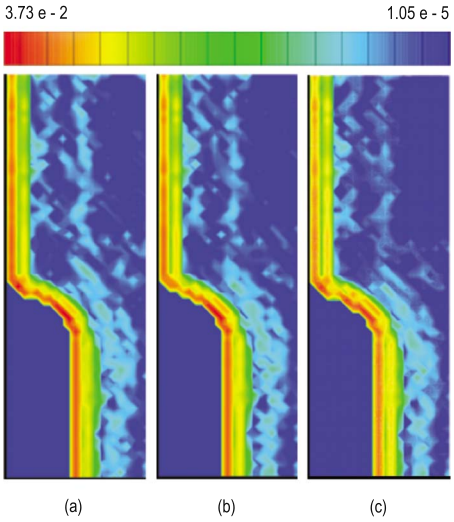

Fig. 11 Thermal entropy generation distribution in the flow at the expansion with rounded shoulders, at a constant surface wall temperature of 90°C, and at flow rates of (a) 100 μl/min, (b) 300 μl/min, and (c) 500 μl/min

500 μl/min, a thin thermal boundary layer forms near the walls and the majority of the flow remains at approximately the inlet temperature.

The contours of constant thermal entropy generation at the rounded expansion are plotted in Fig. 11 for the flow rates of 100 μl/min, 300 μl/min, and 500 μl/min. As demonstrated in both the experimental data and the theory, the entropy generation exhibits its maximum value adjacent to the side walls where the temperature gradient is highest.

The total amount of thermal entropy generation in the contraction and expansion sections of the microchannels are calculated and presented in Fig. 12. In general, the thermal entropy production rates are decreasing with flow rate. The reason is the reduction in the thermal boundary layer thickness (see Fig. 10) and steeper temperature gradient at the side walls, which increases the convection heat transfer coefficient. Higher convection heat transfer rates result in smaller thermal entropy generation rates (see Chap. 4 of Ref. [4]). No strong geometry dependence is observed, due to relatively high measurement uncertainties.

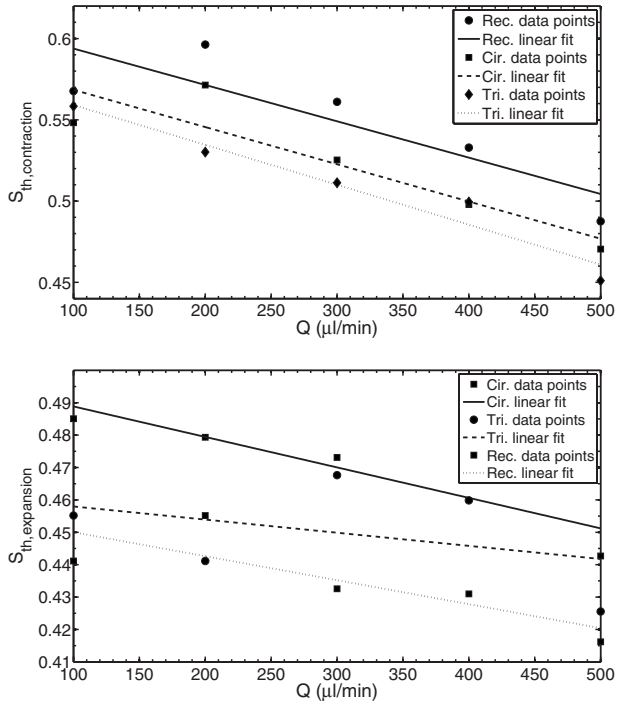

Fig. 12 Variations of thermal entropy generation with flow rate in the contraction (*a*) and expansion (*b*) of the microchannels

6 Summary and Conclusions

An experimental technique for measuring entropy production in microscale systems is described. The method is used to measure entropy generation of laminar, forced convection flow in a microchannel, widely utilized in electronics cooling devices. The entropy generation is obtained by postprocessing the velocity and temperature fields measured with microparticle image velocimetry and laser induced fluorescence methods. This method provides whole field entropy generation data and helps designers identify regions of high destruction rates of available energy and redesign them. This technique was used to measure the frictional and thermal entropy generation components in the transition between a 100 μm wide and a 200 μm wide microchannel and satisfactory results were attained. Better resolutions and accuracies can be obtained by using more powerful lenses and smaller particles.

The results of the measurements in the flow area expansion and contraction show that the largest frictional entropy generation occurs in the triangular expansion geometry. The reason is the increased length of the side walls exposed to nonseparated flow and the resulting high wall shear effects. No geometry dependence was observed in the thermal entropy generation results due to relatively large uncertainties. The measurement results indicate that the frictional and thermal entropy generation rates have inverse trends of variation with flow rate. Thus, there is an optimum flow rate at which the losses due to the combined frictional and heat transfer effects are minimized. In this work, the thermal entropy generation rate is orders of magnitude larger than the frictional entropy generation rate. Practical limitations did not allow increasing the flow rate to capture the optimum point.

Acknowledgment

The authors acknowledge the financial support of the Natural Sciences and Engineering Research Council of Canada (NSERC). They also appreciate the staff of the Microelectronics Heat Transfer Laboratory and Microfluidics Laboratory in the University of Waterloo for their help with the experimental setup.

Nomenclature

C = concentration, M/m^3
I = light intensity, W
L = length, m
M = magnification
Re = Reynolds number
S = entropy, J/K
T = temperature, K
$\overline{U}$ = average velocity, m/s
V = local Velocity, m/s
X = Displacement, pixel
d = diameter, m
$f^{\#}$ = f-number of the lens
k = thermal conductivity of the fluid, W/m K
$\mathbf{q}$ = vectorial heat transfer rate, W
s = specific entropy, J/kg K
t = time, s
u,v = velocity components in x and y directions, m/s
x,y = Cartesian coordinates, m

Greek

α = absorptivity, 1/M m
δ = uncertainty
η = sensitivity coefficient

λ = wavelength, m
μ = dynamic viscosity, N s/m^2
ϕ = quantum efficiency
ρ = density, kg/m^3
σ = standard deviation

Subscripts

0 = excitation light
e = effective
flow = related to flow
g = generation
hyd = hydraulic
image = related to image
p = particle
ref = reference
s = diffraction limited
u,b = bias
u,c = calibration
u,p = precision

References

[1] 2000, "Technology Roadmap for Semiconductors (ITRS): Executive Summary," Official Website, www.itrs.net
[2] 2007, "Technology Roadmap for Semiconductors (ITRS): Executive Summary," Official Website, www.itrs.net
[3] Tuckerman, D. B., and Pease, R. F. W., 1981, "High Performance Heat Sinking for VLSI," IEEE Electron Device Lett., **2**, pp. 126–129.
[4] Bejan, A., 1996, *Entropy Generation Minimization*, 1st ed., CRC, Boca Raton, FL.
[5] Khan, W. A., Yovanovich, M. M., and Culham, J. R., 2006, "Optimization of Microchannel Heat Sinks Using Entropy Generation Minimization Method," 22nd Annual IEEE Semiconductor Thermal Measurement and Management Symposium (Semi-Therm), Dallas, TX.
[6] Abbassi, H., 2007, "Entropy Generation Analysis in a Uniformly Heated Microchannel Heat Sink," J. Energy, **32**, pp. 1932–1947.
[7] Chen, K., 2005, "Second-Law Analysis and Optimization of Microchannel Flow Subjected to Different Thermal Boundary Conditions," Int. J. Energy Res., **29**, pp. 249–263.
[8] Erbay, L. B., Yalcin, M. M., and Ercan, M. S., 2007, "Entropy Generation in Parallel Plate Microchannels," Int. J. Heat Mass Transfer, **43**, pp. 729–739.
[9] Hooman, K., 2007, "Entropy Generation for Microscale Forced Convection: Effects of Different Thermal Boundary Conditions Velocity Slip, Temperature Jump, Viscous Dissipation, and Duct Geometry," Int. Commun. Heat Mass Transfer, **34**, pp. 945–957.
[10] Ogedengbe, E. O. B., Naterer, G. F., and Rosen, M. A., 2006, "Slip-Flow Irreversibility of Dissipative Kinetic and Internal Energy Exchange in Microchannels," J. Micromech. Microeng., **16**, pp. 2167–2176.
[11] Adeyinka, O. B., and Naterer, G. F., 2005, "Particle Image Velocimetry Measurement of Entropy Production With Free Convection Heat Transfer," Trans. ASME, **127**, pp. 614–623.
[12] Naterer, G. F., and Adeyinka, O. B., 2006, "New Laser Based Method for Non-Intrusive Measurement of Available Energy Loss and Local Entropy Production," Exp. Therm. Fluid Sci., **31**, pp. 91–95.
[13] Santiago, J. G., Wereley, S. T., Meinhart, C. D., Beebe, D. J., and Adrian, R. J., 1998, "A Particle Image Velocimetry System for Microfluidics," Exp. Fluids, **25**, pp. 316–319.
[14] Natarjan, V. K., and Christensen, K. T., 2009, "Two-Color Laser-Induced Fluorescent Thermometry for Microfluidic Systems," Meas. Sci. Technol., **20**, pp. 015401.
[15] Ross, D., Gaitan, M., and Locascio, L. E., 2001, "Temperature Measurement in Microfluidic Systems Using a Temperature-Dependent Fluorescent Dye," Anal. Chem., **73**, pp. 4117–4123.
[16] Sakakibara, J., and Adrian, R. J., 1999, "Whole Field Measurement of Temperature in Water Using Two-Color Laser Induced Fluorescent," Exp. Fluids, **26**, pp. 7–15.
[17] Kim, H. J., Kihm, K. D., and Allen, J. S., 2003, "Examination of Ratiometric Laser Induced Fluorescence Thermometry for Microscale Spatial Measurement Resolution," Int. J. Heat Mass Transfer, **46**, pp. 3967–3974.
[18] Yu, L., Tay, F. E. H., Xu, G., Chen, B., Avram, M., and Iliescu, C., 2006, "Adhesive Bonding With SU-8 Wafer Level for Microfluidic Devices," J. Phys.: Conf. Ser., **34**, pp. 776–781.
[19] Adeyinka, O. B., and Naterer, G. F., 2005, "Experimental Uncertainty of Measured Entropy Production with Pulsed Laser PIV and Planar Laser Induced Fluorescence," Int. J. Heat Mass Transfer, **48**, pp. 1450–1461.
[20] Meinhart, C. D., Wereley, S. T., and Santiago, J. G., 1999, "PIV Measurements of a Microchannel Flow," Exp. Fluids, **27**, pp. 414–419.
[21] Devasenathipathy, S., Santiago, J. G., Wereley, S. T., Meinhart, C. D., and Takehara, K., 2003, "Particle Imaging Techniques for Microfabricated Fluidic Systems," Exp. Fluids, **34**, pp. 504–514.
[22] Lee, S. Y., Wereley, S. T., Gui, L., Qu, W., and Mudawar, I., 2002, "Microchannel Flow Measurement Using Micro Particle Image Velocimetry," ASME International Mechanical Engineering Congress and Exposition, New Orleans, LA.
[23] Tsuei, L., and Savas, O., 2000, "Treatment of Surfaces in Particle Image Velocimetry," Exp. Fluids, **29**, pp. 203–214.
[24] Figliola, R. S., and Beasley, D. E., 2006, *Theory and Design for Mechanical Measurements*, 4th ed., Wiley, Hoboken, NJ.
[25] Bourdon, C. J., Olsen, M. G., and Gorby, A. D., 2004, "Validation of an Analytical Solution for Depth of Correlation in Microscopic Particle Image Velocimetry," Meas. Sci. Technol., **15**, pp. 318–327.
[26] White, F. M., 2005, *Viscous Fluid Flow*, 3rd ed., McGraw-Hill, Columbus, OH.

3D Integrated Water Cooling of a Composite Multilayer Stack of Chips

Fabio Alfieri

Manish K. Tiwari

Igor Zinovik

Dimos Poulikakos
e-mail: poulikakos@ethz.ch

Department of Mechanical and Process Engineering,
Laboratory of Thermodynamics in Emerging Technologies,
ETH Zurich,
8092 Zurich, Switzerland

Thomas Brunschwiler

Bruno Michel

Advanced Thermal Packaging,
IBM Zurich Research Laboratory,
IBM Research GmbH,
8803 Rueschlikon, Switzerland

New generation supercomputers with three dimensional stacked chip architectures pose a major challenge with respect to the removal of dissipated heat, which can reach currently as high as 250 W/cm^2 in multilayer chip stacks of less than 0.3 cm^3 volume. Interlayer integrated water cooling is a very promising approach for such high heat flux removal due to much larger thermal capacity and conductivity of water compared with air, the traditional cooling fluid. In the current work, a multiscale conjugate heat transfer model is developed for integrated water cooling of chip layers and validated with experimental measurements on an especially designed thermal test vehicle that simulates a four tier chip stack with a footprint of 1 cm^2. The cooling heat transfer structure, which consists of microchannels with cylindrical pin-fins, is conceived in such a way that it can be directly integrated with the device layout in multilayer chips. Every composite layer is cooled by water flow in microchannels (height of 100 μm), which are arranged in two port water inlet-outlet configuration. The total power removed in the stack is 390 W at a temperature gradient budget of 60 K from liquid inlet to maximal junction temperature, corresponding to about 1.3 kW/cm^3 volumetric heat flow. The computational cost and complexity of detailed computational fluid dynamics (CFD) modeling of heat transfer in stacked chips with integrated cooling can be prohibitive. Therefore, the heat transfer structure is modeled using a porous medium approach, where the model parameters of heat transfer and hydrodynamic resistance are derived from averaging the results of the detailed 3D-CFD simulations of a single streamwise row of fins. The modeling results indicate that an isotropic porous medium model does not accurately predict the measured temperature fields. The variation of material properties due to temperature gradients is found to be large; therefore, variable properties are used in the model. It is also shown that the modeling of the heat transfer in the cooling sublayers requires the implementation of a porous medium approach with a local thermal nonequilibrium, as well as orthotropic heat conduction and hydrodynamic resistance. The improved model reproduces the temperatures measured in the stack within 10%. The model is used to predict the behavior of multilayer stacks mimicking the change of heat fluxes resulting from variations in the computational load of the chips during their operation. [DOI: 10.1115/1.4002287]

Keywords: 3D chip stack, micropin-fin, integrated water cooling, conjugate heat transfer modeling, variable properties, thin porous medium, nonthermal equilibrium

1 Introduction

Vertical integration of circuit dies has tremendous potential to tackle the ever increasing performance requirement of high speed computing (Moore's law). This technology has already been shown to be feasible using through-silicon-vias (TSVs). However, such break-through fabrication strategies notwithstanding, the key requirement of maintaining a below threshold chip temperature is an enormous challenge. In fact, from the thermal perspective, vertically integrated high performance integrated circuits (ICs) are even more demanding than traditional 2D fabricated ICs, since the chip stacking process requires higher heat dissipation per unit area. For the cooling of such state-of-the-art 3D chip stacks [1], traditional air-cooling techniques are inadequate. Water with its nearly four times higher heat capacity and an order of magnitude higher thermal conductivity is a much superior choice as coolant. Several studies in the literature have therefore demonstrated the feasibility of water as electronic chip cooling liquid starting with the work of Tuckerman and Pease [2]. Backside heat removal using sophisticated thermal interfaces [3] and microchannel coldplates [4–8] have been shown effective in handling a single logic layer. Combining two or more logic layers can already result in unacceptably high junction temperatures with single sided water cooling [9]. Therefore, novel and scalable heat-removal strategies are needed to allow a high degree of freedom for fabrication and electrical design.

A possible strategy is to use interlayer integrated cooling [10], where a cooling network is integrated between the layers and optimized concerning the electrical layout of a multilayer chip stack. The proof of principle for this idea is provided in a recent publication [11] assessing micropin-fins and microchannel heat transfer structures. In the current work, we focus on developing a model for such 3D integrated water cooling of chip stacks and validating the model with experimental measurements. We introduce a novel way of modeling the microscale heat transfer structures as a porous medium with local thermal nonequilibrium (the so called two-temperature approach [12]) between water and solid matrix of the porous medium. Although the porous medium approach has been used previously starting with the work of Koh and Colony [13], to the best of our knowledge, the local thermal nonequilibrium approach for modeling microstructures was intro-

Contributed by the Heat Transfer Division of ASME for publication in the JOURNAL OF HEAT TRANSFER. Manuscript received February 9, 2010; final manuscript received July 21, 2010; published online September 22, 2010. Assoc. Editor: W. Q. Tao.

duced in a preliminary work [14]. The porous medium model has some inherent advantages when modeling high density microstructures in chip cooling applications, for which the computational cost of modeling the detailed flow structure and geometry can be restrictive. The two-temperature model adopted here is expected to better capture local thermal transport and result in better prediction of local thermal hot-spots. The effect of variable flow and heat transfer resistance through the heat transfer structure is also accounted for using anisotropic thermal conductivity of the porous medium. The computationally economic porous medium approach allowed us to incorporate temperature dependent water properties into the model. The pressure drop through the heat transfer structure (a key cost criterion) is shown to be clearly influenced by the variation of the properties of water with temperature. The developed model is applied for modeling of the experiments on a heat transfer structure consisting of aligned arrays of micropin-fins confined between the heating elements.

In order to accurately model the heat transfer coefficient and the pressure drop in a typical heat transfer structure using the porous medium approach, reliable correlations for these quantities in terms of temperature dependent flow variables are necessary. The correlations developed for standard large scale heat exchangers can lead to significant errors due to the influence of boundary walls on the microscale heat transfer structures used in chip cooling. Although some recent studies have modeled the heat transfer in microscale pin-fin structures using experimental data [15–17], they obtain average Nusselt number correlations, which provide estimations of the outlet temperature of flow but cannot be used to reliably predict local temperature variations. These investigators recourse to classical correlations, such as the ones compiled by Žukauskas and Ulinskas [18], to interpret their results and to clarify the differences thereof due to the scale of the problem and the influence of boundaries. However, previous works in the literature have brought forth several important finding in terms of heat transfer enhancement and optimization at microscale using pin-fin structures. The influence of pin shape [19,20], orientation [21], and the consequences of using pin array with nonuniform pin heights [22] has been clarified. Novel strategies to reduce the pressure drop, such as by forming recesses in the lid [23], have also been demonstrated. The number of previous studies on stacked chip cooling is relatively limited. In most of these studies on stacked chip cooling, pragmatic approaches of analytical one dimensional [24] or thermal resistance network type models rooted in experimental or reduced conjugate heat transfer solutions [10,25,26] are used to evaluate the performance of heat transfer structures. However, such reduced modeling can suffer from inability to accurately predict the local thermal gradients arising due to increasingly complex and time varying hot-spots, which are critical in determining the safe performance of the 3D chips. In the current work, we have developed a detailed CFD model of conjugate heat transfer, exploiting symmetry conditions, to predict local heat transfer and fluid flow through a heat transfer structure consisting of a micropin-fin array. Appropriate correlations for Nu and pressure drop based on local water bulk temperature and variable properties were developed from this CFD model. The effect of using variable thermophysical material properties as opposed to constant ones is also analyzed. In a way this is analogous to sensitivity analysis of the results with respect to variation in properties; however, our primary focus is to illustrate the influence of using temperature dependent property values on the results of integrated water cooling of 3D chip stacks. These correlations are then used in a two-temperature porous medium model of an entire chip stack with realistic heat flux conditions. The model results are also validated using the experimental measurements performed on a thermal demonstration test vehicle. The two-temperature model adopted is shown to accurately capture the local temperature gradients arising due to the presence of step changes in the wall heat flux through the discrete hot-spots.

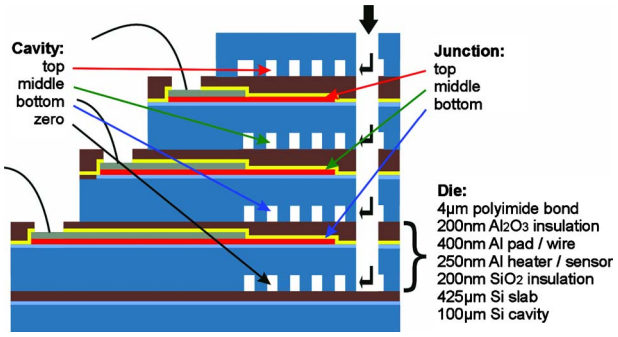

Fig. 1 Cross section of the pyramid chip stack in transversal direction

2 Experimental Setup

To validate the modeling results, a test vehicle was built using microfabrication techniques. It consists of four fluid cavities with the pin-fins etched into the silicon. Three power dissipating layers utilizing joule heating in metal thin films represent the nonuniform power map of a vertical integrated chip stack (Fig. 1). The dissipated heat was determined by calculating the electrical power with measured values of voltage and current through the heater. The electrical power should be equal to the enthalpy increase from inlet to outlet, calculated by means of inlet/outlet temperatures, mass flow, and fluid properties at average fluid temperature. Typically the ratio between the two values was found to 96% or higher in all our measurements. Wire bond electrical connections are used to deliver power and read the temperature signals from the layers. Therefore, the size of the subsequent lower die is increased to be able to place bonding pads on one side of each die. A detailed description of the test vehicle fabrication can be found in Ref. [14].

Compared with actual chip stacks, the test vehicle silicon slab thickness is 425 μm instead of 50 μm to reduce wafer handling complexity. This will enhance the heat spreading capability in each layer. A realistic slab-thickness results from a maximal TSV height of typically 150 μm minus the cavity depth. Furthermore, we used a compliant polyimide layer for leak-tight bonding. This layer represents a thermal impedance of 20 K mm^2/W and emulates the wiring levels of a real processor die with a typical thermal resistance of 7 K mm^2/W. The offset of 13 K mm^2/W needs to be considered in further discussion of the thermal performance.

The thermofluidic characterization of the test vehicles was performed on a single-phase fluid-loop with water as coolant, temperature controlled through a secondary chiller loop (ProLine RP855, Lauda). The primary loop is equipped with a magnetically coupled gear pump (Fluidotech), a 10 μm particle filter, a Coriolis-flow mass flow meter (MFS 3000-S03) with an accuracy of 0.3% of measured values, a differential pressure sensor (PD23-V-2, Omega, accuracy 0.1% at full scale of 2 bars), and T-type thermocouples measuring the inlet and outlet fluid temperatures (accuracy of $\pm$0.1 K). The standard deviations in the measured temperature values for any given operation point were below 0.14 K. The hot-spots are powered by multipurpose DC power supplies. The dissipated power and the hot-spot temperature are measured with a Keithley 2701 multimeter and a Keithley 7700 multiplexer card. The data acquisition was performed through a LABVIEW platform. A schematic of the entire experimental setup is depicted in Fig. 2.

3 Model Development

3.1 Temperature Dependent Material Properties. In all the simulations, material properties of fluid and solid subdomains are incorporated as functions of temperature. Typical temperature

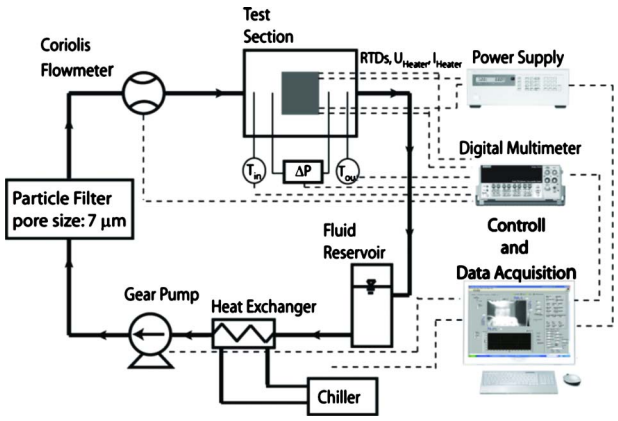

Fig. 2 Detailed schematic of the experimental setup

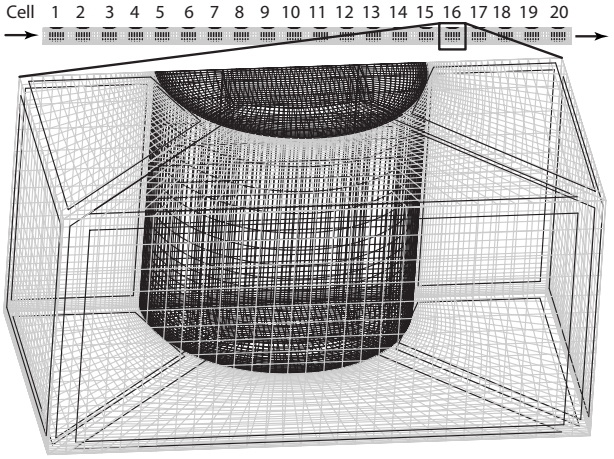

Fig. 3 Geometry with 20 inline pins simulated using detailed 3D conjugate heat transfer model and a zoom in into a single cell (pin-fin and fluid)

changes in chip cooling applications lie in the range from 273 K to 373/363 K (water/silicon), from inlet to outlet. For such a large variation in temperature, material properties can change significantly (see Table 1, which summarizes the two extreme end values in the range [27]).

The temperature dependent change in the dynamic viscosity μ, more than 200% from 273 K to 373 K, stands out compared with the other properties. Although not as high as viscosity, the variation for other properties such as thermal conductivity κ, specific heat capacity c_p, and density ρ is also 20–50%. The variation of the material properties indicates that the commonly used assumption that the properties are constant is not suitable for the present problem, where we would like to capture important local temperature gradients and flow characteristics due to the high heat fluxes being generated by the chip.

Furthermore, since we are working with a very thin layer of heat transfer structure (the layer height is only 100 μm), the boundary is also expected to play a significant role in heat transfer characteristic of stacked and bounded micropin-fin array being modeled here. Although the flow can be fully developed after four to five pins in streamwise direction [11], the thermal boundary layer will not develop so quickly. Depending on the coolant mass flow, the inlet temperature, and the amount of heat dissipated, the thermal boundary layer might not be fully developed until 10–15 pins. The thermal entrance length is therefore much longer than the hydrodynamic entrance length. This leads to a large region in the chip where the heat transfer coefficient cannot be assumed to be constant. The effect needs to be carefully considered in order to develop an effective ultrathin porous medium model for heat transfer structure.

The development of the model is divided into two parts. In the first part, a conjugate heat transfer problem for a row of inline pin-fins with water as a coolant is solved using ANSYS CFX®. From these first set of simulations, the heat transfer coefficient and pressure drop are obtained in correlation forms, $\mathrm{Nu}(v,T)$ and $\Delta p(v,T)$, to be used in the porous medium based simulations performed on the entire 3D stacked chip geometry in the second part.

Table 1 Minimal and maximal values of material properties

Variable		Min	Max	Units
Water	c_p	4180	4218	J/kg K
	μ	2.8×10^{-4}	1.8×10^{-3}	Pa s
	ρ	958	1000	kg/m^3
	k	0.57	0.68	W/m K
Silicon	c_p	678	767	J/kg K
	k	109	169	W/m K

3.2 Detailed Geometry. The computational domain for the three dimensional CFD model developed in order to obtain correlations for the pressure loss $\Delta p(v,T)$ and the heat transfer coefficient $h(v,T)$ in heat sinks with inline cylindrical pin-fins is shown in Fig. 3. The domain consists of a row of 20 inline pins in the direction of the flow, each with 50 μm diameter and 100 μm height, enclosed between two heated plates and arranged at a pitch of 100 μm.

Exploiting the symmetry of the computational domain, we can simulate one-half of the height and one-half of the width, reducing the computation time by 75%. Only one row is simulated, meaning that we assume to have an infinite number of contiguous rows. The limitation simulating only one row and not an array is that the lateral walls and the respective boundary layers are not taken into account. However, since in practice these walls are well insulated and the entrance length is about four to five pins, they should not influence the results much.

With the realistic setting in mind, the following boundary conditions are specified. The inlet is defined by means of mass flow rate and static temperature. The outlet uses an opening boundary condition with zero static pressure and the static temperature set as equal to the average temperature over the outlet. A constant heat flux is imparted onto the plate. At the interface of the fluid and the pins, the heat flux conservation is imposed. Symmetry condition is used at all other boundaries. Table 2 summarizes settings for the boundary conditions.

The solver used is ANSYS CFX®, which is fed with the temperature dependent material properties in the form of a polynomial function of temperature. The polynomial coefficients were obtained by simple linear least squares fitting of the corresponding temperature dependent property values obtained from Ref. [27]. All simulations are performed in steady state mode.

A mesh independence study was performed for several mesh

Table 2 Boundary conditions for the inline pin-fin model

Position	Variable	Value
Inlet	Static temperature	293 K
	Mass flow	$0.1-35\times10^{-7}$ kg/s
Outlet	Static temperature	Average outlet temperature
	Relative pressure	0 Pa
Plate	Heat flux/plate	0/25/50/75/100/125 W/cm^2
The other boundary conditions are symmetry walls		

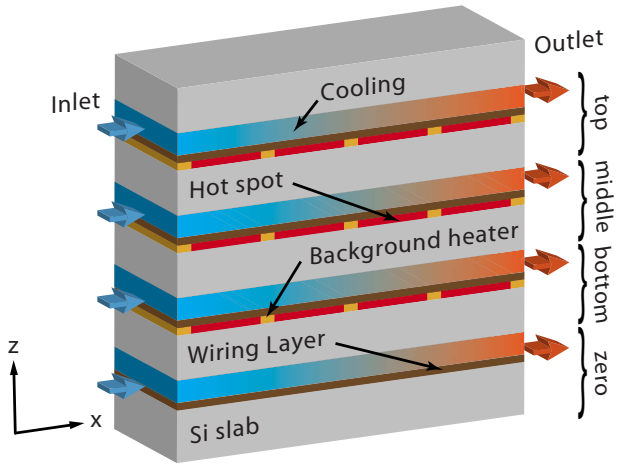

Fig. 4 Cross section of the CFD model in streamwise direction

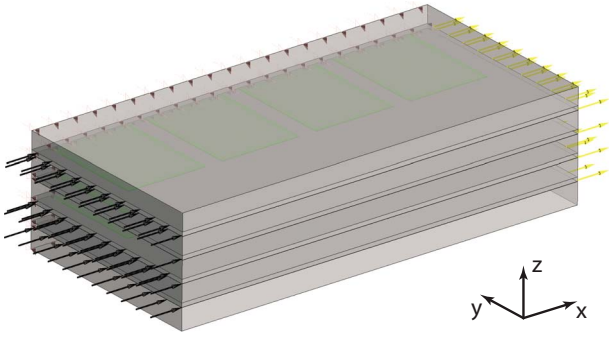

Fig. 5 CFD model of a two-port multilayer stack of chip

sizes and types. A tetrahedral mesh with prism layers failed to resolve the boundaries and therefore structured meshes with hexahedral cell are used. Series of simulations with three different meshes (1,000,000, 5,000,000, and 12,000,000 nodes) were carried out. The meshes were created using the ANSYS ICEM® meshing tool and own exactly the same blocks for each cell, consisting in two half O-grids both inside the cylinder and outside in the fluid region. The change lies in the number of nodes on the edges and on their arrangement on it. Due to the high fluid temperature gradients near the walls, finer mesh is used near boundaries. The results of simulation of the temperature field were found to be more sensitive to the mesh refinement than the velocity and pressure fields. In fact, velocity and pressure fields do not show important differences for the three meshes. While the temperature field showed greater dependency on the mesh size, the difference between the medium and finest mesh was still above 1% and therefore the mesh with 12,000,000 nodes is used for all subsequent simulations.

The convergence criteria are set to 10^{-7} for the normalized residuals from the momentum and energy equations, which is reached after about 700 computational steps. Four monitor points are used to check local temperature and convergence.

3.3 Three Dimensional Stack. Figure 4 shows the schematic of the pyramid test vehicle used to perform experimental measurements (see also Fig. 1) and validate the porous medium modeling results. The structure consists of four dies called respectively "zero," "bottom," "middle," and "top." The first one does not include heating elements and contains only a 525 μm thick silicon layer and the cooling channel of 100 μm in height. The other three dies placed on the top of the die zero own the same arrangement and dimensions. On the top of a 425 μm thick Si slab, a layer composed of hot-spots surrounded by background heaters is created, which is covered by a wiring layer.

The computational domain used to simulate the multilayer chip stack is illustrated in Fig. 5. Only half of the real stack in the y direction is simulated because of symmetry.

Boundary conditions are defined similar to the simulation of the detailed pin-fin model illustrated before. The inlet is described by means of mass flow rate and static temperature, whereas at the outlet cross section the average static pressure has been set to zero. The cooling heat transfer structure is modeled as porous medium. In the dielectric layer, hot-spots are placed equidistant and modeled as volumetric heat sources. All other walls are considered adiabatic and with no-slip. The summary of boundary conditions that remain unchanged for all the following results can be found in Table 3.

A detailed mesh sensitivity study is done with four meshes containing 500,000, 1,000,000, 2,500,000, and 6,000,000 nodes with uniform and nonuniform distributions. The best resolved mesh with nonuniform node distribution is chosen in order to capture the gradients around the hot-spots and in the water boundary layers. The convergence of the simulations, decided by a value of 10^{-9} for the residuals, is reached between 100 and 200 time steps. The solver used is still ANSYS CFX® and all material properties are temperature dependent. In addition, orthotropic thermal conductivity is used for pin-fin heat transfer structure being modeled as a porous medium. The orthotropic thermal conductivity can be expressed as

$$k_{ii} = \begin{pmatrix} k_{xx} & 0 & 0 \\ 0 & k_{yy} & 0 \\ 0 & 0 & k_{zz} \end{pmatrix} \tag{1}$$

The components of k_{ii} are determined differently for the equilibrium and nonequilibrium porous medium models. For the nonequilibrium case, we impose a zero thermal conductivity in the x and y directions, since the pin-fins are not connected together, and the conductivity of silicon in the z direction. For the thermal equilibrium case, following the Rayleigh [28] proposition for a cylinder/fluid arrangement similar to the current modeled geometry, the effective conductivity in z direction (the direction parallel to the pin height) is computed as

$$\frac{k_{zz}}{k_{pf}} = 1 + \left(\frac{k_{ps} - k_{pf}}{k_{pf}}\right)(1 - \varepsilon) \tag{2}$$

and those in the other two directions as

$$\frac{k_{xx}}{k_{pf}} = \frac{k_{yy}}{k_{pf}} = 1 + \frac{2(1 - \varepsilon)}{\left(\frac{k_{ps} + k_{pf}}{k_{ps} - k_{pf}}\right) - 1 + \varepsilon} \tag{3}$$

The pin-fin size and pitch values used in the current study correspond to a high value of porosity ($\varepsilon = 0.841$), so that k_{xx} and k_{yy} approach the thermal conductivity of water, and k_{zz} is lower than the arithmetic mean of water and silicon conductivities. Equation (3) is a simplified form of the equation proposed by Rayleigh [28], which can be utilized in the high porosity range without any significant loss in accuracy. However, the complete form should be

Table 3 Boundary conditions for the two-port model

Position	Variable	Value
Inlet	Static temperature	293 K
	Mass flow	2.16×10^{-3} kg/s
Outlet	Pressure	0 Pa
Porous	Porosity	0.841
Hot-spots	Volumetric heat flux	$5.8/12 \times 10^{11}$ W/cm^3
The other boundary walls are adiabatic with no-slip		

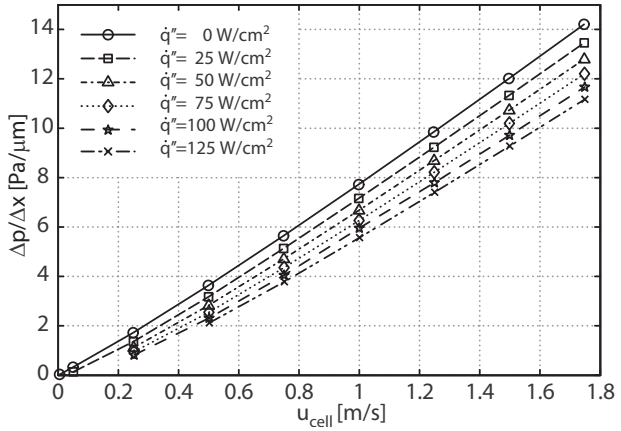

Fig. 6 Pressure drop as a function of the average cell velocity for different plate heat fluxes

used when modeling a heat transfer structure with low porosity.

Since we incorporate the porous fluid thermal conductivity k_{pf} as a function of temperature in our models, the effective thermal conductivities become temperature dependent. In addition, for the porosity corresponding to our geometry, the difference between k_{zz} values for common used coolant temperatures is higher than 20%. This underscores the importance of using temperature dependent thermal conductivity values for the porous medium.

The governing equation for fluid momentum can be expressed as [29]

$$\frac{1}{\varepsilon^2}\rho \boldsymbol{u}\,\nabla\cdot\boldsymbol{u} = -\nabla p + \frac{1}{\varepsilon}\mu\nabla^2\boldsymbol{u} - \frac{\mu}{\kappa}\boldsymbol{u} \tag{4}$$

The heat transports in the water and the solid parts of the porous medium in nonequilibrium situation are modeled as [29]

$$\nabla\cdot(\boldsymbol{u}\rho c_p T)_{pf} = \nabla\cdot(k\,\nabla\,T)_{pf} + h_{fs}(T_{ps} - T_{pf})A_0 \tag{5}$$

and

$$\nabla\cdot(k\,\nabla\,T)_{ps} - h_{fs}(T_{ps} - T_{pf})A_0 = 0 \tag{6}$$

where $A_0 = A_{\text{pin}}/V_{\text{cell}}$ is the contact area density and $\boldsymbol{u}$ is the superficial velocity vector.

The solid wall heat transfer is modeled with heat conduction and heat generation given by

$$\nabla\cdot(k\,\nabla\,T)_s + \dot{Q}''' = 0 \tag{7}$$

where $\dot{Q}'''$ denotes the volumetric heat source used in the dielectric layer. The boundary conditions on the interface between solid and porous medium are

$$(1-\varepsilon)k_s\,\nabla\,T_s = k_{ps}\,\nabla\,T_{ps} \tag{8}$$

$$\varepsilon k_s\,\nabla\,T_s = k_{pf}\,\nabla\,T_{pf} \tag{9}$$

$$T_s = T_{ps} = T_{pf} \tag{10}$$

The continuity of heat flux is assumed at the interface between porous-fluid and porous-solid.

4 Results and Discussion

4.1 Pressure Drop. Figure 6 shows the average pressure drop per unit length for the fully developed flow around a row of inline pins computed at different mass flow rates and wall heat flux. It is calculated as

$$\frac{d\overline{p}}{dx} = \frac{\overline{p}_{1500} - \overline{p}_{1600}}{L_{x,\text{cell}}} \tag{11}$$

where $\overline{p_x}$ represents the average pressure over the cross section of the channel at the position x (μm) in the streamwise direction and $L_{x,\text{cell}}$ corresponds to the length of a cell. From hereinafter, a cell denotes the local representative volume around each pin. The boundaries of the cell in the streamwise direction are located exactly halfway between two adjacent pins. Cell 16 is chosen to represent the pressure drop and water properties in order to ensure both full thermal and hydrodynamic development of the flow and avoid disturbance from the outlet.

It can be observed from Fig. 6 that for a given average cell velocity (i.e., mass flow rate) the pressure drop is not constant and for increasing heat fluxes it decreases. This is mainly due to the high temperature dependency of water viscosity, which strongly decreases with rise in temperature. The difference in pressure drop due to increasing heat flux rises with increasing average cell velocity. This leads to higher momentum diffusion across any given cross section and therefore the pressure loss is enhanced. This effect is responsible for slope changes in the pressure drop curves shown in Fig. 6. To describe this variation of pressure drop using the Darcy's law

$$\frac{dp}{dx} = \frac{\mu}{\kappa}\boldsymbol{u} \tag{12}$$

would lead to a correlation with a substantial error because it does not take into account the nonlinear temperature and velocity dependencies. Therefore, a modified form of Darcy's law is introduced as

$$\frac{d\overline{p}}{dx} = \frac{\mu_{\text{cell}}}{\tilde{\kappa}\ \text{Re}_{D,\text{cell}}^{\gamma}\ \text{Pr}_{\text{cell}}^{\delta}}u_{\text{cell}} \tag{13}$$

where the average cell velocity u_{cell} is calculated by volume averaged on the cell as

$$u_{\text{cell}} = \frac{1}{V_{f,\text{cell}}}\int_{V_{f,\text{cell}}} u_i dV_{f,\text{cell},i} \tag{14}$$

and the permeability κ is expressed as

$$\kappa = \tilde{\kappa}\ \text{Re}_{D,\text{cell}}^{\gamma}\ \text{Pr}_{\text{cell}}^{\delta} \tag{15}$$

with $\tilde{\kappa}$ denoting the modified permeability, Pr_{cell} denoting the cell Prandtl number, and $\text{Re}_{\text{D,cell}}$ denoting the Reynolds number, which is defined as

$$\text{Re}_{D,\text{cell}} = \frac{u_{\text{cell}}D}{\upsilon} \tag{16}$$

The fitting parameters $\tilde{\kappa}=2.4067\times10^{-10}$ m^2, $\gamma=-0.044207$, and $\delta=-0.21322$ employed in Eq. (13) are found using the multiple linear regression method. Any temperature dependent property in the cell is computed at an average temperature in the cell given by

$$T_{f,\text{cell}} = \frac{T_{\text{bulk}}|_{@\text{cell,in}} + T_{\text{bulk}}|_{@\text{cell,out}}}{2} \tag{17}$$

The local fluid bulk temperature at inlet and outlet of each cell is found by means of an energy balance as

$$T_{\text{bulk}} = \frac{\displaystyle\int_{A_{\text{cross}}} \rho u c_p T_f dA_{\text{cross}}}{\displaystyle\int_{A_{\text{cross}}} \rho u c_p dA_{\text{cross}}} \tag{18}$$

Figure 7 clearly shows that the correlation for the pressure drop (Eq. (13)) is fitting our data very well.

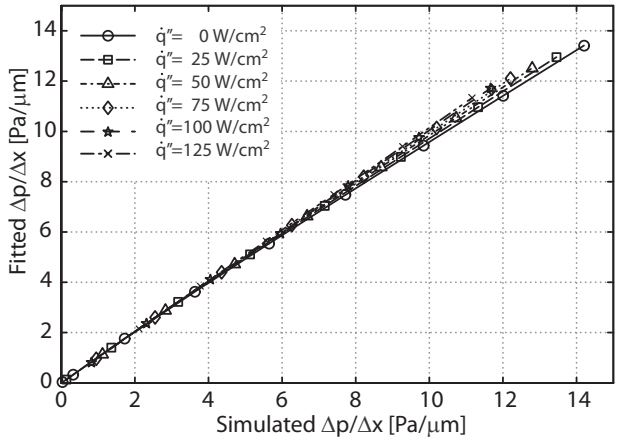

Fig. 7 Comparison between simulated and fitted pressure drop

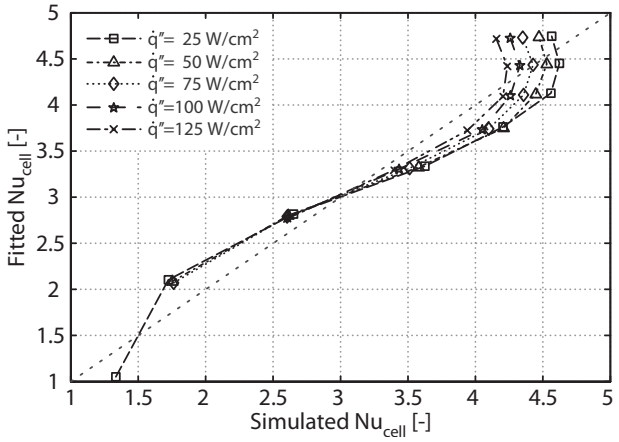

Fig. 9 Comparison between simulated and fitted Nusselt number

4.2 Heat Transfer Coefficient. The other parameter required by the nonequilibrium porous medium model is the heat transfer coefficient. The thermal development of the flow for all the heat fluxes used is shown in Fig. 8, which depicts the total local Nusselt number (Nu_{tot}) for different mass flows. Nu_{tot} accounts for the heat transfer to the liquid from both pins and the plate. It is calculated in terms of the corresponding total heat transfer coefficient, which is defined as

$$h_{\text{tot}} = \frac{\dot{q}''_{\text{tot,cell}}}{T_{\text{tot,cell}} - T_{f,\text{cell}}} \tag{19}$$

where

$$\dot{q}''_{\text{tot,cell}} = \frac{1}{A_{\text{pin}} + A_{\text{plate}}}\left(\int_{A_{\text{pin}}} \dot{q}''_{w,i} dA_{\text{pin},i} + \int_{A_{\text{plate}}} \dot{q}''_{w,i} dA_{\text{plate},i}\right) \tag{20}$$

and

$$T_{\text{tot,cell}} = \frac{1}{A_{\text{pin}} + A_{\text{plate}}}\left(\int_{A_{\text{pin}}} T_{w,i} dA_{\text{pin},i} + \int_{A_{\text{plate}}} T_{w,i} dA_{\text{plate},i}\right) \tag{21}$$

As it is clear from Fig. 5, at high mass flow rates the Nu_{tot} curves are flattened after ten pins, which confirms the thermal development of the flow.

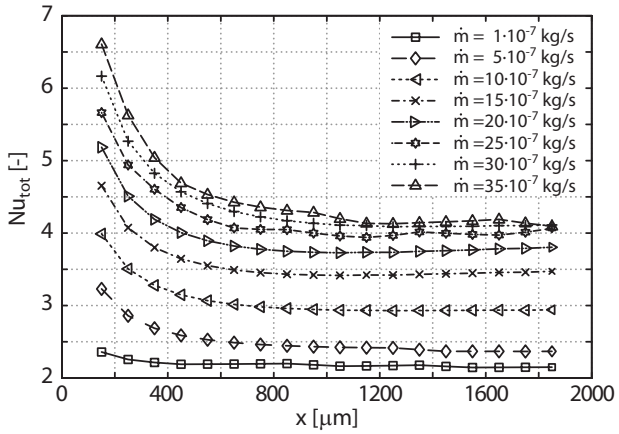

Fig. 8 Total local Nusselt number for different mass flow rates and $\dot{Q}''$=25 W/cm²

The cell averaged heat transfer coefficient from pins to water can be defined as

$$h_{\text{cell}} = \frac{\dot{q}''_{\text{pin,cell}}}{T_{\text{pin,cell}} - T_{f,\text{cell}}} \tag{22}$$

with the wall heat flux from the pins given by

$$\dot{q}''_{\text{pin,cell}} = \frac{1}{A_{\text{pin}}}\int_{A_{\text{pin}}} \dot{q}''_{w,i} dA_{\text{pin},i} \tag{23}$$

and the average temperature at the pin surface in a cell computed as

$$T_{\text{pin,cell}} = \frac{1}{A_{\text{pin}}}\int_{A_{\text{pin}}} T_{w,i} dA_{\text{pin},i}. \tag{24}$$

The Nusselt number of each cell can be obtained as

$$\text{Nu}_{\text{cell}} = \frac{h_{\text{cell}} D_{\text{pin}}}{k_{\text{cell}}} \tag{25}$$

and averaged for cells 10–16, where the flow is found to be thermally fully developed.

The importance of using Eq. (22) to define the heat transfer coefficient from pin to the fluid lies in the fluid temperature, which is influenced by the heat transfer to the fluid from the pin and the plates combined. Clear distinction of these heat fluxes is necessary in order to accurately model the pin-finned heat transfer structure as a nonequilibrium porous medium that can predict the local thermal gradients. The cell averaged Nusselt number (Nu_{cell}), defined using the heat transfer coefficient in Eq. (22), to be used in the porous medium model is correlated using the relation

$$\text{Nu}_{\text{cell}} = C \ \text{Re}_{D,\text{cell}}^{\alpha} \ \text{Pr}_{\text{cell}}^{\beta} \tag{26}$$

The parameters $C=0.33088$, $\alpha=0.41347$, and $\beta=0.42252$ are obtained using the multiple linear regression fitting. Figure 9 shows the result of this fitting. It is clear that the correlation provides a good approximation to the data spread from a perfect fit (as indicated by the dotted line with 45 deg slope). The deviation is limited to less than $\pm 30\%$ at low mass flow rates.

4.3 Model Validation. The results on the three dimensional chip stack, modeled using porous medium approach, are described next. In this study the focus is on the two-port microchannel configuration with inline pin-fins, where inlet and outlet are aligned in the same direction.

Figures 10 and 11 show the performance of the nonequilibrium

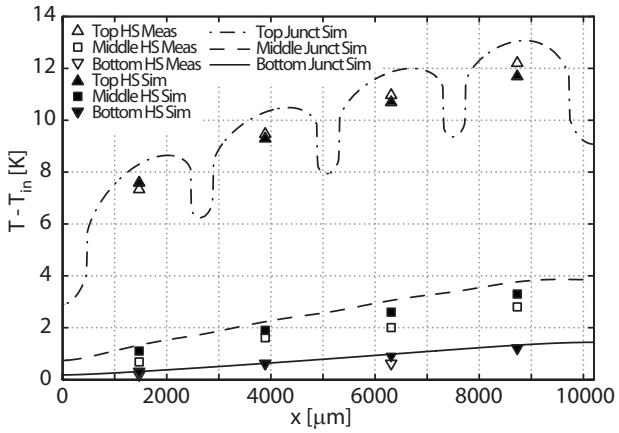

Fig. 10 Validation of the porous medium model with measurements for 4 hot-spots operating in the "top" layer

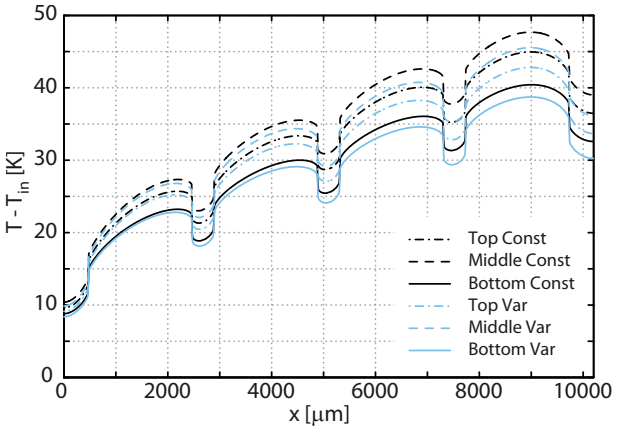

Fig. 12 Impact of constant and variable material properties on temperature rise at benchmark operation condition in different chip levels

porous medium model with respect to predicting experimental measurements and also serve the purpose of validating the simulations. The figures depict, for different sequences of hot-spot (HS) operation, the streamwise variation of the junction temperature (Junct), as well as simulated (Sim) and measured (Meas) hot-spot temperatures at different stack levels (see Fig. 4). The junction temperature needs to be distinguished from the hot-spot temperature. The former is the maximal temperature along a streamwise directed line, in the symmetry plane, lying between silicon slab and hot-spot layers. The latter is the line averaged temperature on the centerline (along y axis in Fig. 5) lying in the central plane of the hot-spot and therefore will be lower than the junction temperature. The junction temperatures are plotted as lines in Figs. 10 and 11 in order to show the trends in temperature variation along the different layers of the stack. The hot-spot temperatures are plotted as symbols in order to validate the simulations with experimental measurements.

Figure 10 shows the junction temperature rise in the streamwise direction and the average hot-spot temperatures in the different levels of the chip stack for the case where all four hot-spots in the top layer are operating at 12 W, whereas the others are turned off. The model predicts the trend well and the simulation results are mostly in good agreement with the experimental measurements. The maximal deviation is below 0.6 K, which is acceptable given the intricacy of the measurements and the corresponding simulations.

Measurements and simulation are compared in another configuration shown in Fig. 11, with the second hot-spot of each layer operating at 12 W, while the others are turned off. The overprediction in this case is observable mostly in the hot-spot region, whereas the rest of the domain is well predicted. As expected the maximal temperature is reached in the middle layer. The maximum deviation between simulation and experimental measurement occurs at the hot-spot temperature of the top layer and is less than 2.5 K. It is important to recognize that the corresponding deviation was much lower for any hot-spot temperature when all hot-spots are in on condition (see Fig. 10). Therefore, the deviation shown in Fig. 11 is really the worst case scenario.

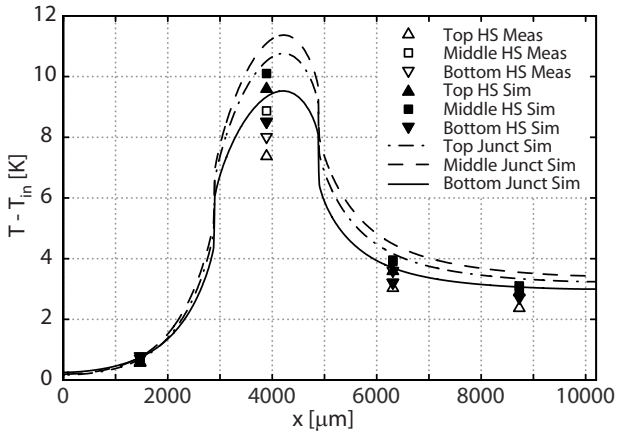

Fig. 11 Validation of the porous medium model with measurements for three hot-spots operating on the top of each other

Validation of the porous medium model with measurements for three hot-spots operating on the top of the consequences of including variable liquid properties in the model are clarified in Fig. 12 and Table 4. The results are obtained with the chip stack operating at benchmark conditions, wherein all hot-spots are switched on and dissipating 25 W each. For the simulation with constant material properties, all the properties were evaluated at the fluid inlet temperature. The figure shows that the error made by this assumption can be as high as 10%.

Moreover, as Table 4 shows, the use of constant material properties leads to a 30% overestimation of pressure drop.

A higher change in pressure drop result compared with temperature rise can be due to a sharper change in viscosity with change in temperature, which has a stronger influence on the pressure drop.

In Fig. 13, we plot the simulation junction temperatures obtained using thermal equilibrium (1-temp) and nonequilibrium (2-temp) porous medium models at benchmark operation with all hot-spots dissipating 25 W each. The effective thermal conductivity values for the entire porous medium used for simulations with the thermal equilibrium model are $k_{xx}=k_{yy}=0.65$ W/m K and $k_{zz}=25$ W/m K.

From Fig. 13, it is clear that the difference between one temperature and two-temperature models can be as high as 50%. The nonthermal equilibrium model, which was validated against our

Table 4 Impact of using constant and variable material properties on pressure drop at benchmark operation condition in different chip levels

	Δp (Pa)		
Material properties	Bottom	Middle	Top
Variable	102,452	103,108	110,520
Constant	129,701	129,701	129,701

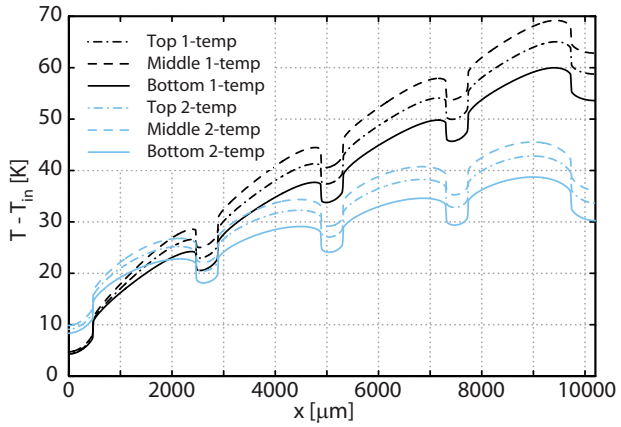

Fig. 13 Comparison of equilibrium and nonequilibrium model at benchmark operating chip

experiments, produced a slight overprediction of the measured temperature, certainly acceptable given the complexity of the system. The thermal equilibrium approach, on the other hand, will lead to a serious overestimation of the chip temperature. Therefore, the cooling structure performance based on the thermal equilibrium model is too conservative and this approach will result in oversized cooling system design and higher costs.

Last but not the least, the computing costs of a 3D chip stack with the heat transfer structures modeled as porous medium are nearly 8000 times lower than a hypothetical case modeling the detailed geometry containing 20,000 pins in the chip stack with four cooling layers. The computational cost of the detailed simulation is extrapolated from the time needed per pin in the detailed geometry simulation of 20 pins (as described in Sec. 3.2). More precisely, however, we should also take into account the 30 simulation runs required on the detailed geometry in order to obtain the parameters designating the porous medium. Even after taking this fact into account, a 30 time reduction in computational time is achieved, which justifies the porous medium approach adopted here.

5 Conclusion

In conclusion, we have developed a nonequilibrium porous medium based model to predict high local thermal gradients in vertically integrated (3D) chip stacks. The cooling cavities with an array of inline cylindrical pins were replaced by ultrathin porous medium layers with orthotropic thermal conductivity and temperature dependent material properties. The correlations for the heat transfer coefficient and pressure drop required for nonequilibrium porous medium simulations were obtained from separate 3D conjugate heat transfer simulations on 20 inline pins under realistic boundary conditions. In deriving the correlations, explicit distinction was made between the heat transfer to the fluid through pins and boundary plates. The porous medium model was shown to be capable of reproducing experimental measurements from a test vehicle composed of three heating layers and four cooling cavities. It was demonstrated that in liquid cooled electronic applications, characterized by very high heat dissipation per unit area and boundary layers sizes comparable to the cooling structures, the use of constant material properties is not suited. It was also shown that the thermal equilibrium assumption in the porous medium model drastically overpredicts the temperature distribution in the three dimensional chip stacks, and thus nonequilibrium model is required.

Nomenclature

A = area (m^2)
A_0 = contact area density (1/m)
c_p = specific heat capacity (kJ/kg K)
D = pin diameter (μm)
H = pin height (μm)
h = heat transfer coefficient (W/m^2 K)
k = thermal conductivity (W/m K)
L = length (μm)
$\dot{m}$ = mass flow (kg/s)
Nu = Nusselt number
p = pressure (Pa)
Pr = Prandtl number
Re = Reynolds number
$\dot{q}''$ = wall heat flux (W/m^2)
$\dot{Q}'''$ = volumetric heat source (W/m^3)
T = temperature (K)
u = velocity (m/s)
V = volume (m^3)
x, y, z = x, y, z coordinates (μm)
$\alpha, \beta, \gamma, \delta$ = exponent for correlations
ρ = density (kg/m^3)
ε = porosity
κ = permeability (m^2)
$\tilde{\kappa}$ = modified permeability (m^2)
μ = dynamic viscosity (Pa s)
υ = kinematic viscosity (m^2/s)
cell = volume containing one pin
cross = cross section
f = fluid
i, j = array indices
in = inlet
out = outlet
pin = pin surface
pf = porous-fluid
ps = porous-solid
s = solid
w = wall

References

[1] Brunschwiler, T., and Michel, B., 2008, *Thermal Management of Vertically Integrated Packages*, Wiley-VCH, Weinheim, Chap. 33, pp. 635–649.
[2] Tuckerman, D. B., and Pease, R. F. W., 1981, "High-Performance Heat Sinking for VLSI," IEEE Electron Device Lett., **2**(5), pp. 126–129.
[3] Linderman, R. J., Brunschwiler, T., Kloter, U., Toy, H., and Michel, B., 2007, "Hierarchical Nested Surface Channels for Reduced Particle Stacking and Low-Resistance Thermal Interfaces," *Proceedings of the 23rd Annual IEEE Semiconductor Thermal Measurement and Management Symposium*, pp. 87–94.
[4] Colgan, E. G., Furman, B., Gaynes, M., Graham, W. S., LaBianca, N. C., Magerlein, J. H., Polastre, R. J., Rothwell, M. B., Bezama, R. J., Choudhary, R., Marston, K. C., Toy, H., Wakil, J., Zitz, J. A., and Schmidt, R. R., 2007, "A Practical Implementation of Silicon Microchannel Coolers for High Power Chips," IEEE Trans. Compon. Packag. Technol., **30**(2), pp. 218–225.
[5] Brunschwiler, T., Rothuizen, H., Fabbri, M., Kloter, U., Michel, B., Bezama, R. J., and Natarajan, G., 2006, "Direct Liquid Jet-Impingement Cooling With Micron-Sized Nozzle Array and Distributed Return Architecture," *Proceedings of the Tenth Intersociety Conference on Thermal and Thermomechanical Phenomena in Electronics Systems*, Vols. 1 and 2, pp. 196–203.
[6] Escher, W., Michel, B., and Poulikakos, D., 2009, "Efficiency of Optimized Bifurcating Tree-Like and Parallel Microchannel Networks in the Cooling of Electronics," Int. J. Heat Mass Transfer, **52**(5–6), pp. 1421–1430.
[7] Escher, W., Brunschwiler, T., Michel, B., and Poulikakos, D., 2010, "Experimental Investigation of an Ultrathin Manifold Microchannel Heat Sink for Liquid-Cooled Chips," ASME J. Heat Transfer, **132**(8), p. 081402.
[8] Wälchli, R., Brunschwiler, T., Michel, B., and Poulikakos, D., 2010, "Combined Local Microchannel-Scale CFD Modeling and Global Chip Scale Network Modeling for Electronics Cooling Design," Int. J. Heat Mass Transfer, **53**(5–6), pp. 1004–1014.
[9] Brunschwiler, T., Michel, B., Rothuizen, H., Kloter, U., Wunderle, B., Oppermann, H., and Reichl, H., 2008, "Forced Convective Interlayer Cooling in Vertically Integrated Packages," *Proceedings of the 11th IEEE Intersociety Conference on Thermal and Thermomechanical Phenomena in Electronic Systems*, Vols. 1–3, pp. 1114–1125.
[10] Koo, J. M., Im, S., Jiang, L. N., and Goodson, K. E., 2005, "Integrated Microchannel Cooling for Three-Dimensional Electronic Circuit Architectures," ASME J. Heat Transfer, **127**(1), pp. 49–58.

[11] Brunschwiler, T., Michel, B., Rothuizen, H., Kloter, U., Wunderle, B., Oppermann, H., and Reichl, H., 2009, "Interlayer Cooling Potential in Vertically Integrated Packages," Microsystem Technol., **15**(1), pp. 57–74.
[12] Nield, D. A., and Bejan, A., 2006, *Convection in Porous Media*, Springer, New York.
[13] Koh, J. C. Y., and Colony, R., 1986, "Heat Transfer of Microstructures for Integrated Circuits," Int. Commun. Heat Mass Transfer, **13**(1), pp. 89–98.
[14] Brunschwiler, T., Michel, B., Paredes, S., Drechsler, U., Cesar, W., Toeral, G. T. Y., and Leblebici, Y., 2009, "Validation of Porous-Media Prediction of Interlayer Cooled 3D-Chip Stacks," *Proceedings of the IEEE International Conference on 3D System Integration, 3DIC*, San Francisco CA, pp. 1–10.
[15] Koşar, A., and Peles, Y., 2006, "Thermal-Hydraulic Performance of MEMS-Based Pin Fin Heat Sink," ASME J. Heat Transfer, **128**(2), pp. 121–131.
[16] Koşar, A., and Peles, Y., 2008, "Micro Scale Pin Fin Heat Sinks: Parametric Performance Evaluation Study," IEEE Trans. Compon. Packag. Technol., **31**(1), pp. 235–235.
[17] Peles, Y., Kosar, A., Mishra, C., Kuo, C. J., and Schneider, B., 2005, "Forced Convective Heat Transfer Across a Pin Fin Micro Heat Sink," Int. J. Heat Mass Transfer, **48**(17), pp. 3615–3627.
[18] Žukauskas, A., and Ulinskas, R., 1988, *Heat Transfer in Tube Banks in Crossflow*, Hemisphere, Washington, DC.
[19] Qu, W. L., and Siu-Ho, A., 2008, "Liquid Single-Phase Flow in an Array of Micro-Pin-Fins-Part I: Heat Transfer Characteristics," ASME J. Heat Transfer, **130**(12), p. 122402.
[20] Kim, K. Y., and Moon, M. A., 2009, "Optimization of a Stepped Circular Pin-Fin Array to Enhance Heat Transfer Performance," Heat Mass Transfer, **46**(1), pp. 63–74.
[21] Fowler, A. J., and Bejan, A., 1994, "Forced-Convection in Banks of Inclined Cylinders at Low Reynolds-Numbers," Int. J. Heat Fluid Flow, **15**(2), pp. 90–99.
[22] Yang, Y. T., and Peng, H. S., 2008, "Numerical Study of Pin-Fin Heat Sink With Un-Uniform Fin Height Design," Int. J. Heat Mass Transfer, **51**(19–20), pp. 4788–4796.
[23] Lee, P. S., and Garimella, S. V., 2005, "Hot-Spot Thermal Management with Flow Modulation in a Microchannel Heat Sink," Proceedings of the ASME Heat Transfer Division, Vol. 376-1, pp. 643–647.
[24] Saidi, M. H., and Khiabani, R. H., 2007, "Forced Convective Heat Transfer in Parallel Flow Multilayer Microchannels," ASME J. Heat Transfer, **129**(9), pp. 1230–1236.
[25] Wei, X. J., and Joshi, Y., 2003, "Optimization Study of Stacked Micro-Channel Heat Sinks for Micro-Electronic Cooling," IEEE Trans. Compon. Packag. Technol., **26**(1), pp. 55–61.
[26] Zhang, H. Y., Pinjala, D., Wong, T. N., Toh, K. C., and Joshi, Y. K., 2005, "Single-Phase Liquid Cooled Microchannel Heat Sink for Electronic Packages," Appl. Therm. Eng., **25**(10), pp. 1472–1487.
[27] Lide, D. R., 2010, *CRC Handbook of Chemistry and Physics*, CRC, Boca Raton, FL/Taylor & Francis, London, pp. 6-1,12-195, and 12-198.
[28] Strutt, J. W., 1892, "On the Influence of Obstacles Arranged in Rectangular Order Upon the Properties of a Medium," Philos. Mag., **5**(34), pp. 481–502.
[29] Kaviany, M., 1991, *Principles of Heat Transfer in Porous Media*, Springer-Verlag, New York.

Heat Transfer Characteristics of Oscillating Heat Pipe With Water and Ethanol as Working Fluids

Haizhen Xian

Yongping Yang
e-mail: yyp@ncepu.edu.cn

School of Energy and Power Engineering,
Beijing Key Laboratory of Energy Safety and Clean Utilization,
North China Electric Power University,
Beijing 102206, China

Dengying Liu
Institute of Engineering Thermophysics,
Chinese Academy of Sciences,
Beijing 100190, China

Xiaoze Du
School of Energy and Power Engineering,
Beijing Key Laboratory of Energy Safety and Clean Utilization,
North China Electric Power University,
Beijing 102206, China

In this paper, experiments were conducted to achieve a better understanding of the oscillating heat pipe (OHP) operating behavior with water and ethanol as working fluid. The experimental results showed that there existed a necessary temperature difference between the evaporator and the condenser section to keep the heat pipe working. The maximum effective conductivity of the water OHP reached up to 259 kW/m K, while that of the ethanol OHP is of 111 kW/m K. Not all the OHPs are operated in the horizontal operation mode. The heat transfer performance of the ethanol OHP was obviously affected by the filling ratio and the inclination angle but the influence law is irregular. The effect of the filling ratio and the inclination angle of the water OHP were smaller than that of the ethanol one. The heat transfer performance of the OHP was improved with increase of operating temperature. The startup characteristics of the OHP depended on the establishment of the integral oscillating process, which was determined by the operating factors. The startup temperature of the ethanol OHP varied from 40°C to 50°C and that of the water, OHP varied from 40°C to 60°C without considering the horizontal operating mode. The water OHP showed a better performance and more stable heat transfer characteristics than the ethanol OHP, which had no obvious advantages of the startup capability as well. [DOI: 10.1115/1.4002366]

Keywords: oscillating heat pipe, heat transfer characteristics, water, ethanol

1 Introduction

The oscillating heat pipe (OHP), also called the pulsating heat pipe, can be classified in a special category of the heat pipe for its particular operating principle. The OHP has some specific advantages over the conventional heat pipe, such as simple wickless structure, excellent heat transfer performance, easy for micromation, and so on. Its excellent heat transfer performance depends on the oscillating flow and phase change of slugs/plugs formed by the capillary force in a capillary channel. This is distinctly different from the conventional one. Miyazaki and Akachi [1] investigated the heat transfer characteristics of the looped OHP with R142b. They proposed a theoretical model that was strongly supported by the experiment results. The results indicated that the pressure oscillation and oscillatory flow had inspirited reciprocally, so as to keep the heat pipe working continuously. Akachi et al. [2] found that the thermal resistance was hardly affected by the heating orientation. Charoensawan et al. [3] experimentally studied the influence of the internal diameter, number of turns, working fluid (water, ethanol, and R-123), and inclination angle of the device. Later a semi-empirical correlations was given in their another paper [4]. Xu et al. [5] provided the high speed flow visualization results for the closed-looped OHP.

Some researches were carried to improve the heat transfer performance of the OHP. For example, Ma et al. [6] investigated experimentally the heat transfer performance of the OHP charged with a diamond nanofluid. Their study indicated that the heat transfer capability of the nanofluid OHP significantly increased. Nonuniformed cross section channels also can be used to enhance the heat transfer of the OHP. The experimental study by Xian et al. [7] showed that the effective thermal conductivity of the nonuniform cross section OHP is 19% higher than that of the uniform cross section. Variations in channel diameters were also employed as a means to enhance the heat transfer of the OHP in the study of Holley and Faghri [8]. They developed a model to study an OHP with sintered porous wicks and investigated the benefits of varying the channel diameter along the flow path. The results indicated that the heat transfer could be enhanced, the sensitivity to inclination angle would be less, and the range of the heat load capability would be larger. Xian et al. [9] adopted the pulse heating instead of the continuous heating to stimulate the working fluid oscillating flow in the heat pipe so as to enhance its heat transfer. Their experimental results indicated that the heat transfer rate of the pulse heating OHP was higher than that of the continuous by 15–35%.

Moreover, OHPs have been put into application as CPU heat sinks, air-preheaters, solar collectors, and so on. For example, Gi et al. [10] designed an "O" shaped flat OHP to connect the cooling fins on the keyboard area, which had very small thermal resistance between a 40 W CPU and cooling fins. Rittidech et al. [11] provided an OHP air-preheater in a dryer to recover the waste heat from exhaust steam. They found that 40% waste heat could be reused when the exhaust temperature of 80°C. Rittidech and Wannapakne [12] applied a closed-end OHP as a flat plate solar collector. An efficiency of approximately 62% was achieved in the efficiency evaluation experiment. In the study of Han et al. [13], they constructed a cryogenic OHP of ultrafast cooling rates for cell cryopreservation using liquid nitrogen as working fluid. The experimental results showed that the apparent heat transfer coefficient of the OHP could reach 2×10^5 W/m^2 K.

However, a comprehensive understanding of the oscillating heat pipe is still lacking because of its extremely complex two phase heat and mass transfer process and multivariate operating mechanism, although many experimental and theoretical approaches have been conducted in these years. The primary influence factors can be summarized as structural, operational, and physical parameters, including the filling ratio, operating orientation, heating mode (top heating, bottom heating, or horizontal heating), temperature difference between evaporator and condenser section, input heat flux, thermophysical properties of working fluids, and so

Contributed by the Heat Transfer Division of ASME for publication in the JOURNAL OF HEAT TRANSFER. Manuscript received April 6, 2010; final manuscript received July 27, 2010; published online September 21, 2010. Assoc. Editor: Giulio Lorenzini.

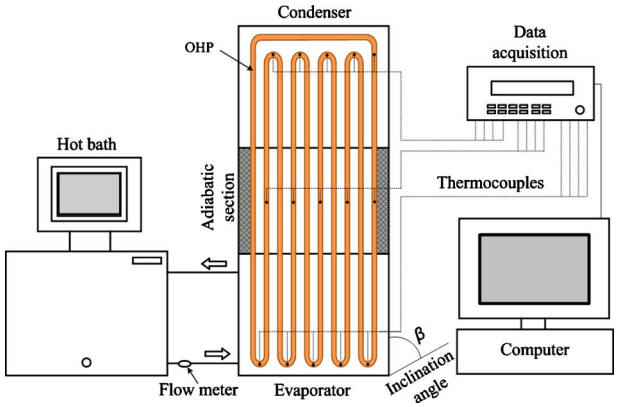

Fig. 1 Schematic experiment system

on. In addition, strong thermal-hydrodynamic coupling interaction can be found among these influence factors. Therefore, it is vital to get much more experimental data to find out the operational regularity. As known, the selection of the working fluid for the heat pipe is dependent on the range of operation temperatures. The saturation temperature of ethanol is 20°C lower than that of water, so it may be a better choice for some working conditions (e.g., relatively lower operating temperature or lower heat load) because it is easier to start up theoretically. Therefore, the main purpose of this paper is to experimentally investigate the heat transfer characteristic of the OHP using ethanol and water as working fluids to provide more experimental data for its better practical application.

2 Experiment System

As shown in Fig. 1, the experimental system comprises an OHP, a hot bath, and a data acquisition system. The closed-loop OHP was made of copper tubes with 3 mm inner diameter, 5 mm outer diameter, and 6.449 m total length. The total number of meandering turns is 10. The evaporator section of 200 mm length was put in a heating box supplied with hot fluid of constant temperatures and mass flow rate by a hot bath (HAKKA, P2-B12) while the condenser section of 200 mm was put in the cooling box charged with 2.3 kg water. The adiabatic section of 200 mm, the heating box, and the cooling box were well insulated with the polyethylene foam insulation to prevent the heat loss. The temperature measurement was performed using HP Benchlink Data Logger (model: Agilent 34970A; resolution: 0.01°C; measuring frequency: 1 Hz), coupled with K type thermocouples of 0.5 mm diameter. Twenty thermocouples were used in this experimental system. Fifteen thermocouples were attached to the tube wall of the heat pipe: five jointed at the evaporator section, five at the adiabatic, and five at the condenser section. One thermocouple was placed at the inlet of heating box and another four thermocouples were respectively placed at four fix positions in the cooling box to measure the water temperature variations. Ethanol and water were employed as the working fluid, and their filling ratios varied among 40%, 50%, and 60%; inclination angles varied among 0 deg, 20 deg, 60 deg, and 90 deg; and operating temperatures varied among 69°C, 79°C, and 88°C. All the experiments were performed more than 2 h to obtain authentic data.

It should be noted that the cooling box was charged with fixed water whose temperature would change against time, so the heat pipe was always operating in the transient state. As a result, its heat transfer rate would decrease with decrease in temperature difference, causing difficulties in determining the appropriate average heat transfer rate to measure the heat transfer performance of the OHP. Despite this, it is necessary to investigate the operating mode like that because it is encountered in the application of the OHP. For example, for the case the OHP used in the natural convection solar collector, the water will be heated to high temperatures as much as possible. The maximum water temperature that can be heated (or the temperature difference between evaporator and condenser section), the startup temperature and the effect of operating factors are very important, so more experiments are needed to reveal the operating laws for the better practical application of the OHP.

In this experiment, the average heat transfer rate of the OHP was determined from

$$Q = c_p m \Delta T / \tau \tag{1}$$

where c_p is the specific heat at a constant pressure, m is the mass of the water inside the cooling box, ΔT represents the water temperature difference during the experience time τ. It is necessary to note that, for the sake of reasonable comparison and accurate analysis by removing the influence of the temperature difference between the water in the cooling box and the OHP tube wall, the average heat transfer rate Q were calculated with the same water temperature difference at the same initial temperature.

The effective thermal conductivity, which is often used to valuate the heat transfer performance for the heat pipe, can be defined as

$$\lambda = \frac{Q \cdot l}{A_c(T_{\text{evap}} - T_{\text{cond}})} \tag{2}$$

where T_{evap} and T_{cond} are the mean wall temperatures at the evaporator and the condenser section respectively, l is the length between the evaporator and condenser section, A_c is the total cross section area of the heat pipe.

3 Results and Discussion

3.1 The Minimum Temperature Difference Between the Evaporator and the Condenser Section. The wall temperature difference between the condenser and evaporator section varied during the operating process, and the phenomena observed also varies correspondingly. At the startup stage, the temperature difference was of the maximum value, as well as comparatively large temperature fluctuations at high frequencies was observed as a result of the serious thermal-hydrodynamic oscillating action inside the heat pipe because of the large pressure difference between evaporator and condensation section caused by rapid evaporation and condensation inside the tube. Subsequently, the temperature difference went down gradually as the water temperature increased in the cooling box, resulting from the reduction of heat dissipation in the condenser section. At the same time, the wall temperature oscillation amplitude and frequency observed also decreased. When the water temperature in the cooling box increased up to a certain maximum temperature that could be heated, the heat pipe would stop work for a short time, no wall temperature oscillation could be observed and a minimum value of the temperature difference between the evaporator and condenser section was achieved. However, when the water temperature in the cooling box decreased (commonly by 1–2°C) after a certain time because of heat loss, the temperature difference between the heating and cooling section rose, the heat pipe restartup, wall temperature oscillations were observed, and the water temperature in the cooling box would increase until up to the maximum value again, so the water was maintained at a maximum temperature by this repeated process. This implies that there exists a necessary temperature difference between evaporator and condenser section to keep the heat pipe working and its value represents the heat transfer performance of the OHP to a certain extent; The smaller the minimum temperature difference, the better the heat pipe performance.

In the experiment, all the OHPs were evacuated to the same vacuum pressure. The minimum temperature differences ΔT_{min} of the ethanol and the water OHP under different operating conditions are given in Fig. 2. It can be seen from the figure that not all of the OHP at the horizontal heating mode can work. For the

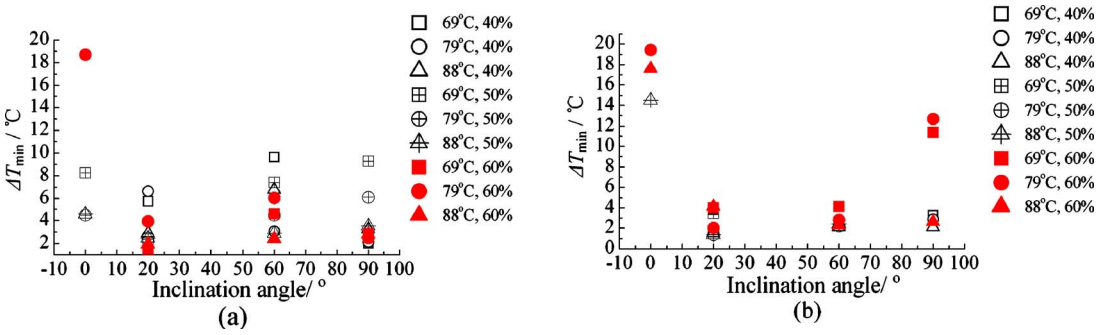

Fig. 2 The minimum temperature difference between the evaporator and the condenser section: (*a*) ethanol and (*b*) water

ethanol OHP, the ΔT_{min}, ranging from 1.4°C to 9.7°C, varied greatly and irregularly when the filling ratio and inclination angle were changed. There exists an optimal inclination angle for each filling ratio, and the difference of ΔT_{min} among each optimal operating condition is small, ranging from 1.5°C to 2.0°C. Comparing at the same filling ratio, the maximum ΔT_{min} was often observed in the cases working at the horizontal inclination angle. Compared with the ethanol OHP, the variations of ΔT_{min} of the water OHP, ranging from 1°C to 4.2°C, are quite small when the filling ratio varies from 40% to 60%, the inclination angle varies from 20 deg to 90 deg, and the operating temperature varies from 69°C to 88°C except in two cases. These cases with ΔT_{min} of 12.7°C and 11.4°C occurred when the filling ratio was 60% and the inclination angle was 90 deg. It can be seen that, the inclination angle has a small effect on the water OHP when the filling ratio is relatively small. However, when the filling ratio increased to 60%, the heat pipe's performance deteriorated when the inclination angle was increased to 90 deg. This is because the effect of gravity will become larger with increase in the filling ratio and the inclination angle, so it requires a greater driving force to push the working fluid from evaporator toward the condenser section. As indicated in Fig. 2, the value of ΔT_{min} decreased significantly, when the operating temperature is increased to 88°C because higher temperatures can offer bigger driving forces.

3.2 Effect of Filling Ratio. The thermal performance of the ethanol OHP under various filling ratios, inclination angles, and operating temperatures is shown in Fig. 3. The maximum effective conductivity achieved reached up to 111 kW/m K. Comparing at the same inclination angle and operating temperature, the heat pipe was obviously affected by the filling ratio in some cases but the influence law is irregular and related to inclination angles and operating temperatures. For example, the effective thermal conductivity variation for each filling ratio is comparatively slight when the OHPs operating at 20 deg inclination angle but their differences became larger with increase of the inclination angle. Additionally, the increasing operating temperature to some extent weakened the effect of filling ratios. The optimal filling ratio was 60% achieved at 60 deg inclination angle when the operating temperatures are 69°C and 79°C, and 50% at 90 deg inclination angle for the operating temperature of 88°C.

The thermal performance of the water OHP is shown in Fig. 4. In the experiment, the water OHP showed an excellent heat transfer performance. The maximum effective thermal conductivity reached up to 259 kW/m K, which was about twice larger than that of the ethanol OHP. It also can be seen that, the effect of the filling ratio of the water OHP is smaller than that of the ethanol one. The performance differences are significant when the operating temperature is 69°C, and these differences decrease with increasing operating temperature. In most cases, the OHP with filling ratio of 60% showed a better and more stable heat transfer performance.

3.3 Effect of Inclination Angle. Experiment results showed that not all OHPs operated in the limiting case of a zero inclination angle: The ethanol OHP with filling ratio of 40% did not work at all operating temperatures but worked well with filling ratio of 50% at all operating temperatures; the OHP with filling

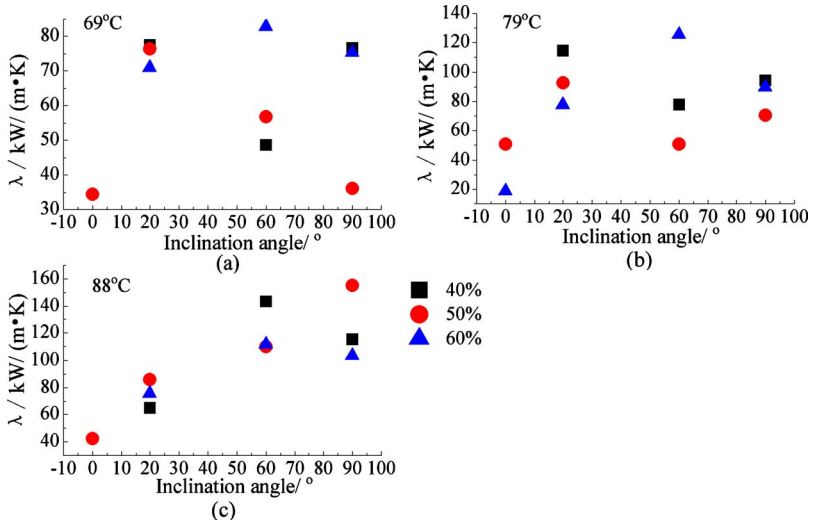

Fig. 3 The thermal performance of the ethanol OHP

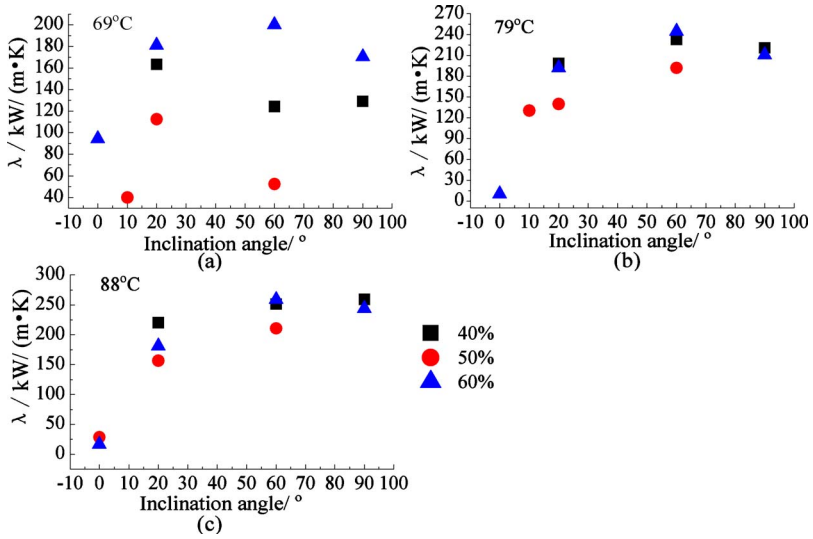

Fig. 4 The thermal performance of the water OHP

ratio of 60% only worked when operating temperature was of 79°C but the heat transfer performance is worse. For the water OHP, the heat pipe could not work when the filling ratio was less than 50%. When the filling ratio was of 60%, the OHP worked well when the operating temperature was 69°C but worked in a worse and unstable state when the operating temperature increased.

The results also exhibited that the OHP, which used ethanol as working fluid, was obviously affected by the inclination angle when the inclination angle changed from 20 deg to 90 deg. In most cases, the optimal value of inclination angle went up when the operating temperature increased: when the operating temperature was of 69°C, the optimal value of inclination angle was 20 deg for the OHP at all filling ratios, while for the cases at a higher operating temperature, the optimal value of the inclination angle mostly located at 60 deg and the heat transfer performance of the OHP at 90 deg inclination angle were improved.

With respect to the water OHP, the effect of the inclination angle was weakened with the increase in operating temperature. The heat transfer performance was improved with increase of inclination angle when the filling ratio is less than 50% but decreased when the filling ratio is 60% because the gravity effect increased with the increase in the filling ratio. The water OHP showed a better and more stable performance than the ethanol OHP.

3.4 Effect of Operating Temperature. As shown in Figs. 3 and 4, the OHP heat transfer performance were improved with the increase of the operating temperature, but the improvement degree of the ethanol OHP was rather smaller than the one using water as working fluid mainly because of the difference in thermal properties. Stronger driving forces caused by the greater heat and mass transfer rate via vaporization were achieved as a result of increasing operating temperature; however, the smaller latent heat of vaporization and the lower saturation temperature made the ethanol OHP easy to vaporize and start up at a relatively lower temperature. Consequently, the heat transfer improvement was very significant at the beginning stage of increasing operating temperature, but the improvement extent became smaller with further increase in operating temperature. With respect to the water OHP, its operating stability and performance was improved significantly with increase in the operating temperature.

3.5 Startup Characteristics. The OHP whether starting up or not can be judged by detecting the wall temperature oscillations and the water temperature increments in the cooling box. All the OHPs were evacuated to the same vacuum pressure and operated stably for more than 40 min to determine the startup temperature. The experimental results are given in Table 1.

For the OHP, the startup characteristics depend on the establishment of the integral oscillating process, which is not only determined by phase-change temperatures, but also by the other factors, such as the effect of gravity, the density, the latent heat of vaporization, the viscosity, and the surface tension, which will definitively determine the action results between driving forces and resistant forces. Among these factors, the driving force caused by phase change and the gravity play the most important roles.

The experimental results showed that the startup temperature of the ethanol OHP varied from 40°C to 50°C and that of the water OHP varied from 40°C to 60°C without considering the horizontal operating mode. For the ethanol OHP, the inclination angle and filling ratio had some influence on the startup temperature. When the filling ratio is relatively small, the startup temperature increases with the increase of the inclination angle. However, when the filling ratio is relatively large, the startup temperature will drop with increase of the inclination angle. The water OHP showed a more stable performance than the ethanol one. The startup temperature kept a constant value of 40°C when the filling

Table 1 Startup temperatures under varied operating conditions

	Water			Ethanol		
Inclination angle (deg)	α=40% (°C)	α=50% (°C)	α=60% (°C)	α=40% (°C)	α=50% (°C)	α=60% (°C)
0	Not run	79	69	Not run	69	69
20	40	40	55	40	50	40
60	40	40	55	45	50	50
90	40	40	60	50	50	40

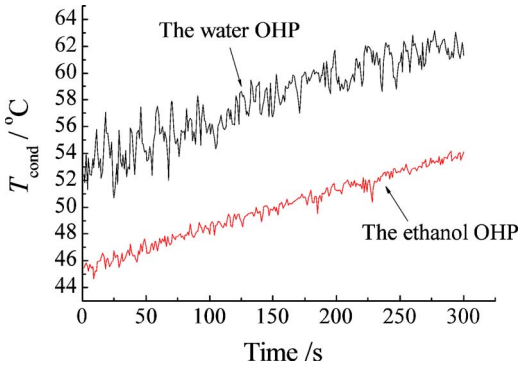

Fig. 5 The wall temperature oscillations at the condenser section

ratio varied from 40% to 50% but increased when the filling ratio is 60%. Its startup temperature was not affected by inclination angle when the filling ratio was small but increased with the increase of the inclination angle when the filling ratio increased to 60%. The startup temperature for the OHP operating horizontally was significantly higher than the others.

3.6 Further Discussion. Comparing the water OHP with the ethanol OHP, the experiment results showed that, in general, the heat transfer performance of the former was much better than the latter and their operating regularities were different in some aspects. In summary, the ethanol OHP was of worse performance and less stable heat transfer characteristics, and no obvious advantages of the startup capability were observed as well. Analyzed qualitatively, the smaller values of latent heat and specific heat of the ethanol can account for its unsatisfactory performance, reflected directly by the different features of the wall temperature oscillations. Typical wall temperature oscillations, operating at the same inclination angle, filling ratio, and operating temperature, are shown in Fig. 5. It can be seen that the wall temperature at the condenser section for the ethanol is much lower than that of the water although both wall temperatures at the evaporator section are equal. In addition, their wall temperature oscillations are different because of the different thermal properties: high frequency and large amplitude for the water and slightly higher frequency and much lower amplitude for the ethanol. This indicates that the thermal impact of the ethanol is much lower than that of the water because of its lower value of latent heat and specific heat. It is necessary to notice that the thermal properties will also affect the internal movement and then will affect the heat transfer performance consequently, so a visualization experiment is necessary for the further investigation on the operating mechanism by directly observing the different operation status of different working fluids.

The working mechanism of the OHP is quite different from the traditional heat pipe. In the traditional heat pipe, the working fluid moving in the form of steam toward the condenser section would cause smaller flow resistance than that in the OHP, whose working fluid moves in liquid and vapor plugs. As mentioned above, the performance of the OHP depends on the establishment of the integral stable movement inside the tube, which is affected by many factors. In addition, strong thermal-hydrodynamic coupling interaction can be found among these factors. A factor would possibly play different roles in operation. For example, the gravity would be a resistance when the liquid and vapor plugs working fluid moves toward the condenser section but would be a driving force when the working fluid flows back to the evaporator section. When the filling ratio increases, the mass of working fluid also increases; it would need a larger driving force to push the working fluid to the condenser section. But if the working fluid reaches condenser section, its velocity back to the evaporator section would be faster than the OHP with lower filling ratios. In the same time, the larger amount of mass carries more heat transferring from the evaporator to the condenser section. In a word, in view of the complex heat and mass transfer process and the multivariate operating mechanism of OHP, further investigation via experiment and theoretical approaches is needed to reveal the operation law.

4 Conclusion

In this paper, experiments were conducted to achieve a better understanding of operating behavior of the OHP using water and ethanol as working fluid. The results obtained in the experiment and conclusions are summarized as follows:

1. There exists a necessary temperature difference between the evaporator and the condenser section to keep the heat pipe working. For the ethanol OHP, the ΔT_{min} varied greatly and irregularly when the filling ratio and inclination angle were changed. Compared with the ethanol OHP, the variations of ΔT_{min} of the water OHP are quite small. The maximum ΔT_{min} was observed in the case working at the horizontal inclination angle at the same filling ratio.
2. Not all the OHPs operated in the limiting case of a zero inclination angle. The maximum effective conductivity of the ethanol OHP reached up to 111 kW/m K, while that of the water OHP reached up to 259 kW/m K, which is about twice larger than that of the ethanol OHP. The ethanol OHP was obviously affected by the filling ratio and the inclination angle but the influence law is irregular. With respect to the water OHP, the effect of the filling ratio and the inclination angle were smaller than that of the ethanol one. The water OHP showed a better and more stable performance than the ethanol OHP. The heat transfer performance of OHP was improved with increase of the operating temperature.
3. The startup characteristics of the OHP depend on the establishment of the integral oscillating process, which is determined by many factors. The startup temperature of the ethanol OHP varied from 40°C to 50°C and that of the water OHP varied from 40°C to 60°C without considering the horizontal operating mode. For the ethanol OHP, the inclination angle and filling ratio had some influence on the startup temperature. With regard to the water OHP, its startup temperature was not affected by inclination angle when the filling ratio was small but increased with the increase of inclination angle when the filling ratio increased to 60%. The startup temperature for the OHP operating horizontally was significantly higher than the others.
4. In summary, the water OHP was of a better performance and more stable heat transfer characteristics than the ethanol OHP, which has no obvious advantages of the startup capability as well.

Acknowledgment

This work is financially supported by the National Natural Science Foundation of China (Grant No. 50876029), the National High-tech R&D Program of China (863 Program) (Grant No. 2009AA05Z418), and the National Basic Research Program of China (973 Program) (Grant No. 2009CB219804).

References

[1] Miyazaki, Y., and Akachi, H., 1996, "Heat Transfer Characteristics of Looped Capillary Heat Pipe," *Proceedings of the Fifth International Heat Pipe Symposium*, Melbourne, Australia, pp. 378–383.
[2] Akachi, H., Polasek, F., and Stulc, P., 1996, "Pulsating Heat Pipes," *Proceedings of the Fifth International Heat Pipe Symposium*, Melbourne, Australia, pp. 208–217.
[3] Charoensawan, P., Khandekar, S., Groll, M., and Terdtoon, P., 2003, "Closed Loop Pulsating Heat Pipes, Part A: Parametric Experimental Investigations," Appl. Therm. Eng., **23**(16), pp. 2009–2020.
[4] Khandekar, S., Charoensawan, P., Groll, M., and Terdtoon, M., 2003, "Closed Loop Pulsating Heat Pipes, Part B: Visualization and Semi-Empirical Modeling," Appl. Therm. Eng., **23**(16), pp. 2021–2033.
[5] Xu, J., Li, Y., and Wong, T., 2005, "High Speed Flow Visualization of a Closed

Loop Pulsating Heat Pipe," Int. J. Heat Mass Transfer, **48**(16), pp. 3338–3351.
[6] Ma, H. B., Wilson, C., Borgmeyer, B., Park, K., and Yu, Q., 2006, "Effect of Nanofluid on the Heat Transport Capability in an Oscillating Heat Pipe," Appl. Phys. Lett., **88**, p. 143116.
[7] Xian, H., Liu, D., Yang, Y., Shang, F., Du, X., Mujumdar, A., and Huang, L., 2007, "Study on Heat Transfer Enhancement of Oscillating-Flow Heat Pipe for Drying," Drying Technol., **25**(4), pp. 723–729.
[8] Holley, B., and Faghri, A., 2005, "Analysis of Pulsating Heat Pipe With Capillary Wick and Varying Channel Diameter," Int. J. Heat Mass Transfer, **48**(13), pp. 2635–2651.
[9] Xian, H., Liu, D., Yang, Y., Shang, F., and Du, X., 2007, "Study on the Heat Transfer Enhancement of Oscillating-Flow Heat Pipe by Pulse Heating," J. Enhanced Heat Transfer, **14**(1), pp. 53–64.
[10] Gi, K., Maezawa, S., Kojima, Y., and Yamazaki, N., 1999, "CPU Cooling of Notebook PC by Oscillating Heat Pipe," *Proceedings of the 11th International Heat Pipe Conference*, Tokyo, Japan, pp. 166–169.
[11] Rittidech, S., Dangeton, W., and Soponronnarit, S., 2005, "Close-Ended Oscillating Heat-Pipe (CEOHP) Air-Preheater for Energy Thrift in a Dryer," Appl. Energy, **81**(2), pp. 198–208.
[12] Rittidech, S., and Wannapakne, S., 2007, "Experimental Study of the Performance of a Solar Collector by Closed-End Oscillating Heat Pipe (CEOHP)," Appl. Therm. Eng., **27**(11–12), pp. 1978–1985.
[13] Han, X., Ma, H., Jiao, A., and Critser, J., 2008, "Investigations on the Heat Transport Capability of a Cryogenic Oscillating Heat Pipe and Its Application in Achieving Ultra-Fast Cooling Rates for Cell Vitrification Cryopreservation," Cryobiology, **56**(3), pp. 195–203.

Imaging of Surface-Tension-Driven Convection Using Liquid Crystal Thermography

T. W. Dutton[1]

L. R. Pate[2]

D. K. Hollingsworth[3]
e-mail: hollingsworth@uh.edu

Department of Mechanical Engineering,
University of Houston,
Engineering Building One,
Houston, TX 77204

Surface-tension forces can drive fluid motion within thin liquid layers with a free surface. Spatial variations in the temperature of the free surface create surface tractions that drive cellular motions. The cells are most commonly hexagonal in shape and they scale on the thickness of the fluid layer. This investigation documents the formation of cells in the liquid film in the presence of a uniform-heat-flux lower boundary condition. Liquid crystal thermography was used to image the cells and measure the temperature distribution on the lower surface of the liquid layer. A 1.1 mm deep pool of silicone oil was supported on a 50 μm thick electrically heated metal foil. The oil was retained inside an independently heated acrylic ring mounted on the top surface of the foil and a dry-ice cooling plate served as the low-temperature sink above the free surface of the oil. Color images of hexagonal convection cells were captured using liquid crystal thermography and a digital image acquisition and processing system. The temperature distribution inside a typical cell was measured using thermographic image analysis. Experimental issues, such as the use of an independently heated retaining ring to control the height of the liquid film and the utility of a flux-based Marangoni number are discussed.
[DOI: 10.1115/1.4002114]

Keywords: Marangoni flow, surface-tension-driven flow, liquid crystal thermography

1 Introduction

When a thin layer of fluid with a free surface is heated from below and cooled from above, cellular flow patterns form in the layer. This phenomenon was first reported by Bénard [1] and has come to be known as "Bénard convection." He attributed the formation of the patterns to the action of buoyancy forces (warm liquid rising and cool liquid falling). First, Block [2] and then more formally, Pearson [3] showed that while cellular motions of this type *appear* to be caused by buoyancy, they are actually caused by *surface-tension forces* acting at the free surface. Small spatial variations in liquid surface temperature produce variations in surface tension. The fluid at the surface is pulled toward the areas that happen to be cooler and these small motions quickly set the entire liquid layer into a highly structured cellular motion. The most typical cellular pattern is a hexagon that is warm in the center and cool at the edges as shown in Fig. 1.

Pearson showed that a dimensionless group now called the "Marangoni number" expresses the ratio of the surface-tension forces to the viscous forces and provides the framework for a stability analysis of surface-tension-driven flows. The Marangoni number, Ma, is defined as

$$\mathrm{Ma} \equiv \frac{-\sigma}{\rho \nu \alpha} \Delta T d \tag{1}$$

where σ is the derivative of surface tension with respect to surface temperature; ΔT is the mean temperature difference across a liquid layer of depth, d; ρ, ν, and α are the density, kinematic viscosity, and thermal diffusivity, respectively, of the liquid. Pearson's analysis showed that Bénard convection patterns would form under appropriate conditions independent of gravity. Since Pearson's work, a number of experimental projects have used particle flow visualization to investigate the flow patterns and to document the critical Marangoni number necessary for cell formation (for example: Koschmieder and co-workers [4,5]).

NASA shuttle flights have explored the advantages of microgravity in the production of new alloys and crystals for use in the next generation of high-technology products. Some of these processes involve thin liquid films that are solidified into the final product. While the microgravity environment removes fluid motions caused by buoyancy forces, surface-tension-driven motions remain. These motions present a considerable complication to the control of thin liquid films in microgravity and their dynamics have become a focus of a several NASA projects. For example, the flight experiment by Ostrach [6] used particle image velocimetry to image and measure flow patterns produced under both uniform-temperature and uniform-heat-flux boundary conditions at the heated surface.

These past studies have typically relied on flow visualization to create images of the cellular patterns. This flow phenomenon is inherently thermally-driven and can be examined effectively by thermal visualization. Through the 1990s, the University of Houston Heat Transfer and Phase Change Laboratory developed liquid crystal thermography as a tool for imaging the complex and dynamic temperature patterns on uniform-heat-flux surfaces in single-phase and two-phase flows. For the details of the technique, see Hay and Hollingsworth [7,8]. For more recent applications see Bayazit et al. [9], and Daniel et al. [10]. This paper reports the final status of our application of this technique to the study of Bénard convection (Dutton [11] and Pate [12]). A uniform-heat-flux lower surface is required by the thermographic technique. This requirement drives our interest in the behavior of Bénard convection with the historically less popular uniform-heat-flux boundary condition. The discussion will focus on the facility construction and operation, imaging the cellular pattern, the measurement of the critical value of Ma through the use of a flux-based definition of the Marangoni number, and the measurement of the temperature distribution on the lower surface.

[1]Present address: Associated Equipment Company, Pearland, TX.
[2]Present address: NASA Johnson Space Center, Houston, TX.
[3]Corresponding author.

Contributed by the Heat Transfer Division of ASME for publication in the JOURNAL OF HEAT TRANSFER. Manuscript received September 26, 2009; final manuscript received June 27, 2010; published online September 20, 2010. Assoc. Editor: Patrick H. Oosthuizen.

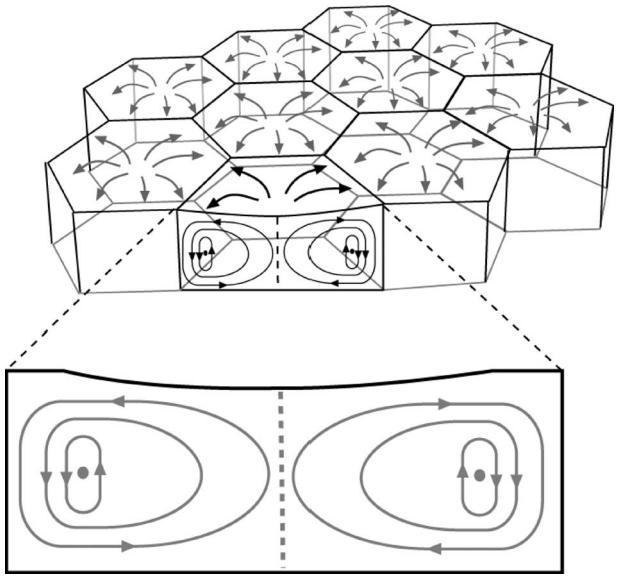

Fig. 1 Sketch of cellular flow pattern [12]

2 Experiment Apparatus and Data Reduction

The experimental facility [11] seeks to create a large, planar field with a cross section as shown in Fig. 2. Dow Corning 200 silicone oil was used to form the liquid layer. This is the same liquid used by Koschmieder and Biggerstaff [4,13] and is frequently chosen because of its relatively high σ and for its low susceptibility to surface contamination. The fluid properties as taken from Koschmieder [13] are given in Table 1. Note that the derivative of surface tension with respect to temperature is negative.

A 50 μm thick, 101.6 mm wide, and 145 mm long stainless steel foil formed the base of the liquid pool. The foil was tensioned across two parallel copper rods by two aluminum clamps connected to springs as shown in Fig. 3(*a*) and 3(*b*). The silicone oil was contained with a Lucite ring glued to the top of the foil with silicone sealer. The inner diameter and height of the ring were 77 mm and 2.6 mm, respectively. An electrically heated wire was embedded in the ring to keep the ring temperature near the foil temperature in order to avoid meniscus creep up the side of the ring. A thermocouple mounted inside the ring was used to monitor its temperature. The lower (dry) side of the foil was guard-heated to effectively eliminate heat flow to the surrounding

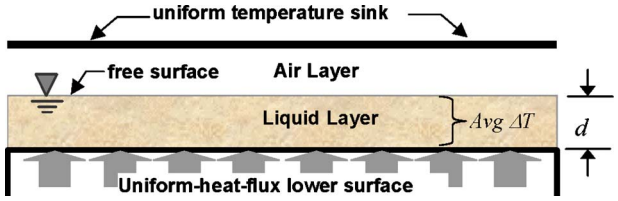

Fig. 2 Diagram of fluid layers with upper and lower boundaries

Table 1 Physical properties of Dow Corning 200 Silicone oil at 25°C

Density, ρ	968 kg/m^3
Kinematic viscosity, ν	1 cm^2/s
Thermal diffusivity, α	0.001095 cm^2/s
Conductivity, k	0.155 W/m K
Derivative of surface tension with respect to temperature, σ	−0.05 dyn/cm K

air. A Lucite cylinder with the same diameter as the retaining ring was installed directly below the foil. The cylinder rested on an aluminum base plate. This base plate was heated with a pair of glued-on resistance heaters so that the air inside the cylinder was held within 4°C of the mean foil temperature. The air temperature was measured by a thermocouple mounted inside the cylinder.

The low-temperature sink was an insulated aluminum and stainless container holding dry ice. A thermocouple was attached to the inside bottom of the container to measure the temperature of the cold surface. The lower surface of the container was machined flat and finished with a medium grade emery cloth. This lower surface formed the uniform-temperature upper boundary condition or "cold-plate" above the air layer. Three independently adjustable micrometer heads supported the dry ice container above the aluminum base plate. These were adjusted to vary the air gap between the liquid surface and the cold-plate.

Liquid crystal thermography was used to image the temperature distribution on the foil test surface at the base of the liquid layer. The underside of the foil was air-brushed with water-soluble black paint followed by several coats of a chiral-nematic liquid crystal paint. Thermochromic liquid crystals (TLC) display a color change across the spectrum from red at the lower end of the active temperature range through blue at the upper end. On either side of the active range, the TLC surface appeared black. While both micro-encapsulated and polymer-dispersed formulations were used in this investigation, the images shown here were obtained with a 50°C to 55°C polymer-dispersed formulation. The surface was illuminated by two 16 W fluorescent bulbs placed to either side of the Lucite cylinder. A hole matching the diameter of the ring and the cylinder was machined into the aluminum base plate and covered with a 3.2 mm thick glass pane. A charge-coupled-device color camera was positioned such that the image was viewed through a 45 deg mirror placed below the base plate. Real-time images were recorded on videotape and single images were digitized directly by a 3×8 bit Matrox color frame-grabber in an Intel-type computer.

A general discussion of quantitative TLC imaging can be found in Hay and Hollingsworth [7]. The intensities of the red, green, and blue primaries (R, G, and B, respectively) as recorded by the camera are cast as magnitudes of *hue*, *saturation*, and *monochromatic intensity*. The hue corresponds most closely to the wavelength of the light and it provides a scalar against which temperature can be calibrated. Hue is defined in terms of the primary intensities as

$$\text{hue} \equiv \arctan\left(\frac{\sqrt{3}(G-B)}{2R-G-B}\right) \tag{2}$$

Following Hay and Hollingsworth [7], a fifth-order polynomial was fit to calibrated examples of this TLC to produce a monotonic active range 2.10°C in width. A computation of uncertainty, using the approach described in Hay and Hollingsworth [7], produced an average *single-pixel* uncertainty equal to ±0.2°C or ±10% of the monotonic range.

Three power sources were used to independently supply power to the foil test surface, the retaining ring, and the aluminum base plate heaters. Power to the test surface was provided by a direct-current power supply and the foil current and voltage were measured for power calculations. The typical operating procedure was as follows. The base plate was heated and the power adjusted until the air temperature inside the Lucite cylinder was within 4°C of the center of the active range of the TLC. The ring was filled with oil using a graduated syringe. The foil was heated by adjusting the current until the TLC became active. The ring heater was then adjusted until its temperature was within 4°C of the mean TLC temperature. The dry-ice container was filled and placed on the facility at a setting that produced a large air gap. The power for the foil and ring were increased to keep the temperatures within the TLC active range while reducing the air gap through adjustment of the micrometer heads. Operating parameters that pro-

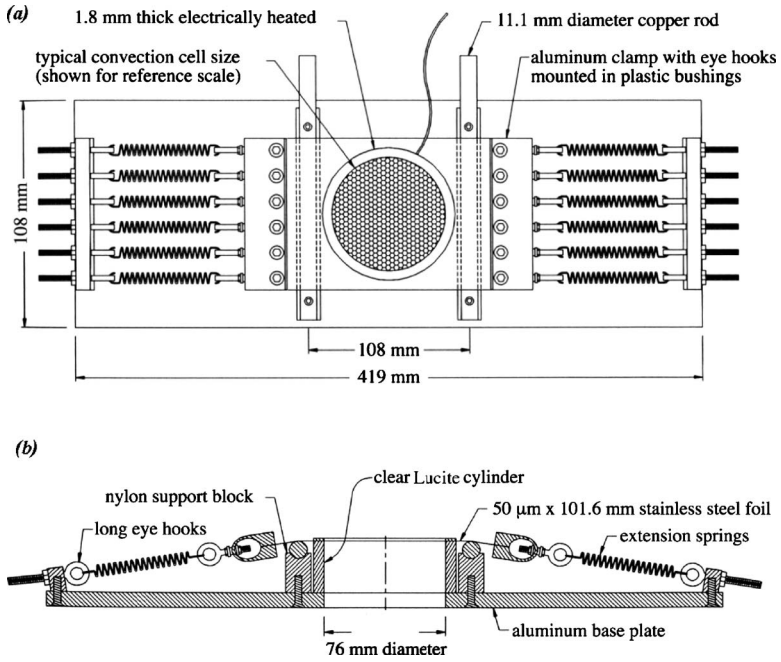

Fig. 3 Drawings of apparatus: (*a*) overhead view and (*b*) side view [11]

duced cells were recorded along with digital images of the TLC surface. These images were analyzed later to determine quantitative temperature distributions.

A unique feature of the apparatus is the independently heated retaining ring. The upper edge of the ring is the closest structural element to the cold plate. An unheated ring thereby becomes the coldest element on the test surface, and as such, liquid at the free surface is drawn to it by surface tension. This motion was so dominant that at unsuitably large air gaps, liquid was observed to flow over the top of the ring where it either froze against the cold plate or flowed down the external side of the ring. This problem was solved by imbedding an independently heated wire inside the retaining ring and providing (by accumulated experience) a power level to the ring so that the ring temperature was sufficiently high to prevent the liquid surface from rising near the ring.

3 Results

3.1 Temperature Field at the Base of the Liquid Layer. A typical cellular pattern in the 77 mm diameter pool as it imprints on the heated surface is shown in Fig. 4. The center of the pattern shows a regular array of hexagons. As the circular outer boundary is approached, that array becomes irregular with three generally colder regions appearing at 120 arc deg separations. Directly adjacent to the boundary, a ring of cells forms that follows the boundary shape and is generally much warmer than the cells toward the center of the pool. A typical cellular pattern from the center of the pool is shown in Fig. 5. This is a roughly 27 mm square image segment from the center of the pool. The spatial

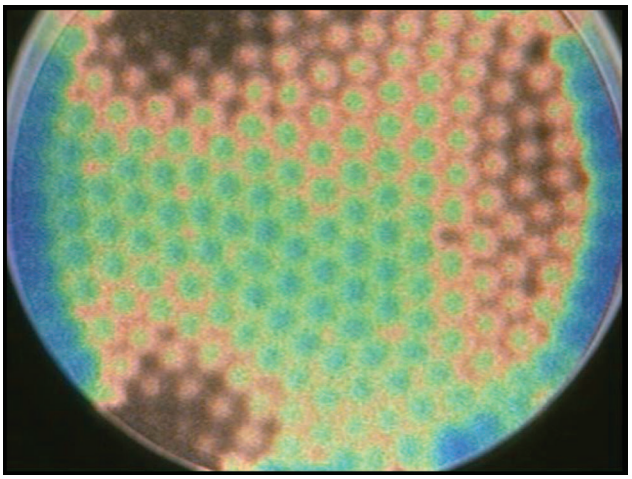

Fig. 4 Typical liquid crystal image of the heated surface beneath the liquid layer

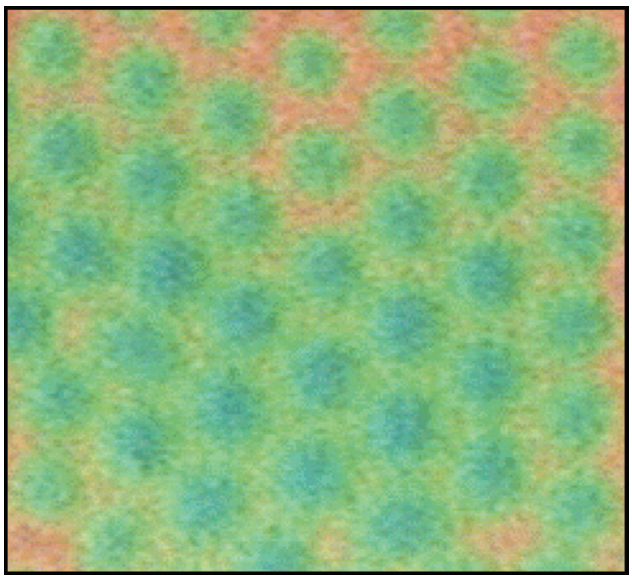

Fig. 5 Typical liquid crystal image of the center of the heated surface beneath the liquid layer

Table 2 Typical values of measurands and associated uncertainty

Measurand	Nominal value	Uncertainty	
Mean liquid depth, d	1.10 mm	$\pm$0.04 mm	4%
Air depth, d_a	2.10 mm	$\pm$0.25 mm	12%
Avg. TLC temperature, T_F	326 K	$\pm$0.75 K	
Cold-plate temperature, T_c	197 K	$\pm$0.5 K	
Overall temperature diff., ΔT_{total}	129 K	$\pm$0.9 K	0.7%
Foil voltage	0.580 V	$\pm$0.001 V	0.17%
Foil current	28.0 A	$\pm$0.25 A	0.9%
Total foil area	0.011 m^2	$\pm$0.0009 m^2	0.7%
Heat flux	1476 W/m^2	$\pm$16.8 W/m^2	1.1%

resolution is 0.11×0.11 mm^2 per pixel. While there are aberrations, most cells have six neighboring cells and all show the characteristic warm centers and cool edges. The cell width is approximately 4.3 mm or four times the liquid layer depth. Typical values of measurands for the formation of cells are given in Table 2.

Uncertainties are estimated at 95% confidence and resultant quantities are computed using constant-odds combinations following Kline and McClintock [14]. At typical settings, the Rayleigh numbers were approximately 11 in the liquid layer and approximately 200 in the air layer. The critical values for the onset of density-driven motions are approximately 700 and 1800, respectively.

The temperature distribution on the TLC surface for a typical group of cells is shown in Fig. 6. This is a roughly 12.75 mm square image region taken from a slightly cooler section near the top of Fig. 5. To reduce the uncertainty in the TLC measurement, a weighted local-area-average temperature was computed using ten contributions to the average: two times the value of the target pixel plus the values from the eight pixels surrounding the target pixel. Baughn et al. [15] found that small-neighborhood filtering produces a large reduction in the uncertainty of a TLC measurement. The reduction they found was of the approximate size one would anticipate if the neighboring pixels were completely uncorrelated and independent measurands. Treating the target pixel and each of its neighbors as independent samples possessing a single-pixel uncertainty of $\pm 0.2\,^\circ$C, one arrives at an uncertainty on the weighted average of $\pm 0.07\,^\circ$C or about 9% of the range of Fig. 6. The center-to-edge variation in temperature within a cell is about $0.6\,^\circ$C or 6% of the temperature drop across the liquid layer at the onset of motion ($10.4 \pm 0.4\,^\circ$C). Also, the temperature distribution near the centers of the cells is more peaked than one might expect from Fig. 5.

Figure 7 is a contour plot showing the temperature distribution in the neighborhood of one cell. The structure of the cell is illustrated by the hexagon superimposed on the figure. The largest lateral temperature gradients are $0.25-0.40\,^\circ$C/mm and occur in a region from 60% to 85% of the width (4.3 mm) of the cell. The lateral heat flow within the foil surface can be estimated using these data, a conductivity for the 0.050 mm foil of 15 W/m K and the assumption that the cell is a 4.3 mm circle. The resulting maximum lateral heat flow (1.5 mW to 3.4 mW) is 7–16% of the product of the heat flux and the cell area (21.4 mW). A lateral heat flow of this relative size is a substantial compromise of the uniform-flux boundary condition once cells are established. However, the only route to a substantial reduction in lateral flow would be a further reduction in foil thickness and our experience indicates that thinner foils cannot be mounted with acceptable surface flatness.

3.2 Estimate of Critical Marangoni Number. Equation (1) gives the standard, or temperature-based, definition of the Marangoni number Ma. The linear stability analysis of Pearson [3] provided theoretical values of Ma at which motion begins in an otherwise quiescent pool. His analysis addressed both the uniform-temperature and uniform-flux boundary conditions, although he did not focus on the details of the latter case. Pate [12] presented the details for the flux-controlled boundary. In general, the theoretical critical value of Ma is dependent on the wavenumber of the disturbance and the Biot number, $\text{Bi} \equiv h_{\text{air}} d / k_{\text{liquid}}$, for the liquid layer. If one assumes that disturbances are naturally

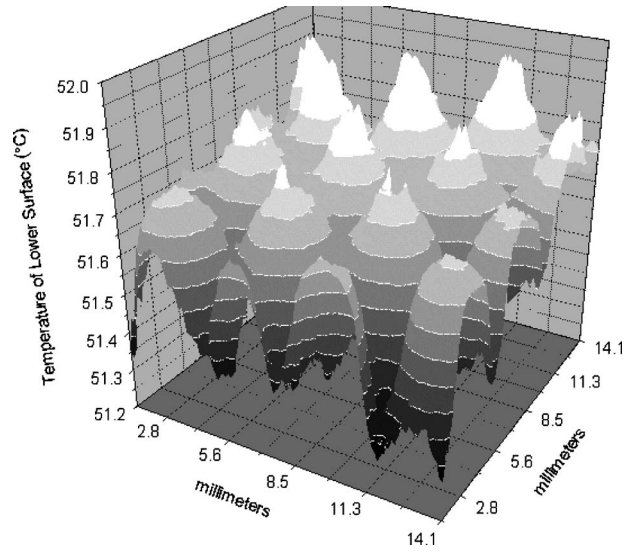

Fig. 6 Measured temperature distribution on the heated surface beneath the liquid layer

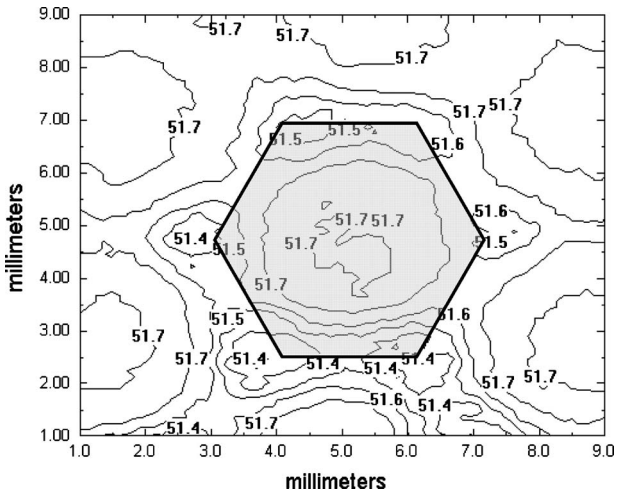

Fig. 7 Contour map of the temperature distribution in the neighborhood of one cell. Hexagon was added to indicate cell structure.

present across a broad spectrum of wavenumbers, the critical Ma will be the minimum Ma for the Bi of the liquid film. Our experiments produce $\mathrm{Bi} \leq 0.1$. For $0 \leq \mathrm{Bi} \leq 0.1$, the critical Ma from linear theory lies between 48.1 and 58.2 for the uniform-flux boundary condition, and between 79.6 and 83.4 for the uniform-temperature condition.

Accurate measurements of Ma are difficult due to the need to infer the temperature difference across the liquid layer ΔT. The liquid layer thickness d can be measured with good precision based on the liquid volume placed in the pool. Experiments can also produce acceptably precise measures of the temperature of the lower surface and of the cold-plate. The area-averaged temperature of the free surface of the liquid must then be estimated using a model of the resistance to heat flow through both the liquid and air layers. Therefore, ΔT is dependent on the thickness and thermal properties of the (assumed quiescent) liquid and air layers, and some knowledge of the radiative coupling between the free surface and the cold-plate. For our facility, the radiative flux was found to be approximately 100 $\mathrm{W/m^2}$ or 7% of the total heat flux [12]. The present experiment used a moderately polished aluminum surface as the cold-plate (measurements by Pate yielded emissivity ≈ 0.2); however, flow visualization experiments that use a glass surface as the cold-plate may have larger radiative fractions. A conduction-only model for the air layer would ignore this contribution and overestimate the temperature drop across the liquid layer by a similar percentage.

Experiments employing a constant-flux lower boundary offer an opportunity to avoid the need to model the heat transfer through the air layer. For such experiments, it is useful to define a flux-based Marangoni number Ma_q in terms of the uniform flux through the quiescent liquid layer just before the onset of motion

$$\mathrm{Ma}_q \equiv \frac{-\sigma c_p}{\nu k^2}\dot{q}''d^2 = \frac{-\sigma}{\rho\nu\alpha}d\left(\dot{q}''\frac{d}{k}\right) = \frac{-\sigma}{\rho\nu\alpha}d\Delta T_{\mathrm{quiescent}} \qquad (3)$$

at the onset of motion, $\mathrm{Ma}_q = \mathrm{Ma}$. After motion begins in a flux-controlled experiment, one expects $\mathrm{Ma}_q > \mathrm{Ma}$ at the same $\dot{q}''$ because of the increased effective conductance in the liquid layer due to fluid motion. The formulation of Ma_q trades the improved precision in $\dot{q}''$ inherent in a flux-based experiment for a greater dependence on a precise measure of the fluid depth d. The use of a 0.050 μm foil as a lower boundary opens the possibility that large-scale wrinkles or waves in the foil created by imperfect tensioning may contribute to the uncertainty in the fluid depth at any one point in the layer. The data given in Tables 1 and 2 produce $\mathrm{Bi} = 0.07$ and $\mathrm{Ma}_q = 54.4$ with an uncertainty of $\pm 8\%$ if the contribution of foil wrinkles to the depth uncertainty is ignored. The uncertainty rises to $\pm 12\%$ if wrinkling equal to ± 1 foil thickness is assumed. This result is in excellent agreement with Pearson's result for the uniform-flux case and was obtained without a thermal resistance model for the air and liquid layers. The uncertainty in Ma_q sources from a constant-odds combination of the present measurement of uncertainties. It does not include uncertainty in the property values given in Table 1 nor is any adjustment in those values made due to the mean liquid layer temperature (47.8°C) differing from the 25°C reference used in Table 1.

Examination of video sequences of the TLC surface showed that the onset of motion originates at the retaining ring and propagates inward [11]. First, a sequence of nested rings or "rolls" form near the retaining ring. Three to four such rolls of approximately 3.5 mm in width could be seen with the roll adjacent to the retaining ring producing the strongest temperature disturbance. Within 1 to 2 s, these rolls fractured into hexagonal cells such that the cell size was consistent with the width of the roll. The origination of motion at the system boundary is consistent with past observations from flow visualization experiments. Given the difficulty maintaining an acceptably flat free surface near the retaining ring, this observation opens the possibility that d near the ring is larger than the average value of d used in computing Ma and Ma_q. The onset of motion near the boundary could be due in part to the critical value of Ma being achieved earlier in this region as Ma is increased from subcritical values.

4 Conclusions

Liquid crystal thermography was used successfully to image the temperature distribution at the base of a thin liquid layer undergoing surface-tension-driven Bénard convection driven by a uniform-flux boundary condition. An independently heated retaining ring used to stabilize the liquid depth near the ring is believed by these authors to be a significant addition to the design of facilities of this type.

Critical values for the Marangoni number at the onset of motion agree with the value predicted by linear stability theory for the uniform-flux case and are markedly lower than the critical value predicted for the uniform-temperature case. Quantitative temperature measurements extracted from these images indicate that, at Marangoni numbers just above the critical value, cell widths are four times the fluid depth and have a center-to-edge temperature difference that is about 6% of the temperature drop across the liquid layer.

For experiments using a uniform-flux lower surface (or for experiments with a uniform-temperature surface but a separate heat flux gage beneath that surface), the flux-based definition of the Marangoni number Ma_q offers a considerable simplification and a possible uncertainty reduction compared with the standard definition. However, flatness of the lower surface over large scales—always an important design issue—becomes a more critical contributor to the uncertainty of Ma_q.

Acknowledgment

The facility development was supported by the University of Houston Institute for Space Systems Operations.

Nomenclature

- Bi = Biot number for the liquid layer $\equiv h_{\mathrm{air}} d / k_{\mathrm{liquid}}$
- c_p = specific heat, J/(kg K)
- d = depth of liquid layer, mm
- d_a = depth of air layer, mm
- h_{air} = effective heat transfer coefficient in the air layer at the free surface, $\mathrm{W/(m^2\ K)}$
- k = thermal conductivity, W/m K
- Ma = Marangoni number based on temperature difference as defined by Eq. (1)
- Ma_q = Marangoni number based on heat flux as defined by Eq. (3)
- $\dot{q}''$ = heat flux through the liquid layer, $\mathrm{W/m^2}$
- R,G,B = eight-bit values of red, green, and blue color primaries
- T_F = temperature of the foil (lower) surface, °C
- T_C = temperature of the cold plate, °C
- α = thermal diffusivity, $\mathrm{cm^2/s}$
- ΔT = temperature drop across liquid layer, °C
- $\Delta T_{\mathrm{total}}$ = $T_F - T_C$, °C
- ν = kinematic viscosity, $\mathrm{cm^2/s}$
- ρ = density, $\mathrm{kg/m^3}$
- σ = derivative of surface tension with respect to temperature, dyn/cm K

References

[1] Bénard, H., 1900, "Les tourbillons cellulaires dans une nappe liquid," Rev. Gen. Sci. Pures Appl., **11**, pp. 1261–1271.

[2] Block, M. J., 1956, "Surface Tension as the Cause of Bénard Cells and Surface Deformation," Nature (London), **178**, pp. 650–651.

[3] Pearson, J. R. A., 1958, "On Convection Cells Induced by Surface Tension," J. Fluid Mech., **4**, pp. 489–500.

[4] Koschmieder, E. L., and Biggerstaff, M. I., 1986, "Onset of Surface-Tension-

Driven Benard Convection," J. Fluid Mech., **167**, pp. 49–64.
[5] Koschmieder, E. L., and Prahl, S. A., 1990, "Surface-Tension-Driven Benard Convection in Small Containers," J. Fluid Mech., **215**, pp. 571–583.
[6] Ostrach, S., and Kamotani, Y., 1995, "Surface Tension Driven Convection Experiment," NASA Lewis Research Center Pamphlet No. B-0806.
[7] Hay, J. L., and Hollingsworth, D. K., 1996, "A Comparison of Trichromic Systems for Use in the Calibration of Polymer-Dispersed Thermochromic Liquid Crystals," Exp. Therm. Fluid Sci., **12**, pp. 1–12.
[8] Hay, J. L., and Hollingsworth, D. K., 1998, "Calibration of Microencapsulated Liquid Crystals Using Hue Angle and a Dimensionless Temperature," Exp. Therm. Fluid Sci., **18**, pp. 251–257.
[9] Bayazit, B. B., Hollingsworth, D. K., and Witte, L. C., 2003, "Heat Transfer Enhancement Caused by Sliding Bubbles," ASME J. Heat Transfer, **125**(3), pp. 503–509.
[10] Daniel, E., Hollingsworth, D. K., and Witte, L. C., 2007, "Transition From Boiling Onset to Fully Developed Nucleate Boiling in a Narrow Vertical Channel," Heat Transfer Eng., **28**(10), pp. 885–894.
[11] Dutton, T. W., 1996, "Liquid Crystal Imaging of Surface-Tension-Driven-Convection," BS honors thesis, Department of Mechanical Engineering, University of Houston, Houston, TX.
[12] Pate, L. R., 1999, "Investigation of Surface-Tension-Driven Flows on a Uniform-Flux Surface," MS thesis, Department of Mechanical Engineering, University of Houston, Houston, TX.
[13] Koschmieder, E. L., 1967, "On Convection Under an Air Surface," J. Fluid Mech., **30**, pp. 9–15.
[14] Kline, S. J., and McClintock, F. A., 1953, "Describing Uncertainties in Single Sample Experiments," Mech. Eng., **75**, pp. 3–8.
[15] Baughn, J. W., Anderson, M. R., Mayhew, J. E., and Wolf, J. D., 1999, "Hysteresis and Uncertainty of Thermochromic Liquid Crystal Temperature Measurement Based on Hue," ASME-JSME Paper No. AJTE99/6294.

An Experimental Investigation of Performance and Exergy Analysis of a Counterflow Vortex Tube Having Various Nozzle Numbers at Different Inlet Pressures of Air, Oxygen, Nitrogen, and Argon

Volkan Kırmacı
Department of Mechanical Engineering,
Faculty of Engineering,
Bartın University,
74100 Bartın, Turkey

Onuralp Uluer
Department of Mechanical Education,
Faculty of Technical Education,
Gazi University,
Teknikokullar, 06503 Ankara, Turkey

Kevser Dincer
Department of Mechanical Engineering,
Faculty of Engineering,
Selcuk University,
42075 Selcuklu, Turkey

An experimental investigation has been carried out to determine the thermal behavior of cooling fluid as it passes through a vortex tube and the effects of the orifice nozzle number and the inlet pressure on the heating and cooling performance of the counterflow type vortex tube (RHVT). Experiments have been performed using oxygen (O_2), nitrogen (N_2), and argon (Ar). Five orifices have been fabricated and used during the experimental study with different nozzle numbers of 2, 3, 4, 5, and 6. The orifices used at these experiments are made of the polyamide plastic material. The thermal conductivity of polyamide plastic material is 0.25 W/m K. To determine the energy separation, the inlet pressure values were adjusted from 150 kPa to 700 kPa with 50 kPa increments for each one of the orifices and each one of the studied fluids. The vortex tube that was used during the experiments has L/D ratio of 15 and the cold mass fraction was held constant at 0.5. As a result of the experimental study, it is determined that the temperature gradient between the cold and hot exits is decreased depending on the orifice nozzle number increase. Exergy analyses have been realized for each one of the studied fluids under the same inlet pressures with the experiments ($P_i = 150-700$). The exergy efficiency of the vortex tube is more affected by inlet pressure than nozzle number.
[DOI: 10.1115/1.4002284]

Keywords: vortex tube (RHVT), exergy, cooling, heating

1 Introduction

The vortex tube, also known as Ranque vortex tube, Hilsch vortex tube, and Ranque–Hilsch vortex tube, is a device that enables the separation of hot and cold pressurized gas that flows tangentially into the vortex chamber through inlet nozzles [1–5]. A Ranque–Hilsch vortex tube contains one or more inlet nozzles, a vortex chamber, a cold-end orifice, a hot-end control valve, and a tube [6]. In a vortex tube, high pressure gas stream enters tangentially, and by lowering the pressure, it splits into a hot and cold temperature streams. Cold gas stream leaves the tube through a center orifice near the entrance nozzle, while hot gas stream flows toward the control valve and leaves the tube there [4,7]. Centrifugal separation of "stagnant" elements and their adiabatic expansion causes the energy separation in the vortex tube system. The vortex tube can be applied to many industrial applications such as cooling equipment of computer numerical control (CNC) machines, refrigerators, cooling suits, heating process, etc. for its being simple, compact, light, and quiet. Since it has no moving parts, it does not break or wear and therefore, it requires little maintenance [8]. There are two types of flow paths in vortex tubes such as parallel flow and counterflow. In Figs. 1 and 2, the schematic representation of the parallel flow and counterflow vortex tubes are shown.

The energy separation of counterflow vortex tube is shown in Fig. 3. Therefore, an energy transfer between cold and hot gases is responsible for the formation of substantial temperature differences in the vortex tube. The temperature decrease due to expansion is comparable to those in a turbine. Although in the vortex tube there are no rotating walls, there are rotating fluid layers exchanging mechanical energy by friction. A model of this mechanism is represented in Fig. 3. The radially expanding cold gas increases its angular velocity ω_c (i.e., the inner layers rotate faster than the outer ones). The shear stresses produce an outward directed mechanical energy flux E_M. This energy, which predominantly dissipates around the boundary layer of the tube wall, is transferred to the hot gas. The diffusive energy flux E_D, however, is directed inward [11].

Ahlborn et al. [12] carried out measurements in the vortex tubes to support their models for calculating limits of temperature separation. They also attributed the heating to the conversion of kinetic energy into heat and the cooling to the reverse process. Ahlborn et al. [13] identified the temperature separation phenomenon of a Ranque–Hilsch vortex tube in which the gas stream is divided into a hot and cold flow as a natural heat pump mechanism, which is enabled by a secondary circulation. Lewins and Bejan [3] suggested that the angular velocity gradients in the radial direction give rise to frictional coupling between different layers of the rotating flow resulting in a migration of energy via shear work from the inner layers to the outer layers. Trofimov [14] verified that the dynamics of internal angular momentum leads to this effect. Saidi and Valipour [15] presented information data on the classification of the parameters affecting vortex tube operation. In

Contributed by the Heat Transfer Division of ASME for publication in the JOURNAL OF HEAT TRANSFER. Manuscript received August 8, 2009; final manuscript received July 15, 2010; published online September 17, 2010. Assoc. Editor: Ali Ebadian.

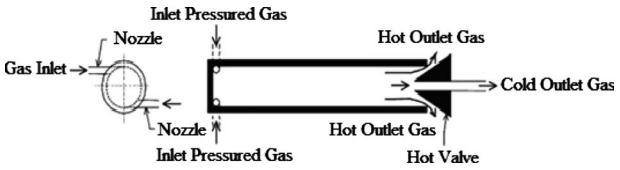

Fig. 1 The schematic representation of a parallel flow vortex tube principle [9]

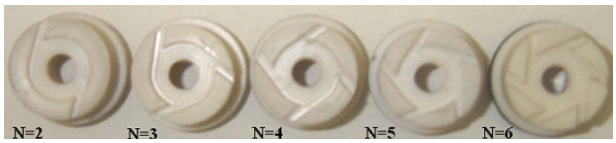

Fig. 4 Orifices used in the experiments

their study, the thermophysical parameters such as inlet gas pressure, type of gas and cold gas mass ratio, moisture of inlet gas, and the geometrical parameters (i.e., diameter and length of main tube diameter of outlet orifice, shape of entrance nozzle) were designated and studied. Singh et al. [16] reported the effect of various parameters such as cold mass fraction, nozzle size, cold orifice diameter, hot outlet of the tube, and L/D ratio on the performance of the vortex tube. Dincer et al. [17] investigated the effect of control valve tip angle on the performance of Ranque–Hilsch vortex tube using different inlet pressures (P_i = 200–420 kPa) and different nozzle numbers (N = 2, 4, 6). Cockerill studied the vortex tubes for use in gas liquefaction and mixture separation as applied to uranium enrichment for determining the basic performance characteristics and the relationship between cold air temperature versus hot air temperature and cold mass fraction, and the variation of the hot discharge tube wall temperature with a hot tube length. Cockerill [9] also reported a mathematical model for the simulation of a compressible turbulent flow in a vortex tube.

Vortex tube system was used to enrich the concentration of methane by Kulkarni and Sardesai [18]. They tried to separate methane and nitrogen gases using vortex tube. This particular separation or the resulting enrichment of methane concentration has applications in the mining industry. Promvonge and Eiamsa-ard [19] experimentally studied the energy and temperature separations in the vortex tube with a snail entrance. Depending on their experimental results, the use of a snail entrance could help to increase the cold air temperature drop and improve the vortex tube efficiency when compared with those of original tangential inlet nozzles. Promvonge and Eiamsa-ard [20] furthermore reported the effects of the number of inlet tangential nozzles, the cold orifice diameter, and the tube insulations on the temperature reduction and isentropic efficiency of the vortex tube. Aydın and Baki [21] investigated experimentally the energy separation in a counterflow vortex tube having various geometrical and thermophysical parameters. Pinar et al. [22] investigated the effects of inlet pressure, nozzle number, and fluid type factors on the Ranque–Hilsch vortex tube performance by means of Taguchi method. As a result, they obtained an optimal factor setting, maximizing temperature gradient and regression model with a correlation coefficient of 0.94.

This study focuses on testing the effects of the orifice nozzle number and the inlet pressure on the heating and cooling performance of counterflow type vortex tube using air, oxygen, nitrogen, and argon as a fluid experimentally. In this work, an experimental study has been carried out to investigate the temperature behavior of air, O_2, N_2, and Ar in a counterflow type vortex tube. This study is different from those of the previous studies in discussing of the four different gases and their cooling and heating effects including exergy analysis by using different inlet pressures and different nozzle numbers.

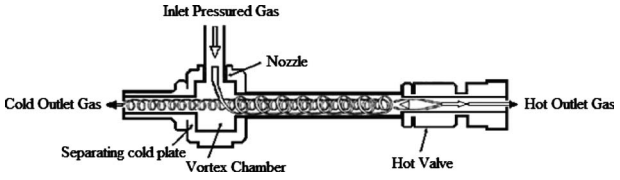

Fig. 2 The schematic representation of a counterflow vortex tube principle [10]

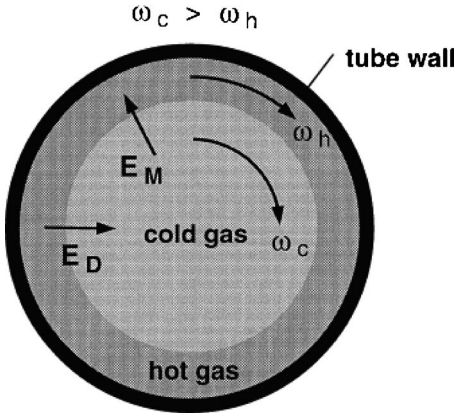

Fig. 3 Energy separation of counterflow vortex tube [11]

2 Experimental Study

In this study, to investigate and discuss the effects of studied gases (air, O_2, N_2 and Ar) as fluid on the vortex tube performance, a counterflow type vortex tube with (L = 150 mm, D = 10 mm) L/D ratio 15 was used. Five different orifices with different nozzle numbers (2, 3, 4, 5, and 6) have been fabricated and used in the experiments as shown in Fig. 4. Polyamide plastic material was used as an orifice material. The thermal conductivity of polyamide plastic is 0.25 W/m °C, the specific heat is 4400 J/kg °C, and its density is 1173 kg/m^3. Each one of the nozzles have the same constant square cross sections (2×2 mm^2). The schematic diagram of the experimental setup is shown in Fig. 5.

The inlet pressures and the hot and cold outlet pressures of the counterflow vortex tube have been measured by a pressure gauge (accuracy ±0.01 bar) as shown in Fig. 5. The mass flow rates at the cold and hot outlets of the counterflow vortex tube have been measured by rotameter with ±0.02 m^3/h precision tolerance. The temperatures of the pressurized air at the inlet and the cold and hot

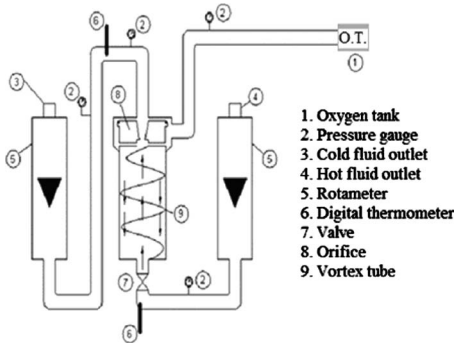

Fig. 5 The schematic diagram of the experimental setup

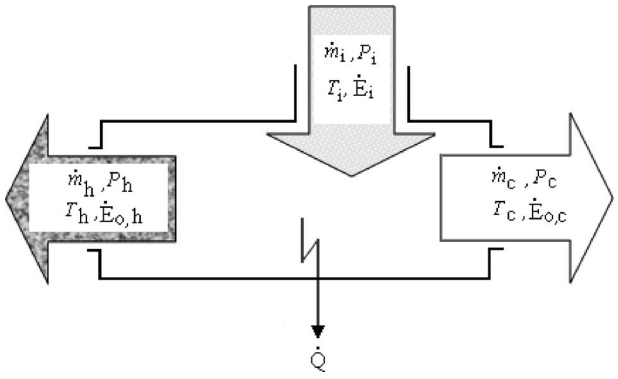

Fig. 6 The schematic diagram of counterflow vortex tube for energy analysis [24]

outlets were measured by a digital thermometer with $\pm 0.5°C$ precision tolerances, and the obtained temperature values have been converted into Kelvin (K) unit.

Temperature probes of the digital thermometer were placed into the ∅1 mm hole, which was drilled at the center of the counterflow vortex tube and 1 cm away from the cold and the hot outlets. The cavities between the probes and the hole were filled with silicon in order to prevent the leakage. A control valve has been mounted on the hot outlet of the tube in order to adjust the mass flow rate of the hot air. With this valve, cold mass fraction (μc) was held constant at 0.5. Before the experiment, the control valve on the hot outlet was kept in fully open position. Then, the air compressor was started and by use of the valve that placed on the counterflow vortex tube inlet side, the beginning pressure value of 150 kPa was reached. Until the constant temperature values have been reached at the cold outlet and at the hot outlet of the counterflow vortex tube, the tank working gases flow is continued. During this stage, the mass flow rates and pressures of the oxygen at the cold outlet and hot outlet were measured by using rotameters and pressure gauges, respectively. This experimental cycle has been repeated three times for the entire inlet pressures selected (150–700 kPa with 50 kPa increments) for each of the studied gases separately and with the different orifices selected (with 2, 3, 4, 5, and 6 nozzle numbers), and mean values were used in the exergy analysis. Since the used system is an adiabatic, there is no heat loss to the environment. In this study, the reference environment temperature is $T_0 = 293.15$ K. The mean values of the measured results have been used to obtain the energy separation.

3 Exergy Analysis of the Vortex Tube

The schematic diagram of counterflow vortex tube for energy analysis is shown in Fig. 6.

The following criteria are assumed for the exergy analysis in the RHVT system.

(i) No friction effect is considered in the RHVT system.
(ii) The flow inside the RHVT is in steady state conditions;,
(iii) RHVT can be assumed adiabatic.
(iv) Inlet and outlet gases were considered as ideal gases.
(v) The reference environmental temperature and pressure are considered as $T_0 = 293.15$ K and $P_0 = 100$ kPa, reflectively.

The second law of thermodynamics can be applied to sections of the RHVT system as shown in Fig. 6. The total inlet exergy $\Sigma \dot{E}_i$ in the RHVT is given as follows [23]:

$$\sum \dot{E}_i = \dot{m}_i \left[C_p(T_i - T_0) - T_0 \left(C_p \ln \frac{T_i}{T_0} - R \ln \frac{P_i}{P_0} \right) \right] + \dot{m}_i \frac{v_i^2}{2} \tag{1}$$

where $\dot{m}_i$ is the mass flow rate of inlet stream, T_i is the inlet temperature, P_i is the inlet pressure, and v_i is the inlet velocity. The total exergy outlet of RHVT system $\Sigma \dot{E}_O$ can be divided into two components, namely, the total exergy of hot outlet $\Sigma \dot{E}_{oh}$ and the total exergy of cold outlet $\Sigma \dot{E}_{oc}$. The total exergy of hot outlet of the RHVT may be written as follows [23]:

$$\sum \dot{E}_{oh} = \dot{m}_h \left[C_p(T_h - T_0) - T_0 \left(C_p \ln \frac{T_h}{T_0} - R \ln \frac{P_h}{P_0} \right) \right] + \dot{m}_h \frac{v_h^2}{2} \tag{2}$$

where $\dot{m}_h$ is the mass flow rate at the hot outlet of the vortex tube, T_h is the temperature at the hot outlet of the vortex tube, P_h is the pressure at the hot outlet of the vortex tube, v_h is the velocity at the hot outlet of the vortex tube [23].

The total exergy of cold outlet of the RHVT can be written as follows [23]:

$$\sum \dot{E}_{oc} = \dot{m}_c \left[C_p(T_c - T_0) - T_0 \left(C_p \ln \frac{T_c}{T_0} - R \ln \frac{P_c}{P_0} \right) \right] + \dot{m}_c \frac{v_c^2}{2} \tag{3}$$

where, $\dot{m}_c$ is the mass flow rate at the cold outlet of the vortex tube, T_c is the temperature at the cold outlet of the vortex tube, P_c is the pressure the cold outlet of the vortex tube, v_c is the velocity at the cold outlet of the vortex tube. In this case, the total exergy outlet may be written as follows [23]:

$$\sum \dot{E}_O = \sum \dot{E}_{oh} + \sum \dot{E}_{oc} \tag{4}$$

The total lost exergy of the RHVT system can be defined as the difference between the total inlet exergy and the total outlet exergy. The total lost exergy of the RHVT system can be calculated by the following equation:

$$\sum \dot{E}_i - \sum \dot{E}_o = \sum \dot{E}_L = \dot{I} \tag{5}$$

where $\Sigma \dot{E}_L$ is the total lost exergy of RHVT [23].

The exergy efficiency based on exergy analysis can be determined using several ways for exergy conversion systems. In this study, the ratio of the total exergy outlet to the total inlet exergy is used as the exergy efficiency (η_{II}) and it is written as follows [23]:

$$\eta_{II} = \frac{\sum \dot{E}_o}{\sum \dot{E}_i} \tag{6}$$

The quantity of the total inlet exergy, the total outlet exergy, the total exergy losses, and the exergy efficiency are calculated from Eqs. (1) and (4)–(6), respectively.

Cold mass fraction is defined as the percentage of inlet pressurized air that is released through the cold end of the tube against the pressurized inlet air mass and can be calculated by using Eq. (7). The cold mass fraction can be controlled by the cone valve, which is placed at the hot tube end. This can be expressed as follows:

$$\mu_c = \frac{\dot{m}_c}{\dot{m}_i} \tag{7}$$

where $\dot{m}_c$ is the mass flow rate at the cold outlet of the vortex tube [15]. The $\dot{m}_c$ and $\dot{m}_i$ were obtained from the COOLPACK software by applying the measured pressures at inlet and at cold and hot air

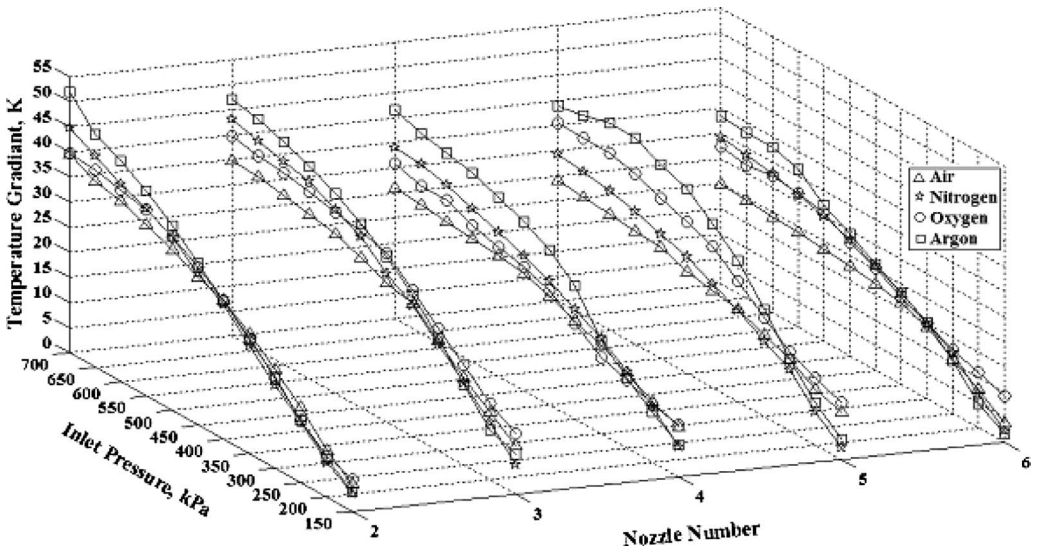

Fig. 7 The temperature gradient versus nozzle numbers and inlet pressures

outlets. The cooling (ΔT_c) and the heating (ΔT_h) effects of the vortex tube are defined as follows, respectively:

$$\Delta T_c = T_i - T_c \tag{8}$$

$$\Delta T_h = T_h - T_i \tag{9}$$

In general, the performance of the vortex tubes was defined as the difference between the heating effect and the cooling effect. Subtracting Eq. (8) from Eq. (9) gives the vortex tube the performance equation as follows (Eq. (10)):

$$\Delta T = T_h - T_c \tag{10}$$

The temperature gradient is defined as the temperature difference between hot outlet temperature (T_h) and cold outlet temperature (T_c) [24].

4 Results and Discussion

In this study, for testing the performance of four types of pressurized fluids (air, O_2, N_2, and Ar) on a counterflow vortex tube having $L/D=15$, $N=2$, 3, 4, 5, and 6, and $P_i=150-700$ kPa experimentally obtained data were used. Cold mass fraction was held constant at 0.5. As shown in Fig. 7, increasing the inlet pressure of the counterflow vortex tube has increased the temperature gradient between the cold and the hot outlets. However, increasing of the orifice nozzle number has decreased the cold and the hot outlet temperature gradient.

In Fig. 7, the cold outlet and hot outlet temperature gradients against the inlet pressure and nozzle number for all of the studied gases are shown. Maximum temperature gradient was obtained at $N=2$ and $P_i=700$ kPa for all of the studied gases. In these conditions, the maximum temperature gradients for air, O_2, N_2, and Ar are 39.6°C, 39.8°C, 44.8°C, and 52°C, respectively. As shown in Fig. 7, the temperature gradients between the cold and hot outlets are decreased for each of the gases (air, O_2, N_2, and Ar) when the effects of the nozzle numbers at high inlet pressures are considered. However, if the nozzles are considered separately, the increase in inlet pressure increases the temperature gradient.

Since there are similar environmental conditions during all of the experiments, the rate of irreversibility and the total inlet exergy are increased exponentially with the increasing of the inlet pressure and it is independent of the orifice nozzle numbers (Fig. 8).

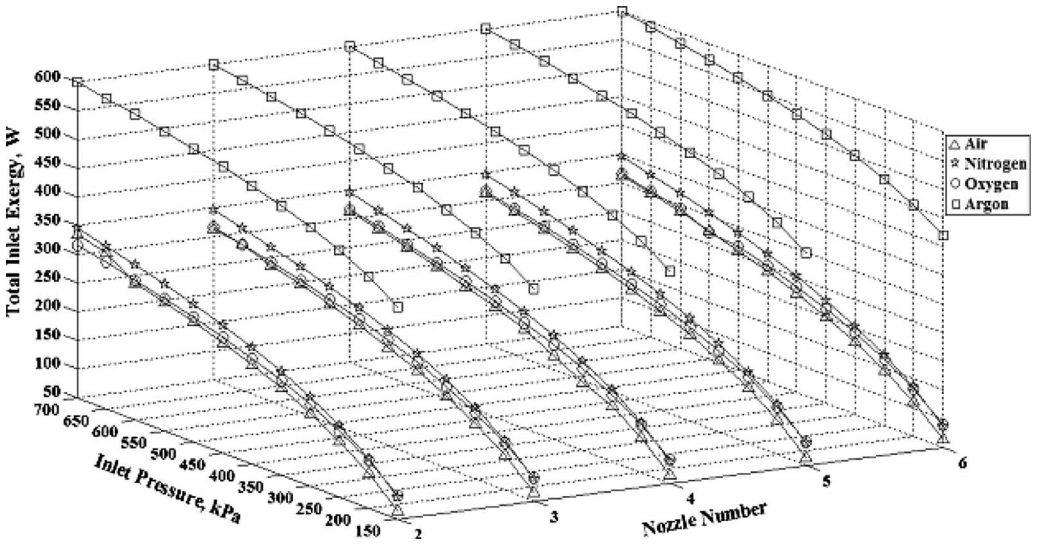

Fig. 8 Total inlet exergy results versus inlet pressure and nozzle numbers

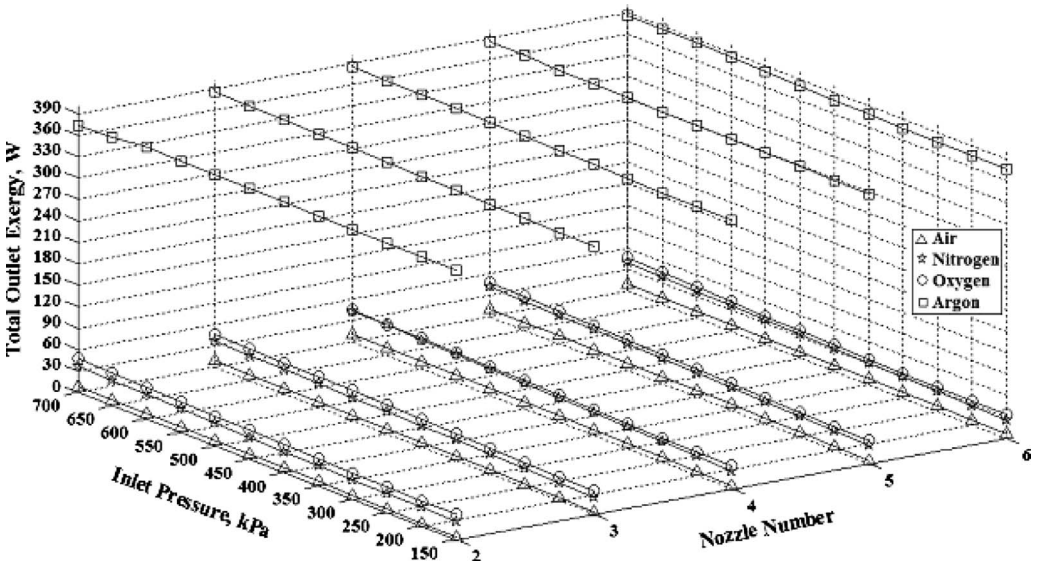

Fig. 9 Total outlet exergy results versus inlet pressure and nozzle numbers

This situation is the same for all of the studied gases. The maximum total inlet exergy is obtained when Ar is used as a fluid. The other gases (air, O_2, N_2) have approximately the same total inlet exergy. As shown in Fig. 9, increasing of the inlet pressure has increased the total output exergy and it is obtained from the results that the nozzle number is less effective than the inlet pressure. It is obtained for each of the gases (air, O_2, N_2, and Ar) that the total outlet exergy of argon is the highest for each of the nozzle numbers and inlet pressures (Fig. 9).

The total lost exergy results versus inlet pressure and nozzle numbers is shown Fig. 10. When P_i increases, it was observed that the velocity at the nozzles increases as well. When Fig. 10 is analyzed simultaneously, one can see that the total lost exergy is increasing with increases in Pi. When the total lost exergies are compared, according to the experimental results, the maximum total lost exergy is nitrogen and the minimum total lost exergy is argon. Maximum total lost exergy is observed for $P_i = 700$ kPa.

It can be seen from Fig. 11 that the exergy efficiency of the vortex tube is more affected by inlet pressure than nozzle number.

The exergy efficiency of vortex tube is decreased logarithmically with increasing of the inlet pressure. The exergy efficiency of Ar is the higher than the other gases (air, O_2, N_2) as shown in Fig. 11.

5 Conclusion

In this study, the experimental data has been obtained for a counterflow Ranque–Hilsch vortex tube having $L/D = 15$, $N = 2$, 3, 4, 5, and 6, and $P_i = 150-700$ kPa using the air, O_2, N_2, and Ar as fluids. The vortex tube performance was tested and an exergy analysis has been realized. Cold mass fraction was held constant at 0.5. It has been seen that increasing of the inlet pressure decreases the cold outlet temperature for each of the gasses. It has also been seen that the cold outlet temperature of Ar is lower than the other gases (air, O_2, and N_2). According to the experimental results, the temperature gradient between the cold and hot outlets has decreased when the effects of the nozzle numbers are taken into account. However, if the nozzles are considered separately,

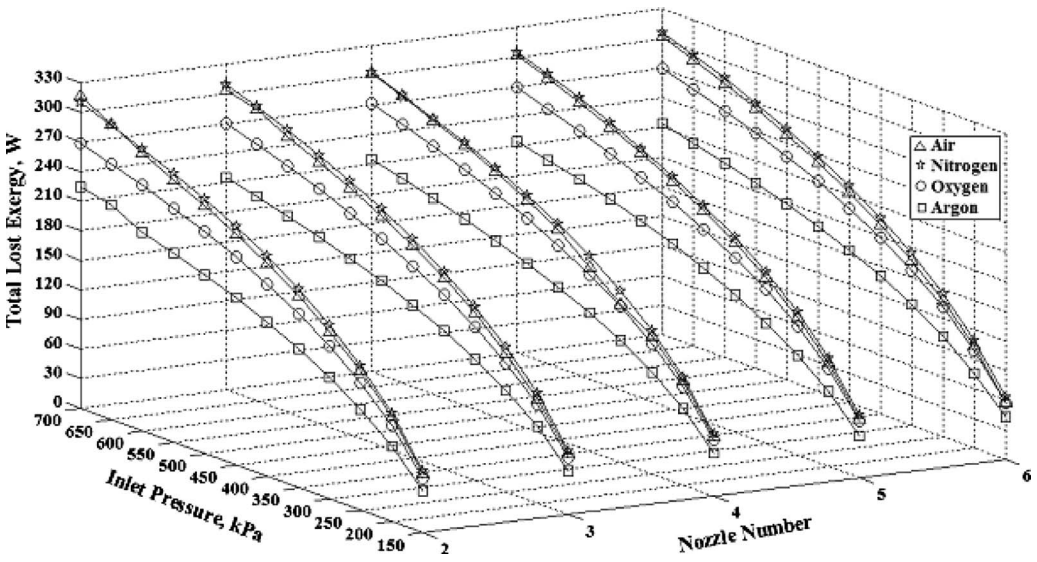

Fig. 10 The total lost exergy results versus inlet pressure and nozzle numbers

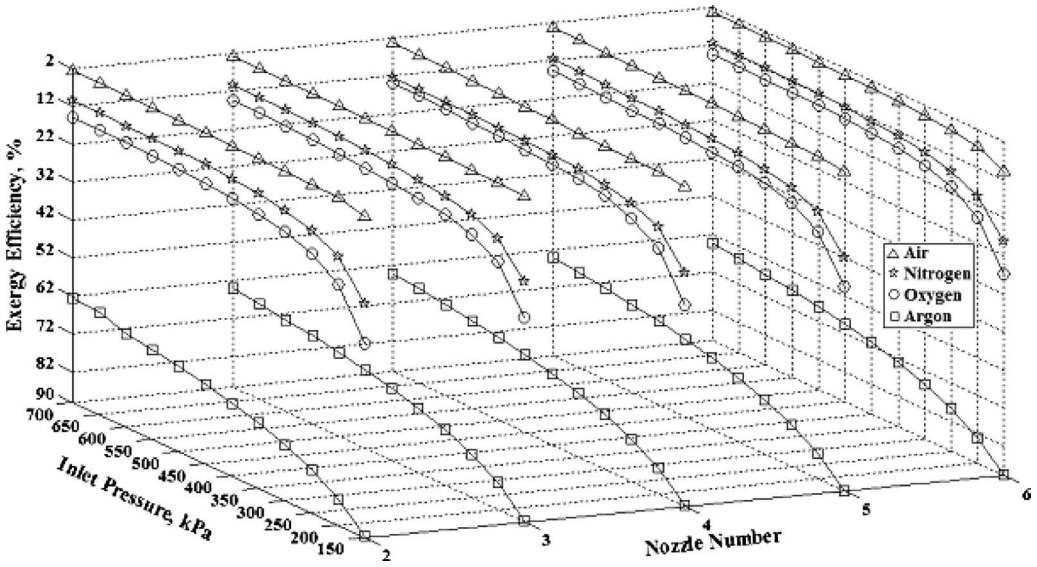

Fig. 11 The exergy efficiency of vortex tube

the increasing of the inlet pressure also increases the temperature gradient. Maximum temperature gradient between the cold and hot outlets is obtained when the orifice number is 2 for all of the studied gases. The temperature gradient between the cold and the hot outlets has been increased with the increase of the vortex tube inlet pressure. Increasing of the orifice nozzle number has decreased the cold and the hot outlet temperature gradient. When the experimental results are taken into account, it is expected that for improving the cold outlet temperature, argon is a better alternative than the other studied gases. For cooling applications (e.g., spot cooling needs, cooling of the cutting tools in manufacturing processes, etc.) for a fixed mass flow rate, the minimum cold mass fraction has to be chosen, and for heating applications (e.g., melting the glues, softening the plastics, humidifying the ambient air, etc.) for a fixed mass flow rate, the cold mass fraction ratio has to be increased.

In this study, the total inlet exergy and the total lost exergy constantly increases from 150 kPa to 700 kPa. From the presented results, it can be seen that the maximum total inlet exergy is obtained when using the Ar and the maximum total lost exergy is obtained when using the N_2. The exergy efficiency of the vortex tube is decreased with the increase of the inlet pressure. It is determined that the highest exergy efficiency is obtained when using Ar under $P_i = 150$ kPa inlet pressure condition.

Nomenclature

C = specific heat (kJ kg^{-1} K^{-1})
D = internal diameter of vortex tube (m)
$\Sigma \dot{E}_{oc}$ = total exergy of cold outlet (kW)
$\Sigma \dot{E}_i$ = total inlet exergy (kW)
$\Sigma \dot{E}_O$ = total outlet exergy (kW)
$\Sigma \dot{E}_{oh}$ = total exergy of hot outlet (kW)
$\Sigma \dot{E}_L$ = total lost exergy (kW)
L = length of vortex tube (m)
$\dot{m}$ = mass flow rate (kg/s)
N = number of nozzles
P = pressure (kPa)
P_0 = reference environmental pressure (=100 kPa)
P_i = pressure of inlet stream (kPa)
P_c = pressure of cold stream (kPa)
P_h = pressure of hot stream (kPa)
T = temperature (K)
T_c = temperature of cold stream (K)
T_h = temperature of hot stream (K)
T_i = temperature of inlet stream (K)
ΔT = temperature gradient (K)
v = velocity of the flow (m s^{-1})
v_c = velocity of hot stream (m s^{-1})
v_h = velocity of hot stream (m s^{-1})
v_i = velocity of inlet stream (m s^{-1})

Greek Letters

ω = angular velocity
ε = exergy efficiency
μ_c = cold mass fraction

Subscripts

a = ambient condition
c = cold outlet
h = hot outlet
i = inlet
0 = outlet

References

[1] Khodorkov, L., Poshernev, N. V., and Zhidkov, M. A., 2003, "The Vortex Tube–A Universal Device for Heating, Cooling, Cleaning, and Drying Gases and Separating Gas Mixtures," Chem. Petrol. Eng., **39**, pp. 409–415.
[2] Wu, Y. T., Ding, Y., Ji, Y. B., Ma, C. F., and Ge, M. C., 2007, "Modification and Experimental Research on Vortex Tube," Int. J. Refrig., **30**, pp. 1042–1049.
[3] Lewins, J., and Bejan, A., 1999, "Vortex Tube Optimization Theory," Energy, **24**, pp. 931–943.
[4] Eiamsa-ard, S., and Promvonge, P., 2008, "Review of Ranque–Hilsch Effects in Vortex Tubes," Renewable Sustainable Energy Rev., **12**, pp. 1822–1842.
[5] Aljuwayhel, N. F., Nellis, G. F., and Klein, S. A., 2005, "Parametric and Internal Study of the Vortex Tube Using a CFD Model," Int. J. Refrig., **28**, pp. 442–450.
[6] Kırmacı, V., and Uluer, O., 2008, "The Effects of Orifice Nozzle Number on Heating and Cooling Performance of Vortex Tubes: An Experimental Study," Instrum. Sci. Technol., **36**, pp. 493–502.
[7] Gao, C. M., Bosschaart, K. J., Zeegers, J. C. H., and de Waele, A. T. A. M., 2005, "Experimental Study on a Simple Ranque–Hilsch Vortex Tube," Cryogenics, **45**, pp. 173–183.
[8] Chengming, G., 2005, *Experimental Study on the Ranque-Hilsch Vortex Tube*, Technische Universiteit Eindhoven, Eindhoven, p. 151.
[9] Cockerill, T., 1995, "Thermodynamic and Fluid Mechanics of Ranque–Hilsch Vortex Tube," MS thesis, University of Cambridge, UK, p. 294.
[10] Cao, Y., Wu, J., Luo, E. C., and Chen, G., 2001, "Research Progress and Overview on Vortex Tube," Cryogenics, **6**(124), pp. 1–5.
[11] Fröhlingsdorf, W., and Unger, H., 1999, "Numerical Investigations of the Compressible Flow and the Energy Separation in the Ranque–Hilsch Vortex

Tube," Int. J. Heat Mass Transfer, **42**, pp. 415–422.
[12] Ahlborn, B., Keller, J. U., Staudt, R., Treitz, G., and Rebhan, E., 1994, "Limits of Temperature Separation in a Vortex Tube," J. Phys. D, **27**, pp. 480–488.
[13] Ahlborn, B., Keller, J. U., and Rebhan, E., 1998, "The Heat Pump in a Vortex Tube," J. Non-Equilib Thermodyn, **23**, pp. 159–165.
[14] Trofimov, V. M., 2000, "Physical Effect in Ranque Vortex Tubes," JETP Lett., **72**, pp. 249–252.
[15] Saidi, M. H., and Valipour, M. S., 2003, "Experimental Modeling of Vortex Tube Refrigerator," Appl. Therm. Eng., **23**, pp. 1971–1980.
[16] Singh, P. K., Tathgir, R. G., Gangacharyulu, D., and Grewal, G. S., 2004, "An Experimental Performance Evaluation of Vortex Tube," J. Inst. Eng. (India), Part AG, **84**, pp. 149–153.
[17] Dincer, K., Baskaya, S., Uysal, B. Z., and Ucgul, I., 2009, "Experimental Investigation of the Performance of a Ranque–Hilsch Vortex Tube With Regard to a Plug Located at the Hot Outlet," Int. J. Refrig., **32**, pp. 87–94.
[18] Kulkarni, M. R., and Sardesai, C. R., 2002, "Enrichment of Methane Concentration via Separation of Gases Using Vortex Tubes," J. Energy Eng., **128**(1), pp. 1–12.
[19] Promvonge, P., and Eiamsa-ard, S., 2004, "Experimental Investigation of Temperature Separation in a Vortex Tube Refrigerator With Snail Entrance," ASEAN J Sci Technol. Dev., **21**, pp. 297–308.
[20] Promvonge, P., and Eiamsa-ard, S., 2005, "Investigation on the Vortex Thermal Separation in a Vortex Tube Refrigerator," ScienceAsia, **31**, pp. 215–223.
[21] Aydın, O., and Baki, M., 2006, "An Experimental Study on the Design Parameters of a Counterflow Vortex Tube," Energy, **31**, pp. 2763–2772.
[22] Pinar, A. M., Uluer, O., and Kırmacı, V., 2009, "Optimization of Counter Flow Ranque–Hilsch Vortex Tube Performance Using Taguchi Method," Int. J. Refrig., **32**, pp. 1487–1494.
[23] Dincer, K., Avcı, A., Baskaya, S., and Berber, A., 2010, "Experimental Investigation and Exergy Analysis of the Performance of a Counter Flow Ranque-Hilsch Vortex Tube With Regard to Nozzle Cross-Section Areas," Int. J. Refrig., **33**, pp. 954–962.
[24] Kırmacı, V., and Uluer, O., 2009, "An Experimental Investigation of the Cold Mass Fraction, Nozzle Number and Inlet Pressure Effects on Performance of Counter Flow Vortex Tube," ASME J. Heat Transfer, **131**(8), p. 081701.

A Semi-Empirical Heat Transfer Model for Forced Convection in Pin-Fin Heat Sinks Subjected to Nonuniform Heating

S. S. Feng
School of Energy and Power Engineering,
Xi'an Jiaotong University,
Xi'an 710049, P.R. China

T. Kim[1]
e-mail: tongbeum@gmail.com

T. J. Lu

SV Laboratory,
School of Aerospace,
Xi'an Jiaotong University,
Xi'an 710049, P.R. China

This paper presents a cost effective semi-empirical analytical model for convective heat transfer in pin-fin heat sinks subjected to nonuniform heating set by a circular hot gas impinging jet. Based on empirical correlations taken from the open literature, temperature variations in the heat sink are obtained from the finite volume solution of the semi-empirical model. Based on a purpose-built experimental setup, measurements of a substrate temperature are performed using an infrared camera. These, along with the convective fluid temperature measured at the exit of the pin-fin array, are compared against analytical model predictions, with overall good agreement achieved. Subsequently, the influences of the convection Reynolds number, substrate thickness, and thermal conductivity of material on the distribution of substrate temperature are quantified by the validated model. It is demonstrated that the present model is capable of predicting local thermal behaviors such as the footprints of the pin fins. In addition, with the spreading resistance captured accurately, the model can be used for the design optimization of pin-fin/substrate systems subjected to nonuniform heating.
[DOI: 10.1115/1.4002285]

Keywords: finite volume method, heat spreading, nonuniform heating, pin-fin heat sink

1 Introduction

Pin fins having either circular or noncircular cross sections are extensively used as heat exchange media in industrial applications such as internal cooling of turbine blades, cooling of electronic devices, and compact heat exchangers. Thus far, numerous studies have been carried out experimentally and numerically to explore the thermal and flow mechanisms associated with pin-fin arrays in forced convection. The majority of these studies focus on pin-fin heat sinks with uniform thermal boundary (temperature or heat flux) conditions imposed through the substrate to which the pin fins are attached.

Tahat et al. [1] measured the convection heat transfer performance in inline and staggered arrangements of cylindrical pin fins protruded vertically from a uniformly heated base plate. The optimal spacing of the pin fins in the longitudinal and transverse directions was examined. Under forced convection with isoflux boundary conditions, Sara et al. [2,3] investigated the heat transfer and flow resistance characteristics of square pin-fin arrays in both inline and staggered arrangements. Performance analysis was carried out to explore the effects of fin pitches and Reynolds number for fixed pumping power of the convective flow.

Kim et al. [4] measured the pressure drop and heat transfer characteristics of inline rectangular pin fins subjected to uniform heating imposed through the base plate. In subsequent analytical modeling, the pin-fin arrays were treated as porous media, and empirical correlations for permeability, Ergun constant, and interstitial heat transfer coefficient covering a wide range of pin-fin pitches were adopted. Using a transient single-blow technique, Jeng and Tzeng [5] measured the interstitial heat transfer coefficient (i.e., heat transfer coefficient on the pin-fin surface) of inline and staggered square pin fins and compared the test data with the correlations reported by Kim et al. [4].

Saha and Acharya [6] studied numerically three-dimensional (3D) unsteady flow and heat transfer in a parallel-plate heat exchanger having an inline array of square pin fins. The 3D unsteady Navier–Stokes and energy equations were solved in a unit cell by taking advantage of the periodical nature of thermal flow fields for asymmetric heating conditions. Naphon and Sookkasem [7] studied the heat transfer characteristics in tapered cylindrical pin-fin heat sinks with isoflux boundary conditions. Full 3D Navier–Stokes and energy equations incorporating the standard k-ε turbulence model were solved. Conduction in the substrate conjugating with forced convection in the pin-fin arrays was considered.

VanFossen [8] measured the overall convective heat transfer from the base-plate and pin-fin surfaces under isoflux boundary conditions. To separate the convection effect from the pin-fin surfaces, thermally active and inactive pin fins having identical geometrical parameters were separately tested. By comparing the overall heat transfer of the two cases, the heat transfer coefficients on the base plate and the pin-fin surfaces were characterized. Consequently, for fixed pin-fin spacing, $S_T/D=S_L/D=3.46$, and pin-fin height ranging $0.5 \le H/D \le 2$, the heat transfer coefficient on the pin-fin surfaces was found to be 35% higher than that on a region of the base plate exposed directly to forced convection (referred to as "end wall heat transfer" in Ref. [8]). Using the same approach, Metzger et al. [9] showed that for $S_T/D=2.5$, $S_L/D=1.5$, 2.5, and $H/D=1.0$, the heat transfer coefficient on the pin-fin surface is twice as high as that on the base plate rooted with staggered cylindrical pin fins. While the end wall heat transfer coefficient was determined in previous studies such as VanFossen [8] and Metzger et al. [9] from thermally inactive pin fins, both the end wall and pin fins are thermally active in reality. To check the accuracy of test data obtained with such unrealistic thermal boundary conditions, Chyu et al. [10] conducted heat transfer experiments with identical thermal conditions prescribed

[1]Corresponding author.

Contributed by the Heat Transfer Division of ASME for publication in the JOURNAL OF HEAT TRANSFER. Manuscript received September 24, 2009; final manuscript received May 11, 2010; published online September 17, 2010. Assoc. Editor: Frank Cunha.

to both the pin fins and base plate using the naphthalene sublimation technique. It was found that the heat transfer coefficients are insensitive to the prescribed thermal boundary conditions and, for $S_L/D=S_T/D=2.5$ and $H/D=1.0$, the heat transfer coefficient on the pin fins is about 20% higher than that on the base plate. Using the thermal liquid crystal technique, Matsumoto et al. [11] measured the base-plate heat transfer coefficient in a rectangular channel with thermally inactive pin fins. Relative to the heat transfer in an empty channel, the heat transfer coefficient on the channel wall is increased by a factor of 3 due to flow mixing enhanced by the thermal inactive pin fins.

In some engineering applications, e.g., jet blast deflector (JBD) in which a flat panel accommodating a specially designed heat exchanger deflects exhaust gas from a jet engine, the thermal boundary conditions imposed on the JBD can be hardly described as uniform. In such cases, heat from the exhaust gas is nonuniformly transferred into the JBD and laterally spread in one of the JBD panels sandwiching the heat exchanger, followed by forced convection. To the best of our knowledge, this scenario has not been studied, either experimentally or theoretically.

To address the above deficiency, this study is concerned with forced convection (air) in square pin-fin heat sinks with an inline arrangement. Particularly, one of the substrates sandwiching the square pin fins is subjected to *nonuniform heating* from a hot gas circular impinging jet, while the other substrate is thermally insulated. To obtain the thermal flow field in such a pin-fin heat sink, computational fluid dynamics (CFD) has been shown to be effective [6,7,12]. When the thermal boundary conditions are uniform, a relatively small computational domain (unit cell) is required, saving computational time by imposing periodical and symmetric boundary conditions. With nonuniform heating, the thermal flow field in the pin fins is no longer periodically distributed. Therefore, CFD calculations based on the unit cell approach can no longer be utilized to characterize thermal flow fields in the entire heat sink. A full 3D CFD calculation for all the pin fins may be performed instead, which is, however, extremely time consuming.

In an attempt to obtain numerically the overall thermal field in the entire heat sink while keeping the computational time acceptable, Khorunzhii et al. [13] set up a finite element model with the commercially available software package ABAQUS for a pin-fin heat sink under uniform heating. Although the substrate and each pin-fin element were meshed to model heat conduction, the flow equations were not solved. Instead, the transfer of heat from pin fins to the convective fluid was modeled by applying the empirical heat transfer coefficient on pin-fin surfaces. With the assumption that the fluid temperature in the flow channel varies only along the longitudinal direction, an explicit expression of the fluid temperature can be obtained analytically. However, for nonuniform heating (as in the present study), the fluid temperature varies not only in the longitudinal direction but also in the transverse direction and hence can no longer be obtained analytically.

This study, therefore, presents a cost effective semi-empirical model capable of predicting detailed thermal fields in a pin-fin heat sink under nonuniform thermal boundary conditions. Heat conduction in the substrate and in each pin fin is considered with an empirical heat transfer coefficient applied on the pin-fin surfaces and nonuniform heat source on the substrate surface, respectively. Particularly, to avoid solving the exhaustive flow equations, uniform fluid temperature within each unit cell is assumed to derive the governing equation. To validate the model predictions, measurements of substrate temperature (with an IR camera) and fluid temperature at the exit of the pin-fin array are separately performed. Local distribution characteristics of substrate temperature as well as heat flux and fluid temperature in the pin-fin channel are analyzed for pin-fin heat sinks subjected to nonuniform impinging jet heating. The influences of convection Reynolds number, substrate thickness and thermal conductivity are quantified with the validated model to demonstrate the potential of the model for a subsequent thermoelastic analysis and design optimization of pin-fin/substrate systems.

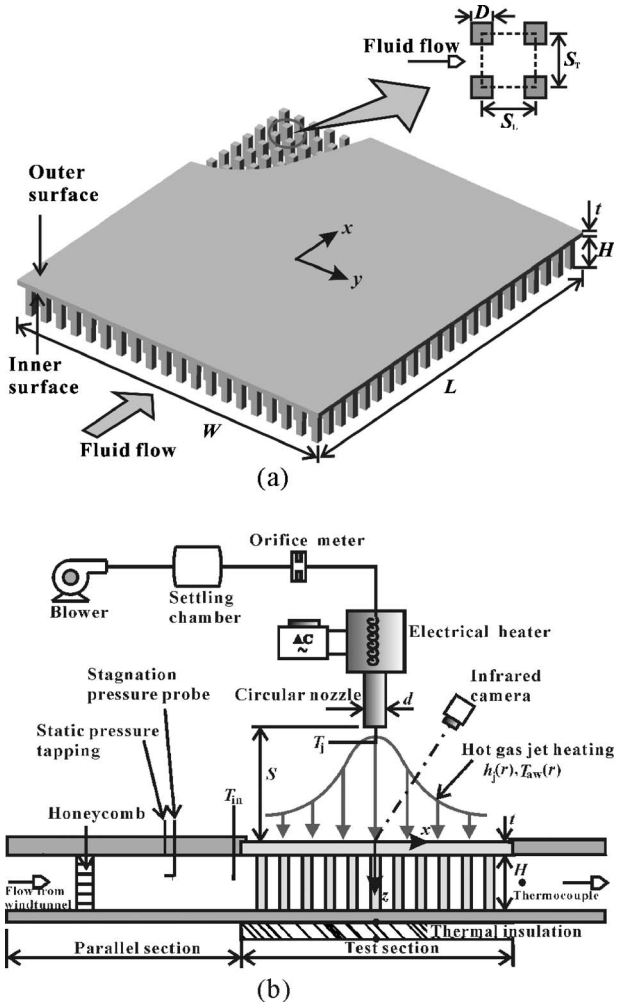

Fig. 1 Schematic of (*a*) square pin-fin heat sink and (*b*) test setup for nonuniform impingement heating

2 Experimental Details

2.1 Pin-Fin Heat Sink and Test Facility. The pin-fin heat sink tested in the present study is shown schematically in Fig. 1(*a*). The pin fins having a square cross section are rooted at a 2 mm thick substrate. Both the pin fins and the substrate were machined using an electric discharge machine (EDM) from a whole Al alloy block ($k_s=169$ W/m K). The square pin fins have identical dimensions of 2.5 mm(D)$\times$2.5 mm(D) and are arranged in an inline manner. The longitudinal (S_L/D) and transverse (S_T/D) pitches are $S_L/D=S_T/D=2.6$, while the pin-fin height is $H/D=4.8$. The other end of the pin fins was attached to a low thermal conducting acrylic plate ($k_s\sim0.2$ W/m K). Other parameters of the pin-fin heat sink are summarized in Table 1.

The pin-fin heat sink was placed in a rectangular test section, and air flow was forced passing through the pin fins to remove heat from the substrate and the pin fins. The Al substrate plate was heated by a circular impinging jet, posing highly nonuniform thermal boundary conditions, as illustrated in Fig. 1(*b*). A circular jet nozzle (diameter d) was positioned normal to the substrate, which discharged hot air to the surrounding air in ambient conditions. The jet exit-to-substrate spacing was fixed at $S/d=6$ during the entire experiment. Before exiting the nozzle, the jet flow was

Table 1 Parameters of test rig and pin-fin heat sink

Test rig	Jet nozzle diameter, d	10 mm
	Jet exit-to-substrate spacing, S	60 mm (or $S/d=6$), fixed
	Hydraulic diameter of rectangular channel, D_h	22 mm
Pin-fin heat sink	Material make	Al alloy (2024T6)
	Substrate dimensions, $(W\times L\times t)$	$130\times 146\times 2$ mm^3
	Pin-fin height, H	12 mm
	Transverse/longitudinal number of pin fins, N_T/N_L	20/22

heated by an electrical heater to approximately 140°C. The averaged mass flow rate of the jet flow was measured by a precalibrated orifice flow meter after a settling chamber. Forced convective flow driven by a centrifugal fan reached the pin-fin section after a parallel section (Fig. 1(*b*)).

2.2 Velocity and Temperature Measurements. To obtain the average mass flow rate of convective flow in the pin-fin section, the velocity profiles along the channel height (H) at the midwidth of the channel were traversed using a stagnation probe (outer diameter 1 mm). The probe was located $9D_h$ upstream of the test section, D_h being the hydraulic diameter of the channel. A static pressure tapping was flush mounted on the inner channel wall at the same upstream location as the stagnation probe. Pressure readings from both the stagnation probe and the static tapping were recorded by a differential pressure transducer.

For heat transfer measurements, three 36-gauge T-type bead thermocouples were used to monitor the ambient temperature (T_{amb}), jet exit temperature (T_j), and inlet temperature (T_{in}) in the heat sink channel. Another bead thermocouple was mounted on a linear transverse system to measure the temperature profile of the exit flow, traversing along the y-axis (channel width) 6 mm from the pin-fin exit. The traverse axis of the temperature probe coincided with the midheight of the channel (i.e., $H/2$). A temperature scanner was used to record the signals from all the thermocouples.

The distribution of surface temperature on the substrate ($z=0$) was mapped using an infrared camera positioned at an angle relative to the jet axis. The images were corrected for nonperpendicular viewing angles during post-image processing. To reduce the reflectivity from the substrate, the substrate was painted in black prior to measurements. The two sidewalls and the bottom substrate of the test section were thermally insulated.

2.3 Data Reduction Parameters. The jet Reynolds number is defined as

$$\mathrm{Re}_j = \frac{4\dot{m}_j}{\pi d\mu_j} \tag{1}$$

where $\dot{m}_j$ is the mass flow rate of jet flow measured by an orifice flow meter, and μ_j is the viscosity of air evaluated at the average adiabatic wall temperature of the substrate surface ($z=0$) [14]. Forced convection Reynolds number is defined as

$$\mathrm{Re}_{D_h} = \frac{\rho u_0 D_h}{\mu_f} \tag{2}$$

where u_0 is the mean inlet velocity in the convection channel.

The substrate surface temperature is evaluated in a dimensionless form defined as

$$\theta_b(z=0) = \frac{(T_b(x,y,0) - T_{in})}{(T_j - T_{amb})} \tag{3}$$

where $T_b(x,y,0)$ is the temperature of the substrate surface experiencing the impinging hot jet, $(T_j - T_{amb})$ represents the strength of heat loading from the hot jet, and $(T_b - T_{in})$ stands for the inlet condition of fluid flow on the cooling effect. The inlet temperature was found to be about 1°C higher than the ambient temperature in experiments. During the entire experiments, the jet Reynolds number Re_j, jet exit temperature T_j, and nozzle exit-to-substrate spacing S/d were fixed at 22,000, 140.0°C, and 6.0, respectively; only the convection Reynolds number was varied in the range of $\mathrm{Re}_{D_h}=3000-12{,}000$.

2.4 Calibration and Validation of Experimental Facility. Before utilizing the present experimental facility, comprehensive calibration and validation were conducted to ensure the correctness of test data obtained from the facility.

To calibrate the orifice meter, for cold free jet, velocity profiles at the nozzle exit were traversed along the radial direction of the circular nozzle using a Pitot tube at three different flow rates. These velocity profiles were then used to calculate the mass flow rate of the jet. The flow rates obtained from the velocity profiles were compared with those obtained from the orifice meter, and the discrepancies were found to be within 2.1%.

Each thermocouple was calibrated in an ice-water mixture filled container. Temperature readings from the temperature scanner were found to be ±0.1°C for each thermocouple. Calibration of the IR camera was also conducted. An aluminum plate was heated uniformly by a film-type heating element attached to one side of the Al plate, with its other side exposed to natural air convection in ambient conditions. To reduce the reflectivity from the Al plate, a black paint was sprayed after a foil-type thermocouple (13 μm thick) was attached at the center of the cooling side of the plate. The IR camera was focused on the center of the Al plate with its focal length and viewing angle identical to those used for testing the pin-fin heat sink.

Temperatures monitored by the IR camera were compared with those measured from the calibrated thermocouple. A systematic deviation of the temperature measured by the IR camera was found and corrected during the data reduction process as

$$T_{\mathrm{thermocouple}}/^\circ\mathrm{C} = 0.9765T_{\mathrm{infrared}}/^\circ\mathrm{C} + 0.1282 \tag{4}$$

The adiabatic wall temperature on the impinging surface was measured and compared with test data available in the open literature. The adiabatic wall boundary was created by a 10 mm thick Perspex plate followed by a 40 mm thick thermal insulation block at the side opposite to the side where the hot gas jet impinges. The hot gas jet system was the same as that used for testing the pin-fin sink. The nondimensional adiabatic wall temperature defined in Ref. [15] is known to be independent of the jet exit temperature,

$$\theta_{aw} = \frac{T_{aw} - T_{amb}}{T_j - T_{amb}} \tag{5}$$

where T_{aw} is the adiabatic wall temperature on the impinging surface measured by the IR camera.

Figure 2 compares the measured distribution of nondimensional adiabatic wall temperature with that reported by Goldstein et al. [15] for $S/d=6$ and $\mathrm{Re}_j=22{,}000$, with good agreement achieved. Consequently, it is believed that the present temperature measurement setup (including the IR camera, thermocouples, and impinging jet system) is reliable.

2.5 Heat Loss Estimation and Uncertainty Analysis. Heat loss from the two sidewalls of the forced convection channel may be ignored as they are not in physical contact with the solid pin

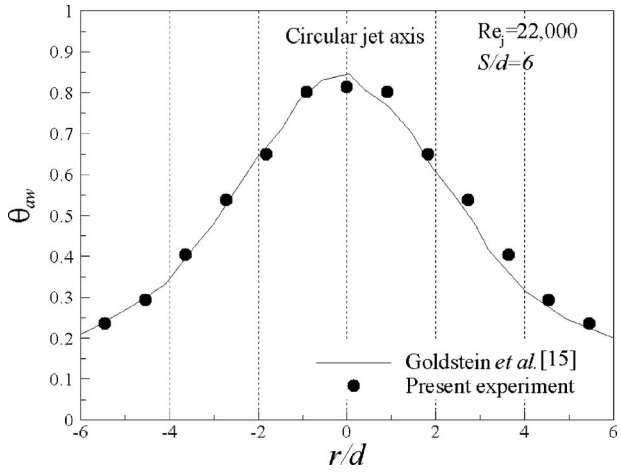

Fig. 2 Comparison of presently measured nondimensional adiabatic wall temperature distribution with that of Goldstein et al. [15]

fins. The four side edges of the substrate were insulated with a thick insulation material polytetrafluoroethylene (PTFE), and the total contact area only accounts for 1.6% of the total heat transfer area of the substrate and pin fins exposed to convective fluid flow. Therefore, it is reasonable to assume that heat lost through these edges is negligible. To evaluate heat loss from the bottom acrylic end wall of the test section, temperatures at the center of both sides of the insulation layer attached beneath the acrylic end wall (see Fig. 1(*b*)) were measured. Based on the measured temperature drop across the insulation layer, heat loss through the acrylic end wall was estimated to be 0.56% of the total heat input.

The uncertainties of pressure drop across the orifice meter (132 ± 1 Pa) and jet Reynolds number were estimated to be 1.1% and 2.1%, respectively. At a typical convection Reynolds number of 10,000, the uncertainty associated with the convection Reynolds number was estimated to be 1.7%. For the nondimensional substrate surface temperature, the uncertainty was evaluated using the root-square method reported in Ref. [16] as

$$\frac{\Delta\theta_b}{\theta_b} = \sqrt{\left(\frac{\Delta T_b}{T_b - T_{\text{in}}}\right)^2 + \left(\frac{\Delta T_{\text{in}}}{T_b - T_{\text{in}}}\right)^2 + \left(\frac{\Delta T_j}{T_j - T_{\text{amb}}}\right)^2 + \left(\frac{\Delta T_{\text{amb}}}{T_j - T_{\text{amb}}}\right)^2} \tag{6}$$

where the error of the temperatures measured by thermocouples, ΔT_j, ΔT_{in}, and ΔT_{amb}, was estimated to be $0.2\,^\circ$C. The average substrate temperature ($T_b - T_{\text{in}}$) was measured to be about $10\,^\circ$C at $\text{Re}_{D_h} = 1.0 \times 10^4$. In the present temperature range, the deviation of the IR measured temperature from that measured by the thermocouple (Eq. (4)) was calculated to be $0.7\,^\circ$C. Therefore, ΔT_b was estimated to be $0.7\,^\circ$C although correction has been performed. Subsequently, the uncertainty in the nondimensional substrate surface temperature was estimated to be within 7.3%.

3 Semi-Empirical Modeling

3.1 Model Description. In the following, to predict local thermal fields in the substrate and each pin fin as well as those in the convective flow, a semi-empirical model independent of the present experiment is developed. For thermal fields in the substrate and in the pin fins, a 3D conduction model and a classical one-dimensional (1D) fin analogy model are separately employed. The thermal field of forced convection flow in the pin-fin channel is estimated by assuming that, upon averaging (to be defined later), the temperature within a unit cell is uniform. Empirical correlations for the heat transfer coefficients of circular hot gas impinging jet and pin-fin cross flow are adopted in the model. Constant thermal properties of air are assumed, and radiation heat transfer is ignored in the analysis.

3.1.1 Heat Conduction in Substrate. Expressed in the Cartesian coordinates (Fig. 1), the temperature field, $T_b(x,y,z)$, in the substrate is governed by

$$(\rho c_p)_s \frac{\partial T_b(x,y,z)}{\partial \tau} = k_s \left(\frac{\partial^2 T_b(x,y,z)}{\partial x^2} + \frac{\partial^2 T_b(x,y,z)}{\partial y^2} + \frac{\partial^2 T_b(x,y,z)}{\partial z^2} \right) \tag{7}$$

where $(\rho c_p)_s$ is a product of the density and specific heat of the substrate material and k_s is its thermal conductivity. As illustrated in Fig. 1, the origin of the coordinates is located at the center of the substrate coinciding with the impinging center of the circular jet.

The boundary conditions applied to solve Eq. (7) are specified as

(a) The sidewalls of the substrate are thermally insulated:

$$\frac{\partial T_b}{\partial x} = 0 \quad \text{at } x = -L/2, \quad x = L/2$$

$$\frac{\partial T_b}{\partial y} = 0 \quad \text{at } y = W/2 \tag{8}$$

(b) Only half of the substrate is considered due to the symmetric nature of the temperature field with respect to the y-axis:

$$\frac{\partial T_b}{\partial y} = 0 \quad \text{at } y = 0 \tag{9}$$

(c) For the substrate surface (i.e., $z=0$) experiencing nonuniform heating via the impinging jet, one has

$$h_j(r)(T_{\text{aw}}(r) - T_b(x,y,0)) = -k_s \frac{\partial T_b}{\partial z} \tag{10}$$

where $h_j(r)$ is the impingement heat transfer coefficient, $T_{\text{aw}}(r)$ is the adiabatic wall temperature on the substrate ($z=0$), and $r=(x^{2+}y^2)^{1/2}$ is the radial coordinate with its origin located at the jet axis. For hot gas impinging jets, numerous studies have argued that the adiabatic wall temperature should be used as the reference in the definition of heat transfer coefficient due to entrainment caused by thermal mixing of jet flow with the surrounding fluid. The heat transfer coefficient thus defined becomes independent of nozzle exit temperature and has the same value as the cold jet case [14,15,17].

(d) On the inner surface of the substrate (i.e., $z=t$) that experiences forced convection cooling, a portion (i.e., the "end wall") is directly exposed to the forced convection flow while the remaining part serves as the root of the pin fins. For the latter, heat transferred from the substrate is conducted to the pin fins and subsequently removed by convective flow. Therefore, thermal boundary conditions for the two different regions are treated separately. For the end wall region, heat balance dictates that:

$$-k_s \frac{\partial T_b(x,y,z)}{\partial z} = h_b(T_b(x,y,t) - T_f(x,y)) \tag{11}$$

where h_b is the end wall heat transfer coefficient and $T_f(x,y)$ is the averaged fluid temperature in the unit cell (to be determined later). For the pin-fin root region, heat balance requires

$$-k_s \frac{\partial T_b(x,y,z)}{\partial z} = q_{\text{fin}} \tag{12}$$

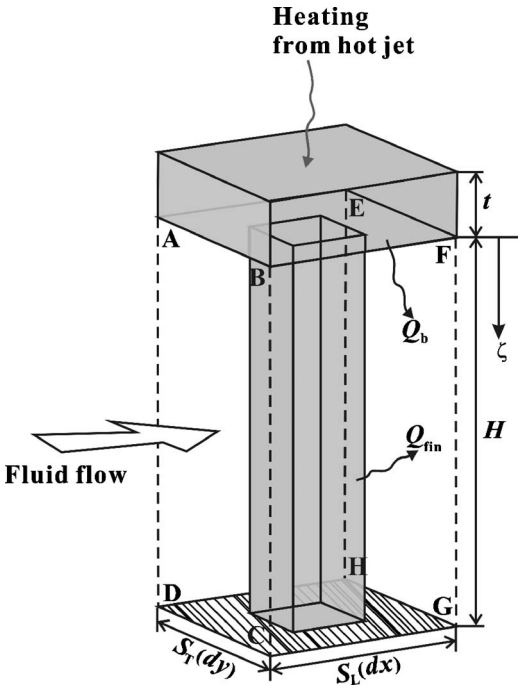

Fig. 3 Heat balance in a representative unit cell of pin-fin heat sink

where q_{fin} is the heat flux conducted by the pin fin from the Al substrate in the unit cell. Note that at different pin-fin roots, the values of q_{fin} are different due to the nonuniform nature of impingement heating. A positive q_{fin} indicates that heat is transferred from the substrate to the pin fin.

3.1.2 Energy Equation for Forced Convective Flow. As previously mentioned, to avoid the calculation of complex flow fields in the channel, we assume that the fluid flow has a uniform temperature within each unit cell so that the in-plane variation of unit-cell-averaged temperature can be analytically predicted. With this assumption, the variation in fluid temperature across the height of the pin-fin channel is not considered in the analysis, which is deemed appropriate for the present problem as the in-plane dimensions of the channel are ten times larger than the channel height. Furthermore, under the highly nonuniform heat input, the in-plane distribution (the *x-y* plane) of fluid temperature is more interesting than that along the channel height.

Figure 3 shows schematically the unit cell used to derive the governing equations. For the entire pin-fin heat sink, 22 and 20 unit cells are distributed in the *x-y* plane along the longitudinal and transverse directions, respectively. Therefore, a distribution of the 22×20 discrete temperatures in the *x-y* plane is obtainable using the unit cell averaging approach.

As shown in Fig. 3, convective flow having an average velocity u_0 enters the unit cell through surface A-B-C-D and exits through surface E-F-G-H. The two side surfaces, B-F-G-C and A-E-H-D, are taken as hydraulically impermeable. However, due to temperature gradient induced by nonuniform heating through the substrate, there is heat transported through the two side surfaces via conduction in the fluid between neighboring cells. The C-D-H-G surface attached to the other end of the pin fin is treated as adiabatic.

Over an infinitesimally small period of time $d\tau$, the rate of net heat entering the unit cell via conduction in the fluid from/to the neighboring unit cells is

$$Q_c = k_f\left(\frac{\partial^2 T_f(x,y)}{\partial x^2} + \frac{\partial^2 T_f(x,y)}{\partial y^2}\right)dxdyHd\tau \tag{13}$$

Because of the ingress and egress of convective flow into and out of the unit cell, the enthalpy increase of the fluid in the unit cell is

$$\Delta H = -(\rho c_p)_f u_0 \frac{\partial T_f(x,y)}{\partial x}dxdyHd\tau \tag{14}$$

Convective heat dissipation from the substrate to convective flow in the unit cell is

$$Q_b = h_b(S_T S_L - A)(\overline{T_b}(x,y,t) - T_f(x,y))d\tau \tag{15}$$

where A is the cross-sectional area of the pin fin and $\overline{T_b}(x,y,t)$ is the average temperature of the end wall (substrate region exposed directly to convective flow). Convective heat dissipation from the pin-fin surface in the unit cell can thence be expressed as

$$Q_{fin} = h_{fin}PH(\overline{T_{fin}} - T_f(x,y))d\tau \tag{16}$$

where h_{fin} is the heat transfer coefficient on the pin surface, P is the perimeter of the pin fin, and $\overline{T_{fin}}$ is the fin temperature averaged along its height (to be determined later).

Heat storage in the fluid during time interval $d\tau$ is

$$\Delta e = (\rho c_p)_f \frac{\partial T_f(x,y)}{\partial \tau}dxdyHd\tau \tag{17}$$

Heat balance of fluid flow in the unit cell is contributed mainly by four mechanisms, namely, heat storage, conduction, streamwise convection, and heat source due to substrate and pin-fin heating, expressed as

$$\Delta e = Q_c + \Delta H + (Q_b + Q_{fin}) \tag{18}$$

Substitution of Eqs. (13)–(17) into Eq. (18) yields a differential equation governing the variation of the unit-cell-averaged fluid temperature as

$$(\rho c_p)_f\left(\frac{\partial T_f(x,y)}{\partial \tau} + u_0\frac{\partial T_f(x,y)}{\partial x}\right) = k_f\left(\frac{\partial^2 T_f(x,y)}{\partial x^2} + \frac{\partial^2 T_f(x,y)}{\partial y^2}\right) + \dot{q} \tag{19}$$

where $\dot{q}$ is the heat source due to heat dissipation from the substrate and pin fin to the fluid:

$$\dot{q} = \frac{Q_b + Q_{fin}}{S_T S_L H d\tau} \tag{20}$$

It should be noticed that the turbulent mixing of fluid flow would induce an additional convective transport, reducing the temperature gradient in the fluid. Due to the lack of relevant information, this effect is not taken into consideration in the present model. However, with the turbulent mixing effect ignored, the good agreement of the lateral distribution of fluid temperature at the channel exit (to be discussed later) suggests that the dominant heat transfer mechanisms for the heat transport of fluid flow in a unit cell are the streamwise convection and heat source.

Equation (19) is solved with the following boundary conditions:

$$T_f = T_{in} \quad \text{at } x = -L/2 \tag{21}$$

$$\frac{\partial T_f}{\partial x} = \frac{\partial T_f}{\partial y} = 0 \quad \text{at } x = L/2 \text{ and } y = 0, W/2 \tag{22}$$

3.1.3 Fin Analogy Model. To determine the heat flux conducted from the substrate to each pin fin, i.e., q_{fin} in Eq. (12), and subsequent dissipation to convective flow, i.e., Q_{fin} in Eq. (16), the concept of fin analogy is adopted. Consider a single square pin fin centered in the unit cell (Fig. 3). At an arbitrary cross section of the pin fin, uniform temperature is assumed. This is considered reasonable because the Biot number based on the pin-fin diameter

D is low, e.g., $Bi_D = 0.005$ for a typical convection Reynolds number of 1.0×10^4. Under the above assumption, the 1D fin analogy may be written as

$$(\rho c_p)_s \frac{\partial T_{\text{fin}}(\zeta)}{\partial \tau} = k_s \frac{\partial^2 T_{\text{fin}}(\zeta)}{\partial \zeta^2} - \frac{h_{\text{fin}} P}{A}(T_{\text{fin}}(\zeta) - T_f(x,y)) \quad (23)$$

where ζ is the local coordinate along the pin-fin height and $T_{\text{fin}}(\zeta)$ is the pin-fin temperature at location ζ.

Equation (23) is solved subjected to the following boundary conditions. At the root of each pin fin, its temperature is identical to that of the substrate:

$$T_{\text{fin}}(\zeta)|_{\zeta=0} = T_b(x,y,t) \quad (24)$$

The tip of the pin fin is thermally insulated:

$$\left.\frac{\partial T_{\text{fin}}(\zeta)}{\partial \zeta}\right|_{\zeta=H} = 0 \quad (25)$$

Once $T_{\text{fin}}(\zeta)$ is determined, the heat conducted to the pin fin from the substrate can be calculated as

$$q_{\text{fin}} = -k_s \left.\frac{\partial T_{\text{fin}}(\zeta)}{\partial \zeta}\right|_{\zeta=0} \quad (26)$$

and the average pin-fin temperature of Eq. (16) is

$$\overline{T}_{\text{fin}} = (1/H)\int_0^H T_{\text{fin}}(\zeta)\, d\zeta \quad (27)$$

3.1.4 Determination of $h_j(r)$, $T_{\text{aw}}(r)$, h_{fin}, and h_b . The governing equations have been obtained hitherto. In addition to the boundary conditions, the values of a few parameters such as $h_j(r)$, $T_{\text{aw}}(r)$, h_{fin}, and h_b need to be prescribed so that thermal fields in the pin-fin heat sink may be calculated. These are obtained from existing empirical correlations, independent of the present experiments. Details for each parameter are described next.

For the impingement heat transfer coefficient, which varies radially along the substrate, $h_j(r)$, the empirical correlation of Goldstein and Franchett [18] as a function of jet Reynolds number and radial location for a given separation distance of $S/d = 6$ was adopted as

$$h_j(r) = \frac{k_f \text{Re}_j^{0.7} 0.155 e^{-0.37(r/d)^{0.75}}}{d} \quad (28)$$

Here, the fluid conductivity k_f is evaluated based on the average adiabatic wall temperature at $z = 0$ [14] given by

$$T_{\text{aw}}(r) = \eta(T_j - T_{\text{amb}}) + T_{\text{amb}} \quad (29)$$

where η is the effectiveness on the substrate, which is independent of the jet Reynolds number and jet exit temperature, but a function of the radial location and separation distance [15]:

$$\eta = 0.35 + 0.6e^{-0.01(S/d-2)^{2.2} - 0.1(r/d)^{2.5}}$$

$$\text{for } 0 \le r/d \le 3.5$$

$$\eta = 1.193(r/d)^{-0.98}$$

$$\text{for } r/d \ge 3.5 \quad (30)$$

The heat transfer coefficient h_{fin} on the pin-fin surface is determined with the empirical correlation reported by Kim et al. [4]:

$$\text{Nu}_{\text{fin}} = \frac{h_{\text{fin}} D}{\varepsilon k_f} = 0.36283 \text{Re}_D^{0.54219} \quad \text{for } \text{Re}_D < 1000$$

$$= 0.04433 \text{Re}_D^{0.82934} \quad \text{for } \text{Re}_D \ge 1000 \quad (31)$$

where ε is the porosity of the pin-fin array and $\text{Re}_D (= \rho_f u_{\max} D/\mu_f)$ is the Reynolds number based on the pin diameter D and maximum velocity $u_{\max} (= u_0 S_T/(S_T - D))$ in the pin-fin array.

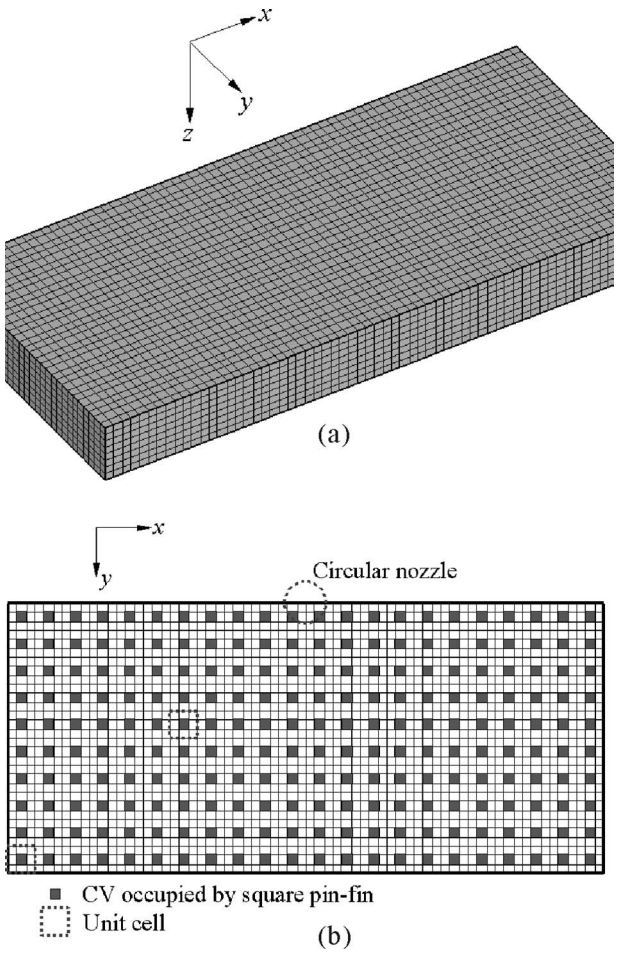

Fig. 4 Computational mesh for substrate: (*a*) 3D mesh for half of substrate; (*b*) plan view from positive *z*-direction showing pin fins (dark squares)

The end wall heat transfer coefficient h_b is affected by complex vortex flow near the substrate. As stated in Ref. [8], the average heat transfer coefficient on the pin-fin surface is approximately 35% higher than that on the end wall for short pin fins having $H/D = 1.0$:

$$h_b = h_{\text{fin}}/1.35 = 0.74 h_{\text{fin}} \quad (32)$$

In the present study, the pin-fin array has $H/D = 4.8$. The effect of this discrepancy will be discussed in Sec. 4.4.

3.2 Calculation Procedure. Equations (7)–(27) were numerically solved using the finite volume method [19]. In order to obtain the temperature field in the substrate, the substrate was divided into a number of nonoverlapping control volumes, as shown in Fig. 4(*a*), over which Eq. (7) was discretized. The unknown temperatures were stored at the center of each control volume. A plan view of the 3D mesh in Fig. 4(*a*) from the positive *z*-direction is presented in Fig. 4(*b*), showing the location of each square pin fin on the inner side of the substrate ($z = t$). In Fig. 4(*b*), the dark square dots denote the pin fins, while the white areas refer to the substrate region (end wall) directly exposed to convective flow. Prior to the calculation, the influence of the numerical grid density on convergence was checked. Based on the results, 39,600 nodes of $66(x) \times 30(y) \times 20(z)$ were distributed in the substrate.

The governing equation for fluid temperature (Eq. (19)) was discretized over a two-dimensional (2D) rectangular domain since

it governs the variation in unit-cell-averaged fluid temperature in the x-y plane. A total of $22(x)\times10(y)$ control volumes were distributed in the computational domain, each covering the projection area of a unit cell in the x-y plane, such as the dashed squares shown in Fig. 4(b). The power-law scheme was used to discretize the convective term of Eq. (19), while the method of central difference was used for the diffusive terms of Eqs. (7), (19), and (23).

The calculation procedures are as follows:

(1) Start calculation with an initial temperature (e.g., ambient temperature) for Eqs. (7), (19), and (23).
(2) Solve 3D conduction equation for the substrate, i.e., Eq. (7), with boundary conditions specified in Eqs. (8)–(12).
(3) Solve fin analogy, Eq. (23), and then calculate q_{fin} and $\overline{T}_{\text{fin}}$. Loop the calculation for each pin fin in all unit cells.
(4) Solve the energy equation for fluid flow, i.e., Eq. (19), with the boundary condition of Eqs. (21) and (22).
(5) Return to step (2) and repeat the calculation till the iteration is complete for the present time step. Then, start the iteration for the next time step with the renewed temperatures of the substrate, pin fins, and fluid in the pin-fin channel as initial values.

4 Discussion of Results

In the previous section, a semi-empirical analytical model for pin-fin heat sink subjected to non-uniform heating has been described along with an experimental model for validation purpose. The present model is first validated by comparing the predicted temperature distribution on the substrate and fluid temperature in the pin-fin channel with those measured. The model is then executed to show its potential in several aspects, such as the prediction of the thermal footprints of the pin fins in terms of heat flux distribution and the capability of capturing the effects of forced convection in the pin-fin channel and heat spreading in the substrate on substrate temperature variation under nonuniform impinging jet heating conditions.

4.1 Substrate Temperature Distribution. Figure 5(a) shows the measured temperature contour on the Al substrate ($z=0$) at the convection Reynolds number of 1.0×10^4. The surface temperature peaks at the impinging center (i.e., $x=y=0$), decreasing monotonically with increasing radial distance from the impinging center. The temperature distribution is symmetric with respect to the y-axis but asymmetric relative to the x-axis. This is attributed to the gradual heating of the cooling flow convecting across the pin fins along the x-axis. As a result, the increased fluid temperature along the x-axis causes a decrease in heat transfer rate from the pin-fin heat sink to the coolant flow. The substrate temperature at the downstream is therefore higher than that at the upstream for the same radial distance. These distribution characteristics are well captured by the semi-empirical model (Fig. 5(b)), validating therefore the proposed model. The warm region at the bottom right of Fig. 5(a) was caused by the image reflection from the jet nozzle when the IR camera was positioned at an angle relative to the jet axis.

4.2 Fluid Temperature in Pin-Fin Channel. With the in-plane distribution of temperature displayed in Fig. 5, the fluid temperature in the pin-fin channel is calculated, and the prediction is shown in Fig. 6(a) at the convection Reynolds number of $\text{Re}_{D_h}=1.0\times10^4$. The convection flow enters the pin-fin section with initial temperature, T_{in}. As it progresses along the x-axis across the pin fins, the heat transferred through the substrate and pin fins is removed by the convective cooling flow. The coolant temperature is thus increased, having its cell-averaged in-plane distribution, as shown in Fig. 6(a). Due to the nonuniform heat input by the impinging jet, C-type isothermals of fluid temperature in the pin-fin heat sink are distinctively observed, differentiating

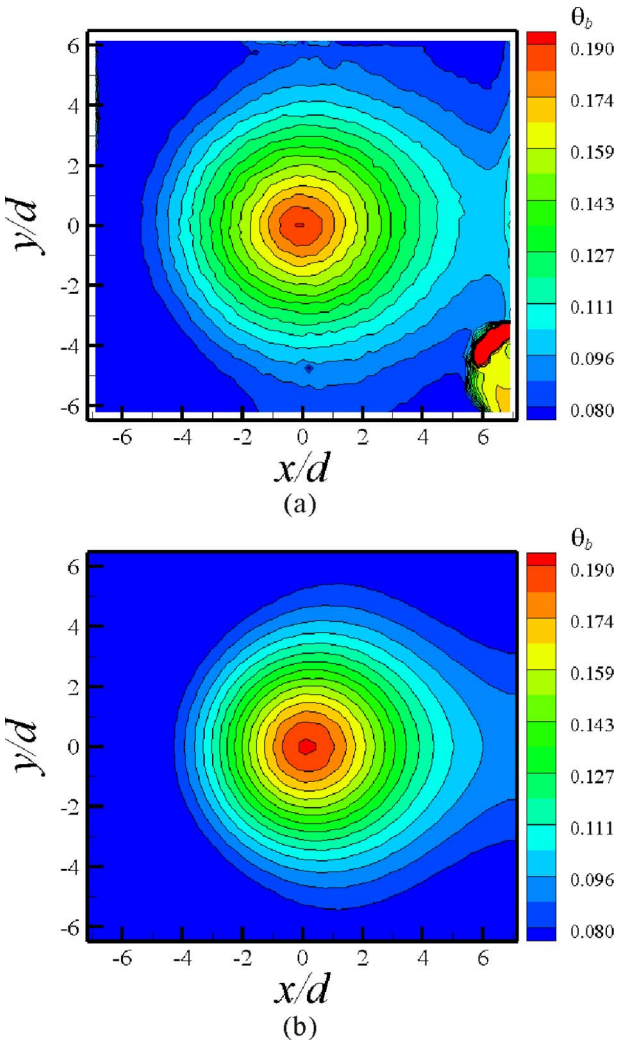

Fig. 5 Surface temperature mappings on substrate ($z=0$) at $\text{Re}_{D_h}=1.0\times10^4$, with convective flow direction from negative x value to positive x value: (a) experiment; (b) prediction from semi-empirical model

the present problem from that under uniform heating conditions.

Figure 6(b) compares the measured fluid flow temperature profiles traversed along the y-axis (widthwise distribution) at the pin-fin exit with model predictions for selected convection Reynolds numbers. The maximum of the flow temperature coincides with the center line of the channel in the widthwise direction ($y=0$). The flow temperature decreases monotonically as moving away from the center line. In general, the predicted fluid temperatures agree well with the measured ones, providing further validation of the proposed model. The maximum deviation between the measurement and prediction for the fluid temperature profile at $\text{Re}_{D_h}=5000$ is found to be 8.2%, greater than the estimated uncertainty (2.8%) for the nondimensional fluid temperature. The larger discrepancy may be attributed to the fact that the fluid temperature at the midheight of the channel (measured) differs from that averaged across the channel height (predicted), although the fluid flow in the pin-fin channel is deemed well mixed.

4.3 Heat Flux Distribution. The predicted heat flux distribution on the substrate surface at $z=t$ is shown in Fig. 7 for $\text{Re}_{D_h}=1.0\times10^4$. The light points denote the locations of the pin-fin roots, which exhibit a much higher heat flux conducted to the solid pin fins than that dissipated directly from the substrate surface by convective fluid flow. For example, the heat flux at the

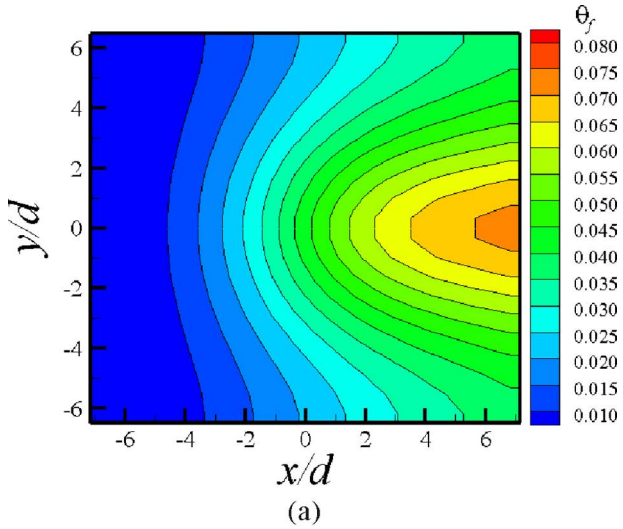

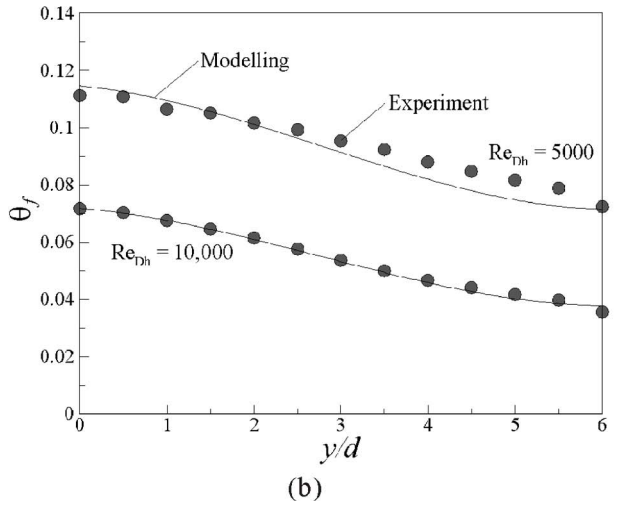

Fig. 6 Fluid temperature in pin-fin heat sink: (*a*) predicted fluid temperature map at $Re_{D_h}=1.0\times10^4$; (*b*) comparison of measured temperature profiles at channel exit ($x=L/2$) along *y*-axis with those predicted

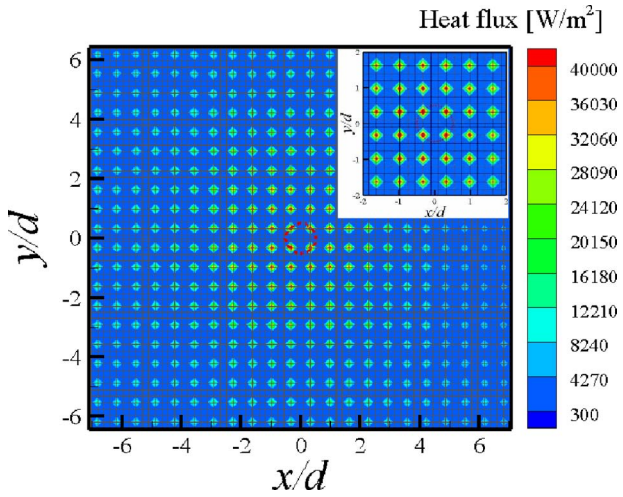

Fig. 7 Heat flux distribution on substrate surface exposed to fluid flow

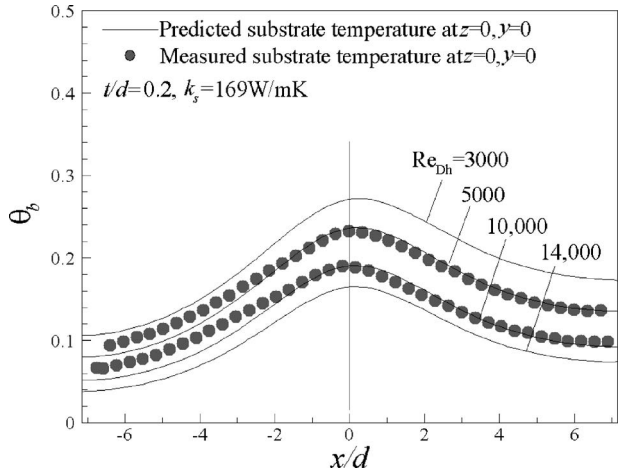

Fig. 8 Effect of convection Reynolds numbers on substrate temperature profile along *x*-axis ($y=0$)

pin-fin root near the impinging center region was predicted to be 5×10^4 W/m^2, whereas that at the substrate region directly exposed to convective fluid flow was only 2.5×10^3 W/m^2. Therefore, the present model is capable of predicting local thermal behaviors such as the footprints of the pin fins.

4.4 Effect of Convection Reynolds Number on Substrate Temperature. Figure 8 plots the predicted profiles of the substrate temperature ($z=0$) along the *x*-axis (i.e., at $y=0$) for selected convection Reynolds numbers, with t/d and k_s fixed at 0.2 and 169 W/m k, respectively. As the convection Reynolds number Re_{D_h} is increased, the substrate temperature is decreased in the whole lateral range. The increase in Re_{D_h} (or mass flow rate of convective flow) enhances the heat transfer coefficients on both the substrate and the pin-fin surface, resulting in increased overall heat dissipation. As a result, the substrate temperature decreases.

For comparison, the measured temperature profiles at $Re_{D_h}=5000$ and 10,000 are also plotted in Fig. 8. Good agreement with the present model predictions is achieved except near the inlet of the pin-fin array where a relatively large discrepancy up to 20% is observed. This may be attributed to the fact that the uniform heat transfer coefficients prescribed on the substrate and pin-fin surface overestimate the actual values near the inlet region. In reality, each of the heat transfer coefficients varies along the streamwise direction in the pin-fin array, increasing for the first few rows to reach a peak and then slowly decreasing toward an asymptotic value [20].

For practical applications associated with nonuniform heating, the high (peak) substrate temperature near the impinging center may be a major concern as this may cause overheating or even failure of the device. Figure 9 plots the normalized peak substrate temperature as a function of the convection Reynolds number. As the convection Reynolds number increases, the peak substrate temperature is seen to decrease monotonically.

The influence of heat transfer coefficient h_b prescribed for the substrate region (end wall) directly exposed to convective cooling in Eq. (32) is now examined. Although the actual value of h_b is influenced by many factors, we believe that it should be higher than the end wall heat transfer coefficient of empty channel flow (lower bound) and lower than that on the pin fin surface (upper bound). Therefore, three cases were calculated, as follows:

(1) h_b selected as the heat transfer coefficient on the pin-fin surface, i.e., $h_b=h_{\text{fin}}$
(2) h_b selected as the heat transfer coefficient associated with empty channel flow, i.e., $h_b=h_{\text{emp}}$

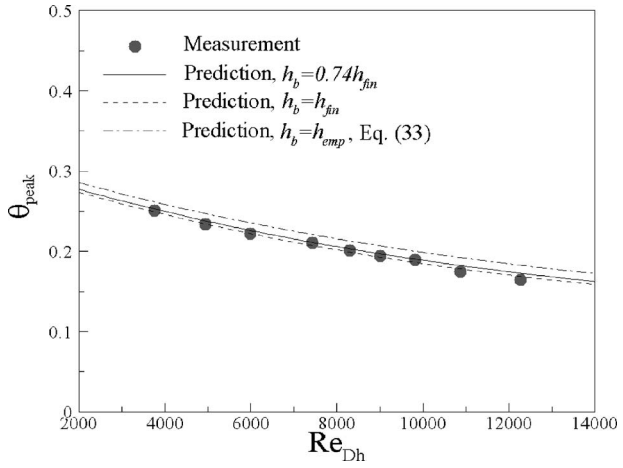

Fig. 9 Peak substrate temperature (θ_{peak}) plotted as a function of convection Reynolds number

(3) h_b selected as the heat transfer coefficient estimated using Eq. (32), i.e., $h_b=0.74h_{\text{fin}}$

Here, the end wall heat transfer coefficient of empty channel flow h_{emp} is calculated using the formulas proposed by Petukhov et al. [21] and Gnielinski [22] as

$$h_{\text{emp}}=\frac{(f/8)(\text{Re}_{D_h}-1000)\text{Pr}}{1+12.7\sqrt{f/8}(\text{Pr}^{2/3}-1)}\frac{k_f}{D_h}$$
$$(2300\le \text{Re}_{D_h}\le 10^4;0.5\le \text{Pr}\le 200)$$

$$h_{\text{emp}}=\frac{(f/8)\text{Re}_{D_h}\text{Pr}}{1+900/\text{Re}_{D_h}+12.7\sqrt{f/8}(\text{Pr}^{2/3}-1)}\frac{k_f}{D_h}$$
$$(10^4\le \text{Re}_{D_h}\le 5\times 10^6;0.5\le \text{Pr}\le 200) \quad (33)$$

where

$$f=(1.82\ \log\text{Re}_{D_h}-1.64)^{-2} \quad (34)$$

It should be noted that to take account of flow acceleration in the pin-fin channel due to the reduced flow area, the velocity u_0/ε is used in Re_{D_h} of Eq. (33).

The predicted peak substrate temperatures for the three cases are presented in Fig. 9. For the case of $h_b=h_{\text{fin}}$, the peak temperature is slightly lower than that of $h_b=0.74h_{\text{fin}}$, although both are fairly close to the measurement data. However, when h_b takes its lower bound h_{emp}, the prediction is about 4.5–10% higher than that measured over the range of convection Reynolds numbers considered. In general, the influence of h_b on the substrate temperature prediction is insignificant due to the fact that the end wall heat transfer area only accounts for 23% of the total wetted surface area in the present case.

4.5 Spreading Resistance in Substrate (Thermal Conductivity and Thickness Effects). The effect of forced convection in the pin-fin channel on substrate temperature has been investigated by applying the validated model. It is also of interest to use this model to explore how the spreading resistance in the substrate affects its temperature distribution. The spreading resistance, commonly involved in the design of electronic cooling devices, exists whenever the heat load is nonuniformly distributed. Lee et al. [23] analytically investigated the spreading resistance in a plate of finite thickness subjected to constant heat flux on the central portion of the plate surface (i.e., nonuniform heating). The spreading resistance is found to be greater than the 1D material resistance (i.e., resistance under uniform heating), contributing significantly to the total thermal resistance.

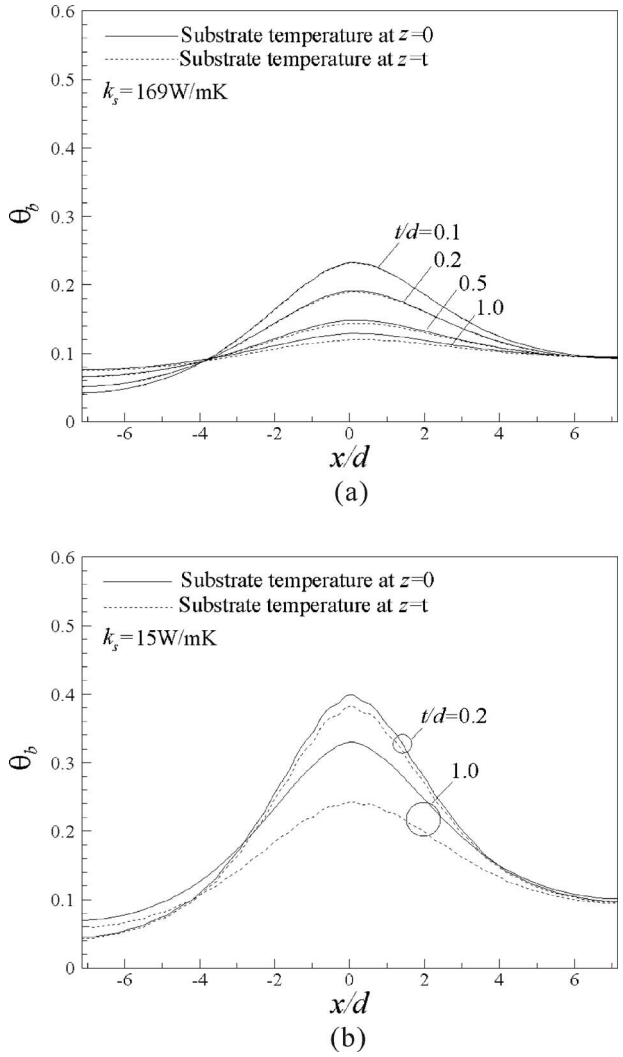

Fig. 10 Influence of substrate thickness on temperature profiles of outer and inner substrate surfaces along *x*-axis at *y*=0 for $\text{Re}_{D_h}=1.0\times10^4$: (*a*) $k_s=169$ W/m K (Al alloy); (*b*) $k_s=15$ W/m K (stainless steel)

Similarly, in the present study, the heat sink substrate experiences concentrated heating from an impinging jet coinciding with the impinging center. The lateral spreading of heat in the substrate is expected to play a crucial role in the overall thermal performance.

Consider first the influence of substrate thickness on the distribution of temperature on both surfaces of the substrate ($z=0$ and $z=t$). When both the substrate and pin fins are made of Al alloy ($k_s=169$ W/m K), Fig. 10(*a*) presents the predicted distribution of substrate surface temperature as a function of substrate thickness (t/d) at $\text{Re}_{D_h}=1.0\times10^4$. The distribution on the outer surface ($z=0$) becomes pronouncedly flatter as the substrate is thickened. This indicates that the resistance to heat spreading is reduced as the substrate thickness is increased, which is consistent with existing findings [23].

Apart from lateral spreading, another component of the thermal resistance exists along the thickness direction (along the z-axis), i.e., the so-called "1D material resistance" [23], which is proportional to t/k. The drop of temperature in the thickness direction increases as t/d is increased from 0.1 to 1.0 (Fig. 10(*a*)) due to increasing material resistance. However, the temperature drop between the outer and inner surfaces of the substrate is, in general,

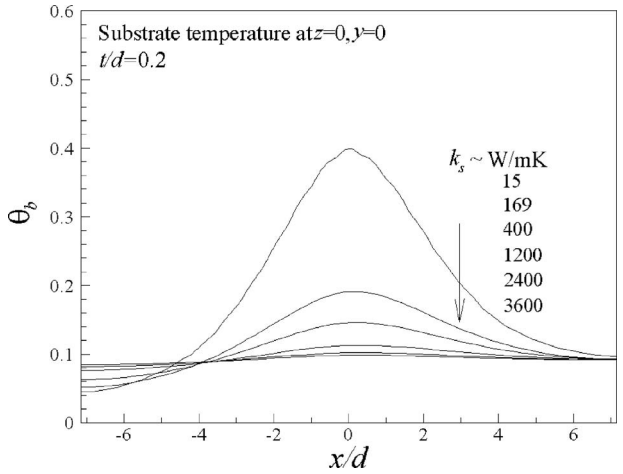

Fig. 11 Distribution of substrate temperature ($z=0$) along x-axis ($y=0$) plotted as a function of substrate thermal conductivity for fixed substrate thickness ($t/d=0.2$) at $Re_{D_h}=1.0\times10^4$

small (e.g., less than 5.7% when $t/d=1.0$), in comparison with that in the lateral direction. This suggests that the material resistance is negligible relative to the spreading resistance. Practically, this is significant as the 3D conduction model currently employed for the substrate can be reduced to a 2D one, leading to reduced computational time and simpler coding procedures if the temperature drop across substrate thickness can be ignored.

When the heat sink is made of stainless steel having a relative low thermal conductivity ($k_s=15$ W/m K), Fig. 10(b) demonstrates that the temperature drop between the outer and inner surfaces is more remarkable than that of the Al heat sink. This indicates that for relative small values of k_s, the material resistance is no longer negligible compared with the spreading resistance. Therefore, the 3D conduction model is necessary for calculating the substrate thermal fields.

To elaborate the influence of thermal conductivity on the lateral distribution of substrate temperature at $z=0$, the substrate thickness is fixed at $t/d=0.2$ while the thermal conductivity is varied over a wide range, as shown in Fig. 11. The substrate temperature becomes substantially flatter as the conductivity is increased due mainly to the decreasing spreading resistance. In particular, when the conductivity exceeds $k_s\approx2400$ W/m K, the substrate temperature appears to increase in a linear fashion along the flow direction (the x-axis) even if the impinging heating is highly nonuniform. The temperature distribution hardly changes with further increases in k_s. Ma and Peterson [24] pointed out that, with the currently available heat pipe technology, a tenfold increase in the thermal conductivity of the heat sink base is readily achievable. The present results indicate that if the heat pipe is constructed into the substrate, the peak temperature and temperature gradient on the substrate would be minimized under nonuniform impinging jet heating.

5 Conclusions

Forced convection in pin-fin heat sinks with inline arrangement subjected to nonuniform heating by circular impinging jet has been investigated experimentally and theoretically. A cost effective semi-empirical heat transfer model is developed to predict the detailed thermal fields in the entire heat sink. The thermal fields in the substrate and each pin fin are described using a 3D conduction model and the classical 1D fin analogy, respectively. To determine the thermal field of fluid flow in the pin-fin channel, the model assumes that the fluid has a uniform temperature within each unit cell, which varies depending on the spatial location of the cell. The model predictions are validated by separate experimental measurements.

In terms of the gradient and magnitude of substrate temperature, increasing the convection Reynolds number leads to decreased substrate temperature in the entire lateral range. Furthermore, increasing the thickness or thermal conductivity of the substrate enhances lateral spreading of heat in the substrate, reducing accordingly the temperature gradient on the substrate. The lateral spreading resistance is found to be dominant over the resistance in the thickness direction of the substrate when its conductivity is high and its thickness moderately small. For a substrate with relatively high conductivity, the present analysis also demonstrates that the 3D conduction model for the substrate can be reduced to a 2D one (computationally advantageous) if the temperature drop in its thickness direction can be ignored.

Acknowledgment

This work is supported by the National Basic Research Program of China (Grant No. 2006CB601203), the National Natural Science Foundation of China (Grant Nos. 50676075 and 10632060), and the National High Technology Research and Development Program of China (Grant No. 2006AA03Z519).

Nomenclature

- A = cross-sectional area of square pin fin (m^2)
- Bi_D = Biot number based on pin-fin diameter ($=h_{fin}D/k_s$)
- c_p = heat capacity (J/kg K)
- D = diameter of square pin fin (m)
- d = diameter of circular nozzle (m)
- D_h = hydraulic diameter of rectangular test section ($=2WH/(W+H)$) (m)
- H = pin-fin height (m)
- h_b = end wall heat transfer coefficient (W/m^2 K)
- h_{fin} = heat transfer coefficient on pin-fin surface (W/m^2 K)
- $h_j(r)$ = impingement heat transfer coefficient (W/m^2 K)
- k = thermal conductivity (W/m K)
- L = length of substrate of pin-fin heat sink (m)
- $\dot{m}_j$ = mass flow rate of hot gas impinging jet (kg/s)
- N_L = number of pin fins in longitudinal direction (x-axis)
- N_T = number of pin fins in transverse direction (y-axis)
- P = perimeter of cross section of square pin fin (m)
- r = radial coordinate (m)
- Re_{D_h} = convection Reynolds number based on hydraulic diameter ($=\rho u_0 D_h/\mu_f$)
- Re_j = jet Reynolds number ($=4\dot{m}_j/\pi d\mu_j$)
- S = nozzle exit-to-substrate spacing (m)
- S_L = longitudinal pin-fin pitch (m)
- S_T = transverse pin-fin pitch (m)
- t = thickness of substrate (m)
- $T_{aw}(r)$ = adiabatic wall temperature on impinging surface (K)
- T_{amb} = ambient temperature (K)
- T_b = local temperature in substrate (K)
- T_{in} = inlet temperature in forced convection channel (K)
- T_f = fluid temperature in pin-fin heat sink (K)
- T_j = impinging jet exit temperature (K)
- T_{fin} = pin-fin temperature (K)
- u_0 = mean inlet velocity of convective flow in rectangular channel (m/s)
- W = width of substrate (m)

Greek Symbols

ε = porosity of pin-fin array
θ_b = dimensionless substrate temperature $(=(T_b - T_{\text{in}})/(T_j - T_{\text{amb}}))$
θ_f = dimensionless fluid temperature $(=(T_f - T_{\text{in}})/(T_j - T_{\text{amb}}))$
ρ = density (kg/m^3)
μ = viscosity (kg/ms)
η = impingement effectiveness (Eq. (30))
τ = time (s)

Subscripts

f = fluid
fin = square pin fin
s = solid
b = substrate plate
j = impinging jet

References

[1] Tahat, M., Kodah, Z. H., Jarrah, B. A., and Probert, S. D., 2000, "Heat Transfers From Pin-Fin Arrays Experiencing Forced Convection," Appl. Energy, **67**, pp. 419–442.
[2] Sara, O. N., Yapici, S., Yilmaz, M., and Pekdemir, T., 2001, "Second Law Analysis of Rectangular Channels With Square Pin-Fins," Int. Commun. Heat Mass Transfer, **28**(5), pp. 617–630.
[3] Sara, O. N., 2003, "Performance Analysis of Rectangular Ducts With Staggered Square Pin Fins," Energy Convers. Manage., **44**, pp. 1787–1803.
[4] Kim, D., Kim, S. J., and Ortega, A., 2004, "Compact Modeling of Fluid Flow and Heat Transfer in Pin Fin Heat Sinks," ASME J. Electron. Packag., **126**, pp. 342–350.
[5] Jeng, T. M., and Tzeng, S. C., 2007, "Pressure Drop and Heat Transfer of Square Pin-Fin Arrays in In-line and Staggered Arrangements," Int. J. Heat Mass Transfer, **50**, pp. 2364–2375.
[6] Saha, A. K., and Acharya, S., 2003, "Parametric Study of Unsteady Flow and Heat Transfer in a Pin-Fin Heat Exchanger," Int. J. Heat Mass Transfer, **46**, pp. 3815–3830.
[7] Naphon, P., and Sookkasem, A., 2007, "Investigation on Heat Transfer Characteristics of Tapered Cylinder Pin Fin Heat Sinks," Energy Convers. Manage., **48**, pp. 2671–2679.
[8] VanFossen, G. J., 1982, "Heat-Transfer Coefficients for Staggered Arrays of Short Pin Fins," ASME J. Eng. Power, **104**, pp. 268–274.
[9] Metzger, D. E., Fan, C. S., and Haley, S. W., 1984, "Effects of Pin Shape and Array Orientation on Heat Transfer and Pressure Loss in Pin Fin Arrays," ASME J. Eng. Gas Turbines Power, **106**, pp. 252–257.
[10] Chyu, M. K., Hsing, Y. C., Shih, T. I.-P., and Natarajan, V., 1999, "Heat Transfer Contributions of Pins and Endwall in Pin-Fin Arrays: Effects of Thermal Boundary Condition Modeling," ASME J. Turbomach., **121**, pp. 257–263.
[11] Matsumoto, R., Kikkawa, S., and Senda, M., 1997, "Effect of Pin Fin Arrangement on Endwall Heat Transfer," JSME Int. J., Ser. B, **40**(1), pp. 142–151.
[12] Moores, K. A., Joshi, Y. K., and Schiroky, G. H., 2001, "Thermal Characterization of a Liquid Cooled AlSiC Base Plate With Integral Pin Fins," IEEE Trans. Compon. Packag. Technol., **24**(2), pp. 213–219.
[13] Khorunzhii, I., Gabor, H., Job, R., Fahrner, W. R., and Baumann, H., 2003, "Modelling of a Pin-Fin Heat Converter With Fluid Cooling for Power Semiconductor Modules," Int. J. Energy Res., **27**, pp. 1015–1026.
[14] Fénot, M., Vullierme, J.-J., and Dorignac, E., 2005, "A Heat Transfer Measurement of Jet Impingement With High Injection Temperature," C. R. Mec., **333**, pp. 778–782.
[15] Goldstein, R. J., Sobolik, K. A., and Seol, W. S., 1990, "Effect of Entrainment on the Heat Transfer to a Heated Circular Air Jet Impinging on a Flat Surface," ASME J. Heat Transfer, **112**, pp. 608–611.
[16] Coleman, H. W., and Steele, W. G., 1999, *Experimentation and Uncertainty Analysis for Engineers*, 2nd ed., Wiley, New York.
[17] Baughn, J. W., Hechanova, A. E., and Yan, X. J., 1991, "An Experimental Study of Entrainment Effect on the Heat Transfer From a Flat Surface to a Heated Circular Impinging Jet," ASME J. Heat Transfer, **113**, pp. 1023–1025.
[18] Goldstein, R. J., and Franchett, M. E., 1988, "Heat Transfer From a Flat Surface to an Oblique Impinging Jet," ASME J. Heat Transfer, **110**, pp. 84–90.
[19] Tao, W. Q., 2001, *Numerical Heat Transfer*, 2nd ed., Xi'an Jiaotong University Press, Xi'an, in Chinese.
[20] Metzger, D. E., Berry, R. A., and Bronson, J. P., 1981, "Developing Heat Transfer in Rectangular Ducts With Arrays of Short Pin Fins," ASME Paper No. 81-WA/HT-6.
[21] Petukhov, B. S., Genin, L. G., and Kovalev, S. A., 1996, *Heat Transfer in Nuclear Power Equipment*, Energoatomizdat, Moscow, in Russian.
[22] Gnielinski, V., 1976, "New Equations for Heat and Mass Transfer in Turbulent Pipe and Channel Flows," Int. Chem. Eng., **16**, pp. 359–368.
[23] Lee, S., Song, S., Au, V., and Moran, K. P., 1995, "Constriction/Spreading Resistance Model for Electronics Packaging," *Proceedings of the Fourth ASME/JSME Thermal Engineering Joint Conference*, Vol. 4, pp. 199–206.
[24] Ma, H. B., and Peterson, G. P., 2002, "The Influence of the Thermal Conductivity on the Heat Transfer Performance in a Heat Sink," ASME J. Electron. Packag., **124**, pp. 164–169.

Laminar Boundary Layer Development Around a Circular Cylinder: Fluid Flow and Heat-Mass Transfer Characteristics

A. Alper Ozalp[1]
Department of Mechanical Engineering,
University of Uludag,
16059 Gorukle, Bursa, Turkey
e-mail: aozalp@uludag.edu.tr

Ibrahim Dincer
Faculty of Engineering and Applied Science,
University of Ontario Institute of Technology,
2000 Simcoe Street North,
Oshawa, ON L1H 7K4, Canada
e-mail: ibrahim.dincer@uoit.ca

This paper presents a comprehensive computational work on the hydrodynamic, thermal, and mass transfer characteristics of a circular cylinder, subjected to confined flow at the cylinder Reynolds number of $Re_d=40$. As the two-dimensional, steady and incompressible momentum and energy equations are solved using ANSYS-CFX (version 11.0), the moisture distributions are computed by a new alternating direction implicit method based software. The significant results, highlighting the influence of blockage ($\beta=0.200-0.800$) on the flow and heat transfer mechanism and clarifying the combined roles of β and moisture diffusivity ($D=1\times10^{-8}-1\times10^{-5}$ m^2/s) on the mass transfer behavior, are obtained for practical applications. It is shown that the blockage augments the friction coefficients (C_f) and Nusselt numbers (Nu) on the complete cylinder surface, where the average Nu are evaluated as $Nu_{ave}=3.66$, 4.05, 4.97, and 6.51 for $\beta=0.200$, 0.333, 0.571, and 0.800. Moreover, the blockage shifts separation (θ_s) and maximum C_f locations ($\theta_{C_{f-max}}$) downstream to the positions of $\theta_s=54.10$, 50.20, 41.98, and 37.30 deg and $\theta_{C_{f-max}}=51.5$, 53.4, 74.9, and 85.4 deg. The highest blockage of $\beta=0.800$ encourages the downstream backward velocity values, which as a consequence disturbs the boundary layer and weakens the fluid-solid contact. The center and average moisture contents differ significantly at the beginning of drying process, but in the last 5% of the drying period they vary only by 1.6%. Additionally, higher blockage augments mass transfer coefficients (h_m) on the overall cylinder surface; however, the growing rate of back face mass transfer coefficients (h_{m-bf}) is dominant to that of the front face values (h_{m-ff}), with the interpreting ratios of $\overline{h}_{m-bf}/\overline{h}_m=0.50$ and 0.57 and $\overline{h}_{m-ff}/\overline{h}_m=1.50$ and 1.43 for $\beta=0.200$ and 0.800. [DOI: 10.1115/1.4002288]

Keywords: heat transfer, fluid flow, mass transfer, confined flow, friction coefficient , moisture diffusivity, moisture transfer coefficient, drying

1 Introduction

Heat and mass transfer aspects of a circular cylinder (CC), subjected to fluid flow, are of considerable interest in many industrial applications, such as unit operations [1], manufacturing [2], and drying [3] processes. From the point of flow around CCs, practical applications such as flow metering devices, support structures, off-shore pipelines, and instrumentation, where small cylindrical wire probes or sensors are made to obstruct the free flow of a fluid and tall buildings, are involved in this industrial frame. As heat transfer mechanisms of CCs are closely interrelated with the operation performance of cooling towers, chimneys, heat exchangers, and cooling of electronic components and equipments, mass transfer behaviors create the technologic base not only for expert systems on food and wood drying but also for nuclear, biological, and chemical filters. For the complete application range, industrial and scientific research on mass transfer operations seeks a proper estimation of the drying time, as well as the behavior of all corresponding operational factors playing an important role in the design and optimization of the related processes. Since mass transfer mechanism depends considerably on the boundary layer development around the dissipating body and on the corresponding heat transfer behavior, the necessity in the idealization of the associated engineering designs becomes apparent. Besides, if the flow around the CC is confined, causing a blockage, both the flow and heat transfer behaviors are structured in accord with this domain dependence, which in return definitely characterizes the mass transfer characteristics. Depending on these facts, research focuses mainly on three key topics: (i) fluid flow and boundary layer development around the CC, (ii) heat transfer from the CC, and (iii) mass transfer within and from the CC.

With the onset of boundary layer investigations, fluid flow around CCs has been the subject of several recent studies. However, due to the needs of certain specific industrial applications, some recent work concentrated on the confined flow, or flow with blockage, around CCs [4–8] and even for square cylinders (SCs) [9,10]. Griffith et al. [4] numerically studied the two-dimensional flow around a CC, where their technical concerns were wake behavior, vortex shedding, recirculation, and separation lengths for the blockage range of $\beta=0.05-0.9$. In a similar computational study, Chakraborty et al. [5] worked on the blockage limits of $\beta=0.05-0.65$; where they additionally studied frictional and total drag coefficients on the CC. For the Reynolds number and blockage ratio ranges of $Re_d=0-280$ and $\beta=0.1-0.9$, numerical com-

[1]Corresponding author.

Contributed by the Heat Transfer Division of ASME for publication in the JOURNAL OF HEAT TRANSFER. Manuscript received April 4, 2010; final manuscript received July 20, 2010; published online September 20, 2010. Assoc. Editor: Ali Ebadian.

putations were performed by Sahin and Owens [6] who reported the neutral stability limit as $Re_d \approx 100$ for $\beta = 0.333-0.800$. In a similar work, Rehimi et al. [7] carried out steady and unsteady regime investigations for the particular blockage case of $\beta = 0.333$ within the Reynolds number range of $Re_d = 30-277$. They stated that for $Re_d < 108$, the streamlines and the pathlines exhibit the characteristics of a steady regime and the flow is characterized by two fixed counter-rotating vortices downstream of the cylinder. Steady numerical computations, in the Reynolds number and blockage ratio ranges of $Re_d = 6-40$ and $\beta = 0-0.8$, were performed by Sen et al. [8], where their findings covered the variation of bubble length, separation angle, and drag force characteristics. Bruer et al. [9] and Camarri and Giannetti [10] studied the identical flow scenarios for SCs for the blockage ratios of $\beta = 0.125$ [9] and $\beta = 0.1-0.17$ [10]. As steady and unsteady flow discussions on recirculation lengths and drag coefficients were presented in Ref. [9], the impact of blockage in unsteady flows, the wake interaction between the wake and the flow close to the confining walls, were clarified in Ref. [10].

There is a limited number of numerical and experimental studies on how local or mean heat transfer aspects of CCs vary with Reynolds and/or Prandtl numbers or with fluid properties. Chang and Mills [11] experimentally studied the effect of aspect ratio on the heat transfer behavior of a cylinder in cross-flow of air. They determined that the circumferentially averaged and total averaged Nusselt numbers increased with decreasing aspect ratio. The integral approach of the boundary layer analysis, to study the fluid flow and heat transfer mechanism around an infinite CC, was applied by Khan et al. [12]. They developed closed form drag and average heat transfer coefficient expressions applicable in wide ranges of Reynolds and Prandtl numbers. In one of their more recent work [13], they investigated the influence of a thin hydrodynamic boundary layer on the heat transfer from a single circular cylinder in liquid metals for a low Prandtl number (between 0.004 and 0.03) under isothermal and isoflux boundary conditions. Bharti et al. [14] numerically studied the effects of Re and Pr on average and local Nu distributions during forced convection heat transfer to incompressible Newtonian and non-Newtonian fluids from a heated circular cylinder in the steady cross-flow regime. Besides the purely CC based fluid flow and heat transfer efforts, there exist a few research that involved different types of cylinder cross sections. An experimental study, to evaluate the convective heat transfer coefficient of liquid cooled various-shaped short pin fins, by means of the infrared thermography was performed by Montelpare and Ricci [15]. Their results demonstrated that the trend of the Nusselt number at different Reynolds numbers depended heavily on the pin shape. In a more comprehensive work, Sparrow et al. [16] collected the average Nusselt number information for circular and noncircular cylinders in cross-flow of air, where some of the noncircular cross sections include squares, diamonds, flat plates perpendicular to the freestream, ellipses, and rectangles.

Considerably limited work dealt with the influence of confining walls on the heat transfer phenomena around cylinders. Buyruk et al. [17] numerically investigated the laminar flow and heat transfer characteristics of a CC for the blockage ratio range of $\beta = 0.17-0.48$. They predicted not only the local static pressure and Nusselt number variations on the CC surface but also the isotherm and streamline contours of the wake region. Through an integral approach of the boundary layer analysis, Khan et al. [18] investigated fluid flow around and heat transfer from a CC between parallel planes for $\beta = 0-0.80$. They found that the blockage ratio controls the fluid flow and the transfer of heat from the cylinder and delays the separation. The blockage effects on the laminar heat transfer mechanism of SCs were also taken into account. As Sharma and Eswaran [19] concentrated on the blockage cases of $\beta = 0.1-0.5$, Dhiman et al. [20] detailed the impact of $\beta = 0.125-0.25$ range. To produce a base for heat transfer discussions, either of the studies presented fluid flow results in terms of velocity profiles, friction and drag coefficient values, and supplied information on the wake structure for different β cases. The growth of drag coefficients and heat transfer rates with blockage were the common outcomes [19,20].

There have been considerable efforts to experimentally/computationally characterize the drying mechanism and mass transfer behavior of moist objects. As some of the work aimed to propose applicable theory for wide range of applications, others focused on specific material. Theoretical and experimental results, on the drying kinetics of bananas, under different air drying conditions, were reported by Queiroz and Nebra [21]. They investigated the effects of surface convective mass transfer by treating the experimental data of moisture content during drying through a diffusion model, where the diffusion coefficient was considered as constant. Dincer et al. [22] developed and verified new drying correlations to determine the moisture transfer parameters, such as moisture diffusivity and moisture transfer coefficients. Akpinar and Dincer [3,23] carried out the experimental and theoretical investigations on the drying of slab cut eggplant slices [3] and potato pieces [23]. As the drying times are determined experimentally, numerical drying models are applied to evaluate the drying process parameters, moisture transfer parameters, and moisture content distributions. Forced convection drying of moist objects was numerically modeled by Kaya et al. [24], where the computational predictions shown that the convective heat and mass transfer coefficients in the upstream side of the cylindrical object are higher than those of the downstream side. Sahin and Dincer [25] proposed a graphical method to estimate the drying moisture transfer parameters and drying times in a quick and efficient manner. The thermogravimetric analysis technique based research, to determine the moisture diffusivity of red apples at high temperatures, was performed by Feng et al. [26]. A two-dimensional numerical analysis of heat and moisture transfer during drying of a cylindrical object was performed by Hussain and Dincer [27], who determined that the moisture gradient was higher in the early drying period and as drying progresses, the moisture gradient remained almost steady. Sahin et al. [28] analytically investigated drying of multidimensional food products and developed a simple method to determine the drying times. Heat and mass transfer coefficients of air chilling and storage of solid food products, for the cases of solids of more complex shapes, were reviewed by Kondjoyan [29]. As Dincer and Hussain [30] developed new Biot number–Dincer number (Bi–Di) correlation for drying applications, microwave drying of sphere, cylinder, half-cylinder, and rectangular prism shaped particles, suspended in an air stream, was considered by Araszkiewicz et al. [31]. McMinn and Magee [32] studied the effects of air velocity and temperature on the drying rate and investigated the kinetics of moisture transport in potato cylinders. Monolayer moisture contents of okra were evaluated by Gogus and Maskan [33] for the drying temperature range of $60-80\,^{\circ}C$. They not only determined the augmentation of effective diffusivity with increasing temperature but also shown that the computed effective diffusivity data had Arrhenius type temperature dependence. Panagiotou et al. [34] retrieved and analyzed a wide collection of moisture diffusivity values, for various foods, from the recent publications. They also classified the data of more than 100 food materials in 11 categories.

The open literature clearly displays the strong need to study the boundary layer development and heat and mass transfer behavior of CCs that are exposed to confined fluid flow. Although several thermofluid CC studies exist in the literature, they are limited to either fluid flow, or fluid flow and heat transfer, or heat and mass transfer. Even though the heat transfer rates are significantly characterized by fluid flow and boundary layer development, and mass transfer coefficients by those of heat transfer, the open literature cannot offer any publication, studying the linkage of hydrodynamic boundary layer development and mass transfer for CCs. The present study aims (i) to develop a complete overview and to bridge the gap between the laminar boundary layer development,

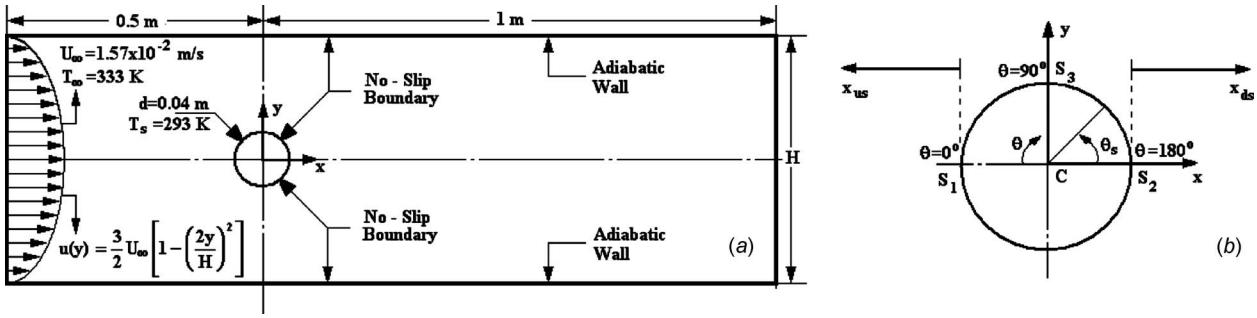

Fig. 1 (*a*) Flow domain around the cylinder and (*b*) the coordinate system

heat transfer rates and mass transfer behavior of CCs in confined flows, and (ii) to establish the impact of blockage on mass transfer mechanism for wide ranges of blockage ratios and moisture diffusivities. The laminar fluid flow and boundary layer development aspects are discussed through streamlines, velocity profiles, separation phenomena, pressure, and friction coefficients. The heat transfer analysis are presented by temperature profiles/contours and Nusselt numbers. The mass transfer results are given in terms of mass transfer coefficients, overall drying times, local drying schemes, and isomoisture contours within the CC.

2 Theoretical Background

2.1 Governing Equations. Figure 1 schematically shows the geometry and the relevant dimensions considered in the analysis. As given in Fig. 1(*a*), on either side of the center of the cylinder, two adiabatic channel walls are placed at a distance of H/2. No-slip boundary condition is applied both to the cylinder surface and to the adiabatic channel walls. A fixed two-dimensional circular cylinder with diameter d is maintained at a constant temperature of T_s. Air enters the duct with a fully developed laminar velocity profile of $u(y)=(3/2)U_\infty[1-(2y/H)^2]$ at a temperature of T_∞, where U_∞ is the average velocity of air at the duct inlet. Additionally, Fig. 1(*b*) displays the geometric notation, adapted for the fluid and heat-mass transfer investigations. As the surface points of S_1, S_2, and S_3 stand for the angular positions of $\theta=0$, 180, and 90 deg, the starting points of the upstream and downstream directions are S_1 and S_2, respectively.

Incropera and De Witt [35] reported that, according to the fundamental fluid mechanics theory, fluid flow around CC remains laminar up to the cylinder Reynolds number of $Re_d \leq 2\times10^5$. Flows with blockage were recently under the inspection of Sahin and Owens [6] and Rehimi et al. [7], where both of the works aimed to investigate the appearance of von Karman vortices and wake instability. As Sahin and Owens [6] recorded the neutral stability as $Re_d \approx 100$ for the blockage range of $\beta=0.333-0.800$, Rehimi et al. [7] evaluated the critical Reynolds number as $Re_d=108$. Since the focus of the present work is to investigate the laminar boundary layer development, heat transfer rates, and mass transfer behavior of CCs in confined flows, the computational analysis is carried out at the constant cylinder Reynolds number of $Re_d=40$, which is not only consistent with the laminar range of [35] but also sufficiently below the critical Reynolds numbers of Refs. [6,7]. Besides, the channel flow aspect of the problem is structured in the computations by adapting the duct height (H) in accordance with the level of blockage ratio ($\beta=d/H$). By simultaneously considering the traditional channel flow critical Reynolds number of Re=2300 [35], for the blockage ratio range of $\beta=0.200\rightarrow0.800$, duct height values are decided as $H=200\rightarrow50$ mm (Fig. 1(*a*)), where the consequent Reynolds number range for the channel flow becomes $Re_{ch}=400\rightarrow100$. Being compatible with these definitions, the fluid flow and heat transfer section of the present problem is structured on incompressible and constant fluid and thermal property characteristics and carried out in steady ($\partial/\partial t=0$) and two-dimensional fluid domain. Under these conditions, equations governing the two-dimensional laminar flow are given in the master Cartesian coordinate system as follows.

For continuity,

$$\frac{\partial u}{\partial x}+\frac{\partial v}{\partial y}=0 \tag{1}$$

For momentum,

$$\rho\left(u\frac{\partial u}{\partial x}+v\frac{\partial u}{\partial y}\right)=-\frac{\partial P}{\partial x}+\mu\left(\frac{\partial^2 u}{\partial x^2}+\frac{\partial^2 u}{\partial y^2}\right) \tag{2a}$$

$$\rho\left(u\frac{\partial v}{\partial x}+v\frac{\partial v}{\partial y}\right)=-\frac{\partial P}{\partial y}+\mu\left(\frac{\partial^2 v}{\partial x^2}+\frac{\partial^2 v}{\partial y^2}\right) \tag{2b}$$

For energy,

$$u\frac{\partial T}{\partial x}+v\frac{\partial T}{\partial y}=\alpha\left(\frac{\partial^2 T}{\partial x^2}+\frac{\partial^2 T}{\partial y^2}\right) \tag{3}$$

Although the hydrodynamic and thermal characteristics around the CC are steady, the moisture content inside the CC will decrease with time due to the drying role of the forced convection acting on the CC surface. It is also certain that the moisture level will not only vary in time but it is also location dependent within the CC. Due to these scientific prospects, moreover to accomplish the aims of the mass transfer section of the present research, the mass transfer mechanism, inside the dried object, is characterized by the two-dimensional moisture transfer equation of Eq. (4), with the assumption that the shrinkage or deformation of the material during drying is negligible.

$$\frac{1}{D}\frac{\partial M}{\partial t}=\frac{1}{r}\frac{\partial M}{\partial r}+\frac{\partial^2 M}{\partial r^2}+\frac{1}{r^2}\frac{\partial^2 M}{\partial \theta^2} \tag{4}$$

2.2 Boundary Conditions. In the fluid flow and heat transfer investigations, no-slip boundary condition ($u=v=0$) is applied to the channel walls and to the cylinder surface. As the cylinder surface is kept at constant temperature (T_s), channel walls are considered as adiabatic. A fully developed duct flow velocity profile and a freestream temperature (T_∞) are employed at the inlet; exit pressure is taken as atmospheric.

In the mass transfer analysis, an initial condition (Eq. (5*a*)) is assigned to the dried object. As the two boundary conditions in the radial direction are located at the center (Eq. (5*b*)) and surface (Eq. (5*c*)), those for the angular direction are both at $\theta=0=2\pi$ (Eqs. (5*d*) and (5*e*)).

$$M(r,\theta,0)=M_i \tag{5a}$$

$$\frac{\partial M(0,\theta,t)}{\partial r}=0 \quad \text{at} \quad r=0 \tag{5b}$$

$$-D\frac{\partial M(R,\theta,t)}{\partial r} = h_m(M - M_a) \quad \text{at} \quad r = R \tag{5c}$$

$$M(r,0,t) = M(r,2\pi,t) \tag{5d}$$

$$\frac{\partial M(r,0,t)}{\partial \theta} = \frac{\partial M(r,2\pi,t)}{\partial \theta} \tag{5e}$$

2.3 Parameter Definitions. Not only to describe the flow type and identify the considered scenarios but also to interpret the evaluated outputs in common scientific notation, the following dimensionless variables and parameters are used:

$$Re_d = \frac{\rho U_\infty d}{\mu} \tag{6a}$$

$$\beta = \frac{d}{H} \tag{6b}$$

$$C_p = \frac{P_\theta - P_\infty}{1/2\rho U_\infty^2} \tag{6c}$$

$$C_f = \frac{\tau_s}{1/2\rho U_\infty^2} \tag{6d}$$

$$\zeta = \frac{T - T_s}{T_\infty - T_s} \tag{6e}$$

$$-k\left.\frac{\partial T}{\partial n}\right|_s = h_\theta(T_s - T_a) \tag{6f}$$

$$Nu_\theta = \frac{h_\theta d}{k} \tag{6g}$$

$$Nu_{ave} = \frac{1}{2\pi}\int_0^{2\pi} Nu_\theta d\theta \tag{6h}$$

$$h_m = h_\theta\left(\frac{DLe^{1/3}}{k}\right) \tag{6i}$$

$$\phi = \frac{M - M_a}{M_i - M_a} \tag{6j}$$

where Re_d is the cylinder Reynolds number, β is the blockage ratio, C_p and C_f are the pressure and friction coefficients, ζ is the dimensionless temperature, h_θ is the local convective heat transfer coefficient, Nu_θ and Nu_{ave} are the local and average Nusselt numbers, h_m is the mass transfer coefficient, and ϕ is the dimensionless moisture content.

2.4 Computational Methods. Computational analyses are carried out in two-different platforms. As the fluid flow and heat transfer simulations are performed with ANSYS-CFX [36], moisture transfer mechanism is taken into consideration by a new alternating direction implicit (ADI) method based software, developed by the authors.

ANSYS-CFX applies the element-based finite-volume method and scalably adopts the multigrid solver to the defined flow domain. Since the overall error in CFD calculations is mainly a combination of grid density and iteration number (or convergence criterion), several successive runs are performed for each individual blockage case to ensure that the numerical outputs are free of the roles of computational items. Table 1 displays a summary of these tests for the four blockage cases of β=0.200, 0.333, 0.571, and 0.800 in terms of the fluid flow and heat transfer parameters that are the primary concerns of the present research. For the complete set of scenarios investigated, a convergence criterion of 1×10^{-7} is used to certain negligibly small iteration errors. Moreover, to predict the velocity and temperature gradients sensitively, refined mesh size is employed in the neighborhood of the solid boundaries (Fig. 1) with the expansion factor of 1.1 (Fig. 2). Since the initial computations indicated stronger gradients in higher blockage cases, to be able to detect the variations with minor geometric steps, the applied number of overall elements is increased accordingly.

Table 1 Grid node effects on fluid flow and heat transfer parameters

β	No. of nodes	$(P_s)_{\theta=0}$ (Pa)	$(\tau_s)_{max}$ (Pa)	Nu_{ave}
0.200	438,732	0.00033	0.00013	3.822
	487,462	0.00041	0.00014	3.697
	503,978	0.00046	0.00014	3.663
	514,318[a]	0.00047	0.00014	3.659
0.333	337,216	0.00081	0.00019	4.172
	408,358	0.00084	0.00019	4.082
	423,137	0.00086	0.00020	4.055
	431,216[a]	0.00086	0.00020	4.051
0.571	293,517	0.00220	0.00032	5.140
	354,713	0.00231	0.00036	5.019
	364,872	0.00233	0.00036	4.977
	374,723[a]	0.00234	0.00037	4.968
0.800	287,437	0.01293	0.00165	6.730
	346,831	0.01321	0.00177	6.547
	358,195	0.01329	0.00182	6.521
	367,048[a]	0.01332	0.00184	6.513

[a]Optimum grid nodes.

The ADI method is a finite difference method for solving parabolic and elliptic partial differential equations in two or more dimensions. For the cylindrical coordinate diffusion equation (Eq. (4)), the idea in ADI is to split the finite difference equations into two: one with the r-derivative (Eq. (7*a*)) and the next with the θ-derivative (Eq. (7*b*)), both taken implicitly.

$$M_{i,j}^{n+1}\left(\frac{2}{D\Delta t} + \frac{2}{\Delta r^2}\right) - M_{i+1,j}^{n+1}\left(\frac{1}{2r\Delta r} + \frac{1}{\Delta r^2}\right) + M_{i-1,j}^{n+1}\left(\frac{1}{2r\Delta r} - \frac{1}{\Delta r^2}\right) = M_{i,j}^{n+1/2}\left(\frac{2}{D\Delta t} - \frac{2}{r^2\Delta\theta^2}\right) + M_{i,j+1}^{n+1/2}\left(\frac{1}{r^2\Delta\theta^2}\right) + M_{i,j-1}^{n+1/2}\left(\frac{1}{r^2\Delta\theta^2}\right) \tag{7a}$$

$$M_{i,j}^{n+1/2}\left(\frac{2}{D\Delta t} + \frac{2}{r^2\Delta\theta^2}\right) - M_{i,j+1}^{n+1/2}\left(\frac{1}{r^2\Delta\theta^2}\right) - M_{i,j-1}^{n+1/2}\left(\frac{1}{r^2\Delta\theta^2}\right) = M_{i,j}^{n}\left(\frac{2}{D\Delta t} - \frac{2}{\Delta r^2}\right) + M_{i+1,j}^{n}\left(\frac{1}{2r\Delta r} + \frac{1}{\Delta r^2}\right) + M_{i-1,j}^{n}\left(\frac{1}{\Delta r^2} - \frac{1}{2r\Delta r}\right) \tag{7b}$$

$$\lambda = \frac{D\Delta t}{(\Delta r^2 + \Delta r^2\Delta\theta^2)} \tag{7c}$$

The solution procedure of Eq. (4) is carried out in conjunction with the initial and boundary conditions of Eq. (5). According to the Lewis analogy [35], mass transfer coefficient (h_m) is significantly related (Eq. (6*i*)) with the convective heat transfer coefficient (h_θ) and characterizes the amount of moisture swept away from the cylinder surface. By obtaining the h distribution on the cylinder surface from ANSYS-CFX solver, h_m variation is also gen-

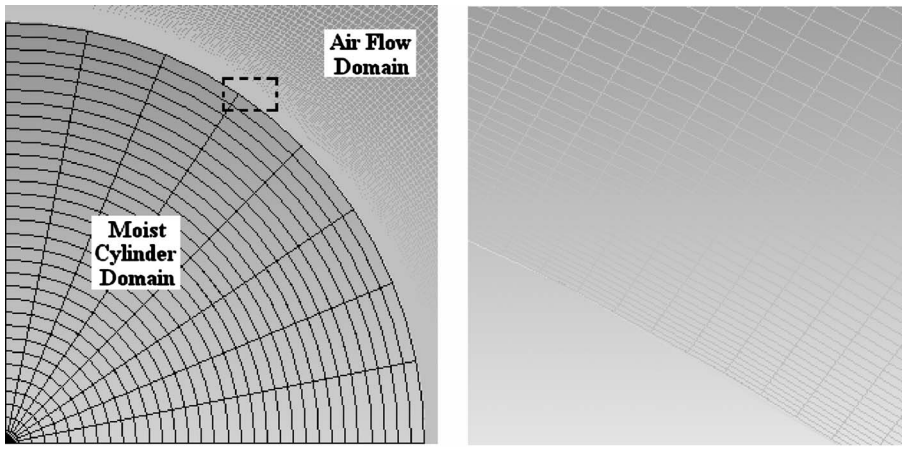

Fig. 2 Grid resolution in and around the cylinder interface

erated. Since computations showed negligible changes with denser meshes, diffusion investigations are performed with the mesh density of 31×31. Moreover, similar to the works of Kaya et al. [24,37], the convergence of ADI is guaranteed with the under-relaxation parameter of $\lambda = 0.5$. As λ is dependent on moisture diffusivity (Eq. (7*c*)), the time step (Δt) in the computations is regulated in accord with the level of diffusivity. Thus, in higher diffusivity cases, adopting lower time steps resulted in extended run-times.

3 Results and Discussion

In order to conduct the study, some physical, hydrodynamic, and thermal data are gathered from the recent publications [4,5,7,8,14,21,23,24,26,27,34,38,39]. The computational studies on the laminar hydrodynamic and thermal boundary layer development and mass transfer characteristics of a circular cylinder are carried out at the constant Reynolds number of $Re_d = 40$, with the average inlet air velocity and cylinder diameter values of $U_\infty = 1.57 \times 10^{-2}$ m/s and $d = 0.04$ m, respectively. Additionally, inlet air temperature, cylinder temperature, and moisture contents of air and cylinder are chosen as $T_\infty = 333$ K, $T_s = 293$ K, $M_a = 0.1$ kg/kg, and $M_{cyl} = 3$ kg/kg, respectively, where these numbers are similar to those of Refs. [8,14,21,23,24,26,27,38,39]. To develop a complete overview on the interactions of hydrodynamic and thermal characteristics with mass transfer behavior, extensive numerical analysis are performed by systematically varying the blockage ratio (β) and moisture diffusivity (D). As the blockage ratio range is selected as $\beta = 0.200 - 0.800$ being similar to those of Griffith et al. [4], Chakraborty et al. [5], Rehimi et al. [7], and Sen et al. [8]; the moisture diffusivity limits are adopted from the real time data of Panagiotou et al. [34] as $D = 1 \times 10^{-8} - 1 \times 10^{-5}$ m^2/s. Fluid flow and heat transfer characteristics are discussed under Secs. 3.1.1 and 3.1.2. As upstream and downstream streamlines, temperature contours, velocity, and temperature profiles are related to the flow domain, hydrodynamic, and thermal boundary layer mechanism on the cylinder surface are enlightened through pressure coefficients, shear stresses, Nusselt numbers, and separation phenomena. Mass transfer results are demonstrated in Sec. 3.2.1 (mass transfer coefficients, drying times), Sec. 3.2.2 (local drying characteristics), and Secs. 3.2.3 and 3.2.4. In Sec. 3, to identify not only the novelty of the findings but also the originality of the work, cross-correlating the evaluations with blockage ratios, moisture diffusivities, and drying times is applied as the presentation strategy.

3.1 Fluid Flow and Heat Transfer Characteristics

3.1.1 Flow Domain Results. Through Fig. 3, it is aimed not only to demonstrate the streamline formation (Fig. 3(*a*)) and temperature contours (Fig. 3(*b*)) around the cylinder but also to further validate the evaluated computational outputs. Numerical outputs, for the streamline and temperature contour formation, come out to be completely symmetric, appearing as a mirror image, having the centerline as the symmetry axis. Indeed this symmetric behavior originates mainly due to two scientific issues: (i) The fluid flow around the cylinder is in the laminar regime and (ii) the centerline of the cylinder coincides with the midplane of the adiabatic duct walls. Thus, both the streamline and temperature contour discussions are carried out in the half fluid domain for the three sections of the upstream, the throat, and the downstream. It can be seen from Fig. 3(*a*) that in the upstream region of the cylinder, centerline streamlines deviate from their route easily in the low β range of $\beta = 0.200 - 0.333$. However, with the increase of blockage ($\beta = 0.571 - 0.800$), they are hydrodynamically forced to keep their route up to the neighborhood of the cylinder surface. The disciplined approach result in smoothly moving upstream streamlines, having tangent paths to the front face of the cylinder and can be further expected to cause significantly augmented static pressure and heat transfer data in the considered region. It can additionally be said that the dominant fluid contact with the cylinder surface can be an apparent source for high friction rates. In the throat, the fluid attains the maximum velocity values computed for the complete flow domain, such that as the maximum velocity values computed for $\beta = 0.200$ and $\beta = 0.333$ are $U_{th\text{-}max} = 2.70 \times 10^{-2}$ m/s ($U/U_\infty = 1.722$) and $U_{th\text{-}max} = 3.27 \times 10^{-2}$ m/s ($U/U_\infty = 2.083$), respectively, the corresponding numbers for $\beta = 0.571$ and $\beta = 0.800$ are $U_{th\text{-}max} = 5.05 \times 10^{-2}$ m/s ($U/U_\infty = 3.217$) and $U_{th\text{-}max} = 1.09 \times 10^{-1}$ m/s ($U/U_\infty = 6.943$). The rise in the $U_{th\text{-}max}$ values is expected due to the narrowing style of the flow domain between the duct wall and the cylinder surface. These numbers, and the continuity theory, further put forward that, in addition to producing augmented $U_{th\text{-}max}$ values, narrower throats result in fuller velocity profiles as well. Indeed, both the accelerated fluid movement and the strictly attaching boundary layer formation on the cylinder surface (due to fuller velocity profiles) delay the separation point toward downstream (zoomed plots in Fig. 3(*a*)). The separation angles of $\theta_s = 54.10$, 50.20, 41.98, and 37.30 deg for $\beta = 0.200$, 0.333, 0.571, and 0.800, respectively, are obtained by the computations, where similar to Refs. [5,8,36–39], the separation locations (θ_s) are measured in the counterclockwise direction,

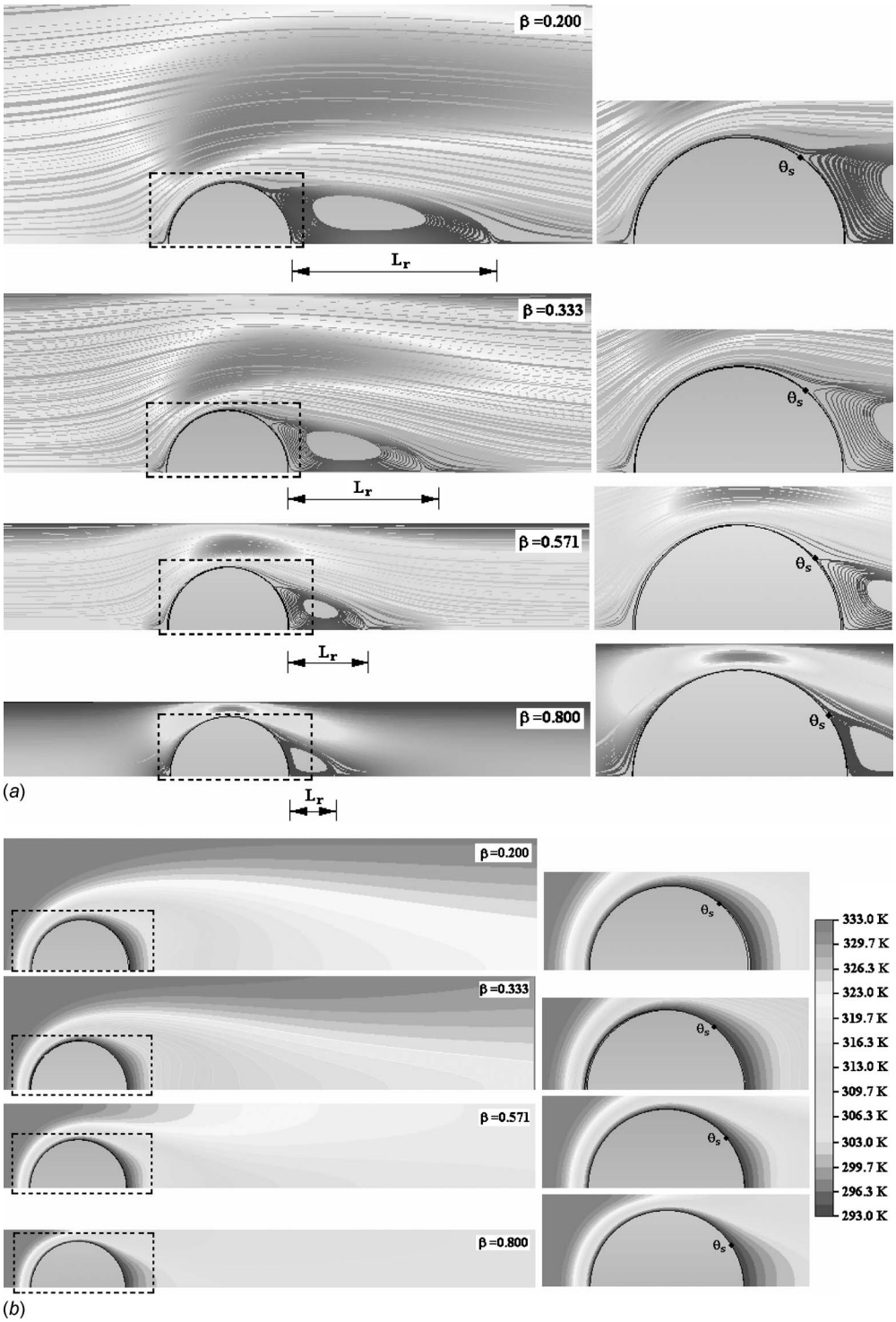

Fig. 3 (*a*) **Streamline formation and** (*b*) **temperature contours around the cylinder for the blockage ratio range of** $\beta = 0.200 - 0.800$

with the origin of S_2 (Fig. 1(*b*)). Several experimental and numerical works considered flows around circular cylinders without blockage. The unconfined flow, for the specific case of Re=40, was investigated by Refs. [5,40–43], where their evaluations on the separation location were relatively comparable being in the range of $\theta_s = 53.1 - 53.8$ deg. Among the considerably fewer work on flows with blockage, Chakraborty et al. [5] and Sen et al. [8] handled the Re=40 flow around CCs. Either of the research computationally determined the shift of separation toward downstream. As the representative outputs were $\theta_s \approx 53$, 50, 48, and 45 deg for $\beta = 0.200$, 0.333, 0.500, and 0.650 in Ref. [5], those of Ref. [8] were reported as $\theta_s \approx 52$, 46, 37.5, and 26.5 deg for $\beta = 0.200$, 0.333, 0.500, and 0.800, respectively. It can be seen that, especially for flows with high blockage, a scientific agreement is not available between Refs. [5,8]; the present findings relatively resemble those of Chakraborty et al. [5]. On the other hand, the present separation

finding ($\theta_s = 54.10°$) at the lowest blockage case ($\beta = 0.200$) is comparable with the identical flow condition data of both Ref. [5] ($\theta_s \approx 53°$) and Ref. [8] ($\theta_s \approx 52°$). It must additionally be pointed out that the separation location of $\beta = 0.200$ is close to the unconfined flow reports ($\theta_s = 53.1-53.8$ deg) of Refs. [5,40–43]. This convergence indicates that the impact of blockage loss strength for $\beta \leq 0.200$, where similar evaluations were as well achieved by Chakraborty et al. [5] and Sen et al. [8]. The onset of the downstream flow domain can be marked by θ_s points, where the following is a vortex structure just at the downstream vicinity of the cylinder (zoomed plots in Fig. 3(*a*)). Figure 3(*a*) indicates that the occupied region of the vortex becomes contracted with higher β. Specifically speaking, the lengths of the recirculation zones are computed as $L_r = \sim 63.9$ mm ($\beta = 0.200$), $L_r = \sim 47.3$ mm ($\beta = 0.333$), ~ 26.9 mm ($\beta = 0.571$), and ~ 16.7 mm ($\beta = 0.800$), indicating that blockage negatively affects the influential domain and the strength of the downstream vortex system. Similar findings on shorter recirculation zones with higher blockage were also reported by Griffith et al. [4] for the blockage range of $\beta = 0.050-0.900$, Chakraborty et al. [5] for the blockage range of $\beta = 0.050-0.650$, and Sen et al. [8] for the blockage range of $\beta = 0-0.800$. Further detailed results on the hydrodynamic characteristics and momentum transfer essentials for the upstream, throat, and downstream sections are presented in Figs. 4(*a*) and 5(*a*).

Throat and downstream temperature contours are given in Fig. 3(*b*). The computational analysis indicated for high blockage cases that the hot fluid domains not only get closer to the cylinder surface but also cover thinner regions; moreover, the forced contact of the hot fluid with the cylinder gives way to higher heat transfer rates. The zoomed plots of Fig. 3(*a*) clearly identify that with the increase of blockage the thermal boundary layer gets thinner up to the separation point (θ_s). The thickening attitude of thermal boundary layers beyond the separation point in the complete blockage cases can also be seen from Fig. 3(*b*). This finding is as well in agreement with the recirculation zone length values of Fig. 3(*a*), indicating the significant interactions of hydrodynamic and thermal characteristics. Buyruk et al. [17] reported the similar impact of β on the isotherm structure in the wake of a cylinder. In the flows with $\beta = 0.200-0.571$, the isotherm contours become similar toward $\theta = 180$ deg (zoomed plots of Fig. 3(*b*)), where this evaluation is an indicator for comparable heat transfer rates in the neighborhood of $\theta = 180$ deg. However, at the highest blockage flow of $\beta = 0.800$ the thermal boundary layer displays a thicker structure, when compared with the milder blockage cases of $\beta < 0.800$. The essentials of this evaluation can be associated with two issues: (i) High backward velocity values exist at $\beta = 0.800$ and (ii) the narrowing nature of the downstream vortex system disturbs the boundary layer and weakens the fluid-solid contact. Further detailed discussions on the thermal characteristics and heat transfer essentials for the upstream, throat, and downstream regions are provided through Figs. 4(*b*) and 5(*b*).

The dimensionless velocity and temperature profiles in the upstream domain of the cylinder are presented in Figs. 4(*a*) and 4(*b*) for the blockage ratio range of $\beta = 0.200-0.800$. Figure 4(*a*) shows that the role of the cylinder on the hydrodynamic behavior of the flowing air becomes apparent at closer sections at the front side of the cylinder for high β cases. Such that for $\beta = 0.200$, 0.333, 0.571, and 0.800, the dimensionless velocity values are computed as $U/U_\infty = 0.26$, 0.34, 0.44, and 0.53, respectively, at the centerline of $x_{us} = 5 \times 10^{-3}$ m. This finding indicates that, due to the late hydrodynamic response of the flow domain at higher β scenarios, flowing air decelerates more rapidly to zero toward the stagnation point ($x_{us5} \rightarrow x_{us1}$), resulting in an augmented momentum velocity in the neighborhood of the cylinder. For $x_{us} = 0$ m, it can be seen from Fig. 4(*a*) that on the cylinder projection lines ($y = \pm 0.02$ m), the dimensionless velocity values (U/U_∞) rise at higher blockage ratios (β). This finding can be related to the downstream movement of the separation point (θ_s) at high β (Fig. 3). On the other hand, the velocity profiles attained at $x_{us} = 0$ m for $\beta = 0.200-0.800$ resemble a fuller form with the increase of β. Indeed, this outcome, together with the presented streamlines of Fig. 3(*a*), point out thinner boundary layer formations at higher blockage ratios. Additionally, the computations clarified the U/U_∞ ranges at $y = \pm 0.02$ m as $1.05 \rightarrow 1.10$, $1.24 \rightarrow 1.33$, $1.41 \rightarrow 1.66$, and $1.35 \rightarrow 2.01$ ($x_{us5} \rightarrow x_{us1}$) for $\beta = 0.200$, 0.333, 0.571, and 0.800, clarifying the rise of velocity values at higher β cases. Moreover, the wider ranges at high β can be attributed to the augmented momentum activity described above. It can also be seen from Fig. 4(*a*) that the order of the upstream velocity profiles reverses at the intersection points. The reverse locations are computed to occur at $y_{rev} = \pm \sim 0.0171$ m ($U/U_\infty = \sim 0.932$), $y_{rev} = \pm \sim 0.0163$ m ($U/U_\infty = \sim 1.076$), $y_{rev} = \pm \sim 0.0148$ m ($U/U_\infty = \sim 1.229$), and $y_{rev} = \pm \sim 0.0126$ m ($U/U_\infty = \sim 1.251$) for β of 0.200, 0.333, 0.571, and 0.800, respectively. The decrease of y_{rev}, the rise of the corresponding U/U_∞ values, and the significantly interacting streamlines with the cylinder (Fig. 3(*a*)) at higher β are clear confirmations for thinner boundary layers and higher momentum rates and trustable evidences for higher frictional activity and heat transfer rates at the cylinder surface.

Figure 4(*b*) demonstrates the variation of dimensionless temperatures (ζ, Eq. (6*e*)), upstream of the cylinder, for the blockage ratio range of $\beta = 0.200-0.800$. It can be seen from the figure that significant decreases in temperature are evaluated while approaching the stagnation point of the cylinder ($x_{us} = 0$ m and $y = 0$ m). The role of blockage is determined to be more sensible in the flow domain of $x_{us} = 0-5 \times 10^{-3}$ m. Within this domain, higher blockage resulted in higher ζ values, which is completely in harmony with the temperature contours of Fig. 3(*b*). In other words, similar to the hydrodynamic boundary layer development, the thermal boundary layer also attains lower thickness values at higher blockage. This cannot only be considered as a matching validation of the hydrodynamic and thermal results but also strengthened the discussions on augmented heat transfer activity at higher β. Computations further indicated that as the centerline dimensionless temperature range is $\zeta = 0.049 \rightarrow 0.039$ ($\beta = 0.800 \rightarrow 0.200$) at $x_{us} = 2 \times 10^{-4}$ m, and the corresponding values for the stagnation point ($x_{us} = 0$ m) are $\zeta = 0.006 \rightarrow 0.005$. The narrowing nature of the dimensionless temperature range points out that the impact of blockage on heat transfer rates reduces in the neighborhood of the cylinder, especially at the stagnation point ($y = 0$ m and $\theta = 0$ deg).

Figures 5(*a*) and 5(*b*) show the dimensionless downstream velocity and temperature profiles for the blockage ratio range of $\beta = 0.200-0.800$. To generate a visual comparison opportunity, velocity profiles for the same flow domain of $x_{ds} = 0-5 \times 10^{-3}$ m are demonstrated in Fig. 5(*a*) for the complete β range investigated. In addition to the presented vortex structure in Fig. 3(*a*), through Fig. 5(*a*), it is aimed to provide a deeper discussion on the downstream velocities, strength of the vortices, and the role of the downstream momentum transfer. As can be seen from Fig. 5(*a*), regardless of the level of blockage ratio, backflow ($U/U_\infty < 0$) exists in the downstream section of the cylinder. However, since the strength of the vortex structure can explicitly be defined not only by the magnitude of the backflow but also with the extension of the flow domain that is influenced by the backflow regime, the impact of blockage on the vortex strength comes out to be significantly important. The computations put forward a rise in the backflow velocity values with higher β. Such that as the centerline dimensionless velocity values at $x_{ds} = 5 \times 10^{-3}$ m are computed as $U/U_\infty = -0.039$ and $U/U_\infty = -0.052$ for $\beta = 0.200$ and $\beta = 0.333$, respectively, for the same location the corresponding records are evaluated as $U/U_\infty = -0.094$ and $U/U_\infty = -0.131$ for $\beta = 0.571$ and $\beta = 0.800$. From the point of momentum transfer around the separation point, it can be said that the growth of the backflow values is highly characterized by the comprehensively augmented throat

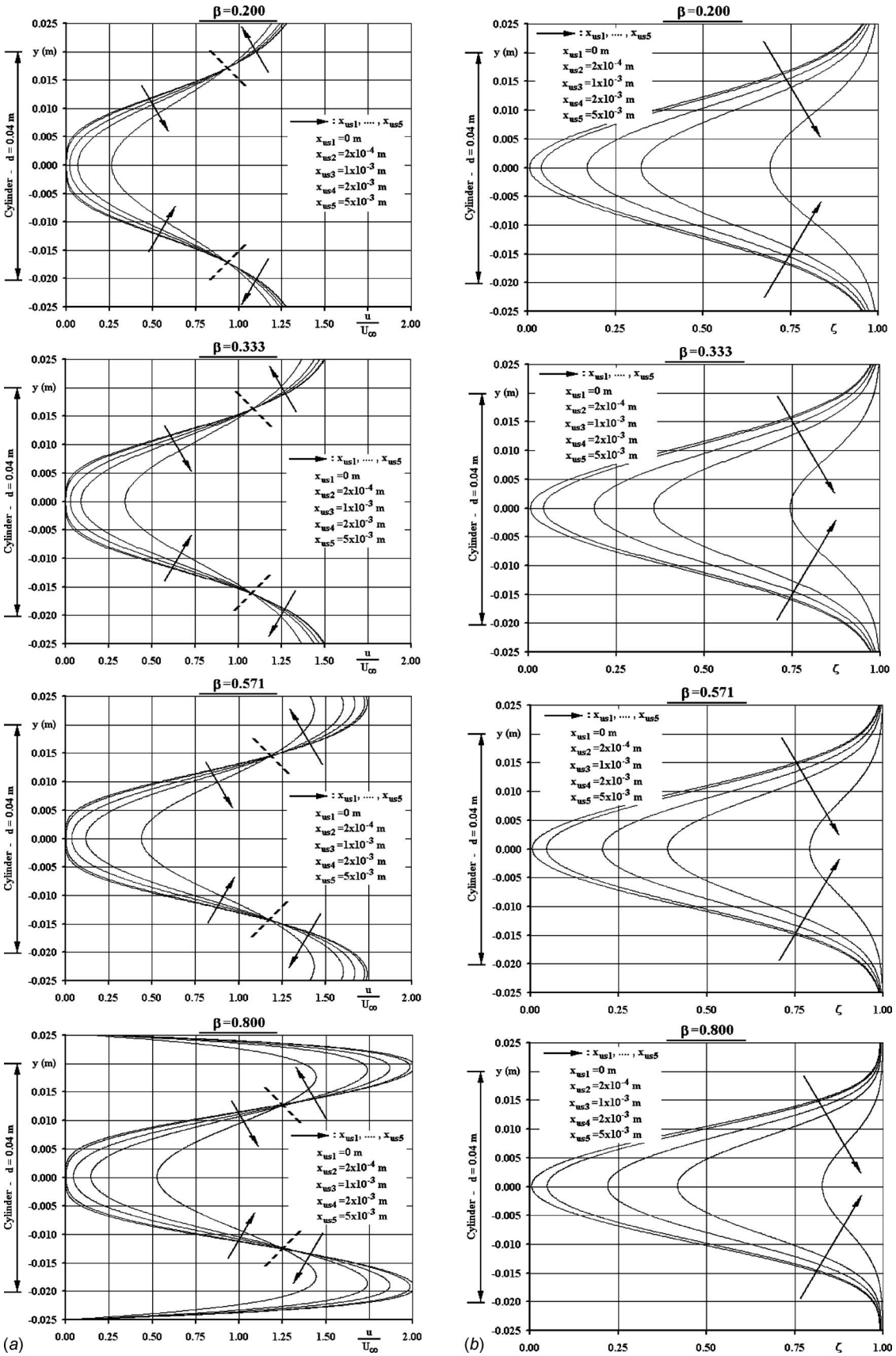

Fig. 4 Dimensionless (*a*) velocity and (*b*) temperature profiles at the upstream of the cylinder for the blockage ratio range of $\beta = 0.200 - 0.800$

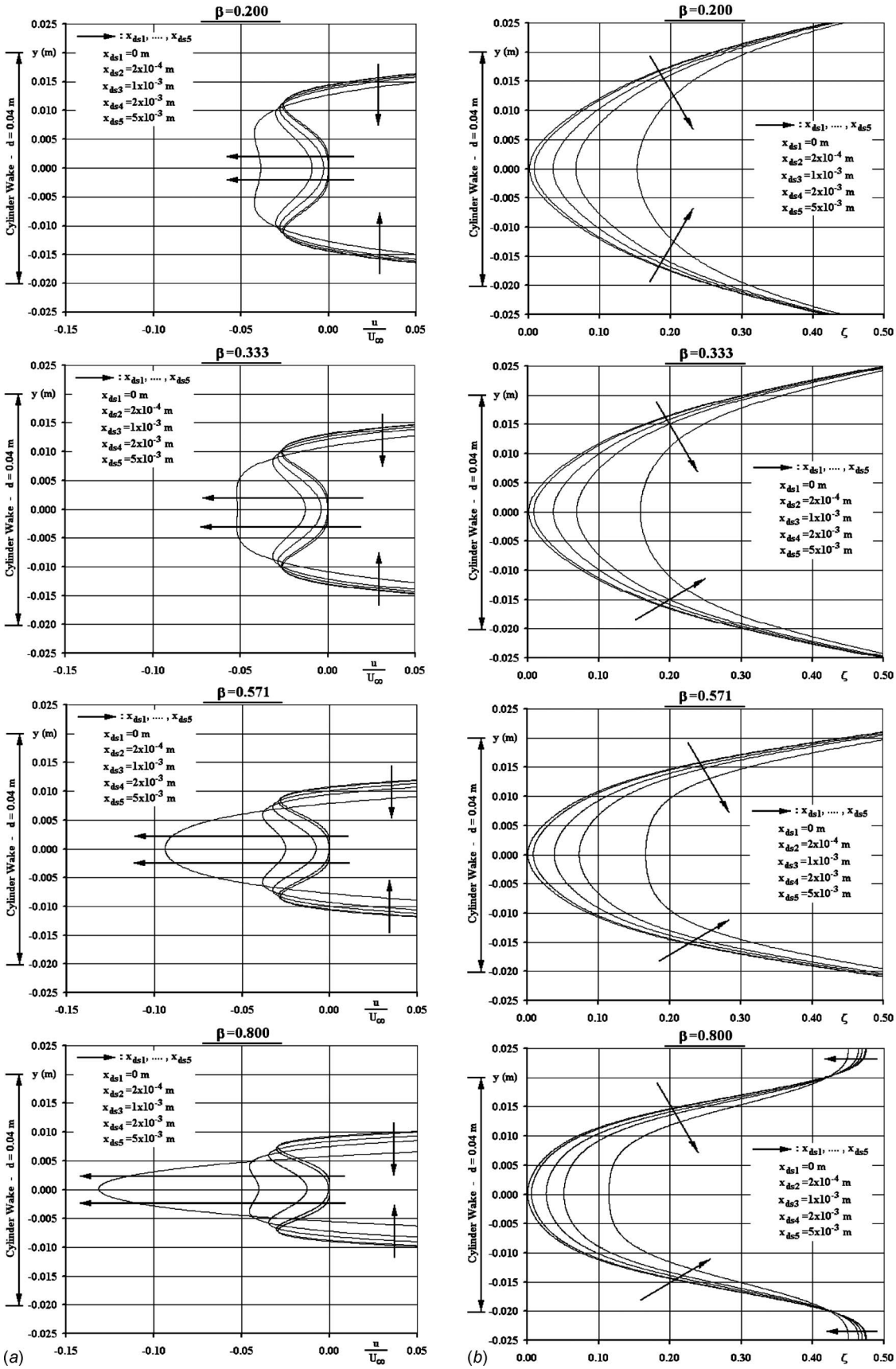

Fig. 5 Dimensionless (*a*) velocity and (*b*) temperature profiles at the downstream of the cylinder for the blockage ratio range of β=0.200–0.800

velocity values of Fig. 4(*a*) at high β. As the downstream shift of θ_s with high blockage ratio (Fig. 3(*a*)) is an outcome of the elevated momentum of fluid motion supporting the boundary layer development by suppressing the negative pressure gradient effects in the decelerating fluid domain, the subsequent hydrodynamic structure is as well characterized by the level of the throat velocity values. In other words, it can be termed as follows: Higher blockage not only augments the throat momentum transfer but also moves the separation point downstream. Not only from the schematic point of view but also according to the role of blockage on the wake (downstream) velocity profiles, the present evaluations match with the circular cylinder findings of Sen et al. [8] (β=0–0.800) and Buyruk et al. [17] (β=0.18–0.47). The downstream velocity profiles additionally verify the determinations on the narrower vortex domain (Fig. 3(*a*)) at high β with the specific width figures of $y=\pm 0.0191 \rightarrow \pm 0.0176$ m, $y=\pm 0.0160 \rightarrow \pm 0.0130$ m, $y=\pm 0.0124 \rightarrow \pm 0.0090$ m, and $y=\pm 0.0110 \rightarrow \pm 0.0064$ m ($x_{ds1} \rightarrow x_{ds5}$) for β=0.200, β=0.333, β=0.571, and β=0.800, respectively. The narrower vortex formation at high β, together with the continuity approach, can be regarded as a secondary factor on the rise of downstream backflow velocities.

The dimensionless downstream temperature profiles are given in Fig. 5(*b*). These results are significant not only to define the heat transfer characteristics in the downstream region of the flow domain but also to distinguish the role of vortex formation (Figs. 3(*a*) and 5(*a*)) on the heat transfer mechanism. The plot interprets for the investigated domain of $x_{ds}=0-5\times10^{-3}$ m that higher blockage ratio causes the fluid movement in the cylinder neighborhood to become hotter. As the isotherms of Fig. 3(*b*) point out, in the neighborhood of θ=180 deg and x_{ds}=0 m the dimensionless temperature values of the confined flow cases of β=0.200–0.571 resemble especially within the separated vortex domain of $x_{ds}=0-1\times10^{-3}$ m (Fig. 3(*a*)). The similar structure of the thermal layouts of β=0.200–0.571 cases is a trustable foresight for comparable heat transfer in the corresponding region. However, the high blockage of β=0.800 results in a unique temperature distribution when compared with those of the lower blockage cases. The lowest view of ζ at β=0.800 (Fig. 5(*b*)) in the complete blockage range results in a narrower temperature gap among the flow and cylinder, a mild temperature gradient, and lower heat transfer rates in that section of the cylinder surface. This outcome can scientifically be detailed by rationalizing the issue of downstream distance in conjunction with the recirculation length (L_r). As L_r is shown to become shorter with high β, the impact of blockage on the thermal activity of the separated domain comes into sight even in the neighborhood of the contact plane of the cylinder and in the downstream vortex system. On the other hand, the contrary evaluation can be set for low blockage scenarios with wider recirculation zones. These findings imply that besides demonstrating the impact of β on ζ, Fig. 5(*b*), as well presents the influence of downstream vortex formation on the flow temperature distribution. Besides, for the complete β range considered the stagnation point (θ=0 deg and x_{us}=0 m) dimensionless temperature values ($\zeta \approx 0.0055$) (Fig. 4(*b*)) are superior to those of the θ=180 deg and x_{ds}=0 m ($\zeta \approx 0.0012$) (Fig. 5(*b*)). This finding is a sign of advanced heat transfer at the upstream of the cylinder. This determination additionally puts forward that the momentum in the vicinity of the stagnation point has major potential, than the downstream vortex system, to bring about significantly augmented heat transfer rates.

3.1.2 Cylinder Surface Results. Figure 6 presents the angular variations of pressure coefficient (C_p), friction coefficient (C_f), and Nusselt number (Nu_θ) on the cylinder surface for the blockage ratio range of β=0.200–0.800. It can be seen from Fig. 6(*a*) that on the front face of the cylinder, the pressure coefficient values are considerably affected by the blockage ratio values, where C_p is determined to rise with β. At the stagnation point (θ=0°),

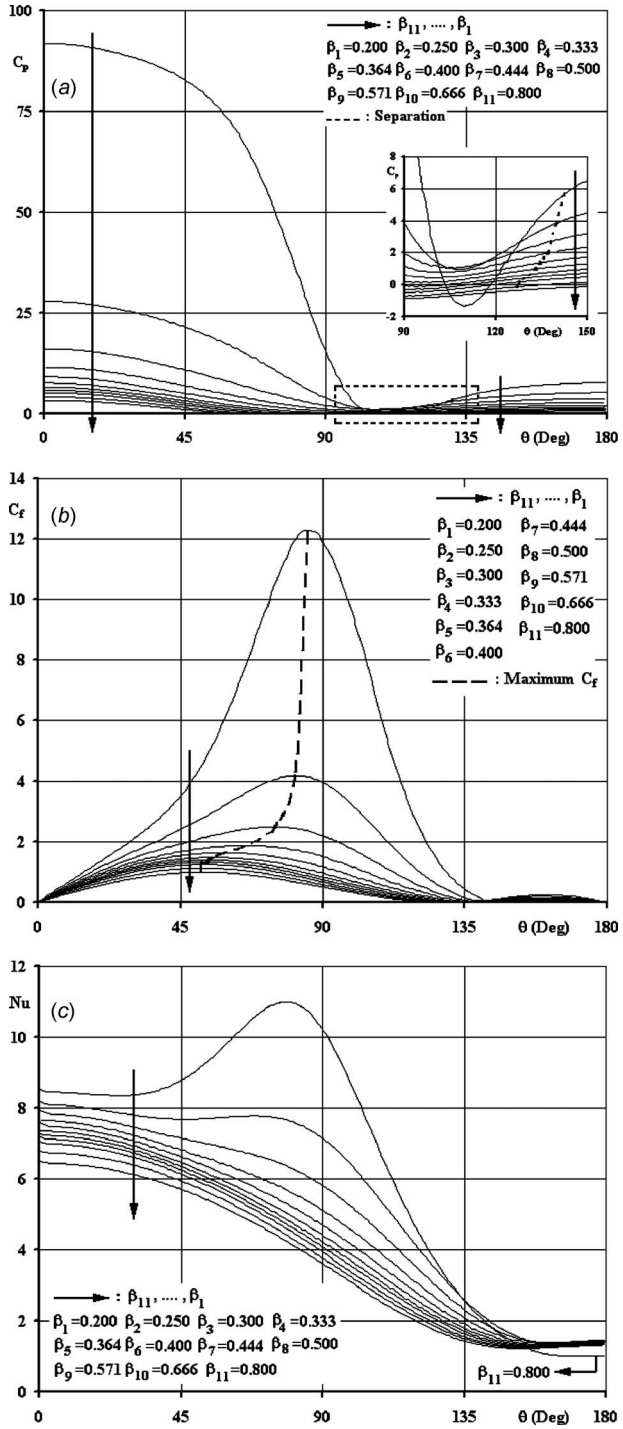

Fig. 6 Variation of (*a*) pressure coefficient, (*b*) friction coefficient, and (*c*) Nusselt number on the cylinder surface for the blockage ratio range of β=0.200–0.800

the highest blockage of β=0.800 creates a pressure coefficient of C_p=91.81, whereas the corresponding values for $\beta=0.500 \rightarrow 0.200$ appear as $C_p=11.51 \rightarrow 3.26$. Showing harmony with the present determinations, the rise of C_p with β was also reported by a few studies; such as the circular cylinder investigations of Chakraborty et al. [5] for Re<200 with β=0.05–0.65, Buyruk et al. [17] for 120<Re<390 with β=0.18–0.47, Sharma and Eswaran [19] for 50<Re<150 with β=0.10–0.50, Khan et al. [18] for laminar and turbulent flows with β=0.30–0.80, and the square cylinder work of Dhiman et al. [20] for Re<45 with β=0.125–0.25. Computations additionally indicated continuous

decreases in C_p toward the throat ($\theta=90°$). The drop in C_p is strictly dependent on the flow acceleration in the associated region; in other words, as the dynamic pressure rises, the contrary arises in the static pressure data. Numerical analysis indicates that the minimum C_p locations are positioned upstream of the separation points (θ_s). Indeed the gap among θ_s and θ_{C_p-min} becomes narrower at high β; such that as the θ_s-θ_{C_p-min} difference is 37.6 deg for $\beta=0.200$, it decreases down to 32.8 deg at $\beta=0.800$. In high β cases, the emergence of minimum C_p values at distant angular positions can be explained by the determinedly attaching boundary layer and delayed separation in these scenarios (Figs. 3(*a*) and 4(*a*)). Downstream of the separation location, Fig. 6(*a*) additionally puts forward an almost constant C_p domain, which is characterized and structured by the vortex regime, in other words the separated flow.

Angular variation of friction coefficient values is displayed in Fig. 6(*b*). It can be seen from the figure that, similar to the results of Chakraborty et al. [5], Khan et al. [18], and Dhiman et al. [20], C_f data are computed to rise with β on the complete cylinder surface. This augmentation can be attributed to the forced fluid contact and significantly interacting streamlines with the cylinder (Fig. 3(*a*)) and fuller velocity profiles (Fig. 4(*a*)) at high blockage cases. The location of maximum C_f are computed to shift downstream with high β, such that as θ_{C_f-max} is 51.5 deg at $\beta=0.200$, it becomes 85.4 deg at $\beta=0.800$. These values match with the maximum C_f location evaluations of Zukauskas and Ziugzda [44] ($\theta_{C_f-max}=\sim 50$ deg) for $\beta=0$ and that of Khan et al. [18] ($\theta_{C_f-max}=\sim 60$ deg) for $\beta=0.4$ case, however, slightly differ from the corresponding reports of Khan et al. [12] ($\theta_{C_f-max}=\sim 58$ deg) and Schonauer [45] ($\theta_{C_f-max}=\sim 57$ deg) for $\beta=0$. The performed analysis additionally puts forward a computational relation among the C_p and C_f variations: The θ_{C_f-max} points match the $\partial^2 C_p/\partial\theta^2=0$ locations. It can be said that maximum C_f are located at the angular points, where the trends in C_p curves reverse to attain the minimum C_p values. Figure 6(*b*) further clarifies the delay of separation with blockage and also the frictionless (no-shear) character in the corresponding domain.

The variation of Nusselt number on the cylinder surface is given in Fig. 6(*c*). The figure clearly puts forward the increase of Nusselt numbers; thus, surface heat transfer rates, with higher blockage, where similar findings were also reported by Bharti et al. [14], Buyruk et al. [17], Khan et al. [18], and Dhiman et al. [20]. Computational studies result in the average Nusselt numbers of $Nu_{ave}=6.51$, 4.97, 4.05, and 3.66 for the blockage ratio cases of $\beta=0.800$, 0.571, 0.333, and 0.200, respectively. For the specific case of Re=40, Biswas and Sarkar [41], Dennis et al. [43], Jafroudi and Yang [46], and Apelt and Ledwich [47] considered flows around circular cylinders without blockage and evaluated average Nusselt numbers in the narrow band of $Nu_{ave}=3.20-3.48$. The close agreement of the unconfined flow values of [41,43,46,47] with the present Nu_{ave} of 3.66 at $\beta=0.200$ strengthens the determination on the negligible impact of blockage for $\beta\leq 0.200$. Moreover, Khan et al. [18] reported the average Nusselt number for the blockage scenario of $\beta=0.200$ as $Nu_{ave}=3.44$, which is quite similar to the present corresponding finding ($Nu_{ave}=3.66$). Besides, the computed Nu_{ave} indicate the augmentation rates of 77.9% among the $\beta=0.800$ and $\beta=0.200$ cases, and 35.8% among the $\beta=0.571$ and $\beta=0.200$ scenarios. On the other hand, it can also be inspected from the figure that the impact of blockage on Nusselt numbers differs depending on the angular position. At the stagnation point, Nusselt numbers for the $\beta=0.800$, 0.571, 0.333, and 0.200 cases are evaluated as Nu=8.53, 7.94, 7.17, and 6.49, respectively, having the $Nu_{\beta=0.800}/Nu_{\beta=0.200}$ and $Nu_{\beta=0.571}/Nu_{\beta=0.200}$ ratios of 1.31 and 1.22. Except for the $\beta=0.800$ case, computations indicated the Nu to decrease in the angular direction, following the stagnation point. Moreover, the above defined ratios are determined as $Nu_{\beta=0.800}/Nu_{\beta=0.200}=1.53$ and 2.85, $Nu_{\beta=0.571}/Nu_{\beta=0.200}=1.23$ and 1.61 at the angular locations of $\theta=45$ and 90 deg, respectively. These records clearly put forward that the impact of blockage on heat transfer mechanism becomes significant toward the throat. This outcome can be enlightened by the close relation of the thermal and hydrodynamic structures. As was reported in Ozalp and Umur's [48,49] experimental studies for external flat and curved flows and in Ozalp's [50,51] computational investigations on internal microduct flows, thinner boundary layers provoke the heat transfer rates to rise. Similar outcomes were also announced by many other researchers both for internal and external flows [52,53]. High blockage based thinner boundary layer formation on the front face was clearly identified through the discussions concerning the role of blockage on the momentum transport and flow pattern (Figs. 3(*a*) and 4(*a*)). The present evaluations on the grow of heat transfer rates with high blockage cannot only be recognized with thinner boundary layer phenomena but can also be considered as a verification for the matching of hydrodynamic and thermal results. Figure 6(*c*) further points out the minimum heat transfer locations as being downstream of the separation points. The nearly constant temperature field in the downstream vortex domain (Fig. 5(*b*)) results in the almost constant heat transfer values in the angular domain of ~ 162 deg $<\theta<180$ deg. Besides, Fig. 6(*c*) further indicates for the cylinder surface section of ~ 162 deg $<\theta<180$ deg that the surface heat transfer rates of the blockage range $\beta=0.200-0.666$ are quite similar, which can be depended on the comparable combined impact of blockage and downstream vortex system on the heat transfer mechanism. But, as clarified in Fig. 3(*a*), the strength of the downstream vortex reduces at the highest blockage of $\beta=0.800$, which as a consequence negatively affects the heat transfer rates. On the other hand, being lower in magnitude, the influential region of the constant heat transfer values becomes narrower (~ 166 deg $<\theta<180$ deg), which can scientifically be linked to the thinner vortex formation at $\beta=0.800$ (Fig. 3(*a*)). It can be extracted from the point of back face heat transfer rates that as the $Nu_{\beta=0.800}/Nu_{\beta=0.200}$ ratio attains the values of 1.86 and 0.79 at $\theta=135$ and 180 deg, the corresponding values for $Nu_{\beta=0.571}/Nu_{\beta=0.200}$ emerge as 1.59 and 1.11. Since the throat ($\theta=90$ deg) ratios come out be superior on the complete cylinder surface, it can be concluded that the impact of boundary layer thinning is dominant to the role of the vortex structure on the heat transfer mechanism.

3.2 Mass Transfer Characteristics

3.2.1 Primary Findings. The mass transfer analysis within the circular cylinder, which is placed in a flow domain having a blockage ratio range of $\beta=0.200-0.800$, requires the knowledge about mass transfer coefficients on the cylinder surface. It is well known that [35] heat and mass transfer coefficients interrelate and in this work this relationship is implemented into the calculations with Eq. (6*i*), as was also applied by Kaya et al. [24]. The semilog plot of Fig. 7 presents the angular variations of mass transfer coefficients for the moisture diffusivity and blockage ratio ranges of $D=1\times10^{-5}-1\times10^{-8}$ m^2/s and $\beta=0.200-0.800$, respectively. The mass transfer coefficient curves are similar to those of Nusselt number (Fig. 6(*c*)) due to the dependent character of h_m on h_θ (Eq. (6*i*)). Moreover, since h_θ values, thus Nu_θ, are evaluated to grow with β (Fig. 6(*c*)), the identical impact can also be visualized on the β driven h_m characteristics. On the other hand, Fig. 7 clarifies that mass transfer coefficients significantly decrease in lower moisture diffusivity cases, which can be regarded as an indicator for considerably augmented overall drying times. Besides, the overall mean $\bar{h}_m$, front face mean $\bar{h}_{m-ff}$, and back face mean $\bar{h}_{m-bf}$ mass transfer coefficients are given in Table 2 for the investigated moisture diffusivity and blockage ratio scenarios. Showing harmony with Fig. 7, the tabulated data indicate that (i) $\bar{h}_{m-ff}$ are higher than $\bar{h}_m$ and $\bar{h}_{m-bf}$, which in return points out that the

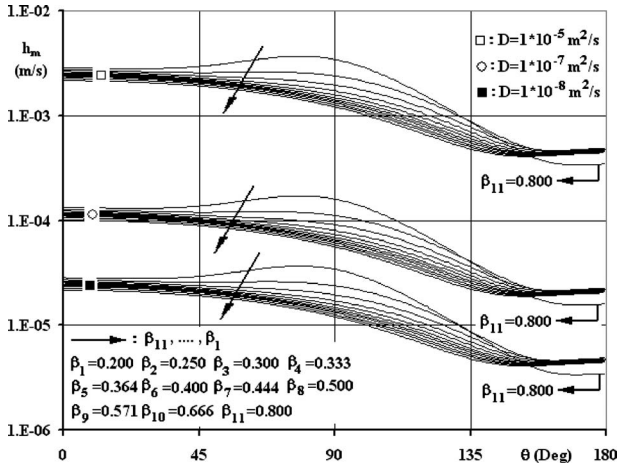

Fig. 7 Variation of mass transfer coefficients for the moisture diffusivity and blockage ratio ranges of $D=1\times10^{-5}-1\times10^{-8}$ m^2/s and $\beta=0.200-0.800$

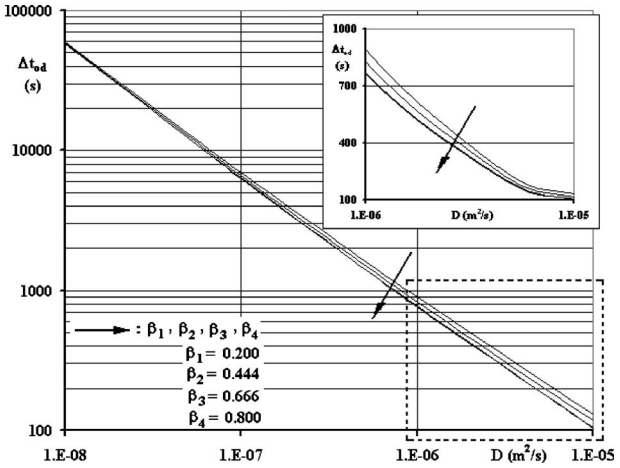

Fig. 8 Variation of overall drying times for the moisture diffusivity and blockage ratio ranges of $D=1\times10^{-5}-1\times10^{-8}$ m^2/s and $\beta=0.200-0.800$

potential of the moisture transfer in the front face of the cylinder is superior to that of the back face; (ii) the increasing role of β on mass transfer rates can be sensed both at the front ($\overline{h}_{m-ff}$) and back ($\overline{h}_{m-bf}$) faces; (iii) being independent of β, lower D decreases the mass transfer coefficients in every angular position of the cylinder surface. Table 2 additionally puts forward specific information regarding the influence of β on h_m. Computations show that as the $\overline{h}_{m-ff}/\overline{h}_m$ and $\overline{h}_{m-bf}/\overline{h}_m$ ratios attain the values of ~1.50 and ~0.50 for $\beta=0.200$, they become ~1.43 and ~0.57 with the rise of β to 0.800, where these proportions are also determined to be independent of D. These ratios identify that, although higher β augments the h_m on the overall cylinder surface (Fig. 7 and Table 2), the growing rate of $\overline{h}_{m-bf}$ is dominant to that of $\overline{h}_{m-ff}$ resulting in the rise of $\overline{h}_{m-bf}/\overline{h}_m$ and drop of $\overline{h}_{m-ff}/\overline{h}_m$ with higher blockage.

Figure 8 presents the overall drying times (Δt_{od}) for the moisture diffusivity and blockage ratio ranges of $D=1\times10^{-5}-1\times10^{-8}$ m^2/s and $\beta=0.200-0.800$. The log-log plot expresses the decrease style of Δt_{od} with both higher diffusivity and higher blockage ratio. As lower Δt_{od} at higher D is an expected outcome, the impact of β on Δt_{od} can be outlined by the direct relation of mass (h_m) and heat transfer (h_θ) coefficients through Eq. (6*i*). As extensively discussed in Sec. 3.1, heat transfer rates grow at higher blockage cases, which in return augments the mass transfer coefficients as presented in Fig. 7. Specifically denoting, computations resulted in the Δt_{od} of 59950→57402 s ($\beta=0.200\rightarrow0.800$) for $D_1=1\times10^{-8}$ m^2/s, 6915.4→6329.6 s for $D_2=1\times10^{-7}$ m^2/s, 894.48→766.12 s for $D_3=1\times10^{-6}$ m^2/s, and 131.41→103.55 s for $D_4=1\times10^{-5}$ m^2/s. These values point out the $\Delta t_{od-\beta=0.200}/\Delta t_{od-\beta=0.800}$ ratios of 1.044, 1.093, 1.168, and 1.269 for D_1, D_2, D_3, and D_4, respectively. The increasing nature of these ratios with higher D clearly puts forward that the impact of β on mass transfer becomes more effective at high D cases. On the other hand, the ratio of the overall drying times, among different diffusivity levels, clarifies the role of D on Δt_{od}. As the $\Delta t_{od-D_1}/\Delta t_{od-D_2}$ ratio is 8.67→9.07 ($\beta=0.200\rightarrow0.800$), the corresponding values for D_2 and D_3, and D_3 and D_4 are 7.73→8.26 and 6.81→7.40, respectively. These ratios indicate that extensive overall drying times can arise for a subject product with sufficiently low moisture diffusivity. This determination is quite important for drying applications, due to the fact that moisture diffusivity property can be as low as $D=1\times10^{-15}$ m^2/s [34].

3.2.2 In-Time Moisture Variations. The in-time variation of cylinder average (ϕ_a) and cylinder center (ϕ_c) dimensionless moisture contents are given in Figs. 9(*a*) and 9(*b*), respectively. As $\phi=1.00$ stands for the initial (t=0 s) moisture content ($M_{cyl}=3$ kg/kg), $\phi=0.00$ indicates the completely dry product and corresponding time is the overall drying time (Δt_{od}). Figure 9

Table 2 Variation of overall, front face, and back face average mass transfer coefficients for the moisture diffusivity and blockage ratio ranges of $D=1\times10^{-5}-1\times10^{-8}$ m^2/s and $\beta=0.200-0.800$

		$\beta=0.200$	$\beta=0.444$	$\beta=0.666$	$\beta=0.800$
$D=1\times10^{-5}$ m^2/s	$\overline{h}_m$ (m/s)	1.23×10^{-03}	1.48×10^{-03}	1.85×10^{-03}	2.18×10^{-03}
	$\overline{h}_{m\text{-}ff}$ (m/s)	1.84×10^{-03}	2.17×10^{-03}	2.61×10^{-03}	3.12×10^{-03}
	$\overline{h}_{m\text{-}bf}$ (m/s)	6.18×10^{-04}	7.94×10^{-04}	1.09×10^{-03}	1.25×10^{-03}
$D=1\times10^{-7}$ m^2/s	$\overline{h}_m$ (m/s)	5.69×10^{-05}	6.87×10^{-05}	8.60×10^{-05}	1.01×10^{-04}
	$\overline{h}_{m\text{-}ff}$ (m/s)	8.52×10^{-05}	1.01×10^{-04}	1.21×10^{-04}	1.45×10^{-04}
	$\overline{h}_{m\text{-}bf}$ (m/s)	2.87×10^{-05}	3.68×10^{-05}	5.07×10^{-05}	5.80×10^{-05}
$D=1\times10^{-8}$ m^2/s	$\overline{h}_m$ (m/s)	1.23×10^{-05}	1.48×10^{-05}	1.85×10^{-05}	2.18×10^{-05}
	$\overline{h}_{m\text{-}ff}$ (m/s)	1.84×10^{-05}	2.17×10^{-05}	2.61×10^{-05}	3.12×10^{-05}
	$\overline{h}_{m\text{-}bf}$ (m/s)	6.18×10^{-06}	7.94×10^{-06}	1.09×10^{-05}	1.25×10^{-05}

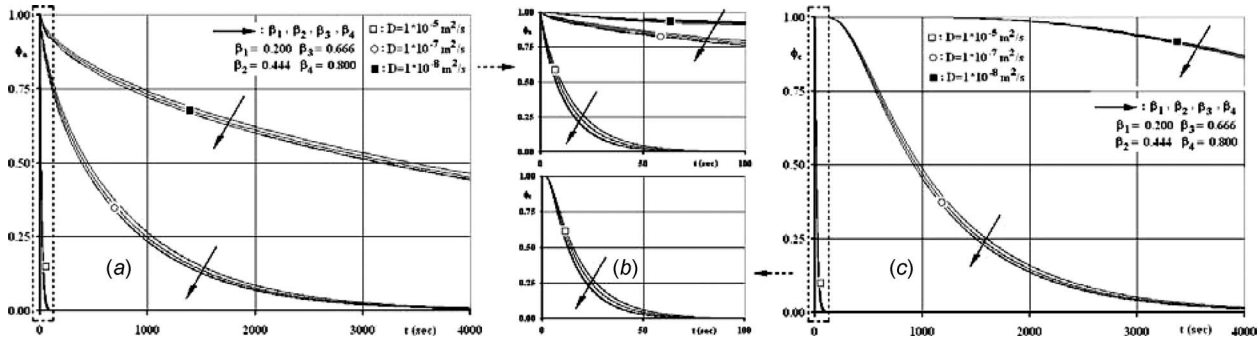

Fig. 9 In time variation of (*a*) cylinder average and (*b*) cylinder center dimensionless moisture content for the moisture diffusivity and blockage ratio ranges of $D=1\times10^{-5}-1\times10^{-8}$ m²/s and $\beta=0.200-0.800$

puts forward that as the ϕ_a and ϕ_c variations of the highest moisture diffusivity case ($D=1\times10^{-5}$ m²/s) are similar, apparent shifts arise among the average and center moisture curves for lower diffusivity products. The ϕ_c/ϕ_a ratios are presented in Table 3 for three diffusivity and two blockage ratio cases at five instants of the overall drying times. Tabulated values mainly indicate the following five issues: (i) Being independent of moisture diffusivity and blockage ratio levels, the gap among the center and average moisture content values is maximum in the early stages of the drying process; (ii) for products with lower diffusivity, the gap is superior to those of the higher diffusivity products; (iii) in higher blockage cases, due to higher mass transfer coefficients, the gap is above those of the lower blockage cases; (iv) in the last 5% of the drying period, center and average moisture content values converge by a ≤1.6% gap, indicating a homogeneous moisture distribution inside the product; (v) during drying, by investigating the weight change of the product, or the amount of lost moisture, the current total moisture content and the average moisture level can be calculated. However the present findings put forward that due to not only the moisture diffusivity of the product but also the blockage ratio of the flow domain, the center moisture value can be significantly above the average moisture level. Thus, the drying period must be decided by considering both the average and center moisture levels. The present computations further point out that 97.75–98.50% of the excess moisture content (M_{cyl}-M_a) leaves the product in the first half of the overall drying time ($\Delta t_{od}/2$). Since operation cost is of high importance in industrial drying applications, this determination enlightens the necessity of accurate estimation of drying period for the desired drying level.

The local dimensionless moisture content variations of three surface points ($S_1-\theta=0$ deg, $S_2-\theta=180$ deg, and $S_3-\theta=90$ deg), as given in Fig. 1(*b*), are plotted in Fig. 10 for the blockage ratio and moisture diffusivity ranges of $\beta=0.200-0.800$ and $D=1\times10^{-5}-1\times10^{-8}$ m²/s, respectively. The figure puts forward that, being independent of β, at the highest moisture diffusivity scenario of $D=1\times10^{-5}$ m²/s, sharp decreases in moisture occur on the cylinder surface with the start of drying ($t\leq100$ s), where the dimensionless moisture values decay down almost to $\phi=0.00$. This outcome can be explained by the simultaneous role of the high mass transfer coefficients and the high moisture diffusion inside the cylinder due to high D. Figure 10 further indicates for $D=1\times10^{-8}$ m²/s, the ϕ difference among S_1 and S_3 locations becomes apparent and wider at lower β. The source of the difference can be clarified by the mass transfer coefficients given in Fig. 7. Figure 7 shows that although the queue of $h_{m-S_1}>h_{m-S_3}$ remains fixed, the gaps among the h_m values become broader at lower β. It can be seen from Fig. 10 that, if each moisture diffusivity case is considered individually, at higher blockage ratios considerably lower moisture exist at S_1 and S_3, but the contrary is true for S_2, which can as well be attributed to the variation of mass transfer coefficients on the cylinder surface (Fig. 7). Computations additionally clarified that, for the complete moisture diffusivity range investigated, as the state of the surface moisture layout, in the highest blockage case of $\beta=0.800$, comes out to be sequenced as $\phi_{S_2}>\phi_{S_1}>\phi_{S_3}$, in the flows with $\beta\leq0.666$ the order of the moisture contents at S_1 and S_3 replaces resulting in $\phi_{S_2}>\phi_{S_3}>\phi_{S_1}$. This finding puts forward the fact that surface moisture levels are characterized significantly by h_m and secondarily by D. These evaluations are extremely important from the point that blockage effect can be adapted to drying applications in which forced-drying is required to be directed to certain angular locations of CC products.

3.2.3 Isomoisture Contour Layouts. Isocontours, at the 10% overall drying times are plotted in Figs. 11(*a*)–11(*c*) for the moisture diffusivities of $D=1\times10^{-5}$ m²/s, $D=1\times10^{-6}$ m²/s, and $D=1\times10^{-7}$ m²/s, respectively. It can be seen from the figure that the front face moisture levels are lower than those of the back face, being independent of moisture diffusivity and blockage ratio. These determinations completely match the in-time moisture variations (Fig. 10) of the surface points S_1 and S_2. Through the numerical analyses the gap among ϕ_{max} and the moisture contents

Table 3 Variation of center to average dimensionless moisture content ratios at five instants of the overall drying times for the moisture diffusivity and blockage ratio ranges of $D=1\times10^{-5}-1\times10^{-8}$ m²/s and $\beta=0.200-0.800$

	ϕ_c/ϕ_a					
	$D=1\times10^{-5}$ m²/s		$D=1\times10^{-7}$ m²/s		$D=1\times10^{-8}$ m²/s	
	$\beta=0.200$	$\beta=0.800$	$\beta=0.200$	$\beta=0.800$	$\beta=0.200$	$\beta=0.800$
5% Δt_{od}	1.337	1.442	1.609	1.674	1.715	1.759
25% Δt_{od}	1.284	1.380	1.539	1.589	1.629	1.664
50% Δt_{od}	1.119	1.160	1.277	1.301	1.334	1.350
75% Δt_{od}	1.024	1.032	1.056	1.060	1.066	1.070
95% Δt_{od}	1.006	1.007	1.012	1.014	1.015	1.016

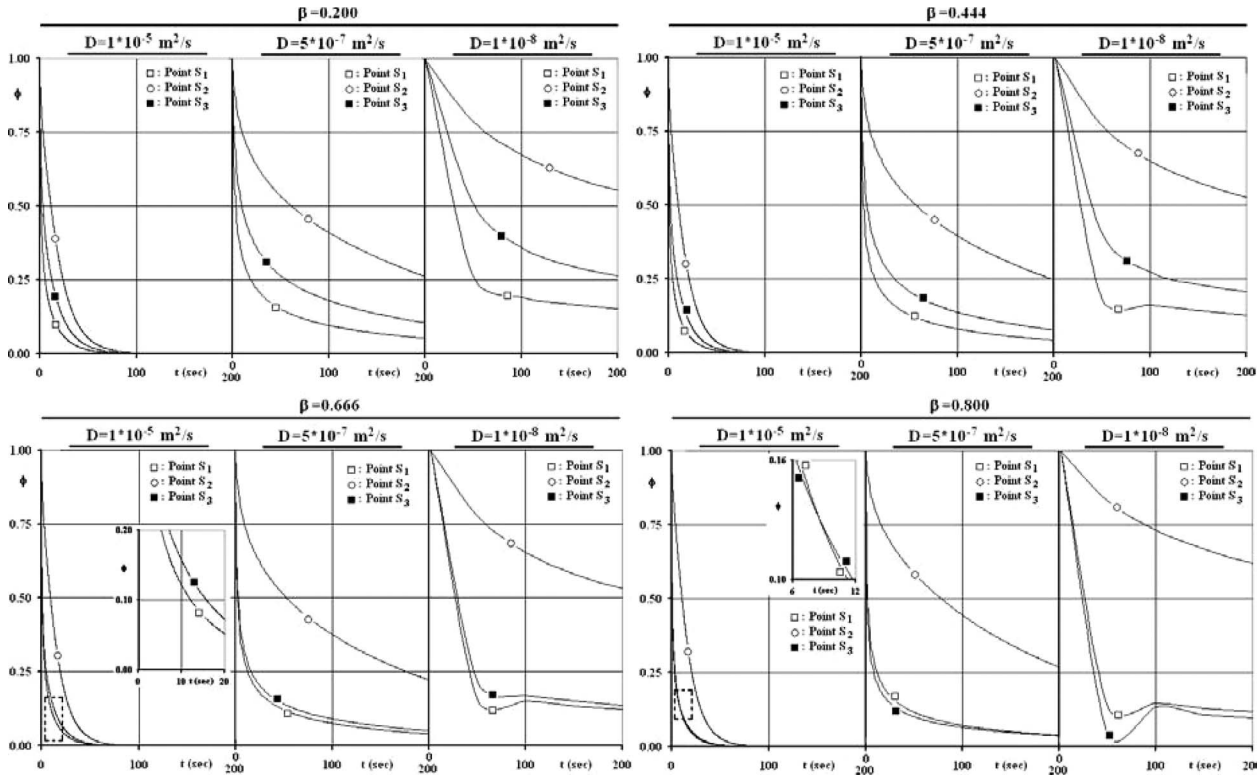

Fig. 10 Drying characteristics at the cylinder surface locations of S_1, S_2, and S_3 for the moisture diffusivity and blockage ratio ranges of $D=1\times10^{-5}-1\times10^{-8}$ m^2/s and $\beta=0.200-0.800$

of S_1 ($\theta=0$ deg) and S_2 ($\theta=180$ deg) (Fig. 1(*b*)) are also identified. As ϕ_{max} exceeds ϕ_{S_1} and ϕ_{S_2} by $0.476\rightarrow0.521$ and $0.146\rightarrow0.122$ ($\beta=0.200\rightarrow0.800$) at $D=1\times10^{-5}$ m^2/s, these differences grow up to $0.650\rightarrow0.676$ and $0.476\rightarrow0.457$ at $D=1\times10^{-7}$ m^2/s. These figures, besides being consistent with the ϕ_c/ϕ_a ratios of Table 3, not only notify the decrease of $\phi_{max}-\phi_{S_2}$ and increase of $\phi_{max}-\phi_{S_1}$ with higher blockage ratios, but also identify the rise of the maximum to surface moisture level gap in cases with lower moisture diffusivities. Figure 11 additionally indicates that as the ϕ_{max} locations are separated from cylinder center in the moisture diffusivity scenario of $D=1\times10^{-5}$ m^2/s, those of $D=1\times10^{-7}$ m^2/s are located in the vicinity of the cylinder center in the complete blockage range considered ($\beta=0.200-0.800$). This evaluation puts forward that in drying applications with high moisture diffusivities ($D=1\times10^{-5}$ m^2/s) surface mass transfer coefficients (h_m) are quite determinative on the front and back face moisture levels. However, in cases with lower diffusivity ($D\leq1\times10^{-7}$ m^2/s) moisture levels on the front and back faces become closer and the ϕ_{max} location shifts toward the cylinder center. The mechanism of this evaluation can further be identified through the converging nature of above $\phi_{max}-\phi_{S_1}$ and $\phi_{max}-\phi_{S_2}$ differences in lower moisture diffusivities. It can further be extracted from the figure that the $\phi_{max(\beta=0.200)}$ and $\phi_{max(\beta=0.800)}$ values diverge at high D cases; such that as the $\phi_{max(\beta=0.200)}$-$\phi_{max(\beta=0.800)}$ difference for $D=1\times10^{-7}$ m^2/s is 0.017, it grows to 0.025 and 0.026 at $D=1\times10^{-6}$ m^2/s and $D=1\times10^{-5}$ m^2/s, respectively. These evaluations put forward the fact that the role of β, and the so occurring h_m distribution, on ϕ_{max} and ϕ_{max} location becomes ineffective at low moisture diffusivities. The discussions presented in Fig. 11 are essential in generating a theoretical approach based scientific relation among the surface and maximum moisture levels.

3.2.4 Verification Analysis. The scientific standard and precision of the new ADI based software is verified by computationally handling the experimental results of Queiroz and Nebra [21] for the drying process of bananas ($D=4.59\times10^{-10}$ m^2/s). Queiroz and Nebra [21] conducted their drying experiments in a laboratory convective chamber dryer. The equipment was supported with a data acquisition device that allowed controlling the air drying conditions, such as temperature and relative humidity, and automatically recorded these parameters and the weight loss data during the entire process. Similar to the present study, the fruit with cylindrical cross section was placed in the perforated tray of the chamber dryer in the direction of air flow. Figure 12 indicates that the outputs of the present model, computed with the experimental conditions of Ref. [21] ($U_\infty=0.33$ m/s, $T_\infty=39.9°C$, $h_m=1.66\times10^{-7}$ m/s, and $M_i=3.43$ kg/kg), and the experimental findings of Ref. [21] coincide well with an acceptable average deviation of 6.4%.

4 Conclusions

The present paper has introduced and discussed the results of a comprehensive numerical investigation on fluid flow and heat-mass transfer characteristics of a circular cylinder, subjected to confined flow. The key concluding remarks of the present study can be summarized as follows:

1. Blockage shifts separation and maximum C_f locations downstream to the positions of $\theta_s=54.10$ deg and 37.30 deg and $\theta_{C_f-max}=51.5$ deg and 85.4 deg for $\beta=0.200$ and 0.800.
2. The lengths of the recirculation zones are computed as to decrease with β, indicating that blockage negatively affects the influential domain and strength of the downstream vortex system.
3. On the overall cylinder surface, blockage is determined to cause thinner hydrodynamic and thermal boundary layers, which in return also rises the frictional and thermal activity.
4. The late hydrodynamic response of the upstream flow do-

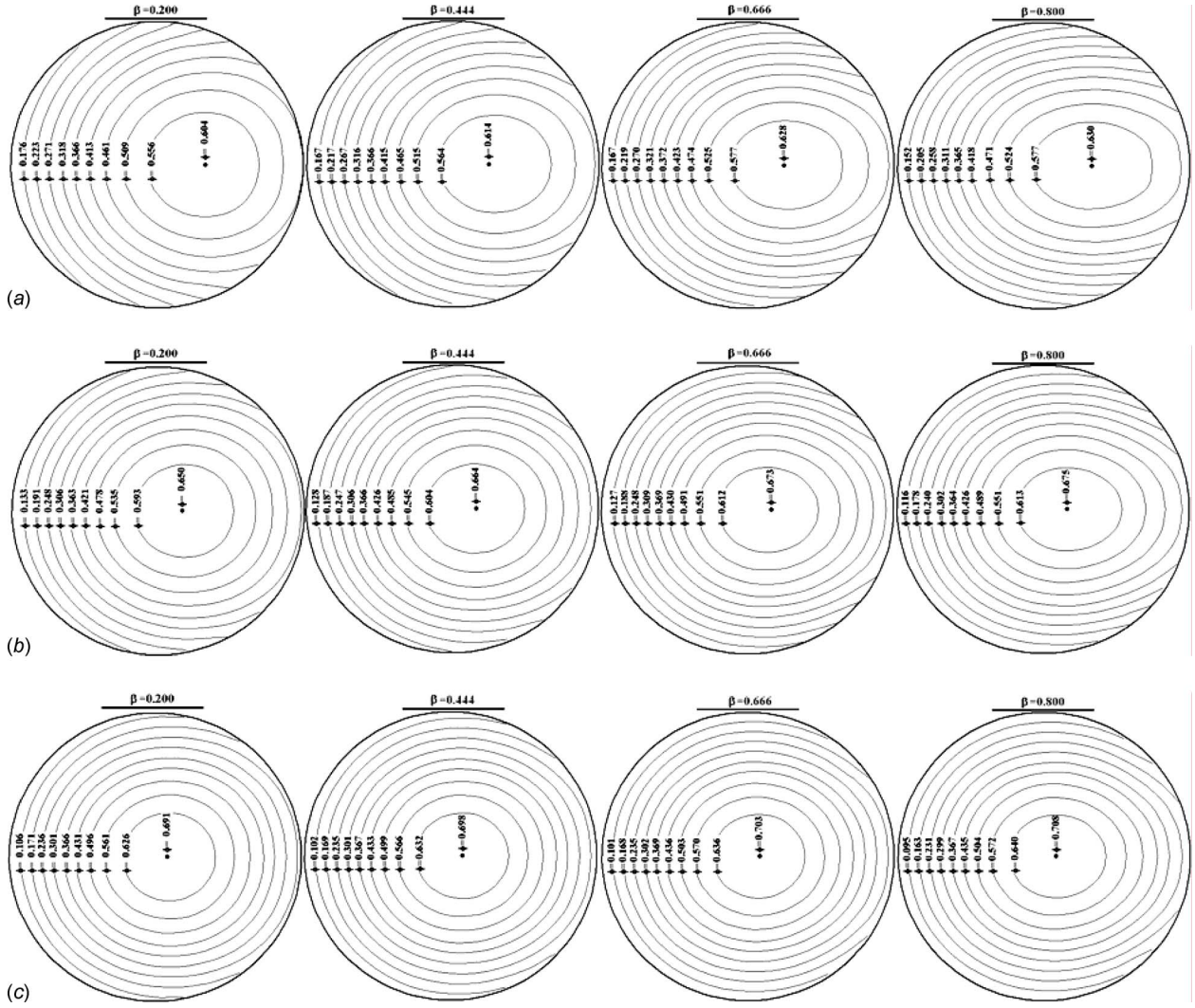

Fig. 11 Isomoisture contours at the 10% drying times of the cases with (*a*) $D=1\times10^{-5}$ m^2/s, (*b*) $D=1\times10^{-6}$ m^2/s, and (*c*) $D=1\times10^{-7}$ m^2/s for the blockage ratios of $\beta=0.200$, 0.444, 0.666, and 0.800

main at higher β scenarios decelerates the flowing air more rapidly to zero toward the stagnation point and results in augmented momentum velocity in the neighborhood of the cylinder and elevated pressure coefficient values.

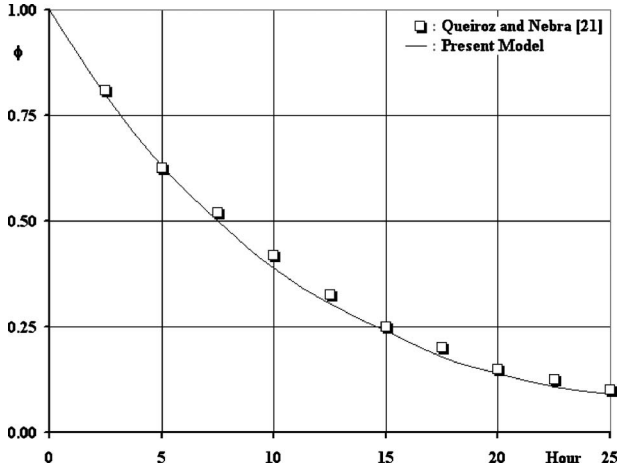

Fig. 12 Comparison of the present model with the experimental outputs of Queiroz and Nebra [21]

5. The Nusselt numbers are determined to be most promoted by blockage at the throat, which in return indicates that the heat transfer mechanism is more influenced by boundary layer thinning than the upstream momentum activity.
6. The higher stagnation point Nusselt number range of $Nu=8.53\rightarrow6.49$ ($\beta=0.800\rightarrow0.200$) than those of the back face values ($Nu=1.03\rightarrow1.31$) at $\theta=180$ deg put forward the superior potential of the stagnation point momentum activity to the downstream vortex system from the point of heat transfer enhancing capability.
7. Besides demonstrating the upstream stand of minimum C_p locations with respect to θ_s, the present computations as well indicated that the gap among θ_s and θ_{C_p-min} becomes narrower at stronger blockage, where the interpreting values are θ_s-$\theta_{C_p-min}=37.6$ deg and 32.8 deg for $\beta=0.200$ and 0.800.
8. The ratios of overall drying times ($\Delta t_{od-\beta=0.200}/\Delta t_{od-\beta=0.800}$), among the limiting blockage scenarios of $\beta=0.200-0.800$, are computed as 1.044–1.269 for $D=1\times10^{-8}$ m^2/s and 1×10^{-5} m^2/s, respectively, identifying the rising role β on mass transfer with higher D.
9. Higher β augments the h_m on the overall cylinder surface;

however, the growing rate of $\overline{h}_{m-bf}$ is dominant to that of $\overline{h}_{m-ff}$.

Nomenclature

C_f = friction coefficient
C_p = constant pressure specific heat (J/kg K), pressure coefficient
d = diameter (m)
D = moisture diffusivity (m^2/s)
h = convective heat transfer coefficient (W/m^2 K)
h_m = mass transfer coefficient (m/s)
H = duct height (m)
k = conductive heat transfer coefficient (W/m K)
Le = Lewis number
L_r = recirculation length (m)
M = moisture content (kg/kg)
n = normal direction
Nu = Nusselt number
P = static pressure (Pa)
r = radical direction
Re_{ch} = channel Reynolds number
Re_d = cylinder Reynolds number
t = time (s)
T = temperature (K)
u = velocity in x-direction (m/s)
U_∞ = average velocity of air at the inlet (m/s)
v = velocity in y-direction (m/s)
w = width (mm)
x = coordinate in x-direction (m)
y = coordinate in y-direction (m)

Greek Symbols

α = thermal diffusivity (m^2/s)
β = blockage ratio
Δ = difference
ϕ = dimensionless moisture
λ = under-relaxation parameter
μ = dynamic viscosity (Pa s)
θ = angular position (deg)
ρ = density (kg/m^3)
τ_s = shear stress (Pa)
ζ = dimensionless temperature

Subscripts

a = air, average
bf = back face
c = center
cyl = cylinder
ds = downstream
ff = front-face
i = initial
od = overall drying
max = maximum
n = normal to the cylinder surface
θ = angular
rev = reverse
s = separation, cylinder surface
th = throat
us = upstream
∞ = inlet air

Superscript

_ = average

References

[1] Bhattacharyya, S., Dhinakaran, S., and Khalili, A., 2006, "Fluid Motion Around and Through a Porous Cylinder," Chem. Eng. Sci., **61**, pp. 4451–4461.
[2] Job, N., Sabatier, F., Pirard, J. P., Crine, M., and Leonard, A., 2006, "Towards the Production of Carbon Xerogel Monoliths by Optimizing Convective Drying Conditions," Carbon, **44**, pp. 2534–2542.
[3] Akpinar, E. K., and Dincer, I., 2005, "Moisture Transfer Models for Slabs Drying," Int. Commun. Heat Mass Transfer, **32**, pp. 80–93.
[4] Griffith, M. D., Thompson, M. C., Leweke, T., Hourigan, K., and Anderson, W. P., 2007, "Wake Behaviour and Instability of Flow Through a Partially Blocked Channel," J. Fluid Mech., **582**, pp. 319–340.
[5] Chakraborty, J., Verma, N., and Chhabra, R. P., 2004, "Wall Effects in Flow Past a Circular Cylinder in a Plane Channel: A Numerical Study," Chem. Eng. Process., **43**, pp. 1529–1537.
[6] Sahin, M., and Owens, R. G., 2004, "A Numerical Investigations of Wall Effects Up to High Blockage Ratios on Two-Dimensional Flow Past a Confined Circular Cylinder," Phys. Fluids, **16**, pp. 1305–1320.
[7] Rehimi, F., Aloui, F., Nasrallah, S. B., Doubliez, L., and Legrand, J., 2008, "Experimental Investigation of a Confined Flow Downstream of a Circular Cylinder Centred Between Two Parallel Walls," J. Fluids Struct., **24**, pp. 855–882.
[8] Sen, S., Mittal, S., and Biswas, G., 2009, "Steady Separated Flow Past a Circular Cylinder at Low Reynolds Numbers," J. Fluid Mech., **620**, pp. 89–119.
[9] Breuer, M., Bernsdorf, J., Zeiser, T., and Durst, F., 2000, "Accurate Computations of the Laminar Flow Past a Square Cylinder Based on Two Different Methods: Lattice-Boltzmann and Finite-Volume," Int. J. Heat Fluid Flow, **21**, pp. 186–196.
[10] Camarri, S., and Giannetti, F., 2007, "On the Inversion of the von Karman Street in the Wake of a Confined Square Cylinder," J. Fluid Mech., **574**, pp. 169–178.
[11] Chang, B. H., and Mills, A. F., 2004, "Effect of Aspect Ratio on Forced Convection Heat Transfer From Cylinders," Int. J. Heat Mass Transfer, **47**, pp. 1289–1296.
[12] Khan, W. A., Culham, J. R., and Yovanovich, M. M., 2005, "Fluid Flow Around and Heat Transfer From an Infinite Circular Cylinder," ASME J. Heat Transfer, **127**, pp. 785–790.
[13] Khan, W. A., Culham, J. R., and Yovanovich, M. M., 2006, "Analytical Study of Heat Transfer From Circular Cylinder in Liquid Metals," Heat Mass Transfer, **42**, pp. 1017–1023.
[14] Bharti, R. P., Chhabra, R. P., and Eswaran, V., 2007, "Effect of Blockage on Heat Transfer From a Cylinder to Power Law Liquids," Chem. Eng. Sci., **62**, pp. 4729–4741.
[15] Montelpare, S., and Ricci, R., 2004, "An Experimental Method for Evaluating the Heat Transfer Coefficient of Liquid-Cooled Short Pin Fins Using Infrared Thermography," Exp. Therm. Fluid Sci., **28**, pp. 815–824.
[16] Sparrow, E. M., Abraham, J. P., and Tong, J. C. K., 2004, "Archival Correlations for Average Heat Transfer Coefficients for Non-Circular and Circular Cylinders and for Spheres in Cross-Flow," Int. J. Heat Mass Transfer, **47**, pp. 5285–5296.
[17] Buyruk, E., Johnson, M. W., and Owen, I., 1998, "Numerical and Experimental Study of Flow and Heat Transfer around a Tube in Cross-Flow at Low Reynolds Number," Int. J. Heat Fluid Flow, **19**, pp. 223–232.
[18] Khan, W. A., Culham, J. R., and Yovanovich, M. M., 2004, "Fluid Flow and Heat Transfer from a Cylinder between Parallel Planes," J. Thermophys. Heat Transfer, **18**, pp. 395–403.
[19] Sharma, A., and Eswaran, V., 2004, "Effect of Channel Confinement on the Two-Dimensional Laminar Flow and Heat Transfer Across a Square Cylinder," Numer. Heat Transfer, Part A, **47**, pp. 79–107.
[20] Dhiman, A. K., Chhabra, R. P., and Eswaran, V., 2005, "Flow and Heat Transfer across a Confined Square Cylinder in the Steady Flow Regime: Effect of Peclet Number," Int. J. Heat Mass Transfer, **48**, pp. 4598–4614.
[21] Queiroz, M. R., and Nebra, S. A., 2001, "Theoretical and Experimental Analysis of the Drying Kinetics of Bananas," J. Food. Eng., **47**, pp. 127–132.
[22] Dincer, I., Hussain, M. M., Sahin, A. Z., and Yilbas, B. S., 2002, "Development of a New Moisture Transfer (Bi–Re) Correlation for Food Drying Applications," Int. J. Heat Mass Transfer, **45**, pp. 1749–1755.
[23] Akpinar, E. K., and Dincer, I., 2005, "Application of Moisture Transfer Models to Solids Drying," Proc. Inst. Mech. Eng., Part A, **219**, pp. 235–244.
[24] Kaya, A., Aydin, O., and Dincer, I., 2007, "Numerical Modeling of Forced Convection Drying of Cylindrical Moist Objects," Numer. Heat Transfer, Part A, **51**, pp. 843–854.
[25] Sahin, A. Z., and Dincer, I., 2002, "Graphical Determination of Drying Process and Moisture Transfer Parameters for Solids Drying," Int. J. Heat Mass Transfer, **45**, pp. 3267–3273.
[26] Feng, H., Tang, J., and Dixon-Warren, J., 2000, "Determination of Moisture Diffusivity of Red Delicious Apple Tissues by Thermogravimetric Analysis," Drying Technol., **18**, pp. 1183–1199.
[27] Hussain, M. M., and Dincer, I., 2003, "Two-Dimensional Heat and Moisture Transfer Analysis of a Cylindrical Moist Object Subjected to Drying: A Finite-Difference Approach," Int. J. Heat Mass Transfer, **46**, pp. 4033–4039.
[28] Sahin, A. Z., Dincer, I., Yilbas, B. S., and Hussain, M. M., 2002, "Determination of Drying Times for Regular Multi-Dimensional Objects," Int. J. Heat Mass Transfer, **45**, pp. 1757–1766.
[29] Kondjoyan, A., 2006, "A Review on Surface Heat and Mass Transfer Coefficients During Air Chilling and Storage of Food Products," Int. J. Refrig., **29**, pp. 863–875.
[30] Dincer, I., and Hussain, M. M., 2002, "Development of a New Bi–Di Correlation for Solids Drying," Int. J. Heat Mass Transfer, **45**, pp. 3065–3069.
[31] Araszkiewicz, M., Koziol, A., Lupinska, A., and Lupinski, M., 2007, "Microwave Drying of Various Shape Particles Suspended in an Air Stream," Transp.

Porous Media, **66**, pp. 173–186.
[32] McMinn, W. A. M., and Magee, T. R. A., 1996, "Air Drying Kinetics of Potato Cylinders," Drying Technol., **14**, pp. 2025–2040.
[33] Gögus, F., and Maskan, M., 1999, "Water Adsorption and Drying Characteristics of Okra (Hibiscus Esculenuts L.)," Drying Technol., **17**, pp. 883–894.
[34] Panagiotou, N. M., Krokida, M. K., Maroulis, Z. B., and Saravacos, G. D., 2004, "Moisture Diffusivity: Literature Data Compilation for Foodstuffs," Int. J. Food Prop., **7**, pp. 273–299.
[35] Incropera, F. P., and De Witt, D. P., 1990, *Fundamentals of Heat and Mass Transfer*, Wiley, New York.
[36] 2005, ANSYS-CFX User Manual.
[37] Kaya, A., Aydin, O., and Dincer, I., 2006, "Numerical Modeling of Heat and Mass Transfer During Forced Convection Drying of Rectangular Moist Objects," Int. J. Heat Mass Transfer, **49**, pp. 3094–3103.
[38] Krokida, M. K., Foundoukidis, E., and Maroulis, Z., 2004, "Drying Constant: Literature Data Compilation for Foodstuffs," J. Food. Eng., **61**, pp. 321–330.
[39] Simal, S., Rossell, C., Berna, A., and Mulet, A., 1998, "Drying of Shrinking Cylinder-Shaped Bodies," J. Food. Eng., **37**, pp. 423–435.
[40] Kawaguti, M., and Jain, P., 1966, "Numerical Study of a Viscous Fluid Flow Past a Circular Cylinder," J. Phys. Soc. Jpn., **61**, pp. 1998–2055.
[41] Biswas, G., and Sarkar, S., 2009, "Effect of Thermal Buoyancy on Vortex Shedding Past a Circular Cylinder in Cross-Flow at Low Reynolds Numbers," Int. J. Heat Mass Transfer, **52**, pp. 1897–1912.
[42] Takami, H., and Keller, H. B., 1969, "Steady Two-Dimensional Viscous Flow of an Incompressible Fluid Past a Circular Cylinder," Phys. Fluids, **12**, pp. II-51–II-56.
[43] Dennis, S. C. R., and Chang, G.-Z., 1970, "Numerical Solutions for Steady Flow Past a Circular Cylinder at Reynolds Numbers up to 100," J. Fluid Mech., **42**, pp. 471–489.
[44] Zukauskas, A., and Ziugzda, J., 1985, *Heat Transfer of a Cylinder in Crossflow*, Hemisphere, New York.
[45] Schönauer, W., 1964, "Ein Differenzenverfahren zur Lösung der Grenzschichtgleichung für Stationäre, Laminare, Inkompressible Strömung," Ing.-Arch., **33**, pp. 173.
[46] Jafroudi, H., and Yang, H. T., 1986, "Steady Laminar Forced Convection From a Circular Cylinder," J. Comput. Phys., **65**, pp. 46–56.
[47] Apelt, C. J., and Ledwich, M. A., 1979, "Heat Transfer in Transient and Unsteady Flows Past a Circular Cylinder in the Range $1<\mathrm{Re}<40$," J. Fluid Mech., **95**, pp. 761–777.
[48] Ozalp, A. A., and Umur, H., 2003, "An Experimental Investigation of the Combined Effects of Surface Curvature and Streamwise Pressure Gradients Both in Laminar and Turbulent Flows," Heat Mass Transfer, **39**, pp. 869–876.
[49] Umur, H., and Ozalp, A. A., 2006, "Fluid Flow and Heat Transfer in Transitional Boundary Layers: Effects of Surface Curvature and Free Stream Velocity," Heat Mass Transfer, **43**, pp. 7–15.
[50] Ozalp, A. A., 2009, "Entropy Analysis of Laminar Forced Convection in a Pipe With Wall Roughness," Int. J. Exergy, **6**, pp. 249–275.
[51] Ozalp, A. A., 2008, "Roughness Induced Forced Convective Laminar-Transitional Micropipe Flow: Energy and Exergy Analysis," Heat Mass Transfer, **45**, pp. 31–46.
[52] Obot, N. T., 2002, "Toward a Better Understanding of Friction and Heat/Mass Transfer in Microchannels—A Literature Review," Microscale Thermophys. Eng., **6**, pp. 155–173.
[53] Turner, A. B., Hubbe-Walker, S. E., and Bayley, F. J., 2000, "Fluid Flow and Heat Transfer Over Straight and Curved Rough Surfaces," Int. J. Heat Mass Transfer, **43**, pp. 251–262.

Performance of Aluminum and Carbon Foams for Air Side Heat Transfer Augmentation

Patrick T. Garrity

James F. Klausner[1]
e-mail: klaus@ufl.edu

Renwei Mei

Department of Mechanical and Aerospace Engineering,
University of Florida,
Gainesville, FL 32611

The air side heat transfer performance of three aluminum foam samples and three modified carbon foam samples are examined for comparison with multilouvered fins often found in compact heat exchangers. The aluminum foam samples have a bulk density of 216 kg/m^3 with pore sizes of 0.5, 1, and 2 mm. The modified carbon foam samples have bulk densities of 284, 317, and 400 kg/m^3 and machined flow passages of 3.2 mm in diameter. The samples were placed in a forced convection arrangement using a foil heater as the heat source and ambient air as the sink. A constant heat flux of 9.77 kW/m^2 is applied throughout the experiments with the mean air velocity ranging from 1 to 6 m/s as the control parameter. The steady volume-averaged momentum equation and a two-equation nonequilibrium heat transfer model are employed to extract the volumetric heat transfer coefficients. Pressure drop measurements are correlated with the Darcy–Forcheimer relation. Empirical heat transfer correlations for the aluminum and carbon foam samples are provided. Using a hypothetical heat exchanger considering only the thermal resistance between the ambient air and the outer tube wall, the air side performance for each sample is modeled based on the local heat transfer coefficients and friction factors obtained from experiments. The performance of each sample is evaluated based on a coefficient of performance (COP, defined as the ratio of the total heat removed to the electrical input of the blower), compactness factor (CF, defined as the total heat removed per unit volume), and power density (PD, defined as the total heat removed per unit mass). Results show the carbon foam samples provide significant improvement in CF but the COP and PD are considerably lower than that for comparable multilouvered fin heat exchangers. [DOI: 10.1115/1.4002172]

Keywords: porous foam, heat transfer augmentation, heat exchanger performance

1 Introduction

Improving condenser and evaporator performance has been a widely studied topic in the context of compact and efficient heat exchanger design. It has been a subject of interest in the process, cryogenic, power, refrigeration, and air conditioning industries, among others. While air flow heat exchangers have been in use by industry for many years, new challenges arise and opportunities for performance enhancement persist. Since most air cooled heat exchangers are limited in performance by the thermal resistance on the air side, focus has been on advancing the air side capabilities. This is achieved by increasing the heat transfer surface area in contact with the flowing air or by increasing the heat transfer coefficient. In many applications it is common to use a louvered fin that acts to break up the thermal boundary layer and improve net heat transfer with an increase in both surface area and heat transfer coefficient [1]. While densely packed louvered fins will greatly enhance heat transfer, the increased pressure drop can make such a configuration undesirable due to increased pumping power. Typically, there is an optimum spacing that represents a tradeoff between enhanced heat transfer and increased pumping power requirements.

Another approach to enhancing the air side heat transfer rate is to replace the fins with a high thermal conductivity porous structure. These structures are capable of increasing the heat exchange surface area while producing a tortuous flow path that breaks up the thermal boundary layer and enhances the heat transfer coefficient. However, the pressure drop across the porous media is amplified, as a result, and increased pumping power is required.

Numerous experiments have considered forced convective air heat transfer enhancement associated with porous metal foams. In general, the experiments can be categorized as those that measure a bulk heat transfer coefficient and those that measure the interstitial heat transfer coefficient. The bulk heat transfer coefficient is defined as the ratio of the surface heat flux to the difference in temperature between the heater wall and inlet air temperature. Convective air bulk heat transfer coefficient measurements for porous metal foams were reported by Hsieh et al. [2], Haak et al. [3], Kim et al. [4], and Tzeng [5]. While such measurements may be useful to test a specialized geometry and flow configuration, their utility is generally limited.

The other approach is to treat the metallic foam as flow through a porous media and solve the solid and fluid coupled energy equations to extract the interstitial heat transfer coefficients from the measured thermal fields. This approach was pursued by Calmidi and Mahajan [6], Jeng et al. [7], and Hwang et al. [8]. The advantage to this approach is that the interstitial heat transfer coefficient only depends on the local interstitial geometry of the metallic foam. Thus, the results may be combined with a solution of the solid and fluid coupled energy equation to analyze porous foam heat exchangers with any arbitrary geometry. Analyses of this type are reported by Lu et al. [9] and Zhao et al. [10].

This paper considers the heat transfer augmentation provided by porous metal foams and compares them against conventional louvered fins. Three types of aluminum and three types of carbon foam are considered. An experimental facility has been set up to measure the pressure drop and volumetric heat transfer coefficient with air flow velocities ranging from 1 to 6 m/s. The Darcy–

[1]Corresponding author.

Contributed by the Heat Transfer Division of ASME for publication in the JOURNAL OF HEAT TRANSFER. Manuscript received March 12, 2009; final manuscript received June 14, 2010; published online September 17, 2010. Associate Editor: Srinivas Garimella.

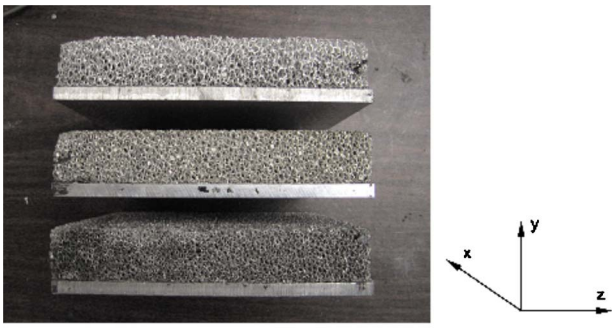

(*a*)

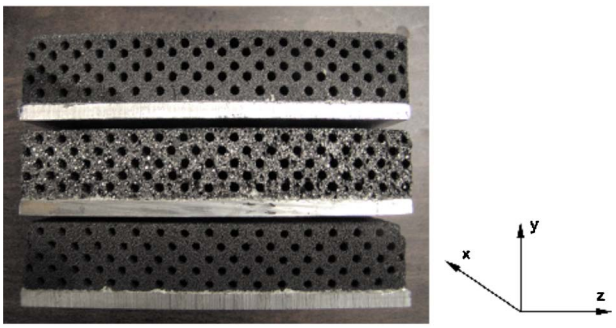

(*b*)

Fig. 1 Foam samples: (*a*) aluminum, 10 PPI, 20 PPI, and 40 PPI (from top to bottom) and (*b*) carbon, L1A, D1, and L1 (from top to bottom)

Forcheimer equation is used to correlate the pressure drop data. The Nusselt number is correlated with Reynolds number based on appropriate length scales. Due to very significant differences in the porous structures, different correlations are used for the aluminum and carbon foams. For comparison against conventional louvered fins, a hypothetical heat exchanger is analyzed and the performance is determined based on a coefficient of performance (COP), compactness factor (CF), and power density (PD).

2 Experimental Facility

Three different aluminum foam samples manufactured by Energy Research and Generation Inc. are studied here along with three carbon foam samples manufactured by Koppers, Inc. The foam samples are shown below in Figs. 1(*a*) and 1(*b*) and the properties are listed in Table 1. The aluminum foams are identified by the manufacturer according to pore density with values of 10 pores per inch (PPI), 20 PPI, and 40 PPI. The bulk density of all aluminum foam samples is 216 kg/m^3. The pore sizes for the 10 PPI, 20 PPI, and 40 PPI aluminum foams are 0.5 mm, 1 mm, and 2 mm, respectively. The three carbon foam samples are identified by the manufacturer as L1, D1, and L1A. The respective pore sizes according to the manufacturer are 600 μm, 650 μm, and 500 μm. Due to the small pore size and large pressure drop required to convey air through the carbon foams, they were modified by machining cylindrical air passages in the axial direction. In each case, 80 passages, 6.7 mm apart, each with a diameter of 3.2 mm, were machined into the foam providing for a uniform, homogeneous geometry. The modified L1, D1 and L1-A, foams have bulk densities of 317 kg/m^3, 400 kg/m^3, and 284 kg/m^3, respectively. Due to the large ratio of passage diameter to pore diameter, there is not a large pressure drop variation between carbon foam samples. It is assumed throughout the analysis that convection heat transfer is dominated by air flow through the machined passages. Therefore, the same surface area per unit volume a for each carbon foam sample is 5.24 m^{-1} and the porosity based on the flow passages is 0.166.

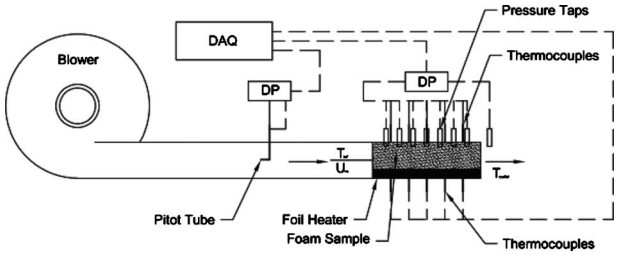

Fig. 2 Experimental facility used to measure the heat transfer augmentation performance of carbon and aluminum foams in a convection arrangement

The experimental facility displayed in Fig. 2 is used to measure the pressure drop and heat transfer coefficient with air blowing through the foam. As shown, a variable speed blower forces air through the foam sample in which a 15.24×15.24 cm^2 aluminum plate is bonded to the foam using S-bond material while the upper surface is insulated with 2.54 cm thick elastomeric foam. A 15.24×15.24 cm^2 foil heater is in contact with the bottom side of the aluminum plate. Five type E thermocouples are embedded into the aluminum plate to measure the lower wall temperature while five more type E thermocouples are located axially along the top surface of the foam to measure the upper wall temperature. The upper wall temperature is used in this analysis instead of the lower wall temperature in order to eliminate the error associated with contact resistance between the heater and the foam. The foam sample is $15.24 \times 15.24 \times 2.54$ cm^3 in volume. Validyne differential pressure transducers measure the pressure drop across the foam. Seven pressure taps are located axially along the foam sample to measure the pressure variation along the channel. A pitot tube is positioned within the air duct leading to the foam sample and a Validyne differential pressure transducer measures the pressure drop across the pitot tube to determine the mean air flow rate. All analog signals are captured using a digital data acquisition system consisting of a measurement and computing CIO-EXP32 multiplexer and PCIM-DAS1602 16 bit analog to digital converter. A custom algorithm was developed to convert measured voltages to pressure, temperature, and velocity.

The experimental facility is used to measure the heat transfer coefficient and pressure drop for each foam sample at different

Table 1 Carbon and aluminum foam properties

Foam sample	K (m^2)	C_F	ε	ε_p	d_p (m)	k_{se} (W/m K)	a (m^{-1})
40 PPI	6.98×10^{-9}	0.020	0.918	NA	5.08×10^{-4}	9.78	2760
20 PPI	1.21×10^{-8}	0.021	0.918	NA	1.02×10^{-3}	9.78	1770
10 PPI	1.98×10^{-8}	0.027	0.918	NA	2.03×10^{-3}	9.78	804
L1-A	1.66×10^{-8}	0.034	0.166	0.806	5×10^{-4}	48.6	5.24
D1	1.66×10^{-8}	0.034	0.166	0.752	6.5×10^{-4}	97.2	5.24
L1	1.66×10^{-8}	0.034	0.166	0.735	6×10^{-4}	61.8	5.24

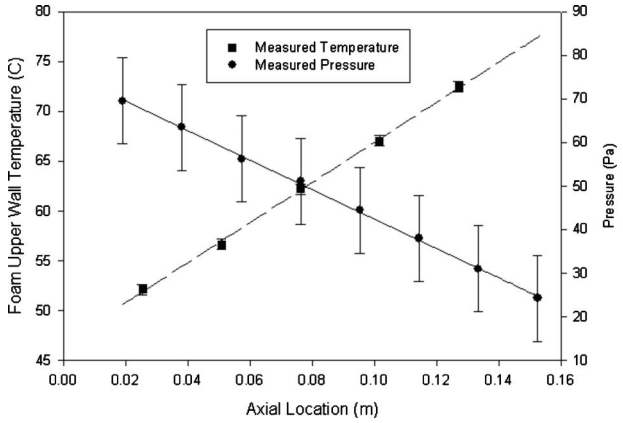

Fig. 3 Axial pressure and upper wall temperature variation for 10 PPI aluminum foam sample u_m=1.13 m/s

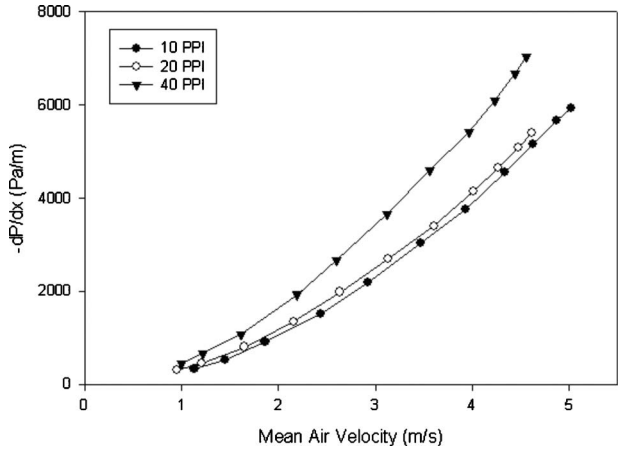

Fig. 5 Aluminum foam pressure gradient variation with respect to mean air velocity

velocity increments. The pressure drop is measured adiabatically. Throughout the heat transfer experiments, the heat flux remains fixed at 9.77 kW/m^2 and the mean air velocity is increased in increments. The mean velocity ranges from approximately 1–6 m/s for the pressure drop and heat transfer experiments, beyond which point there is a substantial increase in pressure drop and only a marginal increase in the heat transfer rate. At each velocity increment, the upper foam temperature is observed until steady state is reached, at which point 500 data points are sampled at 1 Hz. The measurement is repeated five times to insure repeatability. The mean air velocity is then increased and the procedure is repeated. The uncertainty in temperature and pressure drop are estimated to be ± 0.5°C and ± 32 Pa, respectively.

3 Experimental Results

The axial pressure variation for the 10 PPI aluminum foam sample is shown in Fig. 3 operating with a mean velocity u_m =1.13 m/s. The observed linear variation is indicative of fully developed flow. For each foam sample considered, the measured pressure gradients are measured and tabulated in Garrity [11] and are also displayed in Figs. 4 and 5 with varying air velocity. In Fig. 3, the error bars are placed on the pressure measurements. It is observed that the pressure gradient is essentially constant, which is indicative of fully developed flow over the length of the foam sample. As expected, the pressure gradient increases parabolically with increasing air velocity as observed in Figs. 4 and 5.

The pressure gradient for carbon and aluminum foams may be correlated using the Darcy–Forcheimer equation [12].

$$-\frac{dP}{dx} = \frac{\mu_{fl}}{K}u_m + \frac{\rho_{fl}C_F}{\sqrt{K}}u_m^2 \tag{1}$$

where K is the permeability, C_F is a dimensionless parameter that accounts for inertia effects, and u_m is the mean velocity. C_F and K, shown in Table 1, are determined from the tabulated pressure drop data by fitting the data to Eq. (1). Since the porosity and form coefficient are properties of the porous media, adiabatic measurements are adequate and changes in temperature are accounted for in the fluid density and viscosity in Eq. (1). In the case of carbon foam, the difference in the pressure drop between data samples is not large because the majority of air flows through the machined passages. The small difference is attributed to flow through the interstitial pores. Figure 5 shows the pressure drop for the aluminum foams increases with decreasing pore size. The foam upper wall axial temperature profile is shown in Fig. 3 for the 10 PPI sample operating at u_m=1.13 m/s. The wall temperature gradient shown in Fig. 3 is used to determine the sensible heat transfer to the fluid, which is compared against the measured heat input to confirm an energy balance. The upper wall temperature of each foam sample at x=7.62 cm is plotted versus mean fluid velocity in Fig. 6 and also shown in Table 2. As expected, the wall temperature decreases with increasing air velocity. The upper wall temperature profiles of the three aluminum foams appear to be

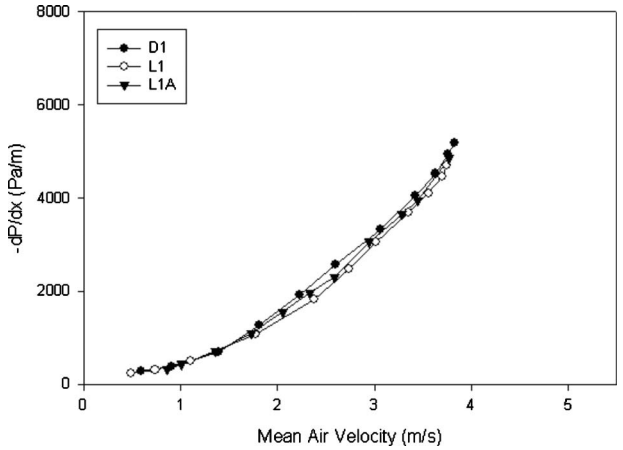

Fig. 4 Carbon foam pressure gradient variation with respect to mean air velocity

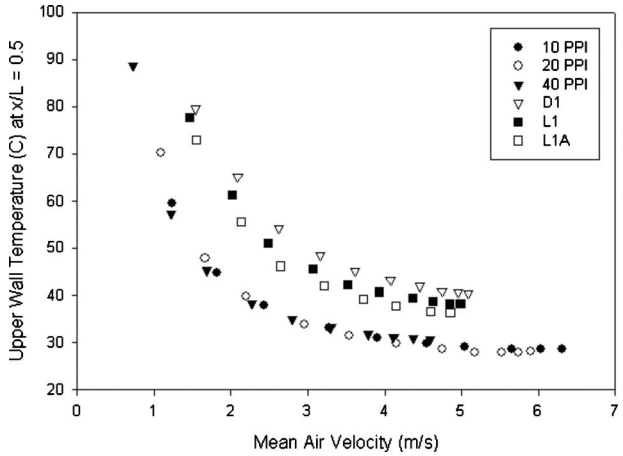

Fig. 6 Foam upper wall temperature variation with respect to mean air velocity for all carbon and aluminum foam samples

Table 2 Volumetric heat transfer coefficient and upper wall temperature for each carbon/aluminum foam

L1A			D1			L1		
u_m (m/s)	h_v (W/m^3 K)	$T_{w,u}$ (°C)	u_m (m/s)	h_v (W/m^3 K)	$T_{w,u}$ (°C)	u_m (m/s)	h_v (W/m^3 K)	$T_{w,u}$ (°C)
1.6	12,400	73.0	1.5	10,100	79.6	1.5	10,500	77.6
2.1	20,500	55.6	2.1	13,600	65.2	2.0	15,100	61.4
2.6	32,500	46.2	2.6	19,400	54.2	2.5	21,700	51.0
3.2	39,500	42.1	3.2	24,100	48.4	3.1	27,100	45.7
3.7	46,400	39.3	3.6	27,800	45.1	3.5	31,800	42.3
4.2	50,400	37.8	4.1	29,800	43.2	3.9	34,000	40.7
4.6	54,300	36.6	4.5	32,200	42.0	4.4	36,400	39.4
4.9	54,400	36.2	4.8	33,700	40.8	4.6	37,300	38.6
10 PPI			20 PPI			40 PPI		
u_m (m/s)	h_v (W/m^3 K)	$T_{w,u}$ (°C)	u_m (m/s)	h_v (W/m^3 K)	$T_{w,u}$ (°C)	u_m (m/s)	h_v (W/m^3 K)	$T_{w,u}$ (°C)
1.2	12,900	59.4	1.1	15,500	70.2	0.7	23,000	88.7
1.8	26,800	44.7	1.7	35,800	47.8	1.2	42,200	57.4
2.4	45,300	37.8	2.2	58,200	39.8	1.7	66,700	45.3
3.3	70,000	33.1	3.0	105,000	33.9	2.3	104,000	38.3
3.9	89,100	31.0	3.5	155,000	31.3	2.8	138,000	35.0

similar. At low velocity an incremental increase in velocity results in a large drop in foam wall temperature and a moderate increase in pressure drop. However, at relatively high air velocities, an incremental change in velocity results in a large increase in pressure drop and only moderate decrease in foam temperature.

4 Heat Transfer Analysis

In order to extract the local heat transfer coefficient from the measured foam temperatures, the steady volume-averaged momentum equation and a two-equation nonequilibrium heat transfer model is employed. In this analysis it is assumed that all thermophysical properties of the solid and fluid are independent of temperature. The foams are modeled as homogenous porous media and the effects of radiation, natural convection, and thermal dispersion are negligible [7]. The governing conservation equations are expressed as follows [9,12].

Momentum

$$-\nabla P - \frac{\mu}{K}\vec{V} + \frac{\mu}{\varepsilon}\nabla^2\vec{V} - \frac{\rho_{fl}C_F}{\sqrt{K}}|\vec{V}|\vec{V} = 0 \tag{2}$$

Energy (solid)

$$(1-\varepsilon)k_s\nabla^2 T_s + h_{sf}a(T_{fl} - T_s) = 0 \tag{3}$$

Energy (fluid)

$$\rho_{fl}C_{p,fl}\boldsymbol{V}\cdot\boldsymbol{\nabla}T_{fl} = \varepsilon k_{fl}\nabla^2 T_{fl} + h_{sf}a(T_s - T_{fl}) \tag{4}$$

where μ_{fl} is the dynamic viscosity of the fluid, ε is the porosity, K is the permeability, h_{sf} is the interstitial heat transfer coefficient, and a is the surface area per unit volume for the porous material. The product of h_{sf} and a is the volumetric heat transfer coefficient h_v. Here, ρ_{fl} and $C_{p,fl}$ are the respective density and specific heat of the fluid while k_{fl} and k_s are the thermal conductivity of the fluid and solid, respectively.

During the experiments, the upper wall of the foam test section is insulated with 2.54 cm thick elastomeric foam. The boundary conditions are $u(y=0)=0$, $u(y=H)=0$, $-k_{se}(\partial T_s/\partial y)|_{y=0} - k_{fe}(\partial T_f/\partial y)|_{y=0} = q_w$, $k_{se}(\partial T_s/\partial y)|_{y=H} + k_{fe}(\partial T_f/\partial y)|_{y=H} = 0$, $T_f(x=0)=T_\infty$, $(\partial^2 T_f/\partial x^2)|_{x=0}=0$, $(\partial^2 T_s/\partial x^2)|_{x=0}=0$, and $(\partial^2 T_s/\partial x^2)|_{x=L}=0$. The following dimensionless variables are introduced [6,9].

$\theta=(T-T_\infty/q_w L/k_{se})$, $x'=x/L$, $y'=y/L$, $U=u/u_m$, $\mathrm{Da}_K = 4K/\varepsilon H^2$, $\lambda=\varepsilon^{1/2}C_F(u_m H/2\nu_{fl})$, $\mathrm{Bi}=(ha_{sf}L^2/k_s)$, $\mathrm{Re}_L=(u_\infty L/\nu_{fl})$, $\mathrm{Re}_K=(u_m\sqrt{K}/\nu_{fl})$, $\mathrm{Pr}=(\nu_{fl}/\alpha_{fl})$, and $\mathrm{St}=(ha_{sf}L/\rho_{fl}C_{p,fl}u_m)$ where u and u_m are the respective local and mean velocities, q_w is the applied heat flux along the lower wall, and $k_{fe}=\varepsilon k_{fl}$ and $k_{se}=(1-\varepsilon)k_s$ are the effective thermal conductivities of the respective fluid and solid. Conservation equations (2)–(4) are nondimensionalized as

$$\left(\frac{H}{2L}\right)^2\frac{\partial^2 U}{\partial y'^2} = \frac{1}{\mathrm{Da}_K}(U-1) + \frac{\lambda}{\sqrt{\mathrm{Da}_K}}(U^2-1) \tag{5}$$

$$\frac{\partial^2\theta_s}{\partial x'^2} + \frac{\partial^2\theta_s}{\partial y'^2} + \mathrm{Bi}(\theta_{fl}-\theta_s) = 0 \tag{6}$$

$$\frac{1}{\varepsilon}U\frac{\partial\theta_{fl}}{\partial x'} = \frac{1}{\mathrm{Re}_L\,\mathrm{Pr}}\left(\frac{\partial^2\theta_{fl}}{\partial x'^2} + \frac{\partial^2\theta_{fl}}{\partial y'^2}\right) + \frac{\mathrm{St}}{\varepsilon}(\theta_s - \theta_{fl}) \tag{7}$$

with boundary conditions $U(y'=0)=0$, $U(y'=H/L)=0$, $(\partial\theta_s/\partial y')|_{y'=0} + (k_{fe}/k_{se})(\partial\theta_f/\partial y')|_{y'=0} = -1$, $(\partial\theta_s/\partial y')|_{y'=H/L} + k_{fe}/k_{se}(\partial\theta_{fl}/\partial y')|_{y'=H/L}=0$, $\theta_{fl}(x'=0)=0$, $(\partial^2\theta_{fl}/\partial x'^2)|_{x'=0}=0$, $(\partial^2\theta_{fl}/\partial x'^2)|_{x'=1}=0$, and $(\partial^2\theta_s/\partial x'^2)|_{x'=1}=0$. The exact solution to the momentum equation has been provided by Vafai and Kim [12] for a slightly modified coordinate system. The exact solution does not apply to the current coordinate system, and a numerical solution for Eq. (5) is used to evaluate the velocity profile subject to a no-slip condition at the upper and lower surfaces of the foam. Solutions to the energy conservation equations were obtained using the Thomas algorithm [13]. For the values of $u_m=0.86$ m/s, $\lambda=1113.7$, $C_f=0.027$ $\mathrm{Da}_K=4.71\times10^{-5}$, $\mathrm{Re}_k=3.67$, $\mathrm{Pr}=0.71$, $\mathrm{St}=9.2$, $\varepsilon=0.92$, and $\mathrm{Bi}=117$, the computed dimensionless velocity profile is shown in Fig. 7 while the dimensionless solid and fluid temperatures are shown in Figs. 8(*a*) and 8(*b*). These dimensionless variables are typical of those falling within the experimental parameter space. As observed, the velocity is uniform along the centerline with a value close to the mean velocity and reduces to zero at the wall where the no-slip boundary condition is imposed. The nearly identical values for centerline and mean velocity suggest that the presence of porous media homogenizes the flow. The solid foam temperature decreases monotonically in the y-direction and increases linearly in the x-direction as expected due to the imposed heat flux boundary on the bottom surface along with the insulated boundary on the upper surface. The fluid temperature initially decreases in the y-direction while increasing in the x-direction as the sensible heat increases in the axial direction.

When solving Eqs. (6) and (7) the heat transfer coefficient is not known a priori. Therefore, a guess is made for the heat transfer coefficient h_{sf} and solutions for Eqs. (6) and (7) yield θ_s and

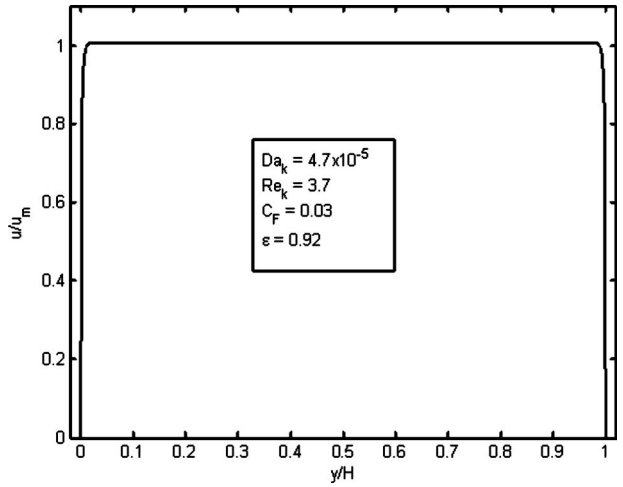

Fig. 7 Dimensionless velocity profile of air flowing through the channel

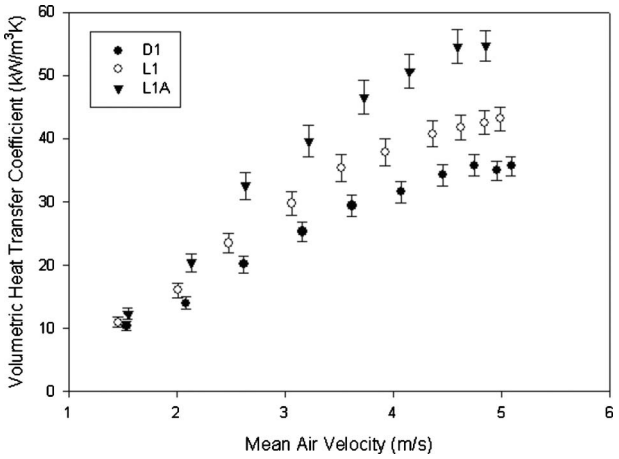

Fig. 9 Carbon foam volumetric heat transfer coefficient variation with respect to mean fluid velocity

θ_{fl}. The upper foam temperature measured at $x=L/2$ is compared with that computed using the guessed value for h_{sf}. If agreement is achieved, the guessed heat transfer coefficient is correct. If they do not agree, a new guess is made for the heat transfer coefficient and the computation is repeated until agreement is achieved. In cases where the mean air velocity is large, the solid foam and air are in near "thermal equilibrium." Thus, large errors arise when extracting the volumetric heat transfer coefficients since most thermal transport is due to conduction through the porous medium. In such cases, a small change in the measured foam upper wall temperature can result in a large change in the computed volumetric heat transfer coefficients.

5 Results

The volumetric heat transfer coefficients $h_v=h_{sf}a$ are computed for each of the six foams and are summarized in Table 2. Variations in volumetric heat transfer coefficient with mean air velocity are shown in Figs. 9 and 10. The aluminum foams have the largest volumetric heat transfer coefficient. The aluminum foams are capable of handling a large heat load because they have large specific surface areas and large effective thermal conductivities. The measured volumetric heat transfer coefficients for the aluminum foams are on the same order as those reported by Hwang et al. [8]. In order to correlate the volumetric heat transfer data, the permeability based Nusselt number is introduced $\mathrm{Nu}_K=(h_v\sqrt{K/a})/k_{fl}$. Figure 11 shows the Nusselt number as a function of the Reynolds number $\mathrm{Re}_K=(u_m\sqrt{K}/\nu_{fl})$, for the three aluminum foams. It is observed that the data are well collapsed for relatively low air velocity. At high air velocity, the solid and the fluid are in the near thermal equilibrium and a large error in the extracted heat transfer coefficient results. The error in the correlation at high velocities

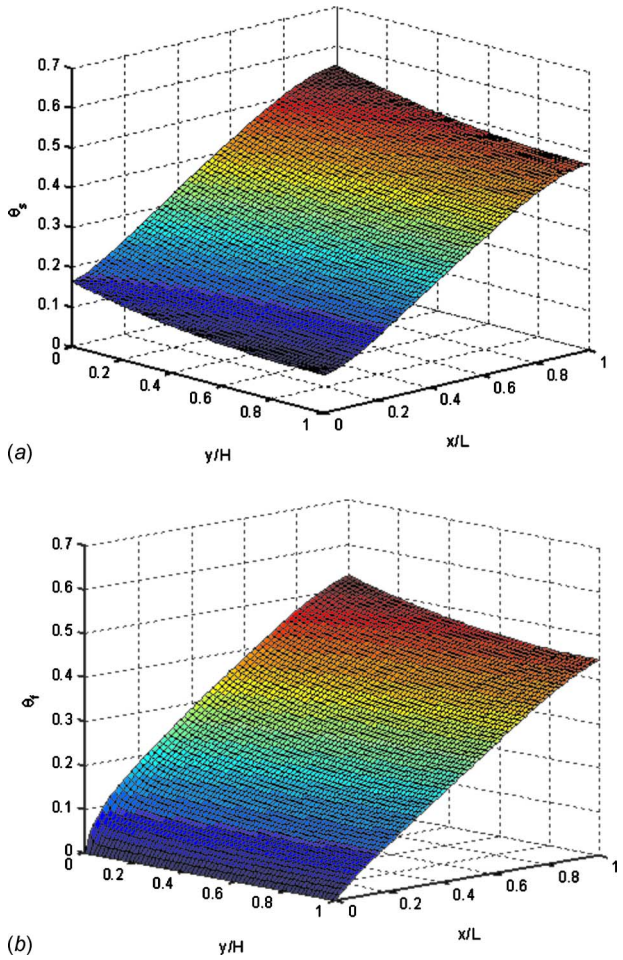

Fig. 8 Dimensionless temperature profiles within the channel: (*a*) solid and (*b*) fluid

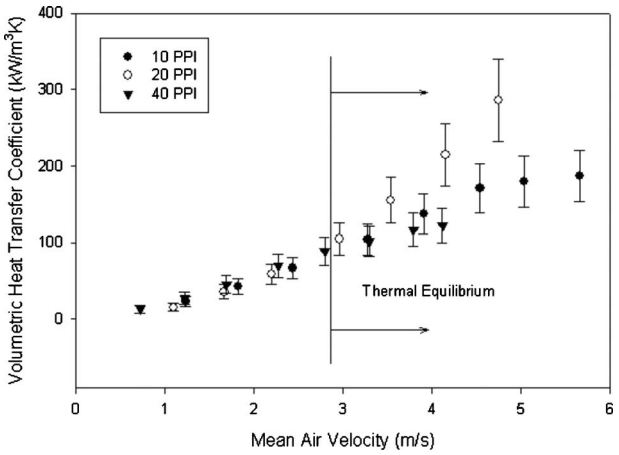

Fig. 10 Aluminum foam volumetric heat transfer coefficient variation with respect to mean fluid velocity

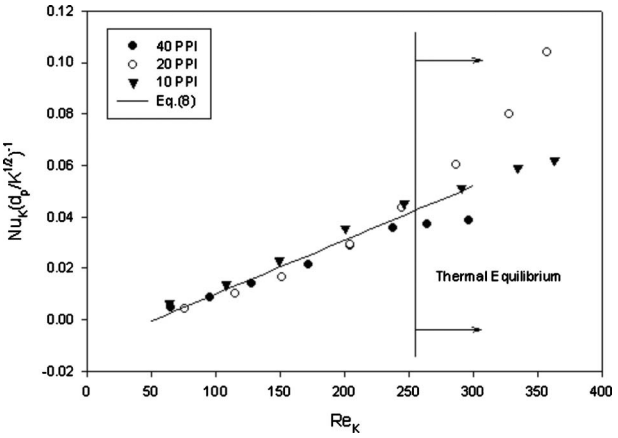

Fig. 11 Nusselt number correlation for aluminum foams showing a transition to thermal equilibrium conditions

has a minimal effect on the computed solid temperature profile since thermal equilibrium conditions minimize convective thermal transport. Overall, the correlation allows for an accurate prediction of wall temperature for the full range of air velocities investigated here. For $Re_k > 50$, the aluminum foam Nusselt number may be expressed as

$$Nu_K = \frac{d_p}{\sqrt{K}}\left[\frac{Re_K}{4887} - 0.01\right] \tag{8}$$

If it is assumed that all of the air passes through the machined channels for the carbon foam samples, ideally each foam sample should have the same volumetric heat transfer coefficient at the same Reynolds number. However, variations in the data are observed. These are explained by the fact that some air passes through the smaller interstitial pores of the foam, thus, convecting heat through the pores. It is reasonable to expect that the data can be correlated using the pore diameter. Figure 12 shows the product of the Nusselt number $Nu_D = (h_v D/k_{fl})$ and $(D/d_p)^{-3/2}$ as a function of Reynolds number $Re_D = u_m D/\nu_{fl}$ for the three carbon foams. As observed, the data are also well correlated and the carbon foam Nusselt number may be expressed as

$$Nu_D = (D/d_p)^{3/2}(8.87\ Re_D^{1/2} - 355) \tag{9}$$

The relative error between the measured and predicted pressure drops and volumetric heat transfer coefficient for the aluminum and carbon foams are summarized in Table 3. As expected, the volumetric heat transfer coefficient is predicted with reasonable accuracy.

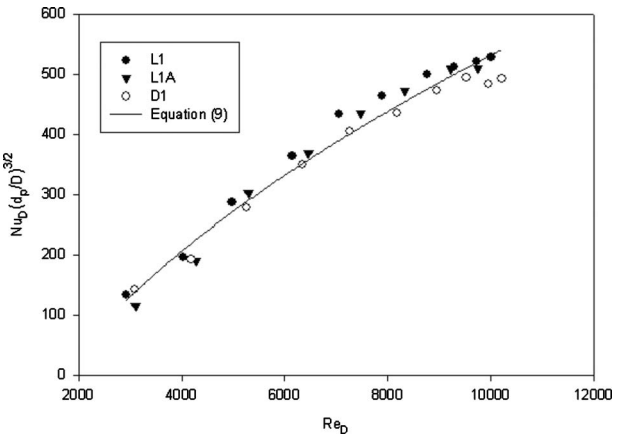

Fig. 12 Nusselt number correlation for carbon foams

Table 3 Relative error for pressure drop and Nusselt number correlations

	Relative error (dP/dz)	Relative error (Nu_k)
10 PPI (%)	4	5
20 PPI (%)	3	19
40 PPI (%)	5	5
L1A (%)	2	4
D1 (%)	9	5
L1 (%)	9	9

Comparing the pressure drops in Figs. 4 and 5 for the aluminum and carbon foams, it is observed that they are on the same order. However, comparing the volumetric heat transfer coefficients in Figs. 9 and 10, it is observed that those for the aluminum foams are significantly greater than those for the carbon foams. Although this may suggest better performance can be derived from the aluminum foams, this is not necessarily the case because the carbon foams have a higher effective thermal conductivity and a more careful assessment on performance is required. This is discussed in the next section. The addition of machined flow passages within the carbon foam results in a significant decrease in the volumetric heat transfer coefficient. These flow passages are necessary in order to reduce the pressure drop through the foam and not overburden the required pumping power. The size and number of the flow passages were chosen such that the pressure drop across the aluminum and carbon foams are on the same order. It is recognized that the size and number of flow passages used for the carbon foams may not yield optimum performance.

As mentioned, the engineering application of carbon foam for heat transfer augmentation requires the addition of flow passages in order to pass air with a reasonable pumping load. However, due to the significant disparity in length scales between the carbon pore structure and the flow passage diameter, it is expected that the interstitial heat transfer coefficient within the pore structure will vary significantly from that in the flow passage. This brings into question the validity of applying Eqs. (5)–(7) to the carbon foam structures. Here, is it understood that the extracted volumetric heat transfer coefficient for the carbon foam represents a mean with contributions from heat transport through the interstitial pores and the flow passages. The data are correlated well using Eq. (9), and the correlation provides a useful tool for comparing heat transfer augmentation performance of carbon foams with aluminum foams and louvered fins, as will be discussed next.

6 Hypothetical Heat Exchanger Performance

For comparison purposes, a hypothetical heat exchanger having specified dimensions is analyzed for each foam sample as well as for louvered fins. An illustration of the heat exchanger geometry is shown in Fig. 13. The louvered fin geometry shown in Fig. 13(*a*) is common in compact heat exchangers and can be further classified as multilouvered. The flat tube configuration has been chosen because it allows for enhanced performance. Fiebig et al. [14] showed that the heat exchanger element with flat tubes gives nearly twice as much heat transfer and only half as much pressure loss as the corresponding heat exchanger element with round tubes allowing for a more compact, efficient design. The foam geometry shown in Fig. 13(*b*) utilizes the same flat tube arrangement as the louvered fin case and is oriented such that the heat exchanger working fluid is in cross flow with the ambient air, as is the case with the louvered fins. Since the only difference in the two designs is the extended surface area between tubes, the configuration allows for a quantitative comparison between each foam sample and the louvered fins.

To determine which configuration or enhanced surface yields the best performance, it is important to first have a clear definition of what constitutes good performance. The ideal heat exchanger

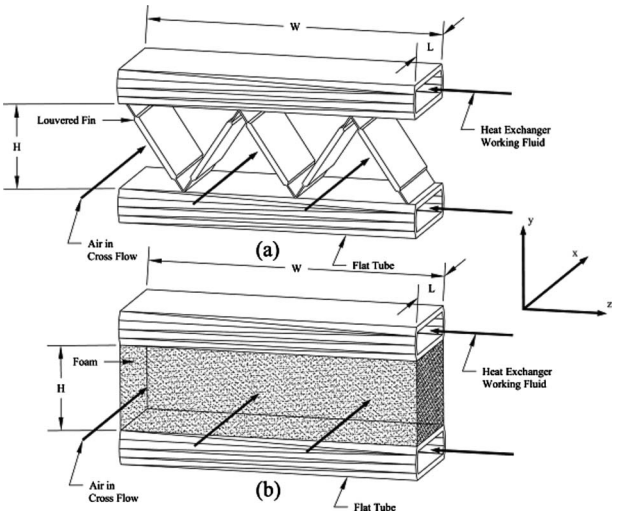

Fig. 13 Hypothetical heat exchanger in cross flow with (*a*) louvered fin and (*b*) carbon/aluminum foam configurations

will be compact in size and capable of removing the required heat load while consuming a minimal amount of electric energy from the blower. Since a more compact heat exchanger must often consume more energy than a less compact heat exchanger under the same heat load, it is important to base the performance on both power consumption and compactness so that the designer can choose an optimal configuration that best suits each specific application. Here, a quantitative evaluation for the performance of each foam sample is made based on a COP (defined as the ratio of the total heat removed to the electrical input of the blower), CF (defined as the total heat removed per unit volume), and PD (defined as the total heat removed per unit mass).

In order to predict the heat removal capabilities for the hypothetical heat exchanger shown in Fig. 14(*b*), the momentum equation for the fluid as well as the coupled energy equations for the solid and fluid are solved using Eqs. (2)–(4). The equations are normalized by the following scales $\theta=(T-T_\infty/T_w-T_\infty)$, $x'=x/L$, $y'=y/L$, and $U=u/u_m$, providing dimensionless equations identical to those shown in Eqs. (5)–(7), the only difference being in the dimensionless temperature θ. The hypothetical heat exchanger described here will have a constant wall temperature of 100°C and an ambient air stream entering at 25°C. By implementing a constant wall temperature, the hypothetical heat exchanger will emulate a configuration with zero thermal resistance from condensation of the inner working fluid on the inner tube wall. The wall temperature is chosen to emulate typical condensation of water at atmospheric pressure while the inlet air temperature is chosen based on typical ambient conditions. In practice, results may differ depending on the temperature difference between the working fluid and ambient air. To extrapolate these results, foam geometries must be carefully chosen. As the temperature difference decreases, the interstitial heat transfer term gets smaller in comparison to the conduction terms, approaching a thermal equilibrium condition. In such cases it may be beneficial to reduce length scales, such as foam height to eliminate material in regions where the heat transfer rates are marginal. Also, care must be given to the large Reynolds numbers encountered for the carbon foams. Typically, large Reynolds number flow can give rise to dispersion effects not accounted for in Eqs. (3) and (4). However, the large Reynolds numbers result from the large diameter of the machined flow passages. The flow through the interstitial foam structure is very low, and it is expected that dispersion effects will be significantly damped by the foam ligaments. Assuming a no-slip condition at the wall, the boundary conditions along the tube wall and the fluid at the inlet are as follows: $U(y'=0)=0$, $U(y'=H/L)=0$, $\theta_{fl}(x',y'=0)=\theta_s(x',y'=0)=1$, $\theta_{fl}(x',y'=H/L)=\theta_s(x',y'=H/L)=1$, $\theta_{fl}(x'=0,y')=0$, $(\partial^2\theta_{fl}/\partial x'^2)|_{x'=1}=0$, and $(\partial^2\theta_s/\partial x'^2)|_{x'=1}=0$. To simplify this analysis, only two tubes of the heat exchanger are considered in the analysis with heat transfer taking place along both boundaries of the foam, simulating a portion of the hypothetical heat exchanger shown in Fig. 14(*b*). Due to symmetry, only this portion of the heat exchanger needs to be computed.

Using the volumetric heat transfer coefficient taken from Eqs. (8) and (9), along with the permeability K and the inertia coefficient C_F taken from Table 1, the governing equations are solved and the temperature field is obtained. The total heat removed $\dot{Q}_{\text{removed}}$ is computed from

$$\dot{Q}_{\text{removed}}=\dot{m}C_{p,f}(T_{f,\text{out}}-T_{f,\text{in}})=2\left(-W\int_0^L(1-\varepsilon)k_s\left.\frac{\partial T_s}{\partial y}\right|_{y=0}dz-W\int_0^L(\varepsilon)k_f\left.\frac{\partial T_f}{\partial y}\right|_{y=0}dz\right) \quad (10)$$

while the pressure gradient is evaluated from Eq. (1). The electrical input to the blower is estimated as the product of the volumetric flow rate of air and the pressure drop.

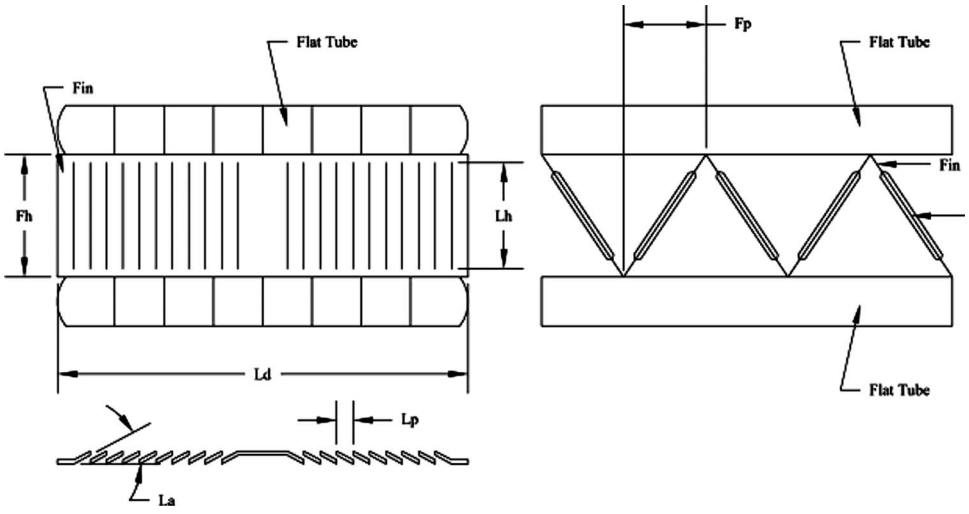

Fig. 14 Depiction of louvered fin geometric parameters

Table 4 Geometric parameters for louvered fin configuration

Fh (mm)	60	Fp (mm)	4
Lh (mm)	58	Lp (mm)	1.2
Ld (mm)	100	La (deg)	22

$$\dot{E}_{\text{input}} = u_m A_c \Delta P \tag{11}$$

where A_c is the frontal area of the heat exchanger seen by the ambient air stream. Finally, the COP, CF, and PD are evaluated as

$$\text{COP} = \frac{\dot{Q}_{\text{removed}}}{\dot{E}_{\text{input}}} \tag{12}$$

$$\text{CF} = \frac{\dot{Q}_{\text{removed}}}{V} \tag{13}$$

$$\text{PD} = \frac{\dot{Q}_{\text{removed}}}{m} \tag{14}$$

where V is simply the volume of the hypothetical heat exchanger and m is the mass.

For proper comparison, the heat removal capabilities of the louvered fins are to be obtained as well. Since there have been numerous experiments conducted on this subject, several correlations exist in literature that provide accurate approximations for the interstitial heat transfer coefficient and pressure drop. Dong et al. [15] provided a correlation for interstitial heat transfer coefficient as well as pressure drop based on a large database for multilouvered fins. Using the correlations provided by Dong et al. [15], the COP, CF, and PD are computed for the louvered fin heat exchangers and compared against those for each foam sample at different air velocities. The geometric parameters chosen to describe the louvered fin configuration are listed in Table 4 and depicted in Fig. 14. The bulk density of the louvered fins is estimated based on these geometric parameters to be 128 kg/m^3. The results of heat exchanger performance analysis are shown in Figs. 15–17 for the foam sample and louvered fin configurations.

Figure 15 shows that the multilouvered fin configuration is favorable over both the carbon and aluminum foam samples when COP is the main consideration. This is due to the added pressure drop resulting from the tortuous flow path for air flow through the foam. In the case of a louvered fin, several independent length scales exist that have an effect on COP including the fin pitch and louver pitch. A small fin pitch will increase surface area while a small louver pitch will break up the thermal boundary layer more frequently. By reducing both of these length scales, the heat removal should increase due to the increase in both surface area and heat transfer coefficient. However, this will also constrict the flow path and induce mixing, giving rise to an increase in pressure drop. These length scales may be controlled to design an optimum louvered fin configuration. In the case of flow through a homogeneous porous structure such as an aluminum foam, the length scales of importance are the pore diameter, and the ligament diameter, or more importantly, the square root of permeability. A more fundamental study on the flow structure within porous media is needed in order develop a designer foam, capable of producing COP comparable to conventional louvered fin configurations. A comprehensive flow study using the Lattice–Boltzmann method may provide insight into the optimal geometric length scales needed to improve overall foam performance, as the current foam structures do not yield comparable COP when compared with louvered fins.

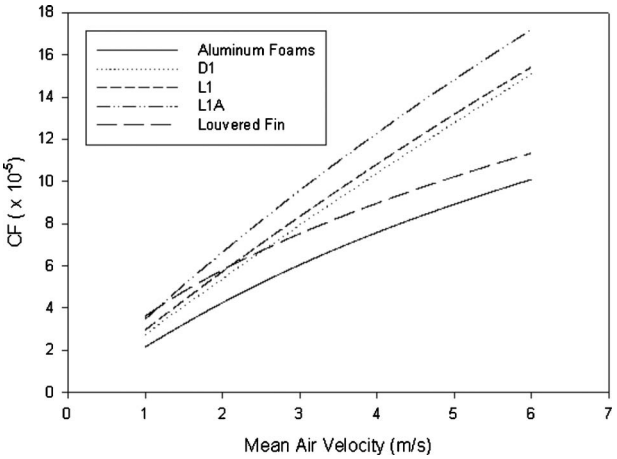

Fig. 16 Comparison of compactness factor for louvered fin and foam configurations

Figure 16 shows that the CF is highest for the D1 carbon foam sample. This is a result of several factors. One is the high thermal conductivity of the carbon foam that helps to increase the effective fin efficiency. Another is due to finite leakage through the pores, which provides a large surface area in contact with the air and a tortuous flow path that induces mixing. However, the power density is largest for the louvered fins, as seen in Fig. 17. This is due to the relatively low density of the louvered fin configuration. It is interesting to note that the CF for the carbon foam configuration increases steadily with increasing air velocity and in contrast the CF for the louvered fins does not increase as rapidly.

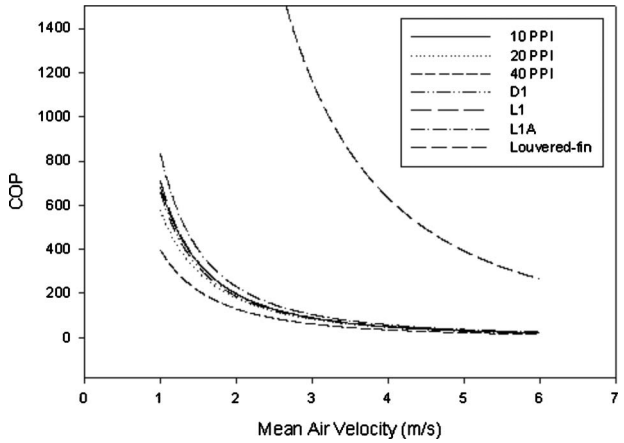

Fig. 15 Comparison of coefficient of performance for louvered fin and foam configurations

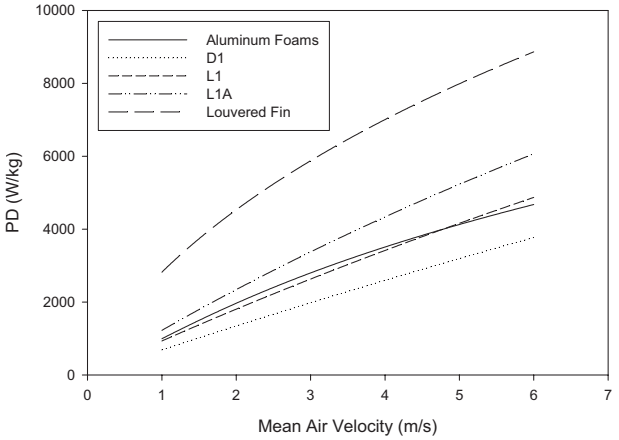

Fig. 17 Comparison of power density for louvered fin and foam configurations

Thus, at high air velocity the CF for the carbon foams is significantly higher than that for the louvered fins. This could be because at low fluid velocity, or low Reynolds number, the thermal boundary layer will be largest at which point it is advantageous to break up the boundary layer frequently. At high Reynolds number however, the boundary layer will be thinner, and the effects of the added mixing will be marginal. Therefore, it should be expected that a foam structure with a tortuous flow path will provide better heat transfer rates at low Reynolds number than the carbon foam configuration that is less effective in breaking up the thermal boundary layer since the majority of flow takes place within the machined passages.

7 Conclusion

The performance of three aluminum foam and three carbon foam samples have been evaluated for heat transfer augmentation. Correlations for computing the pressure drop and volumetric heat transfer coefficient based on the geometric properties of the foam are provided. Results show that aluminum foam samples yield the highest volumetric heat transfer coefficient while the 10 PPI aluminum foam sample yields the smallest pressure drop. To better quantify the heat transfer performance of these foam samples, comparison with conventional louvered fin geometries is made using a coefficient of performance, compactness factor, and power density as the basis for comparison. Results show the carbon foam samples provide significant improvement in CF but the COP and PD are considerably lower. The highest COP and PD are achieved with the multilouvered fin configuration; however, the resulting CF is substantially lower than that for carbon foam. In conclusion, carbon foam performs better than conventional plate-fin heat exchangers in applications where a reduced heat exchanger volume is favored over reduced mass and/or COP but in cases where reduced mass and/or COP are important, a multilouvered fin type configuration proves to be more advantageous.

Acknowledgment

Financial Support for this work was funded by NASA Glenn Research Center under Contract No. NA63-2750.

Nomenclature

A = area (m^2)
a = surface area per unit volume (m^{-1})
Bi = Biot number
C_F = inertia coefficient
$C_{p,f}$ = constant pressure specific heat of fluid (J/kg K)
CF = compactness factor (W/m^3)
COP = coefficient of performance
D = machined passage diameter (m)
Da = Darcy number
$\dot{E}_{\text{input}}$ = electrical energy (W)
F_h = fin height (mm)
F_p = fin pitch (mm)
h_{sf} = Interstitial heat transfer coefficient (W/m^2 K)
h_v = Volumetric heat transfer coefficient (W/m^3 K)
K = Permeability (m^2)
k = Thermal conductivity (W/m K)
L_a = louver angle (deg)
L_d = louver depth (mm)
L_H = louver height (mm)
L_p = louver pitch (mm)
Nu = Nusselt number
P = pressure (Pa) or (kPa)
PD = power density (W/kg)
Pr = Prandtl number
$\dot{Q}_{\text{removed}}$ = heat removed from hypothetical condenser (W)
q_w = heat flux along heater wall (W/m^2)
Re = Reynolds number
St = Stanton number
T = temperature (°C)
U = normalized axial fluid velocity
u = axial fluid velocity (m/s)
u_m = mean axial fluid velocity (m/s)
V = volume (m^3)
W = width (m)

Greek Symbols

ε = porosity
μ = dynamic viscosity (Ns/m^2)
ν = kinematic viscosity (m^2/s)
ρ = density (kg/m^3)
ΔP = pressure drop (Pa)

Subscripts

D = passage diameter based length scale
fl = fluid
fe = effective fluid property
K = permeability based length scale
s = solid
se = effective solid property
w = wall

References

[1] Chang, Y. J., and Wang, C. C., 1997, "A Generalized Heat Transfer Correlation for Louver Fin Geometry," Int. J. Heat Mass Transfer, **40**(3), pp. 533–544.
[2] Hsieh, W. H., Wu, J. Y., Shih, W. H., and Chiu, W. C., 2004, "Experimental Investigation of Heat-Transfer Characteristics of Aluminum-Foam Heat Sinks," Int. J. Heat Mass Transfer, **47**, pp. 5149–5157.
[3] Haack, D. P., Butcher, K. R., Kim, T., and Lu, T. J., 2001, "Novel Lightweight Metal Foam Heat Exchangers," *2001 ASME Congress Proceedings*, New York.
[4] Kim, S. Y., Paek, J. W., and Kang, B. H., 2000, "Flow and Heat Transfer Correlations for Porous Fin in a Plate-Fin Heat Exchanger," ASME J. Heat Transfer, **122**, pp. 572–578.
[5] Tzeng, S. C., 2007, "Spatial Thermal Regulation of Aluminum Foam Heat Sink Using Sintered Porous Conductive Pipe," Int. J. Heat Mass Transfer, **50**, pp. 117–126.
[6] Calmidi, V. V., and Mahajan, R. L., 2000, "Forced Convection in High Porosity Metal Foams," ASME J. Heat Transfer, **122**, pp. 557–565.
[7] Jeng, T. M., Liu, L. K., and Hung, Y. H., 2005, "A Novel Semi-Empirical Model for Evaluating Thermal Performance of Porous Metallic Foam Heat Sinks," J. Electron. Packag., **127**, pp. 223–234.
[8] Hwang, J. J., Hwang, G. J., Yeh, R. H., and Chao, C. H., 2002, "Measurement of Interstitial Convective Heat Transfer and Frictional Drag for Flow Across Metal Foams," ASME J. Heat Transfer, **124**, pp. 120–129.
[9] Lu, W., Zhao, C., and Tassou, S., 2006, "Thermal Analysis on Metal-Foam Filled Heat Exchangers. Part I: Metal-Foam Filled Pipes," Int. J. Heat Mass Transfer, **49**(15–16), pp. 2751–2761.
[10] Zhao, C., Lu, W., and Tassou, S., 2006, "Thermal Analysis on Metal-Foam Filled Heat Exchangers. Part II: Tube Heat Exchangers," Int. J. Heat Mass Transfer, **49**(15–16), pp. 2762–2770.
[11] Garrity, P., 2009, "A Flow Boiling Microchannel Thermosyphon for Fuel Cell Thermal Management," Ph.D. thesis, University of Florida.
[12] Vafai, K., and Kim, S. J., 1989, "Forced Convection in a Channel Filled With a Porous Medium: An Exact Solution," ASME J. Heat Transfer, **111**, pp. 1103–1106.
[13] Conte, S. D., and de Boor, C., 1972, *Elementary Numerical Analysis*, McGraw-Hill, New York.
[14] Fiebig, M., Valencia, A., and Mitra, N. K., 1994, "Local Heat Transfer and Flow Losses in Fin-and-Tube Heat Exchangers With Vortex Generators: A Comparison of Round and Flat Tubes," Exp. Therm. Fluid Sci., **8**(1), pp. 35–45.
[15] Dong, J., Chen, J., Chen, Z., Zhang, W., and Zhou, Y., 2007, "Heat Transfer and Pressure Drop Correlations for the Multi-Louvered Fin Compact Heat Exchangers," Energy Convers. Manage., **48**(5), pp. 1506–1515.

Calibration of a Computational Model to Predict Mist/Steam Impinging Jets Cooling With an Application to Gas Turbine Blades

Ting Wang
e-mail: twang@uno.edu

T. S. Dhanasekaran
e-mail: tdhanase@uno.edu

Energy Conversion and Conservation Center,
University of New Orleans,
New Orleans, LA 70148-2220

In heavy-frame advanced turbine systems, steam is used as a coolant for turbine blade cooling. The concept of injecting mist into the impinging jets of steam was experimentally proved as an effective way of significantly enhancing the cooling effectiveness in the laboratory under low pressure and temperature conditions. However, whether or not mist/steam cooling is applicable under actual gas turbine operating conditions is still subject to further verification. Recognizing the difficulties of conducting experiments in an actual high-pressure, high-temperature working gas turbine, a simulation using a computational fluid dynamic (CFD) model calibrated with laboratory data would be an opted approach. To this end, the present study conducts a CFD model calibration against the database of two experimental cases including a slot impinging jet and three rows of staggered impinging jets. The calibrated CFD model was then used to predict the mist cooling enhancement at the elevated gas turbine working condition. Using the experimental results, the CFD model has been tuned by employing different turbulence models, computational cells, and wall y^+ values. In addition, the effects of different forces (e.g., drag, thermophoretic, Brownian, and Saffman's lift force) are also studied. None of the models is a good predictor for all the flow regions from near the stagnation region to far-field downstream of the jets. Overall speaking, both standard k-ε and Reynolds stress model (RSM) turbulence models perform better than other models. The RSM model has produced the closest results to the experimental data due to its capability of modeling the nonisotropic turbulence shear stresses in the 3D impinging jet fields. The simulated results show that the calibrated CFD model can predict the heat transfer coefficient of steam-only case within 2–5% deviations from the experimental results for all the cases. When mist is employed, the prediction of wall temperatures is within 5% for a slot jet and within 10% for three-row jets. The predicted results with 1.5% mist at the gas turbine working condition show the mist cooling enhancement of 20%, whereas in the laboratory condition, the enhancement is predicted as 80%. Increasing mist ratio to 5% increased the cooling enhancement to about 100% at the gas turbine working condition.
[DOI: 10.1115/1.4002394]

Keywords: impinging jets, mist cooling, heat transfer enhancement, two-phase flow, gas turbine blade cooling

1 Introduction

Jet impingement heat transfer has been employed for many industrial applications such as the cooling of turbine blades and electrical equipment, the drying of paper and textiles, and the annealing of metals. In the gas turbine (GT) industry, there is a continuous need for increasing the turbine inlet temperature to achieve higher thermal efficiency, which eventually demands significant cooling enhancement on the turbine blades. For example, advanced turbine systems (G or H-type land-based gas turbine systems) have been designed to utilize steam as the coolant to cool the combustor transition piece and/or first-stage vanes and blades and return the heated steam to the bottom steam cycle to augment the system thermal efficiency. To further enhance the above closed-loop steam cooling arrangement, a series of extensive experimental studies under laboratory conditions have been conducted to prove that the concept of injecting mist (tiny water droplets) into the single-phase coolant flow is an effective approach to enhance cooling in a straight pipe [1,2], in a 90 deg bend [3], in a slot impinging jet on both flat and concave surfaces [4,5], and in multiple impinging jets [6,7]. Typically, an average cooling enhancement of 50–100% was achieved by injecting 1–3 wt % mist into the steam flow. Very high local cooling enhancement of 200–300% was observed in the tube and on a flat surface and cooling enhancement above 500% was observed when steam flow passed the 90 deg bend.

The concept of using mist/steam to enhance cooling effectiveness is based on the following features: (a) latent heat of evaporation, (b) increased specific heat, (c) steeper temperature gradient near the wall, (d) lower bulk temperature, (e) increased flow mixing induced by steam-droplet interactions and droplet dynamics, and (f) additional momentum and mass transfer induced by the thrust of evaporation of liquid droplets on/near the wall. A model for mist/steam jet cooling was developed by Li et al. [8]. This model considered the total heat flow to be comprised of three components: single-phase like heat flow, boundary layer quenching effect accounting for heat flow, leaving the surface through the steam, and added heat flow occurring in brief contacts with impacting droplets. Their analysis showed that the heat conduction from the wall to the droplet was the dominant enhancement

Contributed by the Heat Transfer Division of ASME for publication in the JOURNAL OF HEAT TRANSFER. Manuscript received April 13, 2009; final manuscript received July 7, 2010; published online September 17, 2010. Assoc. Editor: Wei Tong.

mechanism. The quenching effect of droplets in the steam flow became important when the mist concentration was high. The heat transfer to small droplets was mainly through the steam while larger droplets hit and cooled the heated wall by direct heat conduction. An extensive review of relevant mist cooling literatures was conducted by Guo et al. [1] and was not repeated here.

Numerous experimental and numerical investigations on the single-phase impinging confined jets have been conducted and are available in literature. Chou and Hung [9] conducted an analytical study for cooling of an isothermal heated surface with a confined slot jet. They also performed a numerical study for the fluid flow and heat transfer of slot jet impingement with an extended nozzle [10]. Laschefski et al. [11] numerically analyzed the velocity field and heat transfer in rows of rectangular impinging jets in the transient state. Cziesla et al. [12] simulated turbulent flow issued from a slot jet array using a subgrid stress model. In 1998, Yang and Shyu [13] presented numerical predictions on the fluid flow and heat transfer characteristics of multiple impinging slot jets with an inclined confinement surface. Tzeng et al. [14] employed eight turbulence models including one standard and seven low-Reynolds number k-ε models to predict the heat transfer performance of multiple impinging jets. Validation results indicated that the prediction by each turbulence model depended on grid distributions and a numerical scheme used in spatial discretization. Recently, Goodro et al. [15] studied the effect of hole spacing on jet array impingement heat transfer on flat plate and showed that spatially averaged Nusselt numbers for 8D hole spacing are generally higher than values for 12D hole spacing.

As far as the studies on two-phase impinging jet are concerned, Shimizu et al. [16] experimentally investigated the heat transfer of an axisymmetric jet impinging on a flat surface. They used a suspension consisting of nitrogen gas and graphite particles of 10 μm diameter and varied the initial loading ratio up to 2.5. They showed that the stagnation point heat transfer coefficient obtained at the highest loading ratio was found to be 6 times as large as the single-phase flow. Yoshida et al. [17] conducted experiments on a two-dimensional impinging jet with gas-solid suspensions. These experiments provided detailed data on the turbulence structure and, on the basis of the information, clarified the heat transfer mechanism of the gas-solid impinging jet. These studies did not include phase change and that will be modeled by the present study.

Impinging liquid spray cooling involves liquid evaporation and bears some similarity to mist impinging cooling but the liquid droplets in the spray cooling are typically very large (50 μm–2 mm) and are transported dominantly by the droplet's inertia with minimal entrained gas flow. Therefore, the two-phase flow physics and flow field of liquid spray cooling are different from mist impinging jet cooling.

Even though there was not much information on the numerical studies of the impinging jet with mist in a steam flow, similar studies applied to mist in the air film cooling were seen in literature. Li and Wang [18,19] simulated mist/air film cooling and showed that a small amount of mist injection (2% of the coolant mass flow rate) could increase the adiabatic cooling effectiveness about 30–50% under low temperature, velocity, and pressure conditions similar to those in the laboratory. The effect of different flow parameters, injection hole configuration, and coolant supply plenum on the cooling effectiveness were also studied. Considering the effect of blade internal cooling on the film cooling over the blade outer surface, Li and Wang [20] further presented the mist/air film cooling heat transfer coefficient under nonadiabatic wall condition including conjugate wall conduction with internal channel cooling beneath the blade surface. The results of conjugate 2D cases indicated that heat conduction from downstream to upstream along the solid wall are strong. The streamwise heat even conducted back from a distance of five-slot widths downstream to the neighborhood of the jet hole. Terekhov and Pakhomov [21] conducted a numerical study of the near-wall droplet jet in a heated tube. They examined the effects of droplet diameter, the blowing ratio, and the wall heat flux on cooling enhancement. Li and Wang [22] computationally investigated the mist cooling performance on the leading edge and curved surfaces of a stationary turbine blade and found that the maximum mist cooling enhancement was approximately 60% on the pressure side and 30% on the suction side.

It should be noted that mist/air flow and mist/steam flow are thermodynamically different. Mist/air is a two-component, two-phase flow, where the evaporation process of the water droplets is initially controlled by the partial pressure of the water vapor in the air and not by the total pressure of the mixture until the boiling temperature is reached. Mist/steam is a one-component, two-phase flow in which the evaporation process of the water droplets is controlled by the steam pressure. Generally, under the same pressure and the same temperature, the droplets within mist/air flow are more likely to evaporate than those within mist/steam flow. When the surrounding temperature is above the boiling temperature, the vaporization process for both mist/steam and mist/air is identical; both are subjected to the total pressure of the mixture.

In open literature, no documents have indicated that this concept of mist/steam cooling has ever been tested under an actual gas turbine (elevated temperature, pressure, heat flux, and Reynolds number) working condition. There are technical challenges involved in introducing mist into the airfoils in an actual gas turbine. Recognizing the difficulty and cost in conducting an experiment at high Reynolds number and under elevated pressure and temperature conditions, implementing CFD simulation will be an opted approach to provide preliminary flow and heat transfer physics to guide decision-making on conducting experiments. It should be noted that these CFD simulations assume that the mist with defined mist/steam ratio enters at the injection point without considering how the mist is transported there. The authors are presently investigating, in parallel, the technique of introducing mist into the turbine vanes and blades to achieve required mist/steam ratio at the desired injection locations.

The present investigation focuses first on calibrating the CFD model with experimental data taken under low temperature and pressure conditions, followed by employing the calibrated CFD model to predict the potential mist/steam heat transfer enhancement under elevated gas turbine operating conditions. The calibration is carried out with the available database of experimental results of a slot jet [4] and multiple rows of staggered jets [7].

2 Numerical Model

2.1 Test Section. Figure 1(*a*) shows the schematic diagram of the confined multiple-row impinging jet experimental test section employed by Wang et al. [7]. The same test section was used for a slot impinging jet by replacing the upper plate. As shown in the figure, the multiple steam jets with mist are impinging on the target wall and are split at the stagnation line in either side of x-direction and then proceed to a settling plenum before exit through circular tubes. The settling plenum is used to minimize disturbance that could be caused by directly exhausting the spent steam to the tubes. From a computational point of view, two different domains are considered: the basic domain (dotted line in Fig. 1(*a*)), which includes only the confined region of 0.125 m long, and the extended domain (dashed line in Fig. 1(*a*)), which includes the settling plenum and a short length of tube. Additional details on the experimental test set-up can be obtained from Refs. [4–7]. The geometry details of the two experimental models are shown in Figs. 1(*b*) and 1(*c*). The slot width is 7.5 mm, the jet hole diameter is 8.1 mm, the target wall distance is 22.5 mm (2.8d), and the confined passage length is 250 mm. For multiple jets, the jet centers are spaced at 25 mm (3d) apart. The dimensions of the target distance and domain length are kept constant for all cases. The target wall is heated uniformly by Joule heating. Due to flow symmetry, only half a portion of the slot jet domain is calculated. For the multiple-row jets, one-quarter of the actual

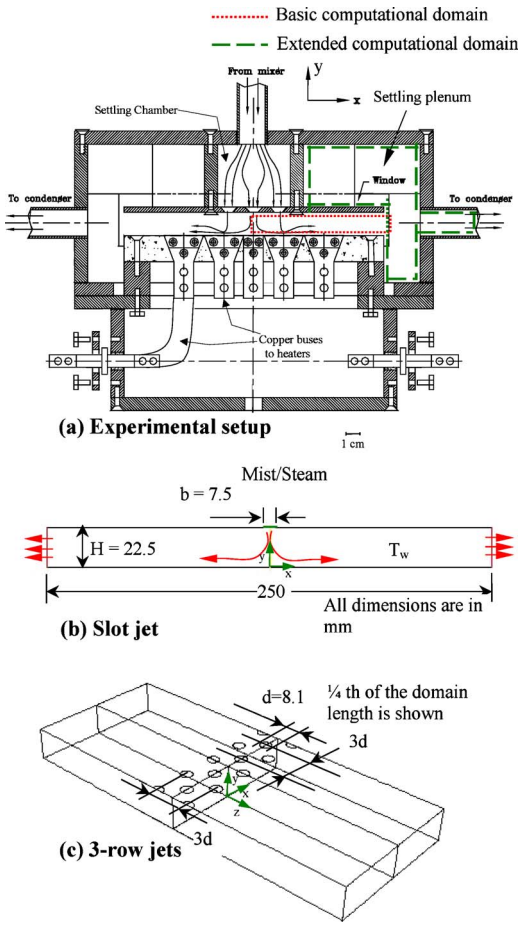

Fig. 1 (*a*) Experimental setup [7] and computational geometry details of (*b*) slot jet and (*c*) three-row jets

flow domain is computationally modeled.

It should be noted that the mist was not generated by an atomizer near the jet issuing slot or holes in the experiment; rather, the mist was generated and mixed with saturated steam in a mixer approximately 3 ft (0.19 m) away from the test section and was then transported to the settling chamber. This process provides a true mist flow with liquid droplets suspending in the main flow, which possess very different characteristics from the sprayed flow. A spray flow will involve active liquid droplet break-up, coalescence, and precipitation.

2.2 Numerical Method. A feasible method to simulate the steam flow with mist injection is to consider the droplets as a dispersed phase since the volume fraction of the liquid is usually small (e.g., 5% mist by weight gives approximately 0.08% in volume). The trajectories of the dispersed phase (droplets) are calculated by the Lagrangian method by tracking each droplet from its origin. The impact of the droplets on the continuous phase is considered as source terms to the governing equations of mass, momentum, and energy. Two components (water and water vapor) are simulated in the impinging jet flow.

2.3 Governing Equations and Turbulence Models (Continuous Phase-Steam). The 3D time-averaged steady-state Navier–Stokes equations as well as the equations for mass and energy are solved. The governing equations for conservation of mass, momentum, and energy are given as

$$\frac{\partial}{\partial x_i}(\rho u_i) = S_m \tag{1}$$

$$\frac{\partial}{\partial x_i}(\rho u_i u_j) = \rho g_j - \frac{\partial P}{\partial x_j} + \frac{\partial}{\partial x_i}(\tau_{ij} - \rho\overline{u_i' u_j'}) + F_j \tag{2}$$

$$\frac{\partial}{\partial x_i}(\rho c_p u_i T) = \frac{\partial}{\partial x_i}\left(\lambda\frac{\partial T}{\partial x_i} - \rho c_p\overline{u_i' T'}\right) + \mu\Phi + S_h \tag{3}$$

where τ_{ij} is the symmetric stress tensor defined as

$$\tau_{ij} = \mu\left(\frac{\partial u_j}{\partial x_i} + \frac{\partial u_i}{\partial x_j} - \frac{2}{3}\delta_{ij}\frac{\partial u_k}{\partial x_k}\right) \tag{4}$$

The source terms (S_m, F_j, and S_h) are used to include the contributions of evaporated water mass, lift, or drag body forces exerted on the droplets and absorption of latent heat from the dispersed phase. $\mu\Phi$ is the viscous dissipation.

In mist/air cooling, water droplets evaporate and vapor is diffused and transported into its surrounding flow. Different from the mist/air flow, no species transport equation is used in the mist/steam flow since steam is the only main flow medium.

The terms of $\rho\overline{u_i' u_j'}$ and $\rho c_p\overline{u_i' T'}$ represent the Reynolds stresses and turbulent heat fluxes. The Reynolds number of the main flow (based on the slot jet width and the inlet condition) is about 22,500 in this study.

2.3.1 Turbulence Models. It is well known that the weakness of the CFD simulation is on the uncertainties produced by various turbulence models. It is difficult to determine a priori, which turbulence model would perform the best in a specific flow field. Therefore, a large part of the calibration process focuses on evaluating the results of five different turbulence models against the experimental data. Five turbulence models are considered including standard k-ε model, renormalization group theory (RNG) k-ε model, k-ω model, shear-stress transport (SST) k-ω model, and Reynolds stress model (RSM). The standard k-ε model, which, based on the Boussinesq hypothesis, relates the Reynolds stresses to the mean velocity and provides two transport equations of turbulence kinetic energy (k) and turbulence energy dissipation (ε). It is robust and has been widely used. The RNG k-ε model was derived using the renormalization group theory [23]. It has an additional term in the ε-equation to improve the accuracy for rapidly strained flows. The effective viscosity is used to account for low-Reynolds number effect. Theoretically, this model is more accurate and reliable than the standard k-ε model. The standard k-ω model is an empirical model based on transport equations for the turbulent kinetic energy (k) and the specific dissipation rate (ω), which can also be considered as the ratio of ε/k [24]. The low-Reynolds number effect is accounted for in the k-ω model. The SST model is a mixture of the k-ω model and the k-ε model: Close to the wall, it becomes the k-ω model while in the far-field, the k-ε model is applied [25]. The turbulence in the impinging flow could be anisotropic and nonequilibrium with multiscaled integral and dissipation length scales. Therefore, the RSM model with a second-moment closure to model anistropic Reynolds stresses is attentively considered in this study. The constants in the k-ε equations were assigned with the recommended values by Launder and Spalding [26]. The turbulence Prandtl number Pr_t is set to 0.85 and the turbulence Schmidt number Sc_t is set to 0.7.

2.3.2 Near-Wall Treatment. Several reports show that the near-wall modeling approach predicts better heat transfer results than the wall function approach in the impinging jet application. Morris et al. [27] used hybrid wall function treatment with different turbulent Prandtl number functions to predict jet impingement heat transfer and found that the predicted stagnation and average heat transfer coefficients agree with experiments to within a maximum deviation of 16% and 20%, respectively. They tested the effect of near-wall node distance (y^+) with heat transfer coefficient and observed the variation in the range of 2%. As the present simulation includes complexity due to dispersed flow (mist), the standard wall function is selected by assuming that the interfer-

ence of droplets on the flow structure in the near-wall region is insignificant and the law of the wall is valid in the two-phase impinging jet flow.

2.4 Discrete Phase Model (Water Droplets)

.

2.4.1 Droplet Flow and Heat Transfer. Based on Newton's second law, the droplet motion in airflow can be formulated by

$$m_p d\mathbf{v_p}/dt = \sum \mathbf{F} \tag{5}$$

where $\mathbf{v_p}$ is the droplet velocity (vector). The right-hand side is the combined force acting on the droplet, which normally includes the hydrodynamic drag, gravity, and other forces such as Saffman's lift force [28], thermophoretic force [29], and Brownian force [30], etc. Saffman force concerns a sphere moving in a shear field. It is perpendicular to the direction of flow, originating from the inertia effects in the viscous flow around the particle. It can be given as

$$F_{\text{saff}} = 1.615\rho\nu^{0.5}(u_g - u_p)(du/dn)^{0.5} \tag{6}$$

where du/dn is the gradient of the tangential velocity. It is valid only when $\text{Re}_p \ll 1$, where Re_p is the particle Reynolds number scaled by the slip velocity between the droplet and the steam.

The thermophoretic force arises from asymmetrical interactions between a particle and the surrounding fluid molecules due to temperature gradient. This force tends to repel particles or droplets from a high-temperature region to a low temperature region. The following equation can be used to model this force:

$$F_n = -K\frac{1}{m_p T}\frac{\partial T}{\partial n} \tag{7}$$

More details can be found in Talbot et al. [29]. The Brownian force considers the random motion of a small particle suspended in a fluid, which results from the instantaneous impact of fluid molecules. It can be modeled as a Gaussian white noise process with spectral intensity given by Li and Ahmadi [30].

Without considering the radiation heat transfer, the droplet's heat transfer depends on convection and evaporation, as given in the following equation:

$$m_p c_p \frac{dT}{dt} = \pi d^2 h(T_\infty - T) + \frac{dm_p}{dt}h_{fg} \tag{8}$$

where h_{fg} is the latent heat. The convective heat transfer coefficient (h) can be obtained with an empirical correlation from Ranz and Marshall [31,32]

$$\text{Nu}_d = \frac{hd}{\lambda} = 2.0 + 0.6\ \text{Re}_d^{0.5}\ \text{Pr}^{0.33} \tag{9}$$

where Nu_d is the Nusselt number and Pr is the Prandtl number.

Theoretically, evaporation can occur at two stages: (a) when the temperature is higher than the saturation temperature (based on local water vapor concentration), water evaporates and evaporation is controlled by the water vapor partial pressure until 100% relative humidity is achieved and (b) when the boiling temperature (determined by the air-water mixture pressure) is reached, water continues to evaporate. In this study, the main flow medium is steam so the evaporation of the water droplets is not controlled by the partial water vapor (as in the mist/air flow), rather, it is controlled by the total pressure of the steam flow, i.e., by the boiling temperature as in Ref. [33].

$$-\frac{dm_p}{dt} = \pi d^2\left(\frac{\lambda}{d}\right)(2.0 + 0.46\ \text{Re}_d^{0.5})\ln(1 + c_p(T_\infty - T)/h_{fg})/c_p \tag{10}$$

where c_p is the specific heat of the bulk flow.

2.4.2 Stochastic Particle Tracking. The turbulence models discussed above can only obtain time-averaged velocity. Using this velocity to trace the droplet will result in an averaged trajectory identical to the streamline. In a real flow, the instantaneous velocity fluctuation would make the droplet move around this averaged track. However, the instantaneous velocity is not simulated in the current computation because the turbulence is modeled in time-averaged terms. One way to simulate the instantaneous turbulent effect on droplet dispersion is to "improvise" the random turbulent fluctuation by using the stochastic tracking scheme [34]. Basically, the droplet trajectories are calculated by imposing the instantaneous flow velocity ($\overline{u}+u'$) rather than the average velocity ($\overline{u}$). The velocity fluctuation is then given as

$$u' = \zeta(\overline{u'^2})^{0.5} = \zeta(2k/3)^{0.5} \tag{11}$$

where ζ is a normally distributed random number. This velocity will apply during the characteristic lifetime of the eddy (t_e), which is a time scale calculated from the turbulent kinetic energy and dissipation rate. After this time period, instantaneous velocity will be updated with a new ζ value until a full trajectory is obtained. Note that when the RSM model is used, the velocity fluctuation is independently decided in each direction. When the stochastic tracking is applied, the basic interaction between droplets and continuous phase stays the same, which is accounted by the source terms in the conservation equations. The source terms are not directly but, rather, indirectly affected by the stochastic method so formulation of the source terms is not affected by implementing the stochastic tracking method. For example, the drag force between a water droplet and the steam flow depends on the slip velocity calculated by the averaged Navier–Stokes equations and the droplet velocity calculated by the Lagrangian Eq. (1). When the stochastic tracking method is used, a random velocity fluctuation is imposed at an instant of time and the drag force will be calculated based on this instantaneous slip velocity. The source term associated with this instantaneous drag force enters into the momentum equation without any additional formulation. For a steady-state calculation, the "instant of time" means "each iteration step."

2.4.3 Droplet Collision and Break-Up Models. The discrete phase model (DPM) estimates the number of collisions and their outcomes (coalescence and bouncing) using the algorithm of O'Rourke [35]. The algorithm uses the probability of collision based on collision volume. The probability distribution of the number of collision is calculated by

$$P(n) = e^{-\overline{n}}\frac{\overline{n}^n}{n!} \tag{12}$$

where n is the number of collisions between the collector and other droplets and $\overline{n}$ is the ratio of collision volume to continuous phase cell volume V. The collision volume is defined as $V_c = n_s\pi(r_b + r_s)^2 v_{\text{rel}}\Delta t$. Here, n_s is the number of small droplet parcels, r_b and r_s are the radius of big and small droplets, v_{rel} is the relative velocity between droplets, and Δt is the time interval. The DPM model uses the Taylor analogy break-up model to consider the droplet break condition. As Weber number is less than 100, the model is well applicable to the present study. More details regarding this model can be found in Refs. [34,36]. The droplets undergoing collision and break-up are negligible: in the order of only four out of 2725 particles injected.

2.5 Boundary Conditions

2.5.1 Continuous Flow (Steam). Various boundary conditions are assigned to the two different impinging cases. In common, steam is considered as continuous flow and mist is considered as discrete flow for all the models. In the slot jet model, the uniform inlet velocity of 27 m/s (Reynolds number of 22,500 based on jet width b) is assigned in negative y-direction. Since no experimen-

tal measurement of the issuing jet velocity profile is available, in view of the thin plate, the jet holes being drilled through the velocity profile should be close to a uniform profile with a very thin boundary layer effect. The saturated temperature of steam at the inlet is 105°C. At the target wall, the constant heat flux of 20,900 W/m^2 is applied. Symmetric boundary condition has been used at the centerline parallel to the impinging direction (Fig. 1(*b*)). The symmetric condition imposes zero normal velocity at the symmetry plane and zero normal gradients of all variables at the symmetry plane. In the case of multiple-row jets model, constant inlet velocity of 32.75 m/s (Reynolds number of 15,000 based on jet diameter *d*) with saturated steam inlet temperature of 103°C is assigned. Due to symmetry, one-quarter of the test domain is considered as the computational domain. A constant heat flux of 13,400 W/m^2 is applied on the target wall. Two symmetric planes are assumed; one at the *x*-*y* plane and another one at the *y*-*z* plane, as shown in Fig. 1(*c*). All the side and top walls in the computational domain are assigned as adiabatic walls with nonslip velocity boundary condition. The inlet turbulence intensity is specified as 1%. The flow exit of computational domain is assumed to be at a constant pressure of 1 atm.

2.5.2 Discrete Flow (Mist). The fine water droplet with various uniform droplet diameters and distributed droplet diameters are considered. In the slot jet cases, the particles are injected from ten equally spaced locations at the inlet. Two mass concentration ratios (mist/steam) of 1% and 2% are simulated. In the 3D multiple-row jets case, mist ratio of 1.5% (0.0000177 kg/s water droplets) is simulated.

2.5.3 Discrete Phase Wall Boundary Condition. When the droplet reaches the wall, the change of the droplet trajectory is determined from the discrete phase wall boundary condition. Each droplet, when it approaches the wall, can undergo any one of the changes [22,37] based on the condition of the wall: dry or flooded. As the experimental investigation shown no flooding on the target surface, in the present numerical model, the wall is considered as dry. In case of the dry wall, the droplets have three major regimes including reflect, break-up, and trap. According to Wachters and Westerling [38], the regimes depend on the incoming Weber number of the droplet. Here, the Weber number is the ratio of kinetic energy of a droplet to the surface energy of a droplet ($We = \rho d_d v_d^2/\sigma$). It was shown from the experimental results that the droplet with incoming Weber number (We_{in}) less than 10 reflects elastically with nearly same outgoing Weber number (We_{out}). Considering the mean droplet size of 10 μm and the jet inlet velocity of 27 m/s, the Weber number lies below the value of 10. Hence, the reflect model is used in the numerical model. The change in momentum due to particle rebound is calculated by coefficient of restitution. The normal coefficient of restitution is defined as $CR_n = v_{a,n}/v_{b,n}$, where v_a and v_b are the particle velocities after and before rebound. Similarly, the change in momentum in tangential direction is calculated from tangent coefficient of restitution $CR_t = v_{a,t}/v_{b,t}$. The normal or tangential coefficient of restitution equal to 1.0 implies that the particle retains all of its normal or tangential momentum after the rebound and 0.0 implies that the particle retains none of its momentum after rebound. In this model, the coefficients are calculated as a function of impact angle.

2.6 Computational Cells. The computational domain has been discretized to fine cells to conduct the simulation. Figure 2(*a*) shows the computational grid of the 2D slot jet, which contains structured quad elements. The total number of 9000 (150×60) elements is used in this model. Figure 2(*b*) shows the computational grid of the three-row jet case. The domain is completely constructed by hexahedral elements. To accurately predict possible recirculation, separation, and reattachment zones, the elements have been clustered toward the wall to obtain the appropriate y^+ value of 12, which is the lowest y^+ value suitable for using the standard k-ε model. Less than $y^+ = 12$, the wall function kicks in. A total of 500,000 ($60 \times 120 \times 70$) elements are used for the 3D three-row jet case.

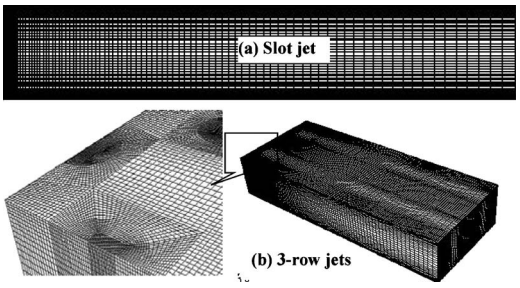

Fig. 2 Computational domain: (*a*) slot jet and (*b*) multiple-row of staggered jets

The computation has been carried out using the commercial CFD software FLUENT (version 6.2.16) from Ansys, Inc. The simulation uses the segregated solver, which employs an implicit pressure-correction scheme and decouples the momentum and energy equations. The SIMPLE algorithm is used to couple the pressure and velocity. Second order upwind scheme is selected for spatial discretization of the convective terms. The second order accuracy is obtained by calculating quantities at cell faces using multidimensional linier reconstruction approach [34]. The computation is conducted for the steam field (continuous phase) first. After obtaining an approximate converged flow field of the steam, the dispersed phase of droplet trajectories are calculated. At the same time, drag, heat, and mass transfer between the droplets and the steam flow are calculated. Variable property values are calculated using polynomial equations for steam and piecewise approximation for water droplets as functions of temperature. Specifically, steam and mist/steam mixture thermal conductivity and viscosity are calculated with the correlation of ideal gas mixing law and density and specific heat are calculated with incompressible ideal gas and mixing law, respectively. It was discovered that the property database for water vapor and steam in FLUENT is not sufficient and gives unreasonable results, such as predicting temperature lower than wet bulb temperature after water droplet evaporation, during the code verification process. A detailed database has been incorporated through function statement.

Iterations proceed alternatively between the continuous and discrete phases. Ten iterations in the continuous phase are conducted between two iterations of the discrete phase. Converged results are obtained after the residuals satisfy mass residual of 10^{-4}, energy residual of 10^{-6}, and momentum and turbulence kinetic energy residuals of 10^{-5}. These residuals are the summation of the imbalance in each cell scaled by a representative for the flow rate. The computation was carried out, in parallel, processing on two dual-core pentium clusters with ten nodes and six nodes, respectively.

2.6.1 Grid Sensitivity Study. A grid sensitivity test has been carried out on both slot jet and three-row jet cases, as shown in Fig. 3. Three different numbers of elements are considered, for example, slot jet case had 2000 (80×25), 5000 (100×50), and 9000 (150×60) elements. The y^+ values of the first near-wall element are kept constant for all cases. The grid sensitivity study is conducted using the RSM turbulence model with standard wall function. It is verified that the result of wall temperature distribution is negligibly affected by the number of cells above 5000 in the slot jet case and above $0.3 \times 10^6 (50 \times 100 \times 60)$ elements in the three-row jet case. In the grid sensitivity test, the wall y^+ values are kept constant as 20 for the slot jet case and 12 for the three-row jet case. The reason for selecting different y^+ values is that the reduction of y^+ value from 20 to 12 did not affect the wall

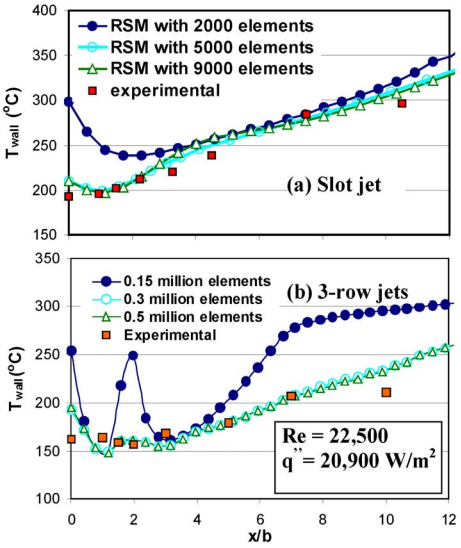

Fig. 3 Grid sensitivity study: (*a*) slot jet and (*b*) three-row jets

temperature prediction much (not shown here) in the 2D configuration but was affected noticeably in the 3D configuration (the details are given in Sec. 3.2).

3 Results and Discussion

3.1 Results of Slot Impinging Jet

3.1.1 Effect of Turbulence Models. In the process of calibrating the CFD model, initially, computation was carried out with various turbulence models including standard k-ε, RNG, RSM, k-ω, and SST on the slot jet for the steam-only case. The computed temperatures on the target wall by all the turbulence models are shown spreading within a $\pm 15\%$ band across the experimental data in Fig. 4(*a*). The RSM model provides the best overall prediction with an average of 5% deviation from the experimental data (the deviation was calculated by $(T_{cfd}-T_{exp})/(T_{max}-T_{sat})$, where T_{max} is the maximum temperature on the target wall and T_{sat} is the saturation temperature). The standard k-ε model provides the second best prediction in excellent agreement with the experimental data near the stagnation point and the region between 3*b* and 5*b* but in the far-field, it did not do well. The predictions from other models, such as RNG, k-ω, and SST, are less promising and show larger deviations from the experimental data.

Following the steam-only case, the effect of the turbulence model on mist/steam case has been compared, as shown in Fig. 4(*b*). The results show that three turbulence models including standard k-ε, RNG, and RSM predict the same value near stagnation region up to $x/b=3.0$ and beyond that standard, k-ε and RSM models predicts closer to experimental values. To investigate the

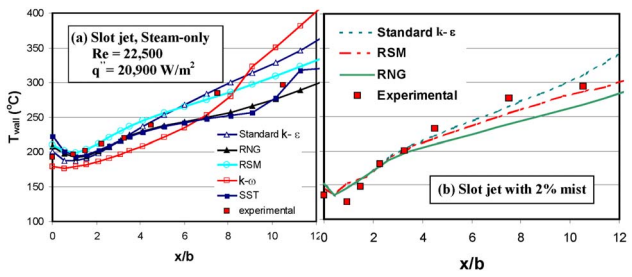

Fig. 4 Wall temperature distribution of a slot jet model

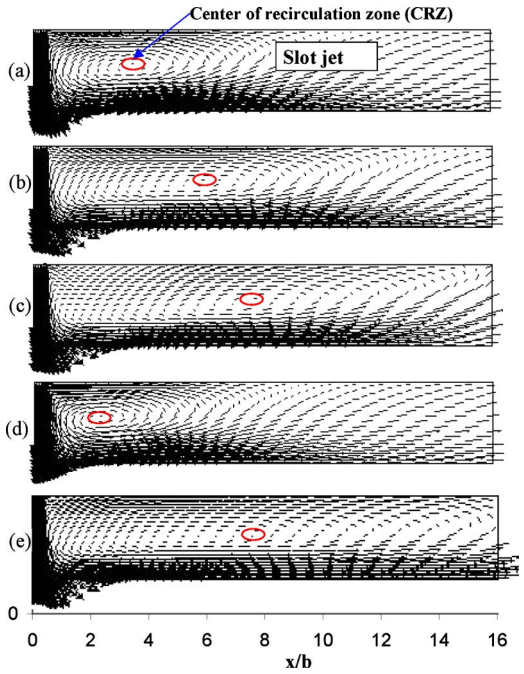

Fig. 5 Velocity vector plot: (*a*) standard k-ε, (*b*) RNG, (*c*) RSM, (*d*) k-ω, and (*e*) SST

reason for the wide range of deviation in the predicted results of the steam-only case, velocity vectors are plotted for various turbulence models, as shown in the Fig. 5. The figure clearly shows the large difference in the flow field predicted by various turbulence models, especially the center location of the recirculation zone (CRZ). The CRZ is located midway between the confined walls at $x/b=3$ in the flow field calculated by the standard k-ε and k-ω models (Figs. 5(*a*) and 5(*d*)). The remaining models predict the center location of the CRZ at about $x/b=6$. It is interesting to observe that the closer the center of the CRZ is to the stagnation line, the stronger the forced convection cooling and the lower the wall temperature near the stagnation point. In the meantime, the closer the center of the CRZ is to the stagnation line, the smaller the recirculation area is induced. This results in a quicker spread of impinging jet and less cooling fluid traveling near the target wall and downstream (e.g., Fig. 5(*d*) versus Fig. 5(*e*)). Hence, warmer wall temperature is in the far-field ($x/b>9$). The closeness of the CRZ's center to the stagnation line follows this order: k-ω, k-ε, RNG, RSM, and SST, which leads to the predicted stagnation temperature following in the ascending order (reduced cooling) and the predicted far-field wall temperature in the descending order (increased cooling). Figure 4 shows that k-ω, k-ε, and RNG turbulence models overpredict the far-field ($x/b>9$) wall temperature.

3.1.2 Effect of Computational Domain. Since all the turbulence models except the RSM do not predict the far-field wall temperature well beyond $x/b=8$, it was suspected that the scattered prediction data might be due to the selection of the computational domain (Fig. 1(*a*)). The exit of the current computational domain (the basic domain) has been placed at the end of the confined channel, whereas in the actual test setup, the fluid enters into a settling plenum from the confined channel before it is finally exhausted through a circular tube. Although the design of the settling plenum was meant to reduce the disturbances outside the test section from affecting the flow inside the channel, it became necessary to include the settling plenum in the computational domain (the extended domain) to examine the effect of the extended computational domain on the far-field temperature data.

The result in Fig. 6 shows that using the extended domain re-

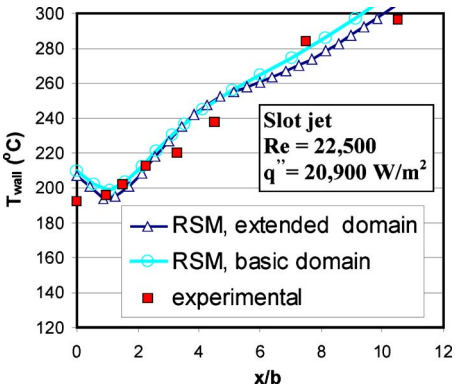

Fig. 6 Effect of computational domain on slot impinging jet cooling (steam-only)

duces the far-field wall temperature values and allows a better prediction of the wall temperature within 3°C at $x/b=10$. On the other hand, the deviation between measured and computed values increases slightly at $x/b=7.5$ when comparing the result of the basic model. Overall speaking, the extended domain predicts the temperature distribution trend better than the basic domain, especially in the far-field location. It is worth noting that the measured heat transfer data had 5–7% uncertainty [4] that would cause the uneven deviation between measured and predicted data. As the present study focuses on cooling enhancement due to mist, which occurs mainly near the stagnation region, this bias error is self-compensated, i.e., both steam-only and mist/steam cases posses the same bias error between basic and extended domains; therefore, the basic computational domain model has been used for all cases and significant computation time has been saved.

3.1.3 Effect of Various Forces on the DPM. After choosing RSM as the best-suited turbulence model for steam and steam/mist flows, computation was carried out to further tune the discrete phase model. As explained previously, the prediction of trajectory of a discrete phase particle is achieved by integrating the force balance on the particle. The dominant main forces are drag and gravitational.

In addition to the main forces, secondary forces, such as thermophoretic, Brownian and Saffman, are included in the computation and the effect of each additional force is investigated individually. Figure 7(*a*) shows the comparison of the experimental and computed target wall temperature distributions under influences of various forces by injecting 2 wt % mist into the steam flow. The wall temperature is approximately 20°C overpredicted near the stagnation point and underpredicted at 10–20°C at $x/b>2$ if only the main drag and gravitational forces are considered. The effect of secondary forces on the wall temperature is negligible except at the stagnation region. The inclusion of Saffman force increases the accuracy of prediction noticeably in the stagnation region. Therefore, three major forces (drag, weight, and Saffman forces) are included in calibrated models.

3.1.4 Effect of Time Scale Used in the Stochastic Particle Tracking. The prediction of stochastic particle dispersion makes use of the concept of the integral time scale, which describes the time spent in turbulent motion along the particle path [34]. The integral time scale constant (ITS) can be approximated as $\mathrm{ITS}=TC\times k/\varepsilon$, where *TC* is the constant, k is the turbulent kinetic energy and ε is dissipation rate. Computations are carried out to seek the most appropriate *TC* value for this study. Different time constants including $TC=0.15$, 0.005, 0.0001, and 0.0005 are provided to investigate the effect of time constant on the heat transfer result. The effect of *TC* on stochastic particle tracking is shown in Fig. 7(*b*), together with a case without employing a stochastic tracking scheme. The results show that the value $TC=0.0005$

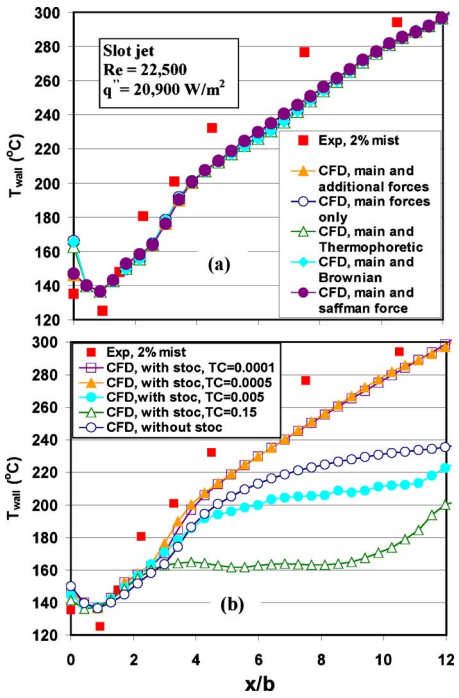

Fig. 7 Effect of (*a*) main and secondary forces on the droplet model and (*b*) stochastic tracking time scale constant (*TC*) on the slot jet model

gives a better match with the experimental results than all other options. The case without stochastic tracking predicts better than those cases with stochastic tracking but are using an improper selection of *TC* values.

3.1.5 Effect of Mist/Steam Mass Concentration Ratio. After the above calibration, the tuned CFD model is used to predict mist cooling enhancement in impingement steam jets. Figure 8(*a*) shows the comparison between experimental and computational results of wall temperature distribution for the slot impingement jet for three cases: steam-only, 1% mist, and 2% mist. The results show that the CFD model with the steam-only case predicts the wall temperature within 5% deviation from the experimental data. The definition of this deviation is already defined in the previous section. In the cases of 1% mist and 2% mist, the CFD predictions are within 10% of the experimental data.

Distributions of heat transfer coefficient for the three cases are plotted in Fig. 8(*b*). Here, the heat transfer coefficient is calculated as

$$h(x)=q''/(T_w(x)-T_j) \tag{13}$$

The steam saturation temperature at 105°C is taken as the jet temperature and the constant wall heat flux q'' is at 20,900 $\mathrm{W/m^2}$. In the steam-only case, the result shows that the CFD model predicts the *h*-value very well in the entire surface except at the stagnation line, where the CFD model underpredicts the *h*-value by about 10%. In the 1% mist case, the CFD model predicts the *h*-value well for region $x/b>3$ but overpredicts the *h*-value by approximately 15% in the region of $x/b<2$ and underpredicts the stagnation line *h*-value. In the 2% mist case, the CFD model also predicts the *h*-value well for $x/b>2$ but underpredicts the *h*-value near the stagnation line for $x/b<2$.

The enhancement ratio (h_{mist}/h_o) in Fig. 8(*c*) largely reflects the deviation trends of *h*-values. Overall, the CFD model can predict mist cooling wall temperature within ±10% and the *h*-value within ±20% from the experimental data. The above discussion bypassed one extremely high *h*-value (1000 $\mathrm{W/m^2\,K}$) in the experimental data at $x/b=1$ of the 2% mist case. It needs to be noted

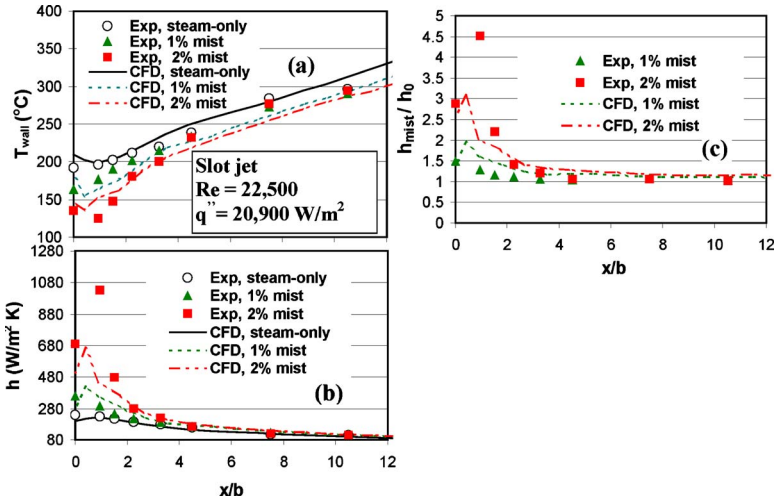

Fig. 8 Heat transfer prediction of the slot impingement jet: (*a*) wall temperature, (*b*) heat transfer coefficient, and (*c*) cooling enhancement

that the prediction of heat transfer coefficient (h) and cooling enhancement ratio (h_{mist}/h_o) is not as accurate as the wall temperature because the wall temperature was directly measured, whereas the h-values and h_o/h_{mist} are derived by calculations. The h-value becomes very sensitive to any minor variation of wall temperature when cooling is effective and the wall temperature approaches the saturation temperature (i.e., when $T_w - T_j$ approaches zero, the heat transfer coefficient approaches infinity). This is what happens to the data at $x/b=1$. One option to avoid infinite large heat transfer coefficient is to replace the saturation temperature with the adiabatic wall temperature.

To obtain an idea of the water droplet evaporation rate, the surviving droplet mass concentration distributions across the channel height are plotted in Fig. 9 at various x/b locations. Figure 9(a) shows that the droplet mass concentration is confined near the wall within a layer of $y/H=0.18$. The near-wall droplets evaporate and are consumed rapidly from $x/b=1$ to $x/b=5$. Beyond $x/b=5$, the near-wall droplets deplete to almost zero within the region $y/H<0.025$. At the end of the test channel, plenty of droplets survive, as can be seen from the concentration distribution at $x/b=10$. A similar trend is observed for the 2% mist case shown in Fig. 9(b).

3.2 Results of Three-Row Impinging Jets

3.2.1 Effect of y^+ Values With Standard Wall Function. From the predicted values of slot jet cases, it was shown that the near-wall Reynolds stresses calculation is very critical in computing wall temperature distribution. In the 3D impinging jet simulation, initially standard wall function with $y^+ \sim 20$ was used as this value gave satisfactory results in 2D slot jet simulation. But in the 3D application, there is an overprediction hump seen at $x/b=2$ and very poor prediction at the stagnation point in Fig. 10. Since the law of the wall is imposed with $y^+ < 11.2$ in the 3D cases, the first near-wall element has been reset at $y^+=12$. The results are very encouraging by showing that the hump is removed and the overall prediction matches the experimental data within 8% except near the stagnation region. The 8% wall temperature prediction band in a complex three-row impinging jets flow field is a much more significant achievement than the 5% prediction band in a 2D slot jet flow field.

3.2.2 Prediction of Mist Cooling Enhancement. The fine-tuned CFD is then used to simulate the cooling enhancement with 1.5% mist injection into three rows of steam impinging jets. The calculations have been made for distributed droplet diameter varying from 5 μm to 50 μm with the mean diameter of about 10 μm, as reported in the experimental studies [8]. The Rosin–Rammler distribution function is used, which is based on the assumption that an exponential relationship exits between the droplet diameter d_d and the mass fraction of droplets with diameter greater than d Y_d

$$Y_d = e^{-(d/d_m)^n} \tag{14}$$

where d_m refers to the mean diameter (10 μm) and n refers to the spread parameter. Figure 11(a) shows the measured distribution of

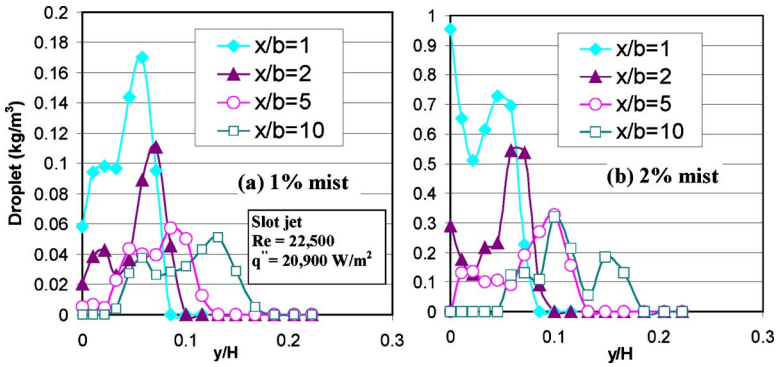

Fig. 9 Droplet concentration distributions across the channel height at various *x*-locations of slot jet cases: (*a*) 1% mist and (*b*) 2% mist

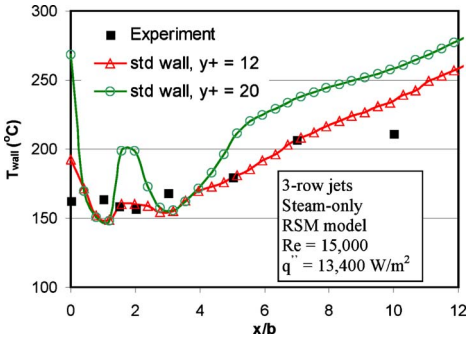

Fig. 10 Effect of y^+ values of 12 and 20 with standard wall function on centerline temperature distribution along the first row jet for three-row impinging jets model (steam-only)

droplet diameter against experimental mass fraction obtained in Ref. [8]. From the relationship, the spread parameter (2.4) is calculated and used to fit the size distribution into the CFD model.

Figure 11(*b*) shows the CFD prediction of wall temperature with distributed droplet diameter. The data presented in Figs. 11(*b*) and 11(*c*) are taken from $z=0$ location, i.e., centerline of the second row jet. Calculations are carried out for the constant droplet sizes of 5 μm, 10 μm, and 50 μm to understand the effect of droplet sizes. Those droplet sizes are selected to cover the minimum, maximum, and mean droplet sizes in the distributed droplet distribution, as found in the experimental result. Apart from the fact that the distributed droplet diameter gives close results to measured values, constant diameter with 5 μm achieves the maximum cooling effect compared with larger sizes of droplets. There is a considerable hike in wall temperature for the cases between 5 μm and 10 μm. Beyond 10 μm, very gradual increase in wall temperature is observed in Fig. 11(*b*). The figure shows that the temperature distribution of distributed diameter case lies between the cases of 5 μm and 50 μm. It is worth to note that the distributed diameter case lies mostly toward uniform 5 μm case near the stagnation region and close to 10 μm and 50 μm in the far-field region. Figure 11(*c*) reveals that the small droplet diameter 5 μm maintains the constant heat transfer coefficient between the jets as the behavior of steam-only case. For example, the *h*-value is almost constant from $x/d=0$ to the second row impinging location of $x/d=1.5$. But in the larger droplet sizes, the value peak in the stagnation location. Furthermore, the *h*-value at the stagnation region reduces drastically as the droplet

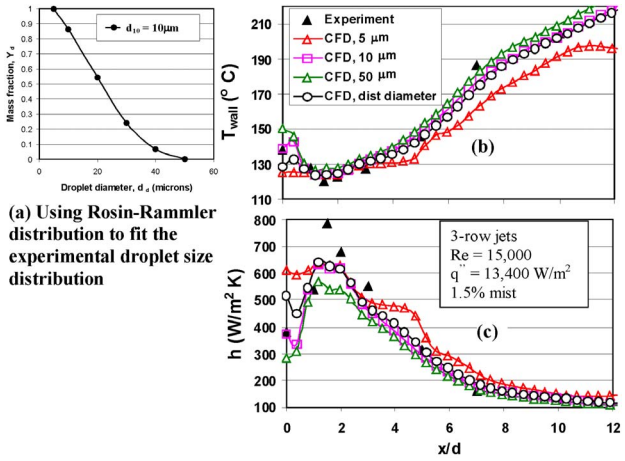

(a) Using Rosin-Rammler distribution to fit the experimental droplet size distribution

Fig. 11 (*a*) Experimental droplet size distribution and heat transfer results of three-row jets: (*b*) wall temperature and (*c*) heat transfer coefficient

diameter increases from 10 μm to 50 μm. This indicates that the wall-droplet contact is critical in the smaller droplet sizes in the heat transfer rate.

The CFD prediction of steam-only and mist/steam cases are shown comparatively in Fig. 12(*a*). The prediction of the steam-only case shows the maximum deviation of 8% from experimental wall temperature values while the prediction for the 1.5% mist/steam case is very good with a deviation of only 2–3%. Figure 12(*a*) (ii) shows that the CFD predicts heat transfer coefficient (*h*) well in the region beyond $x/d=5$ but at the impinging region, there is an overprediction of about 20%.

Due to the underpredicted steam-only *h*-values and the overpredicted mist *h*-values, the cooling enhancement (h_{mist}/h_o) prediction is significantly higher than the experimental data at the impinging point, as shown in Fig. 12(*a*) (iii). Again, this is caused by the reason stated earlier that the *h*-value becomes very sensitive to any minor variation of wall temperature when cooling is effective and the wall temperature approaches the saturation temperature. The ratio of h_{mist}/h_o further amplifies this effect. For example, at $x/b=1.5$, the experimental data are $T_w=120°\text{C}$ and $h=788$ W/m^2 K while the predicted wall temperature is at 124°C. This 4°C difference results in a *h*-value of 637 W/m^2 K (or 20% off).

3.3 Simulated Results Under Elevated Gas Turbine Operating Conditions. With sufficient confidence being built on the validation process against the laboratory experimental work under the low pressure, temperature, heat flux, and Reynolds number conditions, computation has been extended to simulate the mist cooling enhancement in real gas turbine environment under elevated conditions. For this purpose, the superheated steam at 750 K and 15 atm pressure is chosen to reflect the elevated gas turbine working condition. The wall heat flux and inlet velocity are increased from 13,400 W/m^2 to 120,000 W/m^2 and 27–40 m/s, respectively (Re=15,000–52,250). The mist ratio of 1.5% is maintained constant for both cases. Table 1 gives the comparison of steam and water properties between low and elevated pressure and temperature conditions. The steam density increases about 6 times and liquid density reduces 14% at elevated condition, which will allow more droplets to suspend in the steam flow and be supported by the steam. The kinematic viscosity of steam increases about 3.5 times, which will reduce the slip velocity and, therefore, reduce heat transfer to the droplet via convection. This allows droplets to last longer to provide the needed cooling further downstream. Furthermore, both increases of liquid specific heat (+7%) and water latent heat (+16%) at the elevated condition are beneficial to achieving more effective mist cooling.

Figure 12(*b*) shows the effect of droplet diameter on mist cooling enhancement at elevated operating conditions. The results are taken at $z=0$, i.e., midaxis of the second row jet. Noticeable reduction in the wall temperature can be seen due to mist cooling in Fig. 12(*b*) (i). The cases of 5 μm, 10 μm, and distributed diameter cases are almost coinciding each other and the 50 μm case is showing the lowest cooling effect among other cases as expected. The corresponding cooling heat transfer coefficients are shown in Fig. 12(*b*) (ii). The average increase in heat transfer coefficient of about 15% is noted at elevated operating conditions in Fig. 12(*b*) (iii), whereas in the low operating conditions, the value is about 40–60% (see Fig. 8(*c*)). At the impingement region of $x/b=1.5$ (second row jet), 80% of the cooling enhancement was previously predicted at the low operating condition, whereas at the elevated operating condition, the cooling enhancement value is reduced to 20%.

Although the cooling enhancements under elevated GT operating conditions are not as attractive as under low pressure and temperature conditions, it is important to point out that in addition to the cooling enhancement value, the actual wall temperature reduction is another important indicator to evaluate the impingement jet cooling performance. The importance of evaluating the

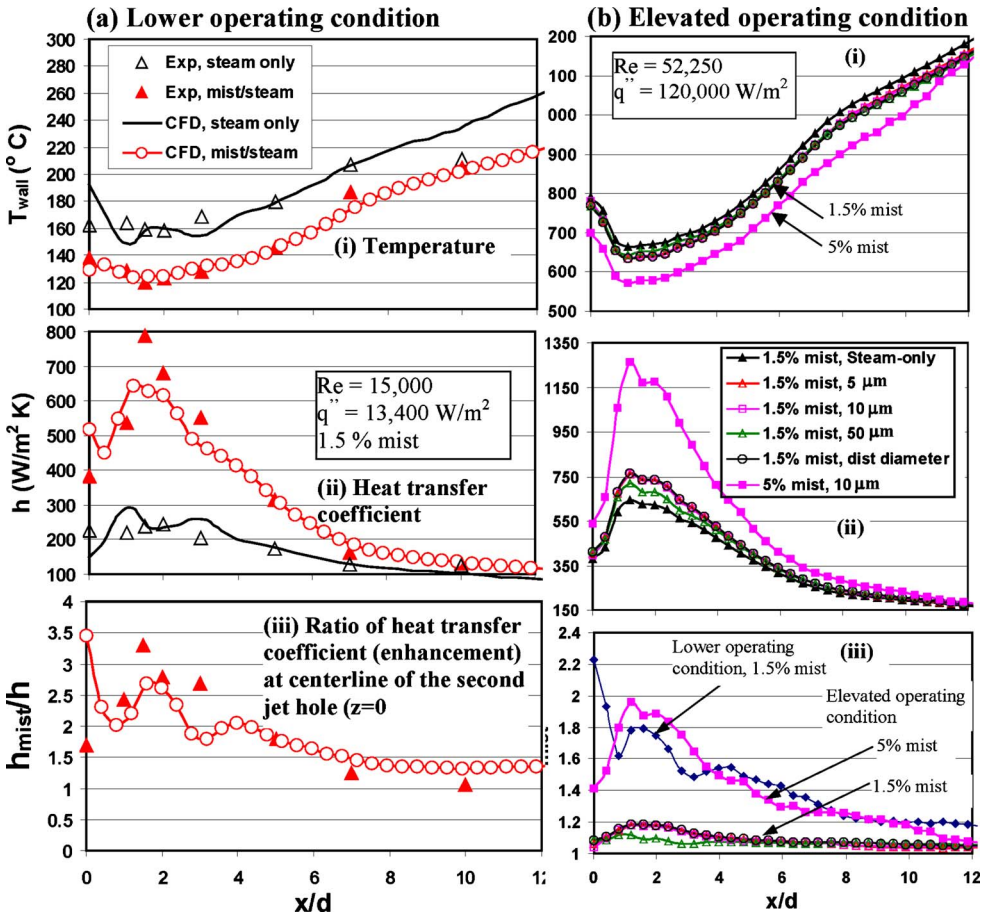

Fig. 12 Heat transfer results of three-row jets: (*a*) lower and (*b*) elevated operating conditions

actual wall temperature reduction originates from the need to veer the wall temperature away from the blade material yield limit. Typically, an additional 50 K wall temperature reduction will be appreciably valued when the wall temperature is close to the material yield point. Under the elevated GT operating conditions, the temperature difference between the wall and the coolant (steam) is approximately 600 K (1350–750 K), whereas this temperature difference is 185 K (573–388 K) under the low temperature and pressure conditions. Therefore, 60% cooling enhancement will reduce wall temperature about 74 K at the low operating condition, whereas a 15% cooling enhancement at elevated condition will contribute to about 90 K wall temperature reduction. Since the increased steam density (+600%) and reduction of liquid density (−14%) at elevated condition allows more droplets to suspend in the steam flow and be supported by the steam, using higher mist ratio should further increase the enhancement ratio. Indeed, the result of 10 μm droplets and 5% mist show a mist enhancement of about 100% with a wall temperature reduction of 365 K, as shown in Fig. 12(*b*) (iii).

Table 1 Steam and water (liquid) properties at low and elevated conditions

	388 K	750 K
Steam	1 atm	15 atm
Density (kg/m^3)	0.7	4.45
Specific heat (J/kg K)	2014	2180
Heat conductivity (W/m K)	0.0261	0.0651
Dynamic viscosity (kg/m s)	1.24×10^{-5}	2.76×10^{-5}
Kinematic viscosity (m^2/s)	1.77×10^{-6}	6.2×10^{-6}
Jet (multiple) temperature	376.15 (saturated)	750 (super heated)
Water		
Saturation temperature (K)	373	472
Specific heat (J/kg K)	4180	4490
Density (kg/m^3)	998	866
Latent heat (kJ/kg)	1950	2260
Boundary conditions		
Jet velocity (m/s)	27	40
Reynolds number	15,000	52,250
Wall heat flux for multiple round jets (W/m^2 K)	13,400	120,000

4 Conclusions

A CFD model has been calibrated against the available experimental results of injecting fine-droplet mist into steam impinging jets of two arrangements, a slot jet and three rows of jets. The following conclusions are drawn.

- The calibration process reveals that the RSM turbulence model with standard wall function gives better results on this application. The standard wall function works satisfactorily on 2D flows with y^+ being set at 20 without needing to resolve the near-wall flow. However, in the 3D flow, the calibration process requires resolution to the near-wall flow down to $y^+\approx12$. The selection of extended computational domain affects the prediction of wall temperature at the far-field locations to approximately 2% but not significantly.
- Drag force and droplet weight are the main forces affecting droplet dynamics. Among various secondary forces, Saff-

man force has been identified as an important factor that affects a more accurate prediction near the stagnation region. Other forces, such as thermophoretic and Brownian, have a negligible effect on the predicted results.
- The stochastic tracking with time scale evaluated with $0.0005k/\varepsilon$ provides better results.
- The calibrated CFD model can predict the wall temperature of the 2D mist/steam slot impinging jet flow within 5% and the 3D multiple rows of impinging jets within 8%.
- The h-value becomes very sensitive to any minor variation of wall temperature when cooling is effective and when the wall temperature approaches the saturation temperature. Therefore, comparisons between the experimental and CFD results are more certain by comparing wall temperatures rather than the h-values.
- The prediction of mist/steam cooling at the gas turbine operating condition with 1.5% mist showed 20% enhancement. This value was much higher as 80% in the low operating condition. Increasing the mist ratio to 5% at the gas turbine operating condition increased the mist enhancement to about 100%.

It should be noted that no rotating effect is included in this study so the application of the present results to gas turbine blades must be cautious by further evaluating the rotating effect. Also, note that the calibration of the computation model is strictly connected to the available experimental data at laboratory working condition.

Acknowledgment

This study was supported by the Louisiana Governor's Energy Initiative via the Clean Power and Energy Research Consortium (CPERC) and was administered by the Louisiana Board of Regents.

Nomenclature

b = slot width (m)
C = concentration (kg/m^3)
d = diameter of round jet (m)
h = convective heat transfer coefficient (W/m^2 K)
H = target distance (channel height, m)
k = turbulent kinetic energy (m^2/s^2)
k_c = mass transfer coefficient
K = thermophoretic coefficient
m = mass (kg)
q'' = wall heat flux (W/m^2)
Re = Reynolds number
T_w = wall temperature (°C)
T_j = jet temperature (°C)
TC = Stochastic tracking time constant
v = velocity (m/s)

Greeks

ε = turbulence dissipation (m^2/s^3)
λ = thermal conductivity (W/m K)

Subscripts

j = jet
p or d = particle or droplet

References

[1] Guo, T., Wang, T., and Gaddis, J. L., 2000, "Mist/Steam Cooling in a Heated Horizontal Tube: Part 1: Experimental System," ASME J. Turbomach., **122**, pp. 360–365.
[2] Guo, T., Wang, T., and Gaddis, J. L., 2000, "Mist/Steam Cooling in a Heated Horizontal Tube: Part 2: Results and Modeling," ASME J. Turbomach., **122**, pp. 366–374.
[3] Guo, T., Wang, T., and Gaddis, J. L., 2000, "Mist/Steam Cooling in a 180-Degree Tube," ASME J. Heat Transfer, **122**, pp. 749–756.
[4] Li, X., Gaddis, T., and Wang, T., 2001, "Mist/Steam Heat Transfer of Confined Slot Jet Impingement," ASME J. Turbomach., **123**, pp. 161–167.
[5] Li, X., Gaddis, J. L., and Wang, T., 2003, "Mist/Steam Heat Transfer With Jet Impingement Onto a Concave Surface," ASME J. Heat Transfer, **125**, pp. 438–446.
[6] Li, X., Gaddis, T., and Wang, T., 2003, "Mist/Steam Cooling by a Row of Impinging Jets," Int. J. Heat Mass Transfer, **46**, pp. 2279–2290.
[7] Wang, T., Gaddis, J. L., and Li, X., 2005, "Mist/Steam Heat Transfer of Multiple Rows of Impinging Jets," Int. J. Heat Mass Transfer, **48**, pp. 5179–5191.
[8] Li, X., Gaddis, J. L., and Wang, T., 2001, "Modeling of Heat Transfer in a Mist/Steam Impinging Jet," ASME J. Heat Transfer, **123**, pp. 1086–1092.
[9] Chou, Y. J., and Hung, Y. H., 1994, "Impingement Cooling of an Isothermally Heated Surface With a Confined Slot Jet," ASME J. Heat Transfer, **116**, pp. 479–482.
[10] Chou, Y. J., and Hung, Y. H., 1994, "Fluid Flow and Heat Transfer of an Extended Slot Jet Impingement," J. Thermophys. Heat Transfer, **116**, pp. 538–545.
[11] Laschefski, H., Cziesla T., Biswas, G., and Mitra, N. K., 1996, "Numerical Investigation of Heat Transfer by Rows of Rectangular Impinging Jets," Numer. Heat Transfer, **30**, pp. 87–101.
[12] Cziesla, T., Tandogan, E., and Mitra, N. K., 1997, "Large Eddy Simulation of Heat Transfer From Impinging Slot Jets," Numer. Heat Transfer, **32**, pp. 1–17.
[13] Yang, Y. T., and Shyu, C. H., 1998, "Numerical Study of Multiple Impinging Slot Jets With an Inclined Confinement Surface," Numer. Heat Transfer, **33**, pp. 23–37.
[14] Tzeng, P. Y., Soong, C. Y., and Hsieh, C. D., 1999, "Numerical Investigation of Heat Transfer Under Confined Impinging Turbulent Slot Jets," Numer. Heat Transfer, **35**, pp. 903–924.
[15] Goodro, M., Park, J., Ligrani, P., Fox, M., and Moon, H. K., 2007, "Effect of Hole Spacing on Jet Array Impingement Heat Transfer," ASME Paper No. GT2007-28292.
[16] Shimizu, A., Echigo, R., and Hasegawa, S., 1979, "Impinging Jet Heat Transfer With Gas-Solid Suspension Medium," Heat Transfer Conference, San Diego, CA, pp. 155–160.
[17] Yoshida, H., Suenaga, K., and Echigo, R., 1990, "Turbulence Structure and Heat Transfer of a Two-Dimensional Impinging Jet With Gas-Solid Suspensions," Int. J. Heat Mass Transfer, **33**(5), pp. 859–867.
[18] Li, X., and Wang, T., 2006, "Simulation of Film Cooling Enhancement With Mist Injection," ASME J. Heat Transfer, **128**, pp. 509–519.
[19] Li, X., and Wang, T., 2007, "Effects of Various Modelling on Mist Film Cooling," ASME J. Heat Transfer, **129**, pp. 472–482.
[20] Li, X., and Wang, T., 2008, "Two-Phase Flow Simulation of Mist Film Cooling on Turbine Blades With Conjugate Internal Cooling," ASME J. Heat Transfer, **130**, p. 102901.
[21] Terekhov, V. I., and Pakhomov, M. A., 2006, "Numerical Study of the Near-Wall Droplet Jet in a Tube With Heat Flux on the Surface," J. Appl. Mech. Tech. Phys., **47**, pp. 1–11.
[22] Li, X., and Wang, T., 2008, "Computational Analysis of Surface Curvature Effect on Mist Film Cooling Performance," ASME J. Heat Transfer, **130**, p. 121901.
[23] Choudhury, D., 1993, "Introduction to the Renormalization Group Method and Turbulence Modeling," Technical Memorandum No. TM-107, Fluent, Inc.
[24] Wilcox, D. C., 1998, *Turbulence Modeling for CFD*, DCW, La Canada, CA.
[25] Menter, F., 1993, "Zonal Two Equation Model for Aerodynamic Flows," AIAA Paper No. 93-2906.
[26] Launder, B. E., and Spalding, D. B., 1972, *Lectures in Mathematical Models of Turbulence*, Academic, London.
[27] Morris, G. K., Garimella, S. V., and Amano, R. S., 1996, "Prediction of Jet Impingement Heat Transfer Using a Hybrid Wall Treatment With Different Turbulent Prandtl Number Functions," ASME J. Heat Transfer, **118**, pp. 562–569.
[28] Saffman, P. G., 1965, "The Lift on a Small Sphere in a Slow Shear Flow," J. Fluid Mech., **22**, pp. 385–400.
[29] Talbot, L., Cheng, R. K., Schefer, R. W., and Willis, D. R., 1980, "Thermophoresis of Particles in a Heated Boundary Layer," J. Fluid Mech., **101**, pp. 737–758.
[30] Li, A., and Ahmadi, G., 1992, "Dispersion and Deposition of Spherical Particles From Point Sources in a Turbulent Channel Flow," Aerosol Sci. Technol., **16**, pp. 209–226.
[31] Ranz, W. E., and Marshall, W. R., Jr., 1952, "Evaporation From Drops, Part I," Chem. Eng. Prog., **48**, pp. 141–146.
[32] Ranz, W. E., and Marshall, W. R., Jr., 1952, "Evaporation From Drops, Part II," Chem. Eng. Prog., **48**, pp. 173–180.
[33] Kuo, K. Y., 1986, *Principles of Combustion*, Wiley, New York.
[34] Fluent, Inc., 2005, Version 6.2.16, Fluent Manual.
[35] O'Rourke, P. J., 1981, "Collective Drop Effects on Vaporizing Liquid Sprays," Ph.D. thesis, Princeton University, Princeton, NJ.
[36] Taylor, G. I., 1963, "The Shape and Acceleration of a Drop in a High Speed Air Stream," *The Scientific Papers of G. I. Taylor*, G. K. Batchelor, ed., Cambridge University Press, Cambridge.
[37] Dhanasekaran, T. S., and Wang, T., 2008, "Validation of Mist/Steam Cooling CFD Model in a Horizontal Tube," ASME Paper No. HT2008-5556280.
[38] Wachters, L. H. J., and Westerling, N. A. J., 1966, "The Heat Transfer From a Hot Wall to Impinging Water Drops in the Spheroidal State," Chem. Eng. Sci., **21**, pp. 1047–1056.

Experimental Investigation on the Heat Transfer of a Leading Edge Impingement Cooling System for Low Pressure Turbine Vanes

Pedro de la Calzada
e-mail: pedro.delacalzada@itp.es

Jose Javier Alvarez
e-mail: josejavier.alvarez@itp.es

ITP, Industria de Turbopropulsores S.A.,
Avda Castilla 2,
San Fernando de Henares, 28830 Madrid, Spain

Impingement cooling through jet holes is a very attractive cooling system for heat rejection at high heat loaded areas as the leading edge of turbine vanes. Although some correlations and tools are available to dimension such systems, the variety and complexity of the flow features present in those systems still require experimental validation of real engine designs. Among the experimental techniques possible to be used, transient liquid crystal method offers good resolution as well as sufficient accuracy. Under this investigation, an impingement cooling system for the leading edge of a contrarotating power turbine (PT) representative of a small turboshaft engine was investigated experimentally. The PT vane features a very thin leading edge with high curvature and side channels rapidly turning backward. Constraints on cooling flow consumption and distribution led to a leading edge configuration with two rows of staggered jets. This particular configuration was experimentally investigated for three different Reynolds numbers around the design point by using a transient liquid crystal technique, which allows the measurement of surface distribution of heat transfer coefficient at the area of interest. Heat transfer results are presented in terms of surface distributions, impingement rows stagnation line local distributions, streamwise distributions along planes over the impingement stagnation points, span averaged streamwise local distributions, and surface averaged values. These results are then compared with available correlations from existing literature showing good matching for both maximum and averaged values. The results are also used as baseline data to discuss some of the flow features that can have effect on the heat transfer on this particular configuration. [DOI: 10.1115/1.4002206]

Keywords: turbine cooling, heat transfer, impingement cooling, liquid crystal

1 Introduction

The increasing operating temperature of modern turbines usually requires internal cooling of the airfoils if acceptable metal temperature levels to fulfill integrity and life targets are to be achieved. In particular, the leading edge (LE) area of the airfoils is critical since it is typically subject to the highest external heat transfer load due to the stagnation nature of flow there, hence, requiring high cooling flow rates to reduce airfoil metal temperature. Although convective cooling through serpentine passages running all along the leading edge area (with or without ribs) is a proven technology for managing the heat load, more complex configurations are needed to further improve the system efficiency. Impingement cooling systems by arrays of jet holes distributed along the surface offer some advantages as reduced cooling flow consumption and the capability of a very localized effect. Furthermore, the use of a tube plenum to feed the jet holes also improves the uniformity of the surface heat transfer compared with serpentine passages of decreasing cooling potential. Therefore, impingement cooling through rows of jet holes is very attractive to turbine cooling designers.

Extensive experimental investigations of cooling systems with impingement on flat surfaces have been conducted for many years. Early investigations of Florschuetz et al. [1] and Florschuetz et al. [2], during the 1980s, until the recent work by Onstad et al. [3] are examples of these contributions focused on flat plates with arrays of impingement jets, taking into account different effects as crossflow or fluid extraction. However, fewer investigations have been performed of jet impingement on concave surface geometries, which are particularly representative of airfoil leading edges.

The early investigations conducted by Chupp et al. [4] and Hrycak [5] already offered valuable experimental data for correlating impingement heat transfer in concave surfaces, focusing on stagnation and surface averaged values. Bunker and Metzger [6] extended the interest to the surface distribution of the heat transfer around the impingement region. The work of Kayansayan and Kucuka [7] also presented some analytical model results to be compared with experimental data for jets impinging on cylindrical concave surfaces. The investigations of Taslim and Setayeshgar [8] and Taslim and Khanicheh [9] offer more surface averaged heat transfer results on airfoil leading edge geometry including more effects as gill film and showerhead holes.

In the present work, an impingement cooling system for the LE of a contrarotating PT vane was investigated experimentally. The PT vane tested featured a very thin LE cooled by two rows of staggered impingement holes. This particular configuration was experimentally investigated for three different Reynolds numbers around the design point by using a transient liquid crystal technique, which allows the measurement of surface distribution of heat transfer coefficient.

2 Real Engine Geometry

The investigation presented in this paper was carried out with the aim at developing and validating the basic technology and

Contributed by the Heat Transfer Division of ASME for publication in the JOURNAL OF HEAT TRANSFER. Manuscript received April 23, 2010; final manuscript received July 2, 2010; published online September 21, 2010. Assoc. Editor: Frank Cunha.

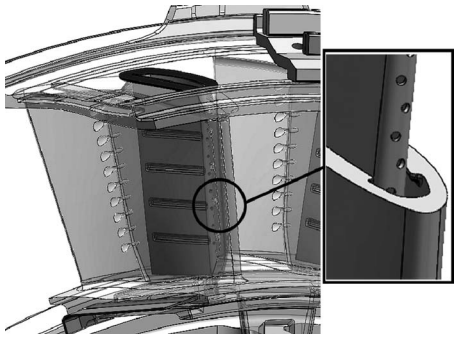

Fig. 1 Real engine NGV geometry (detail of insert tube LE impingement orifices)

tools to be used in the real engine design, hence, focusing on the particular geometry and conditions required in the real case.

The engine geometry model, corresponding to a contrarotating PT vane of a small turboshaft, is shown in Fig. 1. The coolant is fed into the insert tube through the open top end and then flows through two staggered rows of holes, impinging on the vane LE area as it can be seen on the right plot of the same figure. After jetting through the holes, the coolant flows along the PS and SS ribbed channels to mix at the TE cavity and eventually discharge through a row of ten holes on the airfoil PS.

The particular configuration of two staggered rows of impingement holes distributed all along the span of the LE was chosen mainly to minimize the coolant flow consumption and decrease the cooling system sensitivity to small deviations in the final real position of holes in production. Longitudinal ribs at both airfoils sides were provided so as to ensure a good distribution of the cooling flow along the airfoil span. Five channels separated by four ribs with four holes each were defined.

3 Test Geometry and Experimental Set-Up

Table 1 details the geometric parameters of the impingement rows in the test specimen. The geometry is common for both PS and SS rows, the only difference being that the two rows are staggered to each other. Figures 2 and 3 are schemes showing further details of the impingement geometry and instrumentation layout. Figure 3 shows the definition of the nominal position of the impingement jet stagnation points (B), which are 90 deg apart

Table 1 Impingement rows geometry

d (mm)	X (mm)	Y (mm)	Z (mm)	D (mm)	X/d	Y/d	Z/d	D/d
2.78	12.71	16.44	15.19	12	4.57	5.91	5.46	4.32

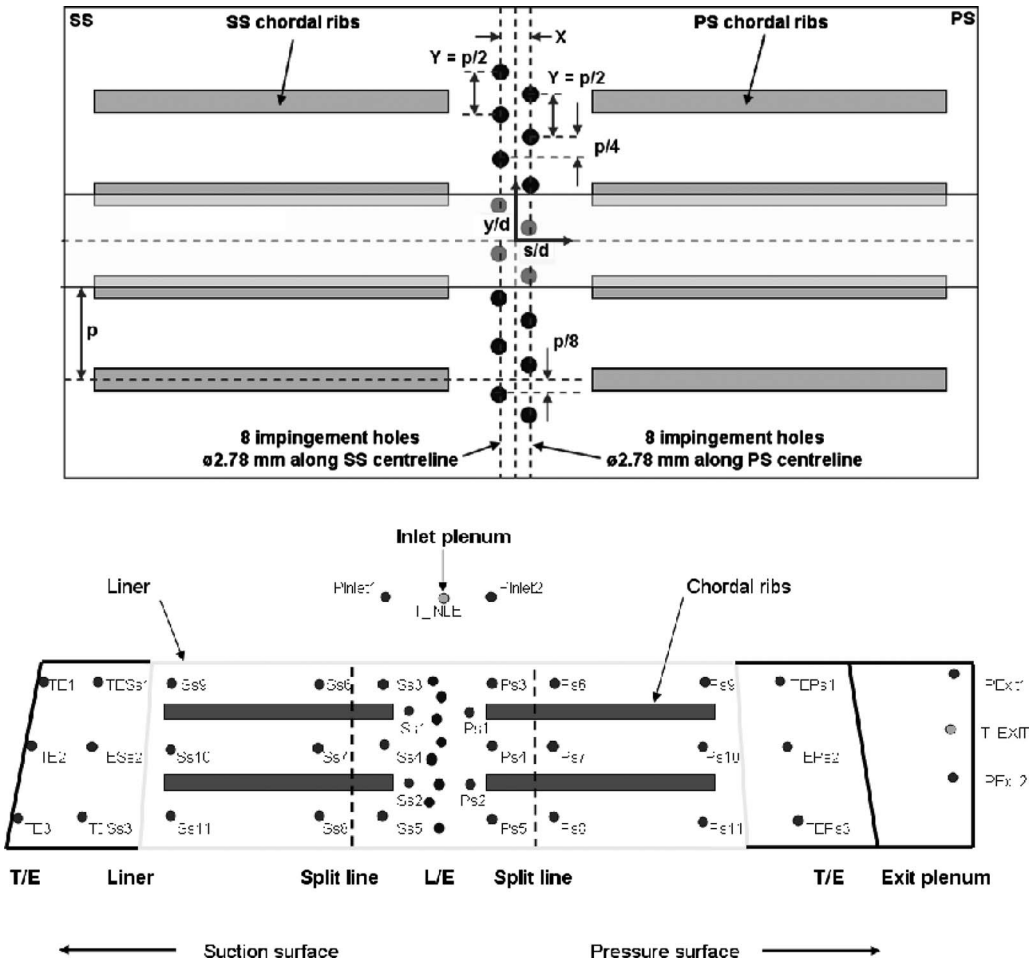

Fig. 2 Impingement and instrumentation layout scheme

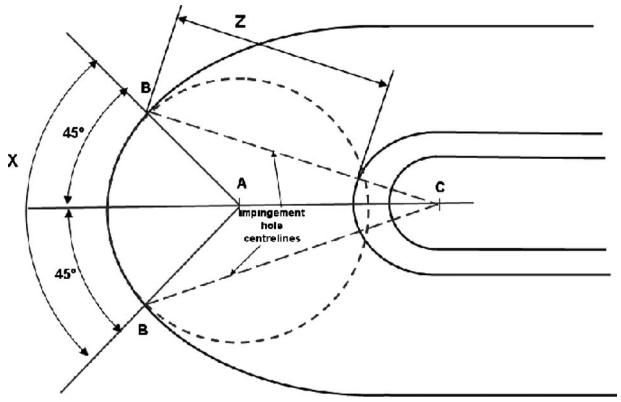

Fig. 3 Impingement geometry scheme

from each other along the LE circular arc. Nominal impingement jet centerlines are then defined by joining points B with point C, which is the impingement insert LE center of curvature.

The test was carried out at three different jet Reynolds number conditions corresponding to the engine design point: Re=3334, design point−30%: Re=2330, and design point+30%: Re=4338. These Re conditions are called low, nominal (or Nom) and high throughout this paper for the sake of simplicity. Test pressures and temperatures were selected such that similar jet Reynolds and Mach numbers to those encountered in engine operation at its design point were attained in the tests.

Table 2 details some of the functional parameters obtained in the tests for the impingement orifices. The results have been averaged for all the impingement orifices of both PS and SS rows. The discharge coefficient values obtained are lower than the 0.821 value that what would be obtained if the Damerow et al. [10] correlation was used.

Since the main interest of the investigation was the performance of the LE impingement area between two ribs, a model with three spanwise repeating equal channels representative of the central channel of the real engine configuration, was built. Feeding of the model impingement tube was through the top end while the lower tube end was fully closed. Although this configuration did not exactly correspond to the real engine geometry, the central channel of the test model was considered sufficiently representative of the central channel in the real engine geometry. Despite the present investigation was focused on the LE impingement cooling area the test model, the test also included the complete internal cooling geometry including the side channels, the TE rear cavity, and the exit holes, which discharged the coolant to an exit plenum from which air was also drawn from the top. The complete model allowed detailed investigation of the LE area while retaining any other phenomena affecting the staggered jets from an uneven flow distribution in the side channels driven by rear cavity asymmetry.

3.1 Perspex Model Design Considerations. The model interior surface shape definitions were generated directly from a computer-aided design and drafting model of the engine component. This ensured that the cooling passage geometry was fully representative of the engine component. This surface was then surrounded with Perspex and arranged with appropriate split faces and clamping arrangements to ensure good sealing and adequate strength. Care was taken during the design phase to ensure a clear optical path to the cooling passage surfaces of interest.

The model scale was chosen through due consideration of expected HTC level and resulting liquid crystal phase change times, rig pressure and mass flow delivery capability, and also ease of handling (size). Excessively long crystal phase change times (>2 min) can lead to poor quality optical signals, introducing uncertainty in the measurement of phase change time. Very short phase change times ($<5-10$ s) go hand in hand with small temperature differences between gas and wall, introducing uncertainties in driving temperature difference due to thermocouple measurement uncertainty. Typically, a HTC in the range of $10-2000$ W/m^2 K can be successfully measured using this approach with air feed temperatures up to 100°C. Higher temperatures may lead to damage to the Perspex model.

The large range of HTC present in impingement cooling systems tests often results in some loss of information due to either very short or very long phase change times. Multiple crystals may be used to capture both high and low heat transfer regions in the same test, however, in this case, the gas-wall temperature difference was too small in the very low heat transfer regions for this approach to be worthwhile.

The model wall thickness was chosen to be as small as possible to commensurate with the diktats of model strength and deflection under pressure load and heat soak depth evaluated through the use of Fourier modulus. The test analysis used was based on the assumption of a semi-infinite solid, i.e. the heat wave conducted through the material does not reach a boundary during the test. The speed at which heat diffuses into the substrate is dependent only on the thermal properties and dimension of the material and not on the thermal boundary conditions themselves. Thus, the minimum wall thickness was set using the following criterion to ensure that the heat pulse failed to reach an external surface during the period of the test:

$$\mathrm{Fo} = \frac{\alpha\theta}{x^2} < 0.2 \tag{1}$$

which is derived from Eq. (3), i.e. the semi-infinite solid analytical solution of the Fourier conduction equation, given a step change in fluid temperature, where θ is taken as the phase change time for an expected level of HTC.

For a low thermal diffusivity material as the Perspex material used in this case, a total phase change time of around 60 s and a model minimum wall thickness of 25 mm, the validity of the semi-infinite assumption is ensured.

3.2 Rig Design. The rig layout is presented in Fig. 4. Air is supplied to the Perspex model from a pressurized (up to 400 psi) storage tank. The line pressure is stepped down through a pressure reducing valve, which maintains a constant pressure upstream of a sonic nozzle. The NPL calibrated sonic nozzle gives a flow measurement uncertainty of $\pm 0.5\%$. Air was drawn from the model through a vacuum pump, which exhausts to atmosphere. Air mass flow and pressure could, thus, be controlled independently, allowing independent control of Mach and Reynolds numbers in the test model.

The rapid change in air temperature required by the transient liquid crystal technique was achieved using an in-line mesh

Table 2 Impingement orifice test data

Re	Tu (K)	Pd (kPa)	PR	Mj	Cd
2330	293.10	12.98	1.102	0.272	0.756
3334	293.20	18.61	1.098	0.273	0.770
4338	293.21	24.31	1.093	0.273	0.784

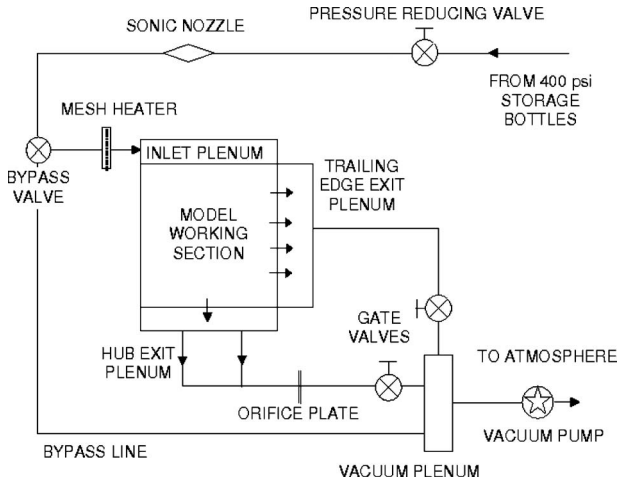

Fig. 4 Test rig schematic layout

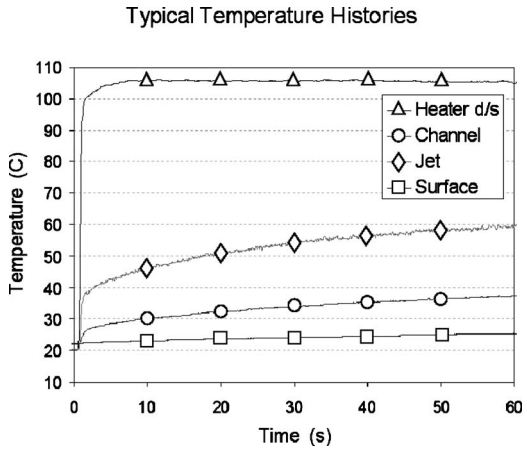

Fig. 5 Typical temperature trajectories

heater, designed and constructed by the Oxford University Osney Laboratory and described in Ireland et al. [11]. The mesh heater was fitted immediately upstream of the inlet plenum to maximize the speed of the gas temperature growth within the model. Model inlet temperature is limited by the softening point of Perspex; typically, inlet temperature is limited to 120°C.

The video capture was performed using bespoke software, which captures digital output from up to four CCD cameras to hard disk in real time without compression, through a VSavant user interface. Software algorithms are used to establish the phase change time at each pixel from the intensity history of each pixel according to the type of liquid crystal used.

Thermocouple and pressure transducer data acquisition is through a bespoke 16 bit turnkey system constructed in house. Rig operation is through an interface generated in LABVIEW.

4 Data Analysis

The transient liquid crystal heat transfer measurement technique is in widespread use and has been already described in literature many times previously, e.g. Ireland and Jones [12], thus, only a brief description will be given here.

The geometrically representative Perspex model is subjected to a sudden change in gas temperature at engine representative flow conditions. The surfaces of interest (the internal NGV wall surface, which is subject to the impingement jets) coated with liquid crystal exhibit color play at a temperature unique to the crystal. The color play is captured on video during the test; the color play resulting from crystal lattice untwists with temperature being referred to as the crystal "phase change." This phase change time information is married with gas temperature histories taken at judicious positions within the model in an iterative time marching analysis of the conduction through the substrate. Taking an initial guess at a certain location, together with a measured gas temperature history, the temperature distribution through the entire depth of the Perspex substrate at that location is predicted using a one-dimensional transient finite element model. Boundary conditions used are the initial uniform pretest temperature of the set-up, and the location dependent gas temperature history. The substrate is assumed semi-infinite, i.e. no heat loss from a back face of the model, and lateral conduction is assumed negligible. The time at which the surface is predicted to reach the crystal calibration temperature is compared with the phase change time. The HTC is adjusted, and the transient substrate temperature prediction iterated until these times match. This analysis is performed for each pixel of video information in the view, yielding full field HTC distributions. The crystal phase change temperature is calibrated in situ with a surface mounted thermocouple in the camera view in every test.

For 1D conduction with diffusivity independent of temperature, the Fourier Equation reduces to

$$\frac{\partial^2 T}{\partial x^2} = \frac{1}{\alpha}\frac{\partial T}{\partial \theta} \tag{2}$$

where

$$\alpha = \frac{k}{\rho C_p}$$

An analytical solution for the substrate temperature subjected to a step change in fluid temperature with HTC constant with time is given in Schneider [13] by

$$\frac{T(x,\theta) - T_0}{T_\infty - T_0} = erfc\left(\sqrt{\frac{x^2}{4\alpha\theta}}\right) - \exp\left(\frac{h^2\theta}{\rho C_p k} + \frac{hx}{k}\right) erfc\left(\sqrt{\frac{x^2}{4\alpha\theta}} + \sqrt{\frac{h^2\theta}{\rho C_p k}}\right) \tag{3}$$

At the fluid washed surface of the substrate, this reduces to

$$\frac{T(\theta) - T_0}{T_\infty - T_0} = 1 - \exp\left(\frac{h^2\theta}{\rho C_p k}\right) erfc\left(\sqrt{\frac{h^2\theta}{\rho C_p k}}\right) \tag{4}$$

This is a solution describing the surface temperature of the substrate as a function of time, HTC, and substrate thermal properties. While not directly used in the analysis approach in this work, it is useful in that the functional relationship between the surface temperature and the HTC is similar and the nature of the influence of the material thermal properties is shown.

Typical temperature trajectories are presented in Fig. 5. The mesh heater generates a very rapid increase in gas temperature, as measured immediately downstream of the mesh. However, given the combination of relatively low mass flow and significant inlet plenum and duct volume (and, thus, wetted surface area) in this particular model, the temperature drop prior to the measuring section is large. Hence, the temperature history near the target surface is not well approximated by a step function. While analytical approaches are possible with this type of gas temperature transient, e.g. Gillespie et al. [14], it is frankly easier and more flexible to form a numerical solution, which is the approach taken in this analysis. Using a numerical rather than analytical scheme also easily enables the use of temperature dependant, i.e. solution dependent, thermal properties ($\rho C_p k$) in the analysis.

Clearly the level of "measured" HTC depends on the driving gas temperature used in the analysis. In an impingement system,

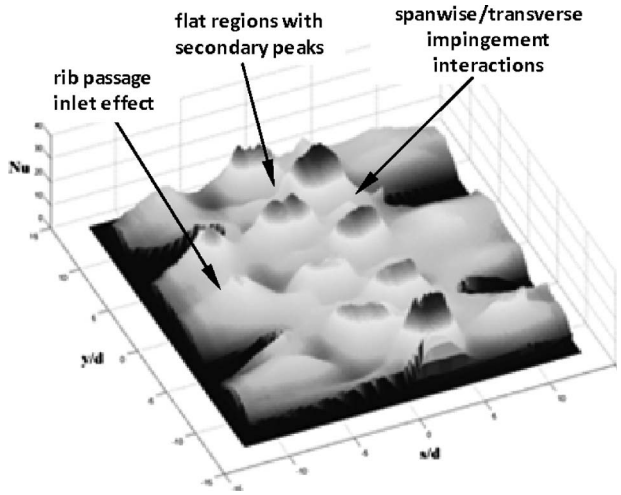

Fig. 6 Design point Nu distribution (3D view)

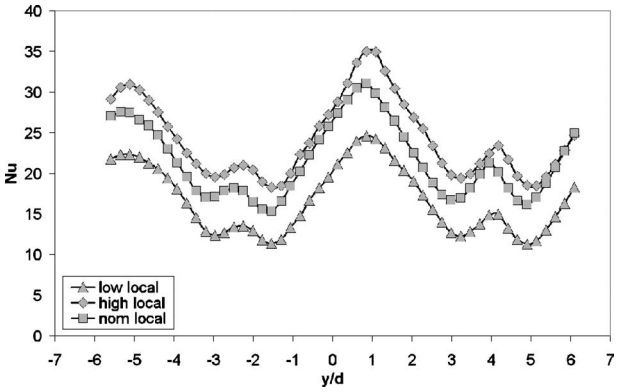

Fig. 7 PS row centerline Nu distribution

there are strong local gradients in gas temperature due to the nature of the flow structure, which render measurement of appropriate local gas temperature difficult. A scheme was developed whereby jet dominated and cross flow dominated regions were identified and treated separately. Reference was made to previous measurements of "jet effectiveness" in Van Treuren et al. [15] and a boundary around the jet footprint equivalent to say 0.7 was chosen as the boundary of the jet dominated surface. Temperature histories from thermocouples in the jet mouths were applied over the jet dominated regions while the cross flow dominated regions were covered by interpolating between the limited channel thermocouple locations and the edge of the jet dominated region. It should be noted that the temperature profile within the feed plenum is significant, thus, there is a significant spatial variation in local driving gas temperature over the impingement array.

While these choices of driving gas temperature definition may appear somewhat ad hoc, the resulting contour map of HTC may be judged against the phase change contour map in terms of smoothness of variation over the array. Poor choice of driving gas temperature results in sharp changes and inappropriate footprints in calculated HTC. The primary source of uncertainty in these measurements is in the choice of appropriate gas temperature. Previous studies have used a multiple crystal technique with an analytical scheme to measure both HTC and local adiabatic wall temperature directly, e.g. Van Treuren et al. [15]. However, the complexity of the model tested results in a gas temperature history that is not amenable to this approach. Relying on the scheme described above to determine local gas temperature history leads to an estimated uncertainty in HTC of $\pm 18\%$. Typically, the transient measurement technique should return an uncertainty of around 10%, primary uncertainty sources being temperature measurement error and liquid crystal calibration error. The one-dimensional conduction assumption introduces very small measurement errors due to the presence of lateral conduction in the substrate. These errors become more significant at sharp corners of geometry, which are not present in this model. Any system repeatability errors are reduced by taking multiple measurements (repeat tests) at the same operating point.

5 Experimental Results

5.1 Local Heat Transfer Distributions. Figure 6 shows the Nusselt number distributions obtained for the nominal Reynolds number test condition in the airfoil LE region.

The Nu distributions were obtained from test data obtained from video camera records and post-processed with a bespoke software code developed in MATLAB®, which provided spatially resolved Nu data in structured arrays of nondimensional streamwise (s/d) and spanwise distances (y/d). This information was used to provide the spanwise, constant spanwise distance, and row averaged data presented in following sections.

The areas of the airfoil surface lacking Nu information in Fig. 6 correspond to the areas of the airfoil surface covered by the longitudinal ribs in the airfoil PS and SS.

Information from the test was manually filtered using the post-processing software to remove spurious data introduced by test bolting features and instrumentation in order to get a single picture of the heat transfer distribution in both sides of the airfoil. Interpolation was done where necessary to ensure a smooth joint of both sides out of the information obtained from the two separate PS and SS recording cameras.

Figure 6 shows the PS impingement row on the right of the picture, i.e. positive s/d. The impingement stagnation areas did not show a clear circular defined peak for each impingement jet as expected but a more flatten regions of high heat transfer levels with, in general, more than one smaller secondary peak over those regions.

Higher heat transfer regions in between rib regions can also be observed, which are induced by fluid acceleration in the center of the passage. The intensity and number of these higher heat transfer level regions is dependent on the relative position of the impingement stagnation points relative to the side ribs. The two distinct SS peaks aligned with the impingement footprint are more intense as the two central impingement stagnation regions show better alignment with the inter-rib channel. This effect does not show up in the PS, as the impingement hole footprint is more shifted toward the bottom end and a single peaks appears in the inter-rib channel.

Spanwise and transverse impingement interaction secondary Nu peak bands appeared in the test although the former are more clearly visible.

5.2 Impingement Rows Centerline Heat Transfer. Figures 7 and 8 show the PS and SS impingement row centerline Nu distribution, respectively, for the three Re conditions tested. The impingement region shift toward the bottom end (negative y/d values) in the PS is clearly visible in the picture as the left hand high Nu distribution is incomplete although its contribution is offset by the flank of the impingement hole from the upper rib channel. The interaction effect between holes can also be seen in the both figures.

Upper holes in both the PS and SS show higher Nu levels than the lower ones. No clear explanation for this effect was found although a 3D effect on the feeding tube, open at the top and closed at the bottom, might play a role on this observation.

PS Nu levels are higher than those in the SS. This effect can be induced by the fact that PS flow through the side channel is higher than in the SS due a shorter and straighter PS path, as discharge holes are in the PS and SS flow has to turn 180 deg at the rear side

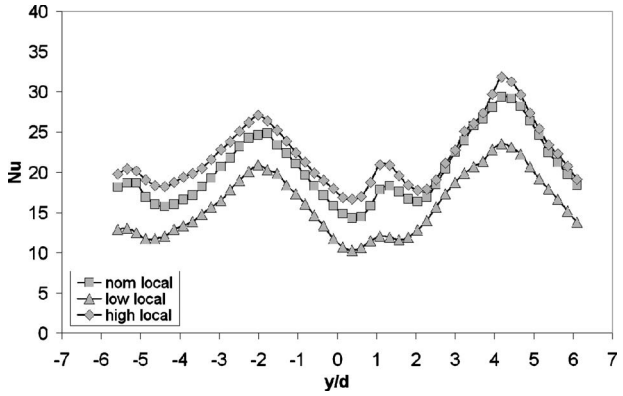

Fig. 8 SS row centerline Nu distribution

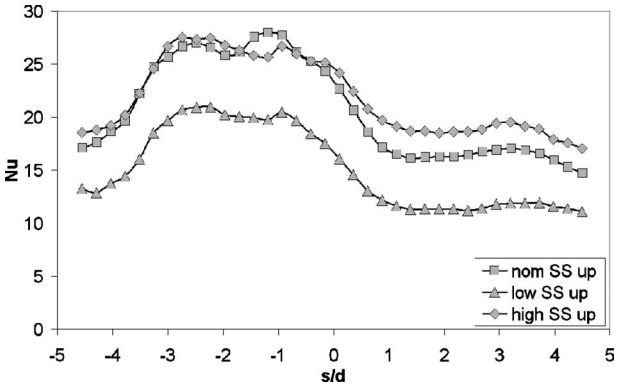

Fig. 11 SS up streamwise local Nu distribution

before discharging through the TE holes. However, impingement orifice discharge coefficients obtained from the tests do not show any difference between PS and SS orifice rows. A further investigation (e.g. by CFD) is proposed to be carried in order to further explain this difference between PS and SS impinging jets.

Figure 9 shows the variation with Re of the mean Nu for both the PS and SS impingement rows. These variations were correlated with Re and the following expressions were obtained:

$$\mathrm{Nu}_{\mathrm{PS\_stg\_avg}} = 0.14785 \cdot \mathrm{Re}^{0.61061} \quad (5)$$

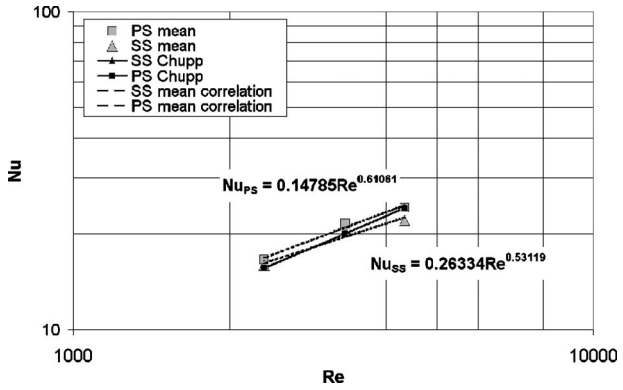

Fig. 9 PS and SS row centerlines

$$\mathrm{Nu}_{\mathrm{SS\_stg\_avg}} = 0.26334 \cdot \mathrm{Re}^{0.53119} \quad (6)$$

The correlation reported in Chupp et al. [4] for stagnation line mean Nu was used as a basis for comparison of the results. This correlation indicated stagnation line Nu should vary with Re to a power of 0.7. This dependence was, however, found to be to a lower power although it can be seen that the three points tested were not aligned in the log plot. The two lower Re points alone showed a higher Re trend than could not be maintained if also considering the higher Re point, which raises some concern on the high Re results.

5.3 Constant Y-Planes Heat Transfer. Figure 10 shows a flat view of the Nu distribution in the region between the central PS and SS ribs. The four y/d constant planes defined by the spanwise position of the intersections of the impingement hole geometric axes with the airfoil target surface are drawn on the figure and called PS up, PS down, SS Up, and SS down for convenience. As said previously, it can be seen that all the jets are deflected toward the bottom end by roughly one impingement hole diameter. The cause of this deflection is not clear but is believed to be due to asymmetry in the discharge conditions induced by the exit holes, which are all different in length.

Figures 11–14 show the Nu distributions along the four constant y/d planes mentioned above. Due to the jet downwards radial deflections, these distribution show different patterns mainly when comparing PS and SS distributions with each other. Figures do not show well defined Nu peaks in the stagnation region but nearly flat shapes.

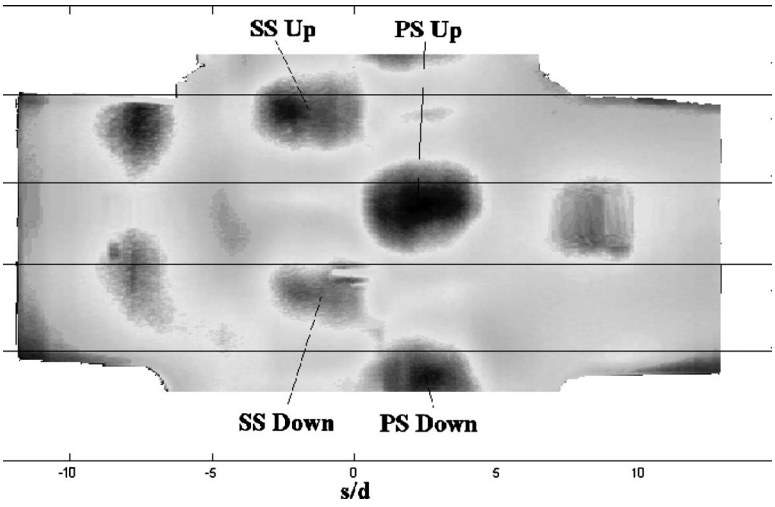

Fig. 10 Design point Nu distribution (flat view)

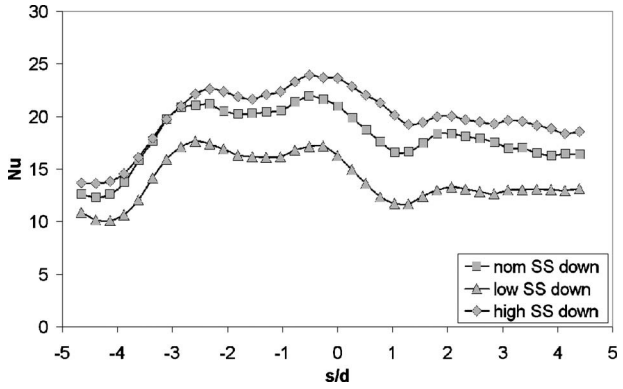

Fig. 12 SS down streamwise local Nu distribution

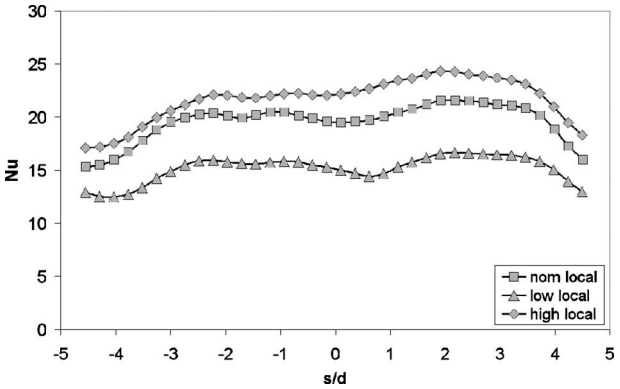

Fig. 15 Local span averaged Nu distribution

5.4 Local Span Averaged Heat Transfer. Figure 15 shows the streamwise distribution of span averaged Nu for the three Re conditions tested. This distribution was obtained for the impingement row extensions defined by the area from −X/2 to X/2 in each impingement row. The resulting Nu distribution in the streamwise impingement influence extension is fairly flat. This is to some extent in contradiction to the expectation of two well defined peaks in the impingement centerlines location with smaller secondary peaks in between the main peaks. However, it has to be taken into account that angled impingement produces elliptical HTC footprints that overlap each other in a staggered configuration of the impingement holes. This helps smooth the HTC level and yield relatively flat span averaged distributions. This distribution, however, is attractive to real engine design since temperature gradients are minimized and so does thermal loads.

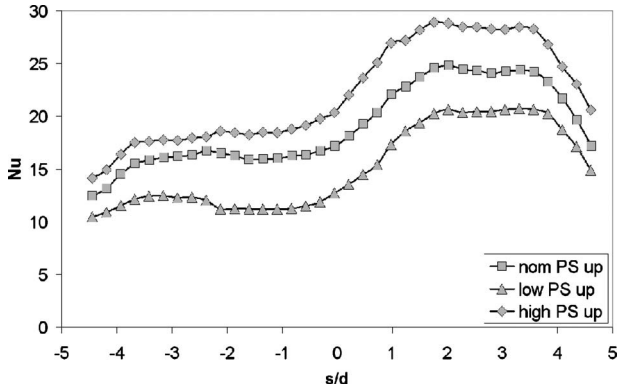

Fig. 13 PS up streamwise local Nu distribution

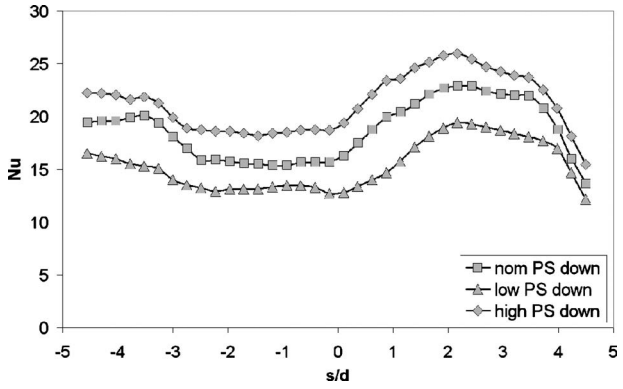

Fig. 14 PS down streamwise local Nu distribution

5.5 Row Averaged Heat Transfer. Figure 16 shows the variation with Re of the row averaged Nu for the PS and SS impingement rows. The row averaged Nu was obtained by averaging all Nu results over the area stretching from −X/2 to X/2 around each impingement centerline (see Figs. 2 and 3 for geometry details). These variations were correlated with Re and the following expressions were obtained:

$$Nu_{PS\_row\_avg} = 0.12321 \cdot Re^{0.62323} \tag{7}$$

$$Nu_{SS\_row\_avg} = 0.20955 \cdot Re^{0.54897} \tag{8}$$

The correlation reported in Chupp et al. [4] for row averaged Nu was used as a basis for comparison of the results. This correlation was developed for single row impingement perpendicular to a semicylindrical target surface with results averaged over the 180 deg of the curved surface. The geometry tested featured, however, a two-row impingement with a 45 deg impingement plane angle between rows with air impinging at a certain angle on a variable curvature surface, which implies geometric conditions between test and correlation are not comparable although it is the best reference identified.

The Re power obtained in the correlations is again smaller than the 0.7 reported by Chupp, and the three Re points in both the PS and SS are not aligned in the plot, which suggested, in view of the results, that the high Re results may be questionable. The row averaged values obtained in the PS are higher than in the SS due to the higher flow spent by the PS, as already discussed.

6 Conclusions

An experimental investigation of the leading edge impingement cooling system of a Low Pressure Turbine vane comprised of two staggered rows of jet orifices was conducted by using a transient liquid crystal technique on a scaled Perspex model. Despite the

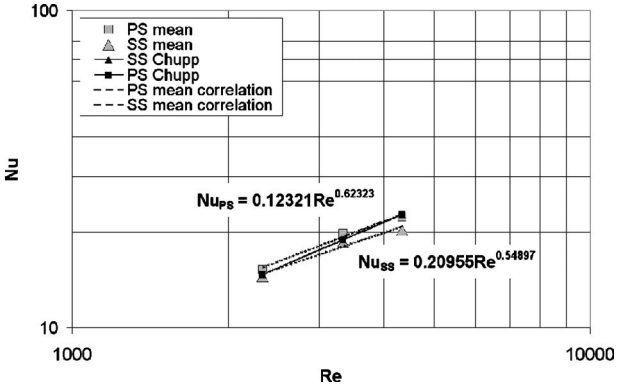

Fig. 16 Row averaged Nu versus Re

low Reynolds number and relatively long crystal phase change times of the experiment, good results were obtained although some lack of resolution for the low HTC regions dominated by duct flow have been identified.

The experimental results showed Nu values at the stagnation regions corresponding to both mean values and row averaged values to vary with the Re to a slightly lower power than the Chupp correlation. However, it is showed that accurate results can be obtained by applying the Chupp correlation to a concave geometry with low radius of curvature.

While clear high single peaks at the impingement points appears when looking to the Nu variation spanwise with secondary smaller peaks being generated at the confluence of two jets, fairly flat regions are found at the stagnation region in streamwise direction, hence, indicating an elliptical shape of the impingement heat transfer with the long axis located streamwise. Secondary high Nu peaks appear for each jet at the inlet of the side channels, which are thought to be due to the effect of the contraction generated by the ribs on the jet secondary impingement region.

Acknowledgment

The authors wish to thank ITP for the permission to publish this paper. We also would like to thank the test team at the Heat Transfer Laboratory at Rolls-Royce Bristol for their effort during the experimental testing and especially to Toby Kohler for his support.

Nomenclature

3D = three-dimensional
CADD = computer-aided design and drafting
C_p = substrate specific heat capacity
D = impingement hole diameter
D = target plate curvature diameter
Fo = Fourier modulus
h, HTC = heat transfer coefficient
k = thermal conductivity, W/m K
LE = leading edge
M = Mach number
NGV = nozzzle guide vane
$\mathrm{Nu}=h\cdot d/k$ = Nusselt number
P = pressure
PS = pressure side
PT = power turbine
$\mathrm{Re}=4\cdot W_j/\pi\cdot d\cdot\mu$ = jet Reynolds number
s = streamwise distance
SS = suction side
T = temperature
TE = trailing edge
W = mass flow
X = streamwise row pitch, mm
y = spanwise distance
Y = spanwise row pitch, mm
Z = impingement to target surface distance

Greek

α = thermal diffusivity
ρ = substrate density
θ = time
μ = dynamic viscosity

Subscripts

avg = average
d = downstream of the impingement orifice
j = jet
stg = stagnation
u = upstream of the impingement orifice

References

[1] Florschuetz, L. W., Berry, R. A., and Metzger, D. E., 1980, "Periodic Streamwise Variations of Heat Transfer Coefficients for Inline and Staggered Arrays of Circular Jets With Crossflow of Spent Air," ASME J. Heat Transfer, **102**, pp. 132–137.
[2] Florschuetz, L. W., Metzger, D. E., and Su, C. C., 1984, "Heat Transfer Characteristics for Jet Array Impingement With Initial Crossflow," ASME J. Heat Transfer, **106**, pp. 34–41.
[3] Onstad, A. J., Elkins, C. J., Moffat, R. J., and Eaton, J. K., 2009, "Full-Field Flow Measurements and Heat Transfer of a Compact Jet Impingement Array With Local Extraction of Spent Fluid," ASME J. Heat Transfer, **131**, p. 082201.
[4] Chupp, R. E., Helms, H. E., McFadden, P. W., and Brown, T. R., 1969, "Evaluation of Internal Heat Transfer Coefficients for Impingement Cooled Turbine Airfoils," J. Aircr., **6**(3), pp. 203–208.
[5] Hrycak, P., 1981, "Heat Transfer From a Row of Impinging Jets to Concave Cylindrical Surfaces," Int. J. Heat Mass Transfer, **24**, pp. 407–419.
[6] Bunker, R. S., and Metzger, D. E., 1990, "Local Heat Transfer in Internally Cooled Turbine Airfoil Leading Edge Regions: Part I: Impingement Cooling Without Film Coolant Extraction," ASME J. Turbomach., **112**(3), pp. 451–458.
[7] Kayansayan, N., and Kucuka, S., 2001, "Impingement Cooling of a Semi-Cylindrical Concave Channel by Confined Slot-Air-Jet," Exp. Therm. Fluid Sci., **25**, pp. 383–396.
[8] Taslim, M. E., and Setayeshgar, L., 2000, "An Experimental Evaluation of Advances Leading Edge Impingement Cooling Concepts," ASME Paper No. 2000-GT-0222.
[9] Taslim, M. E., and Khanicheh, A., 2005, "Experimental and Numerical Study if Impingement on and Airfoil Leading Edge With and Without Showerhead and Gill Film Holes," ASME Paper No. 2005-GT-68037.
[10] Damerow, W. P., Murtaugh, J. P., and Burgraff, F., 1972, "Experimental and Analytical Investigation of the Coolant Flow Characteristics in Cooled Turbine Airfoils," NASA Paper No. CR-120883.
[11] Ireland, P. T., Gillespie, D. R. H., and Wang, Z., 1996, "Heater Element," U.S. Patent No. 6,181,874.
[12] Ireland, P. T., and Jones, T. V., 2000, "Liquid Crystal Measurements of Heat Transfer and Surface Shear Stress," Meas. Sci. Technol., **11**(7), pp. 969–986.
[13] Schneider, P. J., 1955, *Conduction Heat Transfer*, Addison-Wesley, Cambridge, MA.
[14] Gillespie D. R. H., Guo, S. M., Wang, Z., Ireland, P. T., and Kohler S. T., 1996, "A Comparison of Full Surface Local Heat Transfer Coefficient and Flow Field Studies Beneath Sharp—Edged and Radiused Entry Impinging Jets," ASME Paper No. 96-GT-428.
[15] Van Treuren, K. W., Wang, Z., Ireland, P., Jones, T. V., and Kohler, S. T., 1996, "The Role of the Impingement Plate in Array Heat Transfer," ASME Paper No. 96-GT-162.

Entropy Generation Analysis for Nanofluid Flow in Microchannels

Jie Li

Clement Kleinstreuer[1]
e-mail: ck@eos.ncsu.edu

Department of Mechanical and Aerospace Engineering,
NC State University,
Raleigh, NC 27695

Employing a validated computer simulation model, entropy generation is analyzed in trapezoidal microchannels for steady laminar flow of pure water and CuO-water nanofluids. Focusing on microchannel heat sink applications, local and volumetric entropy rates caused by frictional and thermal effects are computed for different coolants, inlet temperatures, Reynolds numbers, and channel aspect ratios. It was found that there exists an optimal Reynolds number range to operate the system due to the characteristics of the two different entropy sources, both related to the inlet Reynolds number. Microchannels with high aspect ratios have a lower suitable operational Reynolds number range. The employment of nanofluids can further minimize entropy generation because of their superior thermal properties. Heat transfer induced entropy generation is dominant for typical microheating systems while frictional entropy generation becomes more and more important with the increase in fluid inlet velocity/Reynolds number.
[DOI: 10.1115/1.4002395]

Keywords: computer simulation, nanofluid flow, entropy minimization, microchannel geometry, microchannel operation

1 Introduction

Nanofluids are dilute suspensions of nanoparticles in liquids, a mixture, which may exhibit remarkable heat transfer characteristics (see Kleinstreuer et al. [1] and literature cited). Nanofluid flow in microchannels, as part of microfluidics and nanotechnology, has the potential for major applications in microscale cooling and nanodrug delivery (see Kleinstreuer et al. [1] and Li and Kleinstreuer [2], among others).

Minimization of entropy generation is potentially a design tool to determine best device geometry and operation for heat exchangers, and has been established for macroscale configurations (see Bejan [3,4], Selvarasu et al. [5], Ratts and Raut [6], Sahin [7,8], Mahmud and Fraser [9], Mansour et al. [10], Khan et al. [11], Ko and Wu [12], and Ko [13], among others). However, fluid flow in microchannels exhibits dominant features often nonexisting or less influential in macrochannels, e.g., wall-slip velocities, entrance effects because of the short conduit length, and significant surface roughness in relation to microchannel height (or hydraulic diameter), to name a few (see Nguyen and Wereley [14]). Clearly, application of entropy generation minimization principles may assist in the optimal design of microchannel heat sinks or bio-micro-electro-mechanical systems (bio-MEMS) in light of geometric and operational conditions [15–19]. Classical methods for enhanced heat transfer, e.g., an increase in heat transfer area and/or inlet Reynolds number are limited options for microchannel flow. Thus, the use of nanofluids as coolants, e.g., CuO or Al_2O_3 nanospheres with diameters in the range of 10 nm$\leq d_p \leq$100 nm in water, oil, or ethylene glycol is a third option.

In this study, entropy generation is minimized for steady laminar pure water and nanofluid flows in a representative trapezoidal microchannel in terms of most suitable channel aspect ratio and Reynolds number range.

2 Theory

Assuming the continuum approach to be valid (i.e., here $D_h > 100$ μm) for steady 3D laminar incompressible nanofluid flow in a microchannel, the continuity, momentum, energy, and species mass transfer equations have to be solved, considering temperature and volume fraction dependent mixture properties. In addition to the conservation laws, mixture properties and the second law of thermodynamics have to be described.

2.1 Governing Equations. Continuity equation

$$\frac{\partial}{\partial x_i}(\rho u_i) = 0 \tag{1}$$

Momentum equation

$$u_j \frac{\partial}{\partial x_j}(\rho u_i) = -\frac{\partial p}{\partial x_i} + \frac{\partial}{\partial x_j}\left[\mu\left(\frac{\partial u_i}{\partial x_j} + \frac{\partial u_j}{\partial x_i}\right)\right] \tag{2}$$

Energy equation

$$u_i\left(\frac{\partial(\rho c_p T)}{\partial x_i}\right) = \frac{\partial}{\partial x_i}\left(k\frac{\partial T}{\partial x_i}\right) + \mu\Phi \tag{3}$$

where

$$\Phi = \left(\frac{\partial u_i}{\partial x_j} + \frac{\partial u_j}{\partial x_i}\right)\frac{\partial u_i}{\partial x_j} \tag{4}$$

Mass transfer equation

$$u_i\frac{\partial c}{\partial x_i} = \frac{\partial}{\partial x_i}\left(D\frac{\partial c}{\partial x_i}\right) \tag{5}$$

For nanofluid flow and pure fluid flow, the corresponding physical properties will be selected, e.g., the thermal conductivities k_{eff} and k_f, respectively.

As hydraulic boundary conditions, uniform velocities were applied at the channel inlet, i.e., $u=U_{in}$, $v=0$, and $w=0$. Exposed to the atmosphere, the outlet pressure was the static pressure, i.e., $p_{\text{gage}}=0$. The no-slip boundary condition was enforced at all solid walls. The thermal boundary condition at the bottom and sidewalls is a constant wall heat flux, i.e., $q=C$ while an adiabatic boundary condition is imposed on the top wall and $T=T_0$ at the microchannel inlet. These thermal boundary conditions are standard assumptions where the channel cover plate functions as a perfect insulator while the sidewalls of the machined or edged microchannel are equally exposed to the heat source, expressed as a constant wall heat flux.

[1]Corresponding author.

Contributed by the Heat Transfer Division of ASME for publication in the JOURNAL OF HEAT TRANSFER. Manuscript received April 30, 2009; final manuscript received May 6, 2010; published online September 17, 2010. Assoc. Editor: Roger Schmidt.

2.2 Mixture Properties. In a recent study, Mansour et al. [20] showed that different published mixture property expressions lead to significantly different results for such fundamental quantities as pumping power or design parameters. Li et al. [21] experimentally investigated the viscosity of $Cu-H_2O$ nanofluids and it was found that temperature was the major factor corresponding to the Cu-mass fraction. Thus, the choice of property model for nanoparticle suspensions is very important.

Typically, the nanoparticle suspensions are dilute so that the effective nanofluid properties can be described as [22]

$$\mu_{\text{eff}} = \mu_f \frac{1}{(1-\varphi)^{2.5}} \tag{6}$$

$$\rho_{\text{eff}} = \varphi\rho_p + (1-\varphi)\rho_f \tag{7}$$

and

$$(\rho c_p)_{\text{eff}} = \varphi(\rho c_p)_p + (1-\varphi)(\rho c_p)_f \tag{8}$$

where φ is the volume fraction of nanoparticles, subscript f indicates the carrier fluid, and subscript p denotes nanoparticles. Equation (6) is an extension of Einstein's postulate by Brinkman to cover higher nanoparticle volume fractions, i.e., $0<\varphi<5\%$, while the density and heat capacity correlations reflect basic mass and energy balances. The effective thermal conductivity is composed of a static part after Maxwell [23] and a kinematic part, i.e., microscale heat transfer due to Brownian particle motion [24]. The final form of k_{eff}, taking into account nanoparticle size and volume fraction as well as type of particle-fluid pairing and temperature dependence, was discussed and compared with measured data sets by Li and Kleinstreuer [2]. Specifically, for k_{eff} the Koo–Kleinstreuer–Li (KKL) model was employed

$$k_{\text{eff}} = k_{\text{static}} + k_{\text{Brownian}} \tag{9}$$

The static part is Maxwell's model and the dynamic part was developed based on kinetic theory together with Stokes' flow of microscale convective heat transfer, i.e., micromixing. Hence, we can write [2]

$$\frac{k_{\text{static}}}{k_f} = 1 + \frac{3\left(\frac{k_{p,\text{eff}}}{k_f} - 1\right)\varphi}{\left(\frac{k_{p,\text{eff}}}{k_f} + 2\right) - \left(\frac{k_{p,\text{eff}}}{k_f} - 1\right)\varphi} \tag{10}$$

and

$$k_{\text{Brownian}} = 5\times 10^4 \varphi\rho_f c_{p,f}\sqrt{\frac{\kappa_B T}{\rho_p d_p}}\, g(T,\varphi,d_p,\rho_p) \tag{11}$$

where ρ is the density, $c_{p,f}$ is the fluid thermal capacity, and again, φ is the volume fraction while the subscripts f and p indicate fluid and particle, respectively. The g-function, determined semi-empirically, was introduced to encapsulate the thermo-hydrodynamic interactions among all nanoparticles and affected microscale fluid parcels. For example, for Al_2O_3-water and CuO-water nanofluids, the nonlinear g-function generated r^2 values of 96% and 98%, respectively [25]. In this study, 4% and 1% CuO-water suspensions were employed for the nanofluid flow applications.

2.3 Entropy Generation. If the mixture is Newtonian and if it obeys Fourier's law of heat conduction, the total entropy generation rate per unit volume ($S_{\text{gen}} \equiv S_G$ in W/K m^3) can be expressed as [3]

$$S_{\text{gen}} \equiv S_G = \frac{k}{T^2}\left[\left(\frac{\partial T}{\partial x}\right)^2 + \left(\frac{\partial T}{\partial y}\right)^2 + \left(\frac{\partial T}{\partial z}\right)^2\right] + \frac{\mu}{T}\left\{2\left[\left(\frac{\partial u}{\partial x}\right)^2 + \left(\frac{\partial v}{\partial y}\right)^2 + \left(\frac{\partial w}{\partial z}\right)^2\right] + \left(\frac{\partial u}{\partial y} + \frac{\partial v}{\partial x}\right)^2 + \left(\frac{\partial u}{\partial z} + \frac{\partial w}{\partial x}\right)^2 + \left(\frac{\partial v}{\partial z} + \frac{\partial w}{\partial y}\right)^2\right\} \tag{12}$$

Equation (12) encapsulates the irreversibilities due to heat transfer and frictional effects, i.e.,

$$S_{\text{gen}} = S_{\text{gen}}(\text{thermal}) + S_{\text{gen}}(\text{frictional}) \tag{13}$$

Specifically, the dimensionless entropy generation rate induced by fluid friction can be defined as follows:

$$S_{G,F} = S_{\text{gen}}(\text{frictional}) \cdot \frac{kT_0^{\,2}}{q^2} \tag{14a}$$

where

$$S_{\text{gen}}(\text{frictional}) = \frac{\mu}{T}\left\{2\left[\left(\frac{\partial u}{\partial x}\right)^2 + \left(\frac{\partial v}{\partial y}\right)^2 + \left(\frac{\partial w}{\partial z}\right)^2\right] + \left(\frac{\partial u}{\partial y} + \frac{\partial v}{\partial x}\right)^2 + \left(\frac{\partial u}{\partial z} + \frac{\partial w}{\partial x}\right)^2 + \left(\frac{\partial v}{\partial z} + \frac{\partial w}{\partial y}\right)^2\right\} \tag{14b}$$

while for the thermal entropy source

$$S_{G,T} = S_{\text{gen}}(\text{thermal}) \cdot \frac{kT_0^{\,2}}{q^2} \tag{15a}$$

where

$$S_{\text{gen}}(\text{thermal}) = \frac{k}{T^2}\left[\left(\frac{\partial T}{\partial x}\right)^2 + \left(\frac{\partial T}{\partial y}\right)^2 + \left(\frac{\partial T}{\partial z}\right)^2\right] \tag{15b}$$

Finally,

$$S_{G,\text{total}} = S_{\text{gen}}\frac{kT_0^{\,2}}{q^2} = S_{G,F} + S_{G,T} \tag{16}$$

where T_0 is the fluid inlet temperature and q is the wall heat flux.

Considering the classic solution for Hagen–Poiseuille (H-P) flow through a smooth tube of radius r_0 with uniform wall heat flux q (W/m^2), the velocity and temperature are given by (e.g., Kleinstreuer [26] and/or Bejan [27])

$$u = 2U\left[1 - \left(\frac{r}{r_0}\right)^2\right] \tag{17}$$

and

$$T - T_s = -\frac{qr_0}{k}\left[\frac{3}{4} - \left(\frac{r}{r_0}\right)^2 + \frac{1}{4}\left(\frac{r}{r_0}\right)^4\right] \tag{18}$$

The wall temperature $T_s = T(r=r_0)$ can be obtained from the condition

$$\frac{\partial T}{\partial x} = \frac{dT_s}{dx} = \frac{2q}{\rho c_p U r_0} = \text{constant} \tag{19}$$

Hence, the dimensionless entropy generation for H-P flow can be expressed as

$$S_G\frac{kT_0^{\,2}}{q^2} = \frac{4k^2}{(\rho c_p U r_0)^2}\frac{T_0^{\,2}}{T^2} + (2R-R^3)^2\frac{T_0^{\,2}}{T^2} + \frac{16kT_0^{\,2}\mu U^2}{q^2 T r_0^{\,2}}R^2 \tag{20a}$$

$$= \underbrace{\frac{16}{\text{Pe}^2}\left(\frac{T_0}{T}\right)^2 + (2R-R^3)^2\frac{T_0^2}{T^2}}_{\text{thermal source}} + \underbrace{\phi\frac{T_0}{T}R^2}_{\text{frictional source}} \tag{20b}$$

where

$$\mathrm{Pe} = \mathrm{Re} \cdot \mathrm{Pr} = \frac{2r_0 \rho c_p U}{k} \tag{21a}$$

$$R = \frac{r}{r_0} \tag{21b}$$

and

$$\phi = \frac{16 k T_0 \mu U^2}{q^2 {r_0}^2} \tag{21c}$$

The parameter values used for model validation included Pe $=1155$, $T_0 = 293$ K, $k{T_0}^2/q = 0.223$, and $\phi = 1.63 \times 10^{-2}$. The inlet temperature T_0 was selected as the reference temperature.

In order to assess the overall entropy generated in the entire flow field for different scenarios, the integral form is used.

$$\hat{S}_{G,\mathrm{total}} = \frac{1}{\dot{m} c_p} \int \int_V \int S_{\mathrm{gen}} dV \tag{22}$$

where the fraction of entropy generation due to friction as well as heat transfer can be defined as

$$\xi_F = \frac{\hat{S}_{G,F}}{\hat{S}_{G,\mathrm{total}}} \tag{23a}$$

and

$$\xi_T = \frac{\hat{S}_{G,T}}{\hat{S}_{G,\mathrm{total}}} \tag{23b}$$

2.4 Numerical Method. The numerical solution of the Eulerian transport equations were carried out with a user-enhanced, unstructured finite-volume based program, i.e., CFX 11 from Ansys, Inc. (Canonsburg, PA). The mesh size of the computational domain used in this study was refined until acceptable levels of grid independence of the solutions were achieved. The final mesh featured about 760,000 elements. Specifically, increasing the mesh density by a factor of 2.0 had a negligible effect on all results. The computations were performed on an IBM Linux Cluster at North Carolina State University's High-Performance Computing Center (Raleigh, NC) and on a local dual Xeon Intel 3.0 G Dell desktop (CM-P Laboratory, MAE Department, NC State University). Furthermore, the solutions of the flow field were assumed to be converged when the dimensionless mass and momentum as well as the thermal energy residual ratios were below 10^{-6}. Improving the convergence criteria to less than 10^{-7} had a negligible effect on the simulation results. A typical simulation run took about 24 h.

3 Model Validations

In order to validate the computer model, pure water flow with constant properties in a microtube of diameter $D = 106.66$ μm and length $L = 4.0$ cm was considered (see Fig. 1(*a*)). The volumetric entropy generation rate, based on the simulated velocity and temperature distributions, was compared with the analytical solution of Eq. (20). Figure 2(*a*) shows the dimensionless entropy generation rate profile in radial direction for the microtube. As expected, at the center, i.e., $R = 0$, only the first term in Eq. (20) contributes to S_G; however, for $\mathrm{Pe} \gg 1$, the irreversibility due to axial conduction is negligible in this case. In contrast, in the wall region both thermal and frictional effects produce entropy with a maximum at $R \approx 0.8$ generated by dominant heat transfer induced entropy generation. The computer simulation results match the exact solution perfectly.

For a validation of the KKL model, the thermal performance of water-based alumina nanofluid flow in a straight 1.02 mm tube was investigated and compared with the experimental data of Lai et al. [28]. As shown in Fig. 2(*b*), employing the same geometry and operational conditions (i.e., a volume flow rate of 5 ml/min),

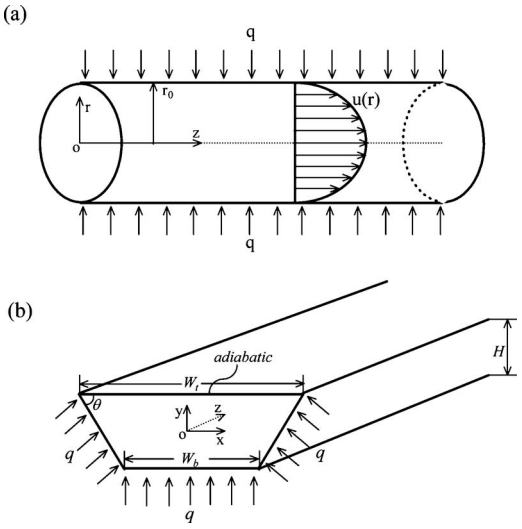

Fig. 1 System sketch: (*a*) validation test tube and (*b*) investigated trapezoidal channel

the use of the KKL model provides very reasonable results for the local heat transfer coefficient. It should be noted that the experimental data sets [28] are actually based on the measured outer wall temperatures, i.e., the inner wall temperatures were calculated with the steady one-dimensional heat conduction equation. The local bulk temperature was obtained using an energy balance based on the nanofluid's thermal properties at the average temperature. Both the pure water and nanofluid flow graphs show the strong entrance-region effect while the use of a very dilute nanoparticle suspension, indeed, increases the local heat transfer coefficient.

Standard numerical tests, i.e., mesh-independence of the results and minimal mass/momentum residuals (10^{-6}), were conducted as well.

4 Results and Discussion

Three cases of trapezoidal microchannels with the same hydraulic diameter ($D_h = 4S/P = 106.66$ μm), where S is the cross-sectional area and P is the perimeter), the same length (i.e., 40 mm), the same base angle (i.e., 54.7 deg, according to Wu and Cheng [29]) but different aspect ratios ($AR = W_b/W_t$) were employed for this study (see Fig. 1(*b*) and Table 1). Pure water as well as a nanofluid (i.e., $\mathrm{CuO}-\mathrm{H_2O}$) were used.

For the three trapezoidal channels, bottom and sidewall were heated by a constant heat flux (typically 0.2 $\mathrm{MW/m^2}$ or higher) while an adiabatic boundary condition was applied on the top. The corresponding heated areas and heat transfer quantities are listed in Table 2.

4.1 Entropy Contours. Figures 3(*a*)–3(*c*), 4(*a*)–4(*c*), and 5(*a*)–5(*c*) depict the dimensionless entropy generation rates at the outlet ($L = 40$ mm and $\mathrm{Re} = 425$) caused by individual and combined sources for pure water flow in microchannels with three different aspect ratios. Friction-induced entropy generation (see Eq. (14)) is dominant at the walls where for $AR = 0.9337$; it resembles slit flow (Fig. 3(*a*)) while at lower *AR*-values (Figs. 3(*b*) and 3(*c*)) the wall locations for $S_{G,F}|_{\max}$ and its extent shift measurably. As expected, the core flow region is nearly $S_{G,F}$-free, which remarkably is also the case for all four corners. This is because within these complex 3D corner flow fields, the velocity gradients (see Eq. (14)) largely cancel each other out.

Heat transfer may generate entropy levels up to three times higher than frictional effects (Figs. 4(*a*)–4(*c*)). Again, the core region is entropy-free, including now part of the adiabatic wall. Strong differences in fluid temperature and surface temperature

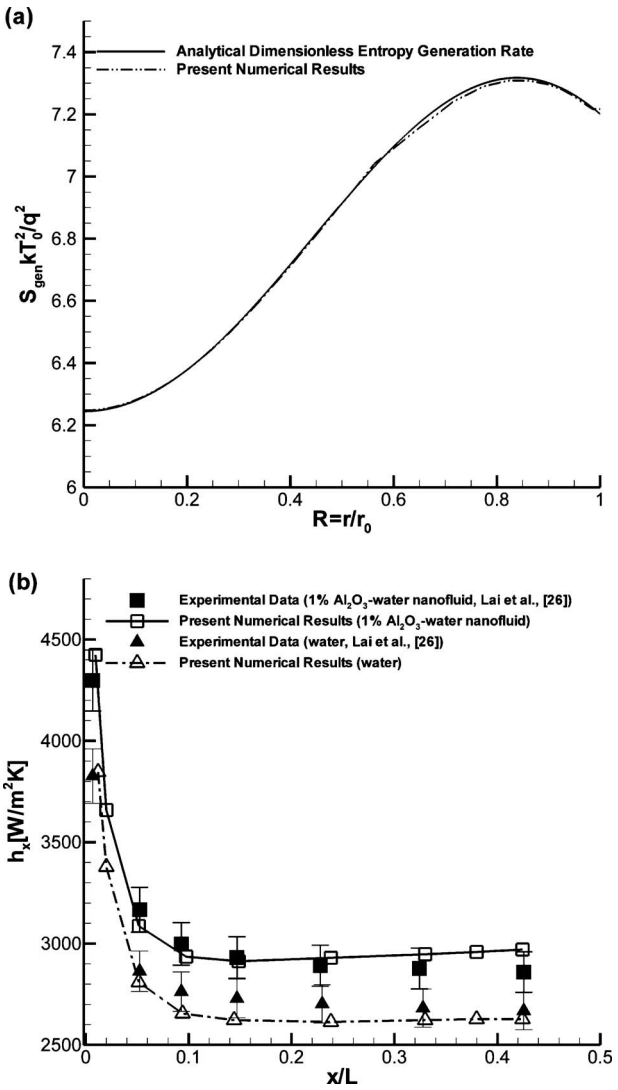

Fig. 2 Model validation: (*a*) dimensionless entropy generation rate profiles in radial direction and (*b*) local heat transfer coefficients in the tubular entrance region for both pure water and nanofluid flows

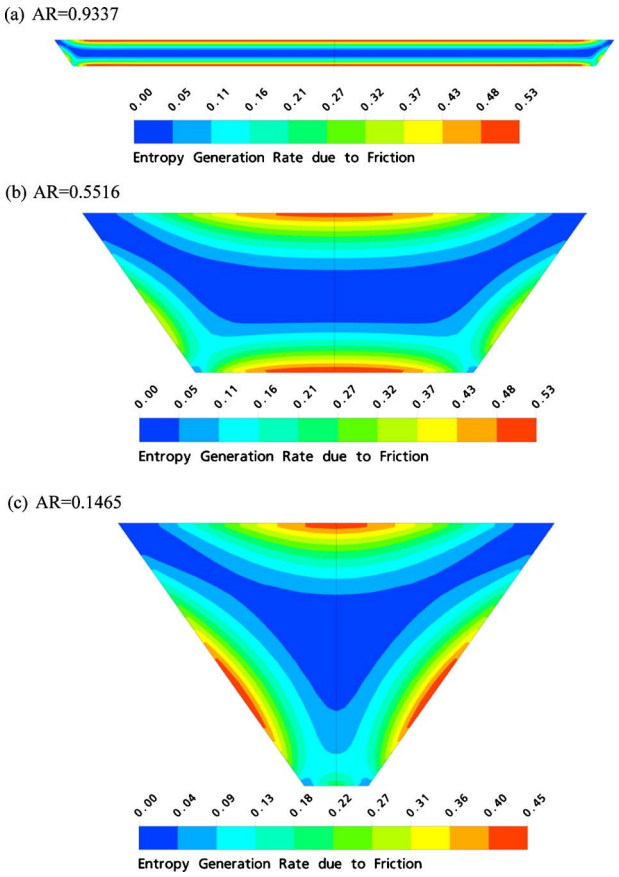

Fig. 3 Entropy generation contours due to friction for pure water flow: (*a*) trapezoidal microchannel case 1, (*b*) trapezoidal microchannel case 2, and (*c*) trapezoidal microchannel case 3

generate gradients and hence, maximum $S_{G,T}$-values near the bottom and side walls (see Eq. (15)). Combining both entropy sources produces for all microchannel aspect ratios closed entropy-free centers (Eq. (12)) with "radially" increasing $S_{G,\text{total}}$-values, reaching maxima at the bottom wall for $AR=0.9337$ and $AR=0.5516$ while for $AR=0.14654$ at the side walls.

Table 1 Trapezoidal microchannel geometry

	H (μm)	W_t (μm)	W_b (μm)	D_h (μm)	AR
Case 1	56.494	1206.73	1126.73	106.66	0.9337
Case 2	80	252.65	139.37	106.66	0.5516
Case 3	122.027	202.47	29.67	106.66	0.1465

Table 2 Thermal boundary conditions

	A_h (m^2)	q (kW/m^2)	Q (W)
Case 1	5.06068×10^{-5}	200	10.12136
Case 2	1.34165×10^{-5}	200	2.68329
Case 3	1.31482×10^{-5}	200	2.62964

4.2 Entropy Profiles. Figures 6(*a*)–6(*c*) provide the entropy generation rate profiles at the vertical midplane along axial direction for $AR=0.5516$ for pure water. Again, the channel length is 40 mm, where for $\text{Re}=425$, the hydraulic entrance effect prevails to $z\approx0.004$ m based on the correlation $L_{\text{entrance}}\approx0.09\,\text{Re}\,D_h$ (Kleinstreuer and Li [19]). Indeed, the graphs in Fig. 6(*a*) confirm such an entropy-rate development in the entrance region where the changes in vertical midplane $S_{G,F}$-profile (Fig. 3(*b*)) reflect the $z=0.005$ m graph in Fig. 6(*a*). Similarly, the $S_{G,T}$-profile for $z=0.01$ m in Fig. 6(*b*) can be correlated with Fig. 4(*b*), implying that the thermal entrance length is much longer than the hydraulic one. Figure 6(*c*) then provides the developing profiles of the total entropy generation rates where at the microchannel bottom, $S_{G,\text{total}}$ is a maximum because of the adiabatic cover plate at $y=4\times10^{-5}$ m.

4.3 Entropy Generation in Thermal Nanofluid Flow. Focusing on the impacts of inlet temperature, Reynolds number, and aspect ratio, entropy generation in trapezoidal microchannels is compared for flow of pure water and nanofluids, i.e., 1% and 4% of CuO-nanoparticles ($d_p=28.6$ nm) in water (see Figs. 7–9).

An increase in fluid inlet temperature, say, $\Delta T_0=15\,^\circ$C, measurably decreases total entropy generation because of higher bulk temperatures and hence, lower gradients in the near-wall region (Fig. 7). More remarkable is the nonmonotonic change in $\hat{S}_{G,\text{total}}$ for nanofluids with their elevated effective thermal conductivities (see Eq. (9)). Specifically, Fig. 8 depicts $\hat{S}_{G,\text{total}}$ as a function of nanoparticle volume fraction, where the optimal volume fraction

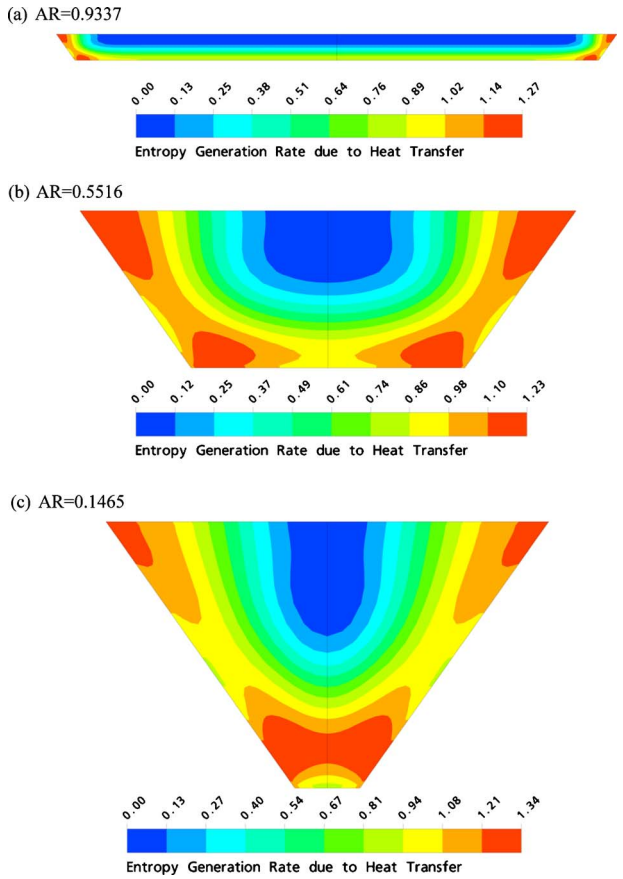

Fig. 4 Entropy generation contours due to heat transfer for pure water flow: (*a*) trapezoidal microchannel case 1, (*b*) trapezoidal microchannel case 2, and (*c*) trapezoidal microchannel case 3

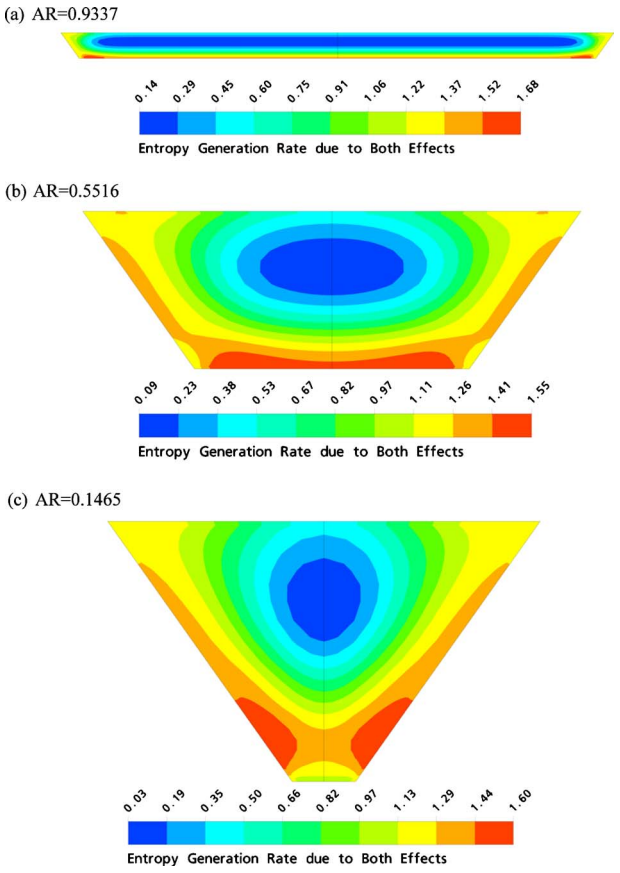

Fig. 5 Entropy generation contours due to both sources for pure water flow: (*a*) trapezoidal microchannel case 1, (*b*) trapezoidal microchannel case 2, and (*c*) trapezoidal microchannel case 3

is around 1.5%. Another effective operational parameter is the inlet Reynolds number where Fig. 9 indicates a desirable range of $425 \leq \mathrm{Re} \leq 1100$ for all fluids and aspect ratios considered, when ignoring "slit flow" for $AR=0.9337$. Due to slightly enhanced frictional effects (see Eq. (6)), the total entropy generated by the mixture is larger than that of the carrier fluid alone; hence, $\hat{S}_{G,\mathrm{total}}^{\mathrm{nanofluid}} > \hat{S}_{G,\mathrm{total}}^{\mathrm{water}}$.

An important geometric design parameter is the aspect ratio. Figure 10 shows $\hat{S}_{G,\mathrm{total}}(AR)$ for three fluids and different inlet Reynolds numbers. Specifically, for $U_{in}=4$ m/s (implying Re =425, 437, and 466 for water, 1% CuO-nanofluids, and 4% CuO-nanofluids, respectively) the larger aspect ratio generates smaller $\hat{S}_{G,\mathrm{total}}$ values while for $U_{in}=10$ m/s (implying Re=1063, 1092, and 1165) the lower aspect ratio generates smaller $\hat{S}_{G,\mathrm{total}}$ values. Clearly, the 1% CuO-water pairing yields more favorable results than the nanofluid with 4% CuO particles. Figure 10 also reveals that there are significant trend changes in $\hat{S}_{G,\mathrm{total}}$ (AR and Re) for all three fluids occurring at critical values, i.e., $AR \approx 0.55$ and $\mathrm{Re} \approx 700$. The main reasons are that with elevated Reynolds numbers temperature gradients are reduced and the frictional effects become dominant, even more pronounced as $AR \rightarrow 1.0$. An additional test run for pure water at Re=638 confirmed that Re ≈ 700 is critical where Fig. 9 has these trend changes in $\hat{S}_{G,\mathrm{total}}$ embedded as well.

5 Conclusions

In the present study, entropy generation in laminar microchannel flow was investigated with a computer model, which was validated with benchmark analytical and numerical results. Nanofluids and pure water were selected as potential coolants for three cases of trapezoidal microchannels with the same hydraulic diameter and base angle but different aspect ratios. The findings can be summarized as follows.

1. For trapezoidal microchannels, the maximum frictional entropy generation rate appears in the middle part of the walls (especially, the relatively longer sidewalls) while the lowest values are located in the acute corner areas and the center area; however, the maximum heat transfer induced entropy generation rates are located at the corners because of the higher heat flow rates.
2. System entropy generation decreases with the increase in the fluid inlet temperature, which reduces local temperature gradients.
3. There exists an optimal Reynolds number range to operate the system due to the characteristics of the two different entropy sources, both related to the inlet Reynolds number.
4. Microchannels with high aspect ratios have a lower optimal operational Reynolds number range.
5. Nanofluids with very low volume fractions of metal nanoparticles are excellent coolants and caused further entropy generation minimization at lower Reynolds numbers due to their excellent thermal properties.
6. For high heat flux conditions, e.g., microheat sinks, heat transfer induced entropy generation is dominant. Frictional entropy generation becomes more and more important with the increase in fluid inlet velocity/Reynolds number.

In summary, it is advisable to select microchannel geometries

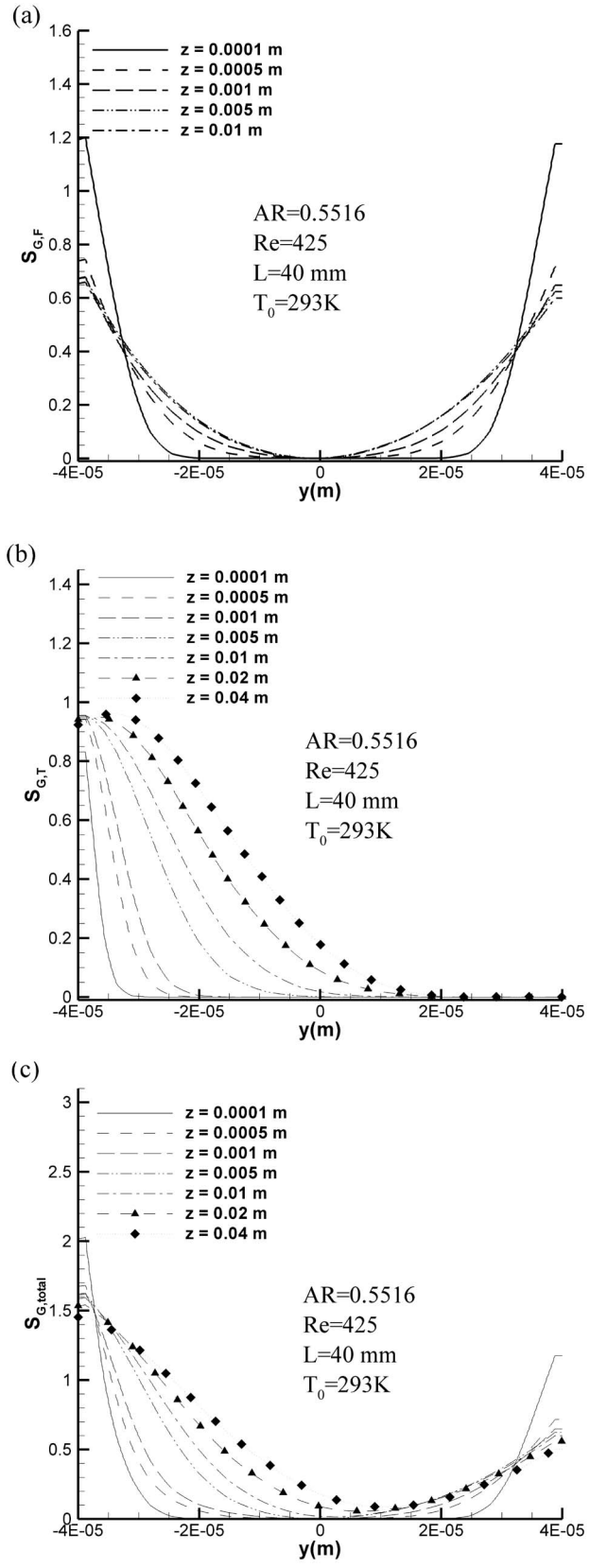

Fig. 6 Entropy generation rate developing along the channel axis for pure water flow: (*a*) developing frictional irreversibilities, (*b*) developing thermal irreversibilities, and (*c*) total irreversibilities

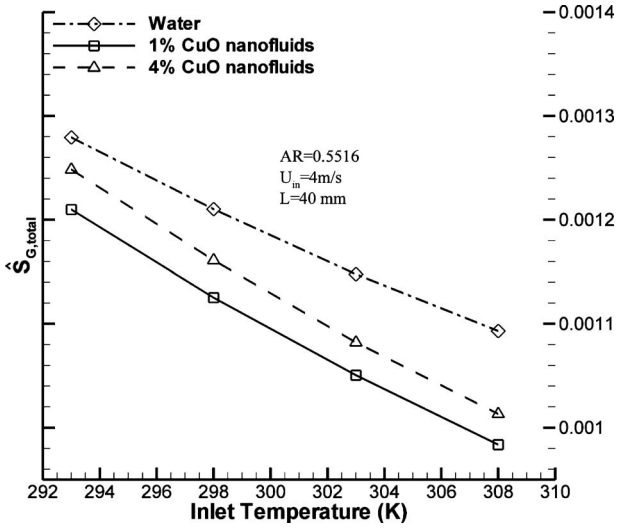

Fig. 7 System entropy generation versus fluid inlet temperature

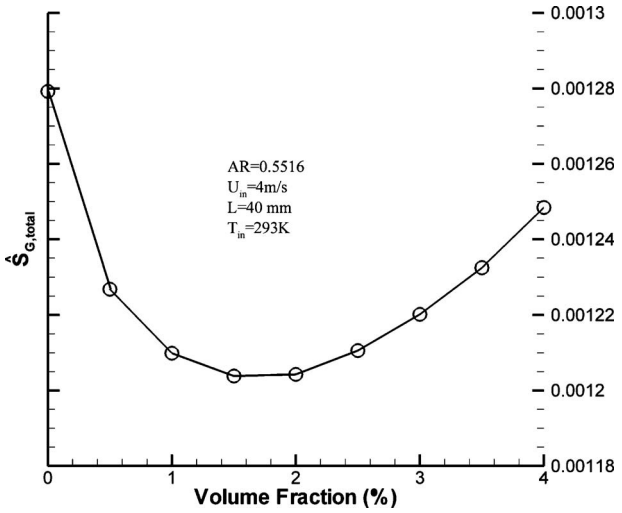

Fig. 8 System entropy generation versus volume fraction

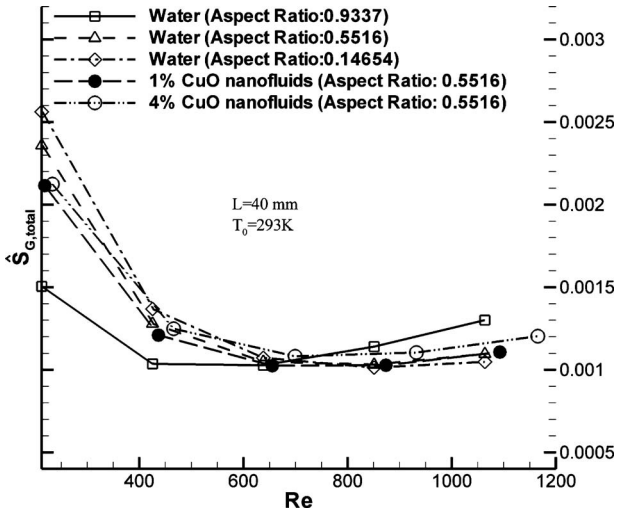

Fig. 9 System entropy generation versus Reynolds number

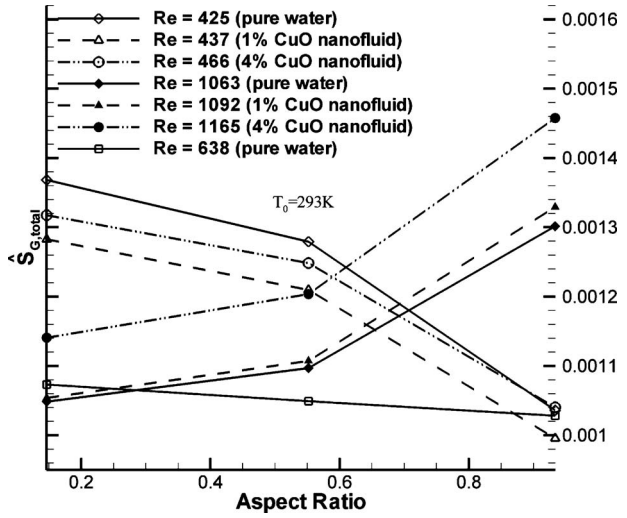

Fig. 10 System entropy generation as a function of aspect ratios and Reynolds number

based on minimization of total entropy generation, subject to encountered thermal and hydraulic boundary conditions. Employing certain nanofluids as coolants may further benefit the minimization of entropy generation in microchannel heat sinks.

Acknowledgment

The generous endowment of the McDonald–Kleinstreuer Fellowship, which supported Jie Li, was provided by Dr. J.P. Archie, Jr. and his wife Sarah, as well as the use of ANSYS-CFX11 (Ansys, Inc., Canonsburg, PA), are gratefully acknowledged.

Nomenclature

AR = aspect ratio ($=W_b/W_t$)
A_h = heated area (m^2)
c = nanoparticle concentration
c_p = specific heat capacity ($J\ kg^{-1}\ K^{-1}$)
d = particle diameter (m)
D_h = hydraulic diameter (m)
D = nanoparticle diffusivity
H = channel height (m)
k = thermal conductivity ($W\ m^{-1}K^{-1}$)
L = channel length (m)
$\dot{m}$ = mass flow rate ($kg\ s^{-1}$)
Pe = Peclet number
q = uniform wall heat flux ($W\ m^{-2}$)
r_0 = tube radius (m)
R = dimensionless radius
Re = ($=\rho UD_h/\mu$) Reynolds number
S_{gen} = entropy generation rate per unit volume ($W\ m^{-3}\ K^{-1}$)
$\hat{S}_{G,F}$ = dimensionless overall frictional entropy generation rate
$\hat{S}_{G,T}$ = dimensionless overall thermal entropy generation rate
T = temperature (K)
u, v, w = velocity components ($m\ s^{-1}$)
U = average velocity ($m\ s^{-1}$)
W_b = channel bottom width (m)
W_t = channel top width (m)

Greek Letters

φ = nanoparticle volume fraction
ϕ = ratio of irreversibilities
ξ = fraction of entropy generation
κ_B = Boltzmann constant
μ = dynamic viscosity ($kg\ m^{-1}\ s^{-1}$)
ρ = density ($kg\ m^{-3}$)

Subscripts

eff = effective
F = frictional effect
f = base fluid
G = generated
in = inlet
p = particle
T = thermal effect
w = wall

References

[1] Kleinstreuer, C., Li, J., and Koo, J., 2008, "Microfluidics of Nanodrug Delivery," Int. J. Heat Mass Transfer, **51**, pp. 5590–5597.
[2] Li, J., and Kleinstreuer, C., 2008, "Thermal Performance of Nanofluid Flow in Microchannels," Int. J. Heat Fluid Flow, **29**(4), pp. 1221–1232.
[3] Bejan, A., 1996, *Entropy Generation Minimization, the Method of Thermodynamic Optimization of Finite-Size System and Finite-Time Processes*, CRC, Boca Raton.
[4] Bejan, A., 2002, "Fundamentals of Exergy Analysis, Entropy Generation Minimization, and Generation of Flow Architecture," Int. J. Energy Res., **26**, pp. 0–43.
[5] Selvarasu, N. K. C., Tafti, D. K., and Blackwell, N. E., 2010, "Effect of Pin Density on Heat-Mass Transfer and Fluid Flow at Low Reynolds Numbers in Minichannels," ASME J. Heat Transfer, **132**, p. 061702.
[6] Ratts, E. B., and Raut, A. G., 2004, "Entropy Generation Minimization of Fully Developed Internal Flow With Constant Heat Flux," ASME J. Heat Transfer, **126**, pp. 656–659.
[7] Sahin, A. Z., 1998, "A Second Law Comparison for Optimum Shape of Duct Subjected to Constant Wall Temperature and Laminar Flow," Heat Mass Transfer, **33**, pp. 425–430.
[8] Sahin, A. Z., 2000, "Entropy Generation in a Turbulent Liquid Flow Through a Smooth Duct Subjected to Constant Wall Temperature," Int. J. Heat Mass Transfer, **43**, pp. 1469–1478.
[9] Mahmud, S., and Fraser, R. A., 2003, "The Second Law Analysis in Fundamental Convective Heat Transfer Problems," Int. J. Therm. Sci., **42**, pp. 177–186.
[10] Mansour, R. B., Galanis, N., and Nguyen, C. T., 2006, "Dissipation and Entropy Generation in Fully Developed Forced and Mixed Laminar Convection," Int. J. Therm. Sci., **45**, pp. 998–1007.
[11] Khan, W. A., Culham, J. R., and Yovanovich, M. M., 2007, "Optimal Design of Tube Banks in Crossflow Using Entropy Generation Minimization Method," J. Thermophys. Heat Transfer, **21**(2), pp. 372–378.
[12] Ko, T. H., and Wu, C. P., 2009, "A Numerical Study on Entropy Generation Induced by Turbulent Forced Convection in Curved Rectangular Ducts With Various Aspect Ratios," Int. Commun. Heat Mass Transfer, **36**(1), pp. 25–31.
[13] Ko, T. H., 2006, "Numerical Investigation on Laminar Forced Convection and Entropy Generation in a Helical Coil With Constant Wall Heat Flux," Numer. Heat Transfer, Part A, **49**, pp. 257–278.
[14] Nguyen, N.-T., and Wereley, S. T., 2006, *Fundamentals and Applications of Microfluidics*, Arten, Boston.
[15] Chein, R., and Chuang, J., 2005, "Analysis of Microchannel Heat Sink Performance Using Nanofluids," Appl. Therm. Eng., **25**, pp. 3104–3114.
[16] Heris, S. Z., Etemad, S. Gh., and Esfahany, M. N., 2006, "Experimental Investigation of Oxide Nanofluids Laminar Flow Convective Heat Transfer," Int. Commun. Heat Mass Transfer, **33**, pp. 529–535.
[17] Jang, S. P., and Choi, S. U. S., 2006, "Cooling Performance of a Microchannel Heat Sink With Nanofluids," Appl. Therm. Eng., **26**, pp. 2457–2463.
[18] Li, J., and Kleinstreuer, C., 2009, "Microfluidics Analysis of Nanoparticle Mixing in a Microchannel System," Microfluid. Nanofluid., **6**, pp. 661–668.
[19] Kleinstreuer, C., and Li, J., 2008, "Microscale Cooling Devices," *Encyclopedia of Micro and Nanofluidics*, D. Li, ed., Springer-Verlag, Heidelberg, Germany.
[20] Mansour, R. B., Galanis, N., and Nguyen, C. T., 2007, "Effect of Uncertainties in Physical Properties on Convection Heat Transfer With Nanofluids," Appl. Therm. Eng., **27**, pp. 240–249.
[21] Li, X., Zhu, D., and Wang, X., 2009, "Experimental Investigation on Viscosity of Cu–H_2O Nanofluids," Journal of Wuhan University of Technology Mater. Sci. Ed., **24**, pp. 48–52.
[22] Xuan, Y., and Roetzel, W., 2000, "Conceptions for Heat Transfer Correlation of Nanofluids," Int. J. Heat Mass Transfer, **43**, pp. 3701–3707.
[23] Maxwell, J. C., 1904, *A Treatise on Electricity and Magnetism*, 2nd ed., Oxford University Press, Cambridge, UK.
[24] Koo, J., and Kleinstreuer, C., 2003, "Liquid Flow in Microchannels: Experimental Observations and Computational Analyses of Microfluidics Effects," J. Micromech. Microeng., **13**, pp. 568–579.
[25] Li, J., 2008, "Computational Analysis of Nanofluid Flow in Microchannels

With Applications to Microheat Sinks and Bio-MEMS," Ph.D. dissertation, MAE Department, NCSU, Raleigh, NC.
[26] Kleinstreuer, C., 1997, *Engineering Fluid Dynamics*, Cambridge University Press, New York.
[27] Bejan, A., 1982, *Entropy Generation Through Heat and Fluid Flow*, Wiley, New York.
[28] Lai, W. Y., Vinod, S., Phelan, P.E., and Prasher, R., 2009, "Convective Heat Transfer for Water-Based Alumina Nanofluids in a Single 1.02-mm Tube," ASME J. Heat Transfer, **131**, p. 112401.
[29] Wu, H. Y., and Cheng, P., 2003, "Friction Factors in Smooth Trapezoidal Silicon Microchannels With Different Aspect Ratios," Int. J. Heat Mass Transfer, **46**(14), pp. 2519–2525.

Influence of Inter- and Intraband Transitions to Electron Temperature Decay in Noble Metals After Short-Pulsed Laser Heating

Patrick E. Hopkins
Engineering Sciences Center,
Sandia National Laboratories,
P.O. Box 5800, Albuquerque, NM 87185-0346
e-mail: pehopki@sandia.gov

This work examines the effects of photonically induced interband excitations from the d-band to states at the Fermi energy on the electron temperature decay in noble metals. The change in the electron population in the d-band and the conduction band causes a change in electron heat capacity and electron-phonon coupling factor. In noble metals, due to the large d-band to Fermi energy separation, the contributions to electron heat capacity and electron-phonon coupling factor of intra- and interband transitions can be separated. The two temperature model describing electron-phonon heat transfer after short-pulsed laser heating is solved using the expressions for heat capacity and electron-phonon coupling factor after intra- and interband excitations, and the predicted electron temperature change of the intra- and interband excited electrons are examined. A critical fluence value is defined that represents the absorbed fluence needed to fill all available states at a given photon energy above the Fermi level. At high absorbed laser fluences and pulse energies greater than the interband transition threshold, the interband and intraband contributions to thermophysical properties differ and are shown to affect temporal electron temperature profiles. [DOI: 10.1115/1.4002295]

Keywords: intraband transition, interband transition, electron-phonon coupling factor, short-pulsed laser heating, electronic band structure, Fermi smearing, two temperature model

1 Introduction

Electron-phonon energy transfer after short-pulsed laser heating is becoming a critical factor in many nanoscale applications. As characteristic length- and time-scales continue to decrease, the thermal resistances associated with electron-phonon energy processes are becoming comparable to typical thermal resistances associated with thermal transport in [1] or across the solid interfaces [2,3] of devices. With the increasing importance of short-pulsed heating and subsequent electron-phonon processes in fundamental research and engineering applications [4–9], the need to accurately predict the thermophysics associated with these processes is rapidly increasing.

The well known two temperature model (TTM) [10], which describes the rate of energy transfer from a hot, thermalized electron system to a cooler phonon system, has been used to predict temperature changes and deduce thermophysical properties in a wide array of studies that are driven or limited by electron-phonon energy transfer, including ablation of metal targets [6,11,12], electron-phonon heat transfer in thin films [5,13,14], effects of microstructural disorder on electron-phonon scattering [15,16], excitations in nanoparticles [17–19], and electron-interface heat transfer [20–24]. In all of these aforementioned studies, a source term from an optical excitation is considered. Experimental works studying optical excitations and electron-phonon coupling from short-pulsed lasers on noble metal targets have used incident laser fluences ranging from a few tenths to 5000 $J\,m^{-2}$ [5,14,25–28]. However, this source term is only considered as a thermal excitation in heat transfer analyses. In the case of an incident optical excitation, such as that delivered by an ultrashort laser pulse, the incident photon energy will cause the electrons in the metal to undergo various inter- and intraband transitions. In the case of interband transitions, the population in the electronic bands participating in thermal processes will change, which will affect the electron heat capacity and electron-phonon coupling factor [8,29], subsequently affecting the predicted temperature change after the optical excitation [30].

In this paper, the effects of optically and thermally excited interband transitions from the d-band (below the Fermi surface) to the Fermi surface on the dynamic response of electron temperatures as predicted by the TMM are considered and compared with the effects of intraband excitations. Both thermal transitions from Fermi smearing [8,29] and optical excitations from incident photon energies [30] cause a change in the electronic density of states, which in turn affects the thermal properties and temperature changes after the excitation. Recently, Hopkins [31] derived expressions for the inter- and intraband contributions to electronic heat capacity and electron-phonon coupling factor. In this work, the TTM is solved using the expressions for heat capacity and electron-phonon coupling factor derived by Hopkins [31], and the predicted electron temperature changes of the intra- and interband excited electrons are examined for various absorbed laser fluences and wavelengths. A critical fluence value is defined that represents the absorbed fluence needed to fill all available states at a given photon energy above the Fermi level.

2 Background

Immediately after partial absorption of an incident laser pulse by the electrons in a solid, the energy of the absorbed photon, $h\nu$,

Contributed by the Heat Transfer Division of ASME for publication in the JOURNAL OF HEAT TRANSFER. Manuscript received July 2, 2009; final manuscript received April 27, 2010; published online September 17, 2010. Assoc. Editor: Patrick E. Phelan.

where h is Planck's constant and ν is the photon frequency, causes the electron to excite to a higher energy state. If the excited state is within the same energy band, this excitation is called an intraband transition. If the energy of the absorbed photon is greater than the energy of an allowable excitation between bands, then the excited electron will undergo an interband transition. Since Fermi smearing affects the available energy states within a few $k_B T_e$ of the Fermi energy, ε_F, where k_B is Boltzmann's constant and T_e is the electron system temperature [16], the various intra- and interband transitions will relocate electrons to states below the Fermi energy to energies as high as the vacuum level, depending on $h\nu$.

The minimum photon energy required to excite an electron to undergo an interband transition to an empty state near the Fermi energy is called the interband transition threshold (*ITT*) [5]. The *ITT* is dependent on the band structures and relative energies of the outermost filled and innermost partially filled or empty electron bands (relative to the nucleus). Therefore, the *ITT* is unique for any given material. For semiconductors and insulators, the *ITT* is the bandgap, and it represents the energy difference between the valence (outermost filled) and conduction (innermost empty) bands. Metals, however, are more complex since electron energy bands can overlap around the Fermi energy allowing these bands to be partially filled. This, in fact, is what makes metals better electrical conductors than semiconductors, and consequently why electron-phonon scattering is such a dominant form of electrical and thermal resistance in metals. In a transition metal, for example, the s-band/d-band crossing is at an energy equal to or greater than the Fermi energy. This produces several allowable low energy d-band (valence d-band) to s-band interband transitions along with intraband transitions in both the d_1-band and the s-band. For example, Cr has interband Fermi transitions at 0.8 eV (*ITT*), 1.0 eV, 1.4 eV, and 1.6 eV [32], W has transitions at 0.85 eV (*ITT*), 1.6 eV, and 1.75 eV [32], and Ni has transitions at 0.25 eV (*ITT*), 0.4 eV, and 1.3 eV [33]. This poses experimental difficulty in isolating the effects of interband transitions thermophysical properties [34]. However, noble metals have a very distinct, high energy *ITT* since the s-band/d-band crossing is significantly lower than the Fermi level, and therefore only the s-band is partially filled. Therefore, the lowest energy d-band to available s-band transition is very large for Cu (2.15 eV), Au (2.4 eV), and Ag (4 eV) [14], making these metals ideal candidates to examine the effects of interband transitions on the electron thermophysics.

Figure 1 shows various transitions in a generic noble metal. This schematic represents a noble metal due to the large separation of the d-band from the Fermi energy. The filled states are represented by the shaded regions and empty states as the nonshaded regions. An intraband transition is depicted as the electron being excited from the state near the Fermi energy in the s/p-band (filled circle) and filling an empty state (empty circle) in a higher energy in the same band. The various interband transitions are depicted by the processes from the d-band edge to the s/p-band. These transitions are shown for various temperatures—$T=0$, T_1, and T_2, where $T_1 < T_2$—to show the effects of Fermi smearing on the *ITT*.

Since the electronic heat capacity, $C_e(T_e)$, and the electron-phonon coupling factor, $G(T_e)$, are dependent on the population of the electron bands within a few $k_B T_e$ of the Fermi surface [16], the density of states and the electronic distribution around the Fermi surface will dictate $C_e(T_e)$ and $G(T_e)$ [16]. In the case of intraband transitions, the population in the electron bands does not change, so $C_e(T_e)$ and $G(T_e)$ are governed by classical, low temperature, solid state theory. However, interband transitions increase/decrease the electron populations at various energies depending on the nature of the excitation, and therefore the density of states of the various bands below the Fermi surface must be taken into account.

The general form for the electron heat capacity is calculated by

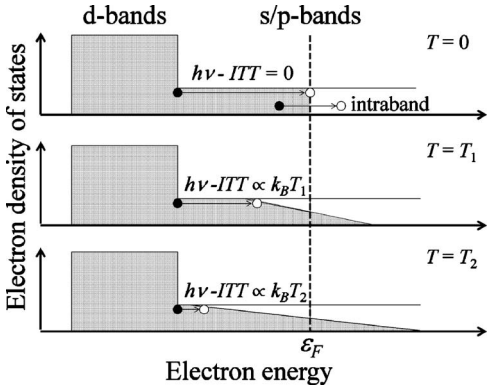

Fig. 1 Schematic depicting intraband transition and various interband transitions in a noble metal in terms of electron density of states as a function of energy. The occupied energies are depicted by the shaded regions and the various transitions are represented as a filled circle to an unfilled circle. Whereas an intraband transition creates an electron/hole pair in the same band, an interband transition creates an electron/hole pair in different bands. The *ITT* is the minimum separation of the d-band edge from the Fermi energy at $T=0$. As the temperature is increased, photons with energies less than the *ITT* can excite an interband transition due to Fermi smearing which creates empty states in the s/p-bands below the Fermi energy.

$$C_e(T_e) = \int_{-\infty}^{\infty} \varepsilon D_T(\varepsilon) \frac{\partial f(\varepsilon, \mu(T_e), T_e)}{\partial T_e} d\varepsilon \tag{1}$$

where ε is the electron energy, $D_T(\varepsilon)$ is the total density of states, and f is the Fermi–Dirac distribution function with $\mu(T_e)$ being the chemical potential, which is a function of electron temperature. In the low temperature limit, $\mu(T_e)$ is approximately equal to ε_F, and Eq. (1) can be expressed as $C_e(T_e) = \gamma T_e$, where γ is commonly called the Sommerfeld coefficient, which is theoretically 62.9 $\mathrm{J\,m^{-3}\,K^{-2}}$ for Au [35]. The reduction of Eq. (1) to $C_e(T_e) = \gamma T_e$ also assumes that only electrons at the Fermi energy participate in energy storage, that is, $C_e(T_e) \propto D_C(\varepsilon_F)$ where $D_C(\varepsilon_F)$ is the conduction band density of states.

The general form for the electron-phonon coupling factor is given by [36]

$$G(T_e) = \pi \hbar k_B \lambda \langle \omega^2 \rangle \int_{-\infty}^{\infty} \frac{(D_T(\varepsilon))^2}{D_T(\varepsilon_F)} \left(- \frac{\partial f(\varepsilon, \mu(T_e), T_e)}{\partial \varepsilon} \right) d\varepsilon \tag{2}$$

where $\hbar$ is the reduced Planck constant, λ is the dimensionless electron-phonon mass enhancement parameter [37], and $\langle \omega^2 \rangle$ is the second moment of the phonon spectrum [38]. For Au, $\lambda \langle \omega^2 \rangle = 23\ \mathrm{meV^2}/\hbar^2$ [39]. In the case of only intraband transitions in the conduction band, Eq. (2) is given by

$$G(T_e) = \pi \hbar k_B \lambda \langle \omega^2 \rangle \int_{-\infty}^{\infty} \frac{(D_C(\varepsilon))^2}{D_C(\varepsilon_F)} \left(- \frac{\partial f(\varepsilon, \mu(T_e), T_e)}{\partial \varepsilon} \right) d\varepsilon \tag{3}$$

At relatively low temperatures, $\partial f(\varepsilon, \mu(T_e), T_e)/\partial \varepsilon \approx \delta(\varepsilon - \mu(T_e)) \approx \delta(\varepsilon)$, and Eq. (3) reduces to

$$G_0 = \pi \hbar k_B \lambda \langle \omega^2 \rangle D_C(\varepsilon_F) \tag{4}$$

which is the original expression derived by Allen [40].

In this case of interband excitations, the number density of the electrons in each band will change. The number of empty states in the conduction band for which there is sufficient photon energy to excite an electron is given by [30]

$$n_{\text{available}} = \int_{-\infty}^{\infty} D_C(\varepsilon)(1 - f(\varepsilon, \mu(T_e), T_e))(1 - H[\varepsilon - (\mu(T_e) - (\varepsilon_{ITT} - h\nu))])d\varepsilon \quad (5)$$

where $H[\cdots]$ is the Heaviside function. Equation (5) will affect the density of states calculations. Separation of the interband and intraband contributions to electron heat capacity and electron-phonon coupling factor is discussed by Hopkins [31]. In short, the interband contribution is dependent on the band structure. In noble metals, since there is a large separation from of the d-band from the Fermi level, the contributions are additive, so $C_{\text{total}}(T_e) = \gamma T_e + C_{\text{inter}}(T_e)$ and $G_{\text{total}}(T_e) = G_0 + G_{\text{inter}}(T_e)$ [31].

3 Effects of Optical Excitations

The key to evaluating $C_e(T_e)$ and $G(T_e)$ lies in determining $\mu(T_e)$, which, when only considering intraband transitions, can be approximated by the Sommerfeld expansion [41], but when taking into account d-band excitations must be calculated by conservation of electron number density by evaluating

$$n_C + n_D = \int_{-\infty}^{\infty} (D_C(\varepsilon) + D_D(\varepsilon)) f(\varepsilon, \mu(T_e), T_e) d\varepsilon \quad (6)$$

where $n_C + n_D$ is a constant and $\mu(T_e)$ is iterated for each temperature. For Au, n_C is 5.9×10^{28} m^{-3} and n_D is 5.9×10^{29} m^{-3}, which is estimated by the atomic density [35] and the number of electrons in the $6s^1$ and $5d^{10}$ bands, respectively [42]. The conduction band density of states is estimated by

$$D_C = 3n_{C,\text{total}}\varepsilon^{1/2}/(2\varepsilon_F^{3/2}) \quad (7)$$

where the Fermi energy of Au is 5.53 eV [35], and $n_{C,\text{total}}$ is the total number of electrons in the conduction band after the excitation, which is given by $n_{C,\text{total}} = n_C + n_{\text{excited}}$. Here, n_{excited} is the number of electrons excited from the d-band to the conduction band from incident photons, which is a function of the number of photons absorbed by the material. If there are enough photons absorbed by the metal to excite all the electrons in the d-band up to available states in the conduction band, then $n_{\text{excited}} = n_{\text{available}}$, where $n_{\text{available}}$ is defined by Eq. (5), and therefore $n_{C,\text{total}} = n_C + n_{\text{available}}$. For this condition to be true, then $n_{\text{available}} \leq n_{\text{photons}}$, where n_{photons} is the number of photons per unit volume in the absorbed laser pulse. The number of photons per volume can be estimated as $n_{\text{photons}} = A/(h\nu\delta)$, where A is the absorbed fluence and δ is the optical penetration depth at $h\nu$. In the case n_{photons} is less than $n_{\text{available}}$, then only $n_{\text{photons}}/n_{\text{available}}$ of the empty states in the conduction band will be filled by electrons undergoing interband transitions.

Assuming that all empty states in the conduction band below the Fermi level are filled by interband excited electrons, that is, $n_{\text{available}} \leq n_{\text{photons}}$ and $n_{C,\text{total}} = n_C + n_{\text{available}}$, the number of states in the d-band after photonically induced interband transitions is given by $n_{D,\text{total}} = n_D - n_{\text{available}}$. The density of states of the $5d^{10}$ band in Au can be approximated by a square function with a width of 5.28 eV [43,44] and the high energy edge of the square function 2.4 eV below the Fermi energy giving rise to the *ITT* energy in Au, so that

$$D_D(\varepsilon) = \frac{n_{D,\text{total}}}{5.28}(-H[\varepsilon - 3.13] + H[\varepsilon + 2.15]) \quad (8)$$

Note the calculation of temperature dependent thermophysical properties using this approximate band structure has shown close agreement with calculations of thermophysical properties using exact ab initio calculations for electronic band structure [7].

If $n_{\text{available}} \leq n_{\text{photons}}$, then the absorbed laser fluence must be greater than the critical fluence, which is defined as

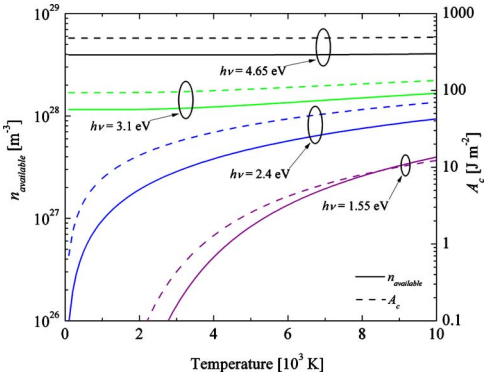

Fig. 2 Number of available states in the conduction band, $n_{\text{available}}$ (solid lines), as a function of temperature in Au and critical absorbed fluence required to excite enough electrons from the d-band to fill all the empty states in the conduction band, A_c (dashed lines)

$$A_c = h\nu\delta n_{\text{available}} \quad (9)$$

Figure 2 shows $n_{\text{available}}$ as a function of temperature for the four different photonic excitations considered, along with A_c for the different photonic excitations. The optical penetration depth, δ, is calculated by $\delta = \lambda/(4\pi n_2)$, where n_2 is the extinction coefficient, or the imaginary part of the complex index of refraction. The extinction coefficients in Au at 1.55, 2.4, 3.1, and 4.65 eV are 5.125, 2.120, 1.956, and 1.803, respectively [45], leading to an optical penetration depth at these energies of 12.4 nm, 19.4 nm, 16.2 nm, and 18.0 nm, respectively. The critical absorbed fluence depends on photon energy.

If the incident absorbed laser fluence is less than the critical absorbed fluence, then $n_{\text{excited}} < n_{\text{available}}$, and the number of electrons excited up to empty states in the conduction band from the absorbed photon energy is only $n_{\text{excited}}/n_{\text{available}}$ of $n_{\text{available}}$. If the absorbed laser fluence is known, then n_{excited} can be determined by

$$n_{\text{excited}} = An_{\text{available}}/(h\nu\delta A_c) \quad (10)$$

and $n_{C,\text{total}} = n_C + n_{\text{excited}}$ and $n_{D,\text{total}} = n_D - n_{\text{excited}}$. Figure 3 shows calculations for $C_e(T_e)$ and $G(T_e)$ for Au excited by a 4.65 eV

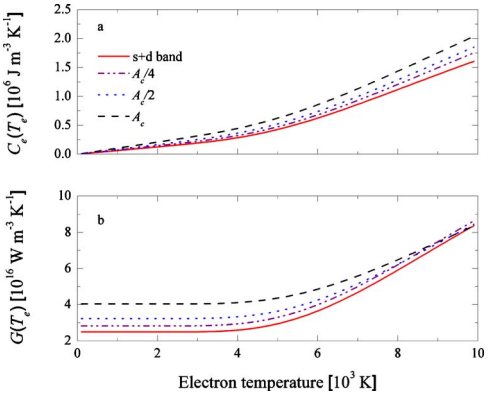

Fig. 3 Predictions of (*a*) $C_e(T_e)$ and (*b*) $G(T_e)$ when only 50% and 25% of the available states 4.65 eV above the conduction band are filled; that is, when the absorbed fluence is only 50% or 25% of A_c. As the absorbed fluence decreases, the change in $C_e(T_e)$ and $G(T_e)$ from the case of no photonic excitation becomes less significant. In the limit of zero electrons excited from the d-band to empty states in the conduction band (i.e., $n_{\text{excited}} = 0$), the predictions of $C_e(T_e)$ and $G(T_e)$ reduce to the case of no photonic excitation (i.e., "s+d band").

laser pulse at the critical fluence, at $A_c/2$ and at $A_c/4$. The calculations for $C_e(T_e)$ and $G(T_e)$ for different laser pulse energies at the critical fluence are given by Hopkins [31]. For comparison, the "s+d bands" calculations, which assume no photonic excitation, are also shown in Fig. 3. As expected, a decrease in the absorbed laser fluence decreases the change in the predicted $C_e(T_e)$ and $G(T_e)$ from that predicted in the case of no photonic excitation.

4 Intra- and Interband Transition-Dependent Two-Temperature Model

In films with thicknesses less than the thermal, or ballistic, penetration depth, δ_B, the temperature gradient in the film is minimal, and the TTM can expressed in a simplified form [5], given by

$$C_e(T_e)\frac{\partial T_e}{\partial t} = -G(T_e)[T_e - T_L] + \frac{0.94A}{t_p d}\exp\left[-2.77\left(\frac{t-2t_p}{t_p}\right)\right] \tag{11}$$

$$C_L\frac{\partial T_L}{\partial t} = G(T_e)[T_e - T_L] \tag{12}$$

where t is the time, t_p is the pulse width, d is the film thickness, and the subscript L refers to the lattice or phonon system. The ballistic penetration depth in Au is about 100 nm [5], so for TTM analyses assuming no thermal gradient, Au film thicknesses will be restricted to less than 100 nm. To separate the intra- and interband contributions to electron system cooling, two separate electron subsystems must be considered, where the intraband subsystem is described by

$$\gamma T_{e,\text{intra}}\frac{\partial T_{e,\text{intra}}}{\partial t} = -G_0[T_{e,\text{intra}} - T_{L,\text{intra}}] \tag{13}$$

and the cooling due to interband excitations is given by

$$C_{e,\text{inter}}(T_{e,\text{inter}})\frac{\partial T_{e,\text{inter}}}{\partial t} = -G_{\text{inter}}(T_{e,\text{inter}})[T_{e,\text{inter}} - T_{L,\text{inter}}] \tag{14}$$

In Eqs. (13) and (14), it is assumed that the entire electron system absorbs the incident laser energy, so the initial conditions for Eqs. (13) and (14) are

$$T_{e,\text{inter}}(t=0) = T_{e,\text{intra}}(t=0) = T_{e,\max} \tag{15}$$

and

$$T_{L,\text{inter}}(t=0) = T_{L,\text{intra}}(t=0) = T_L(t|_{T_{e,\max}}) \tag{16}$$

where $T_{e,\max}$ is determined by Eqs. (11) and (12) and $t|_{T_{e,\max}}$ refers to the time corresponding to $T_{e,\max}$. Figure 4 shows Eq. (13) and (14) calculations of the change in electron temperatures in a 75 nm Au film irradiated with a 500 fs laser pulse, 475 J m^{-2} absorbed fluence and 4.65 eV photon energy (approximately the critical fluence from Fig. 2) and (b) 237 J m^{-2} absorbed fluence and 4.65 eV photon energy (approximately half of the critical fluence from Fig. 2). Only the data after the maximum electron temperature are shown so that a delayed electron system thermalization due to the high energy pulse need not be considered [46]. Note that there is a difference in the predicted electron temperatures and rates of change (slope) of electron temperature between the intra- and interband processes. These same trends are expected for the other noble metals (Ag and Cu) since the large separation of the d-band density of states from the Fermi energy is characteristic of the noble metals [29].

The insets of Figs. 4(*a*) and 4(*b*) show the electron energy density for the inter- and intraband electron systems (the product of the heat capacity and the temperature), along with the sum of these energy densities, and the energy density obtained from the temperature predictions of Eq. (11) assuming the total values for $C_e(T_e)$ and $G(T_e)$ (i.e., including both intra- and interband transitions) as a function of time after the maximum electron temperature. The calculations in the inset were used to ensure that total electron energy density was conserved in the intra- and interband processes.

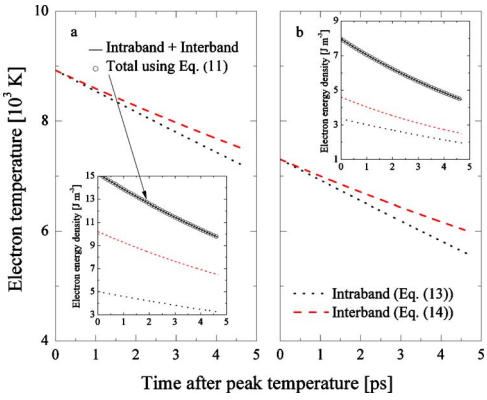

Fig. 4 Change in temperature of electrons excited via inter- (dashed lines) and intraband (dotted lines) transitions in a 75 nm Au film irradiated with a 4.65 eV, 500 fs laser pulse assuming (*a*) 475 J m^{-2} absorbed fluence (approximately the critical fluence) and (*b*) 237 J m^{-2} absorbed fluence (approximately 50% of the critical fluence). This temperature change was calculated with the intra- (Eq. (13)) and interband (Eq. (14)) TTMs, and assumes that the pulse has been completely absorbed and the electron system is fully thermalized. The insets show calculations of the energy densities in the inter- and intraband excited electron systems.

The traditional TTM, as described in Eqs. (11) and (12), is based on free electron theory. However, measurements using optical pulses that excite interband transitions often use this form of the TTM to determine G. As seen in Fig. 4, exciting only intraband transitions (free electrons) gives a different cooling profile than when considering only interband transitions. Since it is the cooling profile that determines G when fitting to the optical data, in the case when interband transitions are excited during these measurements, care must be taken to ensure that the thermophysical properties that account these excitations are considered.

To quantify the effects of not accounting for interband transitions after short pulse absorption, the slope of the data shown in Fig. 4 can be related to the observed electron-phonon coupling factor through the expression derived by Hohlfeld et al. [5] for a homogeneous heated film after short-pulsed laser absorption given by

$$G = -\frac{m\gamma}{1 - \dfrac{300}{T_{e,\max}}} \tag{17}$$

where m is the observed slope of the transient temperature profile. Using Eq. (17) to calculate G from the intraband profiles in Figs. 4(*a*) and 4(*b*) gives 2.4×10^{16} W m^{-3} K^{-1}, in excellent agreement with the intraband G calculated with Eq. (4) for Au (2.49×10^{16} W m^{-3} K^{-1}). This is expected since Eq. (17) does not take into account any subconduction band excitations; using Eq. (17) to calculate G from the interband profiles in Figs. 4(*a*) and 4(*b*) gives 2.0×10^{16} W m^{-3} K^{-1} and 1.8×10^{16} W m^{-3} K^{-1} for the high and low fluence cases, respectively. However, as seen in Fig. 3(*b*), the value for G when accounting for the subconduction band calculations in the temperature range 6000–9000 K ranges from $\sim$5.0–8.0$\times10^{16}$ W m^{-3} K^{-1}. Therefore, if the interband transitions and d-band excitations are not accounted for when analyzing the transient electron temperature profiles, then the electron-phonon coupling factor will be under predicted of by a factor of 2.6–4.2 over the temperature range in Fig. 4. It is important to note that the differences between the inter- and intraband profiles in Fig. 4 assume that the conduction band electrons and d-band

holes excited from the laser pulse have not relaxed. After low laser fluence excitation, the electron-hole relaxation rate in metals is typically only a few tens of femtoseconds [13]. However, as the absorbed laser fluence is increased, the electron-hole relaxation time increases, and previous studies on noble metals have shown that this relaxation time can approach the electron-phonon thermalization time at laser fluences less than 1% of those of interest in this study [46–51]. Therefore, the assumption of an excited electron system that has not relaxed with the d-band holes is valid in this work and at these laser fluences, but future works should examine the low laser fluence regimes where electron-hole relaxation would be faster than electron-phonon equilibration.

5 Conclusions

This work examines the effects of photonically induced interband excitations from the d-band to states at the Fermi energy on the electron temperature decay in noble metals. The change in the electron population in the d-band and the conduction band causes a change in electron heat capacity and electron-phonon coupling factor, which in turn impacts the evolution of the temperature after pulse absorption and electron thermalization. In noble metals, due to the large d-band to Fermi energy separation, the contributions to electron heat capacity and electron-phonon coupling factor of intra- and interband transitions can be separated. At high absorbed laser fluences and pulse energies greater than the interband transition threshold, the interband and intraband contributions to thermophysical properties differ and are shown to affect electron temperature predictions by the two temperature model.

Acknowledgment

The author is grateful for support from the LDRD program office through the Sandia National Laboratories Harry S. Truman Fellowship. Sandia is a multiprogram laboratory operated by Sandia Corporation, a Lockheed-Martin Co., for the United States Department of Energy's National Nuclear Security Administration under Contract No. DE-AC04-94AL85000.

Nomenclature

C_e = electron heat capacity, J m^{-3} K^{-1}
D = electron spectral density of states per unit volume, m^{-3} eV^{-1}
f = Fermi–Dirac distribution function
G = electron-phonon coupling factor, W m^{-3} K^{-1}
H = Heaviside function
h = Planck's constant, J s
$\hbar$ = Planck's constant divided by 2π, J s
k_B = Boltzmann constant, J K^{-1}
m = slope of transient temperature change, K s^{-1}
n = number density, m^{-3}
T_e = electron temperature, K

Greek Symbols

ε = electron energy, eV
γ = Sommerfeld coefficient (linear coefficient to heat capacity), J m^{-3} K^{-2}
λ = electron-phonon mass enhancement parameter
$\langle\omega^2\rangle$ = second moment of the phonon spectrum
μ = chemical potential, eV
ν = photon frequency, Hz

Subscripts

C = conduction band
D = d-band
F = Fermi
inter = interband transition
intra = intraband transition
T = total

References

[1] Majumdar, A., Fushinobu, K., and Hijikata, K., 1995, "Effect of Gate Voltage on Hot-Electron and Hot-Phonon Interaction and Transport in a Submicrometer Transistor," J. Appl. Phys., **77**, pp. 6686–6694.
[2] Hopkins, P. E., and Norris, P. M., 2007, "Substrate Influence in Electron-Phonon Coupling Measurements in Thin Au Films," Appl. Surf. Sci., **253**, pp. 6289–6294.
[3] Majumdar, A., and Reddy, P., 2004, "Role of Electron-Phonon Coupling in Thermal Conductance of Metal-Nonmetal Interfaces," Appl. Phys. Lett., **84**, pp. 4768–4770.
[4] Hohlfeld, J., Matthias, E., Knorren, R., and Bennemann, K. H., 1997, "Nonequilibrium Magnetization Dynamics of Nickel," Phys. Rev. Lett., **78**, pp. 4861–4864.
[5] Hohlfeld, J., Wellershoff, S. S., Gudde, J., Conrad, U., Jahnke, V., and Matthias, E., 2000, "Electron and Lattice Dynamics Following Optical Excitation of Metals," Chem. Phys., **251**, pp. 237–258.
[6] Ivanov, D. S., and Zhigilei, L. V., 2003, "Combined Atomistic-Continuum Modeling of Short-Pulse Laser Melting and Disintegration of Metal Films," Phys. Rev. B, **68**, pp. 064114.
[7] Lin, Z., and Zhigilei, L. V., 2006, "Thermal Excitation of d Band Electrons in Au: Implications for Laser-Induced Phase Transformations," Proc. SPIE, **6261**, p. 62610U.
[8] Lin, Z., and Zhigilei, L. V., 2007, "Temperature Dependences of the Electron-Phonon Coupling, Electron Heat Capacity and Thermal Conductivity in Ni Under Femtosecond Irradiation," Appl. Surf. Sci., **253**, pp. 6295–6300.
[9] Wellershoff, S.-S., Hohlfeld, J., Gudde, J., and Matthias, E., 1999, "The Role of Electron-Phonon Coupling in Femtosecond Laser Damage of Metals," Appl. Phys. A: Mater. Sci. Process., **69**, pp. S99–S107.
[10] Anisimov, S. I., Kapeliovich, B. L., and Perel'man, T. L., 1974, "Electron Emission From Metal Surfaces Exposed to Ultrashort Laser Pulses," Sov. Phys. JETP, **39**, pp. 375–377.
[11] Zhigilei, L. V., and Ivanov, D. S., 2005, "Channels of Energy Redistribution in Short-Pulse Laser Interactions With Metal Targets," Appl. Surf. Sci., **248**, pp. 433–439.
[12] Jiang, L., and Tsai, H.-L., 2005, "Improved Two-Temperature Model and Its Application in Ultrashort Laser Heating of Metal Films," ASME J. Heat Transfer, **127**, pp. 1167–1173.
[13] Qiu, T. Q., and Tien, C. L., 1993, "Heat Transfer Mechanisms During Short-Pulse Laser Heating of Metals," ASME J. Heat Transfer, **115**, pp. 835–841.
[14] Eesley, G. L., 1986, "Generation of Nonequlibrium Electron and Lattice Temperatures in Copper by Picosecond Laser Pulses," Phys. Rev. B, **33**, pp. 2144–2151.
[15] Hostetler, J. L., Smith, A. N., Czajkowsky, D. M., and Norris, P. M., 1999, "Measurement of the Electron-Phonon Coupling Factor Dependence on Film Thickness and Grain Size in Au, Cr, and Al," Appl. Opt., **38**, pp. 3614–3620.
[16] Qiu, T. Q., and Tien, C. L., 1993, "Size Effects on Nonequilibrium Laser Heating of Metal Films," ASME J. Heat Transfer, **115**, pp. 842–847.
[17] Arbouet, A., Voisin, C., Christofilos, D., Langot, P., Del Fatti, N., Vallee, F., Lerme, J., Celep, G., Cottancin, E., Gaudry, M., Pellarin, M., Broyer, M., Maillard, M., Pileni, M. P., and Treguer, M., 2003, "Electron-Phonon Scattering in Metal Clusters," Phys. Rev. Lett., **90**, p. 177401.
[18] Hartland, G. V., 2004, "Electron-Phonon Coupling and Heat Dissipation in Metal Nanoparticles," International Journal of Nanotechnology, **1**, pp. 307–327.
[19] Hodak, J. H., Henglein, A., and Hartland, G. V., 2000, "Electron-Phonon Coupling Dynamics in Very Small (Between 2 and 8 nm) Diameter Au Nanoparticles," J. Chem. Phys., **112**, pp. 5942–5947.
[20] Hopkins, P. E., 2009, "Effects of Electron-Boundary Scattering on Changes in Thermoreflectance in Thin Metal Films Undergoing Intraband Transitions," J. Appl. Phys., **105**, p. 093517.
[21] Hopkins, P. E., Kassebaum, J. L., and Norris, P. M., 2009, "Effects of Electron Scattering at Metal-Nonmetal Interfaces on Electron-Phonon Equilibration in Gold Films," J. Appl. Phys., **105**, p. 023710.
[22] Hopkins, P. E., and Norris, P. M., 2009, "Contribution of Ballistic Electron Transport to Energy Transfer During Electron-Phonon Nonequilibrium in Thin Films," ASME J. Heat Transfer, **131**, p. 043208.
[23] Hopkins, P. E., Norris, P. M., Stevens, R. J., Beechem, T., and Graham, S., 2008, "Influence of Interfacial Mixing on Thermal Boundary Conductance Across a Chromium/Silicon Interface," ASME J. Heat Transfer, **130**, p. 062402.
[24] Norris, P. M., and Hopkins, P. E., 2009, "Examining Interfacial Diffuse Phonon Scattering Through Transient Thermoreflectance Measurements of Thermal Boundary Conductance," ASME J. Heat Transfer, **131**, p. 043207.
[25] Chan, W.-L., Averback, R. S., Cahill, D. G., and Ashkenazy, Y., 2009, "Solidification Velocities in Deeply Undercooled Silver," Phys. Rev. Lett., **102**, p. 095701.
[26] Chan, W.-L., Averback, R. S., Cahill, D. G., and Lagoutchev, A., 2008, "Dynamics of Femtosecond Laser-Induced Melting of Silver," Phys. Rev. B, **78**, p. 214107.
[27] Eesley, G. L., 1983, "Observation of Nonequilibrium Electron Heating in Copper," Phys. Rev. Lett., **51**, pp. 2140–2143.
[28] Smith, A. N., and Norris, P. M., 2001, "Influence of Intraband Transitions on the Electron Thermoreflectance Response of Metals," Appl. Phys. Lett., **78**, pp. 1240–1242.
[29] Lin, Z., Zhigilei, L. V., and Celli, V., 2008, "Electron-Phonon Coupling and Electron Heat Capacity of Metals Under Conditions of Strong Electron-

Phonon Nonequilibrium," Phys. Rev. B, **77**, p. 075133.
[30] Hopkins, P. E., Duda, J. C., Salaway, R. N., Smoyer, J. L., and Norris, P. M., 2008, "Effects of Intra- and Interband Transitions on Electron-Phonon Coupling and Electron Heat Capacity After Short Pulsed Laser Heating," Nanoscale Microscale Thermophys. Eng., **12**, pp. 320–333.
[31] Hopkins, P. E., 2010, "Contributions of Inter- and Intraband Excitations to Electron Heat Capacity and Electron-Phonon Coupling in Noble Metals," ASME J. Heat Transfer, **132**, p. 014504.
[32] Colavita, E., Franciosi, A., Mariani, C., and Rosei, R., 1983, "Thermoreflectance Test of W, Mo and Paramagnetic Cr Band Structures," Phys. Rev. B, **27**, pp. 4684–4693.
[33] Hanus, J., Feinleib, J., and Scouler, W. J., 1967, "Low-Energy Interband Transitions and Band Structure in Nickel," Phys. Rev. Lett., **19**, pp. 16–20.
[34] Hopkins, P. E., Klopf, J. M., and Norris, P. M., 2007, "Influence of Interband Transitions on Electron-Phonon Coupling Measurements in Ni Films," Appl. Opt., **46**, pp. 2076–2083.
[35] Kittel, C., 1996, *Introduction to Solid State Physics*, Wiley, New York.
[36] Wang, X. Y., Riffe, D. M., Lee, Y.-S., and Downer, M. C., 1994, "Time-Resolved Electron-Temperature Measurement in a Highly Excited Gold Target Using Femtosecond Thermionic Emission," Phys. Rev. B, **50**, pp. 8016–8019.
[37] Grimvall, G., 1981, *Selected Topics in Solid State Physics*, North-Holland, New York.
[38] McMillan, W. L., 1968, "Transition Temperature of Strong-Coupled Superconductors," Phys. Rev., **167**, pp. 331–344.
[39] Brorson, S. D., Kazeroonian, A., Moodera, J. S., Face, D. W., Cheng, T. K., Ippen, E. P., Dresselhaus, M. S., and Dresselhaus, G., 1990, "Femtosecond Room-Temperature Measurement of the Electron-Phonon Coupling Constant γ in Metallic Superconductors," Phys. Rev. Lett., **64**, pp. 2172–2175.
[40] Allen, P. B., 1987, "Theory of Thermal Relaxation of Electrons in Metals," Phys. Rev. Lett., **59**, pp. 1460–1463.
[41] Pathria, R. K., 2006, *Statistical Mechanics*, Elsevier Butterworth-Heinemann, Burlington.
[42] Gray, D. E., 1972, *American Institute of Physics Handbook*, McGraw-Hill, New York.
[43] Harrison, W. A., 1980, *Electronic Structure and the Properties of Solids: The Physics of the Chemical Bond*, W. H. Freeman and Company, San Francisco, CA.
[44] Heiner, E., 1988, "Nonequilibrium Thermalized Stage of Noble Metals," Phys. Status Solidi B, **148**, pp. 599–609.
[45] Palik, E. D., 1985, *Handbook of Optical Constants of Solids*, Academic, Orlando, FL.
[46] Sun, C. K., Vallee, F., Acioli, L., Ippen, E. P., and Fujimoto, J. G., 1993, "Femtosecond Investigation of Electron Thermalization in Gold," Phys. Rev. B, **48**, pp. 12365–12368.
[47] Fann, W. S., Storz, R., Tom, H. W. K., and Bokor, J., 1992, "Direct Measurement of Nonequilibrium Electron-Energy Distributions in Subpicosecond Laser-Heated Gold Films," Phys. Rev. Lett., **68**, pp. 2834–2837.
[48] Fann, W. S., Storz, R., Tom, H. W. K., and Bokor, J., 1992, "Electron Thermalization in Gold," Phys. Rev. B, **46**, pp. 13592–13595.
[49] Groeneveld, R. H. M., Sprik, R., and Lagendijk, A., 1992, "Effect of a Nonthermal Electron Distribution on the Electron-Phonon Energy Relaxation Process in Noble Metals," Phys. Rev. B, **45**, pp. 5079–5082.
[50] Groeneveld, R. H. M., Sprik, R., and Lagendijk, A., 1995, "Femtosecond Spectroscopy of Electron-Electron and Electron-Phonon Energy Relaxation in Ag and Au," Phys. Rev. B, **51**, pp. 11433–11445.
[51] Sun, C. K., Vallee, F., Acioli, L., Ippen, E. P., and Fujimoto, J. G., 1994, "Femtosecond-Tunable Measurement of Electron Thermalization in Gold," Phys. Rev. B, **50**, pp. 15337–15348.

Formation Mechanism and Characteristics of a Liquid Microlayer in Microchannel Boiling System

Yaohua Zhang
Graduate School of Engineering,
Yokohama National University,
Tokiwadai, Hodogaya,
Yokohama 240-8501, Japan
e-mail: d08sb191@ynu.ac.jp

Yoshio Utaka
Faculty of Engineering,
Yokohama National University,
Tokiwadai, Hodogaya,
Yokohama 240-8501, Japan
e-mail: utaka@ynu.an.jp

Yuki Kashiwabara
Tokyo Electric Power Company,
2-1377 Soga-cho,
Chuo-ku 260-0822Chiba, Japan
e-mail: kashiwabara1986@hotmail.co.jp

Experiments were performed using the laser extinction method to measure the thickness of the liquid film formed by growing flattened bubbles in a microchannel for gap sizes of 0.5 mm, 0.3 mm, and 0.15 mm. Water, ethanol, and toluene were used as test fluids. A high-speed camera was also used to simultaneously measure the bubble growth process. It was confirmed that the gap size and bubble forefront velocity determined the initial microlayer thickness. The variation trend of the microlayer thickness relative to the velocity of the interface was divided into two regions: region I, where the velocity is small and the thickness increases linearly with increasing velocity, and region II, where the thickness is almost constant or decreased slightly with increasing velocity. Furthermore, a nondimensional correlation for investigating the effects of test materials and gap sizes on microlayer thickness is presented. An analysis of the results showed that the boundaries of the two regions correspond to a Weber number of approximately 110, and in the region where the Weber number was smaller than 110, the thickness of the microlayer was thinner for the liquid whose value of $\rho^{0.62}\nu^{0.42}\sigma^{-0.62}$ *was relatively small. However, for the region where Weber number was larger than 110, the smaller the kinematic viscosity of the liquid, the thinner the microlayer became.* [DOI: 10.1115/1.4002365]

Keywords: microlayer, microchannel, phase change, laser extinction method

1 Introduction

Boiling in mini-/microscale channels is becoming increasingly important in many diverse applications as it is capable of removing large amounts of heat over small areas. For example, in order to realize fast response and compactness for a fuel cell vehicle with a reformer, the use of a microchannel type vapor generator composed of parallel plates is one possible approach to satisfy the requirements of high efficiency heat exchange and low heat capacity. However, phase-change heat transfer mechanisms and characteristics for the microscale show distinct differences from the macroscale behavior. In microchannels, bubbles nucleate and quickly grow to the channel size such that the elongated bubbles are formed, which are confined by the channel walls and grow very fast in length, with a dynamic tip defined as the forefront part of the bubble where the curvature of interface between the bubble and liquid is obviously bigger than zero, and a microlayer is formed between the bubbles and the inner heating plate walls simultaneously after the dynamic tip of the bubble, as shown in Fig. 1. The bubble inside the microchannel is confined so much that the tip is just an extremely small part of the bubble, whereas most part of it is surrounded by the microlayer that is almost parallel with the heating plate. Also, as the fluid system becomes progressively smaller, the relative importance of surface tension increases. Moreover, the bulk liquid, superheated microlayers, and vapor bubbles in the microchannel affect each other in complex ways. The transient evaporation of the microlayer elongated bubbles has been considered to be a major heat transfer mechanism. Accordingly, several investigations on the microlayer formed by the movement of the vapor-liquid interface have been conducted theoretically and experimentally.

Taylor [1] conducted experiments on a glass tube (diameter 2–3 mm) filled with a glycerin-water solution that could be varied to cover a wide range of capillary numbers and measured the amount of liquid remaining on the tube wall when an air bubble penetrated through the glass tube. It was shown that the thickness of the film deposited on the wall by the propagating bubble increases with an increase in capillary number. Bretherton [2] theoretically derived a prediction method for the microlayer thickness based on a lubrication approximation for the limit of $\mathrm{Re} \ll 1$ and neglecting gravitational forces. It was suggested in that study that the liquid layer thickness could scale with the capillary number. Katto and Yokoya [3] measured the temperature of a heating surface set on the base of a water pool and the microlayer thickness under a growing flattened bubble in a narrow gap less than 2.5 mm. They classified boiling patterns into three regimes, in the second of which the formation of the microlayer that led to heat transfer enhancement was confirmed. Using a technique based on video vapor front tracking and transient wall temperature analysis, Moriyama and Inoue [4] experimentally measured the thickness of a thin liquid layer formed by flattened bubbles growing in a superheated liquid between two horizontally parallel, heated, and transparent plates. Tests were conducted with R-113, and the gap between the two plates ranged from $d=100$ to 400 μm. They showed that for a large superheat or large velocity, the viscous boundary layer controlled the formation thickness δ, while at a low bubble velocity or small gap between the plates, the surface tension force was dominant. Thome et al. [5] presented a three-zone flow boiling model formulated to describe the evaporation of elongated bubbles in microchannels, which they compared with experimental data. In a previous report on the present work, Utaka et al. [6] reported measurements of the microlayer thickness of water that formed on a heating surface by vapor growth using the method of laser extinction. The heat transfer characteristics of boiling in a narrow gap microchannel were also investigated

Contributed by the Heat Transfer Division of ASME for publication in the JOURNAL OF HEAT TRANSFER. Manuscript received October 23, 2009; final manuscript received May 17, 2010; published online September 20, 2010. Assoc. Editor: Satish G. Kandlikar.

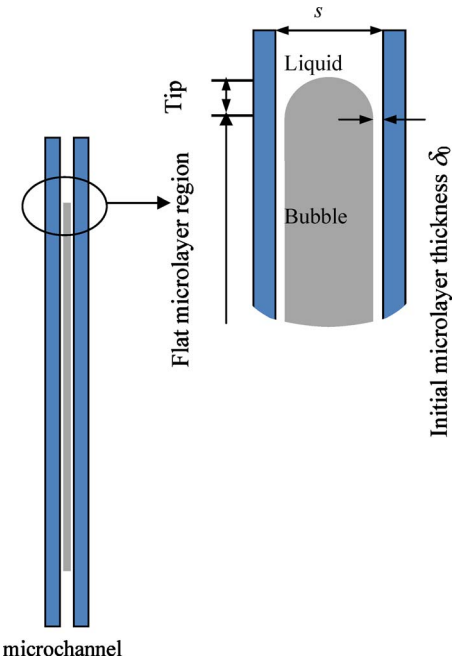

Fig. 1 Schematic diagram of bubble

quantitatively. It was found that the trend in the variation in microlayer thickness relative to the velocity of the bubble forefront could be divided into two regions.

From the review of literature reported, it is clear that many studies have been carried out to clarify the characteristics of the microlayer, most of which were performed in adiabatic conditions. However, how the microlayer is built up in the case of boiling inside microchannels is still a problem of importance. In this research, in order to clarify the formation mechanism of the microlayer, a series of experiments was conducted to observe the formation and growth processes of bubbles. The initial microlayer thickness that is defined as the thickness of the microlayer after the bubble tip at the location where the interface between the vapor and liquid almost parallel with the heating plate, as shown in Fig. 1, was measured directly with a laser extinction method for the test liquid ethanol and toluene. Furthermore, a nondimensional correlation was produced based on the results of the experiments, which is considered to be useful in giving fundamental insight into the basic relations among system variables that are valid for different fluids under different operating conditions.

2 Experimental Apparatus and Procedure

A schematic diagram of the experimental apparatus is shown in Fig. 2(*a*). The vapor generator is located between a He–Ne laser emitter and a Pb–Se detector. A liquid reservoir and a heating tank were placed upstream in the microchannel test apparatus. The cross-section area of the liquid reservoir was large enough to maintain a constant liquid level in the microchannel, which could ensure that it was close to pool boiling in the microchannel but not flow boiling. The liquid supplied to the microchannel apparatus was boiled in a heating tank that was open to the atmosphere. An orifice on the inlet of the microchannel was used to restrain the fluctuation of the liquid flow rate caused by the bubble growth and collapse. Vapor generated from the microchannel vapor generator and the heating tank flowed through a condenser and back to the reservoir. Figure 2(*b*) shows the details of the microchannel test apparatus. A quartz glass with a high transparency for infrared light was mainly utilized for the test apparatus to enable more accurate measurements. The channel thickness between two parallel quartz glass plates has a variable thickness by altering the spacers. Three different gap sizes of 0.15 mm, 0.3 mm, and 0.5

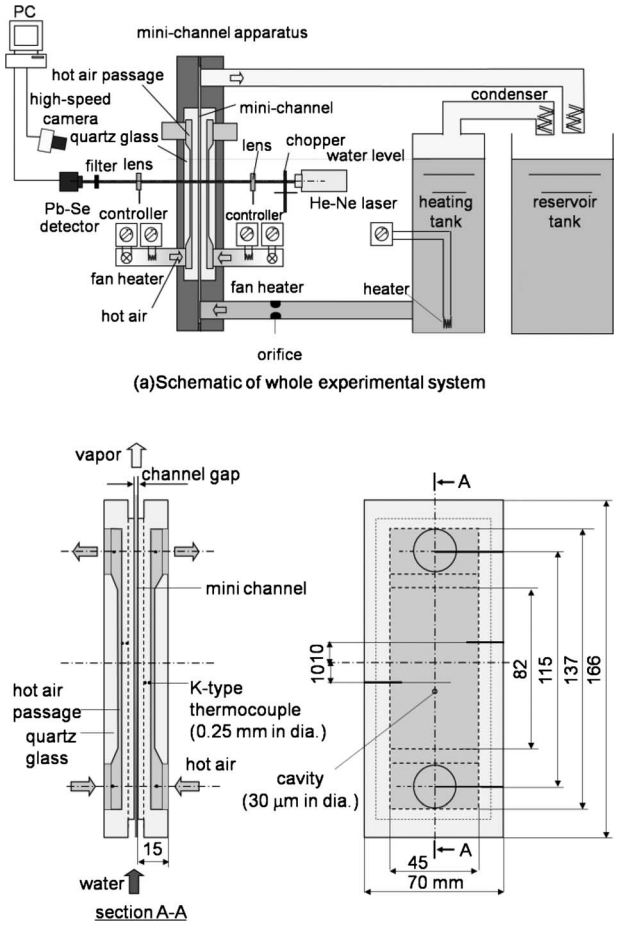

Fig. 2 Experimental apparatus for measuring microlayer thickness

mm were adopted in this study. The real gap size of the microchannel, as measured with a plastic gauge, was in the range of 0.147–0.158 mm for a 0.15 mm test gap size. Therefore, it was confirmed that the gap size was constant and sufficiently accurate with respect to the target value, as reported by Utaka et al. [6].

Passages for high temperature air used as the heating source to heat the microchannel were positioned at the back and the front of the microchannel. The central part of the 82 mm high passage, which essentially served as the heating area, was narrowed to enhance heating. The width of the passage was 45 mm. The heat flux into the microchannel was controlled by varying the air temperature. A cavity of 30 μm diameter was located 12 mm below the center of the microchannel to provide an incipient bubble site on the heating plate. The principle of the laser extinction method was used to determine the microlayer thickness by using Lambert's law as follows:

$$\delta = -\left(\frac{1}{A}\right)\ln(I/I_0) \tag{1}$$

δ denotes the thickness of the liquid layer the laser travels through. In this experiment, because the bubble formed symmetrically in the microchannel, the initial microlayer thickness δ_0 cited in this paper was calculated as $\delta_0 = 0.5\delta$. Regarding the experiment, it refers to the first signal appearing on the laser ray detector when the bubble passed through the point where the laser ray passed through the minichannel, which has been reported by Utaka et al. in Ref. [6]. *A* represents the extinction coefficient, as shown in Table 1. The light intensity at the detector when the microchannel being measured is filled with steam is denoted by I_0, and when filled with both a thin liquid layer and steam, it is

Table 1 Extinction coefficient of the test fluids

	Water	Ethanol	Toluene
A (m^{-1})	5.42×10^4	1.22×10^5	3.15×10^4

denoted by I. This method is sufficiently accurate to measure the microlayer thickness on a micron scale, and a detailed investigation about its measurement precision was carried out by Utaka and Nishikawa [7] for measuring the thickness of thin condensates of liquid mixtures during the process of water-ethanol Marangoni dropwise condensation. The effects of ambient temperature change, reflection of laser rays, etc., on the values of I_0/I were examined. As a result, it was shown that ambient temperature change was the main effect for the accuracy, and the measurement error of the liquid condensates was approximately ±0.3 μm. In this study, the accuracy of microlayer thickness measurement is different for the three kinds of testing liquid and laser measurement devices. Figure 3 shows the variation in detector output due to ambient temperature change, where $I_{0\,\max}$ is the maximum value of I_0 during all the test period. The largest errors for microlayer thickness due to the instability of the detector were 1.3 μm, 0.6 μm, and 2.3 μm for water, ethanol, and toluene, respectively. The laser signals were recorded in synchronization with the process of bubble growth, which was recorded with a high-speed camera, as shown in Fig. 2. The relative location of the incident laser ray on the heating surface was adjusted to vary the distance from the incipient bubble site.

3 Results and Discussion

The microlayer forms as a result of liquid remaining on the heating surface immediately after the liquid is pushed away by the bubble growth. The microlayer thickness varies due to the effects of the bubble growth rate and movement. In this study, attention was focused on the initial microlayer thickness δ_0.

The variation in the initial microlayer thickness versus the bubble forefront velocity is shown in Fig. 4 for water, ethanol, and toluene for three different microchannel gap sizes of 0.5 mm, 0.3 mm, and 0.15 mm. Based on the results for water and toluene, the initial microlayer thickness was strongly affected by the gap size, and it increased with increasing gap size. For ethanol, there was no result in the present study on gap size, except for the minimum size of 0.15 mm. This was because of the large extinction coefficient for the laser used in the present experiment, as shown in Fig. 5. Moreover, the results for ethanol and toluene showed a similar tendency as water for any size of gap. That is, in low velocity regions, the microlayer thickness increases with forefront velocity; however, as velocity increases, the thickness becomes almost constant or decreases slightly for sufficiently high bubble fore-

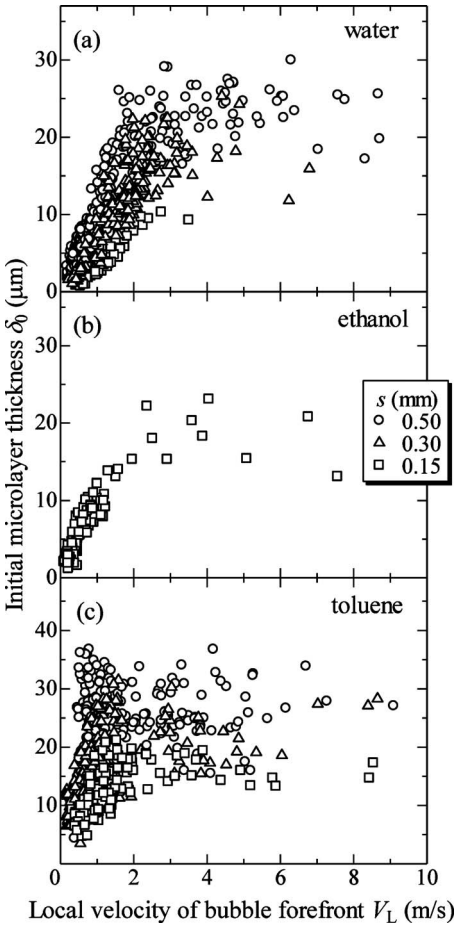

Fig. 4 Microlayer thicknesses versus local bubble forefront velocity for water, ethanol, and toluene

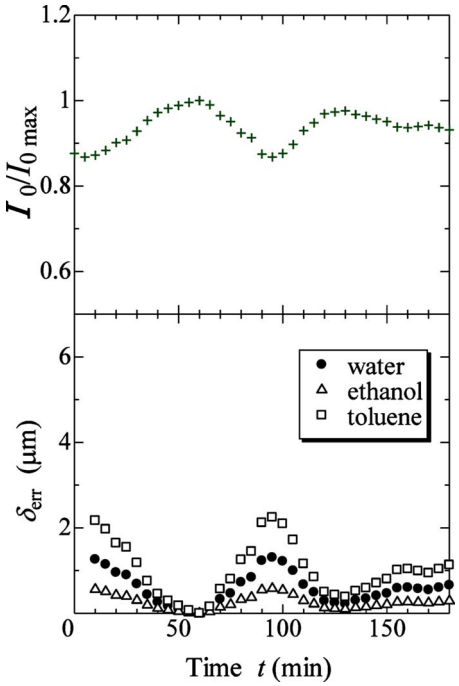

Fig. 3 Error of microlayer thickness measurement due to variation in ambient temperature

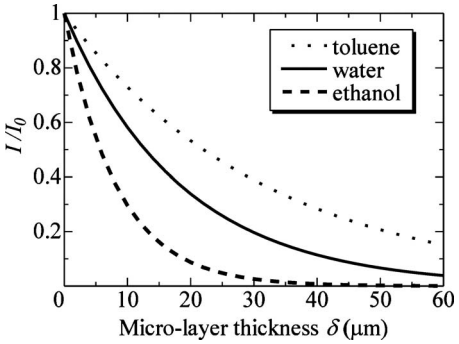

Fig. 5 Relationship between microlayer thickness and ratio of I to I_0

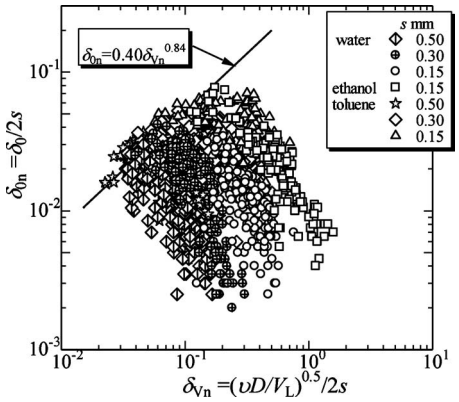

Fig. 6 Microlayer thickness versus viscous boundary layer thickness

front velocities. This fact indicates that a transition in the controlling mechanism occurred when the velocity increased beyond some critical value.

In the next step, in order to gain general insight into the controlling mechanism without considering the kind of fluid and operating conditions, the dimensionless parameters $\mathrm{Re}=\rho V_L d_h/\mu$ and $\mathrm{We}=\rho V_L^2 d_h/\sigma$ (based on the hydrodynamic diameter $d_h=2s$) were used to analyze the experimental results. The Reynolds number Re prescribes the relative magnitudes of inertial and viscous forces in the system, while the Weber number We prescribes those of inertial and curvature forces within a fluid. In order to identify the role played by the different parameters, a quantitative analysis of the experimental data was provided. First, in the region of high velocity, the viscous boundary layer is well developed in the liquid ahead of the dynamic tip of the bubble with the motion of fluid, which was caused by the bubble growth. With increasing distance from the bubble incipient site, the boundary layer thickness increases continuously, which is similar to the liquid motion along a flat plate in the Prandtl law. In this limit, the microlayer thickness could be decided by the viscous boundary layer thickness because the boundary layer thickness becomes thinner with high velocity according to the classical Prandtl law. Then, the relationship between the dimensionless microlayer thickness

$$\delta_{0n} = \delta_0/2s \tag{2}$$

and the dimensionless viscous boundary layer thickness

$$\delta_{Vn} = \frac{\delta_V}{2s} = \frac{1}{2s}\sqrt{\frac{\mu D}{\rho V_L}} = \sqrt{\frac{D}{2s}}\cdot\frac{1}{\sqrt{\mathrm{Re}}} \tag{3}$$

is shown in Fig. 6. Most of the data are distributed to the right of the diagonal line given by

$$\delta_{0n} = 0.35\delta_{Vn}^{0.84} = 0.35\left(\frac{D}{2s}\right)^{0.42}(\mathrm{Re})^{-0.42} \tag{4}$$

The results shown in Fig. 6 could be interpreted similarly to Moriyama and Inoue [4] for R113. That is, the data on the line correspond to the region where the forefront velocity is so fast that the viscous boundary layer δ_{Vn} is thin enough to limit the formation of δ_{0n}, and the surface tension effect to push out the stagnant liquid is diminished. According to Eq. (3), in the region aforementioned, for a given bubble forefront velocity and dynamic viscosity, the microlayer thickness increases with increasing distance D between the incipient bubble site and the bubble forefront. Figure 7 shows, for the three kinds of liquid and three gap sizes, the variations in bubble forefront velocity against the microlayer thickness, with D as a parameter. It could be observed that in the region of high velocity, the initial microlayer thickness increases with increasing D, whereas in the region of low velocity the effect of D vanishes. This is because when V_L becomes slower, δ_{Vn} increases and becomes too thick to limit the formation of the microlayer, which is changed to be determined by the balance between capillarity and viscosity. Correspondingly, in the region of small velocity, the boundary layer law becomes invalid for the formation of microlayers between the bubble and the heating surface. In the limit of small velocity, the effect of inertia force becomes weak and the deformation of interface between vapor and liquid caused by the motion is strongly opposed by the surface tension. At the same time, the flow of liquid caused by the Laplace pressure difference due to the difference in curvature between the almost flat microlayer and the dynamic tip becomes obvious and effected by the surface tension coefficient. Therefore, the microlayer remaining on the heating surface changes to be predominantly determined by the surface tension effect that could make the microlayer thinner than that determined by the boundary layer. With an aim at analyzing the data in the latter region, all of

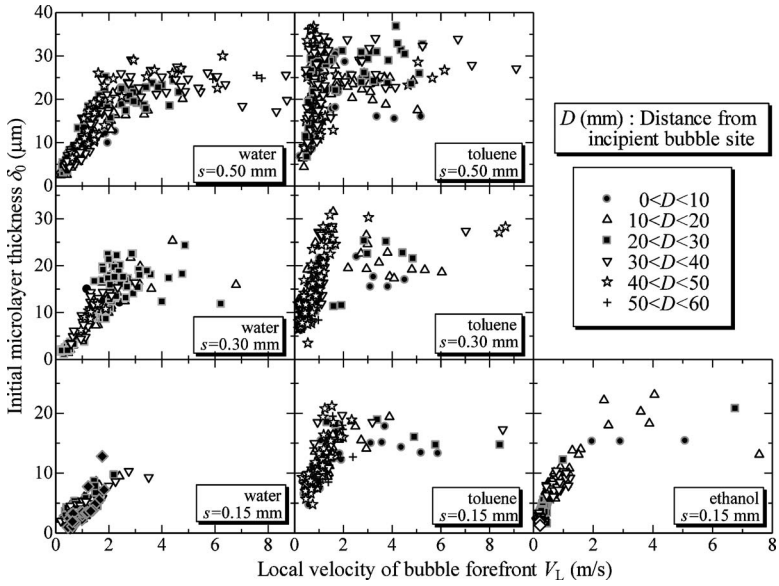

Fig. 7 Effect of bubble forefront traveling distance

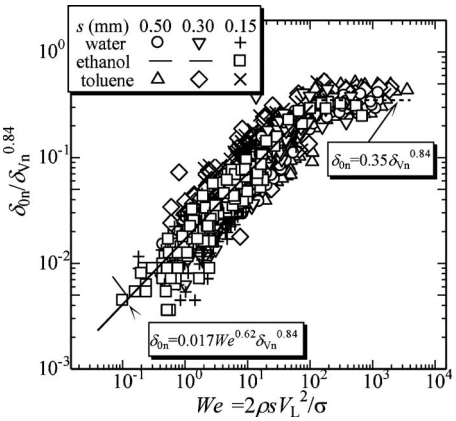

Fig. 8 Nondimensional viscous microlayer thickness versus Weber number for all test liquids and gaps

the data were normalized with $\delta_{Vn}^{0.84}$ and plotted as a function of Weber number, as shown in Fig. 8. It was found that in the region of about We >110, the data do not depend on the Weber number but are correlated instead by Eq. (4), corresponding to that located around the dashed line in Fig. 8 for all test liquids and gaps. For We <110, the figure shows that the normalized data correlated well with the Weber number, as described by Eq. (5), which was obtained by a least-squares fit,

$$\delta_{0n} = 0.017\mathrm{We}^{0.62}\delta_{Vn}^{0.84} = 0.017\mathrm{We}^{0.62}\left(\frac{D}{2s}\right)^{0.42}(\mathrm{Re})^{-0.42} \quad (5)$$

What is shown in Fig. 9 for the test liquid of water and toluene indicates clearly again that the gap size hardly affects the conclusions mentioned above. Therefore, this method of analyzing with Weber number could be used regardless of the liquid type or gap size, and it could be used to analyze the basic mechanism of the microlayer formation.

According to Eqs. (3)–(5) and the definition of Weber number, at the region of small velocity the thickness is proportional to $\rho^{0.62}\nu^{0.42}\sigma^{-0.62}$, and these are 1.75, 1.40, and 0.74 for ethanol, toluene, and water, respectively, according to their properties, as

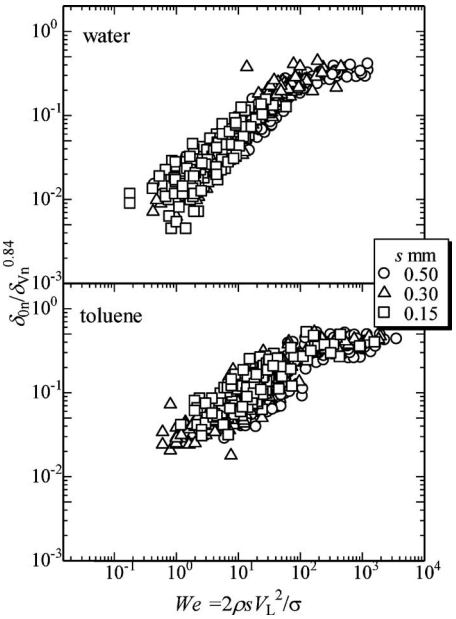

Fig. 9 Nondimensional microlayer thickness versus Weber number for water and toluene to examine the effect of gap sizes

Table 2 Properties of the test fluids at 1 atm and saturation temperature

	Water	Ethanol	Toluene
ρ (kg/m^3)	958.1	737.4	779.7
ν (mm^2/s)	0.295	0.612	0.318
σ (mN/m)	58.9	18.5	18.1

shown in Table 2, a finding also supported by the experimental results. Figure 10 shows the effect of fluid properties on the initial microlayer thickness for $s=0.5$, 0.3, and 0.15 mm. As shown in Fig. 10(c), for the liquids toluene and ethanol, whose values of $\rho^{0.62}\nu^{0.42}\sigma^{-0.62}$ are close to each other, their thicknesses are approximate in the region of relatively lower velocity. Because the value of $\rho^{0.62}\nu^{0.42}\sigma^{-0.62}$ for water is remarkably smaller than ethanol and toluene, and especially its large surface tension that conduces a bigger pressure difference between the flat microlayer region and the tip region causes greater flow of liquid, its microlayer is significantly thinner in the region of low velocity, as shown in Fig. 10(c). However, when it comes to the region of high velocity, the microlayer thickness becomes thin as the order of ethanol, toluene, and water, in accordance with their kinematic viscosities. So, the microlayer thickness of water is the smallest one in all the region of velocity and every size of gap for its relatively small $\rho^{0.62}\nu^{0.42}\sigma^{-0.62}$ and low viscosity compared to toluene and ethanol.

In order to use a continuous relation involving δ_0 within the

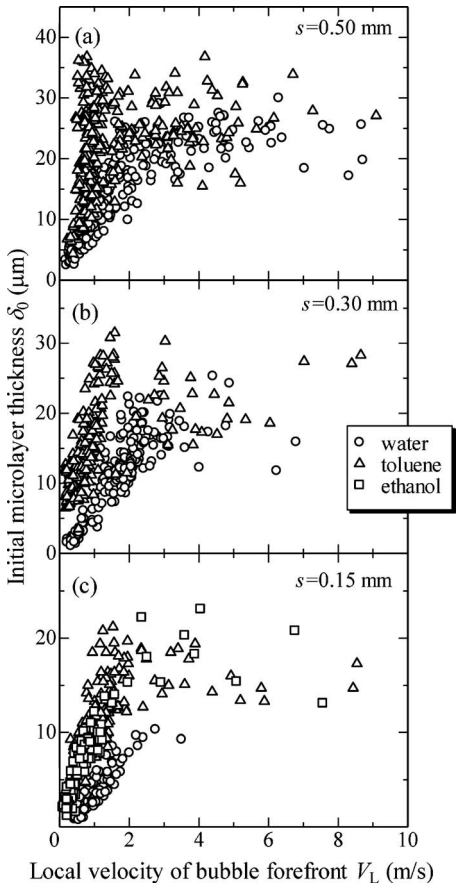

Fig. 10 Effect of fluid properties on initial microlayer thickness for $s=0.5$ mm, 0.3 mm, and 0.15 mm

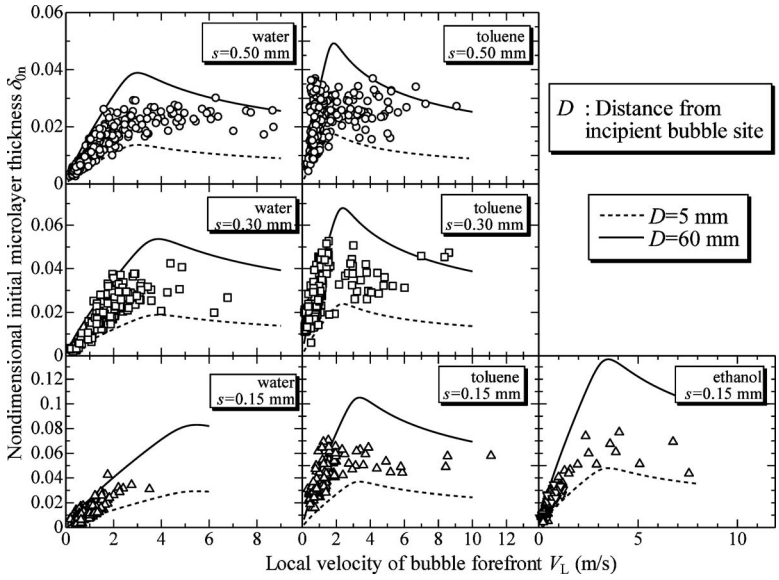

Fig. 11 Comparison between the prediction and the experiment

two regions, the asymptotic expression was applied here by a method similar to that used by Thome et al. [5]. Thus, the asymptotic relation for Eqs. (4) and (5) is

$$\delta_{0n} = \left(\frac{D}{2s}\right)^{0.42} (\mathrm{Re})^{-0.42}\{0.35^{-10} + (0.017\mathrm{We}^{0.62})^{-10}\}^{-1/10} \quad (6)$$

The predicted variation in the dimensionless thickness of the initial microlayer is provided in Fig. 11 for the three kinds of liquid and gap size, with $D=5$ mm represented by solid lines and $D=60$ mm represented by broken lines. The comparison between the prediction of Eq. (6) and the experimental data shows that the error falls in an acceptable range.

In this paper, the boiling was conducted in the microchannel formed by two parallel quartz glass plates. Liquid inside the microchannel was heated by the forced convection of hot air that flows along the outside of the glass plate; the uniform heating was realized. Since the bubbles grew so rapidly that little influence of heat conduction in the direction of the surface of the glass of plate could be realized, it is possible to consider as one-dimensional heat conduction on the direction normal to the surface. The heating conduction should be influenced by the substrate material, and if it was changed to another kind of material with totally different thermal properties, the growth of the bubble becomes different because the unsteady heat transfer inside the substrate material changed. But that does not influence the illumination for the basic mechanism of the microlayer formation. Summing up, the research in this paper could be considered to give fundamental insight into the basic mechanism of bubble formation.

4 Conclusions

Experiments were performed to directly measure, by the laser extinction method, the microlayer that forms on a heating surface by vapor growth during boiling in the mini-/microchannel that formed by two parallel quartz glasses. Microlayer thickness became smaller as the gap size became smaller. A dimensionless correlation for investigating the effects of test liquids and gap sizes on microlayer thickness was presented. At a small Weber number ($\mathrm{We}<110$), the microlayer is controlled mainly by the Weber number, its thickness being smaller for the liquid whose value of $\rho^{0.62}\nu^{0.42}\sigma^{-0.62}$ was relatively large. As the Weber number increased, namely, as the bubble forefront velocity became faster, the mechanisms of microlayer formation change to the viscous boundary layer. Therefore, the smaller the kinematic viscosity of the liquid, the smaller the thickness of the microlayer becomes.

Acknowledgment

This work was supported in part by a Grant-in-Aid for Scientific Research of the Ministry of Education, Culture, Sports, Science and Technology, Japan (Grant No. (B) 17360096).

Nomenclature

A = extinction coefficient (m^{-1})
d_h = hydraulic diameter
D = distance from incipient bubble site (mm)
I = laser intensity
I_0 = incident laser intensity
s = gap size (mm)
d_h = hydrodynamic diameter (mm)
V_L = local bubble forefront velocity (m/s)
δ = thickness of liquid layer the laser travels through (μm)
δ_0 = initial thickness of microlayer (μm)
δ_{0n} = nondimensional initial thickness of microlayer
δ_{Vn} = nondimensional viscous boundary thickness
ν = kinematic viscosity (mm^2/s)
μ = viscosity (μPa s)
σ = surface tension coefficient (mN/m)
We = Weber number
Re = Reynolds number

References

[1] Taylor, G. I., 1961, "Deposition of a Viscous Fluid on the Wall of a Tube," J. Fluid Mech., **10**, pp. 161–165.
[2] Bretherton, F. P., 1961, "The Motion of Long Bubbles in Tubes," J. Fluid Mech., **10**, pp. 166–188.
[3] Katto, Y., and Yokoya, S., 1966, "Experimental Study of Nucleate Pool Boiling in Case of Making Interference Plate Approach to the Heating Surface," *Proceedings of the Third International Heat Transfer Conference*, Vol. 3, pp. 219–227.
[4] Moriyama, K., and Inoue, A., 1996, "Thickness of the Liquid Film Formed by a Growing Bubble in a Narrow Gap Between Two Horizontal Plates," ASME Trans. J. Heat Transfer, **118**, pp. 132–139.
[5] Thome, J. R., Dupont, V., and Jacobi, A. M., 2004, "Heat Transfer Model for Evaporation in Microchannels, Part I: Presentation of the Model," Int. J. Heat Mass Transfer, **47**, pp. 3375–3385.
[6] Utaka, Y., Okuda, S., and Tasaki, Y., 2009, "Configuration of the Micro-Layer

and Characteristics of Heat Transfer in a Narrow Gap Mini/Micro-Channel Boiling System," Int. J. Heat Mass Transfer, **52**, pp. 2205–2214.
[7] Utaka, Y., and Nishikawa, T., 2003, "An Investigation of Liquid Film Thickness During Solutal Marangoni Condensation Using Laser Absorption Method: Absorption Property and Examination of Measuring Method," Heat Transfer Asian Res, **32**(8), pp. 700–711.

Prediction of Local Heat Transfer in a Vertical Cavity Using Artificial Neutral Networks

M. Ebrahim Poulad[1]
e-mail: mpoulad@ryerson.ca

D. Naylor

A. S. Fung

Department of Mechanical and Industrial Engineering,
Ryerson University,
350 Victoria Street,
Toronto, ON, M5B 2K3, Canada

A time-averaging technique was developed to measure the unsteady and turbulent free convection heat transfer in a tall vertical enclosure using a Mach–Zehnder interferometer. The method used a combination of a digital high speed camera and an interferometer to obtain the local time-averaged heat flux in the cavity. The measured values were used to train an artificial neural network (ANN) algorithm to predict the local heat transfer. The time-averaged local Nusselt number is needed to study local phenomena, e.g., condensation in windows. Optical heat transfer measurements were made in a differentially heated vertical cavity with isothermal walls. The cavity widths were $W = 12.7$ *mm, 32.3 mm, 40 mm, and 56.2 mm. The corresponding Rayleigh numbers were about* 3×10^3, 5×10^4, 1×10^5, *and* 2.7×10^5, *respectively, and the enclosure aspect ratio (H/W) ranged from* $A = 18$ *to 76. The test fluid was air and the temperature differential was about 15 K for all measurements.* ALYUDA NEUROINTELLIGENCE *(version 2.2) was used to generate solutions for the time-averaged local Nusselt number in the cavity based on the experimental data. Feed-forward architecture and training by the Levenberg–Marquardt algorithm were adopted. The ANN was designed to suit the present system, which had 4–13 inputs and one output. The network predictions were found to be in a good agreement with the experimental local Nusselt number values.*
[DOI: 10.1115/1.4002327]

Keywords: local heat transfer, artificial neural network, Mach–Zehnder interferometry, free convection

1 Introduction

Architects and building designers are not generally knowledgeable in computational fluid dynamics (CFD) and the complex solution techniques for obtaining the heat transfer inside double glazed windows. So, it would be useful to have a tool to give them a reasonable idea of the impact of their designs on window performance. Condensation of the water on the window due to the humidity is a phenomenon of particular interest. Condensation happens because of the heat transfer between window and humid air at that level. This is a complicated process for nonmechanical engineers. This paper aims to train an artificial neural network (ANN) based on experimental data to predict the local heat transfer at different levels. Therefore, it would be easy to use this trained ANN to predict the heat transfer by just entering the physical conditions (e.g., temperatures, window size, etc.). Abodahab and Muneer [1] measured the longitudinal temperature along double glazed window to investigate the condensation occurrence. Wright [2] developed a model that takes four inputs (internal temperature, external temperature, U-value of the window, and indoor relative humidity to determine the risk of condensation).

In recent years, there has been a renaissance of interest in interferometry in part because of the rapid developments in computer modeling of heat transfer. In the current study, measurements of free convection have been made in a tall air-filled vertical enclosure. Figure 1 shows the test geometry and the three-dimensional coordinate system. The enclosure consisted of two differentially heated plates, which were temperature controlled using constant temperature baths. The side walls that sealed the enclosure were machined from acrylic. This geometry was chosen because the flow regimes are well known.

The current optical method uses the beam-averaged temperature field to measure the instantaneous and time-averaged convective heat transfer flux. The beam-averaged temperature gradient, normal to the measurement surface, was used to calculate the local convective heat flux. This was obtained by applying the conduction heat transfer equation at the surface ($x=0$). After some manipulation, it can be shown that the instantaneous local convective heat flux can be expressed as

$$q_y'' = -k_s \left.\frac{\overline{\partial T}}{\partial x}\right|_{x=0} = -\frac{k_s R \lambda_o T_s^2}{LPG} \left.\frac{\partial T}{\partial x}\right|_{x=0} \tag{1}$$

where k_s is the fluid thermal conductivity evaluated at the surface temperature. Equation (1) has been used to evaluate the instantaneous local heat flux at each time interval using the surface fringe shift gradient ($\partial\varepsilon/\partial x|_{x=0}$) measured in each interferogram. The instantaneous local Nusselt number (Nu_y) for the enclosure can be defined as

$$\mathrm{Nu}_y = \frac{h_y W}{K_f} = \frac{q_y'' W}{k_f (T_H - T_c)} \tag{2}$$

where k_f is the conductivity of the test fluid (air) at mean enclosure temperature, i.e., $(T_H + T_c)/2$. Finally, average Nusselt number was measured by integrating the local Nusselt number distribution using the trapezoidal rule. The details of this technique have been published by Poulad et al. [3].

One hundred and fifty experiments were implemented to measure the time-averaged local Nusselt number for three different enclosure gaps (W). A combination of a high speed digital camera and a Mach–Zehnder interferometer (MZI) was used to record the

[1]Corresponding author.

Contributed by the Heat Transfer Division of ASME for publication in the JOURNAL OF HEAT TRANSFER. Manuscript received January 7, 2010; final manuscript received June 28, 2010; published online September 22, 2010. Assoc. Editor: William P. Klinzing.

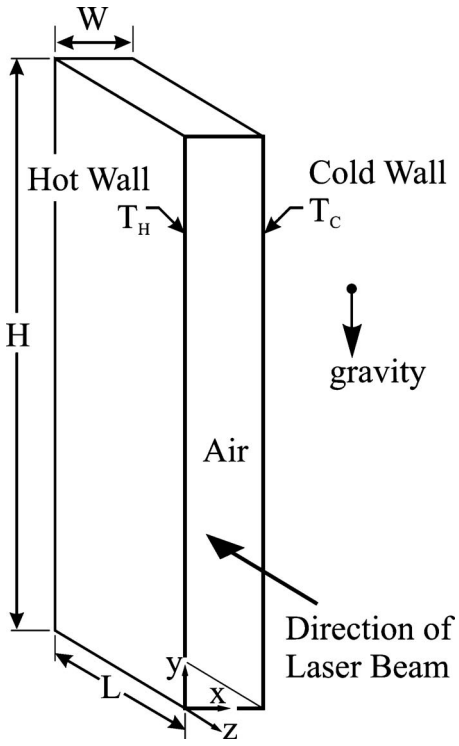

Fig. 1 Experimental geometry and coordinate system

interferograms. Those images were used to calculate Nu_y. Figure 2 shows the steps of the experimental process. As step 6 in the figure shows, the MATLAB IMAGE PROCESSING TOOLBOX was used to process the images.

Interferometry has some limitations. Due to the diffraction, interferometry cannot measure temperature gradient at the surface, $x=0$, as required in Eq. (2). Another problem with interferometry is it is expensive and like all measurement, there is some uncertainty (about $\pm 5\%$) in the measurements. Also, when the fringes are very wide or fine, the measurement accuracy is reduced [4]. Therefore, the ANN technique is a good option to predict the local heat transfer. Neural network is a method of computing, based on the interaction of multiple connected processing elements.

2 Artificial Neural Network

2.1 Major Components of an Artificial Neuron. This section describes the seven major components, which make up an artificial neuron. These components are valid whether the neuron is used for input, output, or is in one of the hidden layers.

1. Weighting factors: A neuron usually interacts with many inputs at the same time. Each input conveys its own relative weight, which gives it the impact that the input needs on the processing element's summation function. The performance of these weights is the same as the varying synaptic strengths of biological neurons. In both cases, some inputs are considered more important than others, therefore, they have a greater effect on the processing element as they combine to produce a neural response [5].
2. Summation function: The weighted sum of all of the inputs is compared by a processing element's operation at first. The

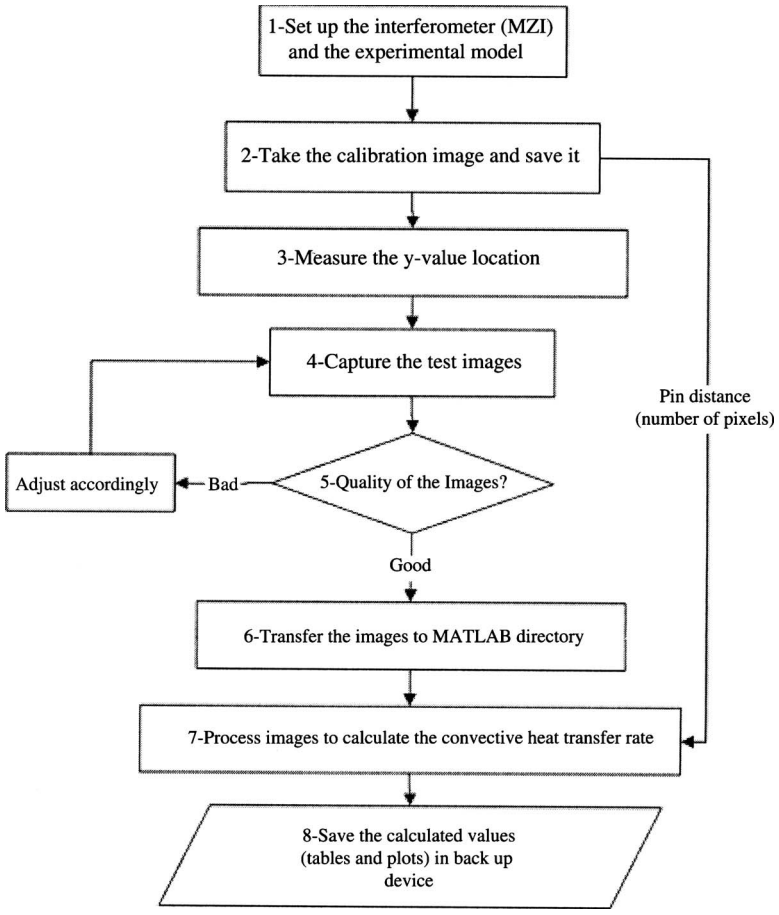

Fig. 2 Steps in the current experiment to calculate Nusselt number

inputs and the corresponding weights are vectors, which are generally represented as $(i_1, i_2, \ldots, i_n)$ and $(w_1, w_2, \ldots, w_n)$, respectively. The dot, scalar, or inner product of these two vectors makes the total input signal. Each component of the i vector is multiplied by the corresponding component of the w vector to find the simplistic summation function and then adding up all the products. $\text{Input}_1 = i_1 \times w_1$, $\text{input}_2 = i_2 \times w_2$, etc., are added as $\text{input}_1 + \text{input}_2 + \cdots + \text{input}_n$. The result is a single number, not a multi-element vector [5].

3. Transfer function: Transfer function is an algorithmic process that transforms the result of the summation function or the weighted sum to a working output. To determine the neural output, the summation total can be compared with some threshold in the transfer function. The processing element generates a signal if the sum is greater than the threshold value. If the sum of the input and weight products is less than the threshold, no signal (or some inhibitory signal) is generated. Both types of responses are significant [5].
4. Scaling and limiting: The result may be scaled or limited just after the processing element's transfer function occurred. The transfer value is multiplied by a scale factor during scaling process and then adds an offset. The scaled result is prevented from exceeding a specified bound by limiting.
5. Output function (competition): Each processing element can have one output signal, which it may output to hundreds of other neurons. This is just like the biological neuron where there are many inputs and only one output action. Generally, the output is the same as the transfer function's result. In order to incorporate competition among neighboring processing elements, however, some network topologies modify the transfer result. It is possible for neurons to compete with each other, inhibiting processing elements unless they have great strength [6].
6. Error function and back-propagated value: In most cases, learning networks calculate the difference between the current output and the desired output. Then, this raw error is transformed by the error function to match the particular network architecture. The most basic architectures use this error directly but some square the error while retaining its sign, some cube the error, and other paradigms modify the raw error to fit their specific purposes. The artificial neuron's error is then typically propagated into the learning function of another processing element. This error term is sometimes called the current error [6].
7. Learning function: According to some neural based algorithms, the learning function modifies the variable connection weights on the inputs of each processing element. This process of changing the weights of the input connections to achieve some desired result can also be called the adaption function, as well as the learning mode [6].

The ANN technique has been receiving increasing attention for simulating engineering systems due to some interesting characteristics, such as its learning capability, fault tolerance, and nonlinearity. Once they are trained, they can provide prediction and generalization at high speed and low cost [7]. Prediction of heat transfer by using ANN based on the experimental data is popular in literature [8]. For example, ANN has been used to optimize solar energy utilization and prediction of residential buildings energy consumption [9]. Kalogirou [10] used the ANN in the field of solar energy. He found that ANN can be used in the fields of use and transformation of energy. To the best of the authors' knowledge, this is the first time that ANN has been used to predict the local Nusselt number for free convection in a cavity.

2.2 Decision on Architecture or Layout. The number of layers and the number of processing elements per layer are important decisions. The selection of these parameters to a feed-forward, back-propagation topology involves more "art" than science. There is no quantifiable best answer to the layout of the network for any particular application. There are only general rules picked up over time and followed by most researchers and engineers applying this architecture to their problems. The following rules are generally followed [11]:

- Rule one: The number of the processing elements in the hidden layer should also increase as the complexity in the relationship between the input data and the desired output increases.
- Rule two: Additional hidden layer(s) may be required if the process being modeled is separable into multiple stages. Additional layers may simply enable memorization and not a true general solution if the process is not separable into stages.
- Rule three: The maximum value for the number of processing elements in the hidden layer(s) is controlled by the amount of training data available. To calculate this upper bound, the number of input-output pair examples in the training set is divided by the total number of the input and output processing elements in the network. Then divide that result again by a scaling factor between 5 and 10. Larger scaling factors are used for relatively noisy data.

Extremely noisy data may require a factor of 20 or even 50 while very clean input data with an exact relationship to the output might drop the factor to around 2. Having few processing elements in the hidden layers is important. The ANN may memorize if there is too many artificial neurons and training set. If that happens, then no generalization of the data trends will occur, making the network useless on new data sets. The process of teaching begins whenever the mentioned rules are used to create a network.

2.3 Training (Learning) Algorithms. Generally, there are three broad learning/training algorithms: supervised, unsupervised, (or self-organized), and reinforcement learning (this is a special case of former learning). For engineering application, the supervised one is mostly used, therefore, only this type of learning is discussed here.

2.3.1 Supervised Learning. Most of artificial neural network solutions have been trained with supervision. In this learning mode, the desired output is compared with the actual output of a neural network. Weights, which are usually randomly set to begin with, are then adjusted by the network so that the next iteration or epoch will produce a closer match between the actual and the desired output. The objective of the learning method is to minimize the current errors of all processing elements. Continuous modification of the input weights reduces the global error over time until acceptable network accuracy is reached [12].

With supervised learning, the artificial neural network must be trained, otherwise, it is not useful. Training consists of presenting input and output data to the network. This data is often referred to as the training set (Tr). That is, for each input set provided to the system, the corresponding desired output set is provided as well. In most applications, actual data must be used.

The training phase can consume a lot of time. In prototype systems with inadequate processing power, learning can take weeks. This training is considered complete when the neural network reaches a user defined performance level. This level signifies that the network has achieved the desired statistical accuracy as it produces the required outputs for a given sequence of inputs. When no further learning is necessary, the weights are typically frozen for the application. Some network types allow continual training at a much slower rate while in operation. This helps a network to adapt to gradually changing conditions. A comprehensive review of the application of ANN in thermal science and engineering readers has been reported by Yang [13].

During experiments, about 153 GB data were gathered from the processing of 162,160 interferograms. The digital images were shaded from 0 (dark) to 255 (bright or saturated). The number of

Fig. 3 The high speed video camera mounted on a *x*,*y*,*z* positioning stage that is equipped with micrometers

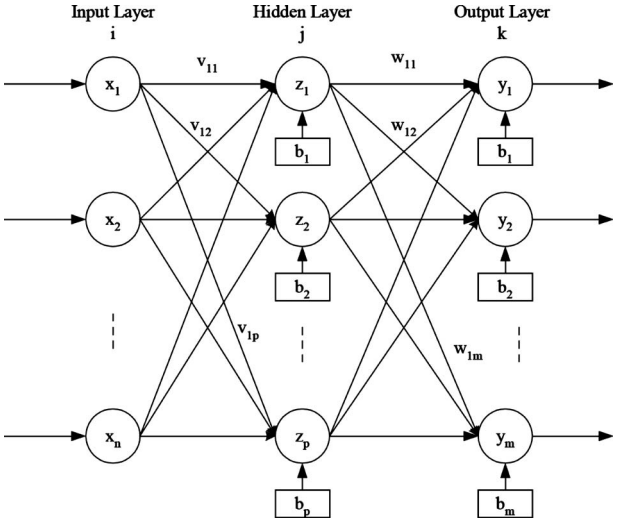

Fig. 4 The structure of the feed-forward ANN

data sets for $W=32.3$ mm, 40 mm, and 56.2 mm is 25, 20, and 61, respectively. These data were used to train an artificial neural network.

The network usually has an input layer, some hidden layers, and an output layer. Simply, each neuron is connected to all the others of previous layer via adaptable weights. As knowledge is stored as a set of connection weight during training, the connection weights are modified. The network uses a learning mode that the input is presented to the network along with the desired output. The weights are adjusted so that the network tries to produce the desired output. The weights after training contain meaningful information, whereas before training, they are random and have no meaning. ALYUDA NEUROINTELLIGENCE 2.2 software is used for simulation in this work [14].

3 Methodology

A combination of MZI with high speed cinematography was used to measure the time-averaged heat transfer flux experimentally. To get the data for training the ANN, the MZI was set up first and the interferograms were transferred to an image processing automatically to calculate the heat transfer flux. The theory of MZI is well documented in open literature [15].

The high speed camera with a resolution of 1280×1024 was used. To get the maximum possible intensity, the lens was removed from camera and images were exposed directly on the camera CCD sensor. In this way, in a single session, the camera was able to capture a maximum area of approximately $\Delta y=20$ mm by $\Delta x=18$ mm on the experimental model. To view the entire model, the camera's "window" was moved within the interferometer beam. Figure 3 shows the camera mounted on a precision *x*-*y*-*z* positioning holder. A preliminary investigation showed that a 10 s capture interval with a frequency of 100 Hz provided an acceptable result.

3.1 NEUROINTELLIGENCE Software. So far, the methodology of the experiments was introduced. Now, the specification or architecture (structure) of the ANN is described. Artificial neural networks are the simple clustering of the primitive artificial neurons. This clustering occurs by creating layers, which are then connected to one another. How these layers connect may also vary. There are various types of ANNs. A few popular ones are multilayer perceptrons (MLPs), radial bias function neural networks (RBFNNs), and counter propagation neural networks (CPNNs). The MLP is the most commonly used NN for prediction in mechanical and chemical engineering [8]. Originally, all artificial neural networks have a similar structure of topology. As Fig. 4 shows, the neurons are grouped into three layers. The input layer consists of neurons that receive input from the external environment. The output layer consists of neurons that communicate the output of the system to the user or external environment. There are usually a number of hidden layers between these two layers. Figure 4 shows a simple feed-forward ANN structure with only one hidden layer. Independent variables (x_i) flow into the input layer with n neurons, pass through the hidden layer with p neurons, and arrive at the output layer with m neurons. Each neuron receives signals from the neurons of the previous layer but the input layer's neurons. The incoming signals are multiplied by the weights (v_{ij}) and summed up with the bias (b_j) contribution [16].

$$\text{inp}_j = \sum_{i=1}^{n} x_i v_{ij} + b_j \tag{3}$$

where inp_j is the total input of the hidden layer neuron j, x_i is the input to the hidden layer neuron j from input layer neuron i, v_{ij} is the weight between the input layer neuron i and hidden layer neuron j, and b_j is the bias of the hidden layer neuron j.

The bias is actually a unit connected to a neuron with a weight of one. The output of a neuron is determined by applying an activation function to the total input (inp_j) calculated using Eq. (3). The bias (b_j) in Eq. (3) has the effect of decreasing or increasing the total input to the activation function Eq. (4), depending on whether it has a negative or positive value, respectively. The bias avoids the tendency of an activation function to get "stuck" in the saturated, limiting value area of the activation function. Sometimes, it is referred to as the classic "error valley" problem. The bias is actually a unit connected to a neuron with a weight of one [16].

Activation functions for the hidden units are needed to introduce nonlinearity into the network. Without nonlinearity, hidden units would not make ANNs more powerful than just plain networks, which do not have any hidden layer units. The sigmoid function, such as the logistic function that is used here, is one of the most commonly used activation functions in networks trained by Levenberg–Marquardt (LM). The logistic function with the output amplitude lying inside the range (0.0–1.0) is

$$Z_j = \frac{1}{1+e^{-\text{inp}_j}} \tag{4}$$

If the predicted outputs do not match the actual (i.e., target) values, NN model is in error. Part of this error is propagated through the network. The weight and bias of each neuron through-

out the network are adjusted to reduce the error so the next iteration error will be less for the same units. The procedure is applied continuously and repetitively for each set of inputs until there are no measurable errors or the total error is smaller than a specified value. In using the NN model, the underlying assumption is that the relationships between the input and the output variables in the training data set, the testing data set, and prediction data set are the same.

In the architecture design of the NEUROINTELLIGENCE, user may manually enter a number of hidden layers (up to five) and a number of hidden units in each layer (up to 256). By default, NEUROINTELLIGENCE proposes a topology with one hidden layer and with the number of hidden units equal to the number of inputs divided by 2. This maybe very wrong in some cases and authors run a search method with different architectures manually and then the result was compared with the architecture proposed automatically by the NEUROINTELLIGENCE. When the input layer receives the input, its neurons produce output, which becomes input to the other layers of the system. The process continues until a certain condition is satisfied or until the output layer is invoked and fires their output to the external environment.

Alyuda shows the structure as n-m_1-,…,-m_k-u, which all of them are scalar numbers, n is the number of inputs, k is the number of hidden layers, m_i is the number of neurons in ith layer, and u is the number of outputs. For example, 9-23-1 means a structure of nine inputs, 23 neurons in one hidden layer, and one output. By default, NEUROINTELLIGENCE divides each data set onto three sets: the training set (Tr), the validation set (Va), and the test set (Te).

3.2 Understanding Input Feature Selection. Input feature selection methods are used to identify input columns that are not useful and do not contribute significantly to the performance of neural network. Insignificant inputs can be removed and help improve the generalization performance of a neural network, in spite of losing some input information. In NEUROINTELLIGENCE, one of the following four methods of feature selection may be used: forward stepwise, backward stepwise, exhaustive search, and genetic algorithms. Details are given in Alyuda Manual [14].

All methods use generalized regression neural networks (GRNN) or probabilistic neural networks (PNN) because they trained quickly and proved to be sensitive to the irrelevant inputs. NEUROINTELLIGENCE automatically uses GRNN for regression problems and PNN for classification problems.

The initial test network architectures were constrained to three layers, one for input, hidden, and output layers, respectively. This architecture was chosen as previous research indicated that multiple hidden layers are rarely effective in terms of both accuracy and training speed [17].

The training set is part of the input data set used for neural network training, i.e., for adjustment of network weights. The validation set is part of the data used to tune network topology or network parameters other than weights. NEUROINTELLIGENCE uses validation set to calculate generalization loss and retain the best network (the network with the lowest error on the validation set). The test set is part of the input data set used only to test how well the neural network will perform on new data. The test set is used after the network is ready (trained) to test what errors will occur during future network application. This set is not used during training and thus, can be considered as consisting of new data entered by the user for the neural network application.

In this work, 68%, 16%, and 16% of the data were selected for training, validation, and test, respectively.

Because of the limitation of the number of data, exhaustive search was used to select the feature of the inputs. Logistic was selected for hidden layer and output activation Z.

The most popular learning algorithms are back-propagation (BP) and its variants [18]. The training set has to be a representative collection of input-output examples. Back-propagation training is a gradient-descent algorithm. It tries to improve the performance of the neural network by reducing the total error by changing the weights along its gradient.

Table 2 Different networks structures to input ANN

Network	Structure	Best fit-R^2	Test-R^2	No. of epoch
A0	13-17-1	0.993	0.981	82
A1	12-26-1	0.931	0.917	51
A2	11-18-1	0.974	0.914	40
A3	9-14-1	0.973	0.966	22
A4	11-13-1	0.997	0.988	20
A4-1	10-15-1	0.979	0.973	10
A4-2	9-12-1	0.978	0.982	27
A5	10-24-1	0.995	0.989	13
B0	8-5-1	0.995	0.978	52
B0-1	7-5-1	0.995	0.972	9
B0*	8-5-1	0.995	0.992	2.5×10^5
B1	7-14-1	0.997	0.998	203
B1-1	6-15-1	0.982	0.983	29
B1-2	5-12-1	0.979	0.977	18
B2	15-7-1	0.961	0.932	300
B3	4-18-1	0.985	0.987	10
B4	5-19-1	0.998	0.997	206
B4-1	4-8-1	0.983	0.988	105
B4-2	3-6-1	0.978	0.975	101
B1*	7-14-1	0.997	0.985	10^5

With a small number of weights (usually, up to 300), LM algorithm is efficient and often performs considerably faster than other algorithms and finds better optima than other algorithms [7]. But its memory requirements are proportional to the square of the number of weights, which is not an issue here. The LM update rule is [17]

$$\Delta W = (J^T J + \mu I)^{-1} J^T \boldsymbol{E} \tag{5}$$

where ΔW is the difference between previous and current weight $(W_{i-1} - W_i)$, J is Jacobean matrix of derivatives of each error to each weight, μ is a scalar, and $\boldsymbol{E}$ is an error vector. Its only drawback is that it requires a matrix inversion step as part of the update, which scales as the N^3 where N is the number of weights. For medium sized networks (let us say, a few hundred weights), this method will be much faster than gradient descent plus momentum. There are seven different algorithms in the NEUROINTELLIGENCE to train the network. The LM and BP were compared before selecting either of them. For this work, the Levenberg–Marquardt algorithm was selected as training algorithm because it always produced better R^2-values (closer to 1). To compare the back-propagation and Levenberg–Marquardt algorithms in training, B0, B1, B1*, and B0* shown in Table 2 are noticeable. As shown in table, 2.5×10^5 epochs in BP (B0*) gives almost the same performance as LM with 52 iterations does. The comparison of the number of iterations of B1 and B1* reveals that BP with 105 epochs cannot even perform as well as LM with 203 epochs.

Automatic feature selection was tried. After 511 iterations, these columns out of nine were rejected: y, y/H, T, P, and Ra. Because this selection, intuitively, does not make sense, therefore, automatic feature selection was overwritten and manual selection was used. The training of all patterns of a training data set is called an *epoch* or *iteration*. Figure 5 shows the process map of this artificial neural networking.

4 Simulation

The following set of data was selected as an input to NEUROINTELLIGENCE: type of the wall (H for hot and c for cold wall), y (height from bottom of the cavity as shown in Fig. 1), y/H, spacing (W), cold wall temperature (T_c), hot wall temperature (T_H), room temperature (T), room pressure (P), ΔT $(T_H - T_c)$, diagonal symmetry (DS), and Rayleigh number (Ra). The Rayleigh number is defined as

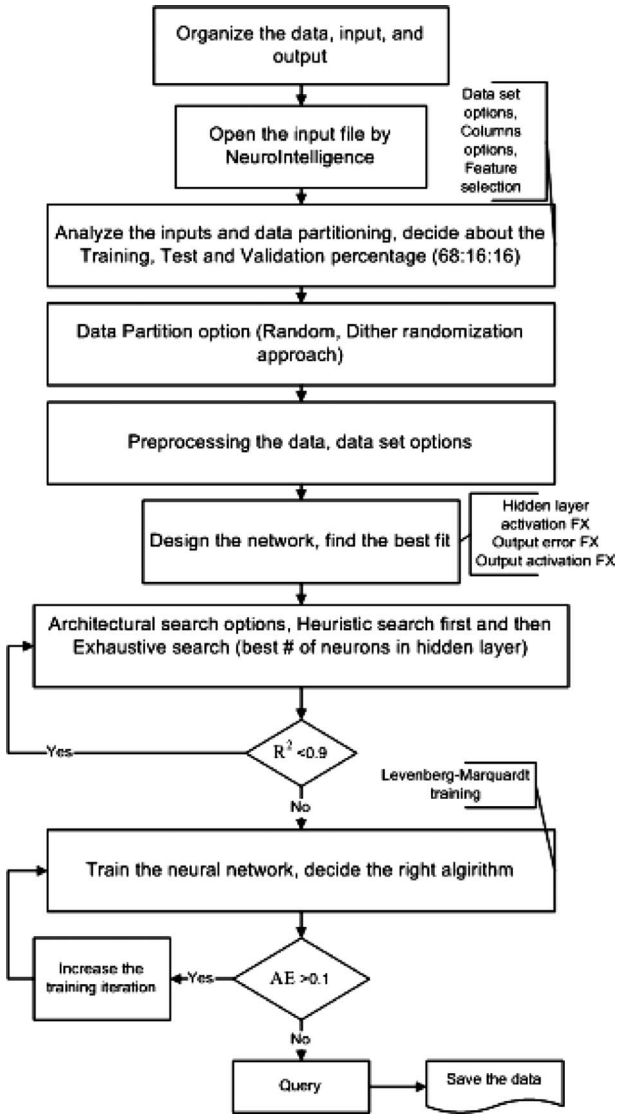

Fig. 5 Process map of the ANN to predict the local Nusselt number using NEUROINTELLIGENCE

$$\mathrm{Ra} = \frac{g\beta\Delta T W^2}{\nu\alpha} \tag{6}$$

where g is the acceleration of gravity, ν is the kinematic viscosity, α is the thermal diffusivity, and β is the coefficient of thermal expansion.

Because of a physical limitation on the height of the interferometer beam, the measurements were made only in the bottom half of the cavity ($0 \le y/H \le 0.5$). It would have been difficult to raise the 350 kg optical bench safely to the height required to make measurements in the upper half. Nevertheless, it was still possible to compute the local time-averaged Nusselt number, using the assumption of "diagonal symmetry" (DS). In this case (DS), measurements on the lower half of the hot wall are considered as the values for upper half of the cold wall diagonally, i.e., $y_{\mathrm{new}} = H - y_{\mathrm{measured}}$.

Room temperature and pressure are not directly related to Nusselt number calculation, they are measured, practically, to adjust the temperature of the water baths and to calculate the air properties inside the cavity. Air is considered an ideal gas. The temperature difference between cold and hot plate has a direct impact on Nusselt number. Considering the above points some sets of inputs are designed. Table 1 shows the network names (net number) and their inputs.

Table 1 Different network names and their respective inputs (B refers to the size $W=56$ data only)

Net No.	Inputs
A0	Wall type, W, y, y/H, T_c, T_H, T, P, Ra
A1	DS, W, y, y/H, T_c, T_H, T, P, Ra
A2	DS, W, y, y/H, ΔT, T, P, Ra
A3	DS, W, y, y/H, ΔT, Ra
A4	Wall type, W, y, y/H, T_c, T_H, Ra
A4-1	Wall type, W, y, T_c, T_H, Ra
A4-2	Wall type, W, y, T_c, T_H
A5	DS, W, y, y/H, T_c, T_H, Ra
B0	Wall type, y, y/H, T_c, T_H, T, P, Ra
B0-1	Wall type, y, T_c, T_H, T, P, Ra
B1	DS, y, y/H, T_c, T_H, T, P, Ra
B1-1	DS, y, T_c, T_H, T, P, Ra
B1-2	DS, y, y/H, T_c, T_H, T, P
B2	DS, y, y/H, ΔT as "C," Ra
B3	DS, y, y/H, ΔT, Ra
B4	DS, y, y/H, T_c, T_H, Ra
B4-1	DS, y, T_c, T_H, Ra
B4-2	DS, y, T_c, T_H

The time-averaged local Nusselt number (Nu) was given to the ANN as a target. Later, inputs were refined to see their effects on the target prediction. In the table, letter "A" means all the above raw data for different sizes were used as inputs. The inputs are entered to ANN as they were measured without any manipulation or adjustments. Letter "B" refers to the data that are classified. In this classification, only the largest cavity ($W=56$ mm) is employed and other sizes' data were rejected. Air flow inside this cavity is fully turbulent, chaotic, and three-dimensional. X-12 is assigned for the network with the same input as X network but y/H excluded. X-2 is assigned for the network with the same input as X-1 network but Ra excluded. Any discrete values would be considered as "category," even if they are number. In network B2, ΔT is considered as category or "C," which is not interpreted as number. It consists of 13 categories (15, 15.1, and 15.2–15.12). To see the effect of "categorization," the network B3 was designed with ΔT as number. Spacing (W) and wall type are always categorized as C. The former is composed of five (i.e., 12.7, 32.3, 40, 56.2, and 56.5) and the latter is composed of two categories (i.e., c and H).

In Table 2, the best fit structures and the related testing R^2 are summarized. To find the best structure, the number of neurons in hidden layer started from 1 and ended at 25, with one in each step. The closer the R^2 parameter to 1, the better the network is. The best fit-R^2 is related to the structure of the network and the test-R^2 shows how well the training process proceeded ($R(X,Y) = [\mathrm{Cov}(X,Y)]/[\mathrm{StdDev}(X).\mathrm{StdDev}(Y)]$). Training iterations were stopped when the absolute error (AE^2) was less than 0.1.

The number of hidden neurons in the network was determined based on the best performance (best fit R^2). The case of one hidden neuron was left out of this trial and error method. If the number of hidden neurons are increase too, this will result in an "over fit." In this case, the network will have a problem being able to generalize. The training set of data will be memorized, making the network useless on new data sets. If the number of neurons is not enough, network will be unable to learn the problem concept. Therefore, to estimate the number of hidden neurons, the network was run with different numbers of hidden neurons. Figure 6 shows

[2]The difference between the actual value of the target column and the corresponding network output.

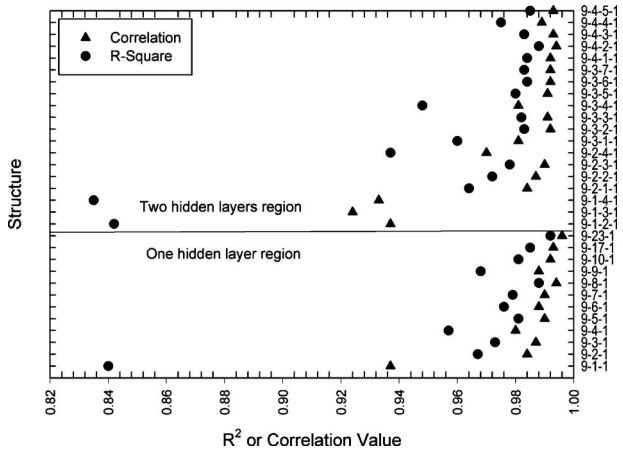

Fig. 6 Effects of structure on R^2 and the correlation

the effect of structure on R^2 and correlation. There results were obtained using a nine input data set to find the best structure. It shows that one hidden layer performed better than two. Also, the correlation value is always bigger than the R^2 value. Correlation is a statistical measure of strength of the relationship between the actual values and network outputs. This coefficient (r) can range from -1 to $+1$. The closer r is to 1, the stronger the positive linear relationship. Based on this preliminary test, three-layer structure was selected for this work.

5 Results and Discussion

The data are partitioned as training set (68.66%), validation set (15.67%), and test set (15.67%). The statistical coefficient of multiple determinations (R^2) was obtained by comparing the performance of each structure. To compare the prediction of different networks, this experiment result is used as actual value: $y=263.4$ mm, $y/H=0.269$, $W=56.7$ mm, $T_c=13.24°C$, $T_H=28.3°C$, $T=23.5°C$, $\Delta T=15.06$ K, $P=758$ mm Hg, and Ra $=2.8\times10^5$. The calculated (actual) value for the local time-averaged Nusselt number was $2.94\pm5\%$. That measurement is the most valid measurement for Nu because it is the average obtained from three sets of measurements, each contained 2000 interferograms.

Table 3 summarizes the deviation of the predicted Nusselt number from actual value for the different networks. A1 provide the worst prediction. A2 is almost the same. The performances of A3 and A4 show that T and P could be omitted from the inputs. Comparison of the percent deviation of A-type with B-type networks reveals that either classification of the data based on the size (W) of cavity is advisable or more data sets are needed for other sizes. On the other hand, manipulation of the input data in neural networking is not recommended. Data should be given to the ANN as they are monitored or measured. That leads the analysis to see the share of each size into the ANN inputs (Table 4).

Table 3 Performance of different networks

Network No.	Nu prediction	Deviation (%)
A0	2.74	7
A1	2.31	27
A2	2.41	22
A3	3.21	8
A4	2.96	1
A4-1	2.75	7
A4-2	2.81	5
A5	3.08	5
B0	2.89	2
B0-1	2.91	1
B1	2.85	3
B1-1	2.86	3
B1-2	2.98	1
B2	2.72	8
B3	2.91	1
B4	3.11	5
B4-1	3.13	6
B4-2	2.88	2

Table 4 Share of different size in ANN input

Size (W)	No. of data sets	% of share
32.3	25	23.6
40	20	18.9
56.2	61	57.5
Total inputs	106	100

5.1 Effect of Dimensionless Values. Removing the Ra and the y/H from the inputs provide better prediction as comparison of networks A4, B1 and B4 with A4-1 and A4-2, B1-1 and B1-2, and B4-1 and B4-2, respectively (Fig. 9). By any math, e.g., dividing y by H or calculating Ra, some round-off error is introduced into ANN, which can falsify neurons during training.

5.2 Effect of Categorization. Analysis of the B-type network performances also implies that about 60 experiments suffice for each size to input the ANN. Moreover, the error-value of B2, which is the worst among of all B-type networks, implies that categorization of ΔT misleads the NEUROINTELLIGENCE software. Thus, it is better to consider ΔT as a number, not a category.

Figure 7 shows how well the training of the network was done. This is the scatter plot obtained from network B4. It can be seen that the outputs of the training are very close to the targets. A linear regression line of the plot, the prediction interval, and the confidence interval (95% method) are shown on the graph to illustrate the performance of the training process.

Figure 8 presents the graph of Nusselt number versus y/H, which was predicted by network B4. The dimensionless location (y/H) is one of the inputs given to the trained network to find the Nu along the cold wall. As Table 3 shows, the prediction from the B4 network is about 5% different from the actual value. This uncertainty, on average, applies to all Nusselt number values in Fig. 8. On the other hand, the trend of the heat transfer is well matched with the experimental findings. On the cold wall, there is low convective heat transfer at the bottom but at the top, the

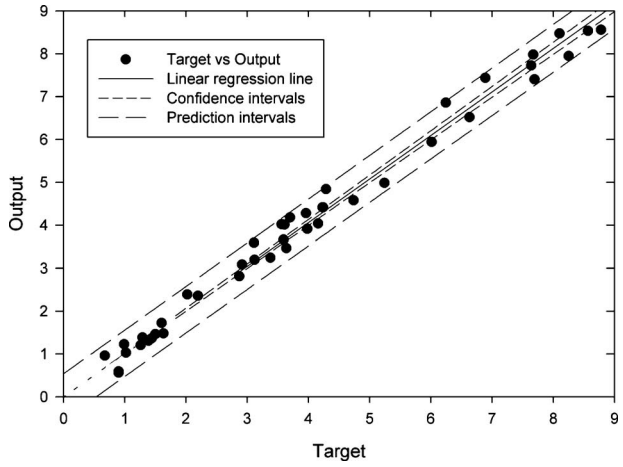

Fig. 7 Scatter plot of the training network B4

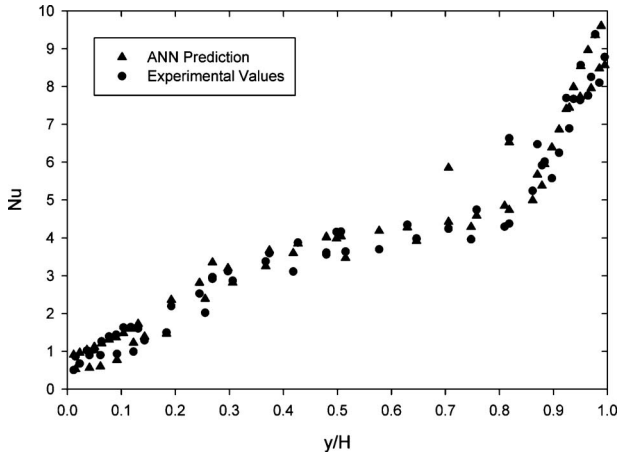

Fig. 8 Local Nusselt number distribution predicted by network B4 compared with the experimental data

convection reaches a maximum due to the impingement of the cold air onto the surface in this region. Along this wall, the central region has almost uniform convective heat transfer. It can be seen that the prediction is in good agreement with the experimental measurements.

The results show that any calculations based on the raw data (or manipulation, e.g., nondimensionalization) does not improve the predictive ability of the ANN. For example, Fig. 9 shows the impact of various manipulations of the data: applying diagonal symmetry, substituting ΔT instead of cold wall and hot wall temperatures, and using the dimensionless values y/H and Ra. Figure 9 shows that these manipulations do not lead to better predictions. Another implication of the better performance of B-type networks is that at least 60 experiments/m of cavity height (H) should be implemented to train the ANN properly. Even with a small set of data, the uncertainty of the ANN is approximately equal to the uncertainty of the experimental measurements. Both were found to have about $\pm 5\%$ uncertainty.

6 Conclusions

The time-averaged local Nusselt number in a tall vertical cavity was measured at different elevations using a combination of MZI and high speed cinematography. Then, an ANN was developed and trained based on the experimental measurements. Finally, the trained neural networks were used to predict the local Nusselt number distribution for the largest cavity size ($W=56$ mm). The application presented here is neither complete nor perfect but merely a sample that demonstrates the usefulness of artificial neural networks. It can predict the local Nu number along the cavity with as few as only three inputs (y, T_c, and T_H). Based on the work presented here, it is believed that ANNs offer an alternative method to predict the local Nu number in the cavity, which should not be underestimated. In order to obtain predictions with higher accuracy, more experimental data is needed as an input for the ANN. This work shows that the ANN technique can perform as well as an experiment in finding the local time-averaged heat transfer. Thus, a well-trained ANN could be used for a wide range of applications where knowledge of the local heat transfer is required. For example, it could be useful in building energy simulation programs or to predict the condensation potential of a window.

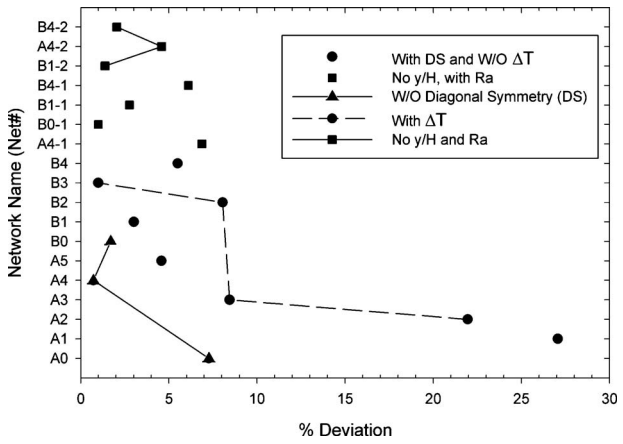

Fig. 9 Performance of different networks

Acknowledgment

This work was funded in part by the Solar Buildings Research Network under the Strategic Network Grants Program and Discovery Grant of the Natural Sciences and Engineering Research Council (NSERC) of Canada.

Nomenclature

AI = artificial intelligence
ANN = artificial neural network
CCD = charge coupled device
CFD = computational fluid dynamics
H = height
L = length of the cavity
LM = Levenberg–Marquardt
k = thermal conductivity
NN = neural network
Nu_y = instantaneous local Nusselt number
q''_y = instantaneous local heat flux ($\mathrm{W/m^2}$)
Ra = Rayleigh number
t = time (s)
T = temperature (K)
ΔT = temperature difference between cold and hot walls (K)
W = width of the cavity (m)
x,y,z = Cartesian coordinate system (m)

Greek Notations

α = thermal diffusivity ($\mathrm{m^2/s}$)
β = thermal expansion coefficient of fluid (1/K)
λ = laser wavelength (m)
μ = dynamic viscosity of fluid ($\mathrm{N\,s/m^2}$)
ν = kinematic viscosity of fluid ($\mathrm{m^2/s}$)
ρ = density of fluid ($\mathrm{kg/m^3}$)
ε = fringe shift

Subscripts

c = cold
f = fluid
H = hot
s = surface
y = local height value

References

[1] Abodahab, N., and Muneer, T., 1998, "Free Convection Analysis of a Window Cavity and Its Longitudinal Temperature Profile," Energy Convers. Manage., **39**(3–4), pp. 257–267.
[2] Wright, L. J., 1998, "Simplified Numerical Method for Assessing the Condensation Resistance of Windows," ASHRAE Trans., **104**, pp. 1222–1229.
[3] Poulad, M. E., Naylor, D., and Oosthuizen, P., 2009, "Measurement of Unsteady Convection in a Complex Fenestration Using Laser Interferometry," *Proceedings of the Canadian Solar Buildings Conference*, Toronto, Ontario, pp. 139–148.
[4] Poulad, M. E., 2009, "A Technique to Measure Turbulent Free Convective Heat Transfer in a Vertical Tall Cavity," MSc. thesis, Ryerson University, Toronto, ON, Canada.

[5] Abdullah, S., and Tiong, E. C., 2008, "Prediction of Palm Oil Properties Using Artificial Neural Network," International Journal of Computer Science and Network Security, **8**(8), pp. 101–107.
[6] Anderson, D., and McNeill, G., 1992, *Artificial Neural Network Technology*, Kaman Sciences, New York.
[7] Gouda, M. M., Danaher, S., and Underwood, C. P., 2002, "Application of an Artificial Neural Network for Modelling the Thermal Dynamics of a Building's Space and Its Heating System," Math. Comput. Model. Dyn. Syst., **8**(3), pp. 333–344.
[8] Ravindranath, G., Prabhukumar, G., and Devaru, B., 2007, "Application of an Artificial Neural Network in Gas-Solid (Air-Solid) Fluidized Bed: Heat Transfer Predictions," ASME International Mechanical Engineering Congress and Exposition, 8, pp. 789–798.
[9] Aydinalp, M., Ugursal, V. I., and Fung, A. S., 2003, "Modelling of Residential Energy Consumption at the National Level," Int. J. Energy Res., **27**, pp. 441–453.
[10] Kalogirou, S. A., 2001, "Artificial Neural Networks in Renewable Energy Systems Applications: A Review," Renewable Sustainable Energy Rev., **5**, pp. 373–401.
[11] Sari Alsmadi, M. K., Bin Omar, K., and Azman Noah, S., 2009, "Back Propagation Algorithm: The Best Algorithm Among the Multi-Layer Perceptron Algorithm," International Journal of Computer Science and Network Security, **9**(4), pp. 378–484.
[12] Gogan, S., 2008, "Fuzzy Set Classified Neural Network for Short-Term Load Forecasting," MS thesis, Thapar University, Patiala, India.
[13] Yang, K. T., 2008, "Artificial Neural Networks (ANNs): A New Paradigm for Thermal Science and Engineering," ASME J. Heat Transfer, **130**, pp. 093001.
[14] Alyuda Research, Inc., 2003, Alyuda User Manual Version 2.1.
[15] Naylor, D., 2003, "Recent Developments in the Measurement of Convective Heat Transfer Rates by Laser Interferometry," Int. J. Heat Fluid Flow, **24**, pp. 345–355.
[16] Aydinalp, M., 2002, "A New Approach for Modeling of Residential Energy Consumption," Ph.D. thesis, Dalhousi University, Halifax, Nova Scotia, Canada.
[17] Neocleous, C., and Schizas, C., 2002, "Artificial Neural Network Learning: A Comparative," LNAI, **2308**, pp. 300–313.
[18] Rumelhart, D., Hinton, G., and Williams, R., 1986, "Parallel Distributed Processing Explorations in the Microstructure of Cognition," *Learning Internal Representations by Error Propagation*, Vol. 1, MIT Press, Cambridge, MA, Chap. 8.

Analytical Solution Under Two-Flux Approximation to Radiative Heat Transfer in Absorbing Emitting and Anisotropically Scattering Medium

Xin-Lin Xia[1]
e-mail: xiaxl@hit.edu.cn

Dong-Hui Li
School of Energy Science and Engineering,
Harbin Institute of Technology,
Harbin 150001, People's Republic of China

Feng-Xian Sun
School of Power and Energy Engineering,
Harbin Engineering University,
Harbin 150001, People's Republic of China

Radiative transfer in absorbing, emitting, and highly anisotropically scattering media is widely encountered in high temperature applications such as pulverized coal firing furnaces and high temperature thermal protection materials. Efficient and effective solution methods for the transfer process are very crucial, especially in thermal radiation related reverse problems and optimization designs. In this study, the analytical solution for radiative heat transfer in an absorbing, emitting, and anisotropically scattering slab between two parallel gray walls are derived under the two-flux approximation. Explicit expression for the radiative heat flux in a slab is obtained under two-flux approximation. The reliability and adaptability of an analytical solution is examined in case studies by comparing with the Monte Carlo results. Comparative studies indicate that the analytical solution can be used in radiative transfer calculation in an absorbing emitting and anisotropically scattering slab. It is much more applicable in a forward and isotropic scattering slab than in an absorbing one, especially in a forward scattering slab. Because of simplicity and high computing efficiency with the analytical solution, it may be useful in reverse radiative transfer problems, in optimization design, and in developing some numerical schemes on radiative heat transfer. [DOI: 10.1115/1.4002326]

Keywords: anisotropically scattering, radiative heat transfer, analytical solution, two-flux approximation

1 Introduction

Radiative heat transfer plays an important role in many engineering applications such as atmosphere remote sensing, aeronautics and space technologies, biological and medical technologies, power engineering, etc. In order to predict the radiative transfer in these engineering applications, many numerical methods have been developed such as the discrete ordinate method (DOM), the finite volume method (FVM) and the Monte Carlo method (MCM). However, because of many advantages including convenience, effectiveness and high computing efficiency with an analytical solution, it still remains attractive to many researchers and may find its potential usage in reverse analysis and optimization design of radiative heat transfer problems or in developing new numerical schemes.

Despite of the complexity and difficulty in radiative transfer problems, many analytical solutions were based on some simplifications. Schuster [1] and Schwarzschild [2] developed an analytical solution for radiative transfer in the atmosphere, which is considered as an absorbing, emitting, and nonscattering medium. Spitzer and Bosch [3] derived an analytical solution for the radiative transfer in an absorbing, nonemitting, and isotropic scattering medium. Ludwig et al. [4] combined MCM with an analytical solution and developed a standard infrared radiation model (SIRRM) for an emitting and isotropically scattering medium, which was widely used for calculating the infrared radiation heat transfer in flames and rocket plumes in the 1980s and 1990s [5,6]. Tian and Dougherty [7] derived an analytical expression for the radiation intensity and radiative heat flux by using a superposition method for a one-dimensional absorbing, emitting, and isotropically scattering medium subjected to collocated irradiance. Andre and Degiovanni [8] analytically studied the one-dimensional transient coupled conduction and radiation transfer in an absorbing, emitting, and isotropically scattering layer by using a Laplace transformation method under the assumption of two-flux approximation. Murthy and Fedorov [9] derived an analytical expression for radiative heat flux by applying the two-flux approximation to an optically thin electrolyte in a SOFC, where absorption, emission, and isotropically scattering is considered. Dombrovsky et al. [10] suggested a modified two-flux approximation and derived an analytical solution for calculating the hemispherical transmittance and reflectance of an absorbing, nonemitting, and isotropically scattering medium. Lapaeva and Rogatkin [11] proposed a general improvement on the two-flux model for a scattering and absorbing medium to derive an analytical solution for one-dimensional light propagation. Musella and Tschudi [12,13] analyzed the transient energy transport in an absorbing, emitting, and isotropically scattering medium subjected to laser heating under the two-flux approximation. It can be inferred from the above studies that either isotropically scattering or nonscattering problems were considered. Radiative transfer in absorbing, emitting, and anisotropically scattering media is widely encountered in high temperature applications such as pulverized coal firing furnaces and high tempera-

[1]Corresponding author.

Contributed by the Heat Transfer Division of ASME for publication in the JOURNAL OF HEAT TRANSFER. Manuscript received December 22, 2009; final manuscript received July 24, 2010; published online September 21, 2010. Assoc. Editor: Walter W. Yuen.

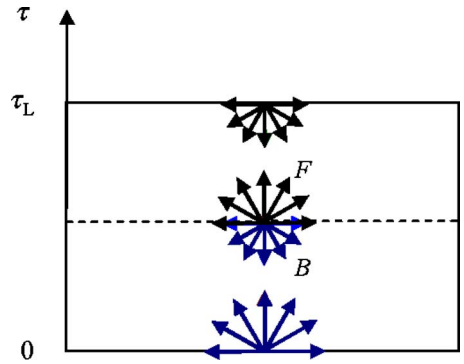

Fig. 1 Schematic diagram of radiative heat transfer in a slab

ture thermal protection materials. Unfortunately, very few solutions on the transfer process in an anisotropically scattering medium can be found except the work by Wang et al. [14], where two new defined parameters describing the anisotropically scattering were introduced instead of using the scattering phase function. In this paper, a fresh method combing a solution matrix and ordinary differential equations theory was attempted to derive an analytical solution for the radiative heat transfer in an absorbing, emitting, and anisotropically scattering slab under the two-flux approximation. Explicit expression for radiative heat flux in the medium was obtained. Case studies were conducted to test the adaptability of the analytical solution in radiative transfer computation by comparing with MCM results.

2 Analytical Solution to the Two-Flux Equations

In this section, the radiative transfer equation in an absorbing emitting and anisotropically scattering slab is solved under the two-flux approximation. Under this approximation, the radiative transfer equation can be transformed into the two-flux equations. For simplicity, detailed deduction to the two-flux equations is omitted in this paper. The two-flux equations in a slab shown in Fig. 1 can be written as [15]

$$\frac{1}{2}\frac{dF}{d\tau} = -(1-\omega f)F + \omega b B + (1-\omega)I_b \tag{1a}$$

$$\frac{1}{2}\frac{dB}{d\tau} = -\omega b F + (1-\omega f)B - (1-\omega)I_b \tag{1b}$$

where F and B are the forward and the backward radiation intensity, respectively, under the two-flux approximation, $\tau = k_e x$ is the optical coordinate, k_e is the extinction coefficient, x is the space coordinate, I_b is the blackbody emission intensity, ω is the scattering albedo, f is the forward scattering fraction, and b the backward scattering fraction. f, b are defined as [16]

$$f = \frac{1}{2}\int_0^{\pi/2} P(\Theta)\sin\Theta d\Theta \tag{2a}$$

$$b = \frac{1}{2}\int_{\pi/2}^{\pi} P(\Theta)\sin\Theta d\Theta \tag{2b}$$

where $P(\Theta)$ is the scattering phase function of the slab and Θ is the scattering angle between the incidence direction and the scattering direction. We suppose that the phase function is invariant with the incidence direction, which is valid because particles in a medium are usually oriented randomly.

The incident radiation and the radiative heat flux under the two-flux approximation are

$$G = 2\pi(F+B) \tag{3a}$$

$$q_r = \pi(F-B) \tag{3b}$$

Consequently, the two-flux equations in Eq. (1) can be transformed into

$$\frac{dq_r}{d\tau} = -(1-\omega)G + 4\pi(1-\omega)I_b \tag{4a}$$

$$\frac{dG}{d\tau} = -4(1-\omega+2\omega b)q_r \tag{4b}$$

Let

$$\Psi_r = \frac{q_r}{n^2\sigma T_r^4}, \quad g = \frac{G}{4n^2\sigma T_r^4}, \quad \theta = \frac{T}{T_r} \tag{5}$$

where T_r is reference temperature and n is the refractive index of the slab. With the above definitions, the two-flux equations in Eq. (4) can be nondimensionalized as

$$\frac{d\Psi_r}{d\tau} = -4(1-\omega)g + 4(1-\omega)\theta^4 \tag{6a}$$

$$\frac{dg}{d\tau} = -(1-\omega+2\omega b)\Psi_r \tag{6b}$$

Equation (6) can be expressed in the following matrix form:

$$\frac{d\mathbf{y}}{d\tau} = \mathbf{A}\mathbf{y} + \mathbf{Q} \tag{7a}$$

with

$$\mathbf{y} = \begin{bmatrix} \Psi_r \\ g \end{bmatrix}, \quad \mathbf{A} = \begin{bmatrix} 0 & -4(1-\omega) \\ -(1-\omega+2\omega b) & 0 \end{bmatrix}, \quad \mathbf{Q} = \begin{bmatrix} 4(1-\omega)\theta^4 \\ 0 \end{bmatrix} \tag{7b}$$

Generally, it is very difficult to solve the equations in Eq. (7) analytically. But if the parameters of ω, f, and b are constants, the system described by Eq. (7) is linear and first-ordered, which can be solved analytically. Based on the theories in ordinary differential equations, the general solution for this system can be expressed as

$$\mathbf{y} = \mathbf{\Phi}(\tau)\mathbf{c} + \mathbf{\Phi}(\tau)\int \mathbf{\Phi}^{-1}(\tau)\mathbf{Q}(\tau)d\tau \tag{8a}$$

where $\mathbf{c} = \begin{pmatrix} c_1 \\ c_2 \end{pmatrix}$ and c_1 and c_2 are two constants depending on boundary conditions, $\mathbf{\Phi}(\tau)$ is called the solution matrix and is described as

$$\mathbf{\Phi}(\tau) = r_1(\tau)\mathbf{P}_0 + r_2(\tau)\mathbf{P}_1 \tag{8b}$$

with

$$\mathbf{P}_0 = \mathbf{E}, \quad \mathbf{P}_1 = \mathbf{A} - \lambda_1\mathbf{E}, \quad \mathbf{E} = \begin{bmatrix} 1 & 0 \\ 0 & 1 \end{bmatrix} \tag{8c}$$

where λ_1 and λ_2 are the eigenvalues of matrix $\mathbf{A}$. The functions $r_1(\tau)$ and $r_2(\tau)$ are solutions of the following two ordinary differential equations, respectively.

$$\frac{dr_1(\tau)}{d\tau} = \lambda_1 r_1(\tau), \quad r_1(0) = 1 \tag{8d}$$

$$\frac{dr_2(\tau)}{d\tau} = r_1(\tau) + \lambda_2 r_2(\tau), \quad r_2(0) = 0 \tag{8e}$$

By solving the eigenfunction of matrix $\mathbf{A}$, the eigenvalues can be derived as

$$\lambda_{1,2} = \pm 2\sqrt{(1-\omega)(1-\omega f+\omega b)} \tag{9}$$

Let

$$\rho = 2\sqrt{(1-\omega)(1-\omega f+\omega b)} \tag{10}$$

then it can be obtained that

$$r_1(\tau) = e^{\rho\tau}, \quad r_2(\tau) = \frac{1}{\rho}sh(\rho\tau), \quad \lambda_1 = \rho, \quad \lambda_2 = -\rho \tag{11}$$

By inserting expression (11) into expression (8) and after some manipulations, the solution matrix can be derived as

$$\mathbf{\Phi}(\tau) = \begin{bmatrix} ch(\rho\tau) & -\dfrac{4(1-\omega)}{\rho}sh(\rho\tau) \\ -\dfrac{\rho}{4(1-\omega)}sh(\rho\tau) & ch(\rho\tau) \end{bmatrix} \tag{12}$$

According to the Cramer's law, the reversion of the solution matrix can be obtained as

$$\mathbf{\Phi}^{-1}(\tau) = \frac{\mathbf{\Phi}^*(\tau)}{|\mathbf{\Phi}(\tau)|} \tag{13}$$

where $|\mathbf{\Phi}(\tau)|$ and $\mathbf{\Phi}^*(\tau)$ are the determinant and the accompanying matrix of $\mathbf{\Phi}(\tau)$. After some manipulations, Eq. (13) can be transformed into

$$\mathbf{\Phi}^{-1}(\tau) = \begin{bmatrix} ch(\rho\tau) & \dfrac{4(1-\omega)}{\rho}sh(\rho\tau) \\ \dfrac{\rho}{4(1-\omega)}sh(\rho\tau) & ch(\rho\tau) \end{bmatrix} \tag{14}$$

By inserting expressions (12) and (14) into expression (8*a*), a general solution to the two-flux equations can be derived. The final results can be expressed as

$$\mathbf{y} = \begin{bmatrix} ch(\rho\tau) & -\dfrac{4(1-\omega)}{\rho}sh(\rho\tau) \\ -\dfrac{\rho}{4(1-\omega)}sh(\rho\tau) & ch(\rho\tau) \end{bmatrix} \times \begin{bmatrix} c_1 + 4(1-\omega)\displaystyle\int_{\tau_0}^{\tau} ch(\rho\tau_\xi)\theta^4(\tau_\xi)d\tau_\xi \\ c_2 + \rho\displaystyle\int_{\tau_0}^{\tau} sh(\rho\tau_\xi)\theta^4(\tau_\xi)d\tau_\xi \end{bmatrix} \tag{15}$$

where τ_ξ is an optical coordinate corresponding to a position with a space coordinate of ξ. The nondimensional radiative heat flux and incidence radiation are

$$\Psi_r = c_1 ch(\rho\tau) - \frac{4(1-\omega)}{\rho}sh(\rho\tau)c_2 + 4(1-\omega)\int_{\tau_0}^{\tau} ch[\rho(\tau-\tau_\xi)]\theta^4(\tau_\xi)d\tau_\xi \tag{16}$$

$$g = -\frac{\rho}{4(1-\omega)}sh(\rho\tau)c_1 + ch(\rho\tau)c_2 - \rho\int_{\tau_0}^{\tau} sh[\rho(\tau-\tau_\xi)]\theta^4(\tau_\xi)d\tau_\xi \tag{17}$$

By inserting the expressions in Eqs. (16) and (17) into Eq. (6), it can be found that the analytical solution satisfies the two-flux equations.

c_1 and c_2 are two constants, which depend on boundary conditions. In this paper, τ_0 is set to be zero. For the opaque, diffuse and gray walls, the boundary conditions can be expressed as

$$\Psi_r = \frac{2\varepsilon_w}{2-\varepsilon_w}(\theta_w^4 - g) \tag{18}$$

By inserting the expressions of Eqs. (16) and (17) into Eq. (18), it can be derived that c_1 and c_2 satisfy the following relation on the lower boundary:

$$A_1c_1 + B_1c_2 = C_1 \tag{19}$$

where

$$A_1 = ch\left(\frac{1}{2}\rho\tau_L\right) + K(\varepsilon_{w1})sh\left(\frac{1}{2}\rho\tau_L\right) \tag{20}$$

$$B_1 = \frac{4(1-\omega)}{\rho}\left[sh\left(\frac{1}{2}\rho\tau_L\right) + K(\varepsilon_{w1})ch\left(\frac{1}{2}\rho\tau_L\right)\right] \tag{21}$$

$$C_1 = \frac{2\varepsilon_{w1}}{2-\varepsilon_{w1}}\theta_1^4 + 4(1-\omega)\int_0^{1/2\tau_L}\left\{ch\left[\rho\left(\frac{1}{2}\tau_L - \xi\right)\right] + K(\varepsilon_{w1})sh\left[\rho\left(\frac{1}{2}\tau_L - \xi\right)\right]\right\}\theta^4(-\xi)d\xi \tag{22}$$

and

$$K(\varepsilon) = \frac{2\varepsilon}{2-\varepsilon}\frac{\rho}{4(1-\omega)} \tag{23}$$

Similarly, another relation between c_1 and c_2 can be obtained on the upper boundary, which is

$$A_2c_1 + B_2c_2 = C_2 \tag{24}$$

where

$$A_2 = -\left[ch\left(\frac{1}{2}\rho\tau_L\right) + K(\varepsilon_{w2})sh\left(\frac{1}{2}\rho\tau_L\right)\right] \tag{25}$$

$$B_2 = \frac{4(1-\omega)}{\rho}\left[sh\left(\frac{1}{2}\rho\tau_L\right) + K(\varepsilon_{w2})ch\left(\frac{1}{2}\rho\tau_L\right)\right] \tag{26}$$

$$C_2 = \frac{2\varepsilon}{2-\varepsilon}\theta_2^4 + 4(1-\omega)\int_0^{1/2\tau_L}\left\{ch\left[\rho\left(\frac{1}{2}\tau_L - \xi\right)\right] + K(\varepsilon_{w2})sh\left[\rho\left(\frac{1}{2}\tau_L - \xi\right)\right]\right\}\theta^4(\xi)d\xi \tag{27}$$

From the equations of Eqs. (19) and (24), it can be derived that

$$c_1 = \frac{B_2C_1 - B_1C_2}{B_2A_1 - B_1A_2} \tag{28}$$

$$c_2 = \frac{A_2C_1 - A_1C_2}{A_2B_1 - A_1B_2} \tag{29}$$

3 Application Analysis

In this section, the analytical solution is tested in some cases by comparing with MCM results, which are usually considered as benchmark solutions. Considering the fact that the divergence of radiative heat flux is a very important physical parameter directly used in coupled heat transfer and the wall heat flux is the other parameter with great significance, each of the two parameters is compared between the analytical and the MCM results.

Consider the radiative heat transfer in a gray slab between two opaque, diffuse, and gray boundaries. The wall emittance of both boundaries is set to be 0.8. The wall temperature at $\tau=0$ is $T_{w1}=1000$ K and the wall temperature at $\tau=\tau_L$ is $T_{w2}=500$ K. The temperature at the two boundaries is continuous and the temperature in the slab is assumed to be linearly distributed as follows:

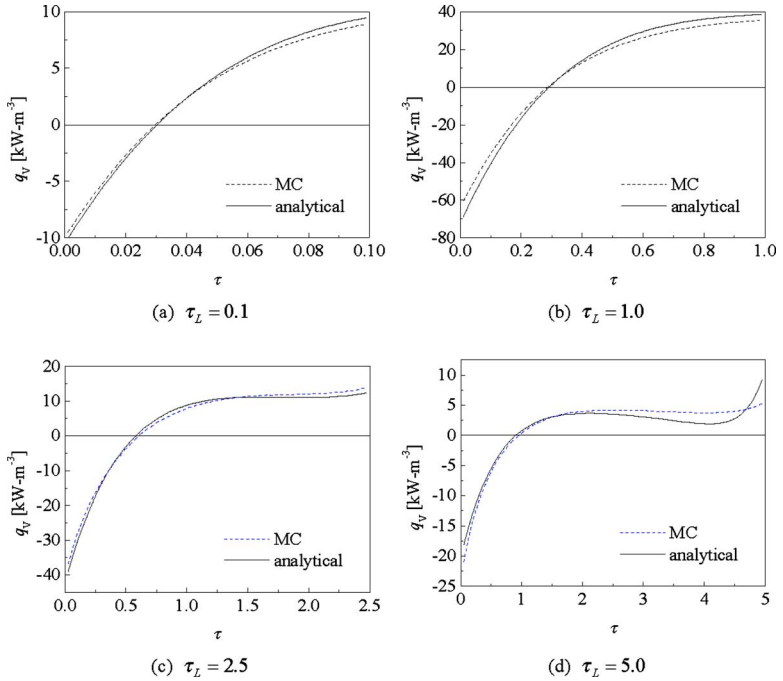

Fig. 2 Profile of radiative heat flux divergence in a nonscattering slab ($\varepsilon = 0.8$)

$$T = \left(T_{\mathrm{m}} + \frac{\Delta T}{2}\right)\frac{\tau_{\mathrm{L}} - \tau}{\tau_{\mathrm{L}}} + \left(T_{\mathrm{m}} - \frac{\Delta T}{2}\right)\frac{\tau}{\tau_{\mathrm{L}}} \tag{30}$$

with an algebraic mean temperature of $T_{\mathrm{m}}=750$ K and a maximum temperature difference of $\Delta T=500$ K. A typical, linearly scattering phase function is selected as an example in this paper.

$$P(\Theta) = 1 + A\cos\Theta \tag{31}$$

where $A=1$ denotes the forward scattering, $A=-1$ denotes the backward scattering, and $A=0$ denotes the isotropic scattering. In order to show the flexibility of the analytical solution in scattering cases, the scattering albedo is selected to be 0.9, which indicates the slab is highly scattering. The refractive index is selected as 1.0.

Figure 2 shows the distribution of radiative heat flux divergence in an absorbing emitting and nonscattering slab. It can be observed that the analytical results agree with MCM results when the slab optical thickness is not larger than 2.5. But when the slab optical thickness is larger than or equal to 5.0, the analytical results have large deviation to MCM results.

Figure 3 gives the profile of radiative heat flux divergence in a

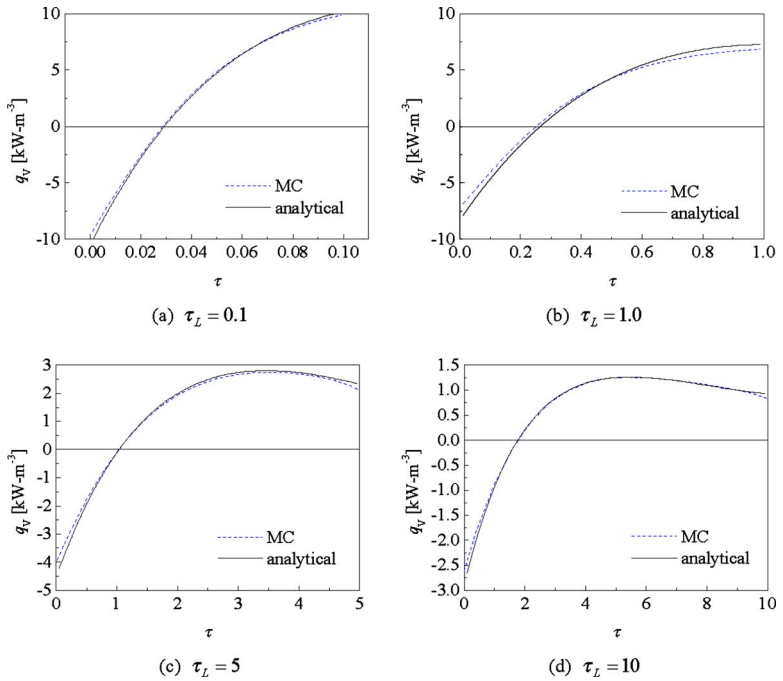

Fig. 3 Profile of radiative heat flux divergence in a forward scattering slab ($\varepsilon = 0.8$)

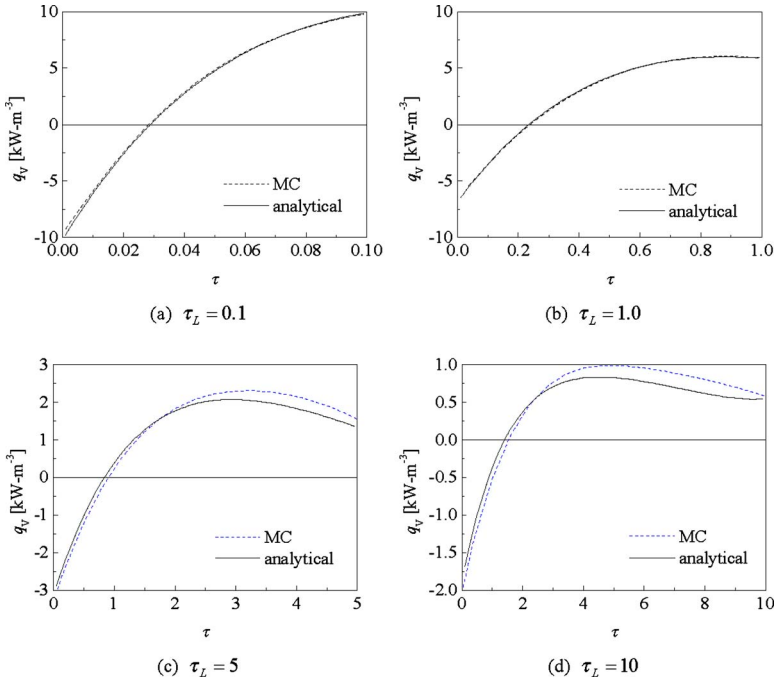

Fig. 4 Profile of radiative heat flux divergence in an isotropic scattering slab ($\varepsilon = 0.8$)

forward scattering slab and the corresponding results from MCM. It can be seen that the analytical results agree well with MCM results when the slab optical thickness is not larger than 10.

Figures 4 and 5 give the profile of radiative heat flux divergence in an isotropic scattering slab and a backward scattering slab, respectively. It can be seen that the analytical results agree well with MCM results when the slab optical thickness is not larger than 1.0. But when the slab optical thickness is equal to 5, the analytical solution has a relatively large deviation to MCM results.

By comparing the results of radiative heat flux divergence in the nonscattering slab, the forward scattering slab, and the isotropic and the backward scattering slab, it can be concluded that the analytical solution has a relatively larger deviation for a nonscattering slab than for a scattering one. The analytical solution is more appropriate for a forward scattering slab than for an isotropic or backward scattering slab. The analytical solution seems to have the least adaptability in a backward scattering slab. The upper threshold in the slab optical thickness under which the solution can be use is the lowest for a backward scattering slab among

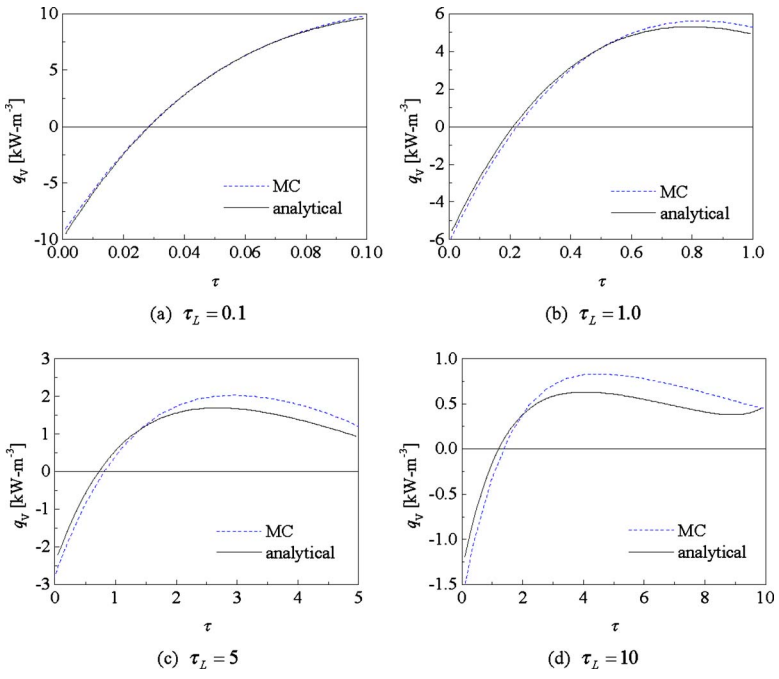

Fig. 5 Profile of radiative heat flux divergence in a backward scattering slab ($\varepsilon = 0.8$)

Table 1 Deviation of radiative heat flux divergence near boundaries in a forward scattering slab

	q_v ($W\,m^{-3}$)							
	$\tau_L=0.1$		$\tau_L=1.0$		$\tau_L=5.0$		$\tau_L=10$	
	$\tau=0$	$\tau=\tau_L$	$\tau=0$	$\tau=\tau_L$	$\tau=0$	$\tau=\tau_L$	$\tau=0$	$\tau=\tau_L$
Analytical	−10,068	10,132	−7904	7274	−4380	2344	−2653	854
MCM	−9284	9867	−6878	6851	−3910	2142	−2484	840
%	8.4	2.7	14.8	6.1	12	9.4	6.8	1.7

scattering cases and the forward scattering slab has the highest threshold in optical thickness. Table 1 gives the relative deviation in radiative heat flux divergence near boundaries in a forward scattering slab. It can be seen that the deviation is almost less than 10%.

Wall radiative heat flux from the analytical solution is compared with MCM results. The wall temperature of both boundaries is set to be 500 K and the temperature in the slab is assumed to be linearly distributed with an algebraic mean temperature of 1000 K and a maximum temperature difference of ΔT in the slab. The temperature at boundaries is not continuous. The slab optical thickness is unity and the refractive index is 1.3.

Table 2 shows the radiative heat flux on boundary walls under different temperature difference of ΔT. It can be observed that the radiative heat flux obtained by the analytical solution is higher than the MCM results. The maximum relative deviation is less than 10% when the temperature difference in the slab is not larger than 200 K. In addition, the analytical solution gives results with less deviation in a scattering slab than in a purely absorbing and emitting slab. The maximum deviation is less than 4% for scattering cases and 10% for nonscattering cases.

High temperature multilayer thermal insulations, which are composed of semitransparent insulation materials and reflecting screens are becoming more and more attractive in thermal protection technologies. In these materials the temperature drop in each insulation layer, generally, does not exceed 100 K and the emittance of reflecting screens is usually low. Study on the adaptability of the analytical solution in radiative transfer calculation for multilayer thermal insulations is conducted. The temperature in the insulation layer is assumed to be linearly distributed with the averaged temperature of 1250 K and the temperature difference ΔT of 100 K. The forward scattering with scattering albedo of 0.9 is considered and the slab optical thickness is assumed to be 5. Figure 6 shows the profile of radiative heat flux divergence in the layer. It can be seen that in the considered situation, the analytical results agree well with MCM results for the wall emittance of both 0.2 and 0.8. It is reasonably inferred that the analytical solution maybe used in the radiative transfer in multilayer thermal insulations.

4 Conditions Where the Analytical Solution is Used

It is obvious that the functions of $sh(\rho\tau)$ and $ch(\rho\tau)$ have no upper bounds and tend to be infinite when the optical coordinate τ

Table 2 Radiative heat flux on boundary walls ($\tau_L=1$)

	q_w (W/m^2)							
	Nonscattering							
ΔT(K)	0		40		80		200	
Wall	$\tau=0$	$\tau=\tau_L$	$\tau=0$	$\tau=\tau_L$	$\tau=0$	$\tau=\tau_L$	$\tau=0$	$\tau=\tau_L$
Analytical	63,869	63,869	62,314	65,549	60,878	67,352	57,268	73,538
MCM	58,647	58,637	57,322	60,163	56,264	61,717	53,295	67,009
%	8.9	8.9	8.7	9.0	8.2	9.1	7.5	9.7
	Forward scattering							
ΔT(K)	0		40		80		200	
Wall	$\tau=0$	$\tau=\tau_L$	$\tau=0$	$\tau=\tau_L$	$\tau=0$	$\tau=\tau_L$	$\tau=0$	$\tau=\tau_L$
Analytical	15,380	15,380	15,258	15,529	15,162	15,705	15,033	16,389
MCM	14,950	14,948	14,803	15,103	14,690	15,292	14,496	16,023
%	2.9	2.9	3.1	2.8	3.2	2.7	3.7	2.3
	Isotropic scattering							
ΔT(K)	0		40		80		200	
Wall	Left	Right	Left	Right	Left	Right	Left	Right
Analytical	15,187	15,187	15,000	15,401	14,842	15,639	14,512	16,519
MCM	14,845	14,859	14,681	15,062	14,535	15,288	14,248	16,114
%	2.3	2.2	2.2	2.3	2.1	2.3	1.9	2.5
	Backward scattering							
ΔT(K)	0		40		80		200	
Wall	$\tau=0$	$\tau=\tau_L$	$\tau=0$	$\tau=\tau_L$	$\tau=0$	$\tau=\tau_L$	$\tau=0$	$\tau=\tau_L$
Analytical	15,000	15,000	14,770	15,256	14,566	15,539	14,101	16,551
MCM	14,763	14,767	14,564	14,989	14,385	15,243	14,015	16,145
%	1.6	1.6	1.4	1.8	1.6	1.9	0.6	2.5

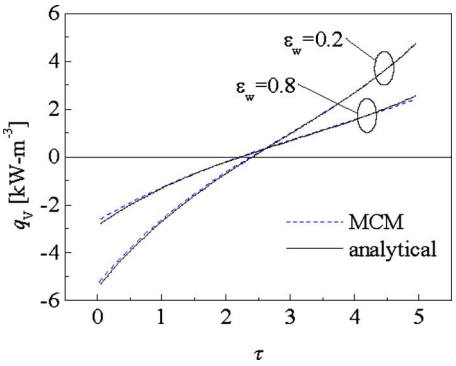

Fig. 6 Profile of radiative heat flux divergence in a forward scattering layer (ε=0.2)

increases to infinity. Consequently, it can be expected that the analytical solution may not be accepted when the optical thickness of the slab is large enough.

Table 3 gives the radiative heat flux divergence varying with optical coordinate in an isothermal and isotropic scattering slab with the optical thickness of 40, the medium temperature of 1000 K, and both wall temperatures of 500 K. It can be observed that the profile of the radiative heat flux divergence almost exhibits symmetry under the prescribed conditions. But asymmetry phenomenon appeared even though it is not obvious.

Table 4 shows that the wall heat fluxes are nearly identical but not the same. In addition, the wall heat flux from the analytical solution is approximately 7% less than the MCM result.

But it has been noticed that either scattering or nonuniform temperature distribution or mean temperature in the slab can lead to the variation in the upper threshold in the slab optical thickness under which the analytical solution can be used.

Comparatively, the functions of $sh(\rho\tau)$ and $ch(\rho\tau)$ have lower bounds, so the analytical solution can be used for any small optical thickness. Tables 5 and 6 give the analytical result and its comparison to MCM result for an isothermal and isotropic scattering slab with an optical thickness of 0.2. It can be observed from Table 5 that the analytical result is approximately 1.7% higher for the radiative heat flux divergence than MCM result. From Table 6, it can be seen that the analytical result for the wall heat flux is approximately 1.3% higher than MCM result.

5 Conclusions

By introducing a solution matrix and applying theories in ordinary differential equations, the radiative transfer equation under the two-flux approximation is solved analytically for a one-dimensional absorbing, emitting, and anisotropically scattering slab with gray and diffuse boundaries. Explicit expression for the radiative heat flux in the slab is obtained. By comparing analytical results with those from MCM in case studies, some useful conclusions can be drawn as follows.

i. The analytical solution derived from the two-flux equations can be used to calculate the radiative heat transfer in an absorbing emitting and anisotropically scattering gray medium. The applicability of the analytical solution, which, generally, can be used for a slab, with a not very large optical thickness, is confined not only by the slab optical thickness but also by some other factors including the mean temperature, the temperature difference in the slab, and the scattering type.
ii. The precision of the analytical solution is influenced by many factors including the medium optical thickness, the medium scattering type (nonscattering, forward scattering, backward scattering, and isotropic scattering), etc.
iii. Although preliminary case studies conducted in this research confirmed the applicability and reliability of the analytical solution on some occasions, much more comprehensive studies need to be conducted further, which include the research on the applicability of the analytical solution in a wide range of optical thickness and mean temperature, the research on the influence of temperature profile in the medium, the research on the modification on the analytical solution to improve its precision, the research on the applicability of the analytical solution in the combined heat transfer, etc.

Table 3 Radiative heat flux divergence in an isothermal and isotropic scattering slab (τ_L=40)

	$\nabla\cdot\mathbf{q}_r$ (W/m^3)						
τ/τ_L	0.06	0.17	0.28	0.5	0.72	0.83	0.94
Analytical	239,609.4	14,492.2	876.5	6.4	876.5	14,492.3	239,610.8

Table 4 Wall heat flux in an isothermal and isotropic scattering slab (τ_L=40)

	q_w (W/m^2)	
Wall	τ=0	$\tau=\tau_L$
Analytic	38,587.9	38,586.2
MCM	41,415.6	41,517.1
%	−6.8	−7.1

Table 5 Radiative heat flux divergence in an isothermal and isotropic scattering slab (τ_L=0.2)

	$\nabla\cdot\mathbf{q}_r$ (W/m^3)						
τ/τ_L	0.06	0.17	0.28	0.5	0.72	0.83	0.94
Analytical	6974	6969	6966	6963	6966	6969	6974
MCM	6906	6881	6865	6850	6870	6873	6902
%	1.0	1.3	1.5	1.7	1.4	1.4	1.1

Acknowledgment

The support on this work from the National Natural Science Foundation of China (Grant Nos. 50776026 and 90816022) is gratefully acknowledged.

Nomenclature

F, B = forward and backward radiation intensity under two-flux approximation, W m^{-2} sr^{-1}
k_e, k_a = extinction coefficient and absorption coefficient, m^{-1}
ω = scattering albedo
f, b = forward and backward scattering fraction
I_b = blackbody emission intensity, W m^{-2} sr^{-1}

Table 6 Wall heat flux in an isothermal and isotropic scattering slab (τ_L=0.2)

	q_w (W/m^2)	
Wall	τ=0	$\tau=\tau_L$
Analytic	3484.2	3484.2
MCM	3438.8	3438.0
%	1.3	1.3

x = space coordinate, m
τ = optical coordinate, $\tau = k_e x$
τ_L = optical thickness of a slab
Θ = scattering angle
$P(\Theta)$ = scattering phase function
G = incident radiation
q_r = radiative heat flux, W m^{-2}
g = dimensionless incident radiation
Ψ_r = dimensionless radiative heat flux
θ = dimensionless temperature
$\mathbf{y}, \mathbf{A}, \mathbf{Q}$ = matrix defined in Eq. (7*a*)
c_1, c_2 = constants depending on boundary conditions
$\mathbf{P}_0, \mathbf{P}_1, \mathbf{E}$ = matrix defined in Eq. (8*c*)
$r_1(\tau), r_2(\tau)$ = variables defined in Eqs. (8*d*) and (8*e*)
λ_1, λ_2 = eigenvalues of matrix **A** in Eq. (9)
ρ = parameter defined in Eq. (10)
$\mathbf{\Phi}(\tau), \mathbf{\Phi}^{-1}(\tau)$ = the solution matrix and its reversion
$|\mathbf{\Phi}(\tau)|$ = determinant of the solution matrix
$\mathbf{\Phi}^*(\tau)$ = accompanying matrix of the solution matrix
$\mathbf{q}_r$ = vector of radiative heat flux, W m^{-2}
ε_w = wall emittance
q_w = radiative heat flux on boundaries, W m^{-2}
n = refractive index
T_w = boundary temperature, K
T = temperature in a slab, K
T_m = mean temperature in a slab, K
ΔT = maximum temperature difference in a slab, K
q_v = minus of radiative heat flux divergence, $q_v = -\nabla \cdot \mathbf{q}_r(\tau)$, W m^{-3}

Subscripts

e = extinction
a = absorbing
b = blackbody
r = radiative, reference
w = boundary walls
0 = position at $\tau = 0$
L = position at $\tau = \tau_L$

References

[1] Schuster, A., 1905, "Radiation Through a Foggy Atmosphere," Astrophys. J., **21**, pp. 1–22.
[2] Schwarzschild, K., 1906, "Equilibrium of the Sun's Atmosphere," Abh. Akad. Wiss. Gottingen, Math.-Phys. Kl, **195**, pp. 41–53.
[3] Spitzer, D., and Bosch, J. T., 1975, "The Absorption and Scattering of Light in Bovine and Human Dental Enamel," Calcif. Tissue Res., **17**, pp. 129–137.
[4] Ludwig, C. B., Malkmus, W., Walker, J., Slack, M., and Reed, R., "The Standard Infrared Radiation Model," AIAA 16th Thermophysics Conference, Palo Alto, CA, Jun. 23–25, Paper No. AIAA-81-1051.
[5] Nelson, H. F., 1984, "Influence of Scattering on Infrared Signatures of Rocket Plumes," J. Spacecr. Rockets, **21**(5), pp. 508–510.
[6] Edwards, Y. S., and Babikian, D. S. A., 1987, "Two-Particle Model for Rocket Plume Radiation," J. Thermophys. Heat Transfer, **1**(1), pp. 13–20.
[7] Tian, Y., and Dougherty, R. L., 1995, "Exact Solution of One-Dimensional Radiative Transfer in an Absorbing Emitting and Isotropically Scattering Medium With Arbitrary Emitting Source," 30th AIAA Thermophysics Conference, San Diego, CA, Jun. 19–22, Paper No. AIAA 95-2024.
[8] Andre, S., and Degiovanni, A., 1998, "A New Way of Solving Transient Radiative-Conductive Heat Transfer Problems," ASME J. Heat Transfer, **120**, pp. 943–955.
[9] Murthy, S., and Fedorov, A. G., 2003, "Radiation Heat Transfer Analysis of the Monolith Type Solid Oxide Fuel Cell," J. Power Sources, **124**, pp. 453–458.
[10] Dombrovsky, L., Randrianalisoa, J., and Baillis, D., 2006, "Modified Two-Flux Approximation for Identification of Radiative Properties of Absorbing and Scattering Media From Directional-Hemispherical Measurements," J. Opt. Soc. Am. A, **23**(1), pp. 91–98.
[11] Lapaeva, L. G., and Rogatkin, D. A., 2006, "Improved Kubelka–Munk Approach for Determination of Tissues Optical Properties in Biomedical Noninvasive Reflectance Spectroscopy," Proc. SPIE, **6536**, pp. 65360Z.
[12] Musella, M., and Tschudi, H. R., 2005, "Transient Radiative and Conductive Heat Transfer in Ceramic Materials Subjected to Laser Heating," Int. J. Thermophys., **26**(4), pp. 981–999.
[13] Musella, M., and Tschudi, H. R., 2008, "Modeling Transient Heat Conduction and Radiative Transport in Semitransparent Media: A Tool for the Interpretation of Reflectivity Data," Int. J. Thermophys., **29**, pp. 706–734.
[14] Wang, F., Cen, K. F., and Girasole, T., 2004, "Two-Flux Method for Radiation Heat Transfer in Anisotropic Gas-Particles Media," Sci. China Ser. E: Technol. Sci., **47**(6), pp. 625–640.
[15] Mital, R., Gore, J. P., and Viskanta, R., 1995, "Measurements of Extinction Coefficient and Single Scattering Albedo of Reticulated Porous Ceramic at High Temperatures," 30th AIAA Thermophysics Conference, San Diego, CA, Jun. 19–22, Paper No. AIAA 95-2036.
[16] Modest, M. F., 1993, *Radiative Heat Transfer*, McGraw-Hill, New York.

A Computational Fluid Dynamics Study on the Effect of Carbon Particle Seeding for the Improvement of Solar Reactor Performance

Nesrin Ozalp
e-mail: nesrin.ozalp@qatar.tamu.edu
Department of Mechanical Engineering,
Texas A&M University at Qatar,
P.O. Box 23874,
Doha, Qatar

Anoop Kanjirakat
e-mail: anoop.baby@qatar.tamu.edu
MEEN Research,
Texas A&M University at Qatar,
P.O. Box 23874,
Doha, Qatar

This study focuses on a technique, referred to as "solar cracking" of natural gas for the coproduction of hydrogen and carbon as byproduct with zero emission footprint. Seeding a solar reactor with micron-sized carbon particles increases the conversion efficiency drastically due to the radiation absorbed by the carbon particles and additional nucleation sites formed by carbon particles for heterogeneous decomposition reaction. The present study numerically tries to investigate the above fact by tracking carbon particles in a Lagrangian framework. The results on the effect of particle loading, particle emissivity, injection point location, and effect of using different window screening gases on a flow and temperature distribution inside a confined tornado flow reactor are presented. [DOI: 10.1115/1.4002173]

Keywords: computational flow dynamics, solar reactor, carbon seeding, solar cracking, hydrogen

1 Introduction

Solar reactors conduct solar thermochemical processes to convert intermittent solar radiation into storable chemical energy in the form of hydrogen, which is a promising fuel for its environmentally friendly characteristic as well as its very high calorific value [1]. Hydrogen production via direct thermal decomposition of natural gas using concentrated solar energy has attracted researchers in recent years for emission-free production of hydrogen [2–6]. In addition to hydrogen, this process yield with carbon black, some of which are in the form of carbon nanotubes [7]. One more advantage of the direct thermal decomposition—or so called "solar cracking"—is that since the hydrogen from this process has high purity, it is suitable for high end applications, such as use in proton exchange membrane (PEM) fuel cell [8].

It is important to reach high exergy efficiency in order to have smaller solar collection area and, therefore, reduced cost for the generation of unit amount of hydrogen. Because of the Carnot limit, it is favorable to run the thermochemical processes at high temperatures. But from the heat transfer point of view, high temperature process causes high losses due to reradiation. For noncatalytic thermal decomposition of methane, temperatures of above 1500 K is required for complete dissociation [9]. Although use of carbon based catalysts, such as activated carbon, graphite, and carbon black does not reduce the high temperature need for complete dissociation, it could significantly improve the thermal decomposition process [9–13]. For example, amorphous form of carbon is observed to have higher catalytic activity in methane decomposition even at temperatures between 1000 K and 1200 K [9]. Finally, since carbon catalysts are cheap and do not require special separation from after decomposition of natural gas, carbon seeding has been the focus of many studies to improve the process efficiency of solar reactors. The direct solar irradiation of particle suspension presents an efficient means of radiative heat transfer due to the multiple scattering of the incoming radiation among the suspended particles.

Kogan and Kogan [14] observed that only 28% conversion was possible with the tornado flow reactor because the methane flow inside the reactor does not get heated uniformly during dissociation. They suggested that the volumetric gas can be heated by carbon particle seeding so that radiation absorption increases, resulting with more uniform temperature distribution inside the reaction chamber. Muradov et al. [15] studied the characteristics of catalytic action of expanded range of carbon materials on the methane decomposition reaction and concluded that "carbon-catalyzed decomposition of methane is an environmentally attractive low emission approach to production of hydrogen." Haueter et al. [16] used ZnO particles as reactant in thermochemical water splitting experiments. ZnO particles served as radiation absorbers as well as thermal barriers for the reactor cavity walls. Thus, as seen in literature, particle seeding inside a reactor is a good option in improving its process efficiency and reactor performance.

The main parameters effecting solar reactor performance are reaction kinetics, absorption, conduction, convection, and heat capacity of the reactor materials [4]. In addition, reactor geometry also has a large effect on the process efficiency. Abanades and Flamant [3] stated that it is possible to achieve almost complete dissociation of methane with proper reactor configuration.

A very useful tool to explore configurations, promising higher efficiencies, is the computational flow dynamic (CFD) analysis of the flow conditions inside the reactor. There have been many CFD studies in recent years for analyzing the solar methane cracking process [7,11,12,17–19] to understand the flow behavior inside the reactor and to improve reactor designs. As it is seen in most of these works, Mie scattering theory has been used to solve radiation heat transfer for gas-particle suspensions [10–12]. In these studies, particles are not tracked individually and a global absorption and scattering coefficients are used in most of them. To the best of our knowledge, there have been no CFD studies involving gas-particle flow, individually tracking the particles, and incorporating radiation and thermal decomposition inside a solar thermo-

Contributed by the Heat Transfer Division of ASME for publication in the JOURNAL OF HEAT TRANSFER. Manuscript received January 25, 2010; final manuscript received June 28, 2010; published online September 22, 2010. Assoc. Editor: He-Ping Tan.

Table 1 Inlet flow conditions of the numerical simulation from the experimental results of Ref. [20]

	F1 (l/min)	F2 (l/min)	FS3 (l/min)	F31 (l/min)	F32 (l/min)
Case 1	9.51	1.74	2.12	0	0
Case 8	9.45	0.77	0.51	1	0.9

chemical reactor except for the studies done by our research group at Sustainable Energy Research Laboratory of Texas A&M University at Qatar.

Our present study aims to explain the gas-particle flow inside a tornado flow solar reactor via Lagrangian particle tracking model by including irradiation and particle radiation interaction. The solar reactor geometry used in our study is that of Kogan et al. [20]. This is mainly due to the fact that they have conducted some experimental gas-particle studies, which can be effectively used in validating our particle tracking simulations.

2 Solar Reactor Geometry

The reactor configuration used in our numerical analysis is that of the works of Kogan et al. [20]. The geometric specifications of this solar reactor are given in Refs. [20,17]. Kogan et al. [20] did some experiments by seeding the reactor with carbon particles at room temperature. The major objective of their work was to understand the particle flow behavior and its probability of deposition on the reactor window at ambient conditions. They were successful in using tornado flow to reduce the auxiliary screening flow by keeping it just below the window screening flow. This reduction is mainly created through the intuitive design of the reactor, e.g., during the design of the reactor, a radial auxiliary screening flow is provided just above the tangential main flow below the window. This helps in exploiting the synergy between the vortex flow of the main flow and the boundary layer flow of the auxiliary screening gas resulting with keeping the auxiliary flow to a minimum level.

The Kogan group studied various reactor configurations with varying inlet parameters to solve carbon deposition problem. They reported several experimental cases with qualitative results of particle deposition on reactor window [20]. Some of the cases showed particles deposit on the window, whereas the window glass was kept clear in some cases. For example, in case #1, it is reported that the reactor window was contaminated by carbon deposition, whereas in case #8, the reactor window was clear. The details of the flow rates used in these two cases are provided in Table 1.

We have run CFD simulations of Kogan's reactor for their two experiments, namely, case #1 and case #8 in Ref. [20], to check the validity of our numerical model. Once we were successful in predicting Kogan's experimental observations numerically, we extended our numerical scheme to incorporate solar irradiation and effects of particle seeding on temperature distribution inside the solar reactor.

The basic geometry used for simulations is shown in Fig. 1. The model geometry primarily consists of a cylindrical portion at the top ($\varnothing$ 140 mm$\times$140 mm) and a conical frustum at the bottom with a height of 70 mm and an exit diameter of 7 mm. The main flow is injected tangentially at locations along the circumference near the reactor window. This flow is labeled as F1. The window screening flow is helium and it is injected underneath the window glass and above the main flow. This flow is labeled as F2. The carbon laden seeding flows (FS1, FS2, and FS3) into the reactor are given at locations as shown in Fig. 1. Tertiary flows, whose aim is to keep the reactor wall clean, are located in the tubular section of the reactor. They are labeled as F31 and F32.

Before going to details of numerical observations made, a brief description on the numerical model used is given below.

3 Numerical Model

We have used three-dimensional geometry for simulations using GAMBIT, which is also used for generating the nonuniform unstructured grid in the geometry. The simulations involve turbulent flow, two-phase, turbulence species transport, solar irradiation, particle tracking, and chemical decomposition using FLUENT 6.3.26. The finite volume method using implicit finite difference scheme is used to discretize the partial differential equations of the model. The SIMPLE algorithm is used for particle velocity coupling and a second order upwinding is used for the interpolation of variables.

In our numerical model, we used ReNormalization Group (RNG) k-ε model since the flow has a low Reynolds number. The swirl effect of the flow has been included in the model. A discrete phase model (DPM) is used to evaluate the trajectories of the carbon particles and to track them through the continuous phase of gas. The motion of particulate phase is obtained based on the force balance equating particle inertial forces on a Lagrangian frame of reference with the forces acting on the particle. Since the particle load is not significant, the interparticle interaction is neglected. Then, the momentum equation of a particle in the x-direction is given as follows:

$$\frac{du_p}{dt} = F_D(\overline{u} + u' - u_p) + g_x\frac{(\rho_p - \rho)}{\rho_p} \tag{1}$$

where $F_D = (18\mu/\rho_p d_p^2)(C_D\,\mathrm{Re}/24)$ and the coefficient for the drag force C_D is as given in Ref. [21]. The particle Reynolds number in Eq. (1) is evaluated as

$$\mathrm{Re} = \frac{\rho d_p |u_p - u|}{\mu} \tag{2}$$

The effects of thermophoretic forces are not considered in the present study.

The concentrated solar energy is the main source of power for the thermal decomposition of natural gas inside the reactor. The solar isolation falling on the reactor window is simulated using FLUENT discrete ordinate (DO) approach. The DO model solves

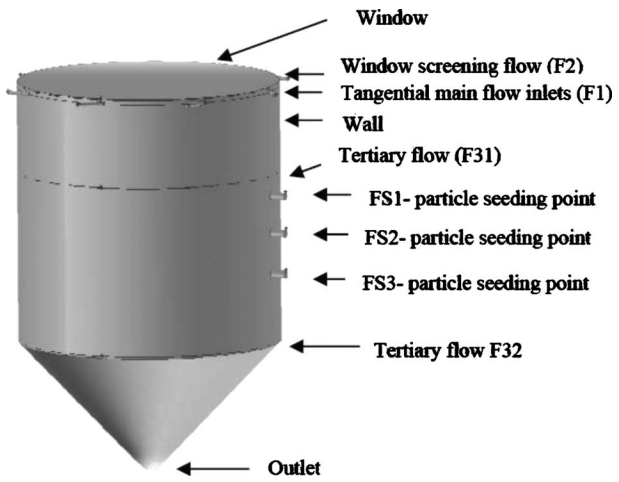

Fig. 1 Geometry used for simulation

the radiative transfer equation for a finite number of discrete angles. For a particle laden flow, this is modified to include the particle radiation effects and is given as

$$\nabla \cdot (I\boldsymbol{s}) + (a + a_p + \sigma_p) I(\boldsymbol{r},\boldsymbol{s}) = an^2 \frac{\sigma T^4}{\pi} + \frac{\sigma_p}{4\pi} \int_0^{4\pi} I(\boldsymbol{r},\boldsymbol{s}') \phi(\boldsymbol{s},\boldsymbol{s}') d\Omega' \tag{3}$$

Here, a_p is the equivalent absorption coefficient due to the presence of particulates and is defined as

$$a_p = \lim_{V \to 0} \sum_{n=1}^{N} \varepsilon_{pn} \frac{A_{pn}}{V} \tag{4}$$

The equivalent particle scattering factor σ_p, which incorporates the particle scattering effects is given as

$$\sigma_p = \lim_{V \to 0} \sum_{n=1}^{N} (1 - f_{pn})(1 - \varepsilon_{pn}) \frac{A_{pn}}{V} \tag{5}$$

where ε_{pn}, A_{pn}, and T_{pn} are the emissivity, projected area, and temperature of particle n, respectively. f_{pn} is the particle scattering factor associated with the n_{th} particle. During particle tracking, the summation is carried over n particles in volume V. It may be noted that when particulate radiation is considered, the individual gas scattering effects are neglected in the simulation. In present study, an angular solid angle discretization of 5×5 and 3×3 are taken in the theta divisions and phi pixels, respectively. Even though, it is computationally intensive, the DO model allows one to incorporate particle radiation effects along with species transport.

The incoming solar flux is simulated as a uniform flux irradiated through a semitransparent window boundary. A flux density of 6000 kW/m^2 is given. A mixed heat transfer with a convective heat transfer coefficient of 5 $W/m^2\,K$ and an external radiation temperature of 300 K is provided at the reactor window [3,8]. The heat transfer from continuous phase to discrete phase (particle phase) is computed from the change in thermal energy of a particle as it passes through each control volume. In FLUENT, particle temperature is evaluated from the balance of energy relating convection and radiation heat transfer as given below.

$$m_p Cp \frac{dT_p}{dt} = hA_p(T_\infty - T_p) + \varepsilon_p A_p \sigma(\theta^4 - T_p^4) \tag{6}$$

The heat transfer coefficient is evaluated using correlations from Rans and Marshall [22]. The heat lost or gain by the particle appears as source or sink of heat in the energy equation as it passes through each computational cell. The particles are assumed to be spherical and the particle scattering factor is assumed to be 0.5 [23]. The inner walls of the reactor are assumed to be opaque with an internal surface emissivity of 0.8. A convective heat loss to outside with a heat transfer coefficient of 5 $W/m^2\,K$ is also provided.

For evaluating reaction kinetics, the first order kinetic law as computed on the basis of an Arrhenius expression assuming plug flow reactor model (Eq. (7)) is used.

$$k(T) = k_o \exp\left(\frac{-E_a}{RT}\right) \tag{7}$$

The activation energy and frequency factor of $E_a = 147$ $kJ\,mol^{-1}$ and $k_o = 1.07 \times 10^6$ s^{-1} are considered when particle seeding is there. With no particle seeding, the activation energy and frequency factor are taken 60.3 $kJ\,mol^{-1}$ and 6.76 s^{-1}, respectively. These values are taken from the experimental data of Trommer et al. [13].

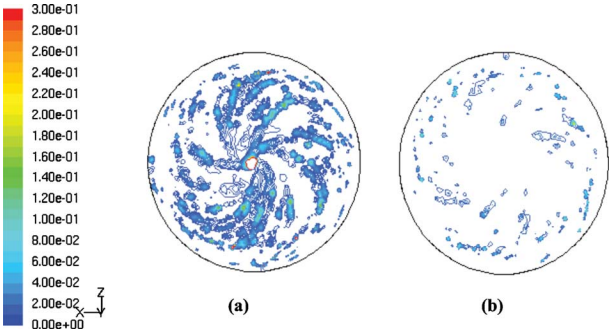

Fig. 2 Particle concentration contour on reactor window: (*a*) for case #1 and (*b*) case #8. Contours colored by DPM concentration (kg/m^3).

The carbon powder used for particle seeding by Kogan et al. was activated charcoal (No. 05105, manufactured by Fluka). However, since the detailed particle size distribution of the samples was not available, we used the particle size distribution of similar carbon particles given in Ref. [12]. The particle size distribution given in Ref. [12] was fitted to a Rosin–Rammler equation with the mean particle size of 20 μm and a spread of 1.2, which we used as the input parameters for FLUENT. The minimum and maximum particle dimensions in the simulations were assumed to be 1 μm and 100 μm, respectively. Density of the carbon particles used was 2000 kg/m^3 and they were injected normally from the injector surface.

Since our present simulations involve mixing of main flow gas (nitrogen) and window screening gas (helium), we have used species conservation by convection and diffusion for solution. In simulations, volume-weighted mixing law was used for density evaluation of gas mixtures and the viscosity was evaluated using mass-weighted mixing laws. Density viscosity, specific heat, and thermal conductivity values of the fluids used in the simulation were evaluated at an average temperature of 1473°C [24]. The mass diffusivity of all components is assumed to be constant and is 2.88×10^{-5} m^2/s.

Grid independence tests were performed to ensure that the solutions do not vary with the number of computational elements. The final adapted grid used for the simulation consisted of 2,084,285 cells. The convergence criterion was set to be 10^{-4} for all the variables. The simulations were carried out in an interactive mode using the supercomputing cluster of the Texas A&M University at Qatar, which consists of 512 cores SGI Altix XE1300 serve computers.

4 Validation

As explained earlier, qualitative validation for particle deposition on reactor window was made for two flow conditions, namely, case #1 and case #8 of Ref. [20]. Figures 2(*a*) and 2(*b*) show the DPM results for particle concentration contours on reactor window for case #1 and case #8, respectively. In the numerical scheme, DPM concentration gives the total concentration of discrete phase (particle) in a continuous cell. The discrete phase concentration inside a cell was determined from the residence time and mass flow in that particular cell using Eq. (8) below.

$$\rho_{\mathrm{DPM}} = \int_t \frac{\dot{m}_p}{V_{\mathrm{cell}}} dt \tag{8}$$

Hence, DPM concentration gave a rough estimate of the density of the solid in a particular region. This basically shows us areas where the particle loading is high and where the maximum probability of deposition is. Thus, it can be noted that the particle concentration near the window region is more for case #1 than when compared with that of case #8 and the particle deposition on

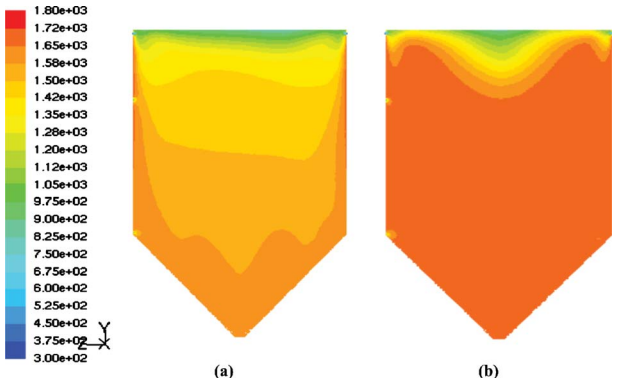

Fig. 3 Temperature distribution inside reactor: (*a*) without particle seeding and (*b*) with particle seeding. Contours colored by static temperature (K).

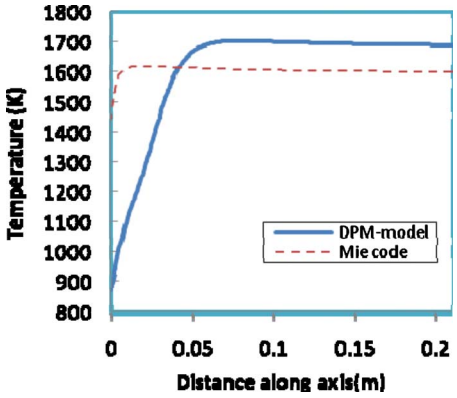

Fig. 4 Comparison of DPM with Mie theory

window. Similar observations are made by Kogan et al. [20] in their experimental observations also. Hence, it can be noted that the discrete phase model utilizing Lagrangian framework is able to track particle behaviors successfully. As the experimental observations were made at ambient conditions, the properties for the validation simulations were also provided as that at room temperature.

This numerical prediction qualitatively validates the experimental observation made in Ref. [20].

5 Results and Discussion

After getting successful preliminary validation runs, we have conducted some parametric studies by varying the inlet flow conditions and gases. Results of these parametric studies can help for the design of solar reactors. Unless otherwise mentioned, the flow conditions used in all simulations are that of case #8 [20].

5.1 Effect of Particle Seeding. Figure 3 shows temperature distribution on a vertical midplane of the reactor geometry. Figure 3(*a*) shows the temperature distribution without particle seeding and Fig. 3(*b*) shows that with particle seeding. The carbon particles are seeded as a laden flow from the injection point FS3 (Fig. 1). A particle flow rate of 2.33×10^{-6} kg/s is given in the simulation. The particles are assumed to have an emissivity value of 0.9. The flow rates and flow conditions used in this simulation were the same as that of case #8 (Table 1). For the simulation, nitrogen gas is provided for the main flow (F1) and helium gas for the window screening flow (F2). As seen from the figure, the particle seeding has brought uniform temperature distribution inside the reactor. Higher temperatures are observed near the reactor walls than at reactor core when no particle seeding is provided. However, by seeding with particles, it is possible to bring more temperatures toward the core of the reactor also. This fact is seen clearly in Fig. 3(*b*) and is one of the main objectives for using particle seeding inside the reactor. In addition, as the chemical reaction inside the reactor is mainly sensitive to temperature distribution, the particle seeding has got great influence in conversion efficiency.

Another observation that can be made is the fact that the simulations with Lagrangian tracking of particles are able to give appropriate temperature distribution inside the reactor. For regions where particle concentrations are more, it is able to show higher temperatures. For regions with lower particle concentrations (near the reactor window region), lower temperatures are shown. The temperature distribution seen in Fig. 3(*b*) near the window is observed mainly due to the cooling effect of the window screening gas. This flow is primarily intended to prevent particle deposition on the reactor window surface. Furthermore, it is given radially below the window surface and turns abruptly by 90 deg and proceeds as a swirling flow along the axis of the reactor. This tornado flow is creating the temperature distribution as seen near the window. It can be seen that the present numerical scheme is able to simulate this effect as well as the particle concentration effects pretty well.

5.2 Comparison With Mie Theory. Our present simulation uses Lagrangian discrete phase approach to solve the flow field. In this section, a comparison of this with that of Mie scattering theory is given. Mie theory can be used as a tool to predict the absorption and scattering coefficients of the particle cloud with sufficient accuracy. Mie efficiency factors calculated from Mie code depends on the wavelength of the solar spectrum and the mean particle radius. The calculations are carried out using the BHMIE algorithm [25]. Along with wavelength of the solar spectrum and equivalent particle diameter, the calculation of the absorption, scattering, and extinction coefficients requires the values of the complex index of refraction of the material. In the present study, the values for the complex index of refraction for carbon black are considered from Dalzel and Sarofim [26]. As an approximation for the complex refraction index, the values for acetylene soot are taken because it has similar carbon content (about 94%) as the charcoal particles used. In the present study, the carbon particles are assumed to have uniform distribution with a volume fraction of 1×10^{-5}. The absorption and scattering coefficients in the reactor are calculated by considering Mie theory. The absorption and scattering coefficients for a wavelength of 2.37 μm and for 20 μm diameter particle is obtained as 0.638 m^{-1} and 1.04 m^{-1}, respectively.

Figure 4 shows the axial temperature variation inside the reactor when using discrete phase model and Mie scattering theory. A good agreement is seen for the two models except near the window region. The temperatures are seen to become almost constant toward the rear of the reactor. This happened mainly due to the uniform mixing of particles with the swirling gas flow toward the exit. This fact is well predicted by both the models. However, the discrete phase model is able to capture the particle concentration effects better. As explained in the earlier section, the particle concentration is lower toward the reactor window region owing to the helium gas window screening flow. This effect is well reflected in the discrete phase model than in Mie theory, which assumes a uniform particle distribution. Hence, it can be observed that DPM can become a better tool in reactor design, especially when there is wide concentration variation within the reactor.

5.3 Effect of Particle Emissivity. Effect of particle emissivity on temperature distribution is analyzed in Sec. 5.3. Temperature variation along the axis of the reactor for three particle emissivities, namely, 0.2, 0.5, and 0.9 are performed. As particle radiation interaction occurs, an increase in particle emissivity is observed to increase the temperature field inside the reactor also. This can be observed in Fig. 5. This effect is brought in the simulation through the second term in the right hand side of Eq. (6). As

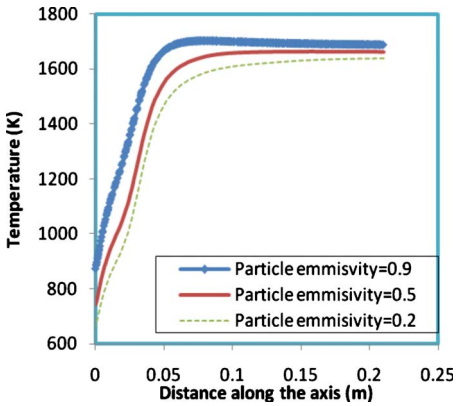

Fig. 5 Effect of particle emissivity on axial temperature distribution

seen from literature [27,28] in all simulations presented in this communication, an emissivity value of 0.9 is considered for carbon particles.

5.4 Effect of Particle Loading. Figure 6 shows the effect of particle loading on temperature inside the reactor. The average exit gas temperature is plotted against various mass flow rates of the particles. As it is seen, the temperature inside the reactor increases with increase in particle loading. This is a straightforward observation and can be tactfully used in some practical situations.

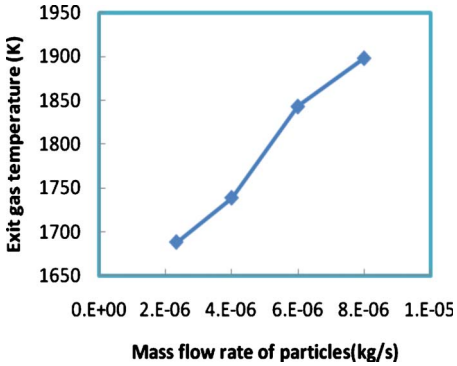

Fig. 6 Effect of particle loading on reactor exit gas temperature

For example, assume a situation in which a sudden reduction in solar irradiation occurs (by clouds and sandstorms) and we still want to maintain the same temperature inside the reactor. One prudent option would be to increase the particle seeding rate at that point to maintain a higher temperature. However, increasing the particle loading could bring in adverse effects, such as particle clogging, and increase the problems associated with particle removal also.

5.5 Effect of Screening Gas. Three window screening gases, namely, hydrogen, helium, and nitrogen are used for comparison. Temperature distribution on the vertical midplane of the reactor for the three gases is plotted in Fig. 7.

Even though the temperature distribution looks similar for all these gases, the temperature spread toward the radial direction near window region is more pronounced when hydrogen is used. In addition, when nitrogen is used, the axial temperature variation from window is different from the other two because of a lower thermal conductivity. However, in order to see the real influence of these screening gases; one has to also investigate the amount of particle deposition on window surface while using them.

Figure 8 shows the DPM concentration on the reactor window surface when hydrogen, helium, and nitrogen are used as screening gases at room temperature. The average DPM concentration is observed to be 0.005 kg/m^3 when hydrogen is used. This is almost half of the deposition value when nitrogen is used (0.011 kg/m^3) for the same flow conditions. Therefore, the reactor window remains cleaner when a lighter gas, e.g., hydrogen, is used as the screening flow. This effect is mainly brought by the ability to maintain a stable flow field when a lighter gas is on top. It is always easier to maintain a stable flow when the lighter gas is on top of the heavier gas than vice versa. This avoids the Taylor instabilities occurring and maintains the screening flow attached to the reactor window. Similar discussion on the advantage of using hydrogen as a sweeping gas is mentioned in the numerical studies of Ref. [29] as well, except, they use different gases for keeping the solar reactor porous walls clean from carbon deposits.

5.6 Effect of Particle Injection Position. Figure 9 shows the effect of particle injection position on temperature. Particle tracks colored by temperature when injected from position FS3 and FS1 (refer Fig. 1) are shown in Figs. 9(*a*) and 9(*b*), respectively. It is noted that a slight increase (around 50 K) in average particle temperature is observed while injecting from top position (FS1) than while injecting from a lower position (FS3). However, a major drift in reactor core temperature is not observed with change in particle seeding position.

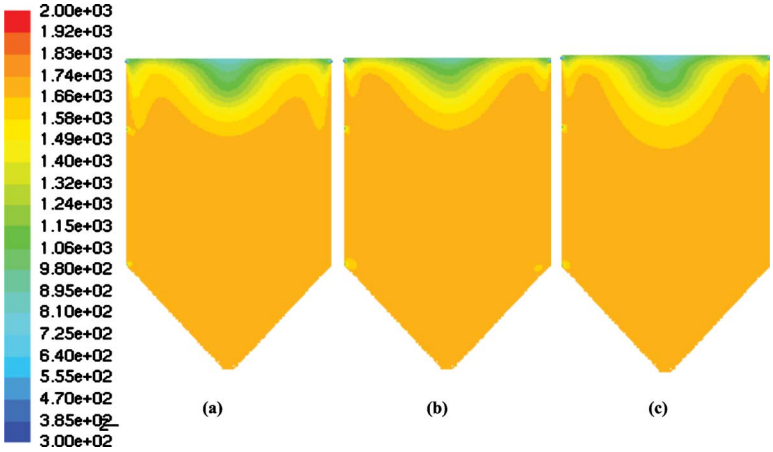

Fig. 7 Temperature distribution inside the reactor when: (*a*) hydrogen, (*b*) helium, and (*c*) nitrogen are used as screening gases. Contours colored by static temperature (K).

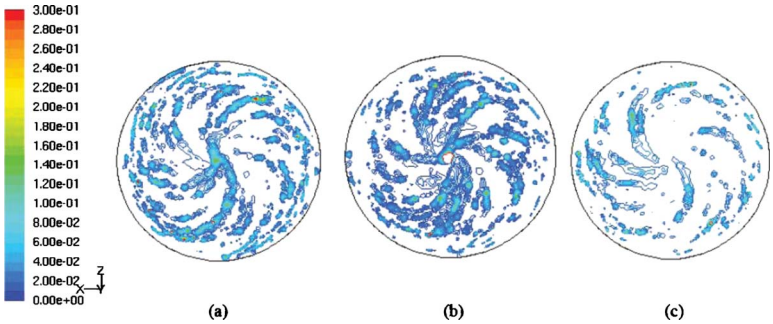

Fig. 8 DPM particle concentration on reactor window when: (*a*) nitrogen, (*b*) helium, and (*c*) hydrogen are used as screening gases. Contours colored by DPM concentration (kg/m^3).

5.7 Effect on Methane Cracking. In Sec. 5.7, effect of particle seeding on the thermal cracking of methane is investigated. In contrast to previous simulations, the main flow is replaced by methane for this case. However, the flow rates and the flow conditions are maintained as that of previous cases. Helium is used as the window screening gas.

The kinetic parameters used in the simulations were taken from Trommer et al. [13]. Figure 10 shows mass fraction contours of methane after reaching steady state. Figure 10(*a*) shows case without particle seeding, whereas Fig. 10(*b*) shows that with particle seeding. The mass fractions at reactor exit with no particle seeding and with particle seeding are observed to be 0.85 and 0.55, respectively. Hence, it can be noted that an increase of 30% in conversion is brought due to the volumetric heating provided by the radiating suspended particles. Hence, it can be concluded that particle seeding is an effective means of improving the reactor performance.

Due to computational complexities involved, only limited runs were possible to simulate thermal cracking of methane along with particle tracking and radiation. However, efforts are being taken by our research group to incorporate more parameters and make a full-fledged optimized reactor design in the near future.

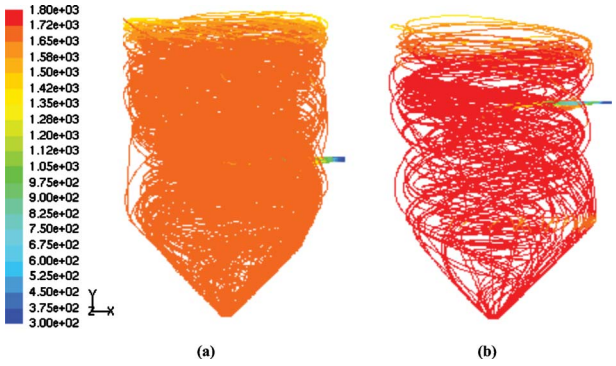

Fig. 9 Particle tracks colored by particle temperature when particle injection is given: (*a*) at a lower position (FS3) and (*b*) at a higher position (FS1)

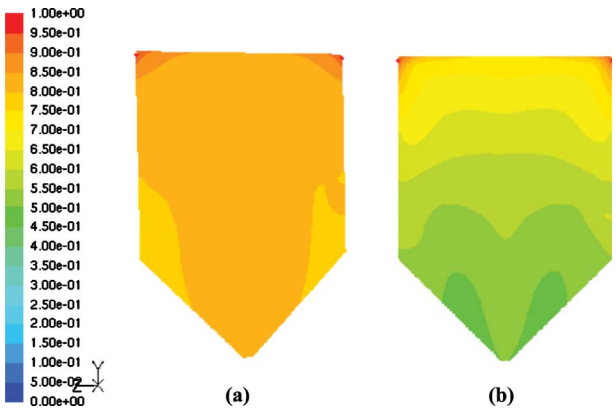

Fig. 10 Mass fraction contours of methane: (*a*) without particle seeding and (*b*) with particle seeding

6 Conclusions

The present study explained the gas-particle flow inside a tornado flow swirling reactor via Lagrangian discrete phase model. Experimentally obtained particle deposition and temperature distribution inside the reactor were numerically predicted successfully. It is observed that computational fluid dynamic simulation along with Lagrangian particle tracking can become a useful tool in thermochemical reactor design. It is also observed that volumetric heating caused by the suspended particle substantially improves the reactor performance. Some of the salient observations made from the parametric studies are as follows.

(a) Carbon particle seeding inside the reactor considerably increases the temperature inside the reactor. Temperature distribution becomes more uniform toward reactor core when there is carbon particle seeding.
(b) Particles with higher surface emissivity show higher temperatures inside the reactor.
(c) Mie scattering theory and discrete phase Lagrangian model show appreciable comparison in portions where particle distribution is uniform.
(d) With increase in particle loading, higher reactor temperatures are observed.
(e) Hydrogen is observed to be a better window screening gas as less particle deposition on reactor window is observed.
(f) Particle injection position is observed to have only marginal effect on reactor core temperature.
(g) Methane conversion increases when the reactor is seeded with carbon particles.

Acknowledgment

This research has been funded by Texas A&M University at Qatar. We would like to thank Khalid Warraich and Faisal Chaudhry of TAMU-Q for their assistance with the supercomputing facilities.

Nomenclature

A = surface area, m^2
A_{pn} = projected area of particle n, m^2

a_p = absorption coefficient
Cp = specific heat, J/kg K
d = diameter, m
DPM = discrete phase model
ε_{pn} = emissivity of particle n
F1 = main gas flow, l/min
F2 = window screening gas flow, l/min
F31, F32 = tertiary gas flow, l/min
FS1, FS2, FS3 = particle seeding flows, l/min
g = gravity, 9.81 m/s^2
h = heat transfer coefficient, W/m^2 K
M = mass, kg
T = temperature, K
T_{pn} = temperature of particle n, K
t = time, s
u = velocity on the x-direction, m/s
V = volume, m^3
μ = dynamic viscosity, kg/m s
θ = radiation temperature, K
ρ = density, kg/m^3
σ = Stefan–Boltzmann constant, 5.67×10^{-8} W/m^2 K^4
σ_p = particle scattering factor

Subscripts

p = particle
α = static condition

References

[1] Ozalp, N., Kogan, A., and Epstein, M., 2009, "Solar Decomposition of Fossil Fuels as an Option for Sustainability," Int. J. Hydrogen Energy, **34**, pp. 710–720.
[2] Ozalp, N., Epstein, M., and Kogan, A., 2010, "Cleaner Pathways of Hydrogen, Carbon Nano-Materials and Metals Production Via Solar Thermal Processing," J. Cleaner Prod., **18**, pp. 900–907.
[3] Abanades, S., and Flamant, G., 2007, "Experimental Study and Modeling of a High-Temperature Solar Chemical Reactor for Hydrogen Production From Methane Cracking," Int. J. Hydrogen Energy, **32**, pp. 1508–1515.
[4] Palumbo, R., Keunecke, M., Möller, S., and Steinfeld, A., 2004, "Reflections on the Design of Solar Thermal Chemical Reactors: Thoughts in Transformation," Energy, **29**, pp. 727–744.
[5] Ozalp, N., Epstein, M., and Kogan, A., 2008, "Cracking of Natural Gas Into Hydrogen and Carbon Black Using Concentrated Solar Energy," International Conference on Harnessing Technology, ICHT Paper No. Sl. No. 9 (i), Vol. 49.
[6] Zhang, J., Fisher, T., Ramachandran, P., Gore, J., and Mudawar, I., 2005, "A Review of Heat Transfer Issues in Hydrogen Storage Technologies," ASME J. Heat Transfer, **127**, pp. 1391–1400.
[7] Rodat, S., Abanades, S., Sans, J., and Flamant, G., 2009, "Hydrogen Production From Solar Thermal Dissociation of Natural Gas: Development of a 10 kW Solar Chemical Reactor Prototype," Sol. Energy, **83**, pp. 1599–1610.
[8] Abanades, S., and Flamant, G., 2008, "Hydrogen Production From Solar Thermal Dissociation of Methane in a High-Temperature Fluid-Wall Chemical Reactor," Chem. Eng. Process., **47**, pp. 490–498.
[9] Muradov, N., 2001, "Catalysis of Methane Decomposition Over Elemental Carbon," Catal. Commun., **2**, pp. 89–94.
[10] Bertocchi, R., Karni, J., and Kribus, A., 2004, "Experimental Evaluation of a Non-Isothermal High Temperature Solar Particle Receiver," Energy, **29**, pp. 687–700.
[11] Klein, H., Karni, J., Ben-Zvi, R., and Bertocchi, R., 2007, "Heat Transfer in a Directly Irradiated Solar Receiver/Reactor for Solid-Gas Reactions," Sol. Energy, **81**, pp. 1227–1239.
[12] Hirsch, D., and Steinfeld, A., 2004, "Solar Hydrogen Production by Thermal Decomposition of Natural Gas Using a Vortex-Flow Reactor," Int. J. Hydrogen Energy, **29**, pp. 47–55.
[13] Trommer, D., Hrisch, D., and Steinfeld, A., 2004, "Kinetic Investigation of the Thermal Decomposition of CH_4 by Direct Irradiation of a Vortex Flow Laden With Carbon Particles," Int. J. Hydrogen Energy, **29**, pp. 627–633.
[14] Kogan, M., and Kogan, A., 2003, "Production of Hydrogen and Carbon by Solar Thermal Methane Splitting. I. The Unseeded Reactor," Int. J. Hydrogen Energy, **28**, pp. 1187–1198.
[15] Muradov, N., Smith, F., and T-Raissi, A., 2005, "Catalytic Activity of Carbons for Methane Decomposition," Catal. Today, **225**, pp. 102–103.
[16] Haueter, P., Moeller, S., Palumbo, R., and Steinfeld, A., 1999, "The Production of Zinc by Thermal Dissociation of Zinc Oxide Solar Chemical Reactor Design," Sol. Energy, **67**, pp. 161–197.
[17] Kogan, A., Israeli, M., and Alcobi, E., 2007, "Production of Hydrogen and Carbon by Solar Thermal Methane Splitting. IV. Preliminary Simulation of a Confined Tornado Flow Configuration by Computational Fluid Dynamics," Int. J. Hydrogen Energy, **32**, pp. 4800–4810.
[18] Meier, A., Ganz, J., and Steinfeld, A., 1996, "Modeling of a novel High-Temperature Solar Chemical Reactor," Chem. Eng. Sci., **51**, pp. 3181–3186.
[19] Abanades, S., and Flamant, G., 2006, "Solar Hydrogen Production From the Thermal Splitting of Methane in a High Temperature Solar Chemical Reactor," Sol. Energy, **80**, pp. 1321–1332.
[20] Kogan, A., Kogan, M., and Barak, S., 2004, "Production of Hydrogen and Carbon by Solar Thermal Methane Splitting. II. Room Temperature Simulation Tests of Seeded Solar Reactor," Int. J. Hydrogen Energy, **29**, pp. 1227–1236.
[21] Morsi, S. A., and Alexander, A. J., 1972, "An Investigation of Particle Trajectories in Two-Phase Flow Systems," J. Fluid Mech., **55**, pp. 193–208.
[22] Ranz, W. E., and Marshall, J., 1952, "Evaporation From Drops, Part 1," Chem. Eng. Prog., **48**, p. 173.
[23] Ho, C. K., Khalasa, S. S., and Siegel, N. P., 2009, "Modeling On-Sun Tests of a Prototype Solid Particle Receiver for Concentrating Solar Power Processes and Storage," *Proceedings of ES2009 Energy Sustainability*.
[24] Yaws, C., 1999, *Chemical Properties Hand Book*, McGraw-Hill, New York.
[25] Bohren, C. F., and Huffman, D. K., 1983, *Absorption and Scattering of Light by Small Particles*, Wiley, New York.
[26] Dalzell, W., and Sarofim, A., 1969, "Optical Constants of Soot and Their Applications to Heat Flux Calculations," ASME J. Heat Transfer, **91**, pp. 100–104.
[27] Stull, R. V., and Plass, G. N., 1960, "Emissivity of Dispersed Carbon Particles," J. Opt. Soc. Am., **50**(2), pp. 121–125.
[28] Rego-Barcena, S., Mani, R., Yang, F., Saari, R., and Thomson, M. J., 2009, "Particle Emissivity in a Full Scale Steel Making Furnace," Metall. Mater. Trans. B, **40**, pp. 158–168.
[29] Dahl, J. K., Weimer, A. W., Graggen, A. Z., and Steinfeld, A., 2005, "Two-Dimensional Axi-Symmetric Model of a Solar-Thermal Fluid Wall Aerosol Flow Reactor," ASME J. Sol. Energy Eng., **127**, pp. 76–85.

On the Analysis of the Aerodynamic Heating Problem

A. Özer Arnas
e-mail: ozer.arnas@usma.edu

Daisie D. Boettner

Gunnar Tamm

Seth A. Norberg

Jason R. Whipple

Michael J. Benson

Bret P. VanPoppel

Department of Civil and Mechanical Engineering,
United States Military Academy,
West Point, NY 10996

A complete analytical solution to the problem of aerodynamic heating is lacking in heat transfer textbooks, which are used for undergraduate and graduate education. There are many issues that are very important from a convective heat transfer point of view. In practice, poor analyses lead to poor design, thus faulty manufacturing. Since, over the years analysis has given way to numerical studies, the instructors do not take the necessary time to go through analytical details. Thus the students just use the results without any awareness of how to get them and the inherent limitations of the analytical solution. The only intent of this paper, therefore, is to present the detailed analytical study of the aerodynamic heating problem. [DOI: 10.1115/1.4001754]

Keywords: aerodynamic heating, convection, flat plate

1 Introduction

The topic of high speed aerodynamic heating in a heat transfer course is important. References to this material are very limited [1,2] and a sampling of graduate heat transfer textbooks [3–5] do not address this subject effectively or not at all, although the fundamental work was done over a century ago [6–9]. Aerospace engineers have utilized these concepts but none have presented detailed analytical results that can be used by the student of heat transfer [10–12]. In some recent heat transfer textbooks [13–15], limited remarks reference the topic but without a robust mathematical analysis. This paper develops the appropriate aerodynamic heat transfer equations through a rigorous analytical study by simplifying the general forms of the conservation equations and the equation of state for the case under consideration.

The four principles that govern this problem are as follows:

1. Newton's Second Law of Motion—Conservation of Momentum

$$\frac{D\boldsymbol{V}}{Dt} = \boldsymbol{F}_b - \frac{1}{\rho}\nabla p + \upsilon\nabla^2\boldsymbol{V} + \frac{1}{3}\upsilon\nabla(\nabla\cdot\boldsymbol{V}) \tag{1}$$

2. Continuity Equation—Conservation of Mass

$$\frac{\partial\rho}{\partial t} + \nabla(\rho\boldsymbol{V}) = 0 \tag{2}$$

3. First Law of Thermodynamics—Conservation of Energy

$$\rho\left[\frac{\partial e}{\partial t} + (\boldsymbol{V}\boldsymbol{\nabla})e\right] = -p(\nabla\cdot\boldsymbol{V}) + \nabla(k\nabla T) + \Phi$$

$$\rho\frac{Di}{Dt} = \frac{Dp}{Dt} + \nabla(k\nabla T) + \Phi \tag{3}$$

where

$$\Phi = 2\mu\left[\left(\frac{\partial u}{\partial x}\right)^2 + \left(\frac{\partial v}{\partial y}\right)^2 + \left(\frac{\partial w}{\partial z}\right)^2\right] + \mu\left[\left(\frac{\partial u}{\partial y} + \frac{\partial v}{\partial x}\right)^2 + \left(\frac{\partial v}{\partial z} + \frac{\partial w}{\partial y}\right)^2 + \left(\frac{\partial u}{\partial z} + \frac{\partial w}{\partial x}\right)^2\right] - \frac{2}{3}\mu\left(\frac{\partial u}{\partial x} + \frac{\partial v}{\partial y} + \frac{\partial w}{\partial z}\right)^2$$

$$i = e + \frac{p}{\rho}$$

4. The Equation of State

$$p = p(\rho, T) \tag{4}$$

These four equations must be solved simultaneously for an exact solution. Since mathematical analysis will not permit an exact solution, certain assumptions must be made to continue with the analysis.

2 Assumptions and Analysis

In general, three methods apply to obtaining the fundamental solution to convective heat transfer problems, as follows:

1. Solve the governing equations using the concept of the boundary layer and suitable similarity parameters.
2. Perform dimensional analysis coupled with extensive experimental data and curve fitting techniques.
3. Use the approximate integral method.

The boundary layer solution to the convection problem is normally demonstrated under the assumptions of steady flow of an incompressible fluid, constant dynamic viscosity and thermal conductivity, and constant specific heats for the case of an ideal gas. Under these assumptions, conservation of mass (Eq. (2)) reduces to

$$\nabla\cdot\boldsymbol{V} = 0 \tag{5}$$

Conservation of momentum (Eq. (1)) reduces to

$$(\boldsymbol{V}\cdot\nabla\boldsymbol{V}) = \boldsymbol{F}_{\text{body}} + \upsilon\nabla^2\boldsymbol{V} \tag{6}$$

Conservation of energy (Eq. (3)) reduces to

$$\rho c_p(\boldsymbol{V}\cdot\nabla T) = k\nabla^2 T + \Phi' \tag{7}$$

where Φ' is obtained from the equation for Φ with the last term eliminated as a result of Eq. (5). The equation of state remains unchanged.

Applying the order of magnitude analysis [2] and assuming two-dimensional flow reduce the conservation of mass (Eq. (5)) to

$$\frac{\partial u}{\partial x} + \frac{\partial v}{\partial y} = 0 \tag{8}$$

Conservation of momentum (Eq. (6)) reduces to

Contributed by the Heat Transfer Division of ASME for publication in the JOURNAL OF HEAT TRANSFER. Manuscript received November 10, 2009; final manuscript received April 17, 2010; published online September 20, 2010. Assoc. Editor: S. A. Sherif.

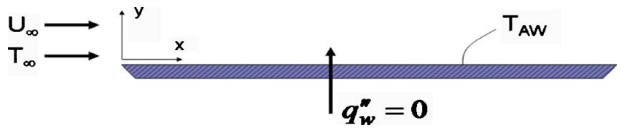

Fig. 1 Schematic of the aerodynamic heating problem

$$u\frac{\partial u}{\partial x}+v\frac{\partial u}{\partial y}=g+\nu\frac{\partial^2 u}{\partial y^2} \tag{9}$$

As a consequence of the order of magnitude analysis for these equations, the additional restriction that $\mathrm{Re}_L \geq 100$ at the end of the plate follows. Conservation of energy (Eq. (7)) reduces to

$$u\frac{\partial T}{\partial x}+v\frac{\partial T}{\partial y}=\frac{u}{\rho c_p}\frac{\partial p}{\partial x}+\alpha\frac{\partial^2 T}{\partial y^2}+\frac{\nu}{c_p}\left(\frac{\partial u}{\partial y}\right)^2 \tag{10}$$

Again as a consequence of the order of magnitude analysis, the additional restrictions that $\mathrm{Ec}=U_\infty^2/c_p(T_w-T_\infty)$ must have an order of magnitude of one (O(1)) and $\mathrm{Pé}\geq 100$ follow.

Consider first an adiabatic flat plate, as shown in Fig. 1. The desired quantity is the value of the temperature of the adiabatic wall T_{aw}. Thus, the boundary conditions of the thermal problem are

$$T(x=0)=T_\infty$$

$$\left.\frac{\partial T}{\partial y}\right|_{y=0}=0 \tag{11}$$

$$T(y\to\infty)=T_\infty$$

Define the following similarity variables as

$$\eta=y\sqrt{\frac{U_\infty}{\nu x}}$$

$$\psi(x,y)=f(\eta)\sqrt{U_\infty \nu x} \tag{12}$$

$$\Theta=\frac{(T-T_\infty)}{\left(\frac{U_\infty^2}{2c_p}\right)}$$

Equation (10) is therefore transformed into Eq. (13)

$$\Theta''+\frac{\mathrm{Pr}}{2}f\Theta'+2\mathrm{Pr}(f'')^2=0 \tag{13}$$

with the transformed boundary conditions of

$$\Theta'(\eta=0)=0$$

$$\Theta(\eta\to\infty)=0 \tag{14}$$

In order to analytically solve Eq. (13) with Eq. (14), let $\zeta=\Theta'$ reduce the order of Eq. (13) by one to give

$$\zeta'=-\frac{\mathrm{Pr}}{2}f\zeta-2\mathrm{Pr}(f'')^2 \tag{15}$$

which is a *first order linear ordinary differential equation with variable coefficients* of the type

$$y'(x)=a(x)y(x)+b(x) \tag{16}$$

To solve this equation, assume a solution in the form of

$$y(x)=u(x)v(x) \tag{17}$$

Then, Eq. (16) becomes

$$u'v+v'u=auv+b \tag{18}$$

or $(u'-au)v+v'u=b$, giving $(u'-au)=0$ and resulting in $(u'/u)=a$, which integrates to $\ln u=\int a dx+C_1''$ and gives

$$u=C_1'\exp\left[\int a dx\right]=C_1'\exp\left[-\frac{\mathrm{Pr}}{2}\int_0^\eta f d\xi\right] \tag{19}$$

Also

$$\left(\frac{dv}{dx}\right)u=b$$

which gives

$$v=\int\frac{b(x)}{C_1'\exp\left[-\frac{\mathrm{Pr}}{2}\int_0^\eta f d\xi\right]}dx+C_2'$$

and simplifies to

$$v=\frac{1}{C_1'}\int_0^\eta\exp\left[\frac{\mathrm{Pr}}{2}\int_0^\beta f d\xi\right]\{-2\mathrm{Pr}(f'')^2\}d\beta+C_2' \tag{20}$$

Therefore, since $\zeta=d\Theta/d\eta=y=uv$, then

$$\frac{d\Theta}{d\eta}=\exp\left[\frac{\mathrm{Pr}}{2}\int_0^\beta f d\xi\right]\left\{\int_0^\eta\exp\left[\frac{\mathrm{Pr}}{2}\int_0^\beta f d\xi\right][-2\mathrm{Pr}(f'')^2]d\beta+C_2'\right\} \tag{21}$$

However, the transformed conservation of momentum equation for no body or pressure forces is [2]

$$2f'''+ff''=0 \tag{22}$$

The numerical solution for Eq. (22) is given in Table 1 including the value of the normal velocity component to verify that it is always an order of magnitude smaller than the component in the flow direction, a fundamental assumption in the order of magnitude analysis, and remembering that $\mathrm{Re}_L\geq 100$ as was mentioned before. This, therefore, is different than the one in Ref. [2]. Therefore, it is important to include this column in Table 1. Therefore, using Eq. (22)

$$\int f d\eta=-2\int\frac{\left(\frac{d^3 f}{d\eta^3}\right)}{\left(\frac{d^2 f}{d\eta^2}\right)}d\eta \tag{23}$$

which simplifies to $\int f d\eta=-2\ln(d^2 f/d\eta^2)=-2\ln(f'')$. Upon substitution into Eq. (21) gives

$$\frac{d\Theta}{d\eta}=(f'')^{\mathrm{Pr}}\left[C_2-2\mathrm{Pr}\int_0^\eta(f'')^{2-\mathrm{Pr}}d\xi\right] \tag{24}$$

Using the boundary condition at $\eta=0$ in Eq. (14), $C_2=0$. This gives $d\Theta/d\eta=[-2\mathrm{Pr}(f'')^{\mathrm{Pr}}\int_0^\eta(f'')^{2-\mathrm{Pr}}d\xi]$, which, upon integration, becomes $\Theta=-2\mathrm{Pr}\int_0^\eta(f'')^{\mathrm{Pr}}[\int_0^\beta(f'')^{2-\mathrm{Pr}}d\xi]d\beta+C_3$. Using Eq. (14) again as $\eta\to\infty$, then C_3 can be evaluated as $C_3=2\mathrm{Pr}\int_0^\infty(f'')^{\mathrm{Pr}}[\int_0^\beta(f'')^{2-\mathrm{Pr}}d\xi]d\beta$, which gives

$$\Theta=2\mathrm{Pr}\left[\int_0^\infty(f'')^{\mathrm{Pr}}\left\{\int_0^\beta(f'')^{2-\mathrm{Pr}}d\xi\right\}d\beta-\int_0^\eta(f'')^{\mathrm{Pr}}\left\{\int_0^\beta(f'')^{2-\mathrm{Pr}}d\xi\right\}d\beta\right] \tag{25}$$

or, in a simplified form, becomes

Table 1 Values for the solution of $2f'''+ff''=0$

$\eta = y\sqrt{\frac{U_\infty}{\nu x}}$	f	$f' = \frac{u}{U_\infty}$	f''	$\frac{1}{2}(\eta f' - f) = \frac{v}{U_\infty}\sqrt{\mathrm{Re}_x}$
0	0	0	0.33206	0
0.2	0.00664	0.06641	0.33199	0.00332
0.4	0.02656	0.13277	0.33147	0.01327
0.6	0.05974	0.19894	0.33008	0.02981
0.8	0.10611	0.26471	0.32739	0.05283
1.0	0.16557	0.32979	0.32301	0.08211
1.2	0.23795	0.39378	0.31659	0.11729
1.4	0.32298	0.45627	0.30787	0.15790
1.6	0.42032	0.51676	0.29667	0.20325
1.8	0.52952	0.57477	0.28293	0.25253
2.0	0.65003	0.62977	0.26675	0.30476
2.2	0.78120	0.68132	0.24835	0.35885
2.4	0.92230	0.72899	0.22809	0.41364
2.6	1.07252	0.77246	0.20646	0.46794
2.8	1.23099	0.81152	0.18401	0.52063
3.0	1.39682	0.84605	0.16136	0.57067
3.2	1.56911	0.87609	0.13913	0.61719
3.4	1.74696	0.90177	0.11788	0.65953
3.6	1.92954	0.92333	0.09809	0.69722
3.8	2.11605	0.94112	0.08013	0.73010
4.0	2.30576	0.95552	0.06424	0.75816
4.2	2.49806	0.96696	0.05052	0.78159
4.4	2.69238	0.97587	0.03897	0.80072
4.6	2.88826	0.98269	0.02948	0.81606
4.8	3.08534	0.98779	0.02187	0.82803
4.91755		**0.99000**		**0.83384**
5.0	3.28329	0.99155	0.01591	0.83723
5.2	3.48189	0.99425	0.01134	0.84410
5.4	3.68094	0.99616	0.00793	0.84916
5.6	3.88031	0.99748	0.00543	0.85279
5.8	4.07990	0.99838	0.00365	0.85535
6.0	4.27964	0.99898	0.00240	0.85712
6.2	4.47948	0.99937	0.00155	0.85831
6.4	4.67938	0.99961	0.00098	0.85906
6.6	4.87931	0.99977	0.00061	0.85959
6.8	5.07928	0.99987	0.00037	0.85992
7.0	5.27926	0.99992	0.00022	0.86009
7.2	5.47925	0.99996	0.00013	0.86023
7.4	5.67924	0.99998	0.00007	0.86031
7.6	5.87924	0.99999	0.00004	0.86034
7.8	6.07923	1.00000	0.00002	0.86039
8.0	6.27923	1.00000	0.00001	0.86039
8.2	6.47923	1.00000	0.00001	0.86039
8.4	6.67923	1.00000	0.00000	0.86039
8.6	8.87923	1.00000	0.00000	0.86039
8.8	7.07923	1.00000	0.00000	**0.86039**

$$\Theta = 2\mathrm{Pr}\int_\eta^\infty (f'')^{\mathrm{Pr}}\left[\int_0^\beta (f'')^{2-\mathrm{Pr}}d\xi\right]d\beta \tag{26}$$

For $\eta=0$, the similarity transform of an adiabatic wall becomes $\Theta(0)=(T_{\mathrm{aw}}-T_\infty)/(U_\infty^2/2c_p)$. Evaluating Eq. (26) at $\eta=0$, which is on the adiabatic wall surface, the result becomes

$$\Theta(0) = 2\mathrm{Pr}\int_0^\infty (f'')^{\mathrm{Pr}}\left[\int_0^\beta (f'')^{2-\mathrm{Pr}}d\xi\right]d\beta \tag{27}$$

which is called the *recovery factor* R_{aw} of the adiabatic wall. Thus, the temperature of the adiabatic wall becomes,

$$T_{\mathrm{aw}} = T_\infty + R_{\mathrm{aw}}\left(\frac{U_\infty^2}{2c_p}\right) \tag{28}$$

For $0.6<\mathrm{Pr}<15$, $\Theta(0)$ may be approximated by

$$\Theta(0) = R_{\mathrm{aw}} = \sqrt{\mathrm{Pr}} \tag{29}$$

or calculated exactly from Eq. (27) for a known free stream function f. From the steady flow energy equation of an ideal gas

$$T_{\mathrm{stagnation}} = T_\infty + \frac{U_\infty^2}{2c_p} \tag{30}$$

if $U_{\mathrm{stagnation}}=0$. Therefore, R_{aw} is a measure of how close the wall temperature is to the stagnation temperature. Thus, for

$$\begin{aligned} &\mathrm{Pr}<1, \quad T_{\mathrm{aw}} < T_{\mathrm{stagnation}} \\ &\mathrm{Pr}=1, \quad T_{\mathrm{aw}} = T_{\mathrm{stagnation}} \\ &\mathrm{Pr}>1, \quad T_{\mathrm{aw}} > T_{\mathrm{stagnation}} \end{aligned} \tag{31}$$

The usual definition for the convective heat transfer coefficient is $h=q/A(T_w-T_\infty)$. However, in this case, $q_w=0$ while $(T_{\mathrm{aw}}-T_\infty)\neq 0$, which implies that the usual definition of the convective heat transfer coefficient does not hold when frictional heating is present. Therefore, a new definition is necessary. For this consider the case of the heated or cooled plate at a uniform temperature T_W. For the case of no frictional heating, $\theta=(T-T_\infty)/(T_w-T_\infty)$. Solving for the temperature, $T=T_\infty+\theta(\eta)(T_w-T_\infty)$. A general solution for T may be written as $T=T_\infty+C(T_w-T_\infty)\theta(\eta)$. Letting

$$\Theta = \left(\frac{T-T_\infty}{T_{\mathrm{stagnation}}-T_\infty}\right) = \frac{(T-T_\infty)}{\left(\frac{U_\infty^2}{2c_p}\right)} \tag{32}$$

for an adiabatic plate, there is a *particular solution* of the form $T=T_\infty+(T_{\mathrm{stagnation}}-T_\infty)\Theta(\eta)$, which gives the complete solution as

$$T = T_\infty + C(T_w-T_\infty)\theta(\eta) + \frac{U_\infty^2}{2c_p}\Theta(\eta) \tag{33}$$

with the appropriate conditions as

$$\begin{aligned} &\eta=0, \quad \theta=1, \quad \Theta = R_{\mathrm{aw}} \\ &\eta\to\infty, \quad \theta\to 0, \quad \Theta\to 0 \end{aligned} \tag{34}$$

Thus, at $\eta=0$, the surface of the wall

$$T_w = T_\infty + C(T_w-T_\infty) + \left(\frac{U_\infty^2}{2c_p}\right)R_{\mathrm{aw}} \tag{35}$$

or using Eq. (28), $C(T_w-T_\infty)=(T_w-T_\infty)-(T_{\mathrm{aw}}-T_\infty)=(T_w-T_{\mathrm{aw}})$. Thus, the general solution becomes

$$(T-T_\infty) = (T_w-T_{\mathrm{aw}})\theta(\eta) + \left(\frac{U_\infty^2}{2c_p}\right)\Theta(\eta) \tag{36}$$

The heat transfer is given by

$$q = -kA\left(\frac{\partial T}{\partial y}\right)_{y=0} = -kA\sqrt{\frac{U_\infty}{\nu x}}\left(\frac{\partial T}{\partial \eta}\right)_{\eta=0} = -kA\sqrt{\frac{U_\infty}{\nu x}}(T_w - T_{\mathrm{aw}})\theta'(0) \tag{37}$$

since $\Theta'(0)=0$ from Eq. (25). Defining the convective heat transfer coefficient for this problem as

$$h = \frac{q}{A(T_w-T_{\mathrm{aw}})} \tag{38}$$

then the Nusselt number becomes

$$\frac{\mathrm{Nu}_x}{\sqrt{\mathrm{Re}_x}} = -\theta'(0) \tag{39}$$

which is the same result as obtained in the case of heat transfer with no friction [1]. Thus, the solution for no frictional heating applies to the frictional heating problem by replacing T_∞ by T_{aw} in the definition of the convective heat transfer coefficient.

The magnitude of $[(T_w - T_\infty)/(T_w - T_{aw})]$ predicts the importance of frictional heating. This is due to the fact that $(T_w - T_{aw}) = T_w - (T_\infty + U_\infty^2/2c_pR_{aw})$. Simplified, this is expressed as

$$\left(\frac{T_w - T_\infty}{T_w - T_{aw}}\right) = \frac{2}{2 - \mathrm{Ec}\, R_{aw}} \tag{40}$$

If $\mathrm{Ec} \ll O(1)$, then $(T_w - T_\infty / T_w - T_{aw}) = 1$ giving $(T_{aw} = T_\infty)$. If $\mathrm{Ec} = O(1)$, then $(T_w - T_\infty / T_w - T_{aw}) \lessgtr 0$ and must be considered. The heat flux is reduced for $\mathrm{Ec} > 0$ and increased for $\mathrm{Ec} < 0$.

In summary, for high speed flow across a flat plate, the ordinary external laminar and turbulent flow relations [14]

$$\mathrm{Nu}_x = 0.33206\sqrt{\mathrm{Re}_x}(\mathrm{Pr})^{1/3}$$
$$\mathrm{Nu}_x = 0.02914(\mathrm{Re}_x)^{4/5}(\mathrm{Pr})^{1/3} \tag{41}$$

apply provided the new definition of the convective heat transfer coefficient is used as given in Eq. (38). For turbulent flow [14]

$$R_{aw} = (\mathrm{Pr})^{1/3} \tag{42}$$

3 Conclusions

The problem of aerodynamic heat transfer is presented in a complete analytical form. The student can understand how this problem is solved and its correct and precise use in the design of systems. It is indeed very important that these details are followed carefully. The mathematical analysis is definitely not beyond the capabilities of students at the graduate level, for sure, and even at the undergraduate level. By not using analysis, we are depriving our students the opportunities of applying their mathematical skills that we so strongly emphasize but neglect to use in our courses. The importance of this problem, of course, cannot be underestimated as tragic events have resulted due to poor design or manufacture.

Acknowledgment

The views expressed herein are those of the authors and do not purport to reflect the position of the United States Military Academy, the Department of the Army, or the Department of Defense.

Nomenclature

A = area (m^2)
a = constant; an arbitrary function of x
b = constant; an arbitrary function of x
C = constant of integration
c = specific heat (kJ/kg K)
D = substantial or material derivative
e = specific energy (kJ/kg)
Ec = Eckert number, $U_\infty^2/(c_p[T_w - T_\infty])$
$\boldsymbol{F}$ = force vector (kN/kg)
f = freestream function
g = (m/s^2) gravitational acceleration
i = specific enthalpy (kJ/kg)
k = thermal conductivity (W/m K)
Nu = Nusselt number, $[(hx)/k]$
p = pressure (kPa)
Pé = Péclet number, $(\mathrm{Re})(\mathrm{Pr}) = [(U_\infty x)/\upsilon]$
Pr = Prandtl number, $[\upsilon/\alpha]$
q = heat transfer rate (W)
R = recovery factor
Re = Reynolds number, $[(U_\infty x)/\upsilon]$
T = temperature (K)
t = time (s)
U = velocity (m/s)
u = x-direction velocity; an arbitrary function of x (m/s)
v = y-direction velocity; an arbitrary function of x (m/s)
w = z-direction velocity (m/s)
$\boldsymbol{V}$ = velocity vector (m/s)
x = Cartesian axis direction (m)
y = Cartesian axis direction (m)
z = Cartesian axis direction (m)

Special Characters

α = thermal diffusivity (m^2/s)
β = integration coordinate
Φ = viscous dissipation function (W/m^3)
η = similarity coordinate
μ = dynamic viscosity ($N\,s/m^2$)
ρ = density (kg/m^3)
θ = dimensionless temperature for no frictional heating
Θ = dimensionless temperature for frictional heating
υ = kinematic viscosity (m^2/s)
Φ = viscous dissipation ($N/s\,m^2$)
ξ = integration coordinate
Ψ = similarity freestream function (m^2/s)
ζ = derivative of the dimensionless temperature, $[\Theta']$

Subscripts and Superscripts

aw = adiabatic wall
b = body
L = based on the length
p = pressure (kPa)
w = wall
∞ = freestream
$'$ = first derivative (1/m)
$''$ = second derivative ($1/m^2$)

References

[1] Eckert, E. R. G., 1956, "Engineering Relations for Heat Transfer and Friction in High-Velocity Laminar and Turbulent Boundary Layer Flow Over Surfaces With Constant Pressure and Temperature," Trans. ASME, **78**, pp. 1273–1284.
[2] Schlichting, H., 1968, *Boundary Layer Theory*, 6th ed., McGraw-Hill, New York.
[3] Cebeci, T., 2002, *Convective Heat Transfer*, Springer, Berlin.
[4] Kays, W. M., and Crawford, M. E., 1993, *Convective Heat and Mass Transfer*, McGraw-Hill, New York.
[5] Oosthuizen, P. H., and Naylor, D., 1999, *Introduction to Convective Heat Transfer Analysis*, WCB/McGraw-Hill, New York.
[6] Blausius, H., 1906, "Grenzschichten in Flüssigkeiten mit Kleiner Reibung," Z. Angew. Math. Phys., **56**(1), pp. 1–37.
[7] Prandtl, L., 1910, "Eine Beziehung zwischen Wärmeaustausch und Strömungswiederstand der Flüssigkeiten," Phys. Unserer Zeit, **10**, pp. 1072–1078.
[8] Pohlhausen, E., 1921, "Der Wärmeaustausch zwishen festen Körpern und Flüssigkeiten mit kleiner Reibung und kleiner Wärmeleitung," Z. Angew. Math. Mech., **1**, pp. 115–121.
[9] von Karman, T., 1921, "Über Laminare und Turbulente Reibung," Z. Angew. Math. Mech., **1**, pp. 233–252.
[10] van Driest, E. R., 1951, "Turbulent Boundary Layer in Compressible Fluids," J. Aeronaut. Sci., **18**(3), pp. 145–161.
[11] Kaye, J., 1954, "Survey of Friction Coefficients, Recovery Factors, and Heat-Transfer Coefficients for Supersonic Flow," J. Aeronaut. Sci., **21**(2), pp. 117–129.
[12] Hayes, W. D., and Probstein, R. F., 1959, *Hypersonic Flow Theory*, Academic, New York.
[13] White, F., 1991, *Viscous Fluid Flow*, McGraw-Hill, New York.
[14] Mills, A. F., 1999, *Basic Heat and Mass Transfer*, Prentice-Hall, Upper Saddle River, NJ.
[15] Kreith, F., and Bohn, M. S., 2001, *Principles of Heat Transfer*, Brooks/Cole, Pacific Grove, CA.

On the Condition for Thermal Rectification Using Bulk Materials

David B. Go[1]
Assistant Professor
Mem. ASME
Department of Aerospace and Mechanical Engineering,
University of Notre Dame,
Notre Dame, IN 46556
e-mail: dgo@nd.edu

Mihir Sen
Professor
Fellow ASME
Department of Aerospace and Mechanical Engineering,
University of Notre Dame,
Notre Dame, IN 46556
e-mail: msen@nd.edu

In conduction, thermal rectification occurs when a material or structure transfers heat asymmetrically. In this work, it is shown that, in the bulk, a necessary condition for thermal rectification is that the thermal conductivity of the material or structure be a function of both space and temperature, and that this function be nonseparable. Practically, this can be achieved using a composite structure consisting of many materials although it could also be achieved with a properly developed single material.
[DOI: 10.1115/1.4002286]

Keywords: rectification, conduction, composite material, analytical

1 Introduction

Thermal rectification is a topic that has begun to receive significant attention in the past decade in both the applied physics and heat transfer communities. It can be broadly defined as a material or structure that transfers heat asymmetrically. That is, for a given temperature difference the heat rate in one direction through the material/structure is not the same as the heat rate when the temperature difference is reversed. More simply, a thermal rectifier can be said to be directional, in that relatively speaking it acts as a heat conductor in one direction and an insulator in the opposite direction. Rectification-like effects are possible in all three of the major heat transfer modes, convection, radiation, and conduction. Although much of the recent focus has been on nanoscale conduction phenomena (e.g., Ref. [1]), it has been recently noted by Peyrard [2] and Dames [3] that it is not necessary to develop exotic nanomaterials to obtain a rectifying effect—it is in fact possible using bulk materials. There has been a considerable amount of work on heat conduction rectification over the past 60–70 years and for a summary of the literature, readers are directed to Dames [3] and the references therein. This work deals only with conduction rectification in the bulk and, in particular, examines the mathematical condition required for rectification to occur.

The recent publications by Peyrard [2] and Dames [3] discussed conduction rectification in the bulk based on solving the heat equation in one dimension, both expanding on earlier bulk analyses by others such as Hoff [4–6]. Peyrard [2] discussed the general case of a material where the thermal conductivity is a function of both location and temperature $k(x,T)$. He proposes that there is a general solution to the heat equation for any thermal conductivity that can be solved numerically and he chooses an artificial form of $k(x,T)$ that is an elaborate function of hyperbolic cosines to demonstrate this. He also suggests rectification can be achieved through a composite material where at least one of them has a temperature-dependent thermal conductivity. In another paper, Dames [3] considered in more detail a two-material composite with $k_j(T)$, and determined a generalized, analytical form for the limit of low rectification when the composite materials both have power-law thermal conductivities.

Although specific examples have been given, necessary and sufficient conditions for the existence of rectification or no rectification have not been discussed in literature. This technical brief expands on the concept of thermal rectification in the bulk, and discusses some of the mathematical bases for thermal rectification across a single material as well as a composite structure. In particular, from a mathematical perspective, the condition on the thermal conductivity necessary to obtain rectification is investigated.

Consider the basic, one-dimensional structure with thermal conductivity of $k(x,T)$ shown in Fig. 1. The system extends from $x=L_1$ to $x=L_2$ with temperatures at each boundary of T_1 and T_2, respectively. Therefore, for there to be rectification, the magnitude of the heat rate when $T_1=T_{\text{hot}}$ and $T_2=T_{\text{cold}}$ must not be equal to that when $T_1=T_{\text{cold}}$ and $T_2=T_{\text{hot}}$. For convenience, the heat rate when $T_1>T_2$ will be called the forward heat rate q^+ and that when $T_1<T_2$ will be called the reverse heat rate q^-. The rectification factor R can be defined simply as the ratio of the magnitude of the larger rate to that of the smaller one, so that

$$R=\begin{cases}\left|\dfrac{q^+}{q^-}\right| & \text{if } |q^+|>|q^-| \\ 1 & \text{if } |q^+|=|q^-| \\ \left|\dfrac{q^-}{q^+}\right| & \text{if } |q^-|>|q^+|\end{cases} \tag{1}$$

If $R=1$, then there is no rectification and if $R>1$ then there is. (N.B. There are other ways to define a rectification factor, such as a percentage difference rather than a simple ratio [3], but the definition is inconsequential to the physical phenomenon.)

2 Conditions for No Rectification

The steady state with no heat generation, one-dimensional governing equation for the temperature distribution $T(x)$ across the material is

$$\frac{d}{dx}\left(k(x,T)\frac{dT}{dx}\right)=0 \tag{2}$$

and this can be directly integrated to give

$$k(x,T)\frac{dT}{dx}=-q \tag{3}$$

Mathematically speaking, $-q$ is an integration constant that is determined through the boundary conditions but it is known from Fourier's law that q is the heat flux. Two boundary conditions are needed to solve the first-order differential equation and also determine q. Equation (3) is integrable only if it is exact or if it can be multiplied by an integrating factor to make it exact.

Consider the case where the thermal conductivity is separable, then $k(x,T)$ can be written as the product of two independent functions of the variables x and T, i.e.,

[1]Corresponding author.

Contributed by the Heat Transfer Division of ASME for publication in the JOURNAL OF HEAT TRANSFER. Manuscript received January 18, 2010; final manuscript received July 14, 2010; published online September 20, 2010. Assoc Editor: Pamela M. Norris.

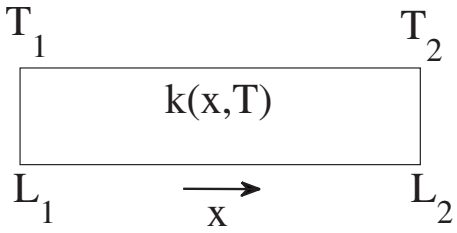

Fig. 1 Schematic of one-dimensional system

$$k(x,T) = f(x)\lambda(T) \tag{4}$$

Integration of Eq. (3) gives

$$\int_{T_1}^{T_2} \lambda(T)dT = -q\int_{L_1}^{L_2} \frac{dx}{f(x)} \tag{5}$$

and this can be rewritten to give the heat rate as

$$q = -\frac{\displaystyle\int_{T_1}^{T_2} \lambda(T)dT}{\displaystyle\int_{L_1}^{L_2} \frac{dx}{f(x)}} \tag{6}$$

When considering rectification, the only difference between q^+ and q^- is that the limits in the integral of $\lambda(T)$ are reversed. Since this changes only the sign but not the magnitude of the integral, it can easily be observed that reversing the boundary temperatures results in $q^+ = -q^-$ and $R=1$; that is, there is no rectification. *Therefore, it can be concluded that separable thermal conductivity is a sufficient condition for no thermal rectification*. That is, if the thermal conductivity $k(x,T)$ is separable, there is no rectification. There are three special cases of separable thermal conductivity that will not be considered separately; $k(x,t)$ is separable if (i) $k(x,T)=$constant, (ii) $k(x,T)=k(x)$, or (iii) $k(x,T)=k(T)$.

However, it cannot be stated that the converse is true—that is, if there is no rectification, the thermal conductivity must be separable. In other words, separability is a sufficient condition for no rectification but not a necessary condition. A necessary condition for no rectification may not exist.

3 Conditions for Rectification

Of greater interest, however, is when thermal rectification does occur. The result of Sec. 2 can be interpreted to mean that *a necessary condition for thermal rectification is that the thermal conductivity of the material be nonseparable*. However, since there is no "if and only if" condition for no rectification, there is no condition either for which rectification is guaranteed. If the thermal conductivity is nonseparable, it is possible that rectification exists. Peyrard [2] demonstrated this by conceiving an arbitrary, nonseparable function for the thermal conductivity and solving Eq. (2) numerically in order to demonstrate rectification although it can easily be demonstrated analytically using simpler $k(x,T)$ functions.

It may be possible to create a material with nonseparable $k(x,T)$, such as an alloy with a nonuniform distribution of one material in the other. However, since homogeneous materials have thermal conductivities that are only a function of temperature, achieving nonseparability can be accomplished simply through composite structures using two or more dissimilar but homogeneous materials where at least one of the thermal conductivities is a function of temperature. When two or more homogeneous materials are conjoined, the thermal conductivity of the composite structure is potentially nonseparable, even if the thermal conductivities of the individual materials *are*. Thus it is possible that a composite wall that is made up of a series of different homogeneous materials with temperature-dependent thermal conductivity provide thermal rectification, as pointed out by both Peyrard [2] and Dames [3]. The mathematics of this case will be considered further below.

3.1 Composite Walls of Homogeneous Materials. Consider a generic composite structure consisting of n materials, each with separable thermal conductivity $k_j(x,T)=f_j(x)\lambda_j(T)$, for $j=1,2,\ldots,n$. The total thermal conductivity of the composite structure depending, therefore, on both x and T, can equivalently be written as

$$k(x,T) = \begin{cases} k_1(x,T) & \text{if } L_1 \le x < \tilde{L}_1 \\ k_2(x,T) & \text{if } \tilde{L}_1 \le x < \tilde{L}_2 \\ \vdots & \\ k_j(x,T) & \text{if } \tilde{L}_{n-1} \le x \le L_2 \end{cases} \tag{7}$$

where $\tilde{L}_1, \tilde{L}_2, \ldots, \tilde{L}_{n-1}$ indicate the locations of the $n-1$ interfaces. The solution for the heat rate is

$$q = -\frac{\displaystyle\int_{T_1}^{\tilde{T}_1} \lambda_1(T)dT}{\displaystyle\int_{L_1}^{\tilde{L}_1} \frac{dx}{f_1(x)}} = -\frac{\displaystyle\int_{\tilde{T}_1}^{\tilde{T}_2} \lambda_2(T)dT}{\displaystyle\int_{\tilde{L}_1}^{\tilde{L}_2} \frac{dx}{f_2(x)}} = \cdots = -\frac{\displaystyle\int_{\tilde{T}_{n-1}}^{T_2} \lambda_n(T)dT}{\displaystyle\int_{\tilde{L}_{n-1}}^{L_2} \frac{dx}{f_n(x)}} \tag{8}$$

where $\tilde{T}_1, \tilde{T}_2, \ldots, \tilde{T}_{n-1}$ are the interface temperatures. By reversing the temperatures at the extreme boundaries (T_1 and T_2), the temperature profile in each material may change, and thus the interface temperatures $\tilde{T}_j$ may change. Therefore, depending on the specific temperature-dependent functions of each material, the integrals may not be equal and opposite when the boundaries are switched, as implied by Eq. (6), leading to rectification.

Consider more closely the case of a two-material composite (materials A and B) with thermal conductivities $k_A(x,T)=f_A(x)\lambda_A(T)$ and $k_B(x,T)=f_B(x)\lambda_B(T)$ and an interface $\tilde{L}$ between L_1 and L_2. From Eq. (3), the temperature distribution for material A is given by

$$\Lambda_A(T) = -q[F_A(x) - F_A(L_1)] + \Lambda_A(T_1) \tag{9}$$

where T_1 is the boundary temperature at L_1 and the antiderivatives are defined as

$$\Lambda_A(T) = \int \lambda_A(T)dT \tag{10a}$$

$$F_A(x) = \int \frac{dx}{f_A(x)} \tag{10b}$$

A similar relation exists for material B. The interface temperature $\tilde{T}$ must be the same for both materials, leading to

$$\Lambda_A(\tilde{T}) = -q[F_A(\tilde{L}) - F_A(L_1)] + \Lambda_A(T_1) \tag{11a}$$

$$\Lambda_B(\tilde{T}) = -q[F_B(\tilde{L}) - F_B(L_2)] + \Lambda_B(T_2) \tag{11b}$$

Equations (11a) and (11b) can be solved for $\tilde{T}$ and the heat flux q. In the case where $\Lambda_A(\tilde{T})=\Lambda_B(\tilde{T})$, the equation for q simplifies to be a linear function of $\Lambda_A(T_1)-\Lambda_B(T_2)$. Defining $\tilde{T}^+$ and $\tilde{T}^-$ as the interface temperatures for the forward and reverse boundary conditions, consider the following conditions:

$$\begin{cases} \Lambda_A(\tilde{T}^+) = \Lambda_B(\tilde{T}^+) \\ \Lambda_A(\tilde{T}^-) = \Lambda_B(\tilde{T}^-) \\ |\Lambda_A(T_{\text{hot}}) - \Lambda_B(T_{\text{cold}})| = |\Lambda_A(T_{\text{cold}}) - \Lambda_B(T_{\text{hot}})| \end{cases} \tag{12}$$

If the functions $\Lambda_A(T)$ and $\Lambda_B(T)$ (or more importantly $\lambda_A(T)$ and $\lambda_B(T)$) are chosen to satisfy these conditions, then $R=1$ always. If $\Lambda_A(T)$ and $\Lambda_B(T)$ do not satisfy this condition, then the overall thermal conductivity is nonseparable and rectification may be possible.

3.2 The Role of Discontinuities. A composite structure inherently creates discontinuities in material properties and a temperature profile that can be described by separate functions across each material, and these can affect the overall thermal conductivity. Consider when $\lambda_A(T)=\lambda_B(T)=\lambda(T)$ but

$$f(x) = \begin{cases} f_A(x) & \text{if } L_1 \le x < \tilde{L} \\ f_B(x) & \text{if } \tilde{L} \le x < L_2 \end{cases} \tag{13}$$

That is, the thermal conductivity of both materials have the same temperature dependence although different spatial dependencies. In this situation, the discontinuity in the function $k(x,T)$ occurs at $\tilde{L}$, and the overall thermal conductivity of the composite could be equivalently written as $k(x,T)=f(x)\lambda(T)$, and it is separable. This case satisfies condition Eq. (12), and the heat rate reduces to

$$q = \frac{\Lambda(T_1) - \Lambda(T_2)}{[F_A(\tilde{L}_i) - F_A(L_1)] - [F_B(\tilde{L}_i) - F_B(L_2)]} \tag{14}$$

Through inspection, it is clear that if T_1 and T_2 are reversed, the heat rate only changes sign but not magnitude and $R=1$. This is the expected result because the overall thermal conductivity is separable.

Now consider the analogous case where $f_A(x)=f_B(x)=f(x)$ and

$$\lambda(T) = \begin{cases} \lambda_A(T) & \text{if } T_1 \le T < \tilde{T} \\ \lambda_B(T) & \text{if } \tilde{T} \le T < T_2 \end{cases} \tag{15}$$

Here, the thermal conductivity of both materials have the same spatial dependence but different temperature dependencies and the discontinuity occurs at $\tilde{T}$. However, the discontinuity $\tilde{T}$ is not known a priori, because it depends on the temperature profile $T(x)$ that results from the boundary conditions at L_1 and L_2. In fact, if $\tilde{T}$ is specified a priori, then the structure may not satisfy conservation of energy without some external heat addition or loss. For this reason, this piecewise assembly of the thermal conductivities is nonseparable because there are no global functions of x and T that satisfy Eq. (4). One possibility, therefore, is that $\tilde{T}^+ \neq \tilde{T}^-$, which leads to $R \ge 1$. But if the functions and boundaries are chosen such that $\tilde{T}^+ = \tilde{T}^-$ in Eq. (15), then $k(x,T)$ is separable and $R=1$. This is in contrast to the previous case where the discontinuity value $\tilde{L}$ is known a priori such that the overall $k(x,T)$ is separable leading to $R=1$ always. In the following section, we consider both of these discontinuities in a two-material case to illustrate this point and demonstrate that nonseparable thermal conductivity leads to rectification.

3.3 Linear Temperature Dependence. Consider the case where the thermal conductivity varies linearly with temperature as described by

$$k(T) = \overline{k}\{1 + \alpha(T - T_0)\} \tag{16}$$

where T_0 is a reference temperature such that $k(T_0)=\overline{k}$, and α is a coefficient that can be positive or negative. Note that, since $k(T)$ must always be positive, the above expression is applicable only for a limited range of temperatures. Now consider when $\alpha_A=\alpha_B=\alpha$, which corresponds to $k_B=Ck_A$, where C is some constant. Here, $\lambda_A(T)=\lambda_B(T)=\lambda(T)=\overline{k}\{1+\alpha(T-T_0)\}$ and

$$f(x) = \begin{cases} 1 & \text{if } L_1 \le x < \tilde{L} \\ C & \text{if } \tilde{L} \le x < L_2 \end{cases} \tag{17}$$

The overall thermal conductivity can be written as $k(x,T)=f(x)\lambda(T)$ and is separable. In this instance, defining the temperature difference $\theta=T-T_0$, the heat rate is

$$q = \frac{C\overline{k}}{(\tilde{L} - L_2) - C(\tilde{L} - L_1)}\left[(\theta_1 - \theta_2) + \frac{1}{2}\alpha(\theta_1^2 - \theta_2^2)\right] \tag{18}$$

For any C and an appropriate temperature range guaranteeing positive thermal conductivity, $q^+=-q^-$ and $R=1$.

Now consider the analogous case when $f_A(x)=f_B(x)=f(x)=1$ and

$$\lambda(T) = \begin{cases} \overline{k}_A\{1 + \alpha_A(T - T_0)\} & \text{if } T_1 \le T < \tilde{T} \\ \overline{k}_B\{1 + \alpha_B(T - T_0)\} & \text{if } \tilde{T} \le T < T_2 \end{cases} \tag{19}$$

The solution for the heat rate is

$$\begin{aligned} q &= -\overline{k}_A\left[\frac{(\theta_1 - \tilde{\theta}) + \frac{1}{2}\alpha_A(\theta_1^2 - \tilde{\theta}^2)}{L_1 - \tilde{L}}\right] \\ &= -\overline{k}_B\left[\frac{(\tilde{\theta} - \theta_2) + \frac{1}{2}\alpha_B(\tilde{\theta}^2 - \theta_2^2)}{\tilde{L} - L_2}\right] \end{aligned} \tag{20}$$

where $\tilde{\theta}$ is at the interface. The interface temperature is given by the positive solution to the quadratic equation

$$\begin{aligned} \frac{1}{2}\tilde{\theta}^2\left[\frac{\overline{k}_A\alpha_A}{\tilde{L} - L_1} - \frac{\overline{k}_B\alpha_B}{\tilde{L} - L_2}\right] + \tilde{\theta}\left[\frac{\overline{k}_A}{\tilde{L} - L_1} - \frac{\overline{k}_B}{\tilde{L} - L_2}\right] - \left[\frac{\overline{k}_A}{\tilde{L} - L_1}\theta_1 + \frac{1}{2}\alpha_A\theta_1^2\right. \\ \left. - \frac{\overline{k}_B}{\tilde{L} - L_2}\theta_2 + \frac{1}{2}\alpha_B\theta_2^2\right] = 0 \end{aligned} \tag{21}$$

Note that, generally, $\tilde{\theta}^+ \neq \tilde{\theta}^-$ because the final term in this equation is dependent on both the boundary temperatures *and* the material at that boundary because of the terms $\frac{1}{2}\alpha_A\theta_1^2$ and $\frac{1}{2}\alpha_B\theta_2^2$. It becomes clear, therefore, that if the boundary conditions are reversed, then this term changes and so does $\tilde{\theta}$. Thus, the overall conductivity $k(x,T)$ is different when the boundary conditions are reversed, and hence it is nonseparable. Therefore, it is anticipated that $R>1$.

Although a closed-form solution for the rectification factor R can be found from Eqs. (20) and (21), its algebraic complexity is such that it is not useful for the purpose of ascertaining if rectification occurs. Therefore, three different arbitrarily chosen two-material composites were considered to demonstrate rectification and that R is as a function of T_2-T_1; this is shown in Fig. 2. In principle, R can be optimized based on the interface location, boundary temperatures, or parameters α and $\overline{k}$ in Eq. (18). Depending on the exact form of the thermal conductivities in the composite wall, there may be special cases of temperature difference or interface location that result in $R=1$.

4 Conclusions

The conditions for thermal rectification and no rectification to occur in bulk materials have been explored. It was shown that if the thermal conductivity of a single material is nonseparable in

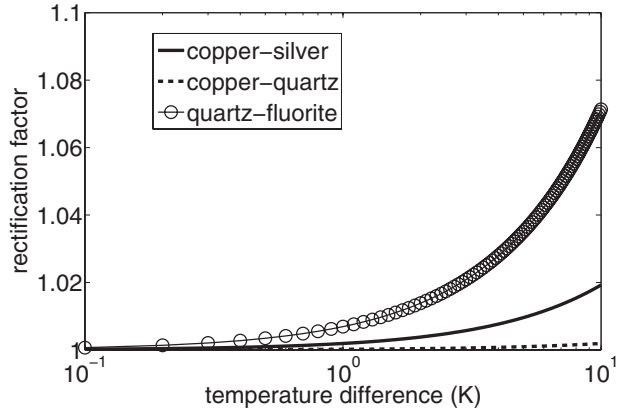

Fig. 2 Rectification as a function of the boundary temperature difference T_2-T_1 for three different two-material composites: metal-metal (copper-silver), metal-insulator (copper-quartz), and insulator-insulator (quartz-fluorite). The constants for each material (α and $\bar{k}$) were estimated from the CRC Handbook [7]) for 300–400 K. The interface was the midplane between the two materials, and the average temperature was held constant at 350 K.

distance and temperature, then rectification is possible. It was also shown that a composite material with different temperature-dependent thermal conductivities can inherently create an overall thermal conductivity that is nonseparable and this is the reason that rectification is possible in composite materials. However, although nonseparability is necessary for rectification, it is not sufficient because there may be special cases of thermal conductivity, boundary conditions, and geometry where rectification does not occur. There likely is no elegant sufficiency condition for rectification that applies universally.

In summary, the following four statements can be made regarding the conditions for existence of rectification in bulk materials:

If $k(x,T)$ is separable, rectification is not possible.

If $k(x,T)$ is nonseparable, rectification may be possible but is not guaranteed.

If there is no rectification, k may either be separable or nonseparable.

If there is rectification, k cannot be separable.

Nomenclature

C = proportionality constant
$f(x)$ = spatially dependent thermal conductivity function
$F(x)$ = integral of one over the spatially dependent thermal conductivity function
k = thermal conductivity
L = length
q = heat rate
R = rectification factor
T = temperature
x = one-dimensional coordinate
α = temperature-dependent thermal conductivity coefficient
θ = temperature difference relative to the reference temperature T_0
$\lambda(T)$ = temperature-dependent thermal conductivity function
$\Lambda(T)$ = integral of temperature-dependent thermal conductivity function

References

[1] Chang, C., 2006, "Solid-State Thermal Rectifier," Science, **314**(5802), pp. 1121–1124.
[2] Peyrard, M., 2006, "The Design of a Thermal Rectifier," Europhys. Lett., **76**, pp. 1–7.
[3] Dames, C., 2009, "Solid-State Thermal Rectification With Existing Bulk Materials," ASME J. Heat Transfer, **131**, p. 061301.
[4] Hoff, H., 1985, "Asymmetrical Heat Conduction in Inhomogeneous Materials," Physica A, **131**, pp. 449–464.
[5] Hoff, H., 1988, "Nonlinear coupling of Steady State Transport Processes. I. Description of the Global Properties," J. Chem. Phys., **88**(1), pp. 371–374.
[6] Hoff, H., 1988, "Nonlinear Coupling of Steady State Transport Processes. II. Determination of Certain Global Properties," J. Chem. Phys., **88**(1), pp. 375–379.
[7] Weast, R. C., ed., 1987, *CRC Handbook of Chemistry and Physics*, 68th ed., CRC, Boca Raton, FL.

Erratum: "A Novel Approach to Low Profile Heat Sink Design" [Journal of Heat Transfer, 2010, 132(9), p. 091401]

J. Stafford, E. Walsh, V. Egan, P. Walsh, and Y. S. Muzychka

The error within this paper is in Eq. (1). The exponent on the square bracket term is given as 1/3 when it should be 1/m. The correct form of Eq. (1) is shown below including the text preceding and following the equation.

For a rectangular duct and an isothermal boundary condition, the dimensionless heat transfer is defined as [11]

$$\mathrm{Nu}_{\sqrt{A}} = \left[\left(\frac{2f(\mathrm{Pr})}{\sqrt{L^*_{\sqrt{A}}}} \right)^m + \left(\left\{ 0.6135 \left(\frac{f\,\mathrm{Re}_{\sqrt{A}}}{L^*_{\sqrt{A}}} \right)^{1/3} \right\}^5 + \left\{ 3.24 \left(\frac{f\,\mathrm{Re}_{\sqrt{A}}}{8\sqrt{\pi}\in^{1/10}} \right) \right\}^5 \right)^{m/5} \right]^{1/m}$$

where $f(\mathrm{Pr})$, $f\,\mathrm{Re}_{\sqrt{A}}$, $L^*_{\sqrt{A}}$, and m are defined in Ref. [11]. The duct aspect ratio $\in$ is b/a.

References

[11] Muzychka, Y. S., and Yovanovich, M. M., 2004, "Laminar Forced Convection Heat Transfer in the Combined Entry Region of Non-Circular Ducts," ASME J. Heat Transfer, **126**, pp. 54–61.

